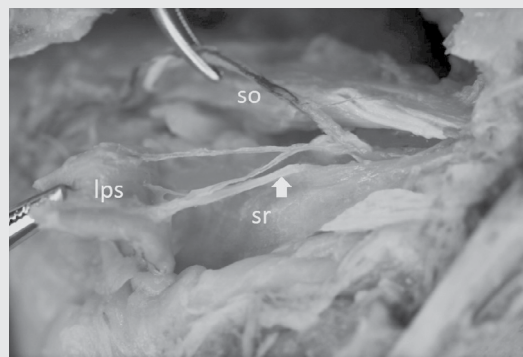


*POLISH ANATOMICAL SOCIETY*

# FOLIA MORPHOLOGICA



*Vol. 80      2021      No. 1*



# FOLIA MORPHOLOGICA

An international multidisciplinary journal devoted to fundamental research in the morphological sciences  
**Official Journal of the Polish Anatomical Society**  
(a Constituent Member of European Federation for Experimental Morphology — EFEM)

**EDITOR-IN-CHIEF**

**Janusz Moryś**

Department of Anatomy and Neurobiology  
Medical University of Gdańsk

**[https://journals.viamedica.pl/folia\\_morphologica](https://journals.viamedica.pl/folia_morphologica)**

*See our website for information on manuscript status, aims and scope,  
instructions for authors as well as editorial board.*

## **Folia Morphologica**

Publishing, Subscription and Advertising Office:

**VM Media sp. z o.o. VM Group sp.k., Grupa Via Medica**

ul. Świątokrzyska 73, 80–180 Gdańsk, Poland  
tel. (+48 58) 320 94 94, fax (+48 58) 320 94 60

Managing editor

Joanna Niezgodą

e-mail: [joanna.niezgoda@viamedica.pl](mailto:joanna.niezgoda@viamedica.pl)

Cover designer

Sylwia Scisłowska

The journal is published at: [www.fm.viamedica.pl](http://www.fm.viamedica.pl) in one volume per year consisting of four numbers. **Subscription rates:** Paper subscription, 4 issues incl. package and postage institutional — 140 euro. The above prices are inclusive of regular postage costs. Payment should be made to: VM Media sp. z o.o. VM Group sp.k., Grupa Via Medica, Bank BGŻ Paribas SA account number: 15 1600 1303 0004 1007 1035 9021; SWIFT: PPABPLPK. Single issues, subscriptions orders and requests for sample copies should be send to e-mail: [prenumerata@viamedica.pl](mailto:prenumerata@viamedica.pl). Electronic orders option available at: [https://journals.viamedica.pl/folia\\_morphologica](https://journals.viamedica.pl/folia_morphologica). The publisher must be notified of a cancellation of access to electronic version not later than two months before the end of a calendar year. After that date electronic access will be automatically prolonged for another year.

**Advertising.** For details on media opportunities within this electronic version of journal please contact the advertising sales department, ul. Świątokrzyska 73, 80–180 Gdańsk, Poland, tel: (+48 58) 320 94 94, e-mail: [viamedica@viamedica.pl](mailto:viamedica@viamedica.pl)

The editors accept no responsibility for advertisement contents.

**Folia Morphologica** is the official journal of the Polish Anatomical Society. For information about the Society, please contact: Prof. Marek Grzybiak, Department of Clinical Anatomy, Medical University of Gdansk, ul. Dębinki 1, 80–211 Gdańsk, Poland, tel: +48 58 349 14 22, e-mail: [grzybiak@gumed.edu.pl](mailto:grzybiak@gumed.edu.pl)

All rights reserved, including translation into foreign languages. No part of this periodical, either text or illustration, may be used in any form whatsoever. It is particularly forbidden for any part of this material to be copied or translated into a mechanical or electronic language and also to be recorded in whatever form, stored in any kind of retrieval system or transmitted, whether in an electronic or mechanical form or with the aid of photocopying, microfilm, recording, scanning or in any other form, without the prior written permission of the publisher. The rights of the publisher are protected by national copyright laws and by international conventions, and their violation will be punishable by penal sanctions.

Editorial policies and author guidelines are published on journal website: [https://journals.viamedica.pl/folia\\_morphologica](https://journals.viamedica.pl/folia_morphologica)

Legal note: [https://journals.viamedica.pl/folia\\_morphologica/about/legalNote](https://journals.viamedica.pl/folia_morphologica/about/legalNote)

**Folia Morphologica** is indexed by: BIOSIS Previews, CAS, CINAHL, CrossRef, Dental Abstracts, EBSCO, Elsevier BIOBASE, EMBIOLOGY, FMJ, Google Scholar, Index Copernicus (154.80), Index Medicus/MEDLINE, Index Scholar, Ministry of Science and Higher Education (70), NCBI/National Center for Biotechnology Information, Polish Medical Bibliography, Scopus, SJR, Thomson Reuters, Thomson Scientific Products — Biological Abstracts, Ulrich's Periodicals Directory, Veterinary Bulletin, WorldCat and Zoological Record. Position in Index Copernicus ranking systems is available at: [www.indexcopernicus.com](http://www.indexcopernicus.com). Current Impact Factor of Folia Morphologica (2019) is 0.941.



# FOLIA MORPHOLOGICA

Editor-in-Chief  
**JANUSZ MORYŚ**

Department of Anatomy and Neurobiology, Medical University of Gdańsk  
ul. Dębinki 1, 80–211 Gdańsk, Poland  
tel. (+48 58) 349 1401, fax (+48 58) 349 1421, e-mail: jmorys@gumed.edu.pl

## EDITORIAL ADVISORY BOARD

**Rafael BOSCOLO-BERTO**, *Department of Neuroscience, University of Padova, Italy*

**Franciszek BURDAN**, *Experimental Teratology Unit of the Human Anatomy Department, Medical University of Lublin, Poland*

**Małgorzata BRUSKA**, *Department of Anatomy, University Medical School, Poznań, Poland*

**Mafalda CACCIOTTOLO**, *USC Leonard Davis School of Gerontology, University of Southern California, Los Angeles, United States*

**Stephen W. CARMICHAEL**, *Department of Anatomy, Mayo Clinic, Rochester, United States*

**Bogdan CISZEK**, *Department of Human Anatomy, Medical University of Warsaw, Poland*

**Om Prakash CHOUDHARY**, *Department of Veterinary Anatomy and Histology, Central Agricultural University, Aizawl, India*

**Carla D'AGOSTINO**, *Neuromuscular Center, University of Southern California, Los Angeles, CA, United States*

**Zygmund Antoni DOMAGAŁA**, *Department of Anatomy, Medical University of Wrocław, Poland*

**Rastislav DRUGA**, *Department of Functional Anatomy, 2<sup>nd</sup> Medical Faculty Charles University, Prague, Czech Republic*

**Jochen FANGHÄNEL**, *Department of Anatomy, Ernst-Moritz-Arndt University, Greifswald, Germany*

**Marek GRZYBIAK**, *Elblag University of Humanities and Economics, Elblag, Poland*

**Hans Jorgen GUNDERSEN**, *Stereological Research Laboratory, University of Aarhus, Denmark*

**Kazimierz JĘDRZEJEWSKI**, *Department of Anatomy, Medical University of Łódź, Poland*

**Leszek KACZMAREK**, *Department of Molecular Cell Neurobiology, Nencki Institute, Warsaw, Poland*

**Zbigniew KMIEĆ**, *Department of Histology, Medical University of Gdańsk, Poland*

**Henryk KOBRYŃ**, *Department of Morphological Sciences, Warsaw, Agricultural University, Poland*

**Przemysław KOWIAŃSKI**, *Department of Human Anatomy and Physiology, Pomeranian University in Slupsk, Poland*

**Dariusz KOZŁOWSKI**, *2<sup>nd</sup> Department of Cardiology, Medical University of Gdańsk, Poland*

**Marios LOUKAS**, *Department of Anatomical Sciences, School of Medicine, St. George's University, Grenada, West Indies*

**Mirosław ŁAKOMY**, *Department of Animal Anatomy, Warmia and Masuria University, Olsztyn, Poland*

**Andrzej ŁUKASZYK**, *Department of Histology and Embryology, University Medical School, Poznań, Poland*

**Alexander J. McDONALD**, *Department of Cell Biology and Neuroscience, USC School of Medicine, Columbia, United States*

**Stanisław MOSKALEWSKI**, *Department of Histology and Embryology, Medical University of Warsaw, Poland*

**Orlando PACIELLO**, *Dipartimento di Patologia e Sanita animale, Univesita degli Studi di Napoli Federico II, Napoli, Italy*

**Asla PITKÄNEN**, *Department of Neurobiology, A.I. Virtanen Institute, University of Kuopio, Finland*

**Michał POLGUJ**, *Department of Angiology, Medical University of Łódź, Poland*

**Michał K. STACHOWIAK**, *Department of Molecular and Structural Neurobiology and Gene Therapy, State University of New York, Buffalo, United States*

**Paweł SYSA**, *Department of Histology and Embryology, Warsaw University of Life Sciences, Poland*

**Michał SZPINDA**, *Department of Anatomy, Nicolaus Copernicus University in Toruń, Collegium Medicum in Bydgoszcz, Poland*

**Edyta SZUROWSKA**, *2<sup>nd</sup> Department of Radiology, Medical University, Gdańsk, Poland*

**Jean-Pierre TIMMERMANS**, *Laboratory of Cell Biology and Histology/Central Core Facility for Microscopic Imaging, Department of Veterinary Sciences, University of Antwerp, Belgium*

**Mirosław TOPOL**, *Department of Angiology, Medical University of Łódź, Poland*

**Mehmet Cudi TUNCER**, *Department of Anatomy, University of Dicle, Medical School, Diyarbakır, Turkey*

**Krzysztof TURLEJSKI**, *Department of Biochemistry and Cell Biology, Cardinal Stefan Wyszyński University, Warsaw, Poland*

**Jiro USUKURA**, *Structural Biology Research Center, Nagoya, Japan*

**Jerzy WALOCHA**, *Department of Anatomy, Jagiellonian University, Collegium Medicum, Kraków, Poland*

**Mark J. WEST**, *Department of Neurobiology, Institute of Anatomy, Århus University, Denmark*

**Maciej ZABEL**, *Collegium Medicum University of Zielona Gora, Poland*

**Marco ZEDDA**, *Department of Veterinary Medicine, University of Sassari, Italy*



# Vertebral artery variations revised: origin, course, branches and embryonic development

E.-P. Magklara, E.-T. Pantelia, E. Solia, E. Panagouli<sup>id</sup>, M. Piagkou, A. Mazarakis, P. Skandalakis, T. Troupis, D. Filippou

Anatomy Department, Medical School, National and Kapodistrian University of Athens, Greece

[Received: 29 November 2019; Accepted: 27 January 2020]

**Background:** The vertebral artery originates from the subclavian artery and is divided into four segments. The aim of this study is to investigate the anatomical variations in the course and branches of the vertebral artery.

**Materials and methods:** A research was performed via PubMed database, using the terms: “variations of vertebral artery AND cadaveric study”, “variations of vertebral artery AND cadavers” and “anomalies of vertebral artery AND cadavers”.

**Results:** A total of 24 articles met the inclusion criteria, 13 of them referring to variations of the origin of the vertebral artery, 9 to variations of the course and 3 to variations of its branches. On a total sample of 1192 cadavers of different populations, origin of the left vertebral artery directly from the aortic arch was observed at 6.7%. In addition, among 311 cadavers, 17.4% were found with partially or fully ossified foramen of the atlas for the passage of the vertebral artery, while the bibliographic review also showed variants at the exit site of the artery from the transverse foramen of the axis.

**Conclusions:** Despite the fact that variations of both the course and the branches of vertebral artery are in most cases asymptomatic, good knowledge of anatomy and its variants is of particular importance for the prevention of vascular complications during surgical and radiological procedures in the cervix area. (Folia Morphol 2021; 80, 1: 1–12)

**Key words:** subclavian artery, brachiocephalic trunk, aortic arch, posterior inferior cerebellar artery

## INTRODUCTION

According to classical anatomical textbooks, the vertebral artery (VA) is divided into four segments [1]. In the first segment, the artery courses dorsally after originating from the subclavian artery until it enters the foramen of the C6. The second segment lies within the transverse foramina of C6 to C2. The third portion is the distal extracranial segment that is short and tortuous. The artery passes through the transverse foramen (TF) of the atlas and then curves backwards and medially behind the lateral mass of the atlas. It then makes a sharp turn to pierce the dura

mater, thereby entering the cranium through the foramen magnum (Fig. 1). The fourth segment is entirely intracranial and terminates when the vertebral arteries join at the lower pontine border to form the basilar artery [10, 27]. The VA typically gives off spinal, muscular, meningeal branches, the anterior spinal artery, ramus choroideus ventriculi quarti, medial and lateral medullary branches and the terminal branch, the posterior inferior cerebellar artery (PICA) [62].

Anatomical variations of the VAs concerning their site of origin, course and branching pattern are

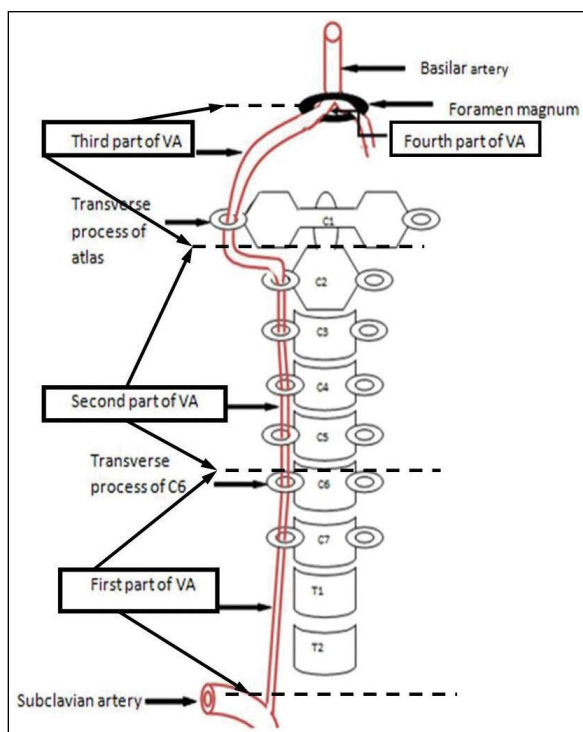


**Figure 1.** Origin and course of vertebral artery (VA). First part: from the origin of the vertebral artery until it enters the foramen of the C6. Second part: between transverse foramina of C6 to C2. Third part: from the transverse foramen until the foramen magnum. Fourth part: entirely intracranial.

not common and present particular clinical interest. Our study has been designed to take into account the reports in the literature so far, in order to investigate the different types of anatomical variations of the VAs and the corresponding incidences.

## MATERIALS AND METHODS

An extensive literature search was conducted using the electronic database PubMed for relevant published articles. The search terms were; “variations of vertebral artery AND cadaveric study”, “variations of vertebral artery AND cadavers” and “anomalies of vertebral artery AND cadavers”. Only cadaveric studies in adults and in English language were included in this study. Computed tomography-scans and angiographic studies were excluded. Additional search filters such as article types, text availability, publication date and species were not applied. Collected data were categorised in tables according to the type of variation. The resulting citations were exported and the articles were screened independently. The references of identified publications and articles were also examined.

## RESULTS

Eventually a total of 24 papers met inclusion criteria, 13 of them referred to variations of the origin of the VA, 9 to variations of the artery’s course and 3 in variations of its branches. It should be noticed that among the 25 papers, one (Lang and Kessler 1991 [27]) referred both to the course and the branches of the artery, so it was counted twice. The articles ranged in date from 1983 to 2019 and included cadaveric studies in different populations.

The 13 studies concerning the VA’s variable origin corresponded to a total number of 1192 cadavers. The results are presented in Table 1 and Figure 2. An atypical VA origin was detected in 7.0% (83 out of 1192 cadavers) of the specimens. A direct origin of the left vertebral artery (LVA) from the aortic arch was observed in 6.7% of cases (80 out of 1192 cadavers). The right vertebral artery (RVA) presented less commonly an aberrant origin (3 cadavers out of 1192, 0.25%). These variations concerned RVA origin from the right common carotid artery (RCCA), from the brachiocephalic trunk (BCT) and double RVA — the one emerging from the aortic arch (AA) and the other from the right subclavian artery (RSCA).

The vertebral level of origin of the RVA and LVA was assessed only in 14 cadavers (1 study, Table 1). The prevalent level of origin of the LVA was between the 7<sup>th</sup> cervical vertebra and the 1<sup>st</sup> thoracic vertebra, while there were also 4 cases emerging between the 1<sup>st</sup> and 2<sup>nd</sup> thoracic vertebra. The RVA arose between the 7<sup>th</sup> cervical vertebra and the 1<sup>st</sup> thoracic vertebra in 5 cases and between the 1<sup>st</sup> and 2<sup>nd</sup> thoracic vertebra in 4 cases.

Concerning the course of the VA, 189 (30.1%) variations were found among 628 cadavers (Table 2, a total of 9 studies). Most of them were observed on second and third segment of the VA. Studies where the VA presented anomalous origin were excluded.

The variations concerning the branching pattern of the VA are represented in Table 3 (3 studies).

## DISCUSSION

According to our review of the literature, the direct origin of the LVA from the AA was observed in 6.7% of the cases. In most occasions the LVA emerged between the left common carotid artery (LCCA) and the left subclavian artery (LSCA). A unique case of a LVA origin between the BCT and the LSCA was reported, while in this specimen the LCCA orig-

**Table 1.** Total number of studies and specimens presenting variations in the origin of the vertebral artery (VA).

Researchers	Year	Specimens	Variations	Per cent
Vorster et al. [56]	1998	60 South African cadavers	LVA origin from the AA (3)	5%
Gluncic et al. [19]	1999	1 cadaver	LVA origin from the AA in a common trunk with LSCA RVA origin from the RCCA	
Yamaki et al. [61]	2006	515 Japanese cadavers	RVA origin from the bifurcation of the BCT (1) LVA origin from the AA (30)	0.2% 5.8%
Ikegami et al. [24]	2007	25 cadavers	LVA origin from the AA (1)	4%
Shin et al. [47]	2008	25 Korean cadavers	LVA origin from the AA (2)	8%
			LVA — level of origin:	
			C7/T1:5	35.7%
			T1/T2:4	28.5%
			T2:1	7.1%
			T2/T3:1	7.1%
			T1:3	21.4%
			RVA — level of origin:	
			C7/T1:6	42.8%
			T1:3	21.4%
			T1/T2:4	28.5%
			C7:1	7.1%
Patil et al. [41]	2012	75 Indian cadavers	LVA origin from the AA (6)	8%
Budhiraja et al. [8]	2013	52 Indian cadavers	LVA origin from the AA (9)	17.3%
Einstein et al. [16]	2016	27 cadavers	LVA origin from the AA (4)	14.8%
Singh [49]	2017	2 Indian cadavers	LVA origin from the AA (1) LVA origin from a common trunk with LSCA (1)	
Motomura et al. [35]	2018	1 cadaver	Duplicated RVA with a proximal leg arising from the AA and a distal one with typical origin from RSCA	
O'Malley et al. [39]	2018	24 Irish cadavers	LVA origin from the AA (2)	8.3%
Li et al. [30]	2018	119 cadavers	LVA origin from the AA (7)	5.89%
Woraputtaporn et al. [60]	2018	266 Thai cadavers	LVA origin from the AA (14)	5.3%

AA — aortic arch; BCT — brachiocephalic trunk; LSCA — left subclavian artery; LVA — left vertebral artery; RCCA — right common carotid artery; RSCA — right subclavian artery; RVA — right vertebral artery

inated from a common trunk with the BCT. Additionally, in two cases the LVA derived from the AA from a common trunk together with the LSCA [19, 49].

In order to understand the majority of VA variations, a deep knowledge of embryological development of the AA and its branching pattern is required. During embryological development, as the heart and aorta move caudally, cervical intersegmental arteries appear from the AA [16]. The 1<sup>st</sup> to 6<sup>th</sup> dorsal intersegmental arteries are anastomosed lengthwise, with their inferior end connected to the 7<sup>th</sup> dorsal intersegmental artery [61]. The first part of the LVA develops close to the origin of the dorsal branch of the 7<sup>th</sup> cervical intersegmental artery and proximal to the postcostal anastomosis, while the second part is derived from longitudinal communications of the

postcostal anastomosis. To enter into the foramen transversarium of 6<sup>th</sup> cervical vertebra, the vessel takes a vertical posterior course [8].

Even though AA variations may be discovered in the very first days of life, the majority are only discovered after death or randomly on imaging methods, due to the absence of symptoms [39]. Even though the exact cause of such variations is unknown [39], a plethora of embryological explanations is contained in the literature. From the aspect of Patil et al. (2012) [41], variations in the branches of the AA might be a result of modified development of certain arteries of the AA during pregnancy. Furthermore, Patil et al. (2012) [41] suggested that a large absorption of embryonic tissue of the LSCA between the origin of the VA and the AA may cause a direct origin of the

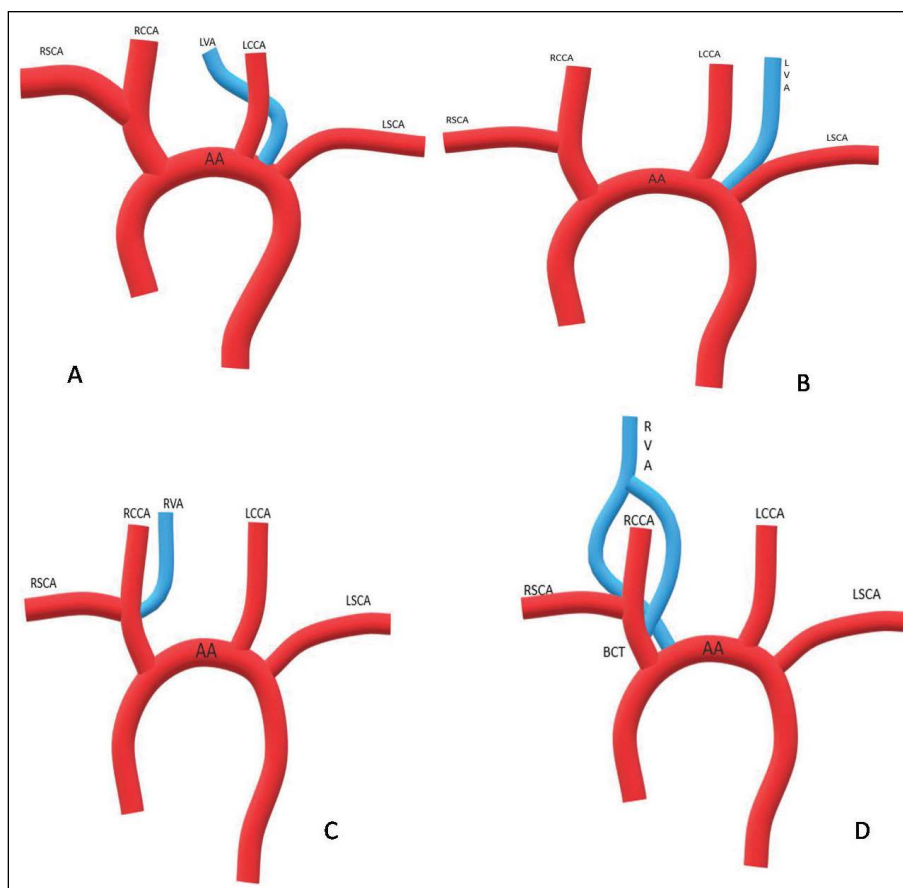


**Figure 2.** Variations of vertebral artery (VA) origin; **A.** Left vertebral artery (LVA) originated from aortic arch (AA); right vertebral artery (RVA) of typical origin; **B.** LVA originated from AA with a common trunk with left subclavian artery (LSCA), RVA of typical origin; **C.** RVA originated from brachiocephalic trunk (BCT), LVA of typical origin; **D.** Duplicated RVA originated from BCT and AA, LVA of typical origin; LCCA — left common carotid artery; RCCA — right common carotid artery; RSCA — right subclavian artery.

LVA from the AA, between the origins of the LSCA and LCCA. Adachi (1928) [2] classified this pattern as type III. Budhiraja et al. (2013) [8] assumed that the first part of VA could be the preserved left 6<sup>th</sup> segmental artery, or there might be a large absorption of the embryonic tissue of LSCA, between the origin of the AA to the origin of VA, causing direct origin of the LVA from the AA. The 6<sup>th</sup> cervical intersegmental artery customarily vanishes, but Einstein et al. (2016) [17] supposed that it might have maintained, permitting blood flow from the arch of aorta. The cause of origin of the LVA from the AA might be the decreased blood flow through the normal origin of the LVA which is the dorsal division of the 7<sup>th</sup> cervical intersegmental artery. According to Yamaki et al. (2006) [61], this anomalous origin of the LVA could be explicated by the fact that the LVA is probably formed through the conjunction of the 4<sup>th</sup> branchial artery with the superior wall of the arch of aorta. Additionally,

growth factors such as transforming growth factor beta and vascular endothelial growth factor may play a significant role in the variable patterns of the AA and its branches [5]. Bhimabhai et al. (2014) [6] suggest that AA variations may be a result of deficient branching of the aortic sac into the right and left limbs during embryonic growth, while Momma et al. (1999) [34] propose that there is a relationship between AA variants and a loss of chromosome 22q11. Moreover, other congenital conditions such as Klippel-Feil syndrome or Down syndrome and rheumatoid arthritis have been associated with VA variations [57].

Concerning the clinical implications of the variations of the LVA origin, Budhiraja et al. (2013) [8] noticed that atherosclerosis often affects the pre-vertebral part of the LVA deriving from the AA. Einstein et al. (2016) [17] stated that an abnormal origin of LVA doesn't have any impact on blood flow, but it might perplex surgical and endovascular



**Table 2.** Variations in the course of the vertebral artery (VA)

Researchers	Year	Specimens	Variations	Per cent
De Oliveira and Rhoton [15]	1985	25 cadaveric heads	In the suboccipital region: • VA was partially, but incompletely, surrounded by bone (6) • Bony ring that completely surrounds the VA (7)	24% 28%
Lang and Kessler [27]	1991	65 head and neck halves	V3 segment Loop formation at the exit from the transverse foramen of C2: • Sideward loop caudally and dorsally (Type II) (9) • Clear loops in the dorsal direction (Type III) (7) • Slant course from the transverse foramen of C2 sideward and upward (Type IV) (7) Variations of V2 segment: • In the space between C6 and C2 it meanders slightly (5) • Clear loops (2)	14% 10.8% 10.8% 7.7% 3.1%
Cacciola et al. [9]	2004	40 cadavers	• Atlas with symmetrical complete bilateral dorsal osseous bridges, passage of VA through the tunnel formed by the dorsal and lateral bridges (1) • VA passage from lateral to medial under the oblique inferior boarder of the partially ossified atlanto-occipital membrane (2)	2.5% 5%
Senoglu et al. [46]	2006	166 dry C1 specimens	Variations of V3 segment: • Bilateral osseous bridges forming a canal for VA (8) • Unilateral osseous bridges forming a canal for VA (10)	4.8% 6%
Tubbs et al. [53]	2006–2007	20 cadavers	Bilateral LAO ligament, dorsally in contact with the VA (20)	100%
Civelek et al. [13]	2007	30 cadavers	Variations at the VA entrance point in the transverse canal (V2 segment): • Entrance into the transverse foramen of C7 (2) • Entrance into the transverse foramen of C4 (1)	7% 3%
Muralimohan et al. [36]	2009	21 Indian cadavers	• On the right side completely ossified bridging fibrous tissue forming a bony tunnel for VA (1) • On the left side partially ossified bridging fibrous tissue forming a bony tunnel for VA (1)	4.7% 4.7%
Ulm et al. [54]	2011	30 cadavers	Variations of V3 segment: Exit of VA from the C2 transverse foramen: • 90° bend (15) • < 90° angle (11) • > 90° angle (4)	50% 37.5% 12.5%
		25 cadavers	Proximal loop formation from its exit from the C2 foramen: • Posteriorly (12) • Directly laterally (5) • Little or no loop present (straight line between C1-C2) (8) • No space between the occipital bone and the horizontal segment (4)	48% 20% 32% 12%
		34 cadavers	Dorsal course through a fully foramen-shaped arterial groove (5)	14.7%
Chanapa and Mahakkanukrauh [12]	2012	181 cervical spines	Entrance of the VA into the transverse foramen of: • C4 (4) • C5 (16) • C7 (20)	1.1% 4.4% 5.5%

processes of AA. The impairment or disengagement of the abnormal vessel might also affect cerebral function. According to the literature, there seems to be a greater hazard during surgical processes of important interruption of cerebral blood flow, if an anomalous VA exists [16]. Thus, a thorough knowl-

edge of variations in the branching pattern of the AA is essential, especially when patients have to experience aortic instrumentation, vessel angiography, or surgery on neck and head [41]. Additionally, a comprehensive understanding of possible abnormal branches emerging from the AA is also vital in the

**Table 3.** Variations in the branches of the vertebral artery (VA)

Researchers	Year	Total specimens	Variations	Per cent	
Lang and Kessler [27]	1991	65 head and neck halves	3 specimens origin from the VA with extradural origins	~4%	
Abd El-Bary et al. [1]	1995	14 cadavers	Branches of the atlantic part of VA		
				<b>Left</b>	<b>Right</b>
			<b>Radiculomuscular</b>	14	14
			<b>Muscular</b>	4	4
			<b>Postmeningeal</b>	4	6
			<b>Postspinal</b>	4	5
				100%	100%
				28.6%	28.6%
				28.6%	42%
				28.6%	35.7%
Wang et al. [58]	2019	1 cadaver	Extradurally bilateral PICA origin between C1 and C2, and a right double-origin PICA		

PICA — posterior inferior cerebellar artery

identification of cranial aneurysms. Moreover, there have been reports that anomalies in the branching pattern of the AA could lead to cerebral anomalies by modifying the pattern of flow in cerebral vessels. Direct origin of LVA from AA seems to increase blood flow in LVA. This direct flow of blood from aorta to brain or absence of equilibrated flow of blood on right and left side at circle of Willis may probably be the cause of greater occurrence of cerebro-vascular diseases in such cases [44].

Our review of the literature retrieved only 1 case of a duplicated RVA (Table 1 [35]). Sim et al. (1976) [48] suggested that this variation may be the result of a remaining portion of the primitive dorsal aorta along with two intersegmental vessels conjoined to the true VA, while Kendi et al. (2009) [25] proposed that the miscarriage of regression of the 5<sup>th</sup> or 6<sup>th</sup> intersegmental arteries may lead to a further potential origin of the VA along with the normal 7<sup>th</sup> segment. Duplicated RVA might be observed only in 1% of Japanese people and it is even rarer in Western Europe population [1]. It occurs mainly in the upper cervical position and is associated with other intracranial anomalies. When duplicated, there is either a main trunk which permeates the dura at the C1-C2 levels and a hypoplastic one or two trunks, one intradural and one extradural, of similar dimension. This probably leads to an acute haematoma below the inner layer of the dura and death, after tapping costal the cervical spine.

In respect to the variations of the RVA origin, our review retrieved a few cases of RVA emerging from the RCCA and the BCT as well as the duplication of the artery which was described above (total incidence of 0.25%). Maiti et al. (2016) [31] mentioned that anomalous origin of the RVA is more frequent

than that of the LVA. This result coincides with the findings of our review. The embryologic explanation is often difficult to understand. Although these findings may be asymptomatic in most cases, detailed information is required before any surgical/endovascular intervention in order to avoid any inattentive injury and misconception of VA [8]. In general, abnormal origin of VA might cause cerebral disorder as it modifies haemodynamic of the brain [8].

Lazaridis et al. (2018) [29] presented in their study an interesting classification system concerning the variable point of origin of both VA. In most of the cases the left or right VA is described to emerge abnormally from different parts of the AA, while extra-aortic points of origin, such as the BCT and carotid arteries are included [29]. Nevertheless, the classification does not mention the point entrance and branching pattern.

Variations related to the entrance point and the course of the second segment in the transverse canal, were noticed in 2 studies and a total of 43 cadavers (20%, Table 2 [12, 53]). The VA entered the TF of C6 in 168 out of 211 specimens (80%). In 5 cadavers it entered in the TF of C4 (2.3%), in 16 cadavers in the TF of C5 (7.6%) and in 22 specimens the entrance point of VA was observed in the TF of C7 (10.4%) [12, 31]. Chanapa and Mahakkanukrauh (2012) [12] reported the 47.5% of the observed variations were on the left side and the 52.5% were on the right side. The 57.5% of the cases which presented variations at the level of entry of the VA were men and the 42.5% were female [12]. Previous studies [7, 22, 31] reported that the VA entered typically at C6 with a range from 90% to 94.9%, while an abnormal entrance at C3, C4, C5, and C7 was observed with a range from 5.1% to 10%.

Chanapa and Mahakkanukrauh (2012) [12] reported that the entrance was found in 89% at the C6, which is compatible with the study of Civelek (2007) [13]. According to our review, the VA entered typically at C6 in 80% of the cases and the abnormal entrance occurred in 20% (C7, C5, and C4 with incidences 10.4%, 7.6%, and 2.3%, respectively). The unilateral entry of VA in the study of Chanapa and Mahakkanukrauh (2012) [12] was 13% similar to the study of Bruneau (2006) [7], which was 12.4%. Ebraheim et al. (1996) [16] reported that serious VA compression, particularly when cervical spondylosis is present, may occur within the TF of C5 spine due to the small diameter of this foramen.

It should be pointed out that LVAs with abnormal origin from the AA tend to present variable and anomalous point of entrance. In the study of Woraputtaporn et al. (2018) [60] the 78.6% of LVAs deriving from the AA entered the TF of C5, with one entering that of the C4. On the right side, no deviations were observed at the origin pattern and the 99.2% of RVA assessed the C6 [60]. That was also the case in the study of Li et al. (2018) [30], where variations with a sinuous course and abnormal entry at the TF of C5 were reported only in LVAs with atypical origin. According to Tardieu et al. (2017) [51], all cases of LVA with this type of origin ascended in a more medial course and presented higher point of origin, being more prompt to injuries.

Concerning the entrance of VA in the transverse canal, in 89% the artery ran nearly straight in this area, in 7.7% it meandered slightly and in 3.1% it formed clear loops [26]. In reference to the third segment of the VA, out of a total sample of 628 cadavers, variations were detected in 119 of them (19%, Table 2). Ulm et al. (2010) [54] found that half of the VA specimens presented a 90° bend at their exit point at the C2 TF, 37.5% made a slightly more acute angle and 12.5% formed an obtuse bend inside the groove. In the same study, 25 dissections at the level of the third segment were examined, specifically at the proximal loop, which is tethered between the bony C1 and C2 foramina. The proximal loop projected posteriorly in 12 (48%) cases and directly laterally in 5 (20%) cases; in 8 (32%) cases there was a small or no loop and the artery coursed in a straight line between C1 and C2. No case in which the proximal loop projected medially or anteriorly was observed. The superior surface of the horizontal segment is in close proximity to the lower

lateral surface of the occipital bone. Ulm et al. (2010) [54] found no separation between the lower surface of the occiput and the superior surface of the third segment in 12% of cadaveric dissections (4/39).

Lang and Kessler (1991) [27] studied the course of the atlantoaxial part of the VA in 65 head and neck halves and presented 4 main types (I–IV) of loop formation in this region. According to their division, the type I which referred to the classical course of the artery was found in 42 (64.6%) specimens. This course was discovered in 64.6% of the cases on the right and in 62.5% on the left. Type II included VAs which formed a loop sideward more or less caudally and slightly dorsally after their exit from the TF of the axis. This form occurred in 9 (14%) specimens, more often on the left (18.8%) than on the right (9.1%). The cases where VA presented clear loops in the dorsal direction and then coursed upward to the TF of the axis belonged to the type III. This type was observed in 7 (10.8%) specimens, more often on the left (12.5%) than on the right (9.1%). Finally, type IV was comprised of the arteries which coursed slantingly from the transverse foramen of the axis sideward and upward, with more or less clear curves of the vessel in the ventral direction before it approached the TF of the atlas. This type occurred in 10.8%; in 15.2% the slanting course was to the right and in 6.3% to the left. Furthermore, they compared both sides in only 32 specimens (12 males, 4 females) and discovered the same type on each side in 56.3%.

Probably the loop formation of the atlantoaxial part was firstly investigated by Kraysenbühl and Yasargil (1957) [26]. These authors as well as Schwedt in 1978 [45] described different subdivisions: slight bendings, small curves, nearly or no loop formation and moderate looping and so on. Toldt and Hoshstetter (1979) [52] presented these bends in their illustrations. Francke et al. (1981) [18] subdivided the loops (concave downward and laterally and inside the TF of C2) and pointed out that these bends seem to increase during aging. According to Muralimohan et al. (2009) [36], the incidence of VA variations in the atlantoaxial region is 2.3%. Ulm et al. (2010) [54] stated that this variant anatomy must be taken into consideration when placing either C2 pars screws or C1-2 transarticular screws, as both these techniques are likely to cause damage of this segment. Thus, detailed knowledge of the anatomy of this arterial segment is critical for the surgeon so that

no accidental injury occurs. In addition, according to Heros (1986) [22], an intraoperative injury to the VA may result in unpredictable neurological deficits depending on contralateral VA flow due to excessive bleeding and disruption of cerebral blood flow.

As the artery exits the transverse foramen of C1, heading towards to the suboccipital region, it typically runs through the groove of the VA found in the posterior arch of C1. One of the most common variations observed in our review study was the presence of an osseous foramen on the posterior arch of the atlas, which is referred in the literature as Foramen Arcuale (FA) (or Ponticulus Posterior) [26]. This foramen, which is formed by the ossification of the atlanto-occipital membrane, transforms the groove of VA in an osseous tunnel inside of which the artery passes through to the suboccipital region. Among 252 cadavers [3, 26, 36, 46, 54] a total (33 out of 41, 80.5%) or partial (8 out of 41, 19.5%) ossification of the atlanto-occipital membrane was observed in 41 (16.3%) (Table 2). Corresponding findings were reported by Senoglu et al. (2006) [46] in 8 cadavers bilateral and in 10 unilateral (166 specimens), while no statistically significant difference between left and right side was reported.

The osseous bridge forming the canal for the VA variant was reported for the first time in the late 19<sup>th</sup> century [32]. According to Manjunath (2001) [32], this variant anatomy was detected on 11.7% of C1 vertebrae observed in 60 southern Indians and was reported to occur in 1.8% to 29.2% of individuals in various geographic locations. Taitz and Nathan (1986) [50] investigated the existence of posterior and/or lateral bone bridges in 672 C1 vertebrae. They found partial posterior bridges in 174 (25.9%) and complete bridges in 53 (7.9%) cases. Paraskevas et al. (2005) [40] examined 176 dried C1 vertebrae and found a canal for the VA in 10.2% and an incomplete canal in 24.4% of their specimens. This variant was observed less frequently in the specimens of Senoglu et al. (2006) [46] (bilaterally in 4.8%, unilaterally in 6%, and partially in 4.8%). Afsharpour et al. (2016) [3] reported that the presence of arcuate foramina may compress the VA as it passes beneath the bony bridge. This compression could result in neurological conditions as vertebrobasilar arterial insufficiency (VBAI). Same symptoms may occur during surgical procedures near the atlas in patients with a FA. Mitchell (1998) [33] and Vanitha (2014) [55] concluded that hyper-

extension of the head or manual pressure in this region during cervical manual manipulation is more likely to provoke VA compression, especially when FA is present, resulting in stenosis. Nevertheless, Haynes (2005) [20] didn't observe any incidence of VA stenosis using a Doppler examination. Cushing et al. (2001) [14] reported that the presence of FA could increase the risk of VA dissection especially with neck rotation. In a comprehensive study of 895 patients, Wight et al. (1999) [59] found out that complaints of neck pain (33%) and cervicogenic headache (22%) were significantly connected with the presence of FA. Pękala et al. (2017) [42] detected that the complete FA was reported to be predominant in North Americans (11.3%) and Europeans (11.2%), and less common among Asians (7.5%). The complete FA was observed more frequently in males (10.4%) than in females (7.3%). On the opposite, an incomplete FA was more commonly observed in females (18.5%) than in males (16.7%). Additional to a complete FA, a contralateral FA was found in 53.1% of the cases. In our review study, the bilateral presence of FA was observed in 44.4% of cases (Table 2). Conclusively, the patient's sex and ethnicity should be taken into consideration by the surgeons while examining the presence of FA. Pre-screening clinical assessment of classic signs and symptoms of VBAI is also of great importance. Radiographic imaging is recommended for assessing the presence of partial or complete FA. In trauma cases, advanced imaging is strongly recommended. In order to minimise the risk of VA injuries from screw placement, attentive evaluation of dorsal-lateral arch thickness is a prerequisite, since FA seems to be a common anomaly. A thorough knowledge of the variants in this region and a detailed appreciation of regional anatomy of the FA are therefore imperative during surgical procedures in this area, as mentioned by Ahn et al. (2018) [4]. However, based on Afsharpour et al. (2016) [3] findings, the presence of such hard bridges over the VA may provide protection from compressive pressures. The same conclusion was reached by Muralimohan et al. (2009) [36] who assumed that although anatomical variations may potentially increase the rate of intraoperative complications, this osseous bridge constitutes an additional barrier which protects the artery, thus it reduces the risk of injury. This is also mentioned in the study of Senoglu et al. (2006) [46].

Tubbs et al. (2007) [53] have reported in their study that all 20 cadavers they had studied presented a lateral atlanto-occipital ligament (LAO) bilaterally, in contact with the VA posteriorly. They reported that this ligament was found to be a distinct band of connective tissue located lateral to the atlanto-occipital junction, separate from the joint capsule and the anterior atlanto-occipital membrane. The insertion of the LAO was observed onto the jugular process of the occipital bone in all specimens [53]. Although Tubbs et al. [53] reported that the presence of the LAO ligament was in close relation with the VA in all their specimens, this ligament is not frequently mentioned in literature and almost absent from all modern textbooks and atlases of anatomy. Some of the texts that have depicted this ligament include the antiquated editions of Gray's anatomy [43]. On the other hand, Hecker (1922) [21], in a landmark treatise on the atlanto-axial-occipital ligaments, didn't mention the LAO. The exclusion of this ligament may be linked to the difficulty to access this region. In case of accidents which might lead to the injury of this ligament, consequential damage in the VA may occur. Therefore, further research of the LAO must be taken into consideration, due to the proximity of this ligament to the VA.

According to Russo et al. (2011) [44], iatrogenic damage in the second segment of the VA is rare. However, the anomalous course of the VA may provoke serious complications during anterior cervical decompression surgery with consequential neurological damage or death. Thus, accurate preoperative planning is prerequisite for anterior cervical decompression [38]. Surgical approaches to the posterolateral craniovertebral junction require working in close proximity to the V3 segment. Therefore, Ulm et al. (2010) [54] concluded that an injury of this segment may occur during procedures of the craniovertebral junction, as well as while its exposure when treating tumours. They also mentioned that an injury of the VA may lead to serious complications such as VA occlusion, formation of an arteriovenous fistula, a pseudoaneurysm, or enormous bleeding that could result in stroke or even death [38, 54].

After the VA enters the suboccipital region, it gives off spinal and muscular branches, which supply the upper portion of the spinal cord and the suboccipital muscles, respectively. During its passage through the dura matter, meningeal branches are emerged. As it courses intercranial, it gives

off its terminal branch, the PICA which is the largest branch of the VA and may be originated from the foramen magnum to the vertebrobasilar junction [1]. According to Lang and Kessler (1991) [25] the PICA emerged from the VA with extradural origins in 3 out of 63 head and neck halves (about 4%), while double-origin PICA extradurally between the vertebrae C1 and C2 is observed in 1–4% of patients [58].

During surgical procedures of the VA, the branches of the VA in the axoatlantal and atlantal segments must be taken into consideration. Lang (1983) [28] was the first who analysed the extradural origins of PICA. It should be noticed that there are a plenty of variations concerning the distance from the lower rim of the TF of the atlas to the dura. Abd et al. (1995) [1] have noticed that the right and left VA often presents an asymmetry. A small VA is difficult to be observed with angiography and perhaps it terminates as PICA. Moreover, PICA termination is highly prevalent in cases of LVA origin from the AA [38]. In case it is ending in the basilar trunk it is termed "hypoplastic"; otherwise it is called "atretic" [38]. Additionally, there is a possibility of absence of this artery, so 4 congenital anastomotic arteries might exist: the trigeminal, otic, and hypoglossal which are intracranial and the proatlantal which is extracranial. All of them constitute embryonic anastomotic arteries among the carotid and basilar circulatory systems. The occipital artery emerges from the internal carotid, it connects the later with the external carotid artery and its proximal portion is formed by a channel of proatlantal artery [1]. From the above, it is clear one proatlantal artery might rise from the external carotid and another from the internal carotid. The VA may be absent or hypoplastic if there is a persistent proatlantal artery. Thus, a proatlantal artery might remain due to abnormalities of VA development [1].

Below the C1 posterior arch is observed a radiculomuscular branch that is formed due to the entrance of the artery. This branch passes between the atlantoaxial joint (forward) and C2 nerve (downward) and was present at all specimens (100%). Moreover, it appears to give two branches; a dural branch that courses to the dura with the C2 nerve and a muscular branch. The origin of this radiculomuscular branch is observed on the entrance point of the VA to the C1 TF and no cadaver presented it lower from the TF (Table 3). Similar were also the findings in the angiography studies of Zhu et al. (2018) [62].

Another muscular branch is formed by the artery above the C1 posterior arch and ran posterosuperiorly and medially. Four cadavers presented this branch both in the left and the right side, respectively (28.6% on each side, Table 3). Distal to this branch, the posterior meningeal artery is formed by the VA posteromedially. This artery was originated 7–11 mm proximal to the entrance point of VA to dural and was detected on the left side in 4 (28.6%) cadavers, on the right side in 6 (42%) specimens and it was missed in 4 (Table 3). Although the meningeal branches of the VA are small, they may become swollen in a plenty of pathologic circumstances. Both anterior and posterior meningeal branches originate from the extracranial VA and supply a portion of the dura of the posterior fossa. The posterior branch emerges from the VA over the arch of C1, under the foramen magnum and it supplies the medial portions of the dura of the occipital posterior fossa and the falx cerebelli. Sometimes it may also continue over the tentorium in order to supply the posterior segment of the falx cerebri and adjacent tentorium [37]. Newton (1968) [37] reported the posterior meningeal artery on the left side in 29.8% of their cases and on the right side in 40% of the cases (angiographic study). According to their study, the posterior meningeal artery originates from the posterior part of the VA among the arch of C1 and the base of the skull.

The posterior spinal artery arose from the posteromedial portion of the VA just at the point of entrance of the dural. It was observed on the left side in 4 (28.6%) cadavers and on the right in 5 (35.7%, Table 3). It also can be emerged from the intradural segment of the artery [11, 23]. In the subarachnoid space, the artery gives off ascendants and descendants branches. The ascendant branch passes through the foramen magnum and divides into branches that are connected to branches of the PICA. The descendant branch course continues on the posterolateral aspect of the spinal cord. It is also connected to the posterior branches of the radicular arteries and is divided into collateral branches, which continue medially across the posterior surface of the spinal cord and they are connected to form an artery located in the midline, parallel to the posterior spinal arteries. Concerning the dural penetration of the VA, the — partial — ligation of the artery at this level is recommend, because the periosteal sheath supports the dura mater. So, in rotations, is more

secure to leave untouched the central part of the dura matter and cutting it around, but not close to the VA. The muscular branch above the posterior arch of C1 is commonly injured during exposure of the artery. Last but not least, the importance of distinguishing the VA from the PICA must be highlighted, as in rare occasions may emerges from the extradural VA [57].

## CONCLUSIONS

It is obvious that, although the variations of VA concerning the origin, the course and the branches are, according to the literature, in most cases asymptomatic, the thorough comprehension and knowledge of the typical VA and its variations is of great importance for the prevention of vascular complications during minimally invasive diagnosis and treatment of cerebral vascular diseases.

## REFERENCES

1. Abd el-Bary TH, Dujovny M, Ausman JI. Microsurgical anatomy of the atlantal part of the vertebral artery. *Surg Neurol.* 1995; 44(4): 392–400; discussion 400, doi: [10.1016/0090-3019\(95\)00033-x](https://doi.org/10.1016/0090-3019(95)00033-x), indexed in Pubmed: [8553261](https://pubmed.ncbi.nlm.nih.gov/8553261/).
2. Adachi B. *Das Arterien system der Japaner*. Vol. 1. Verlag der Kaiserlich-Japanischen Universitat, Kenyusha Press, Kyoto 1928.
3. Afsharpour S, Hoiriis KT, Fox RB, et al. An anatomical study of arcuate foramen and its clinical implications: a case report. *Chiropr Man Therap.* 2016; 24: 4, doi: [10.1186/s12998-016-0082-2](https://doi.org/10.1186/s12998-016-0082-2), indexed in Pubmed: [26811743](https://pubmed.ncbi.nlm.nih.gov/26811743/).
4. Ahn J, Duran M, Sylldort S, et al. Arcuate foramen: anatomy, embryology, nomenclature, pathology, and surgical considerations. *World Neurosurg.* 2018; 118: 197–202, doi: [10.1016/j.wneu.2018.07.038](https://doi.org/10.1016/j.wneu.2018.07.038), indexed in Pubmed: [30026164](https://pubmed.ncbi.nlm.nih.gov/30026164/).
5. Bhatia K, Ghabriel MN, Henneberg M. Anatomical variations in the branches of the human aortic arch: a recent study of a South Australian population. *Folia Morphol.* 2005; 64(3): 217–223, indexed in Pubmed: [16228958](https://pubmed.ncbi.nlm.nih.gov/16228958/).
6. Bhimabhai MP. A study of the branching pattern of aortic arch. *Nat J Integr Res Med.* 2014; 5: 27–30.
7. Bruneau M, Cornelius JF, Marneffe V, et al. Anatomical variations of the V2 segment of the vertebral artery. *Neurosurgery.* 2006; 59(1 Suppl 1): ONS20–4; discussion ONS20, doi: [10.1227/01.NEU.0000219931.64378.B5](https://doi.org/10.1227/01.NEU.0000219931.64378.B5), indexed in Pubmed: [16888547](https://pubmed.ncbi.nlm.nih.gov/16888547/).
8. Budhiraja V, Rastogi R, Jain V, et al. Anatomical variations in the branching pattern of human aortic arch: a cadaveric study from central India. *ISRN Anat.* 2013; 2013: 828969, doi: [10.5402/2013/828969](https://doi.org/10.5402/2013/828969), indexed in Pubmed: [25938106](https://pubmed.ncbi.nlm.nih.gov/25938106/).
9. Cacciola F, Phalke U, Goel A. Vertebral artery in relationship to C1-C2 vertebrae: an anatomical study. *Neurol India.* 2004; 52(2): 178–184, indexed in Pubmed: [15269464](https://pubmed.ncbi.nlm.nih.gov/15269464/).
10. Caplan LR. *vertebrobasilar system syndromes*. In: Vinken PJ, Bruyn GW, Klawans, eds. *Handbook of clinical neurology*.

- ascular disease. Part 1. Elsevier Science Publisher B.V., Amsterdam 1988: 371–409.
11. Carpenter MB. Neuroanatomy. 4th ed. Williams and Wilkins, Philadelphia 1991: 449.
  12. Chanapa P, Mahakkanukrauh P. Anatomical variations of the V2 vertebral artery study by measuring the width of transverse foramen. *J Med Assoc Thai.* 2012; 95(4): 569–573, indexed in Pubmed: [22612013](#).
  13. Civelek E, Kiris T, Hepgul K, et al. Anterolateral approach to the cervical spine: major anatomical structures and landmarks. Technical note. *J Neurosurg Spine.* 2007; 7(6): 669–678, doi: [10.3171/SPI-07/12/669](#), indexed in Pubmed: [18074695](#).
  14. Cushing KE, Ramesh V, Gardner-Medwin D, et al. Tethering of the vertebral artery in the congenital arcuate foramen of the atlas vertebra: a possible cause of vertebral artery dissection in children. *Dev Med Child Neurol.* 2001; 43(7): 491–496, doi: [10.1017/s0012162201000901](#), indexed in Pubmed: [11463182](#).
  15. De Oliveira E, Rhoton A, Peace D. Microsurgical anatomy of the region of the foramen magnum. *Surg Neurol.* 1985; 24(3): 293–352, doi: [10.1016/0090-3019\(85\)90042-4](#).
  16. Ebraheim NA, Lu J, Brown JA, et al. Vulnerability of vertebral artery in anterolateral decompression for cervical spondylosis. *Clin Orthop Relat Res.* 1996(322): 146–151, indexed in Pubmed: [8542690](#).
  17. Einstein EH, Song LH, Villela NLA, et al. Anomalous origin of the left vertebral artery from the aortic arch. *Aorta (Stamford).* 2016; 4(2): 64–67, doi: [10.12945/j.aorta.2015.15.022](#), indexed in Pubmed: [27757404](#).
  18. Francke JP, di Mario V, Pannier M, et al. The vertebral arteries (arteria vertebralis). The V3 atlantoaxial and V4 intracranial segments-collaterals. *Anat Clin (Berl).* 1981; 2: 229–242.
  19. Gluncic V, Ivkic G, Marin D, et al. Anomalous origin of both vertebral arteries. *Clin Anat.* 1999; 12(4): 281–284, doi: [10.1002/\(SICI\)1098-2353\(1999\)12:4<281::AID-CA8>3.0.CO;2-6](#), indexed in Pubmed: [10398389](#).
  20. Haynes MJ, Cala LA, Melsom A, et al. Posterior ponticles and rotational stenosis of vertebral arteries. A pilot study using Doppler ultrasound velocimetry and magnetic resonance angiography. *J Manipulative Physiol Ther.* 2005; 28(5): 323–329, doi: [10.1016/j.jmpt.2005.04.003](#), indexed in Pubmed: [15965406](#).
  21. Hecker P. Appareil ligamenteux occipito-atloïdo-axoïdien etude d'anatomie comparée: Archives d'Anatomie, D'Histologie et d'Embryologie. 1922; 1: 417–433.
  22. Heros RC. Lateral suboccipital approach for vertebral and vertebrobasilar artery lesions. *J Neurosurg.* 1986; 64(4): 559–562, doi: [10.3171/jns.1986.64.4.0559](#), indexed in Pubmed: [3950739](#).
  23. Hong JT, Park DK, Lee MJ, et al. Anatomical variations of the vertebral artery segment in the lower cervical spine: analysis by three-dimensional computed tomography angiography. *Spine.* 2008; 33(22): 2422–2426, doi: [10.1097/BRS.0b013e31818938d1](#), indexed in Pubmed: [18923317](#).
  24. Ikegami A, Ohtani Y, Ohtani O. Bilateral variations of the vertebral arteries: the left originating from the aortic arch and the left and right entering the C5 transverse foramina. *Anat Sci Int.* 2007; 82(3): 175–179, doi: [10.1111/j.1447-073X.2006.00163.x](#), indexed in Pubmed: [17867344](#).
  25. Kendi AT, Brace JR. Vertebral artery duplication and aneurysms: 64-slice multidetector CT findings. *Br J Radiol.* 2009; 82(983): e216–e218, doi: [10.1259/bjr/26005109](#), indexed in Pubmed: [19890113](#).
  26. Krayenbühl H, Yasargil MG. Die vaskulären Erkrankungen im Gebiet der Arteria vertebralis. Eine anatomische und pagängzungband der Fortschritte auf dem Gebiete der Röntgenstrahlen und der Nuklearmedizin. Thieme, Stuttgart 1957.
  27. Lang J, Kessler B. About the suboccipital part of the vertebral artery and the neighboring bone-joint and nerve relationships. *Skull Base Surg.* 1991; 1(1): 64–72, doi: [10.1055/s-2008-1056982](#), indexed in Pubmed: [17170824](#).
  28. Lang J. Clinical anatomy of the head: neurocranium, orbit and craniocervical regions. Springer-Verlag, New York 1983.
  29. Lazaridis N, Piagkou M, Loukas M, et al. A systematic classification of the vertebral artery variable origin: clinical and surgical implications. *Surg Radiol Anat.* 2018; 40(7): 779–797, doi: [10.1007/s00276-018-1987-3](#), indexed in Pubmed: [29459992](#).
  30. Li X, Guan L, Zilundu PLM, et al. The applied anatomy and clinical significance of the proximal, V1 segment of vertebral artery. *Folia Morphol.* 2019; 78(4): 710–719, doi: [10.5603/FM.a2019.0039](#), indexed in Pubmed: [30949997](#).
  31. Maiti TK, Konar SK, Bir S, et al. Anomalous origin of the right vertebral artery: incidence and significance. *World Neurosurg.* 2016; 89: 601–610, doi: [10.1016/j.wneu.2015.11.018](#), indexed in Pubmed: [26897702](#).
  32. Manjunath KY. Posterior bridging of the atlas vertebra in south Indians. *Indian J Med Sci.* 2001; 55(9): 488–490, indexed in Pubmed: [11887298](#).
  33. Mitchell J. The incidence of the lateral bridge of the atlas vertebra. *J Anat.* 1998; 193 (Pt 2): 283–285, doi: [10.1046/j.1469-7580.1998.19320283.x](#), indexed in Pubmed: [9827643](#).
  34. Momma K, Matsuoka R, Takao A. Aortic arch anomalies associated with chromosome 22q11 deletion (CATCH 22). *Pediatr Cardiol.* 1999; 20(2): 97–102, doi: [10.1007/s002469900414](#), indexed in Pubmed: [9986884](#).
  35. Motomura M, Watanabe K, Tabira Y, et al. A case of duplicated right vertebral artery. *Kurume Med J.* 2018; 64(3): 69–73, doi: [10.2739/kurumemedj.MS643004](#), indexed in Pubmed: [29553097](#).
  36. Muralimohan S, Pande A, Vasudevan MC, et al. Suboccipital segment of the vertebral artery: a cadaveric study. *Neurol India.* 2009; 57(4): 447–452, doi: [10.4103/0028-3886.55610](#), indexed in Pubmed: [19770546](#).
  37. Newton TH. The anterior and posterior meningeal branches of the vertebral artery. *Radiology.* 1968; 91(2): 271–279, doi: [10.1148/91.2.271](#), indexed in Pubmed: [4298412](#).
  38. Ohkura K, Shiya N, Washiyama N, et al. Vertebral artery variations in thoracic aortic patients. *Eur J Cardiothorac Surg.* 2014; 46(1): 27–31, doi: [10.1093/ejcts/ezt609](#), indexed in Pubmed: [24446475](#).
  39. O'Malley AM, El Kininy WH, Debebe H, et al. A cadaveric study of aortic arch variation in an Irish population. *Ir J Med Sci.* 2018; 187(3): 853–858, doi: [10.1007/s11845-017-1729-2](#), indexed in Pubmed: [29288397](#).
  40. Paraskevas G, Papaziogas B, Tsonidis C, et al. Gross morphology of the bridges over the vertebral artery groove on the

- atlas. *Surg Radiol Anat.* 2005; 27(2): 129–136, doi: [10.1007/s00276-004-0300-9](https://doi.org/10.1007/s00276-004-0300-9), indexed in Pubmed: 15800734.
41. Patil ST, Meshram MM, Kamdi NY, et al. Study on branching pattern of aortic arch in Indian. *Anat Cell Biol.* 2012; 45(3): 203–206, doi: [10.5115/acb.2012.45.3.203](https://doi.org/10.5115/acb.2012.45.3.203), indexed in Pubmed: 23094209.
  42. Pękala PA, Henry BM, Pękala JR, et al. Prevalence of foramen arcuale and its clinical significance: a meta-analysis of 55,985 subjects. *J Neurosurg Spine.* 2017; 27(3): 276–290, doi: [10.3171/2017.1.SPINE161092](https://doi.org/10.3171/2017.1.SPINE161092), indexed in Pubmed: 28621616.
  43. Pick TP, Howden R. *Gray's anatomy, descriptive and surgical.* Bounty Books, New York 1901.
  44. Russo VM, Graziano F, Peris-Celda M, et al. The V(2) segment of the vertebral artery: anatomical considerations and surgical implications. *J Neurosurg Spine.* 2011; 15(6): 610–619, doi: [10.3171/2011.7.SPINE1132](https://doi.org/10.3171/2011.7.SPINE1132), indexed in Pubmed: 21905775.
  45. Schwedt K. Form- und Lagervariationen der extrakraniellen Arteria vertebralis im Angiogramm. Medical Dissertation, Würzburg 1978.
  46. Senoglu M, Gümüşalan Y, Yüksel KZ, et al. The effect of posterior bridging of C-1 on craniovertebral junction surgery. *J Neurosurg Spine.* 2006; 5(1): 50–52, doi: [10.3171/spi.2006.5.1.50](https://doi.org/10.3171/spi.2006.5.1.50), indexed in Pubmed: 16850956.
  47. Shin IY, Chung YG, Shin WH, et al. A morphometric study on cadaveric aortic arch and its major branches in 25 Korean adults: the perspective of endovascular surgery. *J Korean Neurosurg Soc.* 2008; 44(2): 78–83, doi: [10.3340/jkns.2008.44.2.78](https://doi.org/10.3340/jkns.2008.44.2.78), indexed in Pubmed: 19096697.
  48. Sim E, Vaccaro AR, Berzlanovich A, et al. Fenestration of the extracranial vertebral artery: review of the literature. *Spine.* 2001; 26: E139–E142.
  49. Singh R. Two rare variants of left vertebral artery. *J Craniofac Surg.* 2017; 28(4): 1105–1106, doi: [10.1097/SCS.00000000000003515](https://doi.org/10.1097/SCS.00000000000003515), indexed in Pubmed: 28207465.
  50. Taitz C, Nathan H. Some observations on the posterior and lateral bridge of the atlas. *Acta Anat (Basel).* 1986; 127(3): 212–217, doi: [10.1159/000146284](https://doi.org/10.1159/000146284), indexed in Pubmed: 3788469.
  51. Tardieu GG, Edwards B, Alonso F, et al. Aortic arch origin of the left vertebral artery: an anatomical and radiological study with significance for avoiding complications with anterior approaches to the cervical spine. *Clin Anat.* 2017; 30(6): 811–816, doi: [10.1002/ca.22923](https://doi.org/10.1002/ca.22923), indexed in Pubmed: 28547783.
  52. Toldt C, Hochstetter F. *Anatomischer Atlas, vol. 2, 27th ed.* Urban & Schwarzenberg, München 1979.
  53. Tubbs RS, Stetler W, Shoja MM, et al. The lateral atlantooccipital ligament. *Surg Radiol Anat.* 2007; 29(3): 219–223, doi: [10.1007/s00276-007-0196-2](https://doi.org/10.1007/s00276-007-0196-2), indexed in Pubmed: 17342571.
  54. Ulm AJ, Quiroga M, Russo A, et al. Normal anatomical variations of the V<sub>3</sub> segment of the vertebral artery: surgical implications. *J Neurosurg Spine.* 2010; 13(4): 451–460, doi: [10.3171/2010.4.SPINE09824](https://doi.org/10.3171/2010.4.SPINE09824), indexed in Pubmed: 20887142.
  55. Vanitha V, Teli CG, Kadlimatti HS. Bilateral posterior and lateral ponticles resulting in the formation of vertebral artery canal for the atlas: case report. *IOSR J Dental Med Sci.* 2014; 13(5): 82–84, doi: [10.9790/0853-13548284](https://doi.org/10.9790/0853-13548284).
  56. Vorster W, du Plooy PT, Meiring JH. Abnormal origin of internal thoracic and vertebral arteries. *Clin Anat.* 1998; 11(1): 33–37, doi: [10.1002/\(sici\)1098-2353\(1998\)11:1<33::aid-ca5>3.0.co;2-t](https://doi.org/10.1002/(sici)1098-2353(1998)11:1<33::aid-ca5>3.0.co;2-t).
  57. Wakao N, Takeuchi M, Nishimura M, et al. Vertebral artery variations and osseous anomaly at the C1-2 level diagnosed by 3D CT angiography in normal subjects. *Neuroradiology.* 2014; 56(10): 843–849, doi: [10.1007/s00234-014-1399-y](https://doi.org/10.1007/s00234-014-1399-y), indexed in Pubmed: 25001076.
  58. Wang X, Tang G, Li M. Bilateral extradural posterior inferior cerebellar artery origins where vertebral artery ascends between transverse foramina of C-2 and C-1, with simultaneous right double origin PICA: rare case report and literature review. *World Neurosurg.* 2019; 125: 234–239, doi: [10.1016/j.wneu.2019.01.233](https://doi.org/10.1016/j.wneu.2019.01.233), indexed in Pubmed: 30771546.
  59. Wight S, Osborne N, Breen AC. Incidence of ponticulus posterior of the atlas in migraine and cervicogenic headache. *J Manipulative Physiol Ther.* 1999; 22(1): 15–20, doi: [10.1016/s0161-4754\(99\)70100-4](https://doi.org/10.1016/s0161-4754(99)70100-4), indexed in Pubmed: 10029944.
  60. Woraputtaporn W, Ananteerakul T, Iamsaard S, et al. Incidence of vertebral artery of aortic arch origin, its level of entry into transverse foramen, length, diameter and clinical significance. *Anat Sci Int.* 2019; 94(4): 275–279, doi: [10.1007/s12565-019-00482-6](https://doi.org/10.1007/s12565-019-00482-6), indexed in Pubmed: 30806941.
  61. Yamaki Ki, Saga T, Hirata T, et al. Anatomical study of the vertebral artery in Japanese adults. *Anat Sci Int.* 2006; 81(2): 100–106, doi: [10.1111/j.1447-073x.2006.00133.x](https://doi.org/10.1111/j.1447-073x.2006.00133.x), indexed in Pubmed: 16800294.
  62. Zhu SW, Yang Y, Liu YG, et al. Anatomical features and clinical significance of radiculomuscular artery variants involving the suboccipital segment of vertebral artery: angiographic and cadaver studies. *Clin Neuroradiol.* 2018; 28(1): 75–80, doi: [10.1007/s00062-016-0520-5](https://doi.org/10.1007/s00062-016-0520-5), indexed in Pubmed: 27325366.



# The morphology and application of stem cells in digestive system surgery

M. Puculek<sup>1</sup>, J. Baj<sup>1</sup>, P. Portincasa<sup>2</sup>, M. Sitarz<sup>3</sup>, C. Grochowski<sup>1</sup>, E. Radzikowska<sup>4</sup>

<sup>1</sup>Department of Anatomy, Medical University of Lublin, Poland

<sup>2</sup>Clinica Medica "A. Murri", Department of Biomedical Sciences and Human Oncology, University of Bari Medical School, Bari, Italy

<sup>3</sup>Department of Conservative Dentistry with Endodontics, Medical University of Lublin, Poland

<sup>4</sup>Department of Plastic Surgery, Saint Elisabeth Hospital in Warsaw, Poland

[Received: 10 December 2019; Accepted: 23 January 2020]

**Background:** Stem cells constitute a group of cells which possess the ability to self-renew as well as the capacity to differentiate into a vast number of different cells within the human organism. Moreover, stem cells are able to undergo a potentially unlimited number of divisions and this characteristic is clinically essential. Specific fields of its application include treatment of diseases mainly in the field of haematology, orthopaedics, surgery, dentistry, and neurology.

**Materials and methods:** In the following work, the current knowledge concerning mechanisms of stem cell treatment in different parts of the digestive system with its diseases as well as adjacent therapy for surgery has been revised.

**Results:** Stem cells therapy may be used in the treatment of various diseases of different parts of the digestive system. This also applies to the end part of the digestive tract (proctological diseases) because stem cells can be used to treat fistulas. Liposuction allows more recovery of mesenchymal stem cells, compared to previous bone marrow harvesting methods. Despite the application of stem cells in the treatment of different diseases used for many years so far, the therapeutic use for the regeneration of the gastrointestinal tract is still rare and unfamiliar.

**Conclusions:** Regenerative medicine seems to be a promising tool in medical research, especially when insulated cells and designed biomaterials are taken into consideration. Major points of discussion include types of stem cells, their origin or differentiation for the treatment of many diseases. (Folia Morphol 2021; 80, 1: 13–19)

**Key words:** stem cell, digestive system surgery, fistula

## INTRODUCTION

Stem cells constitute a group of cells able to self-renew (i.e., have the ability to undergo a potentially unlimited number of divisions). Stem cells can differentiate into other, various types of cells. These unique attributes allow stem cells to be widely used in clinical medicine in at least three fields, namely: 1) therapy to replace lost or destroyed cell lines, or to modify the behaviour of other cells; 2) targets

of drug therapy, and 3) growth of differentiated tissue for studying disease models in vitro for drug development.

Specific areas of stem cell application allow treatment of different diseases in the field of haematology, orthopaedics, surgery, dentistry, and neurology [17]. Stem cells are used as a group of healing agents against cancer next to chemotherapy or hormone therapy (in leukaemia, lymphoma, myelodysplastic

**Table 1.** Various types of stem cells

Embryonic stem cells	Adult (somatic) stem cells	Induced pluripotent stem cells (artificial)	Foetal stem cells	Amniotic stem cells
Totipotent	Hematopoietic stem cells	–	Proper foetal stem cells	–
Pluripotent	Mesenchymal stem cells	–	Extraembryonic foetal stem cells	–
Multipotent	Neural stem cells	–	–	–
Oligopotent	Epithelial stem cells	–	–	–
Unipotent	Skin stem cells	–	–	–

syndrome and other haematopoietic cancers, as well as kidney and breast cancer or Ewing sarcoma), but they are also widely spread in aesthetic medicine [28, 43]. Moreover, stem cells constitute great potential to be applied in regenerative medicine, as well. In this context, the use of stem cells falls within an interdisciplinary area of medicine, and combines knowledge from such branches like tissue engineering and molecular biology, while supporting healing, regeneration and repair of damaged tissues.

In this review, we want to depict the current knowledge and importance of stem cell therapy in digestive system surgery.

## HEADING

Cell therapy takes advantage of human cells for the regeneration of damaged tissues or even the whole organs of the patient. The major problem of transplant rejection by the recipient organism can be significantly reduced or even eliminated by creating and transplanting organs which are grown in the laboratory from patient's own stem cells. Stem cells or progenitor cells are often used because of their internal regenerative potential for damaged tissues. The presence of stem cells in transplanted tissues increases angiogenesis (vascular formation), reduces inflammation, and prevents cell death. Furthermore, stem cells secrete numerous growth factors into their surrounding environment, including vascular endothelial growth factor (VEGF), and tumour growth factor [25, 52].

There are several types of stem cells, as reported in Table 1.

Stem cells are divided into embryonic stem cells and somatic (adult) stem cells. Among the embryonic stem cells there are totipotent stem cells (derived from a multi-cell embryo) which can differentiate into cell of any type, while the pluripotent stem cells can differentiate into any type of adult cell except for placental cells (when derived from the embryonic stem cell). Adult stem cells are multipotential, which

may give rise to several different types of cells, usually with similar properties (including haematopoietic cells) or unipotent cells, which may give rise to only one cell type.

Most of stem cells occur in foetal tissues and have the greatest regenerative capacity. Because of ethical reasons, stem cells used for treatment are received from adults. Mesenchymal stem cells (MSCs), which are primarily used, are isolated from almost all tissues (e.g., umbilical cord, periosteum, tendon, skin or muscle). MSCs are easily gained from adipose tissue by liposuction or by surgical excision of the tissue. This method is more effective than obtaining MSCs from bone marrow. Intensive research done by academia and industry has focused on mesenchymal stromal cells (MSCs) because of their unique features. Full use of MSCs' self-renewing ability is enabled because they can be easily isolated and expanded through in vitro culture [34].

Human MSCs derived from Wharton jelly (hWJ-hMSC) are multipotent cells which can differentiate into distinct branches of cells: osteogenic, chondrogenic, adipogenic cells, also can trans-differentiate into neural and glial cells. hWJ-hMSC line presents plasticity and has become an interesting and promising tool for the treatment of cellular and neurogenic regenerative medicine [5]. In addition, MSCs exert immunomodulatory activity and can differentiate into different lines, making them highly attractive for clinical applications in cell therapy according to the concept of developmental engineering [30]. Lenas et al. [30] studied the role of bone morphogenetic protein (BMP) signalling in the differentiation of adult mesenchymal progenitor cells, namely hMSC, towards articular cartilage. The combination of microfluidic system for screening soluble factors on three-dimensional microaggregates and synthetic compounds that selectively and specifically silenced the BMP pathway by targeting ALK2 and ALK3 receptors successfully developed a strategy effective in targeting the hMSC towards

stable articular cartilage, both in vitro and in vivo. Thus, restricting BMP signalling can program adult hMSC to stable chondrogenesis [38].

Stem cell therapy also has an important role in heart regeneration, i.e. MSCs (also isolated from adipose tissue), cardiac cell progenitor cells (CPC) and iPSC cells [11].

Usage of stem cells in medicine begins in 1950s when James Alexander Thomson and his associates of the University of Wisconsin-Madison transplanted bone marrow in order to treat leukaemia. Stem cell surgery started in the late 1990s by Dr. Thompson of the University of Wisconsin and researchers at Johns Hopkins University who reestablished the acquisition from human body tissues. High hopes are placed in MCS, but currently the American Society of Plastic Surgeons, World Health Organization (WHO) or other organizations do not publish official statistics on trends associated with the use of MCS in reconstructive surgery [21].

The mechanisms of action to use stem cells safely to regenerate the human body must be further explored. The United States Food and Drug Administration (FDA) in 2006 developed procedures to ensure the security of patients using stem cell therapy [26].

So far, stem cell treatment methods have been used in more than 70 diseases, including haematopoietic, cardiovascular [16, 18], tumour [6], metabolic [15], dermatological, immune, nervous, bone-joint, digestive, and some genetic diseases. Stem cells can be available in reconstructive surgery to replenish subcutaneous tissue defects. Applications include cancer treatment, radiotherapy, bone grafting, e.g. cranioplasty (filling of skull lid defects), filling of bone tissue defects, e.g. after resection of mandible tumours, cleft palate, treatment of chronic wounds (pressure sores, diabetic foot or as a result of ischaemia, infection), treatment of deep burns, aesthetic medicine and gastrointestinal surgery.

## **APPLICATION OF STEM CELLS IN ENDODONTICS**

The pulp of a human tooth is composed of a basic substance and cellular components, including odontoblasts, fibroblasts and dental stem cells (DSCs), which are MSCs. DSCs include dental pulp stem cells (DPSCs), stem cells from human exfoliated deciduous teeth (SHEDs), periodontal ligament stem cells (PDLSCs), stem cells from apical papilla (SCAP), and dental follicle progenitor cells (DFPCs). DPSCs are classified as specialised (postnatal) adult

stem cells, differentiated by the effects of external factors, leading to the interruption of the process of self-renewal of DSCs. DPSCs, unlike the MSCs, have a multipotential character, so they can vary to at least three different cell lines, such as osteoblasts, endothelial cells, nerve, and fat cells.

Dental pulp stem cells were first isolated in 2000 from perivascular tissue. It is essential to take into consideration the source of tissue donor cells. In general, the younger and less diverse tissue, the better conditions for obtaining DPSCs. Fully retained third molar teeth seems to be the best tissue sample to use. There are no breeding conditions at the present time that would only increase the number of DPSCs without discriminating. The characteristic properties of DPSCs allow them to be widely used in both dental and medical research as well as controlled tissue regeneration. Other options for using DPSCs include treatment of neurodegenerative diseases such as Parkinson's disease, filling bones in orthopaedics, and primarily in regenerative endodontics — regeneration of tissues in the newly emerging field of dentistry. Bone defects which are caused by malignancy, congenital deformities, traumas, osteoporosis, iatrogenic (surgical) and periodontal disease can be successfully treated using DPSCs and not only MSCs derived from bone marrow as it was in the past.

Regenerative endodontics uses stem cells to treat tooth pulp, perforation of root canal walls and bottom of the chamber, as well as necrosis of permanent teeth pulp with incomplete root formation by revascularisation and regeneration. Stem cells are an excellent source of controlled tissue regeneration. Obtaining poorly differentiated cells is difficult; however, possibilities of using DPSCs are very promising and, therefore, scientific studies in this area are still being conducted.

Stem cells are also used in therapy of different organs of digestive system. Despite using these cells for treatment of different diseases for many years, therapeutic use for the regeneration of gastrointestinal tract is still very rare and new [19, 24, 33, 46].

## **STOMACH**

Rashed et al. [42] studied the combined effect in rat model of MSCs gained from the bone marrow and nitric oxide (NO) inducer on injured gastric mucosa. Administration of either MSCs, NO, or MSCS with NO may exert a therapeutic effect on the mucosal lesion in gastric ulcer. Effects were tested by histopathology

after IV injection of MSCs and NO inducer. Mucosal regenerative changes and complete restoration in gastric ulcer occurred in the group receiving both stem cells and NO. Wang et al. [50] performed a study using the group of 48 clean grade male Wistar rats. The aim was to establish the model of gastric ulcer with acetic acid. Bone marrow mesenchymal stem cells (BMSCs) can accelerate ulcer healing by the secretion of VEGF, and improve the quality of ulcer cure. In the regenerative mucosa, the ulcer area, the mucosal thickness and the number of dilated glands by histology was measured by the authors. It turned out that the expression of VEGF was detected at ulcerative margin, using immunohistochemical method [50].

### LIVER

In animal models, BMSC have cured animal liver fibrosis. Only few studies exist which have been performed on humans. Zhang [53] studied 60 patients with liver fibrosis secondary to hepatolenticular degeneration. The efficacy of treatment (penicillamine group vs. combination penicillamine plus BMSCs group) was evaluated based on hepatic fibrosis, liver function, and serological markers. Combination therapy was related to lower cytokine levels, meaning a significant positive effect on liver fibrosis [53].

### PROCTOLOGY

Healing fistulas using stem cells is more accessible in proctology. Indeed, liposuction allows more recovery of fat cells, compared to previous bone marrow harvesting methods.

Anorectal abscesses and anal fistula are acute and chronic phase of inflammation of the anal crypt. They can also be the result of earlier abscess or rectal fistula. The causes include inflammatory bowel disease (Crohn's disease, ulcerative colitis), trauma, foreign body, radiotherapy, diseases of rectum and adjacent organs, immunosuppressive diseases and less common causes (endometriosis, radiation, tuberculosis etc.) [12, 13]. Fistula surgeries should save sphincter muscle without inducing postoperative incontinence. Sparing treatment aimed at avoiding complications, however, is less radical, which may result in recurrences. Furthermore, operations that save sphincter muscle apply only to simple fistulas [27]. Patients with high, branched fistulas cannot be operated by traditional surgical techniques. By the stem cell procedure, the excision of walls and light of the fistula includes specially prepared cell suspension and the

simultaneous stamping of the internal fistula. The cost of the extra procedure of picking and preparing the autogenous material for the slurry is certainly limited by the method. The method is effective in approximately 50% of the cases, with low invasiveness and repeatability [20]. Complications which can appear are associated with infection of the operated site and may refer to the liposuction stage and the fistula area [27]. The incontinence because of anal sphincter damage may also be a complication of surgical treatment, especially more aggressive. Several studies have been projected to elaborate minimally invasive treatment of rectovaginal and anal fistulas. The properties of adipose-derived stem cells significantly enhance a natural healing potency [4, 27, 39, 41, 51].

At the beginning of 21<sup>st</sup> century, stem cell therapy of perianal fistulas was introduced. In 2005, phase I clinical study was published, reporting the treatment of Crohn's disease with autologous adipose tissue-derived MSCs (ADSCs) [12]. Later on the same department conducted phase II study that evidenced that fistulas treated with ADSCs showed higher healing rates (71%) in comparison with fibrin glue treatment (16%) [13]. However, only few ADSC-treated patients remained free of recurrence for more than 3 years in long term observation [20].

In 2012, Herreros et al. [23] performed a multi-centre, randomized, single-blind, add-on clinical trial in 200 adult patients from 19 centres. Patients were randomly assigned to receive 20 million stem cells (group A, 64 patients), 20 million adipose-derived stem cells plus fibrin glue (group B, 60 patients), or fibrin glue (group C, 59 patients) after closure of the internal opening. Fistula healing was defined as reepithelisation of the external opening and absence of collection > 2 cm by magnetic resonance imaging. If the fistula had not healed at 12 weeks, a second dose (40 million stem cells in groups A and B) was administered. Patients were evaluated at 24 to 26 weeks (primary end point) and at 1 year (long-term follow-up). Serious adverse events were absent. In treatment of complex fistula-in-ano, a dose of 20 or 60 million adipose-derived stem cells alone or in combination with fibrin glue was a safe treatment. In the comparison of three groups no statistically significant differences were found [23].

Garcia-Olmo et al. [14] reported similar findings. They check the results of stem-cell therapy under a Compassionate-use Programme for patients with recurrent anal fistulae. There were found ten patients

who had previously undergone multiple surgical interventions that had failed to resolve the fistula. During this research they closed the internal opening, which was followed by local implant of stem cells in the fistula-tract wall. The main cell type selected for implant was autologous expanded adipose-derived stem cells. Outcome at 8 weeks was classified as response or partial response. Evaluation 1 year after the intervention confirmed if complete healing of the fistula occurred. No adverse reactions or complications related to stem-cell therapy occurred during the study period. Both studies independently of each other proved that stem cells are safe and useful for treating anal fistulae [14, 47].

A recent multicentre phase III study by Panes et al. [40] showed that 50% of the patients receiving ADSC treatment had 6 months remission, compared to 34% of patients on placebo treatment. Dietz et al. [10] showed complete recovery in 83% of treated patients. A meta-analysis performed by Lightner et al. [31], which analysed severe phase I, II and III trials, reports healing rates ranging from 27–83%, with positive early results in more than half of analysed studies.

## **GASTROINTESTINAL TRACT**

Recently, results of first human phase 1/2 trial using genetically modified MSCs for treatment of adenocarcinomas of the hepatobiliary and gastrointestinal tract have been published. During the progression of the tumour, MSCs are recruited into the stroma of the tumour. That process causes its growth and metastasis [22, 29, 32, 45]. MSCs have several abilities, which make them perfect vehicle for tumour directed therapy. They have the ability to migrate into deep layers of the tumour microenvironment and differentiate into the tumour stroma cells. Moreover, they have low immunogenicity and can be easily isolated and multiplied [9, 36, 37, 44]. The therapy was confirmed to be acceptably safe and tolerable, which was consistent with phase 1 study results [49]. One study presented signs of activity with stable disease in five of ten patients; however, no impact on tumour markers and size was observed [48].

## **WOUNDS**

The process of wound healing involves multiple growth factors and stem cells and should be studied both in terms of research and clinical relevance. One of the surgical challenges is the problematic wound healing and ulceration in radiation-damaged tissue.

These problems may appear in non-healing surgical wounds, especially in patients with cachexia or with cancers after radiotherapy. Some ongoing clinical trials with growth factors have already produced very promising therapeutic results which can be used in earlier mentioned cases [1–3, 7, 8].

Grafting fat tissue in an irradiated area can improve the quality of the skin and has regenerative effects. The case study by Mohan and Singh [35] describes healing of a chronic ulcer resistant to other ways of treatment using fat tissue transfer (which contains adipose-derived stem cells). A 67-year-old woman with a chronic, non-healing ulcer in her leg had a squamous cell carcinoma excised, followed by radiotherapy. After each of the multiple excisions, ulcer continued to cause symptoms. The patient underwent a wide local excision and split-thickness skin grafting. Afterwards fat was infiltrated around and under the ulcer. In the histological examination there was a post-radiation dermatitis with no evidence of malignancy. After a period in which dressings were used, a reduction in ulcer size was observed and more fat was infiltrated around the lesion. Two months later, the ulcer had been fully healed without recurrence. This case shows the potential of adipose tissue to improve damaged skin. Its use will be able to change the need for complex surgical procedures [35].

Such cases prove that modern therapies, especially cellular and protein therapies, are the future of skin treatments such as burns and chronic wounds. The increased amount of growth factors associated with inflammation, which is often seen in chronic wounds, may also carry a potential risk of cancer transformation. Cellular and humoral mechanisms of neoplasm have many similarities with physiological wound healing (stem cell involvement, inflammation, increased proliferation, similar growth factors). However, proper wound healing is strictly controlled and after it is completed, it begins a natural self-limitation process which is completely different compared to the neoplasm process [1–3, 7, 8].

## **SUMMARY**

One of the most promising directions in medical research is regenerative medicine, which main tools are insulated cells and specially designed biomaterials. Discussions in recent years deal with the type of stem, their origin or differentiation that will be most useful in the treatment of many diseases but there is no clear answer. However, it is obvious that different types of cells will play different roles in relation to the



tasks they are supposed to fulfil. Bone marrow cells have been introduced into clinical practice earlier than other types of cells. The ability of mesenchymal bone marrow stem cells to differentiate into many cell types makes their use an attractive cell source for tissue and organ regeneration. However, the challenge still remains to effectively differentiate MSCs towards the desired cell lines and to maintain the phenotype of previously differentiated cells. Fully verifiable results of stem cell treatment are still growing [1, 7].

## REFERENCES

1. Abdallah BM, Kassem M. The use of mesenchymal (skeletal) stem cells for treatment of degenerative diseases: current status and future perspectives. *J Cell Physiol.* 2009; 218(1): 9–12, doi: [10.1002/jcp.21572](https://doi.org/10.1002/jcp.21572), indexed in Pubmed: [18726996](https://pubmed.ncbi.nlm.nih.gov/18726996/).
2. Auxenfans C, Lequeux C, Perrusel E, et al. Adipose-derived stem cells (ASCs) as a source of endothelial cells in the reconstruction of endothelialized skin equivalents. *J Tissue Eng Regen Med.* 2012; 6(7): 512–518, doi: [10.1002/term.454](https://doi.org/10.1002/term.454), indexed in Pubmed: [21755603](https://pubmed.ncbi.nlm.nih.gov/21755603/).
3. Bielefeld K, Amini-Nik S, Alman B. Cutaneous wound healing: recruiting developmental pathways for regeneration. *Cell Mol Life Sci.* 2012; 70(12): 2059–2081, doi: [10.1007/s00018-012-1152-9](https://doi.org/10.1007/s00018-012-1152-9).
4. Blumetti J, Abcarian A, Quinteros F, et al. Evolution of treatment of fistula in ano. *World J Surg.* 2012; 36(5): 1162–1167, doi: [10.1007/s00268-012-1480-9](https://doi.org/10.1007/s00268-012-1480-9), indexed in Pubmed: [22362043](https://pubmed.ncbi.nlm.nih.gov/22362043/).
5. Bonilla-Porras AR, Velez-Pardo C, Jimenez-Del-Rio M. Fast transdifferentiation of human Wharton's jelly mesenchymal stem cells into neurospheres and nerve-like cells. *J Neurosci Methods.* 2017; 282: 52–60, doi: [10.1016/j.jneumeth.2017.03.005](https://doi.org/10.1016/j.jneumeth.2017.03.005), indexed in Pubmed: [28286110](https://pubmed.ncbi.nlm.nih.gov/28286110/).
6. Budny A, Grochowski C, Kozłowski P, et al. Obesity as a tumour development triggering factor. *Ann Agric Environ Med.* 2019; 26(1): 13–23, doi: [10.26444/aaem/100664](https://doi.org/10.26444/aaem/100664), indexed in Pubmed: [30922023](https://pubmed.ncbi.nlm.nih.gov/30922023/).
7. Chen Ye, Shao JZ, Xiang LX, et al. Mesenchymal stem cells: a promising candidate in regenerative medicine. *Int J Biochem Cell Biol.* 2008; 40(5): 815–820, doi: [10.1016/j.biocel.2008.01.007](https://doi.org/10.1016/j.biocel.2008.01.007), indexed in Pubmed: [18295530](https://pubmed.ncbi.nlm.nih.gov/18295530/).
8. Cherubino M, Rubin JP, Miljkovic N, et al. Adipose-derived stem cells for wound healing applications. *Ann Plast Surg.* 2011; 66(2): 210–215, doi: [10.1097/SAP.0b013e3181e6d06c](https://doi.org/10.1097/SAP.0b013e3181e6d06c), indexed in Pubmed: [21200308](https://pubmed.ncbi.nlm.nih.gov/21200308/).
9. Chulpanova DS, Kitaeva KV, Tazetdinova LG, et al. Application of mesenchymal stem cells for therapeutic agent delivery in anti-tumor treatment. *Front Pharmacol.* 2018; 9: 259, doi: [10.3389/fphar.2018.00259](https://doi.org/10.3389/fphar.2018.00259), indexed in Pubmed: [29615915](https://pubmed.ncbi.nlm.nih.gov/29615915/).
10. Dietz AB, Dozois EJ, Fletcher JG, et al. Autologous mesenchymal stem cells, applied in a bioabsorbable matrix, for treatment of perianal fistulas in patients with crohn's disease. *Gastroenterology.* 2017; 153(1): 59–62.e2, doi: [10.1053/j.gastro.2017.04.001](https://doi.org/10.1053/j.gastro.2017.04.001), indexed in Pubmed: [28400193](https://pubmed.ncbi.nlm.nih.gov/28400193/).
11. Gapska P, Kurpisz M. Perspective in optimization of stem cell therapies for heart regeneration. *Postepy Hig Med Dosw (Online).* 2017; 71(0): 975–987, doi: [10.5604/01.3001.0010.6665](https://doi.org/10.5604/01.3001.0010.6665), indexed in Pubmed: [29225198](https://pubmed.ncbi.nlm.nih.gov/29225198/).
12. García-Olmo D, García-Arranz M, Herreros D, et al. A phase I clinical trial of the treatment of Crohn's fistula by adipose mesenchymal stem cell transplantation. *Dis Colon Rectum.* 2005; 48(7): 1416–1423, doi: [10.1007/s10350-005-0052-6](https://doi.org/10.1007/s10350-005-0052-6), indexed in Pubmed: [15933795](https://pubmed.ncbi.nlm.nih.gov/15933795/).
13. Garcia-Olmo D, Herreros D, Pascual I, et al. Expanded adipose-derived stem cells for the treatment of complex perianal fistula: a phase II clinical trial. *Dis Colon Rectum.* 2009; 52(1): 79–86, doi: [10.1007/DCR.0b013e3181973487](https://doi.org/10.1007/DCR.0b013e3181973487), indexed in Pubmed: [19273960](https://pubmed.ncbi.nlm.nih.gov/19273960/).
14. Garcia-Olmo D, Guadalajara H, Rubio-Perez I, et al. Recurrent anal fistulae: limited surgery supported by stem cells. *World J Gastroenterol.* 2015; 21(11): 3330–3336, doi: [10.3748/wjg.v21.i11.3330](https://doi.org/10.3748/wjg.v21.i11.3330), indexed in Pubmed: [25805941](https://pubmed.ncbi.nlm.nih.gov/25805941/).
15. Grochowski C, Blicharska E, Baj J, et al. Serum iron, magnesium, copper, and manganese levels in alcoholism: a systematic review. *Molecules.* 2019; 24(7), doi: [10.3390/molecules24071361](https://doi.org/10.3390/molecules24071361), indexed in Pubmed: [30959950](https://pubmed.ncbi.nlm.nih.gov/30959950/).
16. Grochowski C, Litak J, Kulesza B, et al. Size and location correlations with higher rupture risk of intracranial aneurysms. *J Clin Neurosci.* 2018; 48: 181–184, doi: [10.1016/j.jocn.2017.10.064](https://doi.org/10.1016/j.jocn.2017.10.064), indexed in Pubmed: [29100674](https://pubmed.ncbi.nlm.nih.gov/29100674/).
17. Grochowski C, Radzikowska E, Maciejewski R. Neural stem cell therapy-Brief review. *Clin Neurol Neurosurg.* 2018; 173: 8–14, doi: [10.1016/j.clineuro.2018.07.013](https://doi.org/10.1016/j.clineuro.2018.07.013), indexed in Pubmed: [30053745](https://pubmed.ncbi.nlm.nih.gov/30053745/).
18. Grochowski C, Staśkiewicz G. Ultra high field TOF-MRA: A method to visualize small cerebral vessels. 7T TOF-MRA sequence parameters on different MRI scanners — Literature review. *Neurol Neurochir Pol.* 2017; 51(5): 411–418, doi: [10.1016/j.pjnns.2017.06.011](https://doi.org/10.1016/j.pjnns.2017.06.011), indexed in Pubmed: [28774679](https://pubmed.ncbi.nlm.nih.gov/28774679/).
19. Gronthos S, Mankani M, Brahimi J, et al. Postnatal human dental pulp stem cells (DPSCs) in vitro and in vivo. *Proc Natl Acad Sci U S A.* 2000; 97(25): 13625–13630, doi: [10.1073/pnas.240309797](https://doi.org/10.1073/pnas.240309797), indexed in Pubmed: [11087820](https://pubmed.ncbi.nlm.nih.gov/11087820/).
20. Guadalajara H, Herreros D, De-La-Quintana P, et al. Long-term follow-up of patients undergoing adipose-derived adult stem cell administration to treat complex perianal fistulas. *Int J Colorectal Dis.* 2012; 27(5): 595–600, doi: [10.1007/s00384-011-1350-1](https://doi.org/10.1007/s00384-011-1350-1), indexed in Pubmed: [22065114](https://pubmed.ncbi.nlm.nih.gov/22065114/).
21. Hall SS. Choroba na szalce. *Świat Nauki.* 2011; 236(4): 40–43.
22. Hanahan D, Coussens LM. Accessories to the crime: functions of cells recruited to the tumor microenvironment. *Cancer Cell.* 2012; 21(3): 309–322, doi: [10.1016/j.ccr.2012.02.022](https://doi.org/10.1016/j.ccr.2012.02.022), indexed in Pubmed: [22439926](https://pubmed.ncbi.nlm.nih.gov/22439926/).
23. Herreros MD, Garcia-Arranz M, Guadalajara H, et al. FATT Collaborative Group. Autologous expanded adipose-derived stem cells for the treatment of complex cryptoglandular perianal fistulas: a phase III randomized clinical trial (FATT 1: fistula Advanced Therapy Trial 1) and long-term evaluation. *Dis Colon Rectum.* 2012; 55(7): 762–772, doi: [10.1097/DCR.0b013e318255364a](https://doi.org/10.1097/DCR.0b013e318255364a), indexed in Pubmed: [22706128](https://pubmed.ncbi.nlm.nih.gov/22706128/).
24. Huang GTJ, Gronthos S, Shi S. Mesenchymal stem cells derived from dental tissues vs. those from other sources: their biology and role in regenerative medicine. *J Dent Res.* 2009; 88(9): 792–806, doi: [10.1177/0022034509340867](https://doi.org/10.1177/0022034509340867), indexed in Pubmed: [19767575](https://pubmed.ncbi.nlm.nih.gov/19767575/).

25. Hunziker R. Regenerative medicine. National Institutes of Health. 2010.
26. Kmiecik B, Skotny-Krakowian A, Rybak Z. Krótki przegląd na temat komórek macierzystych. *Acta Bio-Optica et Informatica Medica. Inżynieria Biomedyczna*. 2015; 21(1): 40–45.
27. Kołodziejczak M, Ciesielski P. Powikłania po leczeniu ropni i przetok odbytu. *Borgis — Nowa Medycyna*. 2016; 3: 114–126.
28. Koźlik M, Wójcicki P. The use of stem cells in plastic and reconstructive surgery. *Adv Clin Exp Med*. 2014; 23(6): 1011–1017, doi: [10.17219/acem/37360](https://doi.org/10.17219/acem/37360), indexed in Pubmed: [25618130](https://pubmed.ncbi.nlm.nih.gov/25618130/).
29. LeBleu VS, Kalluri R. A peek into cancer-associated fibroblasts: origins, functions and translational impact. *Dis Model Mech*. 2018; 11(4), doi: [10.1242/dmm.029447](https://doi.org/10.1242/dmm.029447), indexed in Pubmed: [29686035](https://pubmed.ncbi.nlm.nih.gov/29686035/).
30. Lenas P, Moos M, Luyten FP. Developmental engineering: a new paradigm for the design and manufacturing of cell-based products. Part I: from three-dimensional cell growth to biomimetics of in vivo development. *Tissue Eng Part B Rev*. 2009; 15(4): 381–394, doi: [10.1089/ten.TEB.2008.0575](https://doi.org/10.1089/ten.TEB.2008.0575), indexed in Pubmed: [19505199](https://pubmed.ncbi.nlm.nih.gov/19505199/).
31. Lightner AL, Wang Z, Zubair AC, et al. A Systematic Review and Meta-analysis of Mesenchymal Stem Cell Injections for the Treatment of Perianal Crohn's Disease: Progress Made and Future Directions. *Dis Colon Rectum*. 2018; 61(5): 629–640, doi: [10.1097/DCR.0000000000001093](https://doi.org/10.1097/DCR.0000000000001093), indexed in Pubmed: [29578916](https://pubmed.ncbi.nlm.nih.gov/29578916/).
32. Lin HJ, Lin J. Seed-in-Soil: pancreatic cancer influenced by tumor microenvironment. *Cancers (Basel)*. 2017; 9(7), doi: [10.3390/cancers9070093](https://doi.org/10.3390/cancers9070093), indexed in Pubmed: [28753978](https://pubmed.ncbi.nlm.nih.gov/28753978/).
33. Mackiewicz A, Lekszycki T, Olczak-Kowalczyk D. Komórki macierzyste z miazgi zęba ludzkiego (DPSCs). Charakterystyka i możliwości zastosowania — przegląd piśmiennictwa. *Borgis — Nowa Stomatologia*. 2014; 4: 178–182.
34. Mizukami A, Swiech K. Mesenchymal stromal cells: from discovery to manufacturing and commercialization. *Stem Cells Int*. 2018; 2018: 4083921, doi: [10.1155/2018/4083921](https://doi.org/10.1155/2018/4083921), indexed in Pubmed: [30057622](https://pubmed.ncbi.nlm.nih.gov/30057622/).
35. Mohan A, Singh S. Use of fat transfer to treat a chronic, non-healing, post-radiation ulcer: a case study. *J Wound Care*. 2017; 26(5): 272–273, doi: [10.12968/jowc.2017.26.5.272](https://doi.org/10.12968/jowc.2017.26.5.272), indexed in Pubmed: [28475446](https://pubmed.ncbi.nlm.nih.gov/28475446/).
36. Moradian Tehrani R, Verdi J, Nouredini M, et al. Mesenchymal stem cells: A new platform for targeting suicide genes in cancer. *J Cell Physiol*. 2018; 233(5): 3831–3845, doi: [10.1002/jcp.26094](https://doi.org/10.1002/jcp.26094), indexed in Pubmed: [28703313](https://pubmed.ncbi.nlm.nih.gov/28703313/).
37. Niess H, Thomas MN, Schiergens TS, et al. Genetic engineering of mesenchymal stromal cells for cancer therapy: turning partners in crime into Trojan horses. *Innov Surg Sci*. 2016; 1(1): 19–32, doi: [10.1515/iss-2016-0005](https://doi.org/10.1515/iss-2016-0005), indexed in Pubmed: [31579715](https://pubmed.ncbi.nlm.nih.gov/31579715/).
38. Occhetta P, Pigeot S, Rasponi M, et al. Developmentally inspired programming of adult human mesenchymal stromal cells toward stable chondrogenesis. *Proc Natl Acad Sci U S A*. 2018; 115(18): 4625–4630, doi: [10.1073/pnas.1720658115](https://doi.org/10.1073/pnas.1720658115), indexed in Pubmed: [29666250](https://pubmed.ncbi.nlm.nih.gov/29666250/).
39. Ortiz H, Marzo J, Ciga MA, et al. Randomized clinical trial of anal fistula plug versus endorectal advancement flap for the treatment of high cryptoglandular fistula in ano. *Br J Surg*. 2009; 96(6): 608–612, doi: [10.1002/bjs.6613](https://doi.org/10.1002/bjs.6613), indexed in Pubmed: [19402190](https://pubmed.ncbi.nlm.nih.gov/19402190/).
40. Panés J, García-Olmo D, Assche GV, et al. Expanded allogeneic adipose-derived mesenchymal stem cells (Cx601) for complex perianal fistulas in Crohn's disease: a phase 3 randomised, double-blind controlled trial. *Lancet*. 2016; 388(10051): 1281–1290, doi: [10.1016/s0140-6736\(16\)31203-x](https://doi.org/10.1016/s0140-6736(16)31203-x).
41. Piejko M, Romaniszyn M, Borowczyk-Michałowska J, et al. Cell therapy in surgical treatment of fistulas. Preliminary results. *Pol Przegl Chir*. 2017; 89(3): 48–51, indexed in Pubmed: [28703110](https://pubmed.ncbi.nlm.nih.gov/28703110/).
42. Rashed L, Gharib DM, Hussein RE, et al. Combined effect of bone marrow derived mesenchymal stem cells and nitric oxide inducer on injured gastric mucosa in a rat model. *Tissue Cell*. 2016; 48(6): 644–652, doi: [10.1016/j.tice.2016.09.006](https://doi.org/10.1016/j.tice.2016.09.006), indexed in Pubmed: [27751517](https://pubmed.ncbi.nlm.nih.gov/27751517/).
43. Reichenberger M, Mueller W, Schäfer A, et al. Fibrin-Embedded adipose derived stem cells enhance skin flap survival. *Stem Cell Rev Rep*. 2012; 8(3): 844–853, doi: [10.1007/s12015-011-9341-8](https://doi.org/10.1007/s12015-011-9341-8).
44. Rhee KJ, Lee JIn, Eom YW. Mesenchymal stem cell-mediated effects of tumor support or suppression. *Int J Mol Sci*. 2015; 16(12): 30015–30033, doi: [10.3390/ijms161226215](https://doi.org/10.3390/ijms161226215), indexed in Pubmed: [26694366](https://pubmed.ncbi.nlm.nih.gov/26694366/).
45. Rizvi S, Khan SA, Hallemeier CL, et al. Cholangiocarcinoma - evolving concepts and therapeutic strategies. *Nat Rev Clin Oncol*. 2018; 15(2): 95–111, doi: [10.1038/nrclinonc.2017.157](https://doi.org/10.1038/nrclinonc.2017.157), indexed in Pubmed: [28994423](https://pubmed.ncbi.nlm.nih.gov/28994423/).
46. Sedgley CM, Botero TM. Dental stem cells and their sources. *Dent Clin North Am*. 2012; 56(3): 549–561, doi: [10.1016/j.cden.2012.05.004](https://doi.org/10.1016/j.cden.2012.05.004), indexed in Pubmed: [22835537](https://pubmed.ncbi.nlm.nih.gov/22835537/).
47. Theodoropoulos G, Mihailidou E, Kolovos G. The role of stem cells in the treatment of anal fistulas. *Digestive System Diseases*. 2019: 113–135, doi: [10.1007/978-3-030-11965-2\\_7](https://doi.org/10.1007/978-3-030-11965-2_7).
48. von Einem JC, Guenther C, Volk HD, et al. Treatment of advanced gastrointestinal cancer with genetically modified autologous mesenchymal stem cells: Results from the phase 1/2 TREAT-ME-1 trial. *Int J Cancer*. 2019; 145(6): 1538–1546, doi: [10.1002/ijc.32230](https://doi.org/10.1002/ijc.32230), indexed in Pubmed: [30801698](https://pubmed.ncbi.nlm.nih.gov/30801698/).
49. von Einem JC, Peter S, Günther C, et al. Treatment of advanced gastrointestinal cancer with genetically modified autologous mesenchymal stem cells — TREAT-ME-1 — a phase I, first in human, first in class trial. *Oncotarget*. 2017; 8(46): 80156–80166, doi: [10.18632/oncotarget.20964](https://doi.org/10.18632/oncotarget.20964), indexed in Pubmed: [29113291](https://pubmed.ncbi.nlm.nih.gov/29113291/).
50. Wang G, Li C, Fan X, et al. Effect of bone marrow mesenchymal stem cells on gas-tric ulcer repairing]. *Zhongguo Xiu Fu Chong Jian Wai Ke Za Zhi*. 2015; 29(7): 889–892.
51. Whiteford MH. Perianal abscess/fistula disease. *Clin Colon Rectal Surg*. 2007; 20(2): 102–109, doi: [10.1055/s-2007-977488](https://doi.org/10.1055/s-2007-977488), indexed in Pubmed: [20011384](https://pubmed.ncbi.nlm.nih.gov/20011384/).
52. Yoshimura K, Asano Y, Aoi N, et al. Progenitor-enriched adipose tissue transplantation as rescue for breast implant complications. *Breast J*. 2010; 16(2): 169–175, doi: [10.1111/j.1524-4741.2009.00873.x](https://doi.org/10.1111/j.1524-4741.2009.00873.x), indexed in Pubmed: [19912236](https://pubmed.ncbi.nlm.nih.gov/19912236/).
53. Zhang D. A clinical study of bone mesenchymal stem cells for the treatment of hepatic fibrosis induced by hepatolenticular degeneration. *Genet Mol Res*. 2017; 16(1), doi: [10.4238/gmr16019352](https://doi.org/10.4238/gmr16019352), indexed in Pubmed: [28301671](https://pubmed.ncbi.nlm.nih.gov/28301671/).

# Course variability of the atlantic (V3) segment of vertebral artery: anatomical study with clinical implications

M.K. Ciołkowski<sup>1, 2</sup> , B. Ciszek<sup>1, 3</sup> 

<sup>1</sup>Department of Descriptive and Clinical Anatomy, Centre of Biostructure Research, Medical University of Warsaw, Poland

<sup>2</sup>Department of Neurosurgery, Children's Memorial Health Institute, Warsaw, Poland

<sup>3</sup>Department of Neurosurgery, Prof. Bogdanowicz Children Hospital, Warsaw, Poland

[Received: 16 November 2019; Accepted: 27 January 2020]

**Background:** The atlantic segment of vertebral artery (V3) located at the centre of the crano-vertebral junction is known for its variability and asymmetry, and is either the target or on the way of numerous procedures in this region. The aim of the study was to visualise variability of V3 segment.

**Materials and methods:** The V3 segment was studied in 49 specimens of the suboccipital region injected with coloured gelatine. Direct measurements were performed and probabilistic maps were created using digital photography.

**Results:** The V3 segment has wavy course with possible lateral and significant postero-inferior expansions. In relation to the foramen transversarium the V3 reached up to 5 mm laterally, 23 mm posteriorly, 27 mm medially and up to 11 mm downward. Looking from the medial aspect the course of the V3 is less predictable compared to the lateral approach. Linear measurements and probabilistic maps revealed significant variability and large range of variation. There were 11 cases of V3 tortuosity found in studied material.

**Conclusions:** The complex and variable spatial conformation of V3 makes individual diagnostic and preoperative approach necessary. (Folia Morphol 2021; 80, 1: 20–25)

**Key words:** atlanto-occipital joint, crano-cervical junction, suboccipital triangle, crano-vertebral junction, vertebral artery anatomy, vertebro-basilar system

## INTRODUCTION

Last decades brought significant advance in diagnosis and treatment of the crano-vertebral junction (CVJ) deformities and injuries. The dedicated instrumentation and surgical techniques have been developed to accommodate specific structure and function of this region. Very close and complex relationships of the vertebral artery (VA) and the CVJ structures make an individual approach with precise vascular imaging a gold standard and necessity in many cas-

es. Nevertheless, awareness of anatomical variability range and spectrum of possible anomalies is essential for surgeon planning and analysing the diagnostic imaging, as well as in any emergency or unexpected situations. The midline approaches to the posterior cranial fossa, foramen magnum and upper part of the cervical vertebral canal are naturally limited on both sides by the VAs piercing the dura and reaching cranial cavity. Moreover the lateral and far-lateral posterior fossa approaches have the VA in the centre



of operative field and frequently involve its dissection or transposition. The arch of VA surrounding the atlanto-occipital joint may be in conflict with spine instrumentation in degenerative or traumatic cases. The aim of this study was to estimate the variability of the atlantic segment of the VA as it is a crucial anatomical structure during procedures around CVJ.

The VA is divided into four segments according to their topography and development: V1 — prevertebral, V2 — cervical (also referred to as intertransversary), V3 — atlantic, and V4 — intracranial (actually — intradural) [8]. Despite some ambiguity in understanding borders of these segments by different authors, the atlantic segment is defined here as the one extending between foramen transversarium of atlas vertebra and dura crossing [10, 17]. This assumption is justified on embryological and topographical grounds.

## MATERIALS AND METHODS

Fifty specimens of the posterior CVJ structures and suboccipital soft tissues harvested during routine forensic autopsies were studied in accordance with local ethico-legal regulations. The studied individuals had no medical records or signs on gross examination of direct trauma or surgical interventions within CVJ. There were no signs of significant atherosclerosis or stenosis of the studied arteries. A case of atlas assimilation was excluded from this cohort and described elsewhere [4], while another case of VA duplication around the posterior arch of atlas [5] was left within the analysed group. Cadavers examined here included 34 males and 15 females, aged 18 to 91 years (mean 53 years, standard deviation 18.25).

The arteries were injected with coloured gelatine and specimens were fixed in formalin. After gross dissection of the nuchal muscles to the level of suboccipital musculature a microsurgical dissection was performed to visualise whole length of the V3 bilaterally — total 98 segments of VA were studied.

All linear measurements of the specimens were taken directly using calliper of 0.02 mm accuracy and basic statistical analysis was performed with Statistica 9.0. Preparations were immobilised with the triangle determined by the tips of the transverse processes and the posterior tubercle set in the horizontal plane. Digital pictures were taken of each specimen in three cardinal planes (superior, posterior and lateral views) with reference ruler. Further analysis was performed separately for each side to avoid influence of variability in the general width of the atlas vertebra. Based

on the calibrated images the simplified models of VA projections were created using the Bézier Curves tool in CorelDraw® X3 graphic platform. If more than four 'nodes' of the Bézier Curves tool were needed to model the superior V3 projections due to sudden turn or inflection of the artery curvature, such vessel was regarded as tortuous. The vector graphics models were superimposed on each other with different landmarks used as a common point. Using the transparency tool in the multi-layered picture, the probabilistic maps of VA position were created (each projection model of all 49 was given transparency level of 98%) and presented on 1 mm grid.

## RESULTS

The VA soon after leaving the foramen transversarium bent posteriorly and downwards above the posterior bar of the transverse process in all studied specimens and started a course curved in all three planes. In some cases the tip of the VA arch 'hanged' down as far as 11 mm below the upper surface of the transverse process as observed from the side (Fig. 1). Thus the proximal arm of the V3 run downward and the distal one — upward to reach the groove on the posterior arch of atlas.

Observation of the superior views revealed three general types of initial VA course after leaving the foramen transversarium of atlas. Rarely the artery directed immediately towards midline (type A — 4.1% on the left and 14.3% on the right). Sometimes it first took sagittal course defined arbitrary as fitting the 10° parasagittal angle (type B — 10.2% on the left and 28.6% on the right). Most often it run slightly lateral (type C — 85.7% on the left and 57.1% on the right) to form wider arch surrounding the atlanto-occipital joint (Fig. 2).

The superior projections were analysed from two points of view. Taking the foramen transversarium and the beginning of the V3 segment as the common point resulted in creation of maps simulating location of the VA as if dissected from the side of the transverse process (Fig. 3). The arch of V3 seems to be predictable and conformed to the geometry of the superior articular surface and the whole joint when seen on these pictures. Relatively large 'danger zone' compared to the probabilistic map should also be noticed — it is caused by cases of tortuous V3 separately presented further. It extends from the common point laterally up to 5 mm, posteriorly up to 23 mm and medially up to 27 mm. In order to simulate dissection

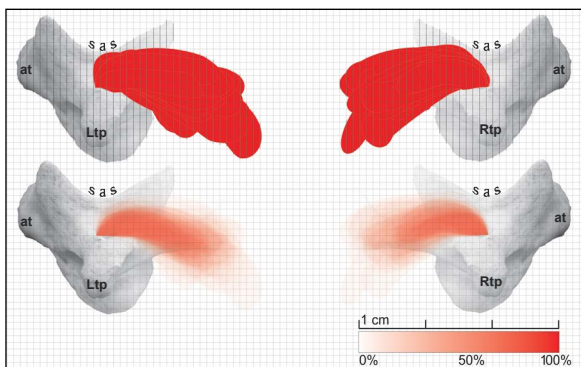


**Figure 1.** Cumulated lateral views of the left and right V3: marking the 'danger zone' above and the probabilistic map below; at — anterior tubercle of atlas; Ltp, Rtp — left and right transverse process; sas — superior articular surface of atlas.

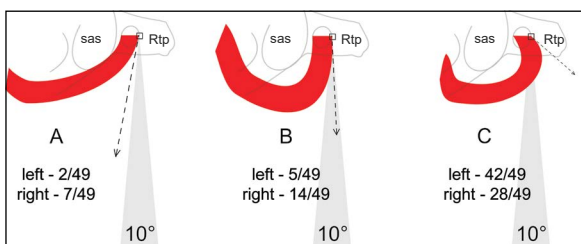


**Figure 2.** Three possible general directions of the V3 course after leaving the foramen transversarium (type A — medial, B — sagittal, and C — lateral) presented on selected cases; Rtp — right transverse process; sas — superior articular surface of atlas.

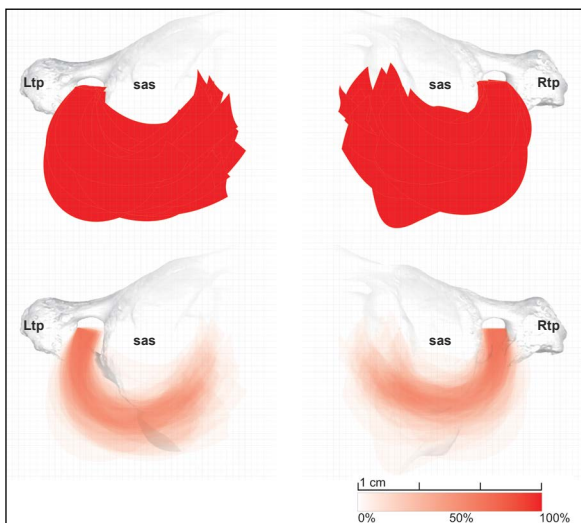


**Figure 3.** Superior views of the left and right V3 with the common origin in the foramen transversarium: the 'danger zone' above and the probabilistic map below; Ltp, Rtp — left and right transverse process; sas — superior articular surface of atlas.

from the midline, other maps were created taking as the common point the crossing of the inner border

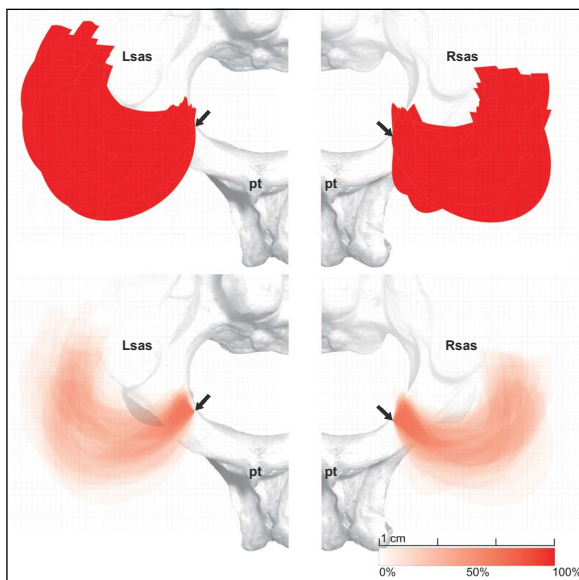


**Figure 4.** Superior views of the left and right V3 with the common point set close to the dura crossing (arrow): the 'danger zone' above and the probabilistic map below; Lsas, Rsas — left and right superior articular surface of atlas; pt — posterior tubercle of atlas.

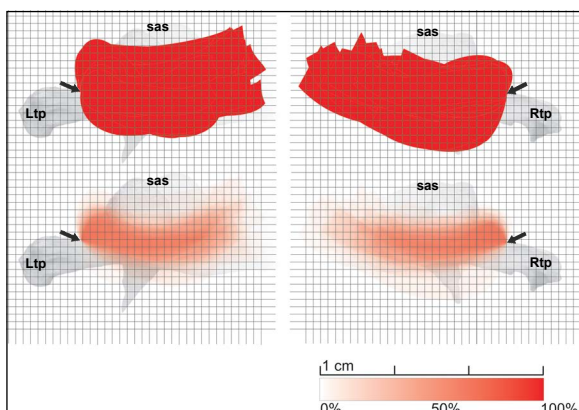


**Figure 5.** Posterior views of the left and right V3 with the common point in the foramen transversarium (arrow): the 'danger zone' above and the probabilistic map below; Ltp, Rtp — left and right transverse process; sas — superior articular surface of atlas.

of the posterior atlantic arch with the outer margin of the VA arch (Fig. 4). These pictures strikingly differ from the previous ones. Except for the part of the V3 located in its bony groove on the posterior arch of atlas the chance of conflict with the VA is evenly distributed in the large area extending up to 30 mm laterally and 16 mm posteriorly.

Analysis of the posterior views of the V3 (Fig. 5) together with the lateral views gives general picture of the waveform course of this artery around the atlanto-occipital joint. The posterior views were also

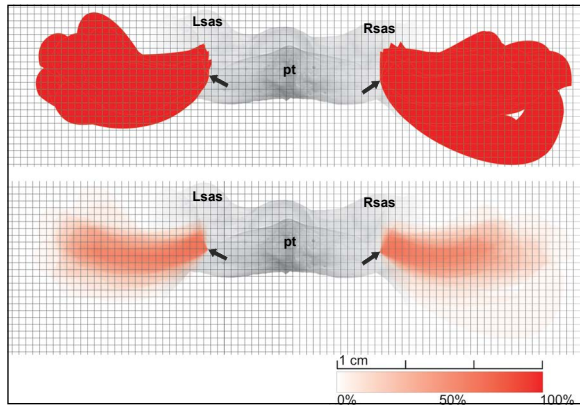


**Figure 6.** Posterior views of the left and right V3 with the common point at the medial (distal) end (arrow): the 'danger zone' above and the probabilistic map below; Lsas, Rsas — left and right superior articular surface; pt — posterior tubercle of atlas.

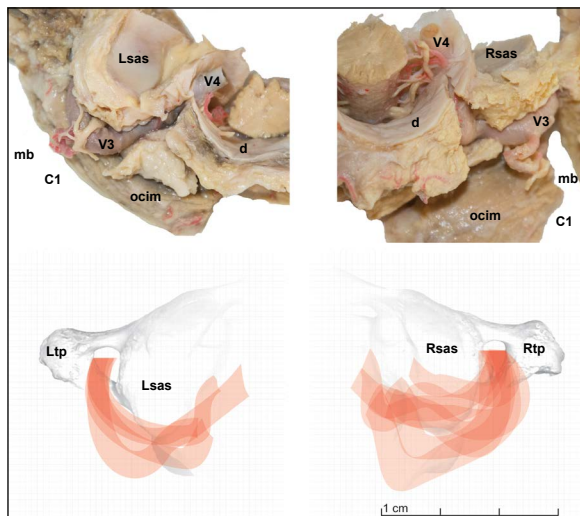


**Figure 7.** Above — left and right exemplary cases of tortuous V3. Pictures taken from oblique perspective. Below — superimposed superior views of all tortuous cases; Lsas, Rsas — left and right superior articular surface of atlas; d — dura mater cut right below foramen magnum; ocim — obliquus inferior capitis muscle; V3, V4 — atlantic and intradural segments of vertebral artery; mb — muscular branch of V3; C1 — dorsal ramus of spinal nerve C1; Ltp, Rtp — left and right transverse process of atlas.

studied taking the distal end of the arteries as the common point with the conclusions similar to these obtained from the horizontal projections (Fig. 6).

In the great majority of cases it was enough to use four 'nodes' of the Bézier Curves tool to model the superior projections of the VA. However in some cases (11.2%) additional nodes were necessary to model the more complex V3 curvature. These cases were referred to as tortuous: 4 on the left and 7 on the right side (Fig. 7). Abnormalities in the course of

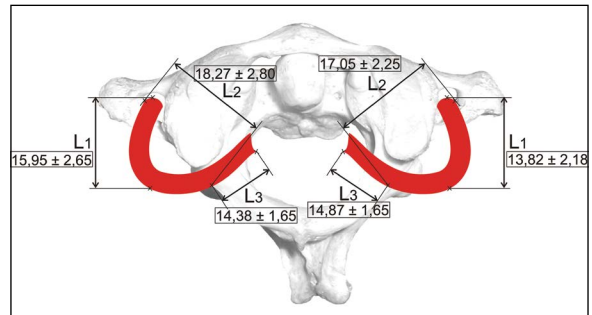


**Figure 8.** The mean values and standard deviations of direct linear measurements of the V3 (L1-L3) — details in text.

the V3 concentrate along its distal part. The tortuous vertebral arteries were found in rather shallow bony grooves of the atlas.

The length of the proximal part of the V3 arch (L1) was measured from the transversary foramen to the tip of the arch — usually located in the axis of the atlanto-occipital joint (Fig. 8). The chord of the V3 arch (L2) was measured between the foramen transversarium and the crossing of the artery with the posterior arch of atlas. The index L1/L2 represents general shape of the arch — the bigger value, the arch is "slimmer". The sagittal dimension of the left V3 arches is significantly longer compared to the right arteries, and the left arches are more "slim" (Table 1). The length of the artery in the bony groove until the dura crossing (L3) was comparable on both sides.

## DISCUSSION

Lang and Kessler [12] described the dorsal course of the VA after leaving the foramen transversarium of atlas vertebra as a rule. Ulm et al. [15] basing on dissections and angiographic studies described course of the VA after leaving the foramen transversarium of atlas as medial. The studies of Abd El-Bary et al. [1] and Cacciola et al. [3] revealed sagittal or medial course of the VA. These discrepancies may originate from subjective observations of the course of the VA, which are difficult because of waveform shape of the artery and oblique axis of the atlanto-occipital joint. On the other hand Yamaguchi et al. [16] in study based on the large radiological material pointed the postero-lateral protrusion of the VA over the posterior arch of atlas. In the material studied for this paper we found wide range of shapes of the V3 arch, where wide arches with initially postero-lateral course prevail. As the arteries dissected in our study were relatively stiff after prior injection *in situ*, fixation and

**Table 1.** Statistical analysis of the V3 linear measurements in millimetres

	Left			Right			P
	Range	Mean	± SD	Range	Mean	± SD	
L1	9.86–23.22	15.95	2.65	9.70–20.70	13.82	2.18	0.000039
L2	12.08–27.84	18.27	2.80	13.24–24.60	17.05	2.25	0.020087
L1/L2	0.55–1.43	0.88	0.16	0.61–1.18	0.82	0.11	0.016084
L3	11.10–18.92	14.38	1.65	10.72–18.46	14.87	1.65	0.139438

L1 — length of the V3 arch, L2 — width of the V3 arch, L3 — length of the V3 in the bony groove. SD — standard deviation, p-value for t-Student test of significant difference between sides

preservation of anchoring bone or dura, observations and measurements are more likely to represent reality.

The asymmetry of the initial course of VA in horizontal plane with more frequent medial deviation of the right artery and lateral course in great majority of left arteries could be explained by handedness; however, there are no data to verify such hypothesis in our material. Right hand and eye domination of the investigator might have also influenced presented results, at least partially.

The authors of clinically oriented papers [1, 6, 9, 11–13, 15] analysed statistically linear measurements taken mainly in cardinal planes or between arbitrary chosen and easily defined points, which is of limited value in the operative field and makes understanding the real position of the vessel difficult. This problem we tried to overcome with our graphic method. General assessment of our probabilistic maps indicates higher uncertainty of VA location when it is dissected from the medial side. Thus the strategy to avoid seeing ‘naked’ artery as long as possible is justified [17]. On the other hand, starting dissection at the transverse process one should remember about possible lateral and significant posterior expansion of the VA. Also the uncertain vertical extent of V3, both above the level of foramen transversarium and below, needs caution when approached from different directions [2].

The course of the VA may interfere with screw trajectory for occipito-cervical fusion procedures. The entry point for occipital condyle screw is located in the middle of posterior aspect of the condyle — i.e. above and anterior to the V3 arch [7, 11, 13]. Lee et al. [13] showed that in a significant number of patients there is no sufficient space between the occipital squama and V3 to perform this procedure. The so-called “slim” V3 arches may give more space for instrumentation. Any approach to the posterior aspect of the occipital condyle may be disturbed

by tortuosity of the VA as well. The screw is inserted into the lateral mass of atlas in the middle of its width, right below the pedicle of posterior arch — i.e. anterior and below the V3 arch. The cases of V3 arch “hanging” down from the plane of transverse process and posterior arch would need cautious transposition.

Few researchers measured the length of the V3 [1, 3, 12] and due to different definitions of the segment or subsegments their results are not comparable. The range of V3 lengths revealed in our study makes any predictions pointless from practical point of view — planning of intravascular interventions or vascular reconstructions evidently needs individual approach. Significant subset of tortuous V3 revealed in our study may explain many unexpected intraoperative difficulties [14].

Comparison between graphic maps with extensive ‘danger zones’ and mean values of linear measurements, even completed with some information on distribution, shows general pitfall of using statistical information derived from anatomical studies. If complications are to be avoided, the range of deviations is to be analysed, not the statistical mean values. Three-dimensional statistical analysis of the VA has not been so far conducted to our best knowledge, and the maps presented here may serve as some simple forerunner of it. In this context, it seems the modern radiological studies allowing volume reconstructions are best suited for exact preoperative planning [4, 5, 9–11].

## CONCLUSIONS

The atlantic segment of the VA usually has wave-form course from the foramen transversarium, behind the atlanto-occipital joint, toward the cranio-spinal dura. Nevertheless, possibility of tortuosity or significant deviations in shape and location of this artery make detailed, three-dimensional preoperative diag-

nostics necessary in cases where direct exposure of the VA is expected. The abilities of navigation devices and virtual reality should be widely used both in patient management and in training to avoid complications and give sense of variability range.

### Acknowledgements

The authors appreciate cooperation and support from Prof. Paweł Krajewski, head of the Forensic Medicine Department in Medical University of Warsaw.

### REFERENCES

1. Abd El-Bary TH, Dujovny M, Ausman JI. Microsurgical anatomy of the atlantal part of the vertebral artery. *Surg Neurol.* 1995; 44(4): 392–400; discussion 400, doi: [10.1016/0090-3019\(95\)00033-x](https://doi.org/10.1016/0090-3019(95)00033-x), indexed in Pubmed: [8553261](https://pubmed.ncbi.nlm.nih.gov/8553261/).
2. Bruneau M, Cornelius JF, George B. Antero-lateral approach to the V3 segment of the vertebral artery. *Neurosurgery.* 2006; 58(1 Suppl): ONS29–35; discussion ONS29, doi: [10.1227/01.neu.0000193930.74183.42](https://doi.org/10.1227/01.neu.0000193930.74183.42), indexed in Pubmed: [16479626](https://pubmed.ncbi.nlm.nih.gov/16479626/).
3. Cacciola F, Phalke U, Goel A. Vertebral artery in relationship to C1-C2 vertebrae: an anatomical study. *Neurol India.* 2004; 52(2): 178–184, indexed in Pubmed: [15269464](https://pubmed.ncbi.nlm.nih.gov/15269464/).
4. Ciołkowski MK, Krajewski P, Ciszek B. A case of atlas assimilation: description of bony and soft structures. *Surg Radiol Anat.* 2014; 36(8): 833–836, doi: [10.1007/s00276-013-1235-9](https://doi.org/10.1007/s00276-013-1235-9), indexed in Pubmed: [24240817](https://pubmed.ncbi.nlm.nih.gov/24240817/).
5. Ciołkowski MK, Krajewski P, Ciszek B. A case of vertebral artery duplication at the level of atlas: anatomical description. *Eur Spine J.* 2014; 23 Suppl 2: 285–287, doi: [10.1007/s00586-014-3304-0](https://doi.org/10.1007/s00586-014-3304-0), indexed in Pubmed: [24748466](https://pubmed.ncbi.nlm.nih.gov/24748466/).
6. Duan S, Lv S, Ye F, et al. Imaging anatomy and variation of vertebral artery and bone structure at craniocervical junction. *Eur Spine J.* 2009; 18(8): 1102–1108, doi: [10.1007/s00586-009-0925-9](https://doi.org/10.1007/s00586-009-0925-9), indexed in Pubmed: [19288143](https://pubmed.ncbi.nlm.nih.gov/19288143/).
7. El-Gaidi MA, Eissa EM, El-Shaarawy EAA. Free-hand placement of occipital condyle screws: a cadaveric study. *Eur Spine J.* 2014; 23(10): 2182–2188, doi: [10.1007/s00586-014-3488-3](https://doi.org/10.1007/s00586-014-3488-3), indexed in Pubmed: [25070792](https://pubmed.ncbi.nlm.nih.gov/25070792/).
8. FIPAT Terminologia Neuroanatomica. Federative International Programme for Anatomical Terminology. 2017. <https://fipat.library.dal.ca/> (February 2017).
9. Ha W, Yang D, Gu S, et al. Anatomical study of suboccipital vertebral arteries and surrounding bony structures using virtual reality technology. *Med Sci Monit.* 2014; 20: 802–806, doi: [10.12659/MSM.890840](https://doi.org/10.12659/MSM.890840), indexed in Pubmed: [24829084](https://pubmed.ncbi.nlm.nih.gov/24829084/).
10. Harnsberger HR, Osborn AG, Macdonald AJ. *Imaging anatomy: brain, head & neck, spine.* Amirsys Pub Inc 2006.
11. La Marca F, Zubay G, Morrison T, et al. Cadaveric study for placement of occipital condyle screws: technique and effects on surrounding anatomic structures. *J Neurosurg Spine.* 2008; 9(4): 347–353, doi: [10.3171/SPI.2008.9.10.347](https://doi.org/10.3171/SPI.2008.9.10.347), indexed in Pubmed: [18939920](https://pubmed.ncbi.nlm.nih.gov/18939920/).
12. Lang J, Kessler B. About the suboccipital part of the vertebral artery and the neighboring bone-joint and nerve relationships. *Skull Base Surg.* 1991; 1(1): 64–72, doi: [10.1055/s-2008-1056982](https://doi.org/10.1055/s-2008-1056982), indexed in Pubmed: [17170824](https://pubmed.ncbi.nlm.nih.gov/17170824/).
13. Lee HJ, Choi DY, Shin MH, et al. Anatomical feasibility for safe occipital condyle screw fixation. *Eur Spine J.* 2016; 25(6): 1674–1682, doi: [10.1007/s00586-016-4399-2](https://doi.org/10.1007/s00586-016-4399-2), indexed in Pubmed: [26831538](https://pubmed.ncbi.nlm.nih.gov/26831538/).
14. Osorio JA, Benet A, Hess CP, et al. Primary vertebral artery reanastomosis during retrosigmoid skull base approach following iatrogenic near-transection with monopolar electrocautery. *Neurosurgery.* 2014; 10 Suppl 4: 631–639, doi: [10.1227/NEU.0000000000000526](https://doi.org/10.1227/NEU.0000000000000526), indexed in Pubmed: [25181436](https://pubmed.ncbi.nlm.nih.gov/25181436/).
15. Ulm AJ, Quiroga M, Russo A, et al. Normal anatomical variations of the V<sub>3</sub> segment of the vertebral artery: surgical implications. *J Neurosurg Spine.* 2010; 13(4): 451–460, doi: [10.3171/2010.4.SPINE09824](https://doi.org/10.3171/2010.4.SPINE09824), indexed in Pubmed: [20887142](https://pubmed.ncbi.nlm.nih.gov/20887142/).
16. Yamaguchi S, Eguchi K, Kiura Y, et al. Posterolateral protrusion of the vertebral artery over the posterior arch of the atlas: quantitative anatomical study using three-dimensional computed tomography angiography. *J Neurosurg Spine.* 2008; 9(2): 167–174, doi: [10.3171/SPI/2008/9/8/167](https://doi.org/10.3171/SPI/2008/9/8/167), indexed in Pubmed: [18764749](https://pubmed.ncbi.nlm.nih.gov/18764749/).
17. Youssef AS, Uribe JS, Ramos E, et al. Interfascial technique for vertebral artery exposure in the suboccipital triangle: the road map. *Neurosurgery.* 2010; 67(2 Suppl Operative): 355–361, doi: [10.1227/NEU.0b013e3181f741f7](https://doi.org/10.1227/NEU.0b013e3181f741f7), indexed in Pubmed: [21099558](https://pubmed.ncbi.nlm.nih.gov/21099558/).

# Stereological analysis of hippocampus in rat treated with chemotherapeutic agent oxaliplatin

J. Sadeghinezhad<sup>1</sup>, I. Amrein<sup>2, 3</sup>

<sup>1</sup>Department of Basic Sciences, Faculty of Veterinary Medicine, University of Tehran, Iran

<sup>2</sup>Institute of Anatomy, Division of Functional Neuroanatomy, University of Zurich, Switzerland

<sup>3</sup>Department of Health Sciences and Technology, ETH, Zurich, Switzerland

[Received: 12 December 2019; Accepted: 27 January 2020]

**Background:** Oxaliplatin (OX) has been widely used for treatment of colorectal and other cancers. Adverse effect of OX and other anticancer agents on cognition have been reported, but studies on the effects of chemotherapy on brain structure are scarce. This study describes the morphometrical features of the hippocampus structures in rat following OX treatment using design-based stereological methods.

**Materials and methods:** Ten male Wistar rats were randomised into two groups. The rats from OX group received 2.4 mg/kg OX in vehicle for 5 consecutive days every week for 2 weeks intraperitoneally. Controls received vehicle only. Cavalieri's method and the optical fractionator method were used for volume and neuron estimation, respectively.

**Results:** Cavalieri's method was used to estimate volume and showed that the volume of the hippocampus was significantly decreased in OX group ( $31.84 \pm 1.24 \text{ mm}^3$ ) compared with the vehicle control group ( $36.95 \pm 3.48 \text{ mm}^3$ ). The optical fractionator method was used to estimate neuron number and showed that the number of neurons in dentate gyrus, cornu ammonis 1 and 3 in OX group ( $8.147 \pm 2.84 \times 10^5$ ,  $4.257 \pm 0.59 \times 10^5$  and  $2.133 \pm 0.22 \times 10^5$ , respectively) did not differ from those of vehicle control group ( $7.36 \pm 1.42 \times 10^5$ ,  $3.521 \pm 0.54 \times 10^5$  and  $1.989 \pm 0.46 \times 10^5$ , respectively).

**Conclusions:** These findings suggested that OX treatment induces loss of hippocampal volume without neuronal loss which might help to clarify the mechanism by which OX affects cognition and to improve preventive treatment strategies. (Folia Morphol 2021; 80, 1: 26–32)

**Key words:** stereology, hippocampus, oxaliplatin, chemotherapy, rat

## INTRODUCTION

Chemotherapy in many cancer types have increased survival times in patients. However, cognitive dysfunctions, referred to as “chemobrain”, such as impairments in attention and concentration, verbal and visual memory and processing speed have been reported after systemic chemotherapy [7, 41]. There are numerous reports regarding adverse effect of different anticancer agents such as methotrexate

[29, 37, 42, 46], 5-fluorouracil [8, 11], cyclophosphamide [9, 36], doxorubicin [23, 27], paclitaxel [19], vincristine [5, 35] and cytosine arabinoside [26] on cognition in human and animal experimental models. Chemotherapy agents, which inhibit tumour cell proliferation, can also effect on non-tumour cell proliferation in the brain [7].

Oxaliplatin (OX) is a third-generation platinum drug which has been widely used alone or with other

chemotherapeutic agents for treatment of colorectal cancer and other carcinomas including ovarian, breast and lung cancers [34, 40]. It is able to react with DNA to create DNA intrastrand adducts, which block DNA synthesis and induce apoptosis in cancer cells and rapidly dividing cells [43]. OX induces peripheral neuropathy [38], crosses the blood–brain barrier and accumulates in cerebrospinal and extracellular fluid in the brain [17, 18], which indicates that the drug can have a direct effect on brain function and structure. Treatment with OX has been shown to induce cognitive impairment in laboratory animals [9, 10, 39]. Furthermore, cellular damage in the hippocampus has been related to the loss of memory function in rats following OX administration [4, 7]. Other platinum compounds such as cisplatin, have also been reported to produce cognitive dysfunction and central neurological problems [28, 48].

The hippocampus, as the key structure in learning and the formation of memory is an appropriate site for investigating the mechanisms involved in some of the cognitive problems arisen by the chemotherapeutic agents [4].

Designed-base stereology enables unbiased and precise quantitative analysis of three-dimensional structures [15]. It is one of the important techniques for the morphometrical evaluation of the hippocampus, which contain important information about the memory function [14]. The morphometrical features of the hippocampus following chemotherapy have not been thoroughly investigated using stereology. Assessment of the effect of OX on hippocampus volume using Cavalieri's method and neuronal number in different regions of the hippocampus using optical disector/fractionator, as a gold standard for efficient, unbiased number estimation in neuroscience, may contribute to evaluate the risks of the treatment and possibly help improve preventive strategies.

## **MATERIALS AND METHODS**

### **Animals**

Ten adult (12–15 weeks) male Wistar rats (Pasteur Institute, Tehran, Iran) were used for the experiment. Animals were housed in large acrylic cages with free access to food and water under controlled light (12 h light and dark cycle) and temperature ( $22 \pm 2^\circ\text{C}$ ). The rats were allowed to acclimatise for 1 week before experimentation.

All experimental procedures involving animals in this study were conducted in accordance with the

standard guide for the care and use of laboratory animals of the University of Tehran, Tehran, Iran.

### **Drug administration**

Rats were randomly divided into OX-treated and vehicle control groups. The rats from OX group received 2.4 mg/kg OX dissolved in 5% glucose solution (vehicle) for 5 consecutive days per week for 2 weeks intraperitoneally (IP) and the vehicle control was administered 5% glucose solution. The chosen dose of OX was in accordance with that commonly used for neurotoxic evaluation of the agent in previous animal studies [4].

### **Tissue sampling and stereological methods**

Rats were euthanized 21 days after treatment using thiopental (50 mg/kg IP). Then, transcardial perfusion fixation of the animals was done using 10% formalin. The brains were removed and the left hemisphere of each animal was fixed in same fixative, dehydrated and embedded in glycol methacrylate (Technovit 7100, Heraeus Kulzer GmbH, Wehrheim/Ts, Germany) according to the manufacturer's instructions.

Embedded brains were cut frontally using a rotary microtome with 20 micrometre thickness. Every 20<sup>th</sup> section was collected using the principle of systematic uniform random sampling, which is known as the section sampling fraction ( $ssf = 1/20$ ). On average, this sampling scheme provided 13 (11–15) sections per animal. Sections were mounted, dried and stained in Giemsa solution [16].

Hippocampal volume and principal cell numbers were estimated using StereoInvestigator 10 software (MBF Bioscience, Williston, VT, USA). The hippocampus including dentate gyrus (DG) and cornu ammonis (CA) were determined in the sections using rat brain atlas of Paxinos and Watson (2007) [33]. DGs were recognised due to horseshoe-shape with small and densely packed neurons. The CA2 region in this study was considered as belong to the CA3 region because the CA2 is very small and the boundaries between these two regions are not detectable. The border between the CA3 and CA1 is defined by a small transition zone between the two regions (Fig. 1) [21].

### **Estimation of the volume**

Estimation of total volume of the hippocampus was done using test points on each section (Fig. 2A). The volume was estimated by Cavalieri estimator us-

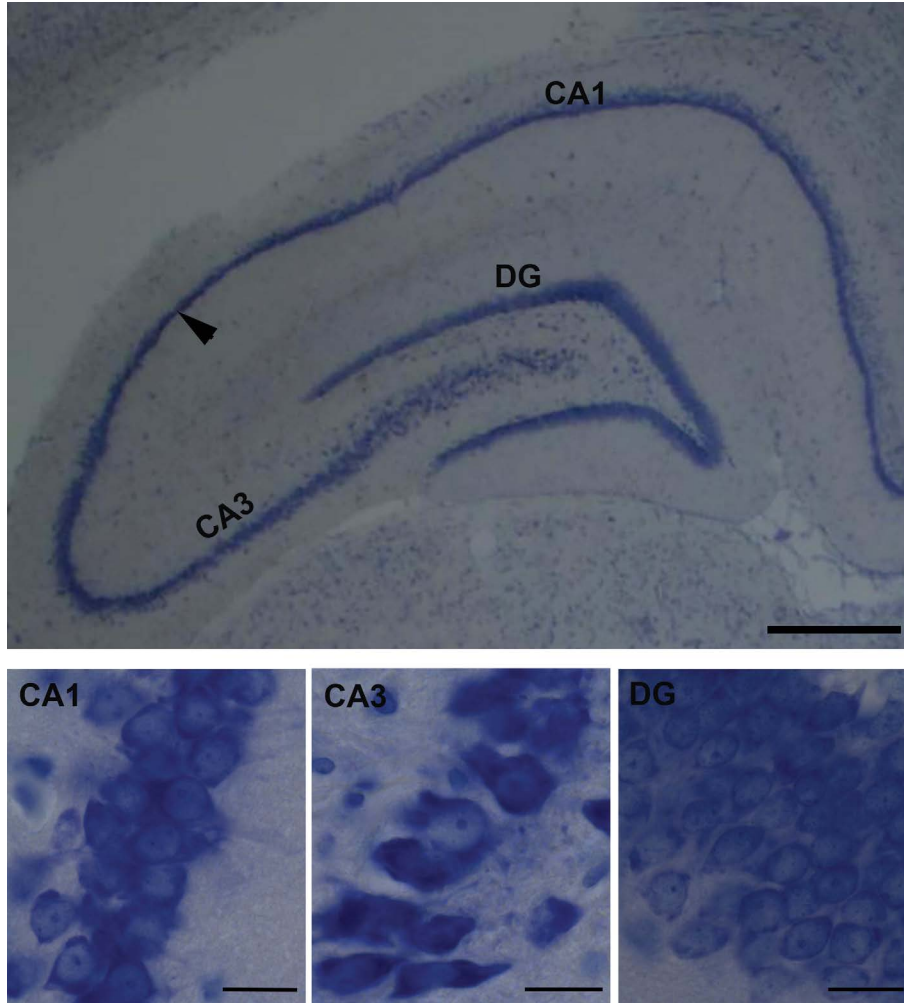


**Figure 1.** Histological coronal section of the hippocampus (scale bar = 200  $\mu\text{m}$ ) with magnification of the CA1, CA3 and dentate gyrus (scale bar = 500  $\mu\text{m}$ ). Arrowhead mark boundary between CA1 and CA3.

ing the following equation [15]:  $V = \Sigma P \times \text{ssf} \times T \times \frac{a}{p}$ , where  $\Sigma P$  is the total number of points hitting the structure;  $\text{ssf}$  (1/20) is the section sampling fraction;  $T$  (20  $\mu\text{m}$ ) is the section thickness and  $a/p$  ( $9 \times 10^4 \mu\text{m}^2$ ) represents the area per point.

#### Estimation of the number of neurons

The optical fractionator was used for number estimation of pyramidal cells and granular cells in CA and DG, respectively. First, the contours of the dentate gyrus and the CA1 and CA3 regions were delineated at low magnification. Then, selected regions were analysed by systematic random sampling at high magnification. A known fraction of the each section was assessed by moving the microscope motorised stage in regular step length in x and y directions and applying an unbiased counting frame sized to count the neurons of specific region (Fig. 2B).

For DG, a step length of 180  $\mu\text{m}$  and counting frame size of  $12 \times 12 \mu\text{m}$  was used, for CA1 a step length of 240  $\mu\text{m}$  and frame size of  $20 \times 20 \mu\text{m}$ , and for CA3 a step length of 190  $\mu\text{m}$  and frame size of  $24 \times 24$  was applied. The counting frame was focused through 10  $\mu\text{m}$  of the section thickness, which corresponds to disector height. Section thickness was measured at every 4–5 sampling location.

The total number of cells in the granular cells (DG) and pyramidal cells (CA1 and CA3) in the left hemisphere was calculated using the following formula [6, 32] —  $N = 1/\text{SSF} \times 1/\text{ASF} \times 1/\text{HSF} \times \Sigma Q^-$ , where  $\text{HSF} = h / tQ^-$  for  $tQ^- = \Sigma t_i q_i^- / \Sigma q_i^-$ ,  $\Sigma Q^-$ : total count of particles sampled;  $\text{SSF}$ : the section sample fraction;  $\text{ASF}$ : the area sample fraction (frame size /  $x, y$  step length);  $\text{HSF}$ : the height sampling fraction;  $h$ : the disector height (10  $\mu\text{m}$  in this study);  $tQ^-$ : the number-weighted mean section thickness;  $t_i$ : the



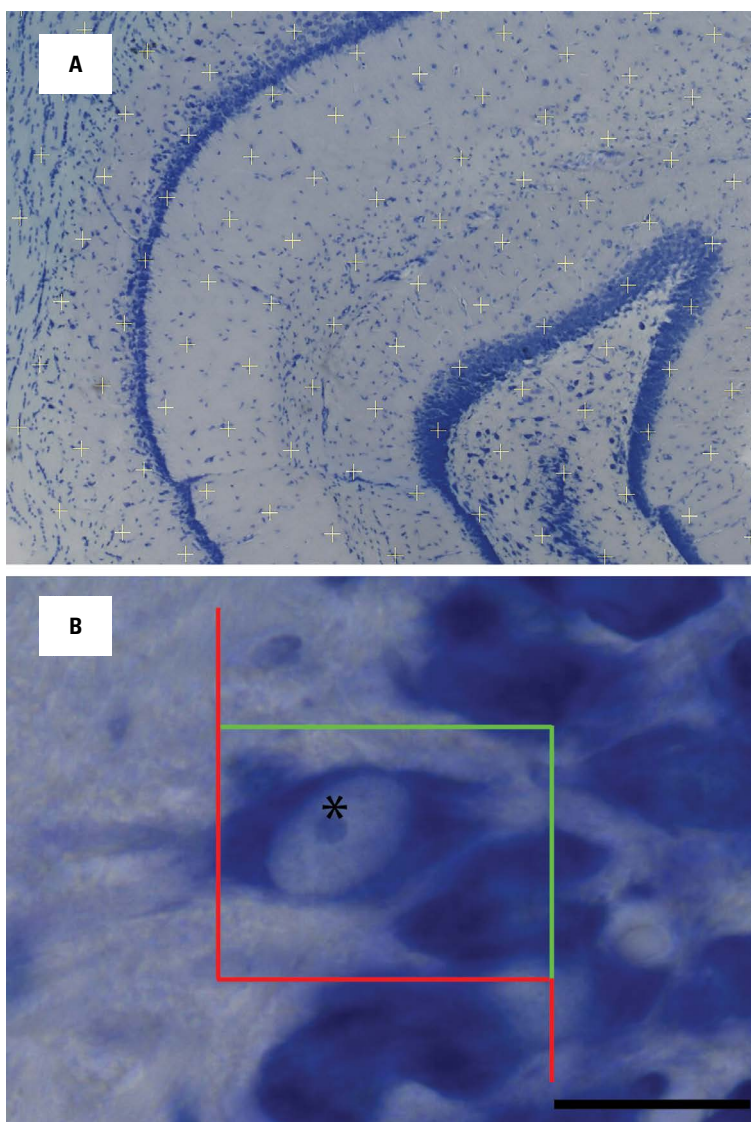


**Figure 2.** Stereological method for estimating hippocampal volume and neuronal number; **A.** Example of a point grid on histological section of the hippocampus. The total number of points hitting the whole hippocampus was counted; **B.** Example of an unbiased counting frame used for optical disector method. The cells which their nucleolus came into focus within dissector’s height if they were completely inside the counting frame or touched the accepted lines (green lines) were counted. Here one neuron (asterisk) was counted (scale bar = 200  $\mu\text{m}$ ).

section thickness in the  $i^{\text{th}}$  counting frame with a cell count of  $q_i^-$  in the disector.

### Statistical analysis

The coefficient of error (CE) of the volume and the number estimates was calculated as previously described [13]. T-test was used for statistical analysis. A value of  $p < 0.05$  was considered significant.

## RESULTS

The results showed that the volume of the hippocampus was significantly decreased after OX treatment compared with the vehicle control group ( $p < 0.05$ ). The related volume of hippocampus in

OX-treated and vehicle control group was  $31.84 \pm 1.24 \text{ mm}^3$  and  $36.95 \pm 3.48 \text{ mm}^3$ , respectively (Table 1). The number of neurons in DG, CA1 and CA3 did not show any significant difference between the two groups. The neuronal number of DG, CA1 and CA3 in the OX-treated group was estimated to be  $8.147 \pm 2.84 \times 10^5$ ,  $4.257 \pm 0.59 \times 10^5$  and  $2.133 \pm 0.22 \times 10^5$ , respectively, while the related neurons in vehicle control group accounted  $7.36 \pm 1.42 \times 10^5$ ,  $3.521 \pm 0.54 \times 10^5$  and  $1.989 \pm 0.46 \times 10^5$ , respectively (Table 1). The  $\text{CE}^2/\text{CV}^2$  ratios (Table 1) are typically  $> 0.5$  indicating that group variances are dominated by the inter-animal differences with only minor contributions of measurement variance to the group variance.

**Table 1.** Estimated hippocampal volume and neuron number

	OX-treated group			Vehicle treated group			P
	Mean $\pm$ SD	CE	CV	Mean $\pm$ SD	CE	CV	
Total volume [mm <sup>3</sup> ]	31.84 $\pm$ 1.24 <sup>a</sup>	0.02	0.03	36.95 $\pm$ 3.48 <sup>b</sup>	0.02	0.09	0.01
Granular cell number [10 <sup>6</sup> ]	7.36 $\pm$ 1.42	0.11	0.19	8.147 $\pm$ 2.84	0.11	0.34	0.69
Pyramidal cell number in CA1 [10 <sup>6</sup> ]	3.521 $\pm$ 0.54	0.11	0.15	4.257 $\pm$ 0.59	0.1	0.13	0.19
Pyramidal cell number in CA3 [10 <sup>6</sup> ]	1.989 $\pm$ 0.46	0.12	0.23	2.133 $\pm$ 0.22	0.12	0.1	0.33

Mean  $\pm$  standard deviation (SD) of hippocampal volume and neurons from one hemisphere (5 animals in each group) estimates with CE (= SEM/mean; inter-animal coefficient of error) and CV (= SD/mean; observed inter-animal coefficient of variation). Different superscript letters in the same rows indicate a significant difference,  $p < 0.05$ .

## DISCUSSION

The hippocampus is pivotal for learning and the formation of memory in the brain. Since the hippocampus shows various forms of plasticity, including the formation of new nerve cells in adult animals, it may be affected by the chemotherapeutic drugs leading to cognitive deficit [25].

In the present study, stereological techniques were used for the quantification of volume and number of neurons of the hippocampus following OX treatment in rat. The results of the current experiment demonstrated that treatment with OX caused a reduction in total volume of the hippocampus. Considering that oxaliplatin penetrates the blood brain barrier and accumulates in the brain [17, 18], an effect on the hippocampus is plausible and may explain memory impairment and other cognitive dysfunctions that have been found in previous studies using behavioural tests [9, 10, 39].

Similar to our results, magnetic resonance imaging (MRI) studies showed a reduced hippocampus volume in breast cancer survivors exposed to chemotherapy [1, 3, 22]. In contrast, Yoshikawa et al. [47] found no adverse effects of adjuvant chemotherapy on hippocampal volume in Japanese breast cancer survivors, using MRI. They implied that brain regions other than the hippocampus, such as the prefrontal cortex, might be involved in memory impairment after chemotherapy.

The neuron numbers did not show any significant loss of either granular cells of the DG or pyramidal cells of the CA1 and CA3 following OX treatment in rat. OX has been reported to induce apoptotic pathway in hippocampus with increasing caspase-3 and caspase-9 [4]. Cyclophosphamide chemotherapy has been suggested to suppress hippocampal neurogenesis and interrupt hippocampal function in mice [45]. Methotrexate also showed inhibition of the formation of immature neurons in the hippocampus [12, 44]. It is interesting that although hippocampal neuronal loss has been explained well in Alzheimer diseases, Joelving

et al. [20] did not find any significant loss of neuron in Parkinson's disease. Korbo et al. [24] also reported no loss of hippocampal neurons in non-Alzheimer dementia.

It should be mentioned that reduction in the number of neurons is not the only mechanism that affect neuronal function. Structurally, decreasing dendritic branching or losing synapses may impair neuronal function without neuronal loss [1]. Changes in hippocampal transmitters and signal transduction pathways are other mechanisms that may disturb hippocampal function [30, 31]. These findings suggest that cognitive disorders may be associated with a variety of changes that may not necessarily include a change in neuronal cell number [20].

It is important to note that the estimating neuron number based on two-dimensional counting is potentially biased. In our study, the potential bias was avoided by the use of the optical fractionator, which is a combination of fractionator sampling and the optical disector principle. This unbiased stereological method is not influenced by tissue deformation like shrinkage or swelling. Importantly, it is also unaffected by changes in the shape or size of the cells that are being counted. The optical fractionator is the gold-standard method for estimating number of neurons [14, 24].

## CONCLUSIONS

This study is the first description of an effect of oxaliplatin on the rat hippocampus using stereology. In conclusion, the results of the present study showed that OX treatment induces a decrease of hippocampal volume without neuronal loss. These findings might help to clarify the mechanism by which OX affects cognition by crossing the blood-brain barrier and accumulating in cerebrospinal and extracellular fluid in the brain and promote the development of treatment strategies that minimise cognitive side effects.

**Acknowledgements**

The authors would like to thank Prof. David Wolfer and Dr. Lutz Slomianka for their excellent scientific collaboration.

**REFERENCES**

- Apple AC, Ryals AJ, Alpert KI, et al. Subtle hippocampal deformities in breast cancer survivors with reduced episodic memory and self-reported cognitive concerns. *Neuroimage Clin.* 2017; 14: 685–691, doi: [10.1016/j.nicl.2017.03.004](https://doi.org/10.1016/j.nicl.2017.03.004), indexed in Pubmed: [28377882](https://pubmed.ncbi.nlm.nih.gov/28377882/).
- Barnes CA, Rao G, Houston FP. LTP induction threshold change in old rats at the perforant path--granule cell synapse. *Neurobiol Aging.* 2000; 21(5): 613–620, doi: [10.1016/S0197-4580\(00\)00163-9](https://doi.org/10.1016/S0197-4580(00)00163-9), indexed in Pubmed: [11016529](https://pubmed.ncbi.nlm.nih.gov/11016529/).
- Bergouignan L, Lefranc JP, Chupin M, et al. Breast cancer affects both the hippocampus volume and the episodic autobiographical memory retrieval. *PLoS One.* 2011; 6(10): e25349, doi: [10.1371/journal.pone.0025349](https://doi.org/10.1371/journal.pone.0025349), indexed in Pubmed: [22016764](https://pubmed.ncbi.nlm.nih.gov/22016764/).
- Bianchi E, Di Cesare Mannelli L, Micheli L, et al. Apoptotic process induced by oxaliplatin in rat hippocampus causes memory impairment. *Basic Clin Pharmacol Toxicol.* 2017; 120(1): 14–21, doi: [10.1111/bcpt.12629](https://doi.org/10.1111/bcpt.12629), indexed in Pubmed: [27273873](https://pubmed.ncbi.nlm.nih.gov/27273873/).
- Di Patre PL, Abbamondi A, Bartolini L, et al. GM1 ganglioside counteracts cholinergic and behavioral deficits induced in the rat by intracerebral injection of vincristine. *Eur J Pharmacol.* 1989; 162(1): 43–50, doi: [10.1016/0014-2999\(89\)90602-x](https://doi.org/10.1016/0014-2999(89)90602-x), indexed in Pubmed: [2721563](https://pubmed.ncbi.nlm.nih.gov/2721563/).
- Dorph-Petersen KA, Nyengaard JR, Gundersen HJ. Tissue shrinkage and unbiased stereological estimation of particle number and size. *J Microsc.* 2001; 204(Pt 3): 232–246, doi: [10.1046/j.1365-2818.2001.00958.x](https://doi.org/10.1046/j.1365-2818.2001.00958.x), indexed in Pubmed: [11903800](https://pubmed.ncbi.nlm.nih.gov/11903800/).
- Dubois M, Lapinte N, Villier V, et al. Chemotherapy-induced long-term alteration of executive functions and hippocampal cell proliferation: role of glucose as adjuvant. *Neuropharmacology.* 2014; 79: 234–248, doi: [10.1016/j.neuropharm.2013.11.012](https://doi.org/10.1016/j.neuropharm.2013.11.012), indexed in Pubmed: [24291465](https://pubmed.ncbi.nlm.nih.gov/24291465/).
- ElBeltagy M, Mustafa S, Umka J, et al. Fluoxetine improves the memory deficits caused by the chemotherapy agent 5-fluorouracil. *Behav Brain Res.* 2010; 208(1): 112–117, doi: [10.1016/j.bbr.2009.11.017](https://doi.org/10.1016/j.bbr.2009.11.017), indexed in Pubmed: [19914299](https://pubmed.ncbi.nlm.nih.gov/19914299/).
- Fardell JE, Vardy J, Shah JD, et al. Cognitive impairments caused by oxaliplatin and 5-fluorouracil chemotherapy are ameliorated by physical activity. *Psychopharmacology (Berl).* 2012; 220(1): 183–193, doi: [10.1007/s00213-011-2466-2](https://doi.org/10.1007/s00213-011-2466-2), indexed in Pubmed: [21894483](https://pubmed.ncbi.nlm.nih.gov/21894483/).
- Fardell JE, Vardy J, Monds LA, et al. The long-term impact of oxaliplatin chemotherapy on rodent cognition and peripheral neuropathy. *Behav Brain Res.* 2015; 291: 80–88, doi: [10.1016/j.bbr.2015.04.038](https://doi.org/10.1016/j.bbr.2015.04.038), indexed in Pubmed: [25934489](https://pubmed.ncbi.nlm.nih.gov/25934489/).
- Foley JJ, Raffa RB, Walker EA. Effects of chemotherapeutic agents 5-fluorouracil and methotrexate alone and combined in a mouse model of learning and memory. *Psychopharmacology (Berl).* 2008; 199(4): 527–538, doi: [10.1007/s00213-008-1175-y](https://doi.org/10.1007/s00213-008-1175-y), indexed in Pubmed: [18463849](https://pubmed.ncbi.nlm.nih.gov/18463849/).
- Goncalves MB, Williams EJ, Yip P, et al. The COX-2 inhibitors, meloxicam and nimesulide, suppress neurogenesis in the adult mouse brain. *Br J Pharmacol.* 2010; 159(5): 1118–1125, doi: [10.1111/j.1476-5381.2009.00618.x](https://doi.org/10.1111/j.1476-5381.2009.00618.x), indexed in Pubmed: [20136845](https://pubmed.ncbi.nlm.nih.gov/20136845/).
- Gundersen HJ, Jensen EB, Ki u K, et al. The efficiency of systematic sampling in stereology--reconsidered. *J Microsc.* 1999; 193(Pt 3): 199–211, doi: [10.1046/j.1365-2818.1999.00457.x](https://doi.org/10.1046/j.1365-2818.1999.00457.x), indexed in Pubmed: [10348656](https://pubmed.ncbi.nlm.nih.gov/10348656/).
- Hosseini-Sharifabad M, Nyengaard JR. Design-based estimation of neuronal number and individual neuronal volume in the rat hippocampus. *J Neurosci Methods.* 2007; 162(1-2): 206–214, doi: [10.1016/j.jneumeth.2007.01.009](https://doi.org/10.1016/j.jneumeth.2007.01.009), indexed in Pubmed: [17368561](https://pubmed.ncbi.nlm.nih.gov/17368561/).
- Howard V, Reed MG. Unbiased stereology: three-dimensional measurement in microscopy. BIOS Scientific Publishers, Taylor & Francis Group, New York 2005.
- Ir iguez C, Gayoso MJ, Carreres J. A versatile and simple method for staining nervous tissue using Giemsa dye. *J Neurosci Methods.* 1985; 13(1): 77–86, doi: [10.1016/0165-0270\(85\)90045-7](https://doi.org/10.1016/0165-0270(85)90045-7), indexed in Pubmed: [3887046](https://pubmed.ncbi.nlm.nih.gov/3887046/).
- Jacobs SS, Fox E, Dennie C, et al. Plasma and cerebrospinal fluid pharmacokinetics of intravenous oxaliplatin, cisplatin, and carboplatin in nonhuman primates. *Clin Cancer Res.* 2005; 11(4): 1669–1674, doi: [10.1158/1078-0432.CCR-04-1807](https://doi.org/10.1158/1078-0432.CCR-04-1807), indexed in Pubmed: [15746072](https://pubmed.ncbi.nlm.nih.gov/15746072/).
- Jacobs S, McCully CL, Murphy RF, et al. Extracellular fluid concentrations of cisplatin, carboplatin, and oxaliplatin in brain, muscle, and blood measured using microdialysis in nonhuman primates. *Cancer Chemother Pharmacol.* 2010; 65(5): 817–824, doi: [10.1007/s00280-009-1085-7](https://doi.org/10.1007/s00280-009-1085-7), indexed in Pubmed: [19662415](https://pubmed.ncbi.nlm.nih.gov/19662415/).
- Janelins MC, Roscoe JA, Berg MJ, et al. IGF-1 partially restores chemotherapy-induced reductions in neural cell proliferation in adult C57BL/6 mice. *Cancer Invest.* 2010; 28(5): 544–553, doi: [10.3109/07357900903405942](https://doi.org/10.3109/07357900903405942), indexed in Pubmed: [20014946](https://pubmed.ncbi.nlm.nih.gov/20014946/).
- Joelving FC, Billeskov R, Christensen JR, et al. Hippocampal neuron and glial cell numbers in Parkinson's disease: a stereological study. *Hippocampus.* 2006; 16(10): 826–833, doi: [10.1002/hipo.20212](https://doi.org/10.1002/hipo.20212), indexed in Pubmed: [16941622](https://pubmed.ncbi.nlm.nih.gov/16941622/).
- Kaae SS, Chen F, Wegener G, et al. Quantitative hippocampal structural changes following electroconvulsive seizure treatment in a rat model of depression. *Synapse.* 2012; 66(8): 667–676, doi: [10.1002/syn.21553](https://doi.org/10.1002/syn.21553), indexed in Pubmed: [22389166](https://pubmed.ncbi.nlm.nih.gov/22389166/).
- Kesler S, Janelins M, Koovakkattu D, et al. Reduced hippocampal volume and verbal memory performance associated with interleukin-6 and tumor necrosis factor-alpha levels in chemotherapy-treated breast cancer survivors. *Brain Behav Immun.* 2013; 30 Suppl: S109–S116, doi: [10.1016/j.bbi.2012.05.017](https://doi.org/10.1016/j.bbi.2012.05.017), indexed in Pubmed: [22698992](https://pubmed.ncbi.nlm.nih.gov/22698992/).
- Konat GW, Kraszpulski M, James I, et al. Cognitive dysfunction induced by chronic administration of common cancer chemotherapeutics in rats. *Metab Brain Dis.* 2008; 23(3): 325–333, doi: [10.1007/s11011-008-9100-y](https://doi.org/10.1007/s11011-008-9100-y), indexed in Pubmed: [18690526](https://pubmed.ncbi.nlm.nih.gov/18690526/).
- Korbo L, Amrein I, Lipp HP, et al. No evidence for loss of hippocampal neurons in non-Alzheimer dementia patients. *Acta Neurol Scand.* 2004; 109(2): 132–139, doi: [10.1034/j.1600-0404.2003.00182.x](https://doi.org/10.1034/j.1600-0404.2003.00182.x), indexed in Pubmed: [14705976](https://pubmed.ncbi.nlm.nih.gov/14705976/).
- Li J, Li Y, Su H, et al. The influence of environment stimulation on learning and memory function in rats with medication chemotherapy. *Annu Int Conf IEEE Eng*

- Med Biol Soc. 2018; 2018: 3537–3540, doi: [10.1109/EMBC.2018.8513084](https://doi.org/10.1109/EMBC.2018.8513084), indexed in Pubmed: [30441142](https://pubmed.ncbi.nlm.nih.gov/30441142/).
26. Li CQ, Liu D, Huang L, et al. Cytosine arabinoside treatment impairs the remote spatial memory function and induces dendritic retraction in the anterior cingulate cortex of rats. *Brain Res Bull.* 2008; 77(5): 237–240, doi: [10.1016/j.brainresbull.2008.07.010](https://doi.org/10.1016/j.brainresbull.2008.07.010), indexed in Pubmed: [18755251](https://pubmed.ncbi.nlm.nih.gov/18755251/).
  27. Liedke PE, Reolon GK, Kilpp B, et al. Systemic administration of doxorubicin impairs aversively motivated memory in rats. *Pharmacol Biochem Behav.* 2009; 94(2): 239–243, doi: [10.1016/j.pbb.2009.09.001](https://doi.org/10.1016/j.pbb.2009.09.001), indexed in Pubmed: [19747935](https://pubmed.ncbi.nlm.nih.gov/19747935/).
  28. Lomeli N, Di K, Czerniawski J, et al. Cisplatin-induced mitochondrial dysfunction is associated with impaired cognitive function in rats. *Free Radic Biol Med.* 2017; 102: 274–286, doi: [10.1016/j.freeradbiomed.2016.11.046](https://doi.org/10.1016/j.freeradbiomed.2016.11.046), indexed in Pubmed: [27908784](https://pubmed.ncbi.nlm.nih.gov/27908784/).
  29. Madhyastha S, Somayaji SN, Rao MS, et al. Hippocampal brain amines in methotrexate-induced learning and memory deficit. *Can J Physiol Pharmacol.* 2002; 80(11): 1076–1084, doi: [10.1139/y02-135](https://doi.org/10.1139/y02-135), indexed in Pubmed: [12489927](https://pubmed.ncbi.nlm.nih.gov/12489927/).
  30. Marksteiner J, Lechner T, Kaufmann WA, et al. Distribution of chromogranin B-like immunoreactivity in the human hippocampus and its changes in Alzheimer's disease. *Acta Neuropathol.* 2000; 100(2): 205–212, doi: [10.1007/s004010000239](https://doi.org/10.1007/s004010000239), indexed in Pubmed: [10963369](https://pubmed.ncbi.nlm.nih.gov/10963369/).
  31. Nowakowski C, Kaufmann WA, Adlassnig C, et al. Reduction of chromogranin B-like immunoreactivity in distinct subregions of the hippocampus from individuals with schizophrenia. *Schizophr Res.* 2002; 58(1): 43–53, doi: [10.1016/s0920-9964\(01\)00389-9](https://doi.org/10.1016/s0920-9964(01)00389-9), indexed in Pubmed: [12363389](https://pubmed.ncbi.nlm.nih.gov/12363389/).
  32. Olesen MV, Needham EK, Pakkenberg B. The optical fractionator technique to estimate cell numbers in a rat model of electroconvulsive therapy. *J Vis Exp.* 2017(125), doi: [10.3791/55737](https://doi.org/10.3791/55737), indexed in Pubmed: [28715378](https://pubmed.ncbi.nlm.nih.gov/28715378/).
  33. Paxinos G, Watson C. *The rat brain in stereotaxic coordinates.* Elsevier, Amsterdam 2007.
  34. Park JH, Chae J, Roh K, et al. Oxaliplatin-Induced Peripheral Neuropathy via TRPA1 Stimulation in Mice Dorsal Root Ganglion Is Correlated with Aluminum Accumulation. *PLoS One.* 2015; 10(4): e0124875, doi: [10.1371/journal.pone.0124875](https://doi.org/10.1371/journal.pone.0124875), indexed in Pubmed: [25928068](https://pubmed.ncbi.nlm.nih.gov/25928068/).
  35. Rebert CS, Pryor GT, Frick MS. Effects of vincristine, maytansine, and cis-platinum on behavioral and electrophysiological indices of neurotoxicity in the rat. *J Appl Toxicol.* 1984; 4(6): 330–338, doi: [10.1002/jat.2550040610](https://doi.org/10.1002/jat.2550040610), indexed in Pubmed: [6542922](https://pubmed.ncbi.nlm.nih.gov/6542922/).
  36. Reiriz AB, Reolon GK, Preissler T, et al. Cancer chemotherapy and cognitive function in rodent models: memory impairment induced by cyclophosphamide in mice. *Clin Cancer Res.* 2006; 12(16): 5000–5001, doi: [10.1158/1078-0432.CCR-06-0138](https://doi.org/10.1158/1078-0432.CCR-06-0138), indexed in Pubmed: [16914590](https://pubmed.ncbi.nlm.nih.gov/16914590/).
  37. Seigers R, Schagen SB, Beerling W, et al. Long-lasting suppression of hippocampal cell proliferation and impaired cognitive performance by methotrexate in the rat. *Behav Brain Res.* 2008; 186(2): 168–175, doi: [10.1016/j.bbr.2007.08.004](https://doi.org/10.1016/j.bbr.2007.08.004), indexed in Pubmed: [17854921](https://pubmed.ncbi.nlm.nih.gov/17854921/).
  38. Sprowl JA, Ciarimboli G, Lancaster CS, et al. Oxaliplatin-induced neurotoxicity is dependent on the organic cation transporter OCT2. *Proc Natl Acad Sci U S A.* 2013; 110(27): 11199–11204, doi: [10.1073/pnas.1305321110](https://doi.org/10.1073/pnas.1305321110), indexed in Pubmed: [23776246](https://pubmed.ncbi.nlm.nih.gov/23776246/).
  39. Sharpe MJ, Fardell JE, Vardy J, et al. The chemotherapy agent oxaliplatin impairs the renewal of fear to an extinguished conditioned stimulus in rats. *Behav Brain Res.* 2012; 227(1): 295–299, doi: [10.1016/j.bbr.2011.11.005](https://doi.org/10.1016/j.bbr.2011.11.005), indexed in Pubmed: [22101173](https://pubmed.ncbi.nlm.nih.gov/22101173/).
  40. Ueno T, Endo K, Hori K, et al. Assessment of antitumor activity and acute peripheral neuropathy of 1,2-diaminocyclohexane platinum (II)-incorporating micelles (NC-4016). *Int J Nanomedicine.* 2014; 9: 3005–3012, doi: [10.2147/IJN.S60564](https://doi.org/10.2147/IJN.S60564), indexed in Pubmed: [24971011](https://pubmed.ncbi.nlm.nih.gov/24971011/).
  41. Vardy J, Tannock I. Cognitive function after chemotherapy in adults with solid tumours. *Crit Rev Oncol Hematol.* 2007; 63(3): 183–202, doi: [10.1016/j.critrevonc.2007.06.001](https://doi.org/10.1016/j.critrevonc.2007.06.001), indexed in Pubmed: [17678745](https://pubmed.ncbi.nlm.nih.gov/17678745/).
  42. Winocur G, Vardy J, Binns MA, et al. The effects of the anti-cancer drugs, methotrexate and 5-fluorouracil, on cognitive function in mice. *Pharmacol Biochem Behav.* 2006; 85(1): 66–75, doi: [10.1016/j.pbb.2006.07.010](https://doi.org/10.1016/j.pbb.2006.07.010), indexed in Pubmed: [16935324](https://pubmed.ncbi.nlm.nih.gov/16935324/).
  43. Wafai L, Taher M, Jovanovska V, et al. Effects of oxaliplatin on mouse myenteric neurons and colonic motility. *Front Neurosci.* 2013; 7: 30, doi: [10.3389/fnins.2013.00030](https://doi.org/10.3389/fnins.2013.00030), indexed in Pubmed: [23486839](https://pubmed.ncbi.nlm.nih.gov/23486839/).
  44. Yang M, Kim JS, Kim J, et al. Acute treatment with methotrexate induces hippocampal dysfunction in a mouse model of breast cancer. *Brain Res Bull.* 2012; 89(1-2): 50–56, doi: [10.1016/j.brainresbull.2012.07.003](https://doi.org/10.1016/j.brainresbull.2012.07.003), indexed in Pubmed: [22796103](https://pubmed.ncbi.nlm.nih.gov/22796103/).
  45. Yang M, Kim JS, Song MS, et al. Cyclophosphamide impairs hippocampus-dependent learning and memory in adult mice: Possible involvement of hippocampal neurogenesis in chemotherapy-induced memory deficits. *Neurobiol Learn Mem.* 2010; 93(4): 487–494, doi: [10.1016/j.nlm.2010.01.006](https://doi.org/10.1016/j.nlm.2010.01.006), indexed in Pubmed: [20109567](https://pubmed.ncbi.nlm.nih.gov/20109567/).
  46. Yanovski JA, Packer RJ, Levine JD, et al. An animal model to detect the neuropsychological toxicity of anticancer agents. *Med Pediatr Oncol.* 1989; 17(3): 216–221, doi: [10.1002/mpo.2950170309](https://doi.org/10.1002/mpo.2950170309), indexed in Pubmed: [2787469](https://pubmed.ncbi.nlm.nih.gov/2787469/).
  47. Yoshikawa E, Matsuoka Y, Inagaki M, et al. No adverse effects of adjuvant chemotherapy on hippocampal volume in Japanese breast cancer survivors. *Breast Cancer Res Treat.* 2005; 92(1): 81–84, doi: [10.1007/s10549-005-1412-6](https://doi.org/10.1007/s10549-005-1412-6), indexed in Pubmed: [15980995](https://pubmed.ncbi.nlm.nih.gov/15980995/).
  48. Zhou W, Kavelaars A, Heijnen CJ. Metformin prevents cisplatin-induced cognitive impairment and brain damage in mice. *PLoS One.* 2016; 11(3): e0151890, doi: [10.1371/journal.pone.0151890](https://doi.org/10.1371/journal.pone.0151890), indexed in Pubmed: [27018597](https://pubmed.ncbi.nlm.nih.gov/27018597/).

# Quantitative analysis of healthy olfactory sulcus depth, olfactory tract length and olfactory bulb volume in the paediatric population: a magnetic resonance study

S. Sahin<sup>1</sup> , A.H. Baykan<sup>1</sup> , E. Altunisik<sup>2</sup> , C.A. Vural<sup>3</sup> , F.D. Sahin<sup>4</sup> , I. Inan<sup>5</sup> 

<sup>1</sup>Department of Radiology, Adiyaman Education and Research Hospital, Adiyaman, Turkey

<sup>2</sup>Department of Neurology, Adiyaman Education and Research Hospital, Adiyaman, Turkey

<sup>3</sup>Department of Orthopaedics, Ankara City Hospital, Ankara, Turkey

<sup>4</sup>Department of Paediatrics, Adiyaman Education and Research Hospital, Adiyaman, Turkey

<sup>5</sup>Department of Radiology, Biruni University, Istanbul, Turkey

[Received: 4 July 2020; Accepted: 25 September 2020]

**Background:** The aim of this study was to determine the normal reference values for olfactory sulcus depth, olfactory tract length and olfactory bulb volume in the paediatric population with routine magnetic resonance imaging (MRI) and determine the relationship, if any, between these values and patient sex and age.

**Materials and methods:** Ninety patients with a median age of 8 years (age range: 3–17 years), consisting of 45 males and 45 females with normal brain MRI scans were evaluated. The patients were divided into three subgroups based on age range, with  $n = 30$  per subgroup; group 1: young children (3–6 years), group 2: children (7–11 years) and group 3: adolescents (12–17 years). In the cranial MRI examination of all groups, the right, left and total olfactory bulb volume values were measured in  $\text{mm}^3$ , the right and left olfactory tract length values and the right and left olfactory sulcus depth values were calculated manually in mm. Demographic data including sex and age were recorded.

**Results:** There was no significant difference between the age groups in terms of sex. Right-left olfactory sulcus depth; right-left olfactory tract length and right-left total olfactory bulb volume values increased significantly when they are compared in terms of age groups ( $p < 0.0001$ ,  $= 0.028$ ;  $< 0.0001$ ,  $< 0.0001$ ;  $< 0.0001$ ,  $< 0.0001$ ;  $< 0.0001$ , respectively). There was no significant difference between right and left olfactory tract length and olfactory bulb volumes in all groups ( $p = 0.792$  and  $p = 0.478$ ), but the right olfactory sulcus depth was significantly larger than the left ( $p = 0.003$ ).

**Conclusions:** Especially as the age progresses, olfactory tract length and olfactory bulb volume dimensions of olfactory nerve and olfactory sulcus depth should be checked during diagnosis of respective illnesses in paediatric population. (Folia Morphol 2021; 80, 1: 33–39)

**Key words:** olfactory sulcus depth, olfactory bulb volume, olfactory tract length, magnetic resonance imaging

## INTRODUCTION

The literature shows that disorders of the olfactory system may be related to many diseases, such as sinonasal disease [14], allergic rhinitis [19], infections [15], trauma [15], epilepsy [8], Behcet's disease [6], migraine [2], idiopathic olfactory loss [15] or disruptions such as gastric excretion in the context of normal digestive physiology [6]. Therefore, determining the anatomical features of olfactory nerve can be very important as it has clinical relevance in the diagnostic process for a clinician.

In this context, the dimensions of olfactory sulcus depth (OSd), olfactory tract length (OTI) and olfactory bulb volume (OBv) can be evaluated radiologically. It has been shown in previous studies that magnetic resonance imaging (MRI) is a reliable method to perform measurements of the olfactory system [10, 11]. The olfactory system was first defined on MRI by Suzuki et al. [16]. Later, in 1998, the standard OBv measurement method on MRI was developed by Yousem et al. [18]. It is not always possible to visualise OT on MRI [12, 16]. The measurement of OTI by using MRI was first performed in a 1989 study [16]. The illustration of olfactory structural elements is shown in Figure 1.

In the literature, studies on the structures constituting the olfactory system are mostly focused on the adult population, while radiological studies on the paediatric population are limited. To the extent of our knowledge, there is not any study presenting OBv, OSd, and OTI dimensions in paediatric population extant in the literature. Therefore, this study was planned to determine the normal reference values of these structures by measuring OBv, OSd, and OTI from MRI studies in a healthy paediatric population and to present the findings to the literature.

## MATERIALS AND METHODS

### Sample size calculation

G\*Power statistical package was used to determine the exact number of cases to be used for analysis. The parameters were determined as follows: effect size = 0.4, type I error = 0.05, power = 0.80, df = 6. The total n number was determined as 92.

### Subjects

Two hundred eighty-six MRI images were examined at baseline in the present study. One hundred thirty-three images were excluded as they did not meet the inclusion criteria, and 63 images were excluded due to artefacts (Fig. 2). Finally, 90 patients

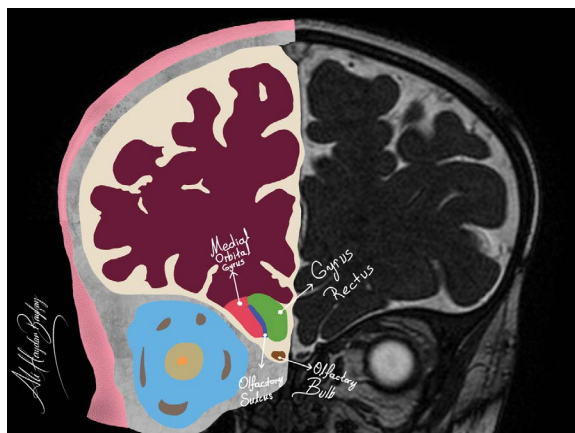


**Figure 1.** Anatomical radiological image of coronal plane (magnetic resonance imaging). Medial orbital gyrus (red area), gyrus rectus (green area), olfactory sulcus (blue area) and olfactory bulb (brown area) are shown in the illustration side.



**Figure 2.** Consort flow diagram.

with MRI images meeting inclusion criteria for normal brain MRI taken from January 2016 to December 2018 were analysed. Patients were considered normal if they had no history of brain trauma, MRI evaluation did not demonstrate sinonasal or brain disease, had no upper respiratory tract infection symptoms; there was no drug use and no environmental exposure that may cause loss of smell. Ethics committee approval was obtained from Adiyaman University Non-Interventional Clinical Research Ethics Board with the number of 2019/1-11. All procedures of this retrospective study were applied according to the principles of the Declaration of Helsinki. "Informed consent" was not obtained from parents as the study was retrospective. Patients included in the study were presented anonymously. The images were obtained retrospectively

from the archives of the Adiyaman University Faculty of Medicine Department of Radiology.

The clinical evaluation of all subjects included ascertainment of personal and family history as well as physical and neurological examination in order to exclude any possible cause of smell dysfunction. Patients with normal reports for non-enhanced brain MRI were included in the study. Patients with pathologic MRI findings like hydrocephalus, tumour, white matter abnormalities, haemorrhage, infarcts, atrophy and cortical dysplasia that have been treated in hospital were excluded. Metabolic, endocrine, neurological and psychiatric diseases were not included in the study.

Following admission, patients were divided into three groups according to age range as follows: group 1: young children (3–6 years), group 2: children (7–11 years) and group 3: adolescents (12–17 years).

### MRI protocol

A single radiologist with more than 10 years' experience re-evaluated MRI images. The operator was blinded throughout the procedure until randomisation, in order to avoid possible influence in the measurement process. The MRIs were performed using a 1.5 T system (Achieva; Philips Medical Systems, Best, Netherlands) using a head coil. Contrast material was not utilised. These images were used for volumetric and morphologic measurements. Coronal images, balanced fast-field echo three-dimensional (3D) T2 weighted images (TR: 6.5 ms; TE: 3.4 ms; field of view [FOV] 180 × 180 mm; number of signal acquisitions [NSA] = 2; slice thickness = 1 mm; slice gap = 0.5 mm; number of slices = 75; matrix = 308 × 308 mm), sagittal images 3D T1 turbo field echo weighted images (TR: 8.2 ms; TE: 4.0 ms; FOV: 140 × 156 mm; NSA = 4; thickness = 1.2 mm; slice gap = 0.5 mm; number of slices = 40; matrix = 252 × 278 mm) were obtained.

### Image analysis

Bilateral OSd, OBv and OTI were measured in all patients. The olfactory bulb was observed as a hypointense ovoid structure surrounded by hyperintense cerebrospinal fluid in T2-weighted series. Sections were obtained at a right angle to the cribriform plate. The volume measurements were obtained semi-automatically using multiplanar reconstructions in a View 3D workstation and manual segmentation based on the contour stack principle. OBv was calculated in mm<sup>3</sup> (Figs. 3, 4). OSd was evaluated in coronal T2 weight-

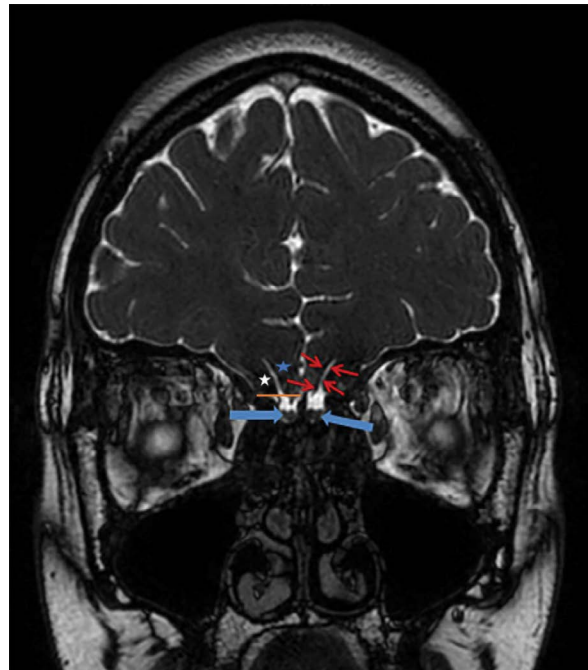


**Figure 3.** A coronal T2-weighted image showing the right and left olfactory bulb as a hypointense ovoid structure (blue arrows). Hyperintense area (red arrows) (olfactory sulcus) is shown between the medial orbital gyrus (white star) and gyrus rectus (blue star). The virtual line that connects the medial orbital gyrus to gyrus rectus is shown with orange line.

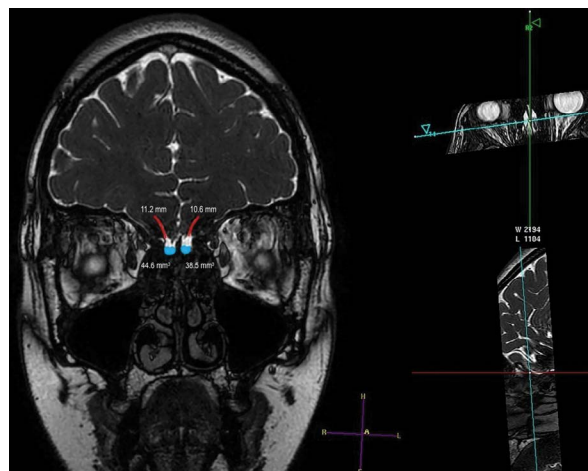


**Figure 4.** Semi-automatic measurement of the olfactory bulb volume using manual segmentation and multiplanar reformations in the three-dimensional workstation. The olfactory bulb is shown in blue on both sides and the volumes are given in mm<sup>3</sup>. Olfactory sulcus are shown as red lines and the measurements are given in mm.

ed series. A virtual tangent line was drawn from the lower end of the medial orbital gyrus, connecting to the lower end of the gyrus rectus in the posterior sections of both eyeballs. This virtual tangential line that

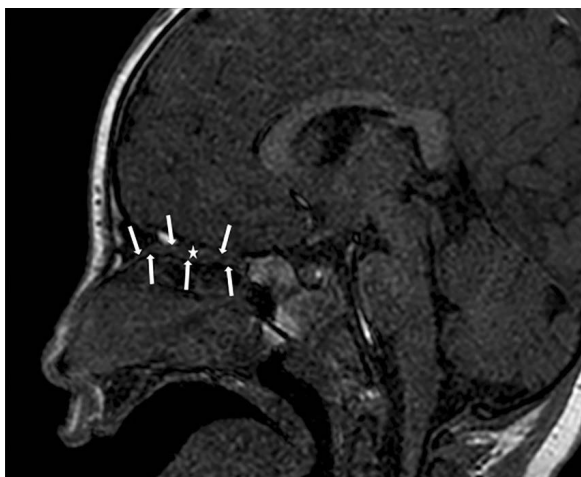


**Figure 5.** A sagittal T1-weighted image showing the boundaries of the right olfactory tract (white arrows). The mid-portion of the tract is indicated by a star.

passes from the deepest part of the olfactory sulcus was connected by free drawing in the cranio-caudal plane to calculate the depth of the OS and recorded in millimetres (Fig. 4). All the measurements were performed by an individual who was blinded to the patient diagnoses. OTI was measured from the area where the nerve tracing was best visualized on the 3D T1-weighted sagittal images and recorded in mm (Fig. 5). The illustration of olfactory structural elements was performed with the Procreate application (Fig. 1).

### Statistical analysis

SPSS Statistics v. 21.0 (IBM Corp. Released 2012. IBM SPSS Statistics for Windows, Version 21.0. Armonk, NY) software was used for statistical analysis. Categorical data were expressed as number and percentage; nonparametric numeric data were expressed as median, minimum and maximum while parametric numeric data were expressed as mean and standard

deviation. The Shapiro-Wilk test was used to evaluate the distribution of numerical data. The Mann-Whitney U was used to evaluate the relationship between sex and OSd and OTI, while Student's t-test was used to evaluate the relationship between sex and OBv. The Kruskal-Wallis test was used to assess the relationship between OSd and OTI in the age groups, and pairwise comparison was used to assess the group that causes the difference in statistically significant patients. The relationship between age groups and OBv was analysed by the ANOVA test and the Bonferroni test was used to evaluate the pairwise comparisons between the groups.

## RESULTS

A total of 90 patients aged between 3 and 17 years (median: 8 years) were included in the study. Forty-five (50%) of the patients were female and 45 (50%) were male. When compared according to age, the right and left OSd and OTI values increased significantly as the mean age increased ( $p < 0.0001$ ,  $p = 0.028$  and  $p < 0.0001$ ,  $p < 0.0001$ , respectively). Right, left and total OBv values increased significantly as the mean age of the group increases. ( $p < 0.0001$ ,  $p < 0.0001$ ,  $p < 0.0001$ ). The OSd, OBv and OTI data according to the age group are summarised in Table 1.

No statistically significant relationship was found between OSd, OTI and OBv values in terms of sex (Table 2).

There was no significant relationship between right and left OTI and OBv values when all age groups were included and compared pairwise; while right OSd was found to be significantly increased compared to left ( $p = 0.003$ ).

The group that causes the difference was assessed based on pairwise comparisons between the age groups. When the first and third groups were com-

**Table 1.** Olfactory sulcus depth (OSd), olfactory tract length (OTI) and olfactory bulb volume (OBv) values according to age groups (n = 90)

	Right OSd [mm]	Left OSd [mm]	Right OTI [mm]	Left OTI [mm]	Right OBv [mm <sup>3</sup> ]	Left OBv [mm <sup>3</sup> ]	Total OBv [mm <sup>3</sup> ]
All groups	8.85 (6–13.6)	8.8 (1.8–16)	23.95 (16.6–39.8)	23.4 (16–39.2)	66.15 (32.7–99.6)	66.2 (31.8–98.3)	133.55 (70–197.9)
Group I (3–6 years)	8.45 (6.9–10.8)	8.25 (5.1–10.8)	20.4 (16.6–28.3)	20.85 (16–25)	54.7 (33–77)	49.3 (31.8–88.8)	99.75 (70–152.8)
Group II (7–11 years)	8.8 (6–11.3)	8.3 (5.5–11)	24.3 (18.3–28.7)	25.8 (16.7–39.2)	66.45 (32.7–84)	66.05 (37.8–88)	131.65 (77.1–170)
Group III (12–17 years)	10.3 (7.5–13.6)	9 (1.8–16)	25.9 (18.7–39.8)	24.45 (19.7–34.6)	78.05 (38.3–99.6)	78.35 (44.9–98.3)	157.6 (83.2–197.9)
p	< 0.0001*	0.028*	< 0.0001*	< 0.0001*	< 0.0001**	< 0.0001**	< 0.0001**

\*Kruskal–Wallis test; \*\*ANOVA test; data are shown as mean (minimum–maximum)



**Table 2.** Olfactory sulcus depth (OSd), olfactory tract length (OTI) and olfactory bulb volume (OBv) values according to sex (n = 90)

	Male	Female	P
Right OSd [mm]	8.8 (6–12.2)	8.8 (6.4–13.6)	0.381*
Left OSd [mm]	8.8 (1.8–10.8)	8.7 (5.6–16)	0.984*
Right OTI [mm]	24 (17.6–39.8)	23.7 (16.6–28.7)	0.103*
Left OTI [mm]	23 (16–39.2)	23.6 (16.8–29.8)	0.904*
Right OBv [mm <sup>3</sup> ]	64 (32.7–94.5)	67.1 (33–99.6)	0.656**
Left OBv [mm <sup>3</sup> ]	65.3 (33.8–90.1)	72 (31.8–98.3)	0.154**
Total OBv [mm <sup>3</sup> ]	128 (77.1–184.6)	136 (77.1–184.6)	0.324**

\*Mann–Whitney U Test; \*\*Student's T-test; data are shown as mean (minimum–maximum)

pared, a statistically significant difference was observed in all values increasing with age. Pairwise comparisons between age groups are presented in Table 3.

Correlation analysis revealed a positive correlation between age and all measurements. Correlation scatter plots are shown in Figure 6.

## DISCUSSION

The evaluation of the olfactory system using MRI has previously been performed in the presence of many diseases, but most studies to date have focused on the adult population [4]. In a study including healthy individuals aged between 19–76 years assessing standard OBv values, the mean value for right OBv was found to be 41–97 mm<sup>3</sup>, while the mean value for left OBv was found to be 37–98 mm<sup>3</sup> [4]. Buschhuter et al. [4] also emphasized that, the OBv values of males were larger compared to females and the mean decrease with age was equal in both sexes. In the present study, OBv values did not show a significant difference in terms of sex. Rombaux et al. [13] reported the minimum OBv value was 58 mm<sup>3</sup> for individuals under 45 years. It was stated that it should be 46 mm<sup>3</sup> for over 45 years of age. Yousem et al. [18]

stated that OBv value increased up to 4<sup>th</sup> decade and decreased with increasing age. Although present study included paediatric age groups, it was found that OBv values increased with age and the results are in parallel with the current literature. Suzuki et al. [16] found that the mean length of the OT was found to be 25 mm. They reported that MRI is an appropriate method for imaging the OT, but it was difficult to evaluate this structure in axial sections [16]. In the present study, OTI measurements were performed on sagittal sections. The current measurement method can be easily applied by physicians in clinical practice, and assessment only takes a short time.

There may be differences between right and left OBv values in humans. Therefore, measurements are made bilaterally [17]. Since OBv is a volumetric value, the total OBv value is calculated as the sum of right and left OBv [5]. In our study, a similar method was used: right, left and total OBv values were calculated separately. In a different study, the right OSd was found to be deeper than the left [9]. In addition, some clinical, electrophysiological and neuroimaging studies have emphasized that the right hemisphere has a greater role in the sense of smell than the left hemisphere [9]. The difference between olfactory structural elements found in these studies may be due to the right hemisphere dominance in the olfactory sense. In our study, no significant difference was found between the right and left sides in terms of OBv and OTI values, but the right OSd was significantly deeper than the left. This result can be explained by the fact that the cerebral cortex (medial orbital gyrus and gyrus rectus) forming the olfactory sulcus is more dominant on the right.

In the literature, we did not find any other study in which normal values of these structures were presented by MRI imaging of olfactory structural elements in a healthy paediatric population. In our study, OBv, OSd and OTI values increased significantly with age. This result reflects the neurodevelopmental integrity of all

**Table 3.** Comparison of age groups with olfactory sulcus depth (OSd), olfactory tract length (OTI) and olfactory bulb volume (OBv) (p values)

	Right OSd*	Left OSd*	Right OTI*	Left OTI*	Right OBv**	Left OBv**	Total OBv**
Group I/Group II (3–6 y/7–11 y)	1	1	0.003	< 0.0001	0.41	0.002	0.005
Group I/Group III (3–6 y/12–17 y)	< 0.0001	0.031	< 0.0001	< 0.0001	< 0.0001	< 0.0001	< 0.0001
Group II/Group III (7–11 y/12–17 y)	0.012	0.152	0.623	1	0.002	0.014	0.002

\*Pairwise comparison (Kruskal Wallis test); \*\*Post-hoc analysis (Bonferroni correction); y — years

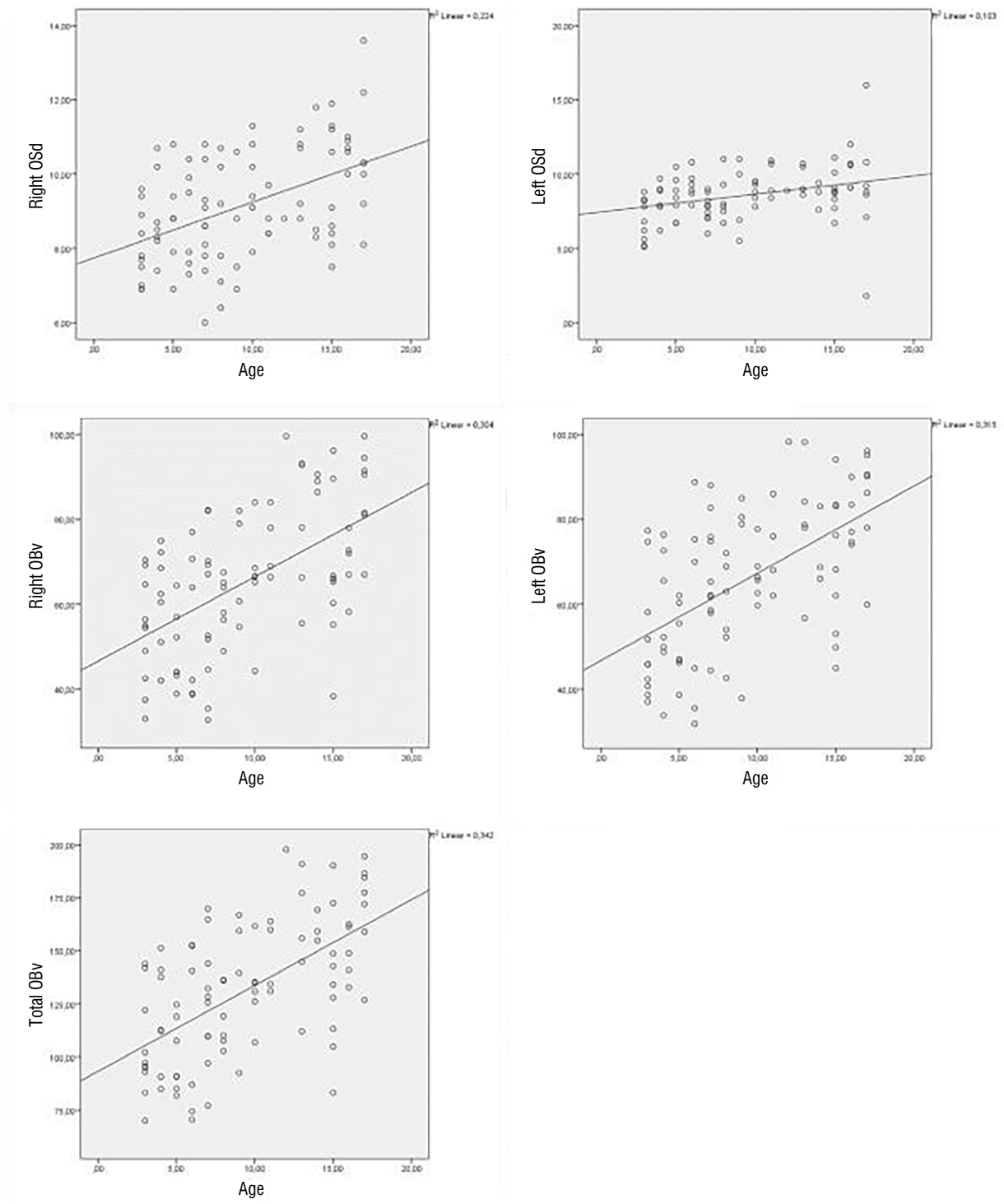


**Figure 6.** Scatter plots showing the correlation between age and olfactory tract length (OTI), olfactory sulcus depth (OSd), and olfactory bulb volume (OBv).

three structures in the paediatric population. In one study, patients with OSd below 4 mm did not develop bilateral olfactory bulbs and olfactory tract aplasia [1]. This result also supports neurodevelopmental integrity between these structures. The olfactory sulcus is an anatomical structure formed by the maturation of the

medial orbital gyri and gyrus rectus, so the structural elements that make up the olfactory system are not only part of a pure sensory component but can also be a neuroanatomic indicator of cortical function.

OBv and OSd measurements have been used to structurally evaluate the effect of olfactory system

in many patients such as isolated congenital anosmia, chronic sinusitis related olfactory dysfunction, post-traumatic, post-infective olfactory dysfunction, epilepsy, migraine, multiple sclerosis, and chemotherapy-related conditions in children [7, 8, 19]. Studies have shown that olfactory structural elements are affected in many of the aforementioned diseases. Most of the diseases and conditions mentioned above are also common in paediatric patients.

Olfactory maturation can give information about cerebral maturation. Hypoplasia and aplasia can be seen in olfactory structures in some diseases such as Kallman syndrome, CHARGE (coloboma, heart defects, choanal atresia, retarded growth and development, genital hypoplasia, ear abnormalities, and/or hearing loss defect) syndrome, and cranio-telencephalic dysplasia [3, 12]. The olfactory system may be affected by certain diseases such as hypoxic ischaemic encephalopathy, cerebral palsy, some paediatric endocrine and metabolic diseases, and kernicterus. In these diseases, reference values will be needed to evaluate the olfactory system. We hope that our study will contribute to the literature on this matter.

### Limitations of the study

There are some limitations in this study. Olfactory function could not be assessed because of retrospective design. Information about the health of the patients was obtained only from the records. The number of patients in the groups was small in our study. A limitation of this study is the difference between determined and recruited n number of the cases. The total n number was determined as 92 but only 90 patients were able to access the data. Measurements were performed by a single radiologist and reliability between measurements was not assessed.

### CONCLUSIONS

In conclusion, the present study gives reference values in terms of age-related normal values in children. These normative data can help to evaluate the olfactory sulcus depth, olfactory tract length and olfactory bulb volume in many diseases in children.








### Acknowledgements

The authors wish to express their gratitude to the officers who are responsible from archiving of cases and MRI technician Kasim Tepe.

### REFERENCES

1. Abolmaali ND, Hietschold V, Vogl TJ, et al. MR evaluation in patients with isolated anosmia since birth or early childhood. *Am J Neuroradiol.* 2002; 23(1): 157–164, indexed in Pubmed: [11827889](#).
2. Aktürk T, Tanik N, Serin Hİ, et al. Olfactory bulb atrophy in migraine patients. *Neurol Sci.* 2019; 40(1): 127–132, doi: [10.1007/s10072-018-3597-6](#), indexed in Pubmed: [30280362](#).
3. Azoulay R, Fallet-Bianco C, Garel C, et al. MRI of the olfactory bulbs and sulci in human fetuses. *Pediatr Radiol.* 2006; 36(2): 97–107, doi: [10.1007/s00247-005-0030-0](#), indexed in Pubmed: [16341529](#).
4. Buschhüter D, Smitka M, Puschmann S, et al. Correlation between olfactory bulb volume and olfactory function. *Neuroimage.* 2008; 42(2): 498–502, doi: [10.1016/j.neuroimage.2008.05.004](#), indexed in Pubmed: [18555701](#).
5. Chen S, Tan Hy, Wu Zh, et al. Imaging of olfactory bulb and gray matter volumes in brain areas associated with olfactory function in patients with Parkinson's disease and multiple system atrophy. *Eur J Radiol.* 2014; 83(3): 564–570, doi: [10.1016/j.ejrad.2013.11.024](#), indexed in Pubmed: [24360232](#).
6. Doğan A, Bayar Muluk N, Asal N, et al. Olfactory bulb volume and olfactory sulcus depth in patients with Behçet's disease. *J Laryngol Otol.* 2018 [Epub ahead of print]: 1–5, doi: [10.1017/S0022215118002141](#), indexed in Pubmed: [30558688](#).
7. Doğan A, Bayar Muluk N, Şahan MH, et al. Olfactory bulb volume and olfactory sulcus depth in migraine patients: an MRI evaluation. *Eur Arch Otorhinolaryngol.* 2018; 275(8): 2005–2011, doi: [10.1007/s00405-018-5029-x](#), indexed in Pubmed: [29876641](#).
8. Hummel T, Henkel S, Negoias S, et al. Olfactory bulb volume in patients with temporal lobe epilepsy. *J Neurol.* 2013; 260(4): 1004–1008, doi: [10.1007/s00415-012-6741-x](#), indexed in Pubmed: [23135292](#).
9. Hummel T, Urbig A, Huart C, et al. Volume of olfactory bulb and depth of olfactory sulcus in 378 consecutive patients with olfactory loss. *J Neurol.* 2015; 262(4): 1046–1051, doi: [10.1007/s00415-015-7691-x](#), indexed in Pubmed: [25712545](#).
10. Hummel T, Witt M, Reichmann H, et al. Immunohistochemical, volumetric, and functional neuroimaging studies in patients with idiopathic Parkinson's disease. *J Neurol Sci.* 2010; 289(1-2): 119–122, doi: [10.1016/j.jns.2009.08.026](#), indexed in Pubmed: [19775703](#).
11. Kim JiY, Lee WY, Chung EJ, et al. Analysis of olfactory function and the depth of olfactory sulcus in patients with Parkinson's disease. *Mov Disord.* 2007; 22(11): 1563–1566, doi: [10.1002/mds.21490](#), indexed in Pubmed: [17534948](#).
12. Leboucq N, Menjot de Champfleure N, Menjot de Champfleure S, et al. The olfactory system. *Diagn Interv Imaging.* 2013; 94(10): 985–991, doi: [10.1016/j.diii.2013.06.006](#), indexed in Pubmed: [23932763](#).
13. Rombaux P, Duprez T, Hummel T. Olfactory bulb volume in the clinical assessment of olfactory dysfunction. *Rhinology.* 2009; 47(1): 3–9, indexed in Pubmed: [19382487](#).
14. Rombaux Ph, Potier H, Markessis E, et al. Olfactory bulb volume and depth of olfactory sulcus in patients with idiopathic olfactory loss. *Eur Arch Otorhinolaryngol.* 2010; 267(10): 1551–1556, doi: [10.1007/s00405-010-1230-2](#), indexed in Pubmed: [20300763](#).
15. Rombaux Ph, Potier H, Markessis E, et al. Olfactory bulb volume and depth of olfactory sulcus in patients with idiopathic olfactory loss. *Eur Arch Otorhinolaryngol.* 2010; 267(10): 1551–1556, doi: [10.1007/s00405-010-1230-2](#), indexed in Pubmed: [20300763](#).
16. Suzuki M, Takashima T, Kadoya M, et al. MR imaging of olfactory bulbs and tracts. *Am J Neuroradiol.* 1989; 10(5): 955–957, indexed in Pubmed: [2505540](#).
17. Wang J, You H, Liu JF, et al. Association of olfactory bulb volume and olfactory sulcus depth with olfactory function in patients with Parkinson disease. *Am J Neuroradiol.* 2011; 32(4): 677–681, doi: [10.3174/ajnr.A2350](#), indexed in Pubmed: [21330398](#).
18. Yousem DM, Geckle RJ, Bilker WB, et al. Olfactory bulb and tract and temporal lobe volumes. Normative data across decades. *Ann N Y Acad Sci.* 1998; 855: 546–555, doi: [10.1111/j.1749-6632.1998.tb10624.x](#), indexed in Pubmed: [9929650](#).
19. Zhang Q, Liu G, Hang W. [Olfactory bulb volume and depth of olfactory sulcus in patients with allergic rhinitis]. *Lin Chung Er Bi Yan Hou Tou Jing Wai Ke Za Zhi.* 2014; 28(24): 1956–1960, indexed in Pubmed: [25895315](#).

# Tractography-guided surgery of brain tumours: what is the best method to outline the corticospinal tract?

T. Szmuda<sup>1</sup>, S. Kierońska<sup>2</sup>, S. Ali<sup>3</sup>, P. Słoniewski<sup>1</sup>, M. Pacholski<sup>3</sup>, J. Dzierżanowski<sup>1</sup>,  
A. Sabisz<sup>4</sup>, E. Szurowska<sup>4</sup>

<sup>1</sup>Neurosurgery Department, Medical University of Gdansk, Poland

<sup>2</sup>Neurology and Neurosurgery Department, University Hospital Collegium Medicum Nicolaus Copernicus University, Bydgoszcz, Poland

<sup>3</sup>Student's Scientific Circle, Neurosurgery Department, Medical University of Gdansk, Poland

<sup>4</sup>Radiology Department, Medical University of Gdansk, Poland

[Received: 7 January 2020; Accepted: 27 January 2020]

**Background:** Diffusion tensor imaging (DTI) is the imaging technique used in vivo to visualise white matter pathways. The cortico-spinal tract (CST) belongs to one of the most often delineated tracts preoperatively, although the optimal DTI method has not been established yet. Considering that various regions of interests (ROIs) could be selected, the reproducibility of CST tracking among different centres is low. We aimed to select the most reliable tractography method for outlining the CST for neurosurgeons.

**Materials and methods:** Our prospective study consisted of 32 patients (11 males, 21 females) with a brain tumour of various locations. DTI and T1-weighted image series were acquired prior to the surgery. To draw the CST, the posterior limb of the internal capsule (PLIC) and the cerebral peduncle (CP) were defined as two main ROIs. Together with these main ROIs, another four cortical endpoints were selected: the frontal lobe (FL), the supplementary motor area (SMA), the precentral gyrus (PCG) and the postcentral gyrus (POCG). Based on these ROIs, we composed ten virtual CSTs in DSI Studio. The fractional anisotropy, the mean diffusivity, the tracts' volume, the length and the number were compared between all the CSTs. The degree of the CST infiltration, tumour size, the patients' sex and age were examined.

**Results:** Significant differences in the number of tracts and their volume were observed when the PLIC or the CP stood as a single ROI comparing with the two-ROI method (all  $p < 0.05$ ). The mean CST volume was 40054U ( $SD \pm 12874$ ) and the number of fibres was 259.3 ( $SD \pm 87.3$ ) when the PLIC was a single ROI. When the CP was a single ROI, almost a half of fibres (147.6;  $SD \pm 64.0$ ) and half of the CST volume (26664U;  $SD \pm 10059U$ ) was obtained (all  $p < 0.05$ ). There were no differences between the various CSTs in terms of fractional anisotropy, mean diffusivity, the apparent diffusion coefficient, radial diffusivity and the tract length ( $p > 0.05$ ). The CST was infiltrated by a growing tumour or oedema in 17 of 32 patients; in these cases, the mean and apparent diffusion of the infiltrated CST was significantly higher than in uncompromised CSTs ( $p = 0.04$ ). CST infiltration did not alter the other analysed parameters (all  $p > 0.05$ ).

*Conclusions: A universal method of DTI of the CST was not developed. However, we found that the CP or the PLIC (with or without FL as the second ROI) should be used to outline the CST. (Folia Morphol 2021; 80, 1: 40–46)*

**Key words: diffusion tensor imaging, diffusion tensor tractography, tractography, corticospinal tract, pyramidal tract, glioma surgery, neurosurgery**

## INTRODUCTION

A neurosurgeon's objective is to achieve maximal tumour resection without producing new neurological defects [24, 29]; this includes preserving the cortico-spinal tract (CST). The CST is a white matter bundle that together with corticobulbar tract composes the pyramidal tract and if damaged it may lead to post-operative paresis [6]. Proper preoperative visualisation of the CST and its integration via an intraoperative neuronavigation system could potentially preserve neurological function and simultaneously increase the resection rate [4, 24]. However, several technical obstacles underlie correct delineation of the CST, including: knowledge of an individual's topographical anatomy, a physician's experience and the degree of destruction of the neuronal pathway through the tumour [14, 21].

Magnetic resonance imaging (MRI) scans are routinely acquired when planning brain tumour surgery. Yet, they provide only general information about the brain's pathology and the surrounding structures. Diffusion tensor imaging (DTI) — which provides a quick and non-invasive method for visualising structural changes of the white matter — can be used for visualisation of the CST [10, 12]. This technique not only plays an important role in neurosurgical planning but may predict the extent of safe resection [1, 22, 27]. However, physicians currently select various regions of interest (ROI) to draw the CST as the optimal DTI-derived method to estimate the course of the CST has not yet been established [11]. Due to this lack of standardisation the reliability of tracking the CST in different centres remains low [21].

Our aim was to determine the optimal DTI-derived method to reconstruct the CST as well as to verify if a single ubiquitous method exists. To accomplish this, we compared CST tracking as determined by various ROIs.

## MATERIALS AND METHODS

### Patients

Thirty-two patients with a brain tumour invading the CST were prospectively collected (11 males,

21 females; age 27–81 years, mean  $\pm$  standard deviation (SD) and median age:  $53.4 \pm 17.1/53.5$ ). These patients were treated at the Neurosurgery Department in Gdańsk, Poland, from 2016 to 2019. The protocol of the study was approved by the local bioethical committee, permission number: NKBBN/65/2019.

### Image acquisition

All patients had a preoperative MRI with a DTI sequence performed on a 1.5T Siemens Magnetom Aera scanner (Erlangen, Siemens Medical Solutions, Erlangen, Germany) which was equipped with a 20-channel head coil. The standard imaging protocol for brain tumours covered T1, T2-weighted sequences and T1-weighted post-gadolinium which served as a neuronavigational sequence. Diffusion-weighted imaging (DWI) was obtained using: three repetitions of 20 directions, a b-factor of  $1000 \text{ s/m}^2$ , a slice thickness of 5.0 mm, a  $128 \times 128$  matrix, a  $240 \times 240$  mm field-of-view, a repetition time of 3500 ms, and an echo time of 83.0 ms. A multivariate linear fitting was used to calculate the orientation for a single voxel. The largest eigenvalue denoted the ultimate fibre direction. A total of 60 diffusion sampling directions were acquired. The in-plane resolution was 1.95313 mm. The slice thickness was 2 mm. The diffusion tensor was calculated and a deterministic fibre tracking algorithm was used [28]. The angular threshold was 90 degrees. The step size was 0.977 mm. Diffusion images were processed and all the analyses were conducted using DSI Studio ([dsi-studio.labsolver.org](http://dsi-studio.labsolver.org)). We calculated the fractional anisotropy (FA), the mean diffusivity (MD) and the apparent diffusion coefficient (ADC). The anisotropy threshold was determined automatically by the software. The fibre trajectories were smoothed by averaging the propagation direction with 30% of the previous direction. Tracks with a length less than 30 mm were discarded. A total of 15000 tracts were calculated. When reconstructing the CST, we obtained tract statistics, including: the number of tracks, the mean length, the volume of the CST, the FA, the AD, and the MD values. The ROI

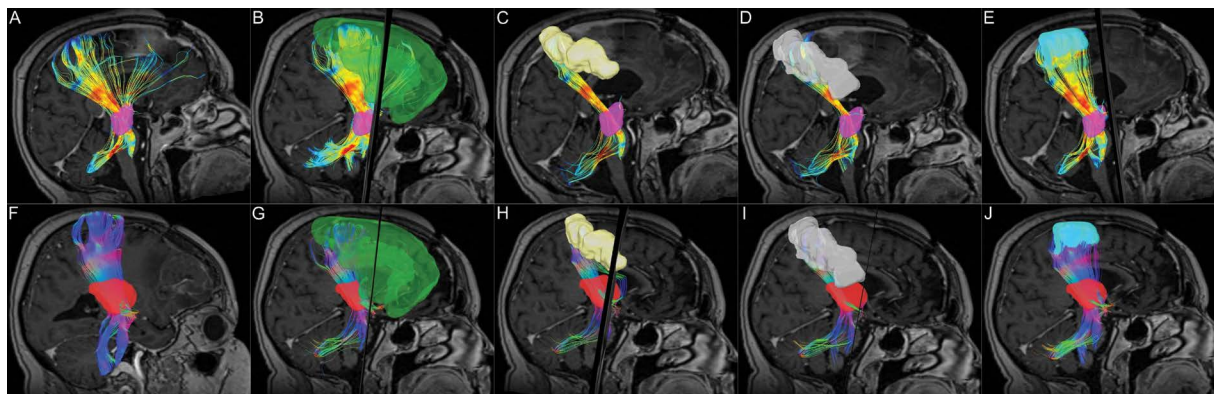


**Figure 1.** A graphic representation of different ways of drawing the cortico-spinal tract, where its course is determined by various regions of interest; **A–E.** Cerebral peduncle (CP, violet); **F–J.** Posterior limb of internal capsule (PLIC, red). **A.** Only CP; **B.** CP and frontal lobe (green); **C.** CP and precentral gyrus (yellow); **D.** CP and postcentral gyrus (white); **E.** CP and supplementary motor area (blue). **F.** Only PLIC; **G.** PLIC and frontal lobe (green); **H.** PLIC and precentral gyrus (yellow); **I.** PLIC and postcentral gyrus (white); **J.** PLIC and supplementary motor area (blue).

**Table 1.** A summary of the average values of the number of tracks of ten corticospinal tracts obtained by a combination of various region-of-interests

ROI	Number of tracts					
	Number	Mean	Median	Minimum	Maximum	SD
CP	32	147.5625	144.5000	22.0000	309.0000	64.01257
CP_preCG	31	31.3548	24.0000	0.0000	211.0000	40.43888
CP_postCG	32	15.1250	12.0000	0.0000	63.0000	15.14819
CP_SMA	32	12.7500	10.0000	0.0000	46.0000	13.77000
CP_FL	32	71.1563	71.0000	3.0000	161.0000	41.26321
PLIC	32	259.2500	248.5000	126.0000	487.0000	87.34581
PLIC_preCG	32	42.3438	39.0000	1.0000	110.0000	27.32199
PLIC_postCG	32	24.0938	22.0000	2.0000	88.0000	20.76654
PLIC_SMA	32	22.4062	18.5000	0.0000	89.0000	21.31614
PLIC_FL	32	115.5938	111.0000	0.0000	287.0000	65.03640

ROI — region of interest, CP — cerebral peduncle, preCG — precentral gyrus, postCG — postcentral gyrus, SMA — supplementary motor area, FL — frontal lobe, PLIC — posterior limb of internal capsule; SD — standard deviation

was selected according to brain landmarks that the CST passed through and the anatomical automatic atlas provided by DSI-Studio. Hence, we verified again all patients and tested methods which were used for drawing CST by other researchers.

After reviewing recent methods of DTI of the CST, we utilised two basic types of ROIs to outline the CST [4, 11, 13, 14, 19, 21, 29]. Two main ROIs were designated as “start points”: the cerebral peduncle (CP) and the posterior limb of internal capsule (PLIC). The following were established as “end points”: the precentral gyrus (PCG), the postcentral gyrus (POCG), the supplementary motor area (SMA) and the frontal lobe (FL). By mixing and matching various combinations of the start point and the end point we obtained ten

different CSTs for analysis. An example is illustrated on Figure 1.

## RESULTS

The CST was reconstructed by 10 different algorithms for each of the 32 patients in the study, resulting in a total of 320 outlines of the CST. The fibres were visualized with DSI-studio to show the anatomical validity of the reconstruction results and we overlay the CST fibres bundles with the FA image. Although the CST was outlined in every patient, a few selected variables could not be calculated due to unknown internal software error(s). The average number of tracts that were obtained with the ten algorithms are summarised in Table 1.

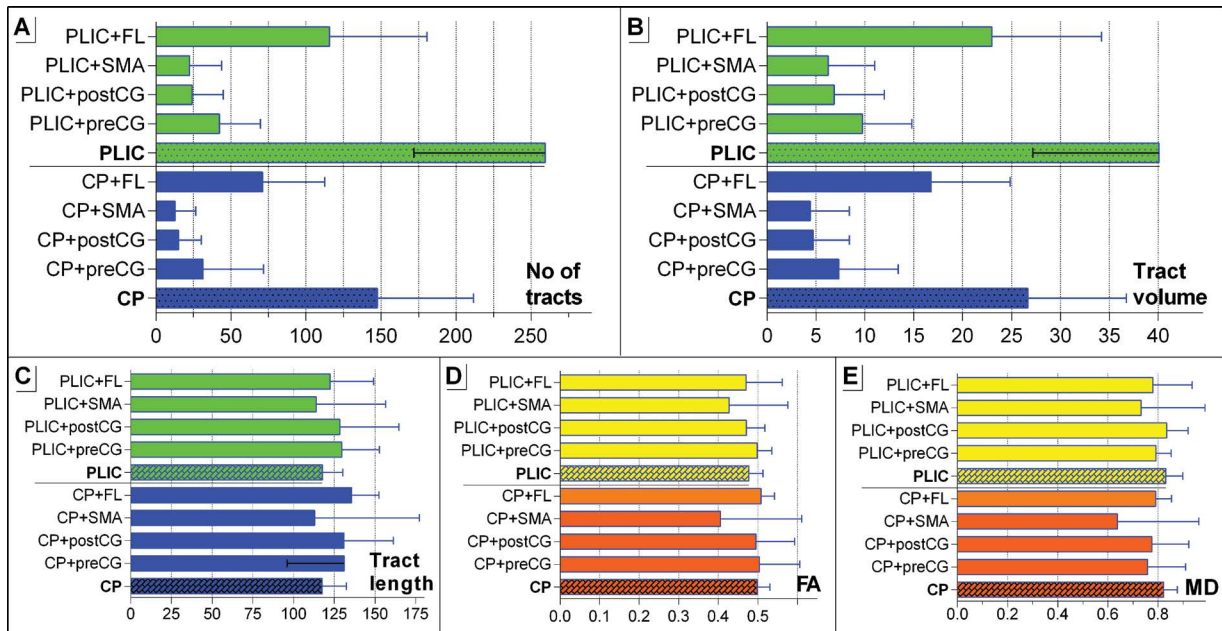


**Figure 2.** The illustration summarises the findings when using 10 different methods of outlining the corticospinal tract, including the mean; **A.** Number of tracts; **B.** Tract volume; **C.** Tract length; **D.** Fractional anisotropy (FA); **E.** The mean diffusivity (MD); PLIC — posterior limb of internal capsule, CP — cerebral peduncle, preCG — precentral gyrus, postCG — postcentral gyrus, SMA — supplementary motor area, FL — frontal lobe.

A significantly higher volume (40054U; SD  $\pm$  12874U) and number of CST tracts (259.3; SD  $\pm$  87.3) were obtained when a single ROI was set at the PLIC comparing to all other ROIs (all  $p < 0.05$ ). In contrast, almost 50% less fibres (147.6; SD  $\pm$  64.0) and volume (26664U; SD  $\pm$  10059U) was achieved when the CP was set as the ROI (both  $p < 0.05$ ) rather than the PLIC. Altogether, the PLIC and CP as starting points comprised a 6.1-fold and 4.7-fold greater number of fibres, respectively than the most common anatomical course of the CST (first ROI set at CP or PLIC, and the cortical ROI set at the precentral gyrus [preCG];  $p < 0.01$ ).

Setting the FL as the endpoint ROI yielded the highest number of tracts (PLIC and FL: 115.6; SD  $\pm$  65.0) and the highest tract volume (CP and FL: 71.1; SD  $\pm$  41.3).

There were no significant differences between the various CSTs in terms of the mean diffusion parameters (FA, MD, apparent diffusion and radial diffusivity) and mean tract length. However, all these values were insignificant when the SMA was set as a ROI (Fig. 2).

Seventeen of the 32 patients (53.1%) with preoperative hemiparesis had a brain tumour or oedema which infiltrated the CST. Even though the degree of infiltration on the CST was not evaluated, the FA, the number of tracts and the tract volumes did not differ between the CSTs drawn in ten configurations

of the ROIs (all  $p > 0.05$ ). However, in patients with CST infiltration through the CP, the MD and the apparent diffusion (AD) was significantly higher than in patients without tract infiltration ( $p = 0.04$ ). This may result from the tumour infiltrating not only the CST but other fibres which are drawn only when the CP is selected as a single ROI. The higher AD was also observed when the postcentral gyrus was added as an additional ROI to the PLIC ( $p = 0.03$ ). This patient group was mostly diagnosed high grade glioblastoma or oligodendroglioma located by the left fronto-parietal lobe, which may explain the finding.

As seen on part D and E on Figure 2, we compared the FA and MD values of the CST between the two brain hemispheres and the patient's sex, yet neither hemisphere yielded significantly different values (all  $p > 0.05$ ). However, patients older than 55 years had a significantly higher MD when the CST was traced from a start point ROI ( $p = 0.031$ ), an endpoint ROI 2 (0.036) and a start point ROI with an end point in the FL ( $p = 0.013$ ). All the statistics comparing the 10 methods of tracking the CST are presented on **Supplementary Table 1** (see journal website) (Fig. 3).

## DISCUSSION

We found that while there is no universal way of determining the CST, the CP or the PLIC should be

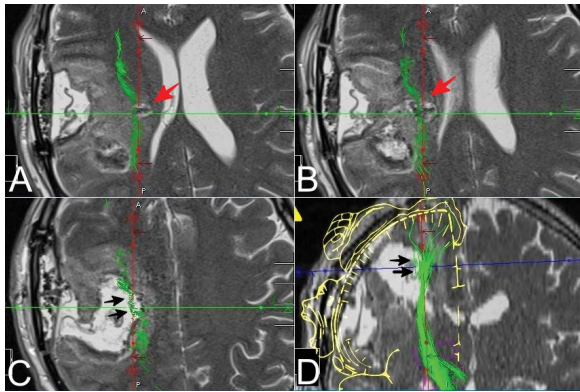


**Figure 3.** A clinical case presentation where an early postoperative magnetic resonance image was fused with a preoperative diffusion tensor imaging (DTI) of the cortico-spinal tract (CST). The subtotal resection of the secondary glioblastoma of the left fronto-parietal region was considered with the preservation of the fibres of the corticospinal tract to preserve foot function. Therefore, only the posterior limb of the internal capsule was selected as a single region of interest to increase DTI sensitivity, regardless of the decreased parallel specificity as many of fibres did not belong to the CST; **A–C.** Axial planes; **D.** Coronal plane, motor homunculus as the injected picture. The red arrows indicate the tumour remnant left deliberately in the CST. The black arrows show the compromised CST fibres responsible for hand movement.

exclusively used as the starting point ROI — regardless of whether the FL is used as the second ROI. This information is invaluable to neurosurgeons as it empowers them to obtain the most optimal view of the CST using DTI. Allowing a surgeon to better understand the spatial orientation between the tumour and the CST fibres may help preserve the CST and therefore minimize the risk of postoperative paresis; since the CST directs the movement of the limbs and the trunk [17]. To the best of our knowledge our findings are novel as our study is the first to compare the various DTI techniques regarding the CST.

It is an established issue that a long fibre bundle may not be recognised as a real fibre. Chenot proved that by using standard ROIs (i.e. PLIC and CP) we obtain a CST far beyond the primary motor cortex [6]. They showed that the CST streamlines from the premotor and parietal cortex. This finding is in contradiction with the well-known course of the pyramidal tract as described by Dejerine in 1901 [7]. To date, the exact origin of CST and the function of its non-primary motor cortex originating fibres remain unclear and unproven [2].

For neurosurgeons, the fibres originating at the precentral gyrus are the most crucial while planning any surgical access near the pyramidal tracts [10, 12, 23, 25]. A study suggests that the remainder of the

CST fibres come from the FL, mainly from the superior frontal gyrus [6]. Our results confirm this since we added the entire frontal lobe as a second ROI to the PLIC or the CP and reduced the number of fibres and the tract volume approximately 2-fold. This suggests that choosing the CP or PLIC as a single ROI does seem to be the most optimal solution when conservative access to the brain pathology is planned to minimise damage to the CST. However, limiting the extent of the ROI-based DTI to the “most anatomical” course of the CST (primary motor cortex as a second ROI to PLIC/CP), decreases the number of potentially valid fibres 6-fold as there is high variability of the CST volume among the population [6, 14]. Thus, there is no universal tractographic approach to delineate the CST due to interference of other crossing fibre tracts (although it may be overcome when the CP or the PLIC stand as a single ROI) [19]. Some authors proposed using the CP and the PLIC as two ROI where all the fibres would run through [13, 29]. At our institution we abandoned this technique and now use a custom DTI technique for all our patients because we believe that estimating the CST around the tumours at the eloquent cortex should utilise a variety of ROIs rather than a standardised set due to several of the reasons indicated before. Of note, DTI operators almost always refer to the CP as a reference for tracking the CST; however, this term is slightly ambiguous. The cerebral crus is a more accurate term anatomically as it refers solely to the anterior part of the CP (which is the correct location for CST tracking).

Setting the ROI at the PLIC was suggested as the approach most resembling the anatomical course of the CST [5]. In our study, the largest volume of the CST was achieved when a single ROI was selected, without indicating any termination points in the brain cortex. In our analysis the ROI point is relatively easy to use and is supported by most DTI data analysis software. The correct ROI may be determined on structural T1-weighted images due to their precisely defined anatomical structures. However, diffusion images that are directionally orientated (DEC sequence) are also useful to define the ROIs especially when white matter structures are being investigated. Thus, special care must be taken when choosing the appropriate ROI [26]. Seeding the termination ROI in a functionally active cortex may be regarded as the most precise method, although, this presurgical task-based functional MRI cannot provide reliable information about the CST in tumours located in the eloquent cortex [15].



In tumours located in or infiltrating the motor cortex the volume of interest (volumetric ROI) may not stand as a single cortical ROI for tracking the CST due to low accuracy [15].

Today, computer software offers automatic (anatomical) atlases to a given brain. This atlas-based method or its combination with DTI has proven to be a similar predictor of clinical outcome when compared with traditional DTI of the CST [21]. Moreover, automatic CST recognition may grant an advantage when planning brain tumour surgery. Recently, O'Donnell et al. [16] proposed the automatic patient-specific method for identifying the CST and the arcuate fasciculus and the DTI predictions corresponded with functional MRIs in 94% of patients. Additionally, the author indicated that the true anatomical termination of the main human tracts remains under debate. Thus, the combination of various techniques, including functional MRI, DTI and computational techniques, could bring scientists closer to discovering the correct CST delineation. On the contrary, the supporters of awake craniotomy for low grade gliomas urge that neuromonitoring and intraoperative stimulation maximize the tumour resection rate while still preserving motor function [8]. Yet, several patients may not be qualified for an awake procedure due to other medical and psychological reasons. We stress that in the absence of functional MRIs, an intraoperative neuromonitoring or motor mapping pathways should be considered to support DTI.

In patients with a high grade glioblastoma, where total resection remains critical, a minor neurological deficit is considered acceptable [24]. In these patients, the CP, the PLIC and the FL were deliberately selected as ROIs as they were the most important CST motor fibres that should be preserved during surgery. With this example, we assert that estimating the CST should be patient-specific as these changes in performing DTI are advantageous. Additionally, literature suggests that the CST's trajectory can change in certain brain pathologies such as a stroke, a brain tumour or a subarachnoid haemorrhage [18]. This may lead to significant alteration in the CST's original route where intraoperative direct stimulation cannot be substituted by other imaging techniques. Bello et al. reported that various types of brain tumours cause modification of white matter fibre trajectory. Based on the DTI analysis, a half of high grade gliomas caused dislocation and some tumours infiltrated or interrupted the course of tracts [3]. On the contrary, low grade gliomas only infiltrated or interrupted

tracts since only a quarter of patients had dislocated fibres. When DTI was compared with intraoperative subcortical mapping, the results illustrated that the CST's course was determined on the basis of DTI depended tumour location and volume [3].

The appropriate choice between these two ROIs lies upon the discretion of the DTI operator. Based on our analysis, seeding the CST from the PLIC results in a significantly greater number of tracks and a larger volume of the CST than seeding from the CP. We postulate that since the CP is smaller than the PLIC, it is less packed in white matter and therefore yields different results [20]. The path of the white matter fibres depends on the degree of precision of the determined ROIs. While plotting points may be determined manually or automatically, in our paper, the CST was determined with an automatic anatomical atlas using two- and three-dimensional planes.

Analysing the CST poses several challenges such as the disturbed anisotropy of water molecules and the reorganisation of nerve fibres. Moreover, tissue swelling around the tumour may disturb the proportions of perpendicular and parallel diffusion, which decreases the FA; this is due to the inversely proportional ratio of average diffusivity and cellularity of the pathology [21]. In addition, the measurement of anisotropy may become a factor differentiating tumours of high and low level of malignancy [21].

In future studies, different tractography methods can be connected with DTI multi-tensor acquisition. Identification of the CST should be carried out based on blood-oxygen-level-dependent and diffusion functional MRIs [9]. These methods may help a physician achieve a better regional and spatial understanding of an area.

## CONCLUSIONS




Our study identified the CST based on various anatomical approaches. We found that while there is no universal method of determining the CST, the CP or the PLIC should be used as the starting point ROIs.

## REFERENCES

1. Anthofer JM, Steib K, Fellner C, et al. DTI-based deterministic fibre tracking of the medial forebrain bundle. *Acta Neurochir (Wien)*. 2015; 157(3): 469–477, doi: [10.1007/s00701-014-2335-y](https://doi.org/10.1007/s00701-014-2335-y), indexed in Pubmed: [25585836](https://pubmed.ncbi.nlm.nih.gov/25585836/).
2. Archer DB, Vaillancourt DE, Coombes SA. A template and probabilistic atlas of the human sensorimotor tracts using diffusion MRI. *Cereb Cortex*. 2018; 28(5): 1685–1699, doi: [10.1093/cercor/bhx066](https://doi.org/10.1093/cercor/bhx066), indexed in Pubmed: [28334314](https://pubmed.ncbi.nlm.nih.gov/28334314/).
3. Bello L, Gambini A, Castellano A, et al. Motor and language DTI fiber tracking combined with intraoperative

- subcortical mapping for surgical removal of gliomas. *Neuroimage*. 2008; 39(1): 369–382, doi: [10.1016/j.neuroimage.2007.08.031](https://doi.org/10.1016/j.neuroimage.2007.08.031), indexed in Pubmed: [17911032](https://pubmed.ncbi.nlm.nih.gov/17911032/).
4. Bonney PA, Conner AK, Boettcher LB, et al. A simplified method of accurate postprocessing of diffusion tensor imaging for use in brain tumor resection. *Oper Neurosurg (Hagerstown)*. 2017; 13(1): 47–59, doi: [10.1227/NEU.0000000000001181](https://doi.org/10.1227/NEU.0000000000001181), indexed in Pubmed: [28931252](https://pubmed.ncbi.nlm.nih.gov/28931252/).
  5. Bürgel U, Amunts K, Hoemke L, et al. White matter fiber tracts of the human brain: three-dimensional mapping at microscopic resolution, topography and intersubject variability. *Neuroimage*. 2006; 29(4): 1092–1105, doi: [10.1016/j.neuroimage.2005.08.040](https://doi.org/10.1016/j.neuroimage.2005.08.040), indexed in Pubmed: [16236527](https://pubmed.ncbi.nlm.nih.gov/16236527/).
  6. Chenot Q, Tzourio-Mazoyer N, Rheault F, et al. A population-based atlas of the human pyramidal tract in 410 healthy participants. *Brain Struct Funct*. 2019; 224(2): 599–612, doi: [10.1007/s00429-018-1798-7](https://doi.org/10.1007/s00429-018-1798-7), indexed in Pubmed: [30460551](https://pubmed.ncbi.nlm.nih.gov/30460551/).
  7. Dejerine J, Dejerine-Klumpke A. *Anatomie des centres nerveux*. Tome 2. Rueff et Cie, Paris 1901.
  8. Duffau H, Taillandier L. New concepts in the management of diffuse low-grade glioma: Proposal of a multistage and individualized therapeutic approach. *Neuro Oncol*. 2015; 17(3): 332–342, doi: [10.1093/neuonc/nou153](https://doi.org/10.1093/neuonc/nou153), indexed in Pubmed: [25087230](https://pubmed.ncbi.nlm.nih.gov/25087230/).
  9. Holodny AI, Ollenschleger MD, Liu WC, et al. Identification of the corticospinal tracts achieved using blood-oxygen-level-dependent and diffusion functional MR imaging in patients with brain tumors. *Am J Neuroradiol*. 2001; 22(1): 83–88, indexed in Pubmed: [11158892](https://pubmed.ncbi.nlm.nih.gov/11158892/).
  10. Kieronska S, Słoniewski P. The usefulness and limitations of diffusion tensor imaging – a review study. *Eur J Transl Clin Med*. 2020; 2(2): 43–51, doi: [10.31373/ejtc/112437](https://doi.org/10.31373/ejtc/112437).
  11. Kim B, Fisher BE, Schweighofer N, et al. A comparison of seven different DTI-derived estimates of corticospinal tract structural characteristics in chronic stroke survivors. *J Neurosci Methods*. 2018; 304: 66–75, doi: [10.1016/j.jneumeth.2018.04.010](https://doi.org/10.1016/j.jneumeth.2018.04.010), indexed in Pubmed: [29684462](https://pubmed.ncbi.nlm.nih.gov/29684462/).
  12. Krakowiak M, Słoniewski P, Dzierżanowski J, et al. Future of the nerve fibres imaging: tractography application and development directions. *Folia Morphol*. 2015; 74(3): 290–294, doi: [10.5603/FM.2015.0044](https://doi.org/10.5603/FM.2015.0044), indexed in Pubmed: [26339808](https://pubmed.ncbi.nlm.nih.gov/26339808/).
  13. Kuczynski AM, Dukelow SP, Hodge JA, et al. Corticospinal tract diffusion properties and robotic visually guided reaching in children with hemiparetic cerebral palsy. *Hum Brain Mapp*. 2018; 39(3): 1130–1144, doi: [10.1002/hbm.23904](https://doi.org/10.1002/hbm.23904), indexed in Pubmed: [29193460](https://pubmed.ncbi.nlm.nih.gov/29193460/).
  14. Leote J, Nunes RG, Cerqueira L, et al. Reconstruction of white matter fibre tracts using diffusion kurtosis tensor imaging at 1.5T: Pre-surgical planning in patients with gliomas. *Eur J Radiol Open*. 2018; 5: 20–23, doi: [10.1016/j.ejro.2018.01.002](https://doi.org/10.1016/j.ejro.2018.01.002), indexed in Pubmed: [29719853](https://pubmed.ncbi.nlm.nih.gov/29719853/).
  15. Niu C, Liu X, Yang Y, et al. Assessing region of interest schemes for the corticospinal tract in patients with brain tumors. *Medicine (Baltimore)*. 2016; 95(12): e3189, doi: [10.1097/MD.00000000000003189](https://doi.org/10.1097/MD.00000000000003189), indexed in Pubmed: [27015212](https://pubmed.ncbi.nlm.nih.gov/27015212/).
  16. O'Donnell LJ, Suter Y, Rigolo L, et al. Automated white matter fiber tract identification in patients with brain tumors. *Neuroimage Clin*. 2017; 13: 138–153, doi: [10.1016/j.nicl.2016.11.023](https://doi.org/10.1016/j.nicl.2016.11.023), indexed in Pubmed: [27981029](https://pubmed.ncbi.nlm.nih.gov/27981029/).
  17. Ottenhausen M, Krieg SM, Meyer B, et al. Functional preoperative and intraoperative mapping and monitoring: increasing safety and efficacy in glioma surgery. *Neurosurg Focus*. 2015; 38(1): E3, doi: [10.3171/2014.10.FOCUS14611](https://doi.org/10.3171/2014.10.FOCUS14611), indexed in Pubmed: [25552283](https://pubmed.ncbi.nlm.nih.gov/25552283/).
  18. Park CH, Kou N, Boudrias MH, et al. Assessing a standardised approach to measuring corticospinal integrity after stroke with DTI. *Neuroimage Clin*. 2013; 2: 521–533, doi: [10.1016/j.nicl.2013.04.002](https://doi.org/10.1016/j.nicl.2013.04.002), indexed in Pubmed: [24179804](https://pubmed.ncbi.nlm.nih.gov/24179804/).
  19. Pujol S, Wells W, Pierpaoli C, et al. The DTI challenge: toward standardized evaluation of diffusion tensor imaging tractography for neurosurgery. *J Neuroimaging*. 2015; 25(6): 875–882, doi: [10.1111/jon.12283](https://doi.org/10.1111/jon.12283), indexed in Pubmed: [26259925](https://pubmed.ncbi.nlm.nih.gov/26259925/).
  20. Radmanesh A, Zamani AA, Whalen S, et al. Comparison of seeding methods for visualization of the corticospinal tracts using single tensor tractography. *Clin Neuro Neurosurg*. 2015; 129: 44–49, doi: [10.1016/j.clineuro.2014.11.021](https://doi.org/10.1016/j.clineuro.2014.11.021), indexed in Pubmed: [25532134](https://pubmed.ncbi.nlm.nih.gov/25532134/).
  21. Ressel V, van Hedel HJA, Scheer I, et al. Comparison of DTI analysis methods for clinical research: influence of pre-processing and tract selection methods. *Eur Radiol Exp*. 2018; 2(1): 33, doi: [10.1186/s41747-018-0066-1](https://doi.org/10.1186/s41747-018-0066-1), indexed in Pubmed: [30426317](https://pubmed.ncbi.nlm.nih.gov/30426317/).
  22. Soni N, Mehrotra A, Behari S, et al. Diffusion-tensor imaging and tractography application in pre-operative planning of intra-axial brain lesions. *Cureus*. 2017; 9(10): e1739, doi: [10.7759/cureus.1739](https://doi.org/10.7759/cureus.1739), indexed in Pubmed: [29209586](https://pubmed.ncbi.nlm.nih.gov/29209586/).
  23. Szmuda T, Ali S. Commentary on: The usefulness and limitations of diffusion tensor imaging – a review study. *Eur J Transl Clin Med*. 2020; 2(2): 85–86, doi: [10.31373/ejtc/114000](https://doi.org/10.31373/ejtc/114000).
  24. Szmuda T, Słoniewski P, Olijewski W, et al. Colour contrasting between tissues predicts the resection in 5-aminolevulinic acid-guided surgery of malignant gliomas. *J Neurooncol*. 2015; 122(3): 575–584, doi: [10.1007/s11060-015-1750-0](https://doi.org/10.1007/s11060-015-1750-0), indexed in Pubmed: [25702194](https://pubmed.ncbi.nlm.nih.gov/25702194/).
  25. Szmuda T, Słoniewski P, Szmuda M, et al. Quantification of white matter fibre pathways disruption in frontal transcortical approach to the lateral ventricle or the interventricular foramen in diffusion tensor tractography. *Folia Morphol*. 2014; 73(2): 129–138, doi: [10.5603/FM.2013.0063](https://doi.org/10.5603/FM.2013.0063), indexed in Pubmed: [24902089](https://pubmed.ncbi.nlm.nih.gov/24902089/).
  26. Van Hecke W, Emsell L, Sunaert S. *Diffusion Tensor Imaging: A Practical Handbook*. Diffus Tensor Imaging A Pract Handb. 2016: 1–440, doi: [10.1007/978-1-4939-3118-7](https://doi.org/10.1007/978-1-4939-3118-7).
  27. Witwer BP, Moftakhar R, Hasan KM, et al. Diffusion-tensor imaging of white matter tracts in patients with cerebral neoplasm. *J Neurosurg*. 2002; 97(3): 568–575, doi: [10.3171/jns.2002.97.3.0568](https://doi.org/10.3171/jns.2002.97.3.0568), indexed in Pubmed: [12296640](https://pubmed.ncbi.nlm.nih.gov/12296640/).
  28. Yeh FC, Wedeen VJ, Tseng WYI. Generalized q-sampling imaging. *IEEE Trans Med Imaging*. 2010; 29(9): 1626–1635, doi: [10.1109/TMI.2010.2045126](https://doi.org/10.1109/TMI.2010.2045126), indexed in Pubmed: [20304721](https://pubmed.ncbi.nlm.nih.gov/20304721/).
  29. Yu Qi, Lin K, Liu Y, et al. Clinical uses of diffusion tensor imaging fiber tracking merged neuronavigation with lesions adjacent to corticospinal tract : a retrospective cohort study. *J Korean Neurosurg Soc*. 2020; 63(2): 248–260, doi: [10.3340/jkns.2019.0046](https://doi.org/10.3340/jkns.2019.0046), indexed in Pubmed: [31295976](https://pubmed.ncbi.nlm.nih.gov/31295976/).

# Comparison of colour difference formulas to best distinguish resected areas of malignant brain tumours from their background using 5-aminolevulinic acid fluorescence

T. Szmuda<sup>1\*</sup>, S. Ali<sup>2\*</sup>, P. Słoniewski<sup>1</sup>

<sup>1</sup>Neurosurgery Department, Medical University of Gdansk, Poland

<sup>2</sup>Student's Scientific Circle, Neurosurgery Department, Medical University of Gdansk, Poland

[Received: 3 February 2020; Accepted: 26 February 2020]

**Background:** Fluorescence-guided surgery (FGS) with 5-aminolevulinic acid (5-ALA) has been proven to assist neurosurgeons to achieve a more complete brain tumour resection. However, 5-ALA-guided surgery is limited since it is often difficult to distinguish the colour difference between the resected areas of malignant brain tumours from their background. Our aim was to evaluate which colour difference formula was optimal to distinguish between malignant brain tumours and the background healthy tissue using 5-ALA fluorescence.

**Materials and methods:** Thirty-seven patients with a primary or secondary malignant brain tumour ingested 5-ALA before the surgery. A 400 nm light was used to excite the fluorescence. Surgical videos were recorded for all the patients and a total of 183 samples were obtained from the fluorescent areas and their respective backgrounds. Three colour differences formulas — contrast ratio (CR), CIELab ( $\Delta E^*$ ) and CIEDE2000 — were applied to the videos and compared using hot-cold maps. Baseline demographics, the tumour's location, the tumour's side, and tumour's World Health Organization (WHO) grade was also analysed for correlations relating to the fluorescence. Chi-square and the Student's *t*-test were used for univariate relations. The three channels of the CIELAB colour space ( $L^*$ ,  $a^*$  and  $b^*$ ) were analysed together and separately (since  $L^*$  of fluorescent areas was significantly higher than the background).

**Results:**  $\Delta E^*$  resulted in good discrimination of  $a^*$  and  $b^*$ , and moderate but acceptable discrimination of  $L^*$ . CIEDE2000 distinguished differences in  $a^*$  and  $b^*$ , although not in  $L^*$ . The CR distinguished only  $L^*$ , whereas the probability of discriminating  $a^*$  and  $b^*$  channels failed. Neither age, sex, tumour location, tumour size nor the WHO grade influenced the  $a^*$ ,  $b^*$  and  $L^*$  colour values ( $p > 0.05$ ). Colour differences measured by  $\Delta E^*$  and CIEDE2000 correlated together ( $r = 0.99$ ,  $p < 0.01$ ), whereas CR correlated only with  $\Delta E^*$  ( $r = 0.21$ ,  $p = 0.01$ ) but not with CIEDE2000 ( $r = 0.07$ ,  $p = 0.32$ ).

**Conclusions:**  $\Delta E^*$  obtained the best colour discrimination between the resected areas of malignant brain tumours and the background when compared to CR and CIEDE2000. Therefore,  $\Delta E^*$  may be the best formula to help neurosurgeons

Address for correspondence: Dr. T. Szmuda, Neurosurgery Department, Medical University of Gdansk, ul. Dębinki 7, 80–952 Gdańsk, Poland, tel: +48 511280369, fax: +48 58 349 33 30, e-mail: tszmuda@gumed.edu.pl

\*Contributed equally to the manuscript

*distinguish the colour differences when operating malignant brain tumours with 5-ALA fluorescence.* (Folia Morphol 2021; 80, 1: 47–54)

**Key words:** 5-aminolevulinic acid, glioma surgery, colour perception, CIEDE2000, fluorescence

## INTRODUCTION

Maximal tumour resection with minimal injury to the surrounding tissue remains the goal for neurological surgeons operating on malignant brain tumours [8, 18, 19, 23]. Fluorescence-guided surgery (FGS) may assist in this matter as it allows better visualisation of a patient's brain tumours, despite brain shift caused by a prolonged surgery or neuronavigational limitations [6]. This allows the physician to perform an optimal resection not only for malignant gliomas but also for recurrent glioblastomas [6, 10]. 5-aminolevulinic acid (5-ALA) is commonly used for FGS as it is a natural haemoglobin metabolite, can be easily administered orally and carries minimal side effects [1].

After ingestion, it accumulates within malignant brain tissues and fluoresces in a violet-red colour after excitation with blue light.

Unfortunately, despite the promise of 5-ALA-guided resection, it remains greatly limited since 5-ALA fluorescence is sometimes difficult to be distinguished from the background healthy tissue. This is crucial since, in practice, the decision to resect a section of a tumour is determined largely by the background colour [19]. To the human eye, slightly different colours may not be able to be distinguished. Thus, to objectively measure colour, the colour space defined by the International Commission on Illumination (CIE LAB) colour system is used to reliably express colour in three quantitative values denoted:  $L^*$ ,  $a^*$  and  $b^*$ . Several colour difference formulas have been proposed including: contrast ratio (CR), CIE Lab ( $\Delta E^*$ ) and CIEDE2000.

$\Delta E^*$  was the very first formula proposed by the International Commission on Illumination (CIE) to measure distance between colours. However, over time, they updated their colour difference formula to CIEDE2000 to account for non-uniformities in human colour vision. CIEDE2000 has also been established as the International Organization for Standardization (ISO) standard. However, these general recommendations may not be optimal to distinguish brain tumours due to the highly specific physical qualities of brain tissue and brain tumours. Studies have shown that

colour perception is highly unique depending on the part of the human body and tissue studied [4, 9]. To our knowledge, no study has yet been done to determine the best colour difference formula(s) regarding brain tumours.

We sought to evaluate which colour difference parameter was optimal to distinguish between malignant brain tumours and the background using 5-ALA fluorescence. To accomplish this, we utilised numerous colour difference formulas (i.e. CR,  $\Delta E^*$  or CIEDE2000) on the neurosurgical recordings of patients with brain tumours.

## MATERIALS AND METHODS

### Patients

Thirty-seven patients with a brain tumour were prospectively collected (22 males and 15 females; age 23–81 years, mean  $\pm$  standard deviation [SD]:  $58.2 \pm 16.3$ , and median age: 64). These patients were treated at the Neurosurgery Department at the Medical University of Gdansk in Gdańsk, Poland, from August 2015 to December 2019. We collected baseline demographic data (age and sex), tumour location (within the lobe and the hemisphere), histopathology, and the World Health Organization (WHO) tumour grade. The protocol of the study was approved by the local bioethical committee (permission number NKBBN/98/2012). The study is a continuation of our previous observations and includes a similar methodology for colour analysis [19].

### Surgery

Four hours prior to anaesthesia, 5-ALA (Gliolan, Medac GmbH; Wedel, Germany) was given orally to each patient. Following craniotomy, magnetic resonance imaging-based navigation helped to remove the gross parts of the tumour under white light. Diffusion tensor tractography highlighted white matter tracts (cerebrospinal tract or arcuate fasciculus) and limited resection of the tumours located near the eloquent areas.

Afterwards, a blue light was used to identify the remaining tumour and a white light was turned on

for further resection. The surgery was carried out in this way until the operating neurosurgeon deemed the tumour to be completely resected. In all the surgeries, the duration from 5-ALA intake to the end of surgical resection was about 9 hours.

### Equipment

Preoperative magnetic resonance imaging was performed on all patients (1.5 Tesla, according to the site-specific protocol, including contrast enhanced [CE] T1, T2-weighted, spectroscopy and diffusion weighed scenes). The StealthViz application (Medtronic Inc., Minneapolis) and StealthStation S7 navigation (Medtronic Navigation; Louisville, CO, USA) assisted all the surgeries. Blue-light filtering of the surgical microscope (OPMI Pentero with fluorescence kit BLU 400, Carl Zeiss, Germany) met the European Medical Device Directive 93/42/EEC requirements. The microscope included an integrated digital camera MKC-500HD (Ikegami Co.; Tokyo, Japan). Camera specifications were as follows: high-definition matrix 1920 × 1080p, 54 dB signal-to-noise ratio, sensitivity of F12 at 2000 lux/3200°K and a 1/3-inch CMOS image sensor. Light sensitivity and white balance remained constant at the default settings. Spectral sensitivity and light filtering in the microscope and camera were unattainable from the manufacturers. The excitation wavelength range was 400–410 nm and the observation wavelength range was 620–710 nm. Room luminance remained constant during the entire surgery and study.

Surgical recordings were examined on a Dell U2410 32" monitor (1920 × 1200p, 16:10 widescreen aspect ratio, 80000:1 dynamic contrast ratio, colour depth of 1.07 billion and 100% coverage of CIE L\*a\*b\* colour gamut 7). Shotcut software v.5.2.0 (Digia Inc.; Santa Clara, CA, USA) was used for video playback without any video filtering.

### Study design and colour analysis

The neurosurgical recordings were watched and points of interest to be included into this study's colorimetric evaluation were chosen if: (1) an area demonstrated fluorescence by the naked eye regardless of its future surgical removal and (2) if an area was delineated by the adjacent background by a different colour.

The points of interests were chosen from the video. Then, Colour Contrast Analyser v.2.5 (WAT

Consortium, int'l) was used to probe the area with RGB colour model values. Both the fluorescent region and the corresponding background of the tumour was analysed in this way. Afterwards, the RGB model was transformed into the CIELAB colour space which consisted of three colour coordinates denoted L\*, a\* and b\* (L\* denotes lightness, a\* describes a red or green value and b\* describes a yellow or blue value).

Using these values, the following formulas found colour differences from the same pool of samples:  $\Delta E^*$ , CIEDE2000 and CR.  $\Delta E^*$  measures the difference between two colours (L\*, a\* and b\*). CR compares relative luminance (i.e. all colours are converted to greyscale) and it is the key parameter distinguishing colours. CIEDE2000 is a complex formula taking into account several metrics to compensate for neutral colours, lightness, chroma and hue.

CIEDE2000,  $\Delta E$  and CR calculated colour differences and their formulas are presented below:

CIEDE2000 (CIE Publ. 142–2001, CIE S 014–6/E:2013)

$$\Delta E^* = \sqrt{([L1-L2]^2 + [a1-a2]^2 + [b1-b2]^2)}$$

$$CR = (L1 + 0.05) / (L2 + 0.05)$$

where L1 and L2 represent relative lighter and darker colour luminance respectively; a1, b1 and a1, b1 signify dimensions of lighter and darker colours respectively.

$\Delta E^*$ , CIEDE2000 and RGB to CIE 1976 L\*a\*b\* transformations were calculated using an electronic spread sheet (Microsoft Office Excel 2010 for Windows). CR was calculated using Colour Contrast Analyser software.

### Statistical analysis

Statistica Software v.10.0 (StatSoft Inc.; Tulsa, OK, USA), was used for performing Chi-square, Student's t-test and their non-parametric equivalents. Continuous variables are expressed as mean ± SD. A p value of < 0.05 was considered statistically significant. Figure 1 illustrates the methodology of probing fluorescent areas and their surroundings. Figure 2 was created using Prism v.6.07 (GraphPad; La Jolla, CA, USA). Hot-cold maps in Figure 3 were created using Past (Hammer and Harper, Øyvind Hammer, Natural History Museum, University of Oslo).

### Study objective

Our aim was to evaluate various colour difference formulas (CR,  $\Delta E^*$  and CIEDE2000) that distinguish fluorescent areas from the background. We attempted this by analysing the area of CIELAB colour space

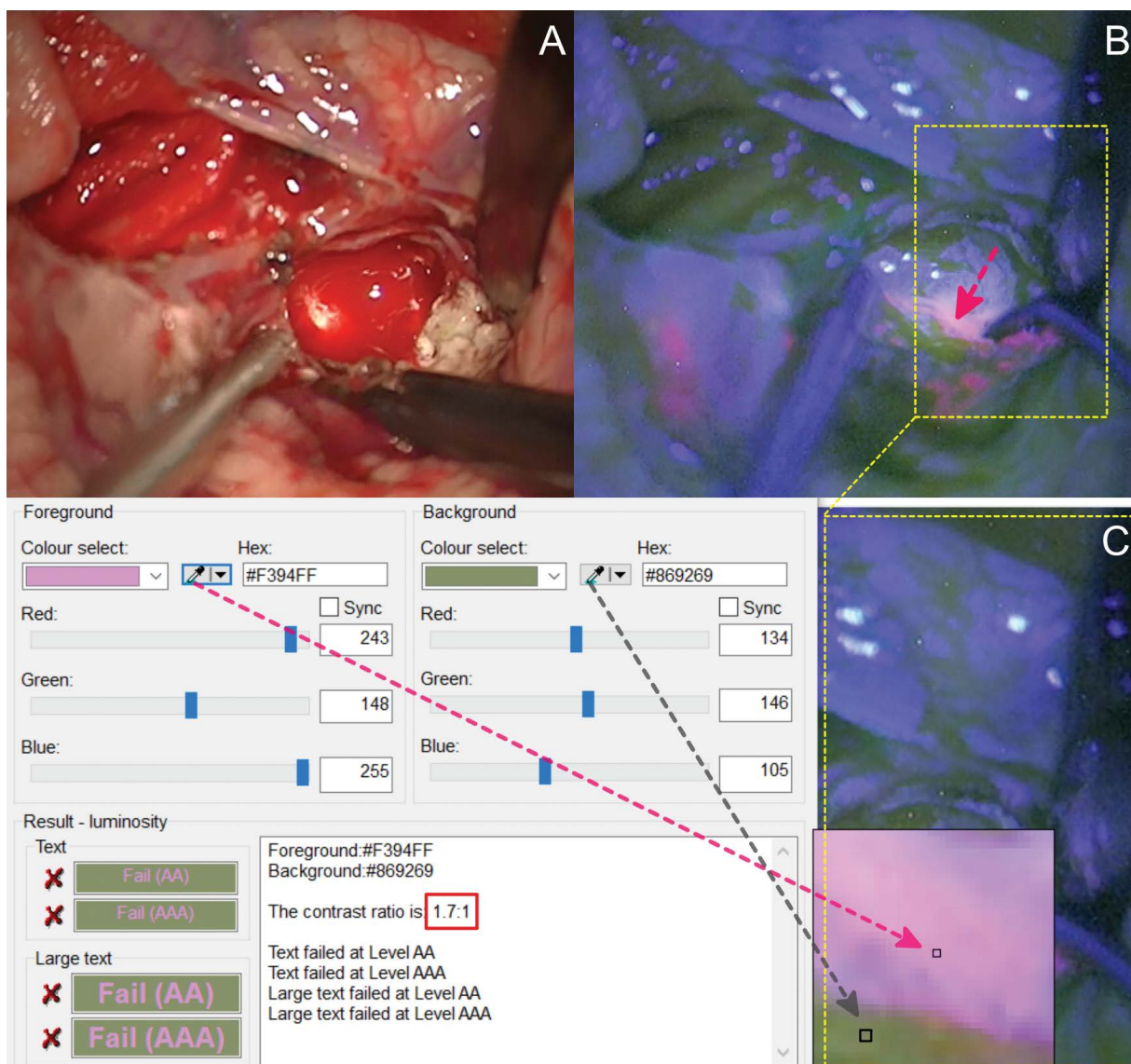


**Figure 1.** This illustration shows how colour parameters were obtained and analysed from the surgery; **A.** The view of the neurosurgical operative area illuminated under normal white-light; **B.** The same view of the operative area; however, illuminated by a 400 nm blue light so that the fluorescence indicated the tumour (pink arrow on panel B); **C.** A picture was taken and was analysed on the computer; the fluorescence (pink arrow) and the background (grey arrow) were chosen and they were coded on the RGB colour space. The contrast ratio was calculated automatically by the software (red rectangle).

under 400 nm illumination and probed fluorescent points and their background.

## RESULTS

The clinical course and outcome were not the scope of the study. Twenty-seven (73.0%) patients had glioblastoma and 2 (5.4%) had gliosarcoma. Out of the primary brain tumours, all were malignant except for 1 patient with gemistic astrocytoma (WHO 2 grade). Out of the total 37 patients, there were 14 (37.8%) surgeries of recurrent or progressive tumours. The most common locations of the tumour were at the temporal lobe (n = 16, 43.2%) and the frontal

lobe (n = 9, 24.3%). We obtained 183 samples of fluorescent areas and 183 samples of their respective background. The detailed chart of sampled values is presented on **Supplementary Table 1**. The results of all the CIELAB colour space channels are illustrated on Figure 2.

### Colour difference

$\Delta E$  and CIEDE2000 correlated together ( $r = 0.99$ ,  $p < 0.01$ ). CR correlated only with  $\Delta E$  ( $r = 0.21$ ,  $p = 0.01$ ) but not with CIEDE2000 ( $r = 0.07$ ,  $p = 0.32$ ). Age, sex, the number of samples, brain hemisphere, location of the tumour and glioblastoma histopathology did not

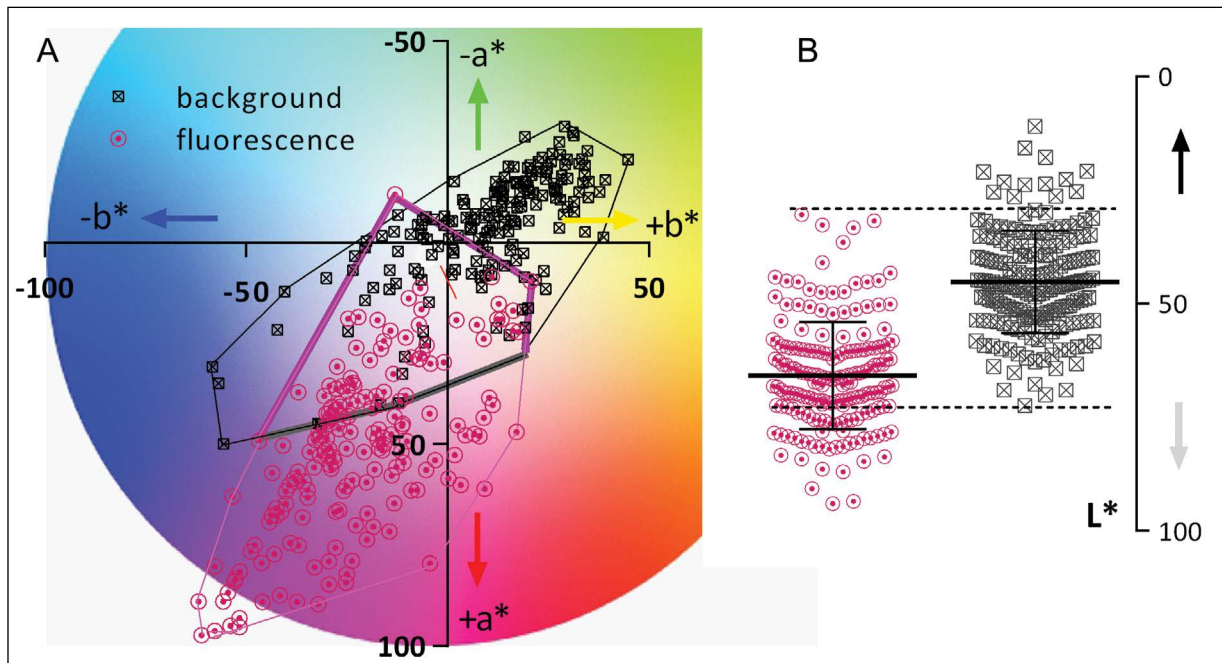


**Figure 2.** Colours of fluorescing areas and the surrounding background in the three channels of the CIELAB colour space:  $a^*$  (green [-] to red [+]),  $b^*$  (blue [-] to yellow [+]) and  $L^*$  for lightness from black to white. Since all three channels could not be represented feasibly on one three-dimensional graph (A) represents  $a^*$  and  $b^*$  while panel B represents only  $L^*$  on the CIELAB colour space. Both panels A and B show a difference in the colour of the background (black crossed square) and the fluorescence (violet encircled dots), however, there is also overlap between the two in  $L^*$ ,  $a^*$  and  $b^*$ ; A. Most of the fluorescent areas were located in Quadrant III (the purple area) while the background colours were located mostly in Quadrant I (the green area); B. The lightness ( $L^*$ ) of most of the fluorescent areas was higher than its background; CIELAB — colour space defined by the International Commission on Illumination.

influence the fluorescent areas or their background colour values ( $a^*$ ,  $b^*$  and  $L^*$ ) ( $p$  always  $> 0.05$ ).

Descriptive statistics of all colour difference parameters are presented on Table 1 and Figure 3 illustrates those findings.  $\Delta E$  resulted in good discrimination of  $a^*$  and  $b^*$ , and moderate but acceptable discrimination of  $L^*$ . CR distinguished only  $L^*$ , whereas the probability of discriminating  $a^*$  and  $b^*$  channels failed. CIEDE2000 distinguished differences in  $a^*$  and  $b^*$  axes, however, not in  $L^*$ .

## DISCUSSION

### Key findings

We found that  $\Delta E^*$  best distinguished colour differences between the resected areas of malignant brain tumours and the background with 5-ALA fluorescence compared to other established colour difference formulas, namely CIEDE2000 and CR. By utilising this optimal colour difference formula for intracranial tumours, neurosurgeons can further appreciate and enjoy the benefits of 5-ALA FGS by performing more complete tumour resections. Our findings are clinically profound since a greater extent of tumour resection may lead to several favourable prognostic

implications for the patient. Even in patients with glioblastoma — a tumour with an especially poor prognosis — a greater extent of resection is still a proven benefit to patients [5, 13, 15]. To our best knowledge, this study is the first to compare the colour difference formulas among intracranial tumours. Moreover, our findings challenge the current ISO colour difference standard (i.e. CIEDE2000, which is recommended by the CIE).

### Context

Gómez-Polo et al. [4, 5] — on their colour experiments conducted on the human gingiva — found that CIEDE2000 imitated colour differences better than  $\Delta E^*$ ; however, in a later experiment found that *both* formulas reflected colour differences in a similar fashion. Our results disagree with Gómez-Polo et al. [4, 5] as we found that  $\Delta E^*$  best distinguished colour differences; however, we reiterate that our experiments were conducted on malignant intracranial tumours which may express 5-ALA fluorescence much different colours than the human gingiva. Therefore, we do not discredit CIEDE2000, but postulate that it may not be the most superior

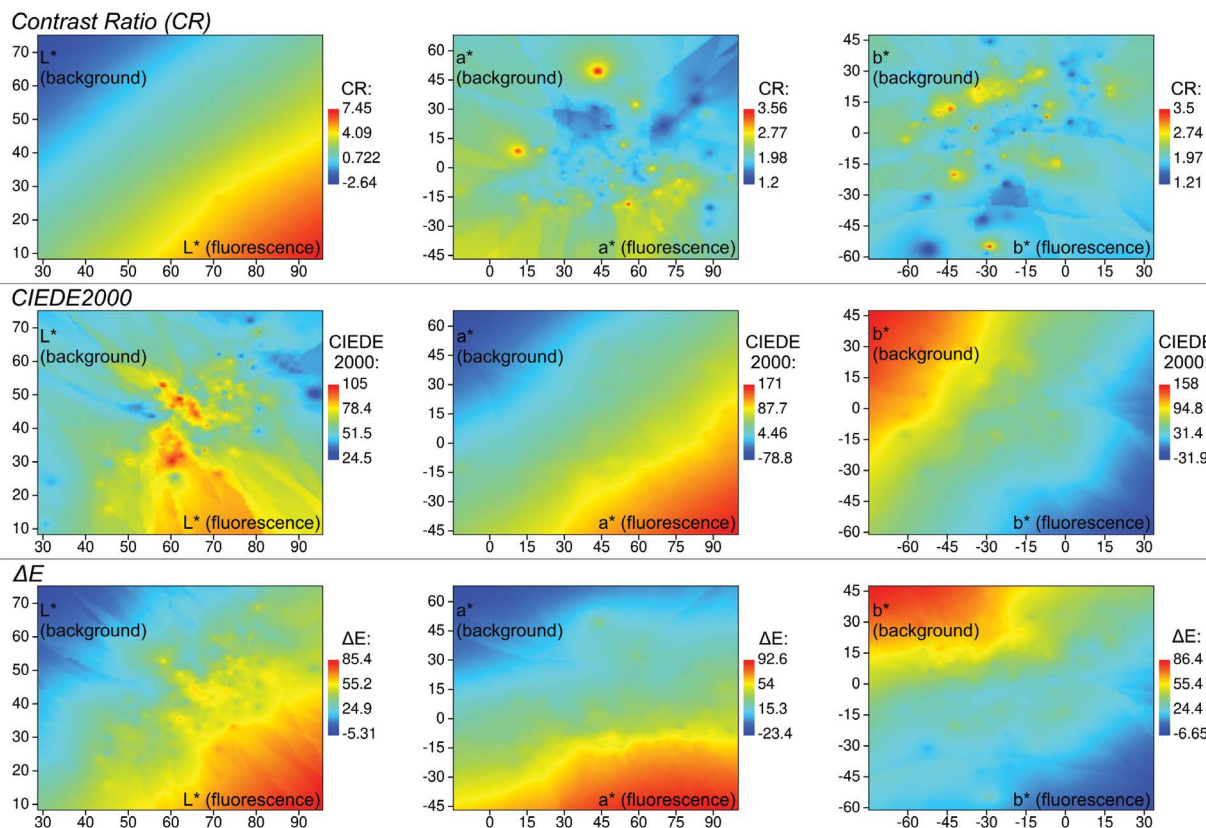


**Figure 3.** Hot-cold probability maps show to what extent the contrast ratio (CR), CIEDE2000 and  $\Delta E$  distinguished colour differences in the three channels of the CIELAB colour space (L\*, a\* and b\*). One may consider “solid or more distinct colour bands” to illustrate significant probabilities (e.g.  $\Delta E$  for a\*, b\* and L\*) while “scattered colours” illustrate non-significant probabilities (CIEDE2000 for L\* and CR for a\* and b\*).

**Table 1.** Colour parameters and colour difference parameters between the fluorescent areas and the background. L\*, a\* and b\* are colour space defined by the International Commission on Illumination (CIELAB) colour space values; colour difference was expressed by means of  $\Delta E$ , contrast ratio and CIEDE2000

Value	Mean	Median	Minimum	Maximum	Lower quartile	Upper quartile	Standard deviation	Standard error of mean	P
Foreground L*	65.80	66.67	30.40	93.97	59.81	72.86	11.81	0.873025	< 0.01
Background L*	45.19	45.62	11.01	72.47	37.47	53.03	11.26	0.832113	
Fluorescence a*	51.03	49.12	-11.93	97.30	38.06	64.56	20.87	1.542679	< 0.01
Background a*	-3.37	-5.78	-28.73	49.91	-13.87	4.3332	14.76	1.090750	
Fluorescence b*	-22.55	-24.69	-61.88	20.67	-33.05	-11.38	17.90	1.323546	< 0.01
Background b*	9.84	13.53	-58.39	44.82	0.27	22.49	18.82	1.391401	
$\Delta E$	42.51	41.55	14.10	78.66	30.58	55.17	14.82	1.096059	
Contrast ratio	2.11	1.90	1.00	4.80	1.70	2.50	0.65	0.047958	
CIEDE2000	66.10	65.19	15.15	145.07	47.41	83.21	25.49	1.884512	

in distinguishing colour differences with malignant brain tumours.

In our previous study on 5-ALA, we proved that surgeons make a decision on tumour resection based on colour L\* contrast (like CR), and not on colour fluorescence [19]. Therefore, in our study, we compared

the CR with  $\Delta E^*$  and CIEDE2000. In this study, the CR formula distinguished colour difference the best in the L\* section of colour space (the shades from black to white) compared to  $\Delta E^*$  and CIEDE2000. However, we realize that since CR is calculated solely on L\*, it has a limited use when discriminating other



colour parameters (e.g. pink fluorescence from a grey background).

A 2011 study on 5-ALA first explored the advantages of measuring 5-ALA-induced fluorescent-metabolites in vivo [20]. Therefore, our study adopted a similar method as the spectra of colours were measured intraoperatively. Their study also concluded that 5-ALA may be used for not only high-grade glioma, but other tumours as well. Our results support these findings as 5-ALA was able to discriminate between normal and malignant tumour tissue in a variety of tumours (i.e. glioblastoma, anaplastic oligodendroglioma and anaplastic astrocytoma).

### Limitations of the study

We realise that there is an inherent challenge in measuring colour difference due to the heterogeneous perception of colour among every individual that is problematic to overcome. However, the formulas used in our study to distinguish colour differences are established and reproducible.

Moreover, it is possible that blood or other organic brain debris might have covered parts of the fluorescing tumour, making colour analysis complicated. Removing unwanted material and preserving a clear view of the operating field is the responsibility of the operating neurosurgeon. We confirm that the neurosurgeons operating on the tumours included in the study had more than 15 years of neurosurgical experience at a university hospital, and thus, assume that they maintained an adequate view of the surgical field at least for the purposes of this study.

### Future directions

In our study, both fluorescence and background colour space sections partially overlapped (see Fig. 2). Therefore, we recommend that future studies on 5-ALA fluorescence include a more specific section of colour space to further highlight fluorescence differences.

We recommend that confirmatory studies be done in other centres around the world to help determine if slight differences in colour perception among populations may be significant enough to warrant colour research specific to a particular population or sub-population [21]. Of note, the neurosurgeons that performed that surgeries were of Polish descent.

Our study was conducted on an adult population. Future research may include a similar study on

a paediatric population as current research suggests that 5-ALA assisted surgery may aid in the resection of paediatric brain tumours as well [12].

### Clinical implications

Several studies have demonstrated that the human visual system may be augmented by fluorescence targeting with 5-ALA and lead to a more extensive tumour resection [3, 11, 17, 22]. Fortunately, the cost of FGS is relatively low when compared to intraoperative magnetic resonance imaging (which has proven to maximise tumour resection) giving FGS an economical and practical advantage [2]. FGS with 5-ALA is one of the most innovative treatments in contemporary neurological surgery as it offers the surgeon intraoperative visualisation of the tumour to a much greater extent than traditional white-light microscopy. By studying which mathematical formula(s) may best distinguish healthy tissue from malignant tissue, neurosurgeons may be empowered to excise a greater extent of the residual tumour tissue while preserving healthy tissue. FGS with 5-ALA has proven to be more effective than conventional neuronavigation-guided neurosurgery in identifying tumour margins, enhancing the extent of malignant tumour resections, promising a longer progression-free survival and increasing the quality of life of patients [14, 16, 24].

## CONCLUSIONS

In our study  $\Delta E^*$  best distinguished fluorescent areas from the background compared to CIEDE2000 and CR. Therefore, we recommend  $\Delta E^*$  to be used by neurological surgeons operating on intracranial tumours as it discriminates colour differences in the optimal way.

### Acknowledgements

We thank Mr. Aleksander Och for his assistance throughout our study.

## REFERENCES

1. Collaud S, Juzeniene A, Moan J, et al. On the selectivity of 5-aminolevulinic acid-induced protoporphyrin IX formation. *Curr Med Chem Anticancer Agents*. 2004; 4(3): 301–316, doi: [10.2174/1568011043352984](https://doi.org/10.2174/1568011043352984), indexed in Pubmed: [15134506](https://pubmed.ncbi.nlm.nih.gov/15134506/).
2. Eljamel MS, Mahboob SO. The effectiveness and cost-effectiveness of intraoperative imaging in high-grade glioma resection; a comparative review of intraoperative ALA, fluorescein, ultrasound and MRI. *Photodiagnosis Photodyn*

- Ther. 2016; 16: 35–43, doi: [10.1016/j.pdpdt.2016.07.012](https://doi.org/10.1016/j.pdpdt.2016.07.012), indexed in Pubmed: [27491856](https://pubmed.ncbi.nlm.nih.gov/27491856/).
3. Floeth F, Stummer W. The value of metabolic imaging in diagnosis and resection of cerebral gliomas. *Nat Clin Pract Neurol*. 2005; 1(2): 62–63, doi: [10.1038/ncpneuro0043](https://doi.org/10.1038/ncpneuro0043).
  4. Gómez-Polo C, Montero J, Gómez-Polo M, et al. Comparison of the CIELab and CIEDE 2000 color difference formulas on gingival color space. *J Prosthodont*. 2020; 29(5): 401–408, doi: [10.1111/jopr.12717](https://doi.org/10.1111/jopr.12717), indexed in Pubmed: [29271041](https://pubmed.ncbi.nlm.nih.gov/29271041/).
  5. Gómez-Polo C, Portillo Muñoz M, Lorenzo Luengo MC, et al. Comparison of the CIELab and CIEDE2000 color difference formulas. *J Prosthet Dent*. 2016; 115(1): 65–70, doi: [10.1016/j.prosdent.2015.07.001](https://doi.org/10.1016/j.prosdent.2015.07.001), indexed in Pubmed: [26412001](https://pubmed.ncbi.nlm.nih.gov/26412001/).
  6. Hadjipanayis CG, Widhalm G, Stummer W. What is the surgical benefit of utilizing 5-aminolevulinic acid for fluorescence-guided surgery of malignant gliomas? *Neurosurgery*. 2015; 77(5): 663–673, doi: [10.1227/NEU.0000000000000929](https://doi.org/10.1227/NEU.0000000000000929), indexed in Pubmed: [26308630](https://pubmed.ncbi.nlm.nih.gov/26308630/).
  7. Haj A, Doenitz C, Schebesch KM, et al. Extent of resection in newly diagnosed glioblastoma: impact of a specialized neuro-oncology care center. *Brain Sci*. 2017; 8(1), doi: [10.3390/brainsci8010005](https://doi.org/10.3390/brainsci8010005), indexed in Pubmed: [29295569](https://pubmed.ncbi.nlm.nih.gov/29295569/).
  8. Krakowiak M, Śloniewski P, Dzierżanowski J, et al. Future of the nerve fibres imaging: tractography application and development directions. *Folia Morphol*. 2015; 74(3): 290–294, doi: [10.5603/FM.2015.0044](https://doi.org/10.5603/FM.2015.0044), indexed in Pubmed: [26339808](https://pubmed.ncbi.nlm.nih.gov/26339808/).
  9. Ling F, Paul E, Furzer R. Colour difference of subcutaneous fat and palmar fat pad in open carpal tunnel release. *ANZ J Surg*. 2014; 84(11): 856–860, doi: [10.1111/ans.12754](https://doi.org/10.1111/ans.12754), indexed in Pubmed: [25040347](https://pubmed.ncbi.nlm.nih.gov/25040347/).
  10. Lu VM, Jue TR, McDonald KL, et al. The survival effect of repeat surgery at glioblastoma recurrence and its trend: a systematic review and meta-analysis. *World Neurosurg*. 2018; 115: 453–459.e3, doi: [10.1016/j.wneu.2018.04.016](https://doi.org/10.1016/j.wneu.2018.04.016), indexed in Pubmed: [29654958](https://pubmed.ncbi.nlm.nih.gov/29654958/).
  11. Roberts DW, Valdés PA, Harris BT, et al. Coregistered fluorescence-enhanced tumor resection of malignant glioma: relationships between  $\delta$ -aminolevulinic acid-induced protoporphyrin IX fluorescence, magnetic resonance imaging enhancement, and neuropathological parameters. *Clinical article. J Neurosurg*. 2011; 114(3): 595–603, doi: [10.3171/2010.2.JNS091322](https://doi.org/10.3171/2010.2.JNS091322), indexed in Pubmed: [20380535](https://pubmed.ncbi.nlm.nih.gov/20380535/).
  12. Schwake M, Schipmann S, Mütter M, et al. 5-ALA fluorescence-guided surgery in pediatric brain tumors: a systematic review. *Acta Neurochir (Wien)*. 2019; 161(6): 1099–1108, doi: [10.1007/s00701-019-03898-1](https://doi.org/10.1007/s00701-019-03898-1), indexed in Pubmed: [30989383](https://pubmed.ncbi.nlm.nih.gov/30989383/).
  13. Shonka NA, Aizenberg MR. Extent of resection in glioblastoma. *J Oncol Pract*. 2017; 13(10): 641–642, doi: [10.1200/JOP.2017.027599](https://doi.org/10.1200/JOP.2017.027599), indexed in Pubmed: [29020534](https://pubmed.ncbi.nlm.nih.gov/29020534/).
  14. Stummer W, Pichlmeier U, Meinel T, et al. Fluorescence-guided surgery with 5-aminolevulinic acid for resection of malignant glioma: a randomised controlled multicentre phase III trial. *Lancet Oncol*. 2006; 7(5): 392–401, doi: [10.1016/S1470-2045\(06\)70665-9](https://doi.org/10.1016/S1470-2045(06)70665-9), indexed in Pubmed: [16648043](https://pubmed.ncbi.nlm.nih.gov/16648043/).
  15. Stummer W, Reulen HJ, Meinel T, et al. Extent of resection and survival in glioblastoma multiforme: identification of and adjustment for bias. *Neurosurgery*. 2008; 62(3): 564–76; discussion 564, doi: [10.1227/01.neu.0000317304.31579.17](https://doi.org/10.1227/01.neu.0000317304.31579.17), indexed in Pubmed: [18425006](https://pubmed.ncbi.nlm.nih.gov/18425006/).
  16. Su X, Huang QF, Chen HL, et al. Fluorescence-guided resection of high-grade gliomas: a systematic review and meta-analysis. *Photodiagnosis Photodyn Ther*. 2014; 11(4): 451–458, doi: [10.1016/j.pdpdt.2014.08.001](https://doi.org/10.1016/j.pdpdt.2014.08.001), indexed in Pubmed: [25131747](https://pubmed.ncbi.nlm.nih.gov/25131747/).
  17. Suero Molina E, Schipmann S, Stummer W. Maximizing safe resections: the roles of 5-aminolevulinic acid and intraoperative MR imaging in glioma surgery-review of the literature. *Neurosurg Rev*. 2019; 42(2): 197–208, doi: [10.1007/s10143-017-0907-z](https://doi.org/10.1007/s10143-017-0907-z), indexed in Pubmed: [28921173](https://pubmed.ncbi.nlm.nih.gov/28921173/).
  18. Szmuda T, Rogowska M, Śloniewski P, et al. Frontal aslant tract projections to the inferior frontal gyrus. *Folia Morphol*. 2017; 76(4): 574–581, doi: [10.5603/FM.a2017.0039](https://doi.org/10.5603/FM.a2017.0039), indexed in Pubmed: [28553860](https://pubmed.ncbi.nlm.nih.gov/28553860/).
  19. Szmuda T, Śloniewski P, Olijewski W, et al. Colour contrasting between tissues predicts the resection in 5-aminolevulinic acid-guided surgery of malignant gliomas. *J Neurooncol*. 2015; 122(3): 575–584, doi: [10.1007/s11060-015-1750-0](https://doi.org/10.1007/s11060-015-1750-0), indexed in Pubmed: [25702194](https://pubmed.ncbi.nlm.nih.gov/25702194/).
  20. Valdés PA, Leblond F, Kim A, et al. Quantitative fluorescence in intracranial tumor: implications for ALA-induced PpIX as an intraoperative biomarker. *J Neurosurg*. 2011; 115(1): 11–17, doi: [10.3171/2011.2.JNS101451](https://doi.org/10.3171/2011.2.JNS101451), indexed in Pubmed: [21438658](https://pubmed.ncbi.nlm.nih.gov/21438658/).
  21. Webster MA, Webster SM, Bharadwaj S, et al. Variations in normal color vision. III. Unique hues in Indian and United States observers. *J Opt Soc Am A Opt Image Sci Vis*. 2002; 19(10): 1951–1962, doi: [10.1364/josaa.19.001951](https://doi.org/10.1364/josaa.19.001951), indexed in Pubmed: [12365615](https://pubmed.ncbi.nlm.nih.gov/12365615/).
  22. Widhalm G, Wolfsberger S, Minchev G, et al. 5-Aminolevulinic acid is a promising marker for detection of anaplastic foci in diffusely infiltrating gliomas with nonsignificant contrast enhancement. *Cancer*. 2010; 116(6): 1545–1552, doi: [10.1002/cncr.24903](https://doi.org/10.1002/cncr.24903), indexed in Pubmed: [20108311](https://pubmed.ncbi.nlm.nih.gov/20108311/).
  23. Yu Qi, Lin K, Liu Y, et al. Clinical uses of diffusion tensor imaging fiber tracking merged neuronavigation with lesions adjacent to corticospinal tract: a retrospective cohort study. *J Korean Neurosurg Soc*. 2020; 63(2): 248–260, doi: [10.3340/jkns.2019.0046](https://doi.org/10.3340/jkns.2019.0046), indexed in Pubmed: [31295976](https://pubmed.ncbi.nlm.nih.gov/31295976/).
  24. Zhao S, Wu J, Wang C, et al. Intraoperative fluorescence-guided resection of high-grade malignant gliomas using 5-aminolevulinic acid-induced porphyrins: a systematic review and meta-analysis of prospective studies. *PLoS One*. 2013; 8(5): e63682, doi: [10.1371/journal.pone.0063682](https://doi.org/10.1371/journal.pone.0063682), indexed in Pubmed: [23723993](https://pubmed.ncbi.nlm.nih.gov/23723993/).

# The craniofacial indicators of aggression: a cross-sectional multiparametric anthropometry study

B. Gülçen<sup>1</sup> , İ.C. Pelin<sup>2</sup>, E.B. Özener<sup>3</sup>

<sup>1</sup>Department of Anatomy, Faculty of Medicine, Balıkesir University, Balıkesir, Turkey

<sup>2</sup>Department of Anatomy, Faculty of Medicine, Başkent University, Ankara, Turkey

<sup>3</sup>Department of Anthropology, Faculty of Letters, Istanbul University, Istanbul, Turkey

[Received: 9 December 2019; Accepted: 12 March 2020]

**Background:** The craniofacial features of a person are unique and critical in the evaluation of age, gender, and ethnicity. The relationships between craniofacial properties and behavioural patterns have been one of the most common research topics.

**Materials and methods:** There are studies on the association of facial width-to-height ratio (fVHR) and aggressive behaviour in men; however, no consensus has been reached as there are inconsistent study results. Most of the studies focus on measuring the pre-determined fVHR in searching for a link to aggression. As the literature lacks data on the associations of multiple craniofacial ratios and aggression, we aimed to study the correlation of aggressive behaviour and multiparametric anthropometric measurements of the craniofacial region in a study group consisting of university students aging 18–38 years.

**Results:** The aggression questionnaire results showed that male students had statistically higher scores than females in all subdomains, except physical aggression. Anthropometric studies revealed that males had higher mean values of craniofacial dimensions and indices than females, except the frontal height, the total lip height, frontal index, and cranial length-head circumference index. The statistical analyses for correlations showed that frontal, upper facial, and total facial height-facial width indices correlated with general and verbal aggression, frontal and upper facial indices correlated with physical aggression, and upper facial and total facial height-facial width indices correlated with indirect aggression only in males.

**Conclusions:** We conclude that our study represents the first example of an extensive craniofacial anthropometric research that correlates several craniofacial measurements and ratios with various aggression subdomains. (Folia Morphol 2021; 80, 1: 55–62)

**Key words:** anthropometry, aggression, craniofacial, anatomy, behaviour

## INTRODUCTION

Every human being is unique in their craniofacial features that are closely related to the overall form and proportions of the body. The human craniofacial

variations in different populations have long been an interesting topic for scientists. The environmental factors and evolutionary mechanisms that act on craniofacial features have been investigated by an-

thropologists, while the related databases are used routinely by forensic scientists, surgeons, dentists, and anatomists for diagnostic and therapeutic purposes. The information on the craniofacial dimensions is especially critical in evaluating the age, gender, and ethnic background of individuals [28].

Many craniofacial properties show dimorphism between sexes; for instance, males are known for the broader zygomatic region, supraorbital ridge, and prominent mandibula, while females have longer and narrower faces, rounder and broader foreheads, and thicker lips compared to males [24, 30]. In addition to the age, nutrition, biomechanical forces, the endocrine factors, especially pubertal sex hormones, have been established as the primary influencers of masculinisation and feminisation of craniofacial features [30]. The influence of pubertal testosterone was shown on facial width/lower facial height and cheekbone prominence decrease, and lower face height/full face height increase [16].

Apart from the dimorphism in craniofacial characteristics, males and females show dimorphism in some behavioural patterns, like aggression. When aggression is kept within normal limits, it provides and defends the required vital sources; however, its inappropriate manifestation can be harmful. Professionals dealing with aggressive behaviour need to know its aetiopathogenesis to provide optimal management strategies [35].

The research demonstrated that males, compared to females, display higher aggressive behaviour under unprovoked conditions [3] and higher physical aggression in real-world settings [2, 13]. The link between craniofacial features and aggression has been studied extensively. The ratio of facial width to height (fWHR) is the most common measurement of masculinity related to aggression [1, 7, 12, 15, 27]. The relationship between fWHR and testosterone levels has been indicated in some research studies [7, 16, 22]. However, the results of other studies did not support the presence of such an association [4, 20, 27]. Moreover, the dimorphism of fWHR had also been questioned [21].

The reasons for those inconsistencies might range from sampling variations to the size of the study group, from ethnicity and socioeconomic status of the investigated population to the unstandardised measurement techniques used in anthropometric studies [26]. The measurement of fWHR as the sole anthropometric factor in most studies that investigate

a link between facial features and aggression has also been considered to be responsible for inconsistent results [19]. To the best of our knowledge, the literature lacks data on correlation studies of aggression and multiple craniofacial features. Hence, we aimed to fill in this gap by designing a study that investigates the association of aggressive behaviour and craniofacial features by using multiple anthropometric parameters in a large study population.

## MATERIALS AND METHODS

### Study group

This study was conducted on university students older than 18 years. The sex distribution of participants showed that there were 156 female and 147 male subjects, aging 18–38 years, with a mean of 20.88 (standard deviation 2.9) and 21.23 (standard deviation 3.38) years for females and males, respectively. No statistically significant difference was observed between the mean age of females and males in the study ( $p > 0.05$ ). The presence of a history of surgery, trauma, and congenital abnormalities in the craniofacial region were considered as exclusion criteria. The study participants provided informed consent, and Institutional Ethics Committee approval was obtained (approval number: KA09/306).

### Study design and protocol

In this prospective cross-sectional study, the subjects who met the study criteria were evaluated by an adapted Turkish version of the "Aggression Questionnaire" [6] constructed originally by Buss and Perry [5]. The responses ranged on a scale of 1 to 5 points (e.g., "1 point" stood for "extremely uncharacteristic of me", and "5 points" stood for "extremely characteristic of me"). Five subdomains of aggressive behaviour assessed by the questionnaire included physical and verbal aggression, indirect aggression, anger, and hostility. Cronbach's alpha for the five aggressiveness scores were as follows: physical aggression: 0.82, verbal aggression: 0.79, anger: 0.81, hostility: 0.75, indirect aggression: 0.87.

The anthropometric studies were performed on all participants. A weighing scale and an anthropometer were used for measuring weight and stature. Craniofacial anthropometric measurements carried out according to a previously described technique [18] and pre-determined craniofacial landmarks were taken twice to minimise operator-related and technical errors. A measuring tape, spreading, and sliding

**Table 1.** Craniofacial anthropometric measurements

	Description
<b>Cranial dimensions</b>	
Cranial length (CL)	Between glabella to opisthocranium
Cranial width (CW)	Between right and left biparietale
Head circumference (HC)	
Frontal breadth (FB)	Between right and left frontotemporale
Frontal height (FH)	From trichion to glabella
Auricular head height (AHH)	From external meatus to vertex
<b>Facial dimensions</b>	
Facial width (FW)	Between right and left zygion
Lower facial heights (LWH)	Between subnasale and gnathion
Upper facial heights (UFH)	Between nasion and stomion
Mandibular breadth (MB)	Between right and left gonion
Mandibular height (MH)	Between sublabiale and gnathion
Mouth width (MW)	Between right and left chelion
Nasal height (NH)	Between nasion and subnasale
Nasal width (NW)	Between right and left alare
Supraorbital depth (SOD)	Between glabella and tragion
Interchantal breadth (ICB)	Between right and left endocanthion
Biocular width (BOW)	Between right and left exocanthion
Total lip height (TLH)	Between labium superius oris and labium inferius oris

callipers were used as required in craniofacial measurements (Table 1).

The body mass index (BMI) of the subjects was determined by dividing the weight to the height squared. A total of 8 craniofacial indices that were relevant to the study were derived from the craniofacial dimensions by formulas described previously [11]. The cranial indices calculated were cephalic index (C-I), the cranial length-head circumference index (CL-HC-I), and frontal index (F-I), while the facial indices consisted of total facial height-facial width index (TFH-FW-I), upper facial index (UF-I), mandible-facial width index (M-FW-I), nasal index (N-I), and total lip height-mouth width (TLH-MW-I) index.

### Statistical analysis

Intraclass correlation coefficient analysis was performed to test the reliability of anthropometric measurements. The descriptive statistics were presented as the mean  $\pm$  standard deviation. The normal distribution of numerical variables was controlled by the Kolmogorov-Smirnov test. Independent samples t-test was used for analysing the results of anthropometric measurements and aggression scores concerning

sex. The correlation among variables was assessed by using the Pearson correlation coefficient. Multiple-regression model was used to evaluate the effect of craniofacial indices on the scores of aggression questionnaire. The statistical analyses were done by using Statistical Package for Social Sciences (SPSS Version 18.0; SPSS Inc. Chicago), and a p-value of or lower than 0.05 was considered significant.

## RESULTS

The responses of participants to the aggression questionnaire were evaluated, and the mean scores of five aggression subdomains were calculated for each gender. The scores of aggressive behaviour of female and male subjects were shown in Table 2. In all subdomains, except in physical aggression, the scores of the male subjects were significantly higher than those of the females ( $p < 0.001$ ). Although the physical aggression scores of males ( $24.44 \pm 7.66$ ) were higher than the females ( $18.41 \pm 7.17$ ), it was not statistically significant ( $p > 0.05$ ). The mean of general aggression score of the male subjects was  $25.86 \pm 4.96$ , while the females had a mean score of  $22.90 \pm 5.55$ , and there was a statistically significant difference between males and females concerning general aggression scores ( $p < 0.001$ ).

The mean values of weight, stature, and BMI of males ( $75.69 \pm 12.94$  kg,  $174.93 \pm 59.75$  cm,  $24.69 \pm 3.66$ , respectively) were significantly higher than those of the females ( $58.67 \pm 9.03$  kg,  $162.2 \pm 57.82$  cm,  $22.28 \pm 3.04$ , respectively;  $p < 0.001$ , Table 2). The mean value of all cranial and facial anthropometric measurements was calculated and compared between genders. Except for the frontal height, all mean values of the cranial measurements were significantly higher in the male subjects than the females ( $p < 0.001$ ). Among the 12 facial anthropometrical measures, the mean value of the total lip height was similar in both genders ( $p = 0.991$ ), while the remaining eleven measurements showed a statistically significantly higher value in male subjects compared to those in the females ( $p < 0.001$ ). The distribution of mean value for all craniofacial anthropometric measurements was presented in Table 2.

We did not find any significant difference in the C-I between sexes ( $p > 0.05$ ). The remaining two cranial indices (CL-HC-I, F-I) were found to be significantly higher in males compared to female subjects ( $p < 0.001$ ). None of the facial indices showed a significant difference between the genders ( $p > 0.05$ ).

**Table 2.** Anthropometric measurements, cranial indices, aggression scores (mean  $\pm$  standard deviation)

	Gender		P	P*
	Male (n = 147)	Female (n = 156)		
Weight	75.69 $\pm$ 12.94	58.67 $\pm$ 9.03	< 0.001	-
Stature	174.93 $\pm$ 59.75	162.2 $\pm$ 57.82	< 0.001	-
Body mass index	24.69 $\pm$ 3.66	22.28 $\pm$ 3.04	< 0.001	-
Cranial measurements:				
Cranial length	189.9 $\pm$ 7.54	178.56 $\pm$ 6.48	< 0.001	0.006
Cranial width	155.44 $\pm$ 6.87	146.97 $\pm$ 5.1	< 0.001	0.0001
Head circumference	562.58 $\pm$ 15.78	537.08 $\pm$ 13.61	< 0.001	0.0001
Frontal breadth	119.33 $\pm$ 4.85	112.37 $\pm$ 4.16	< 0.001	0.0001
Frontal height	53.77 $\pm$ 7.58	53.63 $\pm$ 5.65	0.855	0.669
Auricular head height	69.81 $\pm$ 8.57	64.52 $\pm$ 10.12	< 0.001	0.001
Facial measurements:				
Facial width	142.22 $\pm$ 5.57	132.31 $\pm$ 4.98	< 0.001	< 0.001
Lower facial height	65.49 $\pm$ 5.20	59.74 $\pm$ 5.17	< 0.001	0.006
Upper facial height	75.57 $\pm$ 6.23	70.45 $\pm$ 5.63	< 0.001	0.020
Mandibular breadth	97.48 $\pm$ 8.25	89.35 $\pm$ 8.2	< 0.001	0.001
Mandibular height	26.03 $\pm$ 3.75	24.09 $\pm$ 3.28	< 0.001	0.061
Mouth width	51.55 $\pm$ 4.64	49.15 $\pm$ 4.53	< 0.001	0.025
Nasal height	51.63 $\pm$ 3.64	48.28 $\pm$ 4.30	< 0.001	0.028
Nasal width	36.71 $\pm$ 2.90	33.16 $\pm$ 2.89	< 0.001	< 0.001
Supraorbital depth	124.2 $\pm$ 5.26	116.48 $\pm$ 4.8	< 0.001	< 0.001
Interchantal breadth	34.10 $\pm$ 3.93	31.85 $\pm$ 3.57	< 0.001	0.191
Biocular width	107.6 $\pm$ 6.03	103.78 $\pm$ 5.79	< 0.001	0.056
Total lip height	16.45 $\pm$ 3.92	16.27 $\pm$ 3.43	0.991	0.907
Indices:				
Cephalic index	82.12 $\pm$ 4.7	82.42 $\pm$ 4.18	> 0.05	-
Cranial length-head circumference index	33.73 $\pm$ 0.92	33.25 $\pm$ 0.85	< 0.001	-
Frontal index	45.06 $\pm$ 6.47	47.68 $\pm$ 5.11	< 0.001	-
Upper facial index	189.63 $\pm$ 19.52	189.07 $\pm$ 17.07	> 0.05	-
Total facial height-facial width index	101.25 $\pm$ 7.73	102.08 $\pm$ 7.42	> 0.05	-
Mandibular-facial width index	68.57 $\pm$ 5.62	67.57 $\pm$ 5.88	> 0.05	-
Total lip height-mouth width index	32.1 $\pm$ 7.6	33.2 $\pm$ 6.79	> 0.05	-
Nasal index	71.42 $\pm$ 7.19	69.15 $\pm$ 7.71	> 0.05	-
Buss and Perry Aggression Score:				
General aggression	25.86 $\pm$ 4.96	22.90 $\pm$ 5.55	< 0.001	-
Physical aggression	24.44 $\pm$ 7.66	18.41 $\pm$ 7.17	> 0.05	-
Verbal aggression	27.67 $\pm$ 6.83	26.37 $\pm$ 6.89	< 0.001	-
Anger	27.71 $\pm$ 6.20	25.43 $\pm$ 6.78	< 0.001	-
Hostility	25.50 $\pm$ 6.63	23.78 $\pm$ 6.87	< 0.001	-
Indirect aggression	24.46 $\pm$ 6.42	21.31 $\pm$ 6.25	< 0.001	-

\*The effects of height and body mass index values were controlled by ANCOVA model

The data and results of statistical analyses regarding the craniofacial indices were presented in Table 2.

We evaluated the correlation between the craniofacial indices and the subdomains of aggressive be-

**Table 3.** Correlation of craniofacial indices and aggression types by multi-regression analysis

Aggression	Dependent variables					
	General	Physical	Verbal	Anger	Hostility	Indirect
<b>Independent variables (Model fit p-value)</b>	<b>0.010</b>	<b>&lt; 0.001</b>	<b>0.004</b>	0.109	0.198	< 0.001
<b>Male</b>	<b>Standardised beta coefficient</b>					
C-I	-0.206	-0.342	-0.244	0.064	0.191	0.279
CL-HC-I	-0.180	-0.230	-0.189	0.063	0.139	0.210
F-I	<b>0.264*</b>	<b>0.224*</b>	<b>0.313*</b>	0.126	0.174	0.114
UF-I	<b>0.551*</b>	<b>0.335*</b>	<b>0.487*</b>	<b>0.586**</b>	0.284	<b>0.598*</b>
TFH-FW-I	<b>0.441*</b>	0.067	<b>0.355*</b>	<b>0.493*</b>	0.166	<b>0.387*</b>
M-FW-I	-0.037	-0.060	0.001	0.039	0.053	-0.049
TLH-MW-I	-0.010	-0.015	0.027	0.076	0.032	-0.186
N-I	0.080	0.102	0.045	0.089	-0.118	0.089
<b>Independent variables (Model fit p-value)</b>	0.120	0.131	0.341	0.093	0.196	0.195
<b>Female</b>	<b>Standardised beta coefficient</b>					
CL-HC-I	-0.083	-0.101	-0.109	-0.017	0.030	0.031
F-I	0.066	-0.174	-0.221	-0.045	0.117	-0.034
UF-I	0.108	0.173	-0.001	-0.021	-0.022	0.089
TFH-FW-I	-0.226	0.255	-0.041	0.002	0.139	-0.103
M-FW-I	-0.048	0.160	-0.046	-0.093	-0.220	-0.099
TLH-MW-I	0.166	-0.055	0.054	-0.010	-0.030	-0.088
N-I	0.160	0.073	0.163	0.197	0.139	0.078

\*p < 0.05; \*\*p < 0.01; abbreviations — see text

haviour by a multi-variant regression model. First, the model fit p-value was used to assess the presence of a statistical significance for the model. Male participants showed a statistical significance for models of indices on physical, verbal, indirect, and general aggression ( $p < 0.001$ ,  $p = 0.004$ ,  $p < 0.01$ ,  $p = 0.01$ , respectively); however, there was no such statistical significance in female subjects (Table 3). Further evaluation of the correlations between subdomains of aggression and craniofacial indices in male subjects revealed that the F-I, UF-I, and TFH-FW-I were significantly related with higher scores of verbal and general aggression, while F-I and UF-I were only significantly related with higher physical aggression scores, and UF-I and TFH-FW-I were only significantly related with indirect aggression ( $p$  values below 0.05 for all correlations). There was no significant relationship between craniofacial indices and anger and hostility ( $p > 0.05$ ). The correlations between the craniofacial indices and the types of aggression were presented in Table 3.

## DISCUSSION

Facial WHR is an important characteristic that emerged as a result of sexual selection in the evolu-

tion of the genus Homo, therefore fWHR provided information about general level of testosterone and masculinisation. Due to its relevance to testosterone and masculinisation, WHR is considered an indirect indicator of aggression. In the current study, we investigated the relationship of craniofacial features and aggression by extensive anthropometric studies and a questionnaire [5, 6] for assessing aggression subdomains in a group of university students. The strength of this study is that not only WHR, but also many craniofacial characters have been studied. The weakness of this study is that it does not contain moderator variables such as social status and income level.

Only one study reported relationships among income, craniofacial features, and aggression. In this study it was shown that the income of subjects could be a moderator in the association of aggression and fWHR; the authors observed that fWHR predicted aggressive behaviour only in subjects with low income [13]. Another study demonstrated the effects of social status moderated the association of fWHR and risk-taking behaviour in males [36]. Noser et al. [26] found that income played a critical role in fWHR and physical aggression relation, so the authors suggested

that social status had to be taken into account in such anthropometric studies.

Aggression was recently defined as “the feelings of anger or antipathy resulting in hostile or violent behaviour” by Im et al. [17]. The manifestation of aggression has been widely studied by using aggression paradigms [35] and self-report questionnaires [5]. Studies on aggression with self-reported data were argued against an inherent social-desirability bias, and a recent study investigating the relationship between fWHR and aggressiveness was designed to incorporate data collected from the colleagues of the study subjects [34]. However, that study design still carries an intrinsic risk of bias, as the colleagues might hesitate to reveal real opinions on the behavioural characteristics of the subjects studied. For nearly three decades, the Buss-Perry questionnaire [5] has been one of the most commonly used instruments for assessing aggression with confirmed statistical relevance. Most studies revealed that aggressive tendencies of males, especially in physical and direct subdomains of aggression were more prominent than females, and under unprovoked conditions [2, 3, 17]. We used an adapted version of the Buss-Perry questionnaire [6], and found that general aggression scores of males were significantly higher than the scores of females. The males had higher scores in verbal aggression, anger, hostility, and indirect aggression subdomains. Although male students scored higher in physical aggression, the statistical analysis did not show any significant difference between genders. In a very recent study, the gender difference was shown to be erased for physical aggression in situations that involved provocative stimulations [35]. Based on those recent findings, it can be speculated that the questions, in particular, the ones assessing the physical aggression subdomain, might have provoked emotionally stimulative responses in female students.

The dimensions and shape of the craniofacial region that are extremely variable among human populations and ethnic groups [23] have been routinely used by anthropologists, forensic experts, anatomists, and surgeons. Although indirect methods of anthropometric measurements have been used, the gold standard is still considered to be the direct in-vivo technique, which is conventional and low-cost. This quantitative method allows an accurate measurement of hair-covered areas and lacks the risk of causing distorted views that are occasionally caused by pho-

tographic images used in indirect anthropometry [23, 33]. Pouya et al. [29] compared the direct and indirect anthropometric measurements for the analysis of cephalofacial dimensions and found that the mean cranial length of males was higher than females. As a negligible difference was found between the two techniques, they suggested using the robust and low-cost direct anthropometric methodology for constructing more extensive normative databases. A complete assessment of the craniofacial region, consisting of the shape and form of cranium and face, can be performed thoroughly by using anthropometrical indices derived from craniofacial measurements [9, 33]. In recent anthropometric studies of the face, the results showed that total facial height, upper facial height, and facial width of males were higher than those of females. The facial indices were also found to be higher in males compared to females [9, 28]. The results of a multiparametric cranial morphometric study in a Turkish population showed that fourteen radiologically assessed measurements were higher in males than females [10]. In the current study, out of the 6 cranial and 12 facial dimensions measured, we found that only the frontal height and the total lip height were not significantly different between male and female students. The remaining 16 craniofacial measurements were significantly higher in males compared to females. The total lip height of males was found to be significantly higher than the females in a study [31]. A recent study showed that the mean value of frontal height in males was significantly more than that of the females [32]. The discrepancy between our findings and the results of the study by Sirinturk et al. [32] might be due to direct and indirect anthropometric techniques used in ours and theirs, respectively.

There is extensive research on the association of physical characteristics and behavioural tendencies, and fWHR appears to be the most common point of consensus on its relationship with aggression in males [1, 12, 13, 15], although there are some study results that did not reveal this relationship [14, 27]. Testosterone has been suggested as the primary mediator of the fWHR and aggression relationship [7, 16, 22]; however, several study results did not support this suggestion [4, 22]. In a recent genetics study, three single nucleotide polymorphisms associated with the testosterone levels in the body were reported to have an apparent effect on mandible shape and fWHR [30]. The considered dimorphic property of fWHR [12] is



also questioned in a meta-analysis [21]. Köllner et al. [19] argued against those negative claims and emphasized the importance of conducting investigative studies without pre-specification of facial features of interest. The authors further suggested the measurement of additional points, ratios, and distances to keep the research from over-focusing on the same subset of indicators with inconsistent results. Moreover, the authors of a study suggested the facial height and width should be tested independently to reduce the ambiguity of using the ratio between these two components [8]. In another study, the authors discussed that the missing link causing inconsistent results between fWHR and aggression could be the lack of control over critical influencing factors such as BMI [25].

In consideration of the arguments and suggestions reviewed from the available literature, we analysed our results statistically for the correlation between aggression and craniofacial characteristics by controlling the BMI. We measured 6 cranial and 12 facial anthropometric dimensions and derived 3 cranial and 5 facial indices from those. None of the facial indices showed a significant difference between the genders, while cranial CL-HC-I and F-I indices were significantly higher in the male students compared to those of the females.

When we analysed the correlation between aggression and craniofacial characteristics, we found that none of the craniofacial indices of female students were significantly correlated with aggression or its subdomains. For male students, no correlation in anger and hostility subdomains was present for any of the craniofacial indices. The general and verbal aggression in males correlated with frontal, upper facial, and total facial height-facial width indices. The physical aggression subdomain in males was found to be correlated with frontal and upper facial indices, while indirect aggression in males correlated with upper facial and total facial height-facial width indices.

To the best of our knowledge, this is the first anthropometric evaluation of multiparametric craniofacial features and their correlation with aggression and subdomains in a large sample size with both genders represented. The strengths and limitations of our study should be acknowledged. The sample size, as well as the sampling homogenisation, the evaluation of multiparametric craniofacial characteristics by using direct measurement technique, constitute the advantages of the current study compared to similar

studies. Nevertheless, we should note that the study population only involves students, so the results cannot be safely extrapolated to the general population. The current study also has the same disadvantages inherent to most anthropometric studies, which is the lack of standardised terminology and methodology. These two points are crucial and need to be improved for reducing the errors in measurement and interpretation of the results.

## CONCLUSIONS

In conclusion, we suggest that further studies designed with multiple anthropometric measurements and a study group reflecting the general structure of the population should be conducted for investigating the association of aggression and craniofacial features, and replicate and extend the current findings.

## REFERENCES

1. Alrajih S, Ward J. Increased facial width-to-height ratio and perceived dominance in the faces of the UK's leading business leaders. *Br J Psychol.* 2014; 105(2): 153–161, doi: [10.1111/bjop.12035](https://doi.org/10.1111/bjop.12035), indexed in Pubmed: [24754804](https://pubmed.ncbi.nlm.nih.gov/24754804/).
2. Archer J. Sex differences in aggression in real-world settings: a meta-analytic review. *Rev Gen Psychol.* 2004; 8(4): 291–322, doi: [10.1037/1089-2680.8.4.291](https://doi.org/10.1037/1089-2680.8.4.291).
3. Bettencourt BA, Miller N. Gender differences in aggression as a function of provocation: a meta-analysis. *Psychol Bull.* 1996; 119(3): 422–447, doi: [10.1037/0033-2909.119.3.422](https://doi.org/10.1037/0033-2909.119.3.422), indexed in Pubmed: [8668747](https://pubmed.ncbi.nlm.nih.gov/8668747/).
4. Bird B, Jofré VC, Geniole S, et al. Does the facial width-to-height ratio map onto variability in men's testosterone concentrations? *Evol Hum Behav.* 2016; 37(5): 392–398, doi: [10.1016/j.evolhumbehav.2016.03.004](https://doi.org/10.1016/j.evolhumbehav.2016.03.004).
5. Buss AH, Warren WL. *Aggression questionnaire: (AQ)*. Western Psychological Services, Los Angeles 2000.
6. Can S. "Aggression Questionnaire" adlı ölçeğin Türk popülasyonunda geçerlilik ve güvenilirlik çalışması. GATA Haydarpaşa Eğitim Hastanesi, İstanbul 2002.
7. Carré JM, McCormick CM. In your face: facial metrics predict aggressive behaviour in the laboratory and in varsity and professional hockey players. *Proc Biol Sci.* 2008; 275(1651): 2651–2656, doi: [10.1098/rspb.2008.0873](https://doi.org/10.1098/rspb.2008.0873), indexed in Pubmed: [18713717](https://pubmed.ncbi.nlm.nih.gov/18713717/).
8. Costa M, Lio G, Gomez A, et al. How components of facial width to height ratio differently contribute to the perception of social traits. *PLoS One.* 2017; 12(2): e0172739, doi: [10.1371/journal.pone.0172739](https://doi.org/10.1371/journal.pone.0172739), indexed in Pubmed: [28235081](https://pubmed.ncbi.nlm.nih.gov/28235081/).
9. Dodangheh M, Mokhtari T, Mojaverrostami S, et al. Anthropometric study of the facial index in the population of medical students in Tehran University of Medical Sciences. *GMJ Med.* 2018: 51–57, doi: [10.29088/gmjm.2018.51](https://doi.org/10.29088/gmjm.2018.51).
10. Ekizoglu O, Hocaoglu E, Inci E, et al. Assessment of sex in a modern Turkish population using cranial anthropometric parameters. *Leg Med (Tokyo).* 2016; 21: 45–52, doi: [10.1016/j.legalmed.2016.06.001](https://doi.org/10.1016/j.legalmed.2016.06.001), indexed in Pubmed: [27497333](https://pubmed.ncbi.nlm.nih.gov/27497333/).

11. Farkas LG, Hreczko TM, Katic MJ, et al. Proportion indices in the craniofacial regions of 284 healthy North American white children between 1 and 5 years of age. *J Craniofac Surg.* 2003; 14(1): 13–28, doi: [10.1097/00001665-200301000-00004](https://doi.org/10.1097/00001665-200301000-00004), indexed in Pubmed: [12544216](https://pubmed.ncbi.nlm.nih.gov/12544216/).
12. Geniole SN, Denson TF, Dixon BJ, et al. Evidence from meta-analyses of the facial width-to-height ratio as an evolved cue of threat. *PLoS One.* 2015; 10(7): e0132726, doi: [10.1371/journal.pone.0132726](https://doi.org/10.1371/journal.pone.0132726), indexed in Pubmed: [26181579](https://pubmed.ncbi.nlm.nih.gov/26181579/).
13. Goetz SMM, Shattuck KS, Miller RM, et al. Social status moderates the relationship between facial structure and aggression. *Psychol Sci.* 2013; 24(11): 2329–2334, doi: [10.1177/0956797613493294](https://doi.org/10.1177/0956797613493294), indexed in Pubmed: [24068116](https://pubmed.ncbi.nlm.nih.gov/24068116/).
14. Gómez-Valdés J, Hünemeier T, Quinto-Sánchez M, et al. Lack of support for the association between facial shape and aggression: a reappraisal based on a worldwide population genetics perspective. *PLoS One.* 2013; 8(1): e52317, doi: [10.1371/journal.pone.0052317](https://doi.org/10.1371/journal.pone.0052317), indexed in Pubmed: [23326328](https://pubmed.ncbi.nlm.nih.gov/23326328/).
15. Haselhuhn MP, Ormiston ME, Wong EM. Men's facial width-to-height ratio predicts aggression: a meta-analysis. *PLoS One.* 2015; 10(4): e0122637, doi: [10.1371/journal.pone.0122637](https://doi.org/10.1371/journal.pone.0122637), indexed in Pubmed: [25849992](https://pubmed.ncbi.nlm.nih.gov/25849992/).
16. Hodges-Simeon CR, Hanson Sobraske KN, Samore T, et al. Facial width-to-height ratio (fWHR) is not associated with adolescent testosterone levels. *PLoS One.* 2016; 11(4): e0153083, doi: [10.1371/journal.pone.0153083](https://doi.org/10.1371/journal.pone.0153083), indexed in Pubmed: [27078636](https://pubmed.ncbi.nlm.nih.gov/27078636/).
17. Im S, Jin G, Jeong J, et al. Gender Differences in Aggression-related Responses on EEG and ECG. *Exp Neurobiol.* 2018; 27(6): 526–538, doi: [10.5607/en.2018.27.6.526](https://doi.org/10.5607/en.2018.27.6.526), indexed in Pubmed: [30636903](https://pubmed.ncbi.nlm.nih.gov/30636903/).
18. Kolar J, Salter EM. Craniofacial anthropometry: practical measurement of the head and face for clinical, surgical, and research use. C C Thomas, Springfield, Illinois 1997.
19. Köllner MG, Janson KT, Schultheiss OC. Commentary: sexual dimorphism of facial width-to-height ratio in human skulls and faces: a meta-analytical approach. *Front Endocrinol (Lausanne).* 2018; 9: 227, doi: [10.3389/fendo.2018.00227](https://doi.org/10.3389/fendo.2018.00227), indexed in Pubmed: [29867760](https://pubmed.ncbi.nlm.nih.gov/29867760/).
20. Kosinski M. Facial width-to-height ratio does not predict self-reported behavioral tendencies. *Psychol Sci.* 2017; 28(11): 1675–1682, doi: [10.1177/0956797617716929](https://doi.org/10.1177/0956797617716929), indexed in Pubmed: [28976810](https://pubmed.ncbi.nlm.nih.gov/28976810/).
21. Kramer R. Sexual dimorphism of facial width-to-height ratio in human skulls and faces: a meta-analytical approach. *Evol Hum Behav.* 2017; 38(3): 414–420, doi: [10.1016/j.evolhumbehav.2016.12.002](https://doi.org/10.1016/j.evolhumbehav.2016.12.002).
22. Lefevre C, Lewis G, Perrett D, et al. Telling facial metrics: facial width is associated with testosterone levels in men. *Evol Hum Behav.* 2013; 34(4): 273–279, doi: [10.1016/j.evolhumbehav.2013.03.005](https://doi.org/10.1016/j.evolhumbehav.2013.03.005).
23. Majeed MI, Haralur SB, Khan MF, et al. An anthropometric study of cranio-facial measurements and their correlation with vertical dimension of occlusion among Saudi Arabian subpopulations. *Open Access Maced J Med Sci.* 2018; 6(4): 680–686, doi: [10.3889/oamjms.2018.082](https://doi.org/10.3889/oamjms.2018.082), indexed in Pubmed: [29731941](https://pubmed.ncbi.nlm.nih.gov/29731941/).
24. Matthews HS, Penington AJ, Hardiman R, et al. Modelling 3D craniofacial growth trajectories for population comparison and classification illustrated using sex-differences. *Sci Rep.* 2018; 8(1): 4771, doi: [10.1038/s41598-018-22752-5](https://doi.org/10.1038/s41598-018-22752-5), indexed in Pubmed: [29556038](https://pubmed.ncbi.nlm.nih.gov/29556038/).
25. Muñoz-Reyes JA, Gil-Burmann C, Turiegano E. Digit Ratio 2D:4D, facial masculinization and aggressiveness in Spanish adolescents/Índice 2D:4D, masculinización facial y agresividad en adolescentes españoles. *Estudios de Psicología.* 2014; 35(2): 319–340, doi: [10.1080/02109395.2014.922259](https://doi.org/10.1080/02109395.2014.922259).
26. Noser E, Schoch J, Ehler U. The influence of income and testosterone on the validity of facial width-to-height ratio as a biomarker for dominance. *PLoS One.* 2018; 13(11): e0207333, doi: [10.1371/journal.pone.0207333](https://doi.org/10.1371/journal.pone.0207333), indexed in Pubmed: [30412629](https://pubmed.ncbi.nlm.nih.gov/30412629/).
27. Özener B. Facial width-to-height ratio in a Turkish population is not sexually dimorphic and is unrelated to aggressive behavior. *Evol Hum Behav.* 2012; 33(3): 169–173, doi: [10.1016/j.evolhumbehav.2011.08.001](https://doi.org/10.1016/j.evolhumbehav.2011.08.001).
28. Pandeya A, Atreya A. Variations in the facial dimensions and face types among the students of a Medical College. *JNMA J Nepal Med Assoc.* 2018; 56(209): 531–534, indexed in Pubmed: [30058638](https://pubmed.ncbi.nlm.nih.gov/30058638/).
29. Pouya F, Eftekhari-Vaghefi SH, Salehinejad P. Anthropometric analysis of cephalofacial dimensions in Kerman, Iran. *Acta Med Iran.* 2017; 55(4): 241–248, indexed in Pubmed: [28532135](https://pubmed.ncbi.nlm.nih.gov/28532135/).
30. Roosenboom J, Indencleef K, Lee MK, et al. SNPs associated with testosterone levels influence human facial morphology. *Front Genet.* 2018; 9: 497, doi: [10.3389/fgene.2018.00497](https://doi.org/10.3389/fgene.2018.00497), indexed in Pubmed: [30405702](https://pubmed.ncbi.nlm.nih.gov/30405702/).
31. Sharma RL, Pancholi P, Sharma S, et al. Anthropometric measurement of lips in adults of MP India. *IJAR.* 2017; 3(2): 210–212.
32. Sirinturk S, Bagheri H, Govsa F, et al. Study of frontal hairline patterns for natural design and restoration. *Surg Radiol Anat.* 2017; 39(6): 679–684, doi: [10.1007/s00276-016-1771-1](https://doi.org/10.1007/s00276-016-1771-1), indexed in Pubmed: [27830323](https://pubmed.ncbi.nlm.nih.gov/27830323/).
33. Torres-Restrepo AM, Quintero-Monsalve AM, Giraldo-Mira JF, et al. Agreement between cranial and facial classification through clinical observation and anthropometric measurement among Envigado school children. *BMC Oral Health.* 2014; 14: 50, doi: [10.1186/1472-6831-14-50](https://doi.org/10.1186/1472-6831-14-50), indexed in Pubmed: [24886038](https://pubmed.ncbi.nlm.nih.gov/24886038/).
34. Wang D, Nair K, Kouchaki M, et al. A case of evolutionary mismatch? Why facial width-to-height ratio may not predict behavioral tendencies. *Psychol Sci.* 2019; 30(7): 1074–1081, doi: [10.1177/0956797619849928](https://doi.org/10.1177/0956797619849928), indexed in Pubmed: [31180794](https://pubmed.ncbi.nlm.nih.gov/31180794/).
35. Weidler C, Habel U, Hüpen P, et al. On the complexity of aggressive behavior: contextual and individual factors in the Taylor aggression paradigm. *Front Psychiatry.* 2019; 10: 521, doi: [10.3389/fpsy.2019.00521](https://doi.org/10.3389/fpsy.2019.00521), indexed in Pubmed: [31404138](https://pubmed.ncbi.nlm.nih.gov/31404138/).
36. Welker K, Goetz S, Carré J. Perceived and experimentally manipulated status moderates the relationship between facial structure and risk-taking. *Evol Hum Behav.* 2015; 36(6): 423–429, doi: [10.1016/j.evolhumbehav.2015.03.006](https://doi.org/10.1016/j.evolhumbehav.2015.03.006).

# Anatomical study on branching pattern and variations of orbital segment of the oculomotor nerve

R. Haładaj<sup>1</sup>, Ł. Olewnik<sup>1</sup>, M. Polgaj<sup>1</sup>

Department of Normal and Clinical Anatomy, Interfaculty Chair of Anatomy and Histology, Medical University of Lodz, Poland

[Received: 14 January 2020; Accepted: 19 January 2020]

**Background:** This study aims to revisit the anatomy of orbital segment of the third cranial nerve (CN III). The study also involved morphometric measurements of CN III muscular branches. Detailed description of observed anatomical variations and their incidence was also included. The study supplements earlier findings with detailed observations of the neuromuscular relations.

**Materials and methods:** The study was conducted on 52 orbits taken from 26 cadaveric heads (10 males and 16 females; Central European population).

**Results:** Anatomical variations of the orbital segment of the CN III observed on the examined material involved both the superior and inferior branch of this nerve. The muscular branch innervating the levator palpebrae superioris muscle occasionally pierces the superior rectus muscle. The nerve to the inferior oblique muscle may pierce and innervate the inferior rectus muscle. In rare instances, duplication of the parasympathetic root of the ciliary ganglion may also occur. Among the muscular branches, the smallest diameter reached the branch to the levator palpebrae superioris muscle. Among the three muscular branches derived from the inferior branch of the CN III, the nerve to the inferior oblique was the longest one. Its length varied from 28.9 mm to 37.4 mm. The shortest was the muscular branch to the inferior rectus muscle. Its length varied from 0 mm (when muscular sub-branches arose directly from the nerve to the inferior oblique muscle) to 7.58 mm.

**Conclusions:** This study presented the characteristic of orbital segment of the CN III, including anatomical variations and morphometric measurements relevant to intraorbital procedures. (Folia Morphol 2021; 80, 1: 63–69)

**Key words:** anatomic variations, oculomotor nerve, orbit

## INTRODUCTION

The oculomotor nerve is the third cranial nerve (CN III). It runs in the superior orbital fissure to enter the orbit. The CN III provides motor innervation to the levator palpebrae superioris and almost all extraocular muscles except the superior oblique and lateral rectus muscle. It also carries preganglionic parasympathetic fibres to the sphincter pupillae and the ciliary muscles

of the eye [1, 10, 22, 24, 27]. Those fibres enter the ciliary ganglion through the motor (parasympathetic) root of the ganglion. The postganglionic fibres leave the ganglion and reach the eyeball through via the short ciliary nerves [11, 17, 25].

The CN III enters the orbit through the superior orbital fissure and from this point the orbital segment of the nerve begins [18, 21]. Just after reaching the

Address for correspondence: Dr. R. Haładaj, Department of Normal and Clinical Anatomy, Chair of Anatomy and Histology, Medical University of Lodz, ul. Żeligowskiego 7/9, 90–752 Łódź, Poland, e-mail: robert.haladaj@umed.lodz.pl

orbit, the CN III is divided into two main subdivisions, namely the superior and inferior branch. The superior branch runs on the lateral and then over the optic nerve and ophthalmic artery and innervates the superior rectus and levator palpebrae superioris muscle [1, 10, 22, 24]. The inferior branch, in turn, is thicker and gives off three muscular branches: the branch to the medial rectus muscle which runs under the optic nerve; the branch to the inferior rectus which is the shortest; and the branch to the inferior oblique muscle (also called the nerve to the inferior oblique muscle) which courses along the lateral side of the inferior rectus muscle. In most of cases the parasympathetic root of the oculomotor nerve branches off the muscular branch to the inferior oblique muscle [11, 17, 25].

When CN III is paralysed, drooping of the upper eyelid (ptosis) may occur. In those cases, the eyeball is directed laterally and downwards (divergent strabismus) [24]. If parasympathetic fibres are affected, the pupil dilates and the accommodation of the eye is also affected [5, 24]. Cases of selective damage of the CN III muscular branches were also described [4, 7].

Occasionally, some deviations from the typical anatomy of the CN III may be observed. Anatomical variations of the CN III may have significant clinical importance both during surgical procedures carried out inside the orbit, and when diagnosing clinical symptoms of damage to CN III or its branches [4, 7, 15, 23, 26]. Thus, the goal of this work was to describe the anatomy of orbital segment of the CN III. The study also involved morphometric measurements of CN III muscular branches. Detailed description of observed anatomical variations and their incidence was also included. The study supplements earlier findings with detailed observations of the neuro-muscular relations.

## MATERIALS AND METHODS

The study was performed on 52 orbits taken from 26 cadaveric heads (10 males and 16 females; Central European population), fixed in 10% formalin solution. Cadavers used for the study did not show any craniofacial deformities, scars or traces of previous surgical interventions within the head. The study was approved by the Bioethics Committee (consent no. RNN/338/17/KE).

Dissection procedure was performed based on previously developed protocols [3, 9]. The superior and lateral walls (and upper part of the medial wall)

of the orbit were removed with a Luer bone rongeur and chisel. Opening of the superior orbital fissure and optic canal was also performed. The periorbita was bluntly separated from the remaining orbital walls, the nerves and vessels were cut at the level of the superior orbital fissure (and the optic canal), and then all orbital content was carefully removed. Subsequent section steps included the removal of the lateral rectus muscle which allowed the exposure of the intraconal space, removal of the fatty tissue and visualisation of the oculomotor nerve with its branches. Ciliary ganglion with its parasympathetic roof was also preserved. At this step anatomical variations involving CN III were recorded.

The measurements were taken with an electronic calliper (Mitutoyo Corporation, Kawasaki-shi, Kanagawa, Japan). Each measurement was taken independently by all authors with accuracy of 0.01 mm and included: the diameter of the CN III, diameters of its superior and inferior branch as well as diameters of all muscular branches. Furthermore, the lengths of all CN III branches were measured (from the origin of a given branch to the place of its division). The length of the superior and inferior branch of the CN III was measured from the level of the superior orbital fissure to the place of subsequent division into muscular branches. The lengths of the muscular branches were measured between their origins and the places of their division into muscular sub-branches, i.e. small divisions that reached the internal, global surface of individual muscles (the lengths of the muscular sub-branches defined in this way were also measured). Basic descriptive statistics (minimal and maximal values, mean, median and standard deviation) were calculated for the collected measurements.

## RESULTS

The measurements of the CN III and its branches are given in Tables 1 and 2. Variability in size of certain CN III branches was observed on the examined material. The length of the superior branch of the CN III ranged from 5.88 mm to 12.96 mm. The length of the inferior branch of the CN III ranged from 6.49 mm to 9.98 mm. In all examined cases the inferior branch was thicker (taking into account all cases examined, the mean diameter of the superior branch was 1.17 mm, while the mean diameter of the inferior branch was 1.61 mm). Among the muscular branches, the smallest diameter reached the branch to the levator palpebrae superioris muscle. Its diameter measured

**Table 1.** Diameters of third cranial nerve (CN III) superior and inferior branch as well as diameters of all muscular branches

Variable	Minimum [mm]	Maximum [mm]	Mean [mm]	Median [mm]	SD [mm]
1	1.96	3.04	2.47	2.34	0.35
2	0.88	1.46	1.17	1.21	0.16
3	0.19	0.37	0.27	0.26	0.06
4	1.27	1.9	1.61	1.68	0.18
5	0.77	1.44	1.04	0.98	0.22
6	0.57	0.96	0.75	0.68	0.15
7	0.51	1.04	0.8	0.83	0.14

1 — diameter of the CN III; 2 — diameter of superior branch of CN III; 3 — diameter of muscular branch to the levator palpebrae superioris; 4 — diameter of inferior branch of CN III; 5 — diameter of muscular branch to the medial rectus muscle; 6 — diameter of muscular branch to the inferior rectus muscle; 7 — diameter of the nerve to the inferior oblique muscle; SD — standard deviation

**Table 2.** Lengths of all branches of the third cranial nerve (CN III)

Variable	Minimum [mm]	Maximum [mm]	Mean [mm]	Median [mm]	SD [mm]
1	5.88	12.96	9.15	8.69	2.44
2	8.39	12.46	10.37	10.48	1.42
3	6.49	9.98	8.33	8.22	1.18
4	4.52	8.86	6.61	6.18	1.62
5	6.9	9.59	8.36	8.36	0.91
6	0	7.58	4.62	5.68	3.24
7	8.79	15.16	11.42	10.99	2.06
8	28.91	37.45	32.72	32.18	2.92

1 — length of superior branch of CN III; 2 — maximal length of the muscular sub-branches reaching the superior rectus muscle; 3 — length of inferior branch of CN III; 4 — length of muscular branch to the medial rectus muscle; 5 — maximal length of the muscular sub-branches reaching the medial rectus muscle; 6 — length of muscular branch to the inferior rectus muscle; 7 — maximal length of the muscular sub-branches reaching the inferior rectus muscle; 8 — length of the nerve to the inferior oblique muscle; SD — standard deviation

from 0.19 mm to 0.37 mm. Among the three muscular branches derived from the inferior branch of the CN III, the nerve to the inferior oblique was the longest one. Its length varied from 28.9 mm to 37.4 mm, its diameter ranged from 0.51 mm to 1.04 mm. The shortest was the muscular branch to the inferior rectus muscle. The length of this branch varied from 0 mm (when muscular sub-branches arose directly from the nerve to the inferior oblique muscle) to 7.58 mm. Its diameter ranged from 0.57 mm to 0.96 mm.

All muscular branches derived from CN III underwent subsequent divisions into sub-branches reaching the internal (global) surfaces of each muscle. The number of muscular sub-branches reaching the superior rectus muscle varied on the examined material

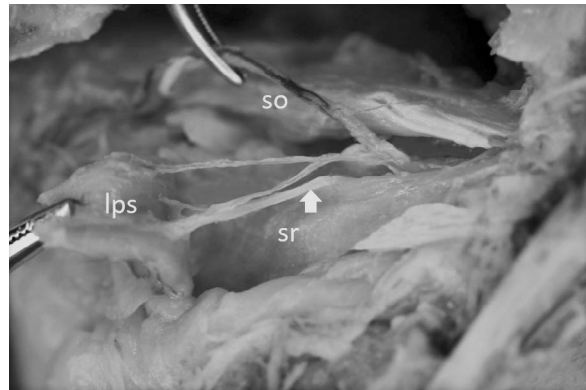


**Figure 1.** Typical variant in which muscular branch to the levator palpebrae superioris (marked by white arrow) wraps around the medial border of the superior rectus muscle (sr) to reach its target muscle. Superior view to the left orbit; lps — levator palpebrae superioris muscle (cut from its origin and reflected); so — superior oblique muscle.

from 4 to 7 (mean: 5.4, median: 5, SD: 0.8). The number of muscular sub-branches reaching the medial rectus muscle varied from 4 to 7 (mean: 5.7, median: 6, SD: 0.9). The number of muscular sub-branches reaching the inferior rectus muscle varied from 2 to 4 (mean: 3.5, median: 4, SD: 0.8). While the number of muscular sub-branches reaching the inferior oblique muscle varied from 3 to 4 (mean: 3.6, median: 4, SD: 0.5).

Anatomical variations of the orbital segment of the CN III observed on the examined material included both the superior and inferior branch of this nerve. Regarding the superior branch of the CN III, anatomical variability was related to the muscular branch innervating the levator palpebrae superioris muscle. In all cases this branch originated on the inferior surface of the superior rectus muscle as one among the terminal sub-branches of the superior branch of the CN III. In most of cases (47/52; 90.4%) the branch wrapped around the medial border of the superior rectus muscle to reach the levator palpebrae superioris muscle (Fig. 1). However, in the remaining 9.6% of cases (5/52; in 1 female head bilaterally, in 1 female head unilaterally and in 2 male heads unilaterally) this branch pierced the superior rectus muscle and then joined the levator palpebrae superioris (Fig. 2).

Regarding the inferior branch of the CN III, anatomical variations involved the nerve to the inferior oblique muscle, muscular sub-branches to the inferior rectus muscle, as well as parasympathetic root of the ciliary ganglion. In most cases (44/52 orbits; 84.6%) the nerve to the inferior oblique muscle ran along the

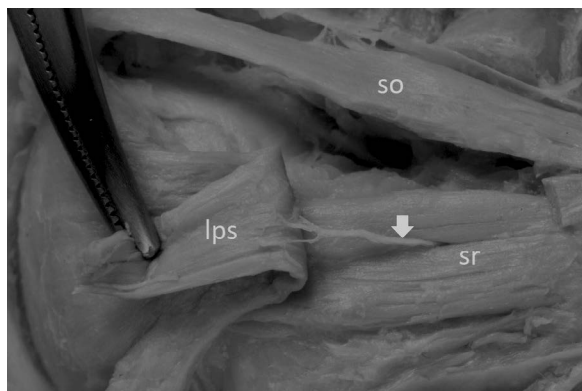


**Figure 2.** Variant in which muscular branch to the levator palpebrae superioris (marked by white arrow) pierces the superior rectus muscle (sr) to reach its target muscle. Superior view to the left orbit; lps — levator palpebrae superioris muscle (cut from its origin and reflected); so — superior oblique muscle.

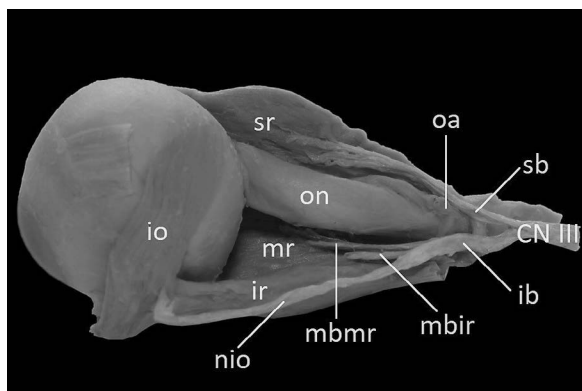


**Figure 3.** Typical anatomy of the third cranial nerve (CN III) and its branches. Lateral view to the left orbit. The lateral rectus muscle was removed to expose the intraconal space. Ciliary ganglion with its roots and short ciliary nerves was removed. The superior branch (sb) of CN III runs lateral and superior to the optic nerve (on) and ophthalmic artery (oa) and innervates the superior rectus (sr) and levator palpebrae superioris muscle (removed on this specimen). The inferior branch (ib) of CN III is thicker and gives off three muscular branches: muscular branch to the medial rectus muscle (mbmr) which runs under the optic nerve; muscular branch to the inferior rectus muscle (mbir) which is the shortest; and the nerve to the inferior oblique muscle (nio) which runs along the lateral border of the inferior rectus muscle (ir); io — inferior oblique muscle.

inferior wall of the orbit, between the inferior and lateral rectus muscles (Fig. 3). However, in 15.4% of cases (8/52 orbits, bilaterally in 1 male and 1 female head, unilaterally in 1 male and 3 female heads), this nerve pierced the inferior rectus muscle; In all those cases, muscular branches to the inferior rectus muscle arose from the nerve to the inferior oblique rather than forming a separate branch (Fig. 4).

Anatomical variation was also observed regarding parasympathetic root of the ciliary ganglion.

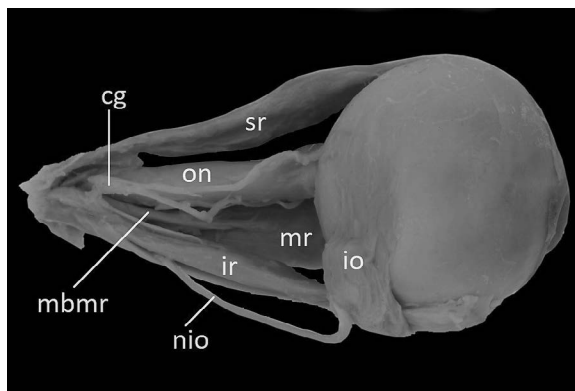


**Figure 4.** Variant in which the nerve to the inferior oblique muscle (nio) pierces the inferior rectus muscle (ir). Lateral view to the right orbit. In this variant, muscular branches to the inferior rectus muscle (ir) arise from the nerve to the inferior oblique instead of forming a separate muscular branch; cg — ciliary ganglion; io — inferior oblique muscle; mbmr — muscular branch to the medial rectus muscle; mr — medial rectus muscle; on — optic nerve; sr — superior rectus muscle.

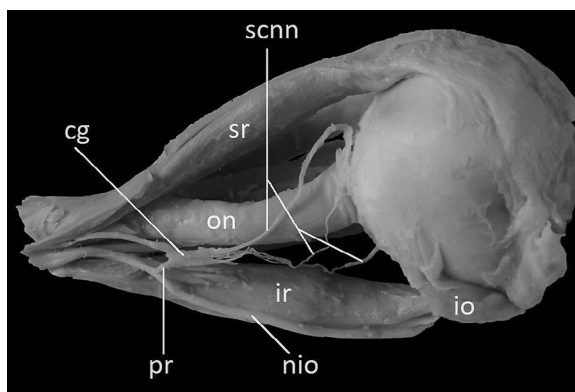


**Figure 5.** Variant with typical, single parasympathetic root (pr) of the ciliary ganglion. Lateral view to the right orbit; cg — ciliary ganglion; io — inferior oblique muscle; ir — inferior rectus muscle; nio — nerve to the inferior oblique muscle; on — optic nerve; scnn — short ciliary nerves; sr — superior rectus muscle.

The length of this root measured from 0.98 mm to 7.91 mm (mean: 4.41; median: 4.91 mm, SD: 2.6 mm). The mean diameter of the parasympathetic root was 0.41 mm (min: 0.15 mm, max: 0.59 mm, SD: 0.14). In majority of cases (47/52; 90.4%) the parasympathetic root was single and originated from the nerve to the inferior oblique muscle (Fig. 5). However, in 5 (9.6%) cases the single parasympathetic root took origin directly from the inferior division of the oculomotor nerve. In 5 cases the parasympathetic root of the ciliary ganglion was double (Fig. 6). In 4 out of those cases both roots emerged from the nerve to the inferior oblique muscle, while in one out of those cases the first root took origin from the inferior division of

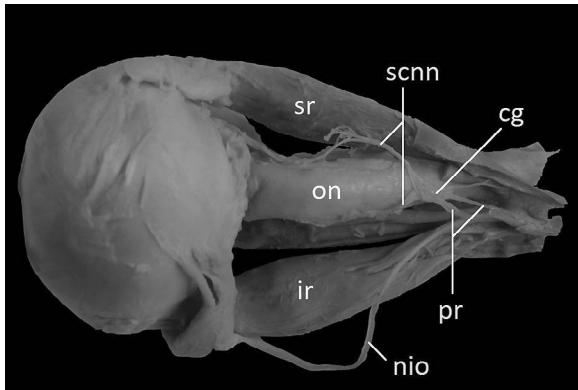


**Figure 6.** Variant in which the parasympathetic root (pr) of the ciliary ganglion is duplicated. Lateral view to the left orbit. In this specimen one root is derived from the inferior branch of the third cranial nerve and the second root takes origin from the initial part of the nerve to the inferior oblique muscle (nio); cg — ciliary ganglion; ir — inferior rectus muscle; on — optic nerve; scnn — short ciliary nerves; sr — superior rectus muscle.

CN III and the second root originated from the nerve to the inferior oblique muscle.

## DISCUSSION

According to Bergman et al. [3], anatomical variations of the CN III “may involve the occurrence of unusual branches or deviations in the course of its branches”. In rare instances a branch from the CN III may replace the abducens nerve or may provide a branch to the superior oblique muscle [3]. However, this was not observed in our material.

The unexpected anatomical variations of CN III branches to the extraocular muscles may have significant meaning during orbital imaging or various surgical and reconstructive procedures performed within the orbit. Black et al. [4] suggest that the nerve to the inferior oblique muscle may be prone to damage due to its long intra-orbital course along the inferior orbital wall; this nerve is located along the lateral edge of the lateral rectus muscle and may be accidentally injured during surgical procedures or inferior orbital wall fractures. Occasionally, the nerve to the inferior oblique muscle or some of its branches may pierce the inferior rectus muscle [3, 4, 12, 20]. In our study an incidence of this variation was estimated at in 15.4% of specimens. In those cases, muscular branches that arise from the nerve to the inferior rectus muscle may cause strong connection between the two structures; Due to traction of the inferior rectus muscle the nerve to the inferior oblique muscle may be paralysed [4]. Since parasympathetic

fibres course most commonly with the nerve to the inferior oblique muscle, damage of this nerve may be accompanied by a tonically dilated pupil [4].

Typically, the muscular branch to the levator palpebrae superioris muscle courses along the medial border of the superior rectus muscle, wraps around this border and reaches its target muscle. The incidences of this typical variant reported by different authors vary between 78.6% and 87.5% [8, 10]. Occasionally, the muscular branch to the levator may pierce the superior rectus muscle and after that enters the inferior surface of the levator palpebrae. The incidence of this variant ranges between 12.5% and 21.4% [8, 10]. The same variation was also described by Bye et al. [6]. Isomura [19], reporting different variations in which two muscular branches to the levator palpebrae superioris united to form a common loop before supplying the muscle. In the presented study a branch to the levator palpebrae superioris muscle was characterised by the smallest diameter. It seems to be additionally fixed in cases where it pierces the superior rectus muscle, which may potentially increase the risk of damage of this branch to injury.

Regarding the parasympathetic root of the ciliary ganglion, variations in number, shape and diameter of this root were reported [11, 14, 17, 25]. Occasionally, duplication or triplication of the parasympathetic root may be observed [3, 11]. In one study the incidence of this variation was estimated at 10% of cases [11]. However, in the study of Tesapirat et al. [25] a single motor root was found in only 62.5% of cases. In the presented study duplication of the parasympathetic root was observed in per cent of specimens. When the parasympathetic root is duplicated one root may arise from the inferior division of the CN III while and another may take origin from the nerve to the inferior oblique muscle, both roots may also originate from those nerve [11]. Both the length of the parasympathetic root of the ciliary ganglion and its origin may also be variable, which was confirmed in the presented study. Knowledge of anatomical relations between the parasympathetic root of the ciliary ganglion and the inferior division of the oculomotor nerve (or the nerve to the inferior oblique muscle) may help with understanding risk to those structures that may occur during specific traumas or surgical procedures. For instance, Bayramlar et al. [2] described the mydriasis associated with the damage of the inferior division of the CN III resulting from complications of sinus surgery. Risk for the ciliary ganglion associated with

orbital floor fractures was stressed by Bodker et al. [5], He et al. [15] and Hornbliss [16]. Those authors analysed association between fractures of inferior wall of the orbit and complications such as traumatic mydriasis.

From the practical point of view, the microsurgical anatomy of orbital segment of the CN III may be crucial in planning surgical accesses that allow extraocular muscles function to be preserved. It may also help to better understand the specific symptoms of damage to this nerve. The two main divisions of the CN III (namely superior and inferior branch) innervate most of the extraocular muscles. The superior branch of the CN III travels along the inferior surface of the superior rectus muscle and gives mean 5 (from 3 to 7) muscular sub-branches to this muscle [22, 27]. Those results are consistent with data provided in presented study, in which the mean number of muscular sub-branches reaching the superior rectus muscle was 5.4 (median: 5). As noted earlier in the discussion, the superior branch supplies also the levator palpebrae superioris muscle.

The inferior division of the CN III is typically divided into three muscular branches: a branch to the medial rectus muscle, muscular branch to the inferior rectus muscle and the nerve to the inferior oblique muscle [12]. According to Park et al. [22] and Zhang et al. [27] the range of muscular sub-branches that may reach the internal surface of the inferior rectus muscle is from 3 to 10. However, in the presented study the number of muscular sub-branches reaching the inferior rectus muscle varied from 2 to 4 (mean: 3.5, median: 4). This difference may be due to the fact that only primary divisions of the muscular branches reaching the inferior rectus muscle were included in this work. The last muscular branch of the inferior division of the oculomotor nerve reaches the medial rectus muscle. This branch may be divided into 3 to 8 sub-branches (mean: 5) innervating the medial rectus muscle. In the presented study the mean number of muscular sub-branches reaching the medial rectus muscle was 5.7 (median: 6). However, in one recent study based on Sihler's stain, the number of nervous branches reaching the medial rectus muscle from 4 to 8 (mean: 5.4, median: 5) [13].

## CONCLUSIONS

This study presented the characteristic of orbital segment of the CN III, including anatomical variations and morphometric measurements relevant to intraor-

bital procedures. Anatomical variations of the orbital segment of the CN III involved both the superior and inferior branch of this nerve. The muscular branches innervating the levator palpebrae superioris muscle occasionally pierce the superior rectus muscle. The nerve to the inferior oblique muscle may pierce and innervate the inferior rectus muscle. The parasympathetic root of the ciliary ganglion may be duplicated. Knowledge of anatomical variations of the CN III orbital segment is important during surgical procedures conducted within the orbit and during diagnosing clinical symptoms of damage to CN III or its branches.

## Acknowledgements

The authors wish to express their gratitude to all those who donated their bodies to medical science.

## REFERENCES

1. Apaydin N, Kendir S, Karahan ST. The anatomical relationships of the ocular motor nerves with an emphasis on surgical anatomy of the orbit. *Anat Rec (Hoboken)*. 2019; 302(4): 568–574, doi: [10.1002/ar.23820](https://doi.org/10.1002/ar.23820), indexed in Pubmed: [29659177](https://pubmed.ncbi.nlm.nih.gov/29659177/).
2. Bayramlar H, Miman MC, Demirel S. Inferior oblique paresis, mydriasis, and accommodative palsy as temporary complications of sinus surgery. *J Neuroophthalmol*. 2004; 24(3): 225–227, doi: [10.1097/00041327-200409000-00009](https://doi.org/10.1097/00041327-200409000-00009), indexed in Pubmed: [15348990](https://pubmed.ncbi.nlm.nih.gov/15348990/).
3. Bergman RA, Afifi AK, Miyauchi R. 2015. Illustrated Encyclopedia of Human Anatomic Variation. Opus III: Nervous System. <https://www.anatomyatlases.org/AnatomicVariants/NervousSystem/Text/OculomotorNerve.shtml>.
4. Black EH, Nesi FA, Gladstone GJ, Levine MR. (Eds). Smith and Nesi's Ophthalmic Plastic and Reconstructive Surgery. Springer, New York, Dodrecht, Heidelberg, London 2012: 186–187.
5. Bodker F, Cytryn A, Putterman A, et al. Postoperative mydriasis after repair of orbital floor fracture. *Am J Ophthalmol*. 1993; 115(3): 372–375, doi: [10.1016/s0002-9394\(14\)73591-3](https://doi.org/10.1016/s0002-9394(14)73591-3).
6. Bye LA, Modi NC, Stanford M. Basic Sciences for Ophthalmology. Oxford University Press, Oxford 2013: 1–57.
7. Cárdenas-Mejía A, Palafox D, Téllez-Palacios D, et al. Levator palpebrae superioris muscle direct neurotization. *J Craniofac Surg*. 2017; 28(8): e747–e748, doi: [10.1097/SCS.00000000000003924](https://doi.org/10.1097/SCS.00000000000003924), indexed in Pubmed: [28953147](https://pubmed.ncbi.nlm.nih.gov/28953147/).
8. Djordjević B, Novaković M, Milisavljević M, et al. Surgical anatomy and histology of the levator palpebrae superioris muscle for blepharoptosis correction. *Vojnosanit Pregl*. 2013; 70(12): 1124–1131, doi: [10.2298/vsp1312124d](https://doi.org/10.2298/vsp1312124d), indexed in Pubmed: [24450257](https://pubmed.ncbi.nlm.nih.gov/24450257/).
9. Haładaj R, Wysiadecki G, Tubbs R. Intramuscular innervation of the lateral rectus muscle evaluated using sihler's staining technique: Potential application to strabismus surgery. *Clin Anat*. 2020; 33(4): 585–591, doi: [10.1002/ca.23452](https://doi.org/10.1002/ca.23452).
10. Haładaj R, Wysiadecki G, Tubbs R, et al. Anatomical variations of the levator palpebrae superioris, including observations on its innervation and intramuscular nerves'



- distribution pattern. *Ann Anat.* 2020; 228: 151439, doi: [10.1016/j.aanat.2019.151439](https://doi.org/10.1016/j.aanat.2019.151439).
11. Haładaj R. Anatomical variations of the ciliary ganglion with an emphasis on the location in the orbit. *Anat Sci Int.* 2020; 95(2): 258–264, doi: [10.1007/s12565-019-00518-x](https://doi.org/10.1007/s12565-019-00518-x), indexed in Pubmed: [31845184](https://pubmed.ncbi.nlm.nih.gov/31845184/).
  12. Haładaj R. Normal anatomy and anomalies of the rectus extraocular muscles in human: a review of the recent data and findings. *Biomed Res Int.* 2019; 2019: 8909162, doi: [10.1155/2019/8909162](https://doi.org/10.1155/2019/8909162), indexed in Pubmed: [31976329](https://pubmed.ncbi.nlm.nih.gov/31976329/).
  13. Haładaj R. Comparison of lateral and medial rectus muscle in human: an anatomical study with particular emphasis on morphology, intramuscular innervation pattern variations and discussion on clinical significance. *Surg Radiol Anat.* 2020; 42(5): 607–616, doi: [10.1007/s00276-019-02400-x](https://doi.org/10.1007/s00276-019-02400-x), indexed in Pubmed: [31897658](https://pubmed.ncbi.nlm.nih.gov/31897658/).
  14. Hamel O, Corre P, Ploteau S, et al. Ciliary ganglion afferents and efferents variations: a possible explanation of postganglionic mydriasis. *Surg Radiol Anat.* 2012; 34(10): 897–902, doi: [10.1007/s00276-012-1000-5](https://doi.org/10.1007/s00276-012-1000-5), indexed in Pubmed: [23076729](https://pubmed.ncbi.nlm.nih.gov/23076729/).
  15. He D, Blomquist PH, Ellis E. Association between ocular injuries and internal orbital fractures. *J Oral Maxillofac Surg.* 2007; 65(4): 713–720, doi: [10.1016/j.joms.2006.09.006](https://doi.org/10.1016/j.joms.2006.09.006), indexed in Pubmed: [17368368](https://pubmed.ncbi.nlm.nih.gov/17368368/).
  16. Hornblass A. Pupillary dilatation in fractures of the floor of the orbit. *Ophthalmic Surg.* 1979; 10(11): 44–46, indexed in Pubmed: [523058](https://pubmed.ncbi.nlm.nih.gov/523058/).
  17. Iaconetta G, de Notaris M, Cavallo LM, et al. The oculomotor nerve: microanatomical and endoscopic study. *Neurosurgery.* 2010; 66(3): 593–601; discussion 601, doi: [10.1227/01.NEU.0000365422.36441.C8](https://doi.org/10.1227/01.NEU.0000365422.36441.C8), indexed in Pubmed: [20173555](https://pubmed.ncbi.nlm.nih.gov/20173555/).
  18. Isomura G. Nerve supply for anomalous ocular muscle in man. *Anat Anz.* 1977; 142(3): 255–265, indexed in Pubmed: [603076](https://pubmed.ncbi.nlm.nih.gov/603076/).
  19. Izci Y, Gonul E. The microsurgical anatomy of the ciliary ganglion and its clinical importance in orbital traumas: an anatomic study. *Minim Invasive Neurosurg.* 2006; 49(3): 156–160, doi: [10.1055/s-2006-944241](https://doi.org/10.1055/s-2006-944241), indexed in Pubmed: [16921456](https://pubmed.ncbi.nlm.nih.gov/16921456/).
  20. Kocabiyik N. Chapter 22: Orbital muscles. In: Tubbs RS, Shoja MM, Loukas M (Eds.). *Bergman's Comprehensive Encyclopedia of Human Anatomic Variation*. Wiley, Hoboken 2016: 207–211.
  21. Natori Y, Rhoton AL. Microsurgical anatomy of the superior orbital fissure. *Neurosurgery.* 1995; 36(4): 762–775, doi: [10.1227/00006123-199504000-00018](https://doi.org/10.1227/00006123-199504000-00018), indexed in Pubmed: [7596508](https://pubmed.ncbi.nlm.nih.gov/7596508/).
  22. Park HK, Rha HK, Lee KJ, et al. Microsurgical anatomy of the oculomotor nerve. *Clin Anat.* 2017; 30(1): 21–31, doi: [10.1002/ca.22811](https://doi.org/10.1002/ca.22811), indexed in Pubmed: [27859787](https://pubmed.ncbi.nlm.nih.gov/27859787/).
  23. Shin HJ, Lee SH, Ha TJ, et al. Intramuscular nerve distribution in the medial rectus muscle and its clinical implications. *Curr Eye Res.* 2019; 44(5): 522–526, doi: [10.1080/02713683.2018.1562556](https://doi.org/10.1080/02713683.2018.1562556), indexed in Pubmed: [30624996](https://pubmed.ncbi.nlm.nih.gov/30624996/).
  24. Standring S. (ed.). *Gray's Anatomy: The anatomical basis of clinical practice*, 41st ed. Churchill Livingstone., Edinburgh, London 2016.
  25. Tesapirat L, Jariyakosol S, Chentanez V. Morphometric study of the ciliary ganglion and its pertinent intraorbital procedure. *Folia Morphol.* 2020; 79(3): 438–444, doi: [10.5603/FM.a2019.0112](https://doi.org/10.5603/FM.a2019.0112), indexed in Pubmed: [31621056](https://pubmed.ncbi.nlm.nih.gov/31621056/).
  26. Tsuda H, Tanaka K. Clinico-anatomical analysis of the fibers to the inferior rectus muscle in the oculomotor fascicles. *Intern Med.* 2012; 51(15): 2031–2034, doi: [10.2169/internalmedicine.51.7914](https://doi.org/10.2169/internalmedicine.51.7914), indexed in Pubmed: [22864132](https://pubmed.ncbi.nlm.nih.gov/22864132/).
  27. Zhang Yi, Liu H, Liu EZ, et al. Microsurgical anatomy of the ocular motor nerves. *Surg Radiol Anat.* 2010; 32(7): 623–628, doi: [10.1007/s00276-009-0585-9](https://doi.org/10.1007/s00276-009-0585-9), indexed in Pubmed: [19885637](https://pubmed.ncbi.nlm.nih.gov/19885637/).

# Anatomy of the superior hypogastric plexus and its application in nerve-sparing paraaortic lymphadenectomy

H. Kim<sup>1</sup> , Y.S. Nam<sup>2</sup>, U.-Y. Lee<sup>1, 2</sup>, I.-B. Kim<sup>1, 2</sup>, Y.-S. Kim<sup>1, 2</sup>

<sup>1</sup>Department of Anatomy, College of Medicine, Catholic University of Korea, Seoul, Korea

<sup>2</sup>Catholic Institute for Applied Anatomy, College of Medicine, Catholic University of Korea, Seoul, Korea

[Received: 7 February 2020; Accepted: 16 February 2020]

**Background:** The purpose of this study was to clarify the anatomy of the superior hypogastric plexus, which would contribute to advancement of nerve-sparing paraaortic lymphadenectomy.

**Materials and methods:** Eighteen cadavers were dissected and morphometrically analysed based on photographic images. Anatomical landmarks such as aortic bifurcation, transitional points of abdominal aorta to bilateral common iliac arteries, and cross point of the right ureter and pelvic brim, and cross point of sigmoid mesentery and pelvic brim were selected as reference points.

**Results:** The left lowest lumbar splanchnic nerve was located more laterally to transitional point of abdominal aorta to in 11/18 specimens, whereas the right lowest lumbar splanchnic nerve passed onto the right transitional point in only one specimen. The lowest lumbar splanchnic nerves or the superior hypogastric plexus covered the aortic bifurcation in 11/18 specimens. The superior hypogastric plexus was separate from the cross point of right ureter and pelvic brim as well as cross point of sigmoid mesentery and pelvic brim.

**Conclusions:** The superior hypogastric plexus is at risk of injury during paraaortic lymphadenectomy because of its topography. Preservation of the superior hypogastric plexus regarding its anatomic basis during paraaortic lymphadenectomy is required. (Folia Morphol 2021; 80, 1: 70–75)

**Key words:** lowest lumbar splanchnic nerves, nerve-sparing surgery, superior hypogastric plexus

## INTRODUCTION

The superior hypogastric plexus (SHP) is a preaortic nervous plexus formed by two lateral roots and one median root [17] around the level of aortic bifurcation [18]. The lateral roots originate mainly from the lowest lumbar splanchnic nerves (LSNs) [2] and contain a sympathetic component [17]. The median root, or a continuation of the abdominal aortic plexus from the inferior mesenteric plexus [15, 17], contains both sympathetic and parasympathetic components [12]. The SHP is divided into paired hypogastric nerves at

the same level or below the sacral promontory [15, 17, 18, 21].

Paraaortic lymphadenectomy is a surgical procedure normally performed concurrently with hysterectomy for diagnostic and therapeutic purposes [19]. Postoperative complications such as urinary, defecatory, and sexual disorders following paraaortic lymphadenectomy have been reported [3, 4, 19]. These postoperative complications are believed to be caused by autonomic denervation during the surgery [19]. Thus, nerve-sparing methods have been established, most of

Address for correspondence: Dr. Y.-S. Kim, Catholic Institute for Applied Anatomy, College of Medicine, Catholic University of Korea, Banpo-Daero 222, Seocho-Gu, Seoul, Republic of Korea, 06591, tel: 82-2-2258-7442, fax: 82-2-537-7081, e-mail: jwkiss@catholic.ac.kr

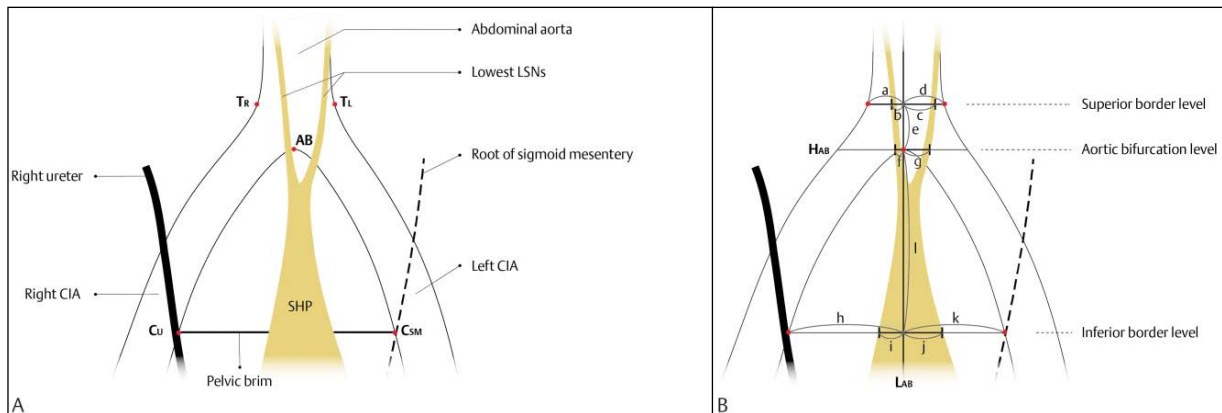


**Figure 1. A.** Anatomical landmarks (indicated by red dots) from the abdominal aorta and the common iliac arteries used in this study. **B.** Definition of 12 measurements to represent relative location of superior hypogastric plexus (SHP) and lowest lumbar splanchnic nerves (LSNs) to anatomic landmarks; CIA — common iliac artery; AB — aortic bifurcation of the abdominal aorta;  $T_R$  — transitional point of the abdominal aorta to the right CIA;  $T_L$  — transitional point of the abdominal aorta to the left CIA;  $C_U$  — cross point of the right ureter and the pelvic brim,  $C_{SM}$  — cross point of the sigmoid mesentery and the pelvic brim;  $H_{AB}$  — a horizontal line passing the aortic bifurcation;  $L_{AB}$  — a longitudinal line passing the aortic bifurcation; a–d were measured at the superior border level; f and g were measured at the aortic bifurcation level; h–k were measured at the inferior border level.

which focus on preservation of pelvic autonomic nerves including hypogastric nerves, pelvic splanchnic nerves, and the inferior hypogastric plexus and its visceral branches [10, 13]. However, autonomic denervation-related complications following non-gynecologic surgery that did not involve the true pelvis but the paraaortic area have been reported [8, 9]. These imply that autonomic denervation-related complications arising after paraaortic lymphadenectomy accompanied by hysterectomy could also be caused by injury to more superiorly located nervous structure, or SHP.

Most previous morphometric studies describing the location of the SHP adopted the midpoint of the sacral promontory [18] or the midsagittal plane [17, 20] as reference points. However, because the sacral promontory is covered by the retroperitoneum, the common iliac vessels and fatty tissue between them, and the anterior longitudinal ligament, it is not clearly observable before being fully dissected. If surgical circumstances, particularly laparoscopic, limit the opportunity for manual palpation, determining the accurate midpoint of the sacral promontory can be a significant challenge. Therefore, easily identifiable anatomical landmarks during the surgery would enhance morphometric analysis of the SHP and clinical applications to laparoscopic surgery.

The purpose of this study was to clarify the anatomy of the SHP by providing relative position of the SHP with morphometric data relevant to anatomical landmarks, which would contribute to advancement of nerve-sparing techniques surgery.

## MATERIALS AND METHODS

The institutional review board of the Catholic University of Korea ruled that a cadaveric study is beyond its review authority. All cadavers used in this study were donated to the Catholic Institute for Applied and Clinical Anatomy under informed consent. Exclusion criteria included any gross evidences of retroperitoneal lesions such as aortoiliac lymph nodes metastasis and vascular malformations, and abdominopelvic surgeries, which could affect quantitative measurements. Eighteen specimens were morphometrically analyzed. Ages at death of specimens were  $83.2 \pm 6.0$  years (range 69.5–91.9). Height and weight of the specimens were  $153.7 \pm 6.6$  cm (range 142.0–168.0) and  $43.4 \pm 11.0$  kg (range 26.0–64.0), respectively. Calculated body mass index was  $18.3 \pm 3.9$  kg/m<sup>2</sup> (range 11.3–25.0).

The method of Paraskevas et al. [17], which involves dissection of the trigone formed by the common iliac arteries and the sacral promontory, was modified. A more enlarged trapezoid-shape incision on the retroperitoneum was required to clarify the positional relationship of the SHP and anatomical landmarks adopted in this study. Five points from the abdominal aorta and the common iliac arteries were palpated and pinned (Fig. 1A). The retroperitoneum overlying the trapezoid formed by the four points, except the aortic bifurcation point, was removed with minimal structural changes. The inferior mesenteric plexus accompanying the inferior mesenteric artery was pushed away to the left. The fatty tissue overlying

**Table 1.** Distances from the aortic bifurcation point to the apices of the trapezoid and the preaortic plexus formed by the lowest lumbar splanchnic nerves and the superior hypogastric plexus. Data were displayed with millimeter (mm) scale

Symbol	Description	Coordinate	Average	SD	Range
At the superior border of the trapezoid level					
a	To right upper apex	x	-10.2	4.9	-21.2 ~ -3.1
b	To outer border of right lowest LSN	x	-3.3	5.2	-12.8 ~ 7.5
c	To outer border of left lowest LSN	x	8.8	4.4	-2.2 ~ 14.8
d	To left upper apex	x	10.5	3.8	0.4 ~ 14.8
e	To the superior border of the trapezoid	y	12.9	3.7	4.2 ~ 18.4
At the aortic bifurcation level					
f	To outer border of the right lowest LSN	x	-1.3	4.0	-9.6 ~ 5.4
g	To outer border of the left lowest LSN	x	7.6	3.7	-0.8 ~ 13.5
At the inferior border of the trapezoid level					
h	To the right lower apex	x	-34.0	7.8	-45.6 ~ -16.1
i	To right border of the SHP	x	-6.8	7.3	-21.1 ~ 5.7
j	To left border of the SHP	x	12.3	6.9	-3.5 ~ 21.0
k	To the left lower apex	x	25.5	8.2	11.7 ~ 46.8
l	To the inferior border of the trapezoid	y	-48.5	13.8	-66.3 ~ -15.3

SD — standard deviation; LSN — lumbar splanchnic nerve; SHP — superior hypogastric plexus

the SHP was removed and the bilateral borders of the SHP were dissected precisely under an OPMI pico surgical microscope with 2.5× magnifying lens (Carl Zeiss, Oberkochen, Germany). The bilateral lowest LSNs were followed to upper limit of the trapezoid. The origin of the SHP was determined as the point at which the bilateral lowest LSNs converged. The dissected SHP was documented by a digital single-lens reflex camera (Canon EOS 650D, Tokyo, Japan) with a two-centimeter scale bar for morphometric analysis in the next step.

Adobe Photoshop CC 2018 (Adobe systems incorporated, California, US) was used to measure distances. A horizontal ( $H_{AB}$ ) and a longitudinal ( $L_{AB}$ ) line passing the aortic bifurcation point were drawn. The aortic bifurcation was regarded as the datum point of the quadrant formed by the horizontal and the longitudinal line. A horizontal line connecting the  $T_R$  and  $T_L$  was drawn for the superior border of the trapezoid. Another horizontal line connecting the  $C_U$  and  $C_{SM}$  was drawn for the inferior border of the trapezoid.

Inside the trapezoid, 10 points at three different levels were marked (Fig. 1B). When the lowest LSN was located more laterally to the apex on the superior border, it was not marked. At each of the three levels, horizontal distances from the  $L_{AB}$  to each marked point were measured (Fig. 1B) and described as x-coordinates. Marked points at right side of the

$L_{AB}$  were given negative values. Likewise, longitudinal distances from the  $H_{AB}$  to each level were measured and described as y-coordinates. Marked points below the  $H_{AB}$  were given negative values. Lengths of the superior and the inferior borders were calculated, as were the horizontal distances from each apex of the trapezoid to the closer border of the lowest LSNs or the SHP.

## RESULTS

Measurement values representing positional relationships of the lowest LSNs and the SHP to the aortic bifurcation are described as coordinate values in the Table 1. Horizontal distances from the four apices of the trapezoid to the lowest LSNs or the SHP are described in Table 2.

At the superior border level, the left lowest LSNs located more laterally to the left upper apex ( $T_L$ ) were observed in 11/18 specimens. In the other seven, the left lowest LSN was located medially to the  $T_L$ . In one specimen, the right lowest LSN passed onto the  $T_R$  at this level. The maximal distance from the  $L_{AB}$  to the outer border of the right lowest LSN was measured as 12.8 mm, but the maximal distance to the outer border of the left lowest LSN could not be measured because of the more lateral location of the left lowest LSN to the  $T_L$ . The maximal distance from the  $L_{AB}$  to the left upper apex was 14.8 mm.

**Table 2.** Lengths from the four apices of the trapezoid to the preaortic plexus. Data were displayed with millimeter (mm) scale

Description	Average	SD	Range
<b>At the superior border</b>			
Horizontal distance from the right upper apex to the closer border of the lowest LSN	6.8	4.7	0 ~ 18.2
Horizontal distance from the left upper apex to the closer border of the lowest LSN	1.7	2.5	0 ~ 7.6
<b>At the inferior border</b>			
Horizontal distance from the right lower apex to the closer border of the SHP	27.2	8.3	12.0 ~ 42.1
Horizontal distance from the left lower apex to the closer border of the SHP	13.2	9.3	2.7 ~ 34.4

SD — standard deviation; LSN — lumbar splanchnic nerve; SHP — superior hypogastric plexus

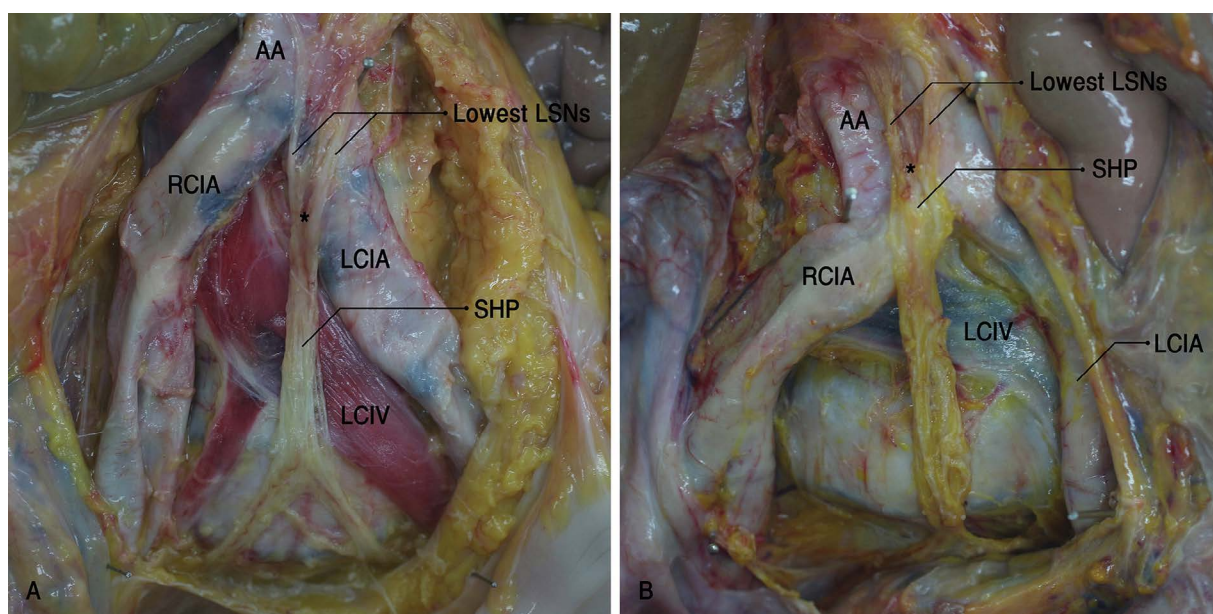


**Figure 2.** Ventral view of the superior hypogastric plexus (SHP); **A.** The SHP is formed by the bilateral lowest lumbar splanchnic nerves (LSNs) below the aortic bifurcation. The SHP is located anterior to left common iliac artery (CIA), the left common iliac vein, and the fifth lumbar vertebral body; **B.** The SHP is formed above the aortic bifurcation. The SHP is located anterior to the right CIA, the left common iliac vein, and the fifth lumbar vertebral body. The asterisk (\*) indicates the origin of the SHP. Between the bilateral LSNs, multiple fibers from the abdominal aortic plexus were observed; AA — abdominal aorta; RCIA — right common iliac artery; LCIA — left common iliac artery; LCIV — left common iliac vein.

At the aortic bifurcation level, the preaortic plexus covered the aortic bifurcation in 11 among 18 specimens despite its slight deviation to either side. In the other cases, the entire plexus was observed to be right (1/18) or left (6/18) of the  $L_{AB}$ . The maximal distances from the  $L_{AB}$  to the outer border of the plexus were 9.6 mm right and 13.5 mm left.

At the inferior border level, the two lower apices ( $C_U$  and  $C_{SM}$ ) were always separate from the SHP. The maximal distances from the  $L_{AB}$  to the outer border of the SHP were 21.1 mm right and 21.0 mm left. The average distance from the right ureter to the SHP was almost twice longer than the average distance from the sigmoid mesentery to the SHP.

The SHP was formed below the aortic bifurcation in 14 of 18 cases (Fig. 2A). In the other cases, the SHP was formed above the aortic bifurcation (Fig. 2B). In average, the gap between the two points at each level was narrower in the middle of the plexus than in the superior and the inferior border. The SHP occupied the widest area at the inferior border level.

## DISCUSSION

The SHP was found to be at risk of injury during paraaortic lymphadenectomy because of its topography. The general appearance of the SHP was inferred through morphometric analysis in this study. The bilateral lowest LSNs converged into and formed the

SHP below the aortic bifurcation in 14/18 cases. The SHP was formed above the bifurcation, as was also reported by Ripperda et al. [18], in four specimens, but even in these cases, the origin of the SHP was located anterior to the lower portion of the abdominal aorta. The SHP, in average, occupied about one third of the space between the right ureter and the root of the sigmoid mesentery at the sacral promontory level and the width of the plexus at this level was wider than any of those at the other two levels. Briefly, the SHP was usually formed below the aortic bifurcation, located anterior to the left common iliac vessels, the fifth lumbar vertebral body, and the sacral promontory down from above. The SHP gradually spread again like a fan from its origin before it divided into hypogastric nerves around the sacral promontory (Fig. 2A). Paraaortic lymphadenectomy involves removal of all lymph nodes around the aorta from the left renal vein superiorly to the mid-portion of the common iliac arteries inferiorly in patients with ovarian cancer or endometrial cancer [1, 11]. Depending on surgeons, the cephalad extent of paraaortic lymphadenectomy may be limited to the level of the inferior mesenteric artery for selected cases of cervical cancer [11]. In both cases of paraaortic lymphadenectomy, the area where the SHP was located is approached.

This study found that the abdominal aortic bifurcation should be avoided as an initiation point of incision during paraaortic lymphadenectomy. Because the preaortic plexus, which is composed of the bilateral LSNs and the abdominal aortic plexus anterior to the aortic bifurcation, was located between approximately 1 cm to the right and 1.4 cm left to the bifurcation in our specimens, an incision at this point [7] would damage the plexus, increasing the possibility of postoperative morbidities. For similar reasons, incisions along the bilateral borders of the abdominal aorta, particularly around the transitional points of the abdominal aorta to the common iliac arteries, are not recommended. On the left side, the lowest LSN ran down from more lateral side to the abdominal aorta and passed anterior to the left common iliac artery in usual (11/18) cases. On the right side, one case of the lowest LSN was observed to pass onto the right transitional points. Incisions placed close to the sidewalls of the lower abdominal aorta could damage the lowest LSNs. Incisions across the right common iliac artery are worth attempting, whereas left-sided incisions could cause a problem running into the sigmoid mesentery. The SHP was about 2.7 cm

from the cross point of the right ureter and the pelvic brim (Table 2). In van Shaik et al. [21], the SHP was reported, at the level of the sacral promontory, 2 cm medial and parallel to the course of the ureters, but the sample size ( $n = 2$ ) was small. Given these observations, an initial incision placed on the retroperitoneum covering the mid-portion of the right common iliac artery would be favorable, and carrying out a longitudinal incision along the right sidewall of the inferior vena cava to the cephalad direction would be a considerable choice to avoid damage to the SHP.

This study provides positional relationships of the SHP to the abdominal aorta and the common iliac arteries. Anatomical landmarks such as the aortic bifurcation, the transitional points of the abdominal aorta to the bilateral common iliac arteries, the cross point of the right ureter and the pelvic brim, and the cross point of the sigmoid mesentery and the pelvic brim were selected for morphometric analysis. The aortic bifurcation and the right ureter were easily identifiable by inspection or palpation under the retroperitoneum even during surgery and have been used successfully as anatomical landmarks in previous radiologic [5, 16] and dissection studies [18, 21]. The root of the sigmoid mesentery was selected because the left ureter was covered by the root of the sigmoid mesentery [6].

Morphometric data regarding the location and general appearance of the SHP would help clinicians identify and preserve the SHP behind the retroperitoneum, but more caution is required before direct and generalised application of this knowledge to the operation. Our results are from the specimens that were older and had lower body mass indices than the average population. This is a limitation of a cadaveric study, which completely depends on post-mortem donation of materials. Radiologic studies using high-resolution magnetic resonance imaging of live human, such as magnetic resonance neurography and combined 3D reconstruction technology [14] might address this limitation.

## CONCLUSIONS

This study provides clinicians with schematic information of the SHP applicable to nerve-sparing paraaortic lymphadenectomies by suggesting morphometric data with relevance to anatomical landmarks. The SHP was proven to be at risk of injury during paraaortic lymphadenectomy because of its topography. A right-sided incision from the mid-portion

tion of the right common iliac artery to the cephalad direction along the right sidewall of the inferior vena cava is recommended to preserve the SHP. Identification and preservation of the SHP regarding its anatomic basis before lymph node dissection is required.


### Acknowledgements

The authors would like to thank Eunah Hong for drawing diagrams, Jeong-Won Oh for gynecological advice, and the donors and their families without whom this research would not be possible. This research was supported by the Basic Science Research Program through the National Research Foundation of Korea (NRF) funded by the Ministry of Education (2018R1D1A1B07048476).

### REFERENCES

- Bae J, Choi JS, Lee WM, et al. Feasibility and efficacy of laparoscopic restaging surgery for women with unexpected ovarian malignancy. *Eur J Obstet Gynecol Reprod Biol.* 2015; 193: 46–50, doi: [10.1016/j.ejogrb.2015.06.027](https://doi.org/10.1016/j.ejogrb.2015.06.027), indexed in Pubmed: [26232726](https://pubmed.ncbi.nlm.nih.gov/26232726/).
- Beveridge TS, Fournier DE, Groh AMR, et al. The anatomy of the infrarenal lumbar splanchnic nerves in human cadavers: implications for retroperitoneal nerve-sparing surgery. *J Anat.* 2018; 232(1): 124–133, doi: [10.1111/joa.12721](https://doi.org/10.1111/joa.12721), indexed in Pubmed: [29159805](https://pubmed.ncbi.nlm.nih.gov/29159805/).
- Bogani G, Cromi A, Uccella S, et al. Nerve-sparing versus conventional laparoscopic radical hysterectomy: a minimum 12 months' follow-up study. *Int J Gynecol Cancer.* 2014; 24(4): 787–793, doi: [10.1097/IGC.000000000000110](https://doi.org/10.1097/IGC.000000000000110), indexed in Pubmed: [24552894](https://pubmed.ncbi.nlm.nih.gov/24552894/).
- Chen Y, Xu H, Li Y, et al. The outcome of laparoscopic radical hysterectomy and lymphadenectomy for cervical cancer: a prospective analysis of 295 patients. *Ann Surg Oncol.* 2008; 15(10): 2847–2855, doi: [10.1245/s10434-008-0063-3](https://doi.org/10.1245/s10434-008-0063-3), indexed in Pubmed: [18649105](https://pubmed.ncbi.nlm.nih.gov/18649105/).
- Chithriki M, Jaibaji M, Steele RD. The anatomical relationship of the aortic bifurcation to the lumbar vertebrae: a MRI study. *Surg Radiol Anat.* 2002; 24(5): 308–312, doi: [10.1007/s00276-002-0036-3](https://doi.org/10.1007/s00276-002-0036-3), indexed in Pubmed: [12497222](https://pubmed.ncbi.nlm.nih.gov/12497222/).
- Coffin A, Boulay-Coletta I, Sebbag-Sfez D, et al. Radioanatomy of the retroperitoneal space. *Diagn Interv Imaging.* 2015; 96(2): 171–186, doi: [10.1016/j.diii.2014.06.015](https://doi.org/10.1016/j.diii.2014.06.015), indexed in Pubmed: [25547251](https://pubmed.ncbi.nlm.nih.gov/25547251/).
- Dottino PR, Tobias DH, Beddoe A, et al. Laparoscopic lymphadenectomy for gynecologic malignancies. *Gynecol Oncol.* 1999; 73(3): 383–388, doi: [10.1006/gyno.1999.5376](https://doi.org/10.1006/gyno.1999.5376), indexed in Pubmed: [10366464](https://pubmed.ncbi.nlm.nih.gov/10366464/).
- Jimenez JC, Smith MM, Wilson SE. Sexual dysfunction in men after open or endovascular repair of abdominal aortic aneurysms. *Vascular.* 2004; 12(3): 186–191, doi: [10.1258/rsmvasc.12.3.186](https://doi.org/10.1258/rsmvasc.12.3.186), indexed in Pubmed: [15586527](https://pubmed.ncbi.nlm.nih.gov/15586527/).
- Johnson R, McGuire E. Urogenital complications of anterior approaches to the lumbar spine. *Clin Orthop Relat Res.* 1981; &NA;(154): 114–118, doi: [10.1097/00003086-198101000-00017](https://doi.org/10.1097/00003086-198101000-00017).
- Kanao H, Fujiwara K, Ebisawa K, et al. Various types of total laparoscopic nerve-sparing radical hysterectomies and their effects on bladder function. *J Gynecol Oncol.* 2014; 25(3): 198–205, doi: [10.3802/jgo.2014.25.3.198](https://doi.org/10.3802/jgo.2014.25.3.198), indexed in Pubmed: [25045432](https://pubmed.ncbi.nlm.nih.gov/25045432/).
- Kavallaris A, Kalogiannidis I, Chalvatzas N, et al. Standardized technique of laparoscopic pelvic and para-aortic lymphadenectomy in gynecologic cancer optimizes the perioperative outcomes. *Arch Gynecol Obstet.* 2011; 283(6): 1373–1380, doi: [10.1007/s00404-010-1580-4](https://doi.org/10.1007/s00404-010-1580-4), indexed in Pubmed: [20607263](https://pubmed.ncbi.nlm.nih.gov/20607263/).
- Kraima AC, van Schaik J, Susan S, et al. New insights in the neuroanatomy of the human adult superior hypogastric plexus and hypogastric nerves. *Auton Neurosci.* 2015; 189: 60–67, doi: [10.1016/j.autneu.2015.02.001](https://doi.org/10.1016/j.autneu.2015.02.001), indexed in Pubmed: [25704391](https://pubmed.ncbi.nlm.nih.gov/25704391/).
- Kyo S, Kato T, Nakayama K. Current concepts and practical techniques of nerve-sparing laparoscopic radical hysterectomy. *Eur J Obstet Gynecol Reprod Biol.* 2016; 207: 80–88, doi: [10.1016/j.ejogrb.2016.10.033](https://doi.org/10.1016/j.ejogrb.2016.10.033), indexed in Pubmed: [27825032](https://pubmed.ncbi.nlm.nih.gov/27825032/).
- Li P, Liu P, Chen C, et al. The 3D reconstructions of female pelvic autonomic nerves and their related organs based on MRI: a first step towards neuronavigation during nerve-sparing radical hysterectomy. *Eur Radiol.* 2018; 28(11): 4561–4569, doi: [10.1007/s00330-018-5453-8](https://doi.org/10.1007/s00330-018-5453-8), indexed in Pubmed: [29728818](https://pubmed.ncbi.nlm.nih.gov/29728818/).
- Lu S, Xu Yq, Chang S, et al. Clinical anatomy study of autonomic nerve with respective to the anterior approach lumbar surgery. *Surg Radiol Anat.* 2009; 31(6): 425–430, doi: [10.1007/s00276-009-0461-7](https://doi.org/10.1007/s00276-009-0461-7), indexed in Pubmed: [19190849](https://pubmed.ncbi.nlm.nih.gov/19190849/).
- McCullough M, Valceus J, Downes K, et al. The ureter as a landmark for robotic sacrocolpopexy. *Female Pelvic Med Reconstr Surg.* 2012; 18(3): 162–164, doi: [10.1097/SPV.0b013e3182544e17](https://doi.org/10.1097/SPV.0b013e3182544e17), indexed in Pubmed: [22543768](https://pubmed.ncbi.nlm.nih.gov/22543768/).
- Paraskevas G, Tsitsopoulos P, Papaziogas B, et al. Variability in superior hypogastric plexus morphology and its clinical applications: a cadaveric study. *Surg Radiol Anat.* 2008; 30(6): 481–488, doi: [10.1007/s00276-008-0352-3](https://doi.org/10.1007/s00276-008-0352-3), indexed in Pubmed: [18465081](https://pubmed.ncbi.nlm.nih.gov/18465081/).
- Ripperda CM, Jackson LA, Phelan JN, et al. Anatomic relationships of the pelvic autonomic nervous system in female cadavers: clinical applications to pelvic surgery. *Am J Obstet Gynecol.* 2017; 216(4): 388.e1–388.e7, doi: [10.1016/j.ajog.2016.12.002](https://doi.org/10.1016/j.ajog.2016.12.002), indexed in Pubmed: [27956200](https://pubmed.ncbi.nlm.nih.gov/27956200/).
- Shi R, Wei W, Jiang P. Laparoscopic nerve-sparing radical hysterectomy for cervical carcinoma: emphasis on nerve content in removed cardinal ligaments. *Int J Gynecol Cancer.* 2016; 26(1): 192–198, doi: [10.1097/IGC.0000000000000577](https://doi.org/10.1097/IGC.0000000000000577), indexed in Pubmed: [26569055](https://pubmed.ncbi.nlm.nih.gov/26569055/).
- Shiozawa T, Huebner M, Hirt B, et al. Nerve-preserving sacrocolpopexy: anatomical study and surgical approach. *Eur J Obstet Gynecol Reprod Biol.* 2010; 152(1): 103–107, doi: [10.1016/j.ejogrb.2010.05.009](https://doi.org/10.1016/j.ejogrb.2010.05.009), indexed in Pubmed: [20542624](https://pubmed.ncbi.nlm.nih.gov/20542624/).
- van Schaik J, van Baalen JM, Visser MJ, et al. Nerve-preserving aortoiliac reconstruction surgery: anatomical study and surgical approach. *J Vasc Surg.* 2001; 33(5): 983–989, doi: [10.1067/mva.2001.113306](https://doi.org/10.1067/mva.2001.113306), indexed in Pubmed: [11331838](https://pubmed.ncbi.nlm.nih.gov/11331838/).

# The terminal branch of the posterior interosseous nerve: an anatomic and histologic study

T. Bonczar<sup>1</sup> , J.A. Walocha<sup>1</sup>, M. Bonczar<sup>2</sup>, E. Mizia<sup>1</sup>, M. Koziej<sup>1</sup>, P. Piekos<sup>1</sup>, M. Kujdowicz<sup>3</sup>

<sup>1</sup>Department of Anatomy, Jagiellonian University Medical College, Krakow, Poland

<sup>2</sup>Intermed Medical Clinic, Zabierzow, Poland

<sup>3</sup>Department of Pathology, Jagiellonian University Medical College, Krakow, Poland

[Received: 17 March 2020; Accepted: 2 April 2020]

**Background:** The aim of this study was to evaluate the terminal branch of the posterior interosseous nerve (PIN) by anatomically and histologically assessing the number, dimension, and area of its individual fascicles, by determining the dimension and area of the whole nerve itself, and by calculating the nerve density ratio (ratio of the sum of the areas of individual fascicles to the area of the whole nerve) of the terminal branch of the PIN.

**Materials and methods:** Twenty-eight terminal branches of the PIN nerve samples were collected from patients undergoing partial denervation of the wrist. The nerve samples were fixed in 10% buffered formalin and stained with haematoxylin and eosin to visualise their nerve bundles. Quantitative analysis of individual fascicles and the whole nerve itself were carried out.

**Results:** Ten nerve samples (35.7%) had one single fascicle (group 1) while the remaining 18 nerve samples (64.3%) contained 2–9 fascicles (group 2). The difference in the sum of the areas of individual fascicles between the two groups did not constitute a statistical difference. Statistically significant between-group differences ( $p < 0.05$ ) were seen in the area of whole nerve, the ratio of fascicle area to the nerve cross-sectional area and the cross-section maximum nerve length and width.

**Conclusions:** The number of nerve fascicles in the terminal branch of the PIN does not affect the overall size of the nerve. The majority of the volume of multi-fascicle nerves, therefore, primarily consists of the internal perineurium. However, due to the low number of nerves, this question cannot be clearly answered. This sets a further direction for further research on a larger group. (Folia Morphol 2021; 80, 1: 76–80)

**Key words:** terminal branch of the posterior interosseous nerve, wrist denervation, posterior interosseous nerve fascicles, nerve graft

## INTRODUCTION

The posterior interosseous nerve (PIN) is one of many nerves that innervate the dorsal wrist [2, 10, 11, 13–15, 22]. The PIN is always excised for both partial and complete wrist denervation as a palliative

method of treatment of a variety of wrist pathologies [5, 11]. Due to its consistent anatomical location and dimensions, accessibility, limited functional deficit after excision [19], and adequate length for reanastomosis, the PIN can be used as a donor graft for digital



nerves injuries [1, 4, 9, 17, 18]. A recent publication has described the technique of thumb digital nerve reconstruction after the excision of a neuroma utilising an arterialised PIN graft [12]. The assessment of the usefulness of PIN as a nerve graft was based on the PIN's similar thickness to that of digital nerves. The purpose of this study was to accurately assess the structure of the terminal branches of PIN.

## MATERIALS AND METHODS

The study material consisted of 28 PIN collected from patients treated for wrist pain who underwent partial denervation of the wrist between January 2015 and September 2016. The cause of wrist pain in the studied patient population was either due to worsening of distal PIN syndrome, degenerative changes after a history of injury, progressing Kienböck's disease, and finally a long course of inflammatory changes. In some cases, the PIN was excised to prevent pain after ligamentous reconstruction of the wrist. Before every wrist denervation, all patients with a diagnosis of distal PIN syndrome had preoperative diagnostics of the PIN performed with ultrasound.

All patients signed a written consent for a PIN neurectomy and to participate in this study. The design of this study was approved by our Regional Ethical Review Board. Intraoperative photographs were taken for documentation. All operations were carried out by the same surgeon who is experienced in wrist surgery, under regional anaesthesia with 3.5× optical magnification. The longitudinal incision was cut 1 cm ulnar to Lister's tubercle. The extensor retinaculum was opened and the PIN was found proximal to or in the floor of the 4<sup>th</sup> dorsal compartment. The samples were then fixed in 10% buffered formalin and stayed fixed for 14 days. Then each sample underwent dehydration and paraffin embedding procedures. The paraffin cubes were cut with a microtome into 4 µm thick sections and stained with haematoxylin and eosin to visualise the nerve bundles. Quantitative analysis of individual fascicles and the whole nerve itself were carried out using the Olympus BX43 microscope. Photographic documentation was achieved using an Olympus SC-100 camera. The photographs were then analysed using Image J. The number of fascicles in each nerve, the surface area of each fascicle, and the thickness of the perineurium of each fascicle were evaluated. The surface area of the fascicle was calculated with the help of the Image J program using a variable scale of

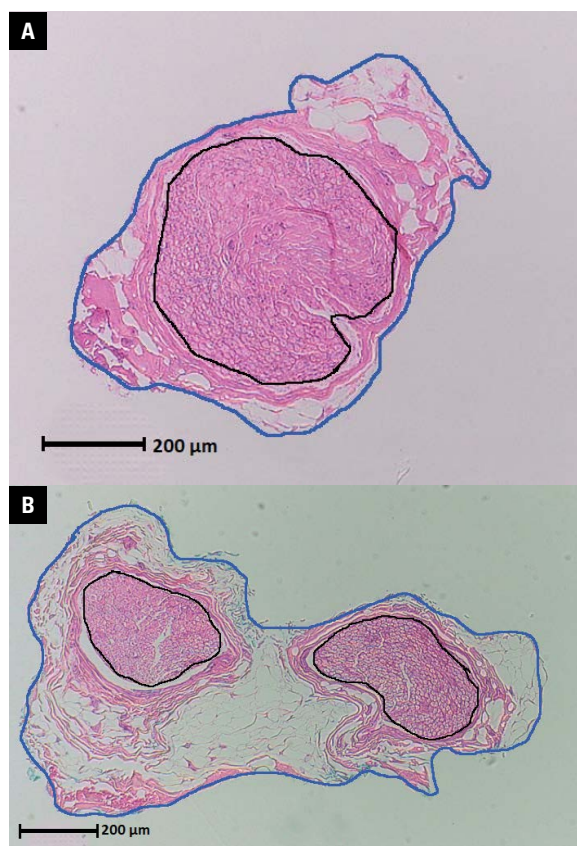


**Figure 1.** Specimen with single fascicle (A) and two fascicles (B) — the black line surrounding the fascicle and the dark blue line around the whole nerve.

enlargement through a computer introduced fascicle contour (Fig. 1). Next the diameter of the each fascicle was measured. Finally, the longitudinal dimensions, transverse dimensions, and the cross-sectional area of the entire nerve were calculated and results of the measurements were recorded.

### Statistical analysis

The data was presented as percentages, mean values with corresponding standard deviations or median with quartiles. The Shapiro-Wilk test was used to determine if the quantitative data was normally distributed. The Student's t-tests and the Mann-Whitney U tests for statistical comparisons were additionally used. Statistical analyses were performed with STATISTICA v13.1 (StatSoft Inc., Tulsa, OK, USA). A p-value of less than 0.05 was considered to be statistically significant.

## RESULTS

The PIN was harvested from 28 patients — 15 males (53.6%) and 13 females (46.4%). Partial

**Table 1.** Causes of posterior interosseous nerve (PIN) excision

Cause of PIN neurectomy	Amount	Percentage
Dorsal PIN syndrome	13	46.4%
SLAC, SNAC	7	25%
SL reconstruction	4	14.3%
Kienböck's disease	3	10.7%
Rheumatoid arthritis	1	3.6%

SL — scapholunate; SLAC — scapholunate advanced collapse; SNAC — scaphoid non-union advanced collapse

denervation of the wrist was performed on the right wrist in 21 (75%) cases, on the left wrist in 7 (25%) cases, and in the dominant hand of the patient in 21 (75%) cases. The mean age of patients was  $36.2 \pm 15.3$  years (range 17–76 years). The causes of PIN excision are shown in Table 1.

Ten nerve samples (35.7%) had one single fascicle (group 1) while the remaining 18 nerve samples (64.3%) contained 2–9 fascicles (group 2). The number of multi-fascicle nerves was as follows: two-fascicles — 4, three-fascicle — 3, four-fascicle — 5, five-fascicle — 1, six-fascicle — 3 and eight and nine-fascicle nerves — 1, respectively. The mean values of selected parameters in mono-fascicles (group 1) and multi-fascicles nerves (group 2) are shown in Table 2. No statistical difference was found between the genders of the patients, between the sizes of the nerves, and between the numbers of fascicles. There

was no correlation between the age and the size of both the nerve and its fascicles. The sum of the areas of the individual fascicles in the single fascicle nerves (group 1) did not differ from the sum of the areas of the individual fascicles in the multi-fascicles nerves (group 2) ( $p = 0.15$ ). However, statistically significant differences ( $p < 0.05$ ) were seen between areas of whole nerve, that was larger in multi fascicles nerves (group 2). Percentage of fascicles to the nerve surface was significantly higher in the mono-fascicle nerves (group 1) than in the multi-fascicles group ( $p = 0.002$ ).

The average nerve density ratio (ratio of the sum of the areas individual fascicles to the area of the whole nerve) was 25.2%. The average sum of the areas of individual fascicles, the cross-sectional area of the whole nerve and nerve density ratio with standard deviation are given in Table 3.

## DISCUSSION

Many publications have shown similarities in the size [3, 6, 8, 21] and in the nerve density [17] of the PIN compared to digital nerves. However, to the knowledge of the authors, this is the first study that describes the anatomical structure of the PIN, taking into account the relationship between the size and number of individual fascicles to the size of the whole nerve. Reissis et al. (1992) [17] compared the usefulness of the PIN as a donor for digital nerve grafts to

**Table 2.** The mean values of selected parameters in mono-fascicles (group 1) and multi-fascicles nerves (group 2)

Parameter	Group	Number	Average	Median	Minimum	Maximum	Bottom quartile	Upper quartile	Standard deviation
Summed area of fascicles [mm <sup>2</sup> ]	1	10	0.19	0.19	0.12	0.27	0.16	0.21	0.05
Area of whole nerve [mm <sup>2</sup> ]	1	10	0.82	0.5	0.23	3.03	0.3	0.97	0.84
Percentage of fascicles to the nerve surface	1	10	36.1	38.2	6.3	69.6	27.8	45.2	17.15
Summed perineurium size [mm]	1	10	0.04	0.04	0.01	0.08	0.03	0.04	0.02
Summed area of fascicles [mm <sup>2</sup> ]	2	18	0.22	0.15	0.01	1.14	0.11	0.19	0.23
Area of whole nerve [mm <sup>2</sup> ]	2	18	3.20	1.55	0.18	10.64	0.72	5.32	3.28
Percentage of fascicles to the nerve surface	2	18	13.41	9.85	0.18	50	2.1	17.8	13.25
Summed perineurium size [mm]	2	18	0.1	0.1	0.04	0.3	0.06	0.1	0.07

**Table 3.** Measurements of 28 posterior interosseous nerve harvested during wrist reconstructive procedures or partial wrist denervation

Parameter	Number	Average	Median	Minimum	Maximum	Lower quartile	Upper quartile	Standard deviation
Summed area of fascicles [mm <sup>2</sup> ]	28	0.2	0.15	0.002	1.14	0.12	0.2	0.21
Area of whole nerve [mm <sup>2</sup> ]	28	2.36	0.88	0.18	10.64	0.52	2.98	2.89
Nerve density ratio [%]	28	21	17	1	68	6	34	18

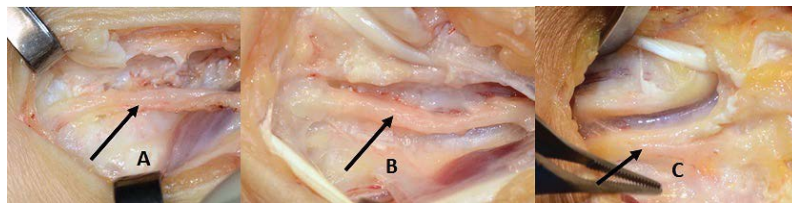


**Figure 2.** Intraoperative photograph of the posterior interosseous nerve before excision. All nerves had similar dimensions regardless of their quantity of fascicles; **A.** Specimen no. 1 with 5 fascicles; **B.** Specimen no. 2 with 3 fascicles; **C.** Specimen no. 5 with 1 fascicle.

15 digital nerves in a microscopic study of 18 fresh terminal branches of the PIN. They defined the nerve density ratio of the PIN as the ratio of the density of neuronal tissue to the density of connective tissue. Their mean nerve density ratio was 90% which ranged from 88–94%. In this study, the results were different and the nerve density ratio, defined as the ratio of the sum of the areas of individual fascicles to the area of the whole nerve, had a mean of only 21% and ranged from 1.0–65%. It is difficult to explain such differences in this study and the study of Reissis et al. (1992) [17], but after using high microscopic magnification it was possible to measure each fascicle in more detail in this study. In addition, the nerves used for the study came from patients with wrist pathology and possible PIN irritation. Ultrasound has shown that nerve irritation causes hypoechoic swollen, mainly of connective tissue [7, 16]. Chevrollier et al. (2014) [3], in a retrospective single-centre study, evaluated emergent nerve grafting for proper palmar digital nerve defects [9]. However, the results of Chevrollier et al. (2014) [3] cannot be compared to the PIN measurements in this study, because of the 12 analysed cases of digital nerve defects, only one patient had the PIN used as a graft. Waters and Schwartz (1993) [20] showed the presence of nerves with a single fascicle in 15 cases (58%) after evaluating 26 PIN using a macroscopic examination at 3.5× magnification. With the use of microdissection without microscopic nerve evaluation, Waters and Schwartz (1993) [20] were able to show the presence of 1 to 5 (average 2) fascicles in the collected nerve samples. The data collected in this studied using high microscopic magnification and appropriate staining has shown that 64.3% of the nerve samples were multi-fascicle nerves. These results differ from previous studies.

This does not mean, however, that multi-fascicle nerves had a larger surface area due to their number of fascicles. On the contrary, the more fascicles the nerve contained, the smaller the fascicles measured. The nerves with more fascicles usually contained one

bigger fascicle with the rest being very small. In these nerves, the majority of the volume, therefore, primarily consisted of the internal perineurium.

## CONCLUSIONS


During surgery, it is impossible to quantitatively assess the PIN after it has been harvested as a nerve graft. Nerves with differing numbers of fascicles are similar in external dimensions (Fig. 2). However, it is crucial to highlight that proper PIN dimensions (the ratio of the nerve tissue to the area of the entire nerve) does not translate to good nerve quality by meaning the nerve density ratio. The number of nerve fascicles in the terminal branch of the PIN does not affect the overall size of the nerve. The majority of the volume of multi-fascicle nerves, therefore, primarily consists of the internal perineurium. However, due to the low number of nerves, this question cannot be clearly answered. This sets a further direction for further research on a larger group.

## REFERENCES

1. Badran H. Digital nerve grafts for insensitve finger tips of thumb and index fingers. *Plastic Reconstr Surg.* 1997; 99(1): 280, doi: [10.1097/00006534-199701000-00081](https://doi.org/10.1097/00006534-199701000-00081).
2. Bonczar T, Walocha JA, Bonczar M, et al. Assessing the innervation of the dorsal wrist capsule using modified Sihler's staining. *Folia Morphol.* 2020 [Epub ahead of print], doi: [10.5603/FM.a2020.0027](https://doi.org/10.5603/FM.a2020.0027), indexed in Pubmed: [32159843](https://pubmed.ncbi.nlm.nih.gov/32159843/).
3. Chevrollier J, Pedoutour B, Dap F, et al. Evaluation of emergency nerve grafting for proper palmar digital nerve defects: a retrospective single centre study. *Orthop Traumatol Surg Res.* 2014; 100(6): 605–610, doi: [10.1016/j.otsr.2014.05.018](https://doi.org/10.1016/j.otsr.2014.05.018), indexed in Pubmed: [25155205](https://pubmed.ncbi.nlm.nih.gov/25155205/).
4. Chong J. Digital nerve grafts with the lateral antebrachial cutaneous nerve. *Plastic Reconstr Surg.* 1977; 59(6): 875, doi: [10.1097/00006534-197706000-00063](https://doi.org/10.1097/00006534-197706000-00063).
5. Dellon AL. Partial dorsal wrist denervation: resection of the distal posterior interosseous nerve. *J Hand Surg Am.* 1985; 10(4): 527–533, doi: [10.1016/s0363-5023\(85\)80077-0](https://doi.org/10.1016/s0363-5023(85)80077-0), indexed in Pubmed: [4020064](https://pubmed.ncbi.nlm.nih.gov/4020064/).
6. Dellon A, Seif S. Anatomic dissections relating the posterior interosseous nerve to the carpus, and the etiology of dorsal wrist ganglion pain. *J Hand Surg.* 1978; 3(4): 326–332, doi: [10.1016/s0363-5023\(78\)80032-x](https://doi.org/10.1016/s0363-5023(78)80032-x).

7. Djurdjevic T, Loizides A, Löscher W, et al. High resolution ultrasound in posterior interosseous nerve syndrome. *Muscle Nerve*. 2014; 49(1): 35–39, doi: [10.1002/mus.23867](https://doi.org/10.1002/mus.23867), indexed in Pubmed: [23559033](https://pubmed.ncbi.nlm.nih.gov/23559033/).
8. Elgafy H, Ebraheim NA, Rezcallah AT, et al. Posterior interosseous nerve terminal branches. *Clin Orthop Relat Res*. 2000(376): 242–251, doi: [10.1097/00003086-200007000-00033](https://doi.org/10.1097/00003086-200007000-00033), indexed in Pubmed: [10906882](https://pubmed.ncbi.nlm.nih.gov/10906882/).
9. Elgafy H, Ebraheim NA, Yeasting RA. The anatomy of the posterior interosseous nerve as a graft. *J Hand Surg Am*. 2000; 25(5): 930–935, doi: [10.1053/jhsu.2000.16359](https://doi.org/10.1053/jhsu.2000.16359), indexed in Pubmed: [11040308](https://pubmed.ncbi.nlm.nih.gov/11040308/).
10. Ferreres A, Suso S, Ordi J, et al. Wrist denervation. *J Hand Surg*. 2016; 20(6): 761–768, doi: [10.1016/s0266-7681\(95\)80043-3](https://doi.org/10.1016/s0266-7681(95)80043-3).
11. Ferreres A, Foucher G, Suso S. Extensive denervation of the wrist. *Tech Hand Up Extrem Surg*. 2002; 6(1): 36–41, doi: [10.1097/00130911-200203000-00007](https://doi.org/10.1097/00130911-200203000-00007), indexed in Pubmed: [16520631](https://pubmed.ncbi.nlm.nih.gov/16520631/).
12. Foo A, Martin-Playa P, Sebastin Muttath SJ. Arterialized posterior interosseous nerve graft for digital neuroma. *Tech Hand Up Extrem Surg*. 2019; 23(4): 152–154, doi: [10.1097/BTH.0000000000000240](https://doi.org/10.1097/BTH.0000000000000240), indexed in Pubmed: [31157733](https://pubmed.ncbi.nlm.nih.gov/31157733/).
13. Fukumoto K, Kojima T, Kinoshita Y, et al. An anatomic study of the innervation of the wrist joint and Wilhelm's technique for denervation. *J Hand Surg*. 1993; 18(3): 484–489, doi: [10.1016/0363-5023\(93\)90096-l](https://doi.org/10.1016/0363-5023(93)90096-l).
14. Gregory T, Goutard M, Gregory J, et al. A cadaveric study of the posterior interosseous nerve and its branches at the level of the distal radius. *J Hand Surg Global Online*. 2019; 1(2): 70–73, doi: [10.1016/j.jhsg.2019.01.001](https://doi.org/10.1016/j.jhsg.2019.01.001).
15. Hofmeister EP, Moran SL, Shin AY. Anterior and posterior interosseous neurectomy for the treatment of chronic dynamic instability of the wrist. *Hand*. 2006; 1(2): 63–70, doi: [10.1007/s11552-006-9003-5](https://doi.org/10.1007/s11552-006-9003-5), indexed in Pubmed: [18780027](https://pubmed.ncbi.nlm.nih.gov/18780027/).
16. Kim Y, Ha DH, Lee SM. Ultrasonographic findings of posterior interosseous nerve syndrome. *Ultrasonography*. 2017; 36(4): 363–369, doi: [10.14366/usg.17007](https://doi.org/10.14366/usg.17007), indexed in Pubmed: [28494524](https://pubmed.ncbi.nlm.nih.gov/28494524/).
17. Reissis N, Stirrat A, Manek S, et al. The terminal branch of posterior interosseous nerve: a useful donor for digital nerve grafting. *J Hand Surg*. 1992; 17(6): 638–640, doi: [10.1016/0266-7681\(92\)90190-d](https://doi.org/10.1016/0266-7681(92)90190-d).
18. Stang F, Stollwerck P, Prommersberger KJ, et al. Posterior interosseous nerve vs. medial cutaneous nerve of the forearm: differences in digital nerve reconstruction. *Arch Orthop Trauma Surg*. 2013; 133(6): 875–880, doi: [10.1007/s00402-013-1731-8](https://doi.org/10.1007/s00402-013-1731-8), indexed in Pubmed: [23536007](https://pubmed.ncbi.nlm.nih.gov/23536007/).
19. Vanden Berge DJ, Kusnezov NA, Rubin S, et al. Outcomes following isolated posterior interosseous nerve neurectomy: a systematic review. *Hand*. 2017; 12(6): 535–540, doi: [10.1177/1558944717692093](https://doi.org/10.1177/1558944717692093), indexed in Pubmed: [28720049](https://pubmed.ncbi.nlm.nih.gov/28720049/).
20. Waters P, Schwartz JT. Posterior interosseous nerve: An anatomic study of potential nerve grafts. *J Hand Surg*. 1993; 18(4): 743–745, doi: [10.1016/0363-5023\(93\)90331-v](https://doi.org/10.1016/0363-5023(93)90331-v).
21. Wilgis E, Maxwell G. Distal digital nerve grafts: Clinical and anatomical studies. *J Hand Surg*. 1979; 4(5): 439–443, doi: [10.1016/s0363-5023\(79\)80038-6](https://doi.org/10.1016/s0363-5023(79)80038-6).
22. Zwart K, Roeling TAP, van Leeuwen WF, et al. An anatomical study to the branching pattern of the posterior interosseous nerve on the dorsal side of the hand. *Clin Anat*. 2020; 33(5): 678–682, doi: [10.1002/ca.23486](https://doi.org/10.1002/ca.23486), indexed in Pubmed: [31581304](https://pubmed.ncbi.nlm.nih.gov/31581304/).

# Assessing the innervation of the dorsal wrist capsule using modified Sihler's staining

T. Bonczar<sup>1</sup> , J.A. Walocha<sup>1</sup>, M. Bonczar<sup>2</sup>, E. Mizia<sup>1</sup>, J. Filipowska<sup>3</sup>

<sup>1</sup>Department of Anatomy, Jagiellonian University Medical College, Krakow, Poland

<sup>2</sup>Intermed Medical Clinic, Zabierzow, Poland

<sup>3</sup>Department of Translational Research and Cellular Therapeutics, City of Hope, Duarte, CA, USA

[Received: 2 January 2020; Accepted: 11 February 2020]

**Background:** The aim of this study was to assess the innervation of the dorsal articular capsule of the wrist using modified Sihler's staining.

**Materials and methods:** Thirty dorsal wrist capsules were collected from 15 donors (both sides) within 12 hours of death. All the capsules were collected in the same manner — using the dorsal incision. The specimens were stained according to the protocol of the modified Sihler's staining technique. The preserved capsules were analysed under 8–16× magnification of an optical microscope for the presence of major nerve trunks, their major and minor branches, and nerve connections.

**Results:** The range of innervation visualised was that the posterior interosseous nerve innervated approximately 60% of the central part; the remaining area was innervated by the dorsal sensory branch of the radial nerve and medial antebrachial cutaneous nerve. The constant findings were the branches departing from the ulnar side of the posterior interosseous nerve and from the radial side, with an exception seen in 2 cases. A communicans branch between the posterior interosseous nerve and medial antebrachial cutaneous nerve was seen in all the specimens. The posterior interosseous nerve innervation extended beyond the level of the carpometacarpal joints II–V.

**Conclusions:** The modified Sihler's staining technique allows for transparent visibility of the nerves that innervate the dorsal wrist capsule. However, it does not allow as accurate assessment as does histological examination, especially regarding the evaluation of nerve endings. Nevertheless, this method provides a significantly larger area of nerve observation than is provided by histological examination. (Folia Morphol 2021; 80, 1: 81–86)

**Key words:** wrist innervation, Sihler's staining technique, posterior interosseous nerve, hand surgery, wrist surgery

## INTRODUCTION

The innervation of the wrist has been a topic of investigation in recent years due to the growing knowledge of wrist pathologies and their treatment. Studies on nerve endings, such as mechanoreceptors, have demonstrated additional important functions of the wrist ligaments in addition to pure stabilisation [8].

However, the extent of innervation of the wrist by individual nerves is yet unclear. Initially, the range of innervation of the wrist was based on the examination of the nerves and their branches with 3.5× magnification, which was then replaced by microdissection using a microscope. Histological examinations of the stained wrist capsule and ligaments have revealed

several features in the area of innervation that are in contrast to the findings of microdissections [6]. Microdissection has made it possible to visualise nerve branches of much smaller sizes and their penetration of the joints within the wrist. The purpose of this study was to assess the nerves within the dorsal wrist capsule using the modified Sihler's staining technique.

## MATERIALS AND METHODS

Thirty dorsal wrist capsules were collected from 15 donors (capsules from both sides) within 12 hours of death. There were 11 male (22 capsules) and 4 female (8 capsules) wrists. The age range at death of these cadavers was 33–72 years (mean age 65.7 years). Donors whose death was caused by polytrauma with associated upper limb injuries were excluded from the study. The limbs were also checked for the presence of postoperative scars in the wrist and forearm region, both on the dorsal and palmar sides. If scars were present, the wrist joint capsules were not collected.

A longitudinal skin incision was made from the proximal 1/3<sup>rd</sup> of the distal forearm to the middle of metacarpal bone III on the dorsal side. The extensor retinaculum was completely dissected, exposing the dorsal wrist joint capsule. The distal cutting line of the capsule was continued along 1 cm above the bases of metacarpal bones II–V, proximally along the edges of the distal end of the radius and ulna; the capsule was detached from the periosteum and dorsal radio-ulnar ligament. A fragment of about 1 cm of the posterior interosseous nerve (PIN) was excised along with its penetration into the capsule.

The lateral and medial edges were determined by the lateral margin of metacarpal II and medial margin of metacarpal V, respectively. The capsules were excised with the extrinsic ligaments detached off its insertions onto the dorsum of the bones of the proximal and distal rows with 3.5× loupe magnification. The side of capsule excision was noted. The proximal part of the excised capsule was determined by presence of the PIN fragment. The specimens were washed under running water and then fixed in a 10% un-neutralised formalin solution for a period of 4 weeks.

The following protocol of staining was applied after 4 weeks of fixation in formalin [22]. Maceration in 3% aqueous potassium hydroxide (KOH) solution for 3 weeks, Sihler's solution I (1 volume glacial acetic acid, 1 volume glycerin, and 6 volumes 1% w/v aqueous chloral hydrate) for staining, Sihler's solution II (1 volume stock Ehrlich's haematoxylin, 1 volume glyc-

erin, and 6 volumes 1% w/v aqueous chloral hydrate) for detaining — each phase for 3 weeks. Lithium carbonate solution 0.05% was then used for neutralisation for 1–2 hours. Finally, dilute 50% glycerin was used for 3 days for clearing the overstained regions (Won et al. 2011 [22]) and all specimens were preserved with 100% glycerin [18]. The preserved capsules were analysed under 8–16× magnification with an optical microscope for the presence of major nerve trunks, their major and minor branches, and nerve connections. The obtained image from the microscope was manually applied to the joint capsule diagram, divided into main quadrants and smaller squares with the wrist (right, left) and sides (radial, ulnar) marked. Each quadrant sustained the 256 small squares (16 rows in 16 columns). Thus the total number of squares in 4 quadrants was 1024. The drawing obtained by hand was scanned and applied to a computer image with accurate reproduction. The area of the innervation of dorsal capsule was determined by two lines running parallel to the long axis of the joint capsule, defined by the outer borders of the furthest reaching and visible nerve branches. Based on the number of squares occupied by the branches of individual nerves, it was possible to calculate the percentage of the area of the joint capsule innervated by a given nerve. The design of this study was approved by our Regional Ethical Review Board.

## RESULTS

The nerves within the 30 wrist capsules in terms of dimensions and course, the number of main trunks and smaller nerve branches, the place of their crossing and the number of small nerves forming the dense network differed in all specimens. In all specimens, the PIN with its branches dominated and covered about 60% of the surface of the articular capsule. This area was determined by two lines running parallel to the long axis of the joint capsule, defined by the outer borders of the furthest reaching and visible PIN branches. All the PINs had at least one large branch on the ulnar side, but most of them had two larger branches (63.3%). Three branches on the ulnar side were visible in 7 (23.3%) cases. Branches on the radial side of the nerve represented similar proportions, although no larger trunks on the radial side were found in two of the 30 specimens. In both these cases, the main trunk or two nerve trunks were clearly passing radially (Fig. 1). Mostly there were two (43.3%) branches, but the total share of the

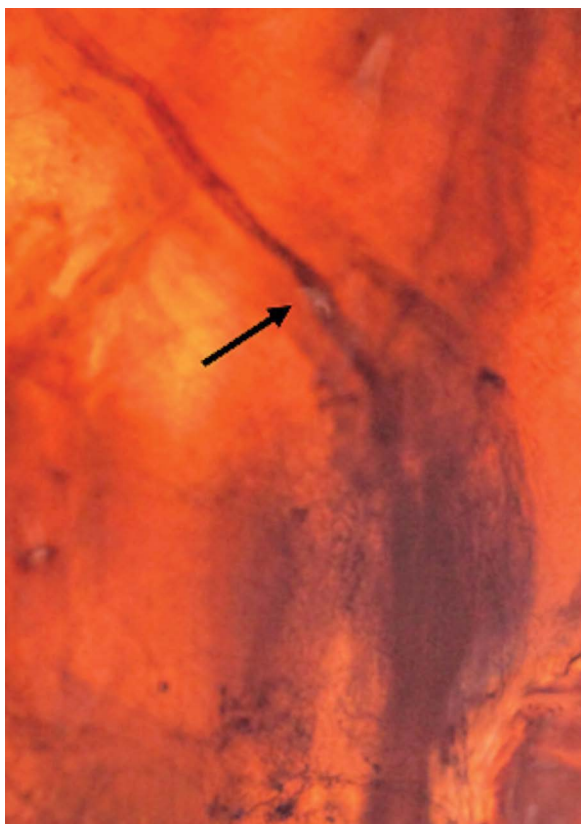


**Figure 1.** Dorsal wrist capsule (right hand) in Sihler's staining technique. Main trunk of the posterior interosseous nerve (arrow) has no branches on the radial side and turns toward the radial side of the capsule.

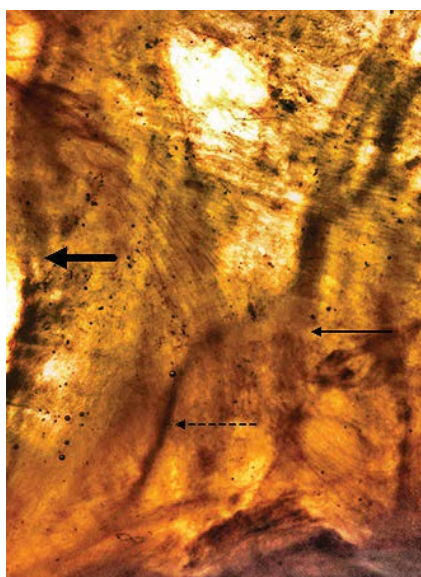


**Figure 2.** Dorsal wrist capsule (right hand) in Sihler's staining technique. Main trunk of the posterior interosseous nerve (thick arrow), main trunk of the medial antebrachial cutaneous nerve (thick arrow). Communicans branch between both nerves (dotted arrow).

number of nerve trunks with 3 or 4 radial branches was identical (43.3%). In all cases, one or two small branches were visible, protruding from the nerve on the ulnar side, which were directed towards the ulnar and distal direction. It was considered that they were branches connecting to the medial antebrachial cutaneous nerve (MACN), because in the 19 capsules wherein the MACN nerve trunks were clearly visible, these branches were communicating with the main trunk of the MACN. The direction of those branches was always the same. Moreover, in all capsules, there were visible branches that crossed the distal cutting line, in an amount of 1–5. If there was one branch (2 cases; 6.7%), it ran centrally or slightly radially. In the case of two branches (8 cases; 26.6%), they constituted the symmetrical endings of the PIN nerve trunk. In the remaining cases, when there were 3, 4, or 5 branches (20 capsules in total; 66.7%), they were branches of the main trunk or its larger branches.

All specimens showed a small nerve mesh that occurred symmetrically in 2 (6.7%) cases. In 16 capsules, a larger number of small nerves were on the radial side of the PIN (78.9%); in the remaining 12 (40%) cases, they were on the ulnar side. In the 19 cases where the MACN was visible, its trunk was slightly smaller than or equal to the PIN. In 2 cases where the PIN had two main trunks, the MACN was larger (Fig. 2). In 4 (21.1%) cases, two MACN trunks were present; in the remaining ones, there was one main trunk (15 cases; 78.9%). No major nerve trunks running on the radial border of the PIN were seen. However, in 15 (78.9%) cases, larger branches crossing the radial cutting line were clearly visible, although they did not show any visible connections with PIN branches. These branches, probably belonging to the superficial branch of the radial nerve (RNSB), were found in numbers of 2 in 8 capsules (53.3%) and 3 in 2 capsules (13.4%). In the remaining 5 (33.3%) cases, there was a single larger branch on the same side. The obtained results are presented in Tables 1–3.

## DISCUSSION

The extent of innervation of the wrist by individual nerves is yet unclear. This is likely because the extent and efficacy of the anatomical examinations keeps changing over time. Initially, the range of innervation of the wrist was based on the preparation of nerves and their branches with 3.5× magnification, which was then replaced by microdissection using a microscope. Histological examinations of the wrist

**Table 1.** Quantitative analysis of the interosseous nerve and its branches based on measurements of 30 joint capsules

Nerve	Amount	Percentage
Posterior interosseous nerve	30	100%
Radial branch	28	93%
0	2	6.70%
1	2	6.70%
2	13	43.30%
3	6	20%
4	7	23.30%
Ulnar branch	30	100%
1	4	13.30%
2	19	63.30%
3	7	23.30%
Terminal branches (crossing distal line incision)	30	100%
1	2	6.70%
2	8	26.60%
3	7	23.30%
4	8	26.70%
5	5	16.70%
Majority of small branches side	Very numerous nerve networks	100%
Equal	2	6.70%
Radial	16	53.30%
Ulnar	12	40%

capsule stained using the S-100 method [20] revealed several conflicting features with what was found in microdissections. This was particularly relevant for the course of the small nerve branches that are invisible during anatomical preparation, the presence of connections between individual nerves, and the places of entry of the nerves into the joint capsule or wrist joints. The exact scope of innervation of the wrist was particularly important in wrist denervation procedures, which are symptomatic treatments for patients experiencing pain originating from a joint. To avoid undesired denervation of other structures, the knowledge of the specific innervation of the joint was essential.

Sihler’s stain is a whole mount nerve staining technique that renders other soft tissues translucent or transparent while staining only the nerves [18]. Wu and Sanders [24, 25] were the first to apply the modified Sihler’s staining technique to investigate the supply patterns of the laryngeal nerves. Liu et al. [16]

**Table 2.** Medial antebrachial cutaneous nerve was present in 19 of 30 wrist capsules. There was constant communicants branch departing from ulnar side of the posterior interosseous nerve running in ulnar and distal direction

Nerve	Amount	Percentage
Medial antebrachial cutaneous nerve	19	63.30%
1	15	78.90%
2	4	21.10%
Ramus communicans	30	100%

**Table 3.** Main trunk of the radial sensory branch was not seen in any specimens. Quantitative analysis of radial branches passing the radial border of the capsule, with no visible connection with branches of posterior interosseous nerve

Nerve	Amount	Percentage
Superficial branch of radial nerve	0	0%
Ramus on the radial border	15	43.30%
1	5	33.30%
2	8	53.30%
3	2	13.40%

were the first to use Sihler’s stain to determine the intramuscular nerve supply of the long head of the triceps muscles in rabbits. Several further studies on the innervation of limb and trunk muscles in humans and monkeys were then carried out in subsequent years [11–14, 23]. Using Sihler’s stained human foetal specimens, Peker et al. [19] investigated the relations between the shape of skeletal muscles and their nerve distribution patterns. To our knowledge, the modified Sihler’s staining technique has never been used to qualitatively assess the course of nerves in the wrist capsule. Our study enabled the visualisation of nerve branches inside the joint capsule that would not be visible during dissection, even at high magnification.

Many studies show that the main innervation of the wrist from the dorsal comes from the PIN [1–3, 6–10, 15, 21]. All the above mentioned studies were based on the preparation of nerve branches or those visible during surgery. In our study, it was possible to determine the range of innervation ratio of the entire joint capsule based on the actual image. Approximately 60% of the central part of the capsule is supplied by the PIN, radial part by the RNSN (approximately 15%) and the MACN innervates approximately 25% of the capsule from the ulnar side. However, the technique we used does not allow us to determine



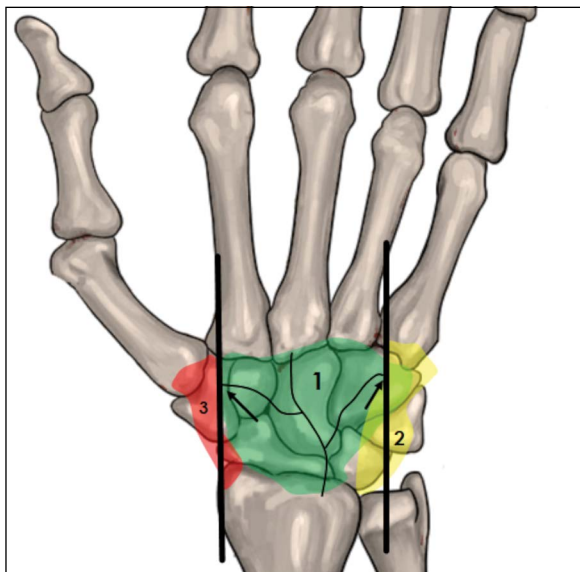


**Figure 3.** Innervation of dorsal aspect of wrist joint. This drawing presents a global overview of innervation and does not show the exact range and possible overlapping. The area of posterior interosseous nerve innervation was determined by two lines running parallel to extend the long axis of the joint capsule, defined by the outer borders of the furthest reaching and visible posterior interosseous nerve branches (arrows); 1 — posterior interosseous nerve innervation area; 2 — dorsal branch of the ulnar nerve innervation area; 3 — superficial branch of radial nerve innervation area.

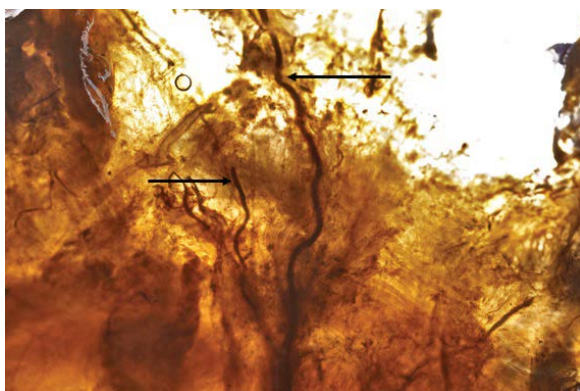


**Figure 4.** Dorsal wrist capsule (left hand) in Sihler's staining technique. Two terminal branches (arrows) of the posterior interosseous nerve crossing the distal border (white area) of the capsule.

where the innervation ranges overlap (Fig. 3). Another important finding of this study is that the terminal branches crossing the distal line incision were found to be fairly consistent; the incision was performed 1 cm distal to the carpometacarpal (CMC) joints II–V (Fig. 4).

Only in 2 of the 30 specimens was single branch noted; in the remaining specimens, the number of branches varied from 2 to 5, on average 3.6 per capsule. In our specimens, these branches were crossing

the cutting line, which did not show the presence of the small end branches. We therefore reached the conclusion that these are not the branches ending in and innervating the CMC joints. Dellon et al. [4, 5] dissected the PIN and its branches in 10 cadavers; they showed that in 2 of the 10 cadavers, the terminal branches of the PIN appeared to extend to the metacarpophalangeal joints, traveling in the deep fascia overlying the interosseous muscles. The methodology of our study did not allow the conclusion that all of these branches innervate the metacarpophalangeal joints, but the number of PIN nerve branches that run through the metacarpals was undoubtedly greater. McCarthy and Breen [17] showed that 14 of 41 (34%) specimens in which the 3.5× magnification of PIN dissection was performed, had innervations of terminal branches that included the CMC joints, the interossei, and the metacarpal periosteum. They also observed three levels of innervation that were present in most specimens: radiocarpal, midcarpal, and terminal branches. However, only fourteen of their specimens had innervations at all three levels. The present study shows that range of PIN innervation reaches beyond the CMC joint's line, which is more distal than the central two-thirds of the posterior wrist joint; this is similar to what was reported by Lin et al. [15].

We realise that there are several limitations to this technique of staining. This method does not enable distinction between sensory and motor neurons, provides less detailed information concerning the relations of the nerve terminal structures, and is time consuming. In addition, differences in staining quality may be seen depending on the thickness and size of the specimen as well as consequent to inaccurate solution changes during the decalcification and clearing steps [18]. However, in our opinion, it can be considered as an interesting supplement to the assessment of the nerves within the wrist capsule along with previously used methods of preparation or histological staining.

## CONCLUSIONS

Modified Sihler's staining allows the clinician to obtain a wider picture of the range of innervation of the wrist joint capsule, much larger than when preparing individual nerves. It provides the opportunity to visualise nerves with much smaller cross sections, smaller than those obtained during microdissection. However, it does not allow assessment as accurate as

that possible with histological examination, especially in evaluation of the nerve endings, but it provides a significantly larger area of nerve observation.

## REFERENCES

1. Apergis E. Wrist anatomy in: Fracture-Dislocations of the Wrist. Springer 2013: 35–37.
2. Braga-Silva J, Román JA, Padoin AV. Wrist denervation for painful conditions of the wrist. *J Hand Surg Am.* 2011; 36(6): 961–966, doi: [10.1016/j.jhsa.2011.03.004](https://doi.org/10.1016/j.jhsa.2011.03.004), indexed in Pubmed: [21549522](https://pubmed.ncbi.nlm.nih.gov/21549522/).
3. Dellon AL. Partial dorsal wrist denervation: resection of the distal posterior interosseous nerve. *J Hand Surg Am.* 1985; 10(4): 527–533, doi: [10.1016/s0363-5023\(85\)80077-0](https://doi.org/10.1016/s0363-5023(85)80077-0), indexed in Pubmed: [4020064](https://pubmed.ncbi.nlm.nih.gov/4020064/).
4. Dellon A, Mackinnon S, Daneshvar A. Terminal branch of anterior interosseous nerve as source of wrist pain. *J Hand Surg.* 1984; 9(3): 316–322, doi: [10.1016/0266-7681\(84\)90051-2](https://doi.org/10.1016/0266-7681(84)90051-2).
5. Dellon A, Seif S. Anatomic dissections relating the posterior interosseous nerve to the carpus, and the etiology of dorsal wrist ganglion pain. *J Hand Surg Am.* 1978; 3(4): 326–332, doi: [10.1016/s0363-5023\(78\)80032-x](https://doi.org/10.1016/s0363-5023(78)80032-x), indexed in Pubmed: [681715](https://pubmed.ncbi.nlm.nih.gov/681715/).
6. Ferreres A, Suso S, Ordi J, et al. Wrist denervation. Anatomical considerations. *J Hand Surg.* 2016; 20(6): 761–768, doi: [10.1016/s0266-7681\(95\)80043-3](https://doi.org/10.1016/s0266-7681(95)80043-3).
7. Grechenig W, Mähring M, Clement HG. Denervation of the radiocarpal joint. *J Bone Joint Surg. British Volume.* 1998; 80-B(3): 504–507, doi: [10.1302/0301-620x.80b3.0800504](https://doi.org/10.1302/0301-620x.80b3.0800504).
8. Hagert E, Forsgren S, Ljung BO. Differences in the presence of mechanoreceptors and nerve structures between wrist ligaments may imply differential roles in wrist stabilization. *J Orthop Res.* 2005; 23(4): 757–763, doi: [10.1016/j.orthres.2005.01.011](https://doi.org/10.1016/j.orthres.2005.01.011), indexed in Pubmed: [16022987](https://pubmed.ncbi.nlm.nih.gov/16022987/).
9. Hagert E, Garcia-Elias M, Forsgren S, et al. Immunohistochemical analysis of wrist ligament innervation in relation to their structural composition. *J Hand Surg Am.* 2007; 32(1): 30–36, doi: [10.1016/j.jhsa.2006.10.005](https://doi.org/10.1016/j.jhsa.2006.10.005), indexed in Pubmed: [17218173](https://pubmed.ncbi.nlm.nih.gov/17218173/).
10. Hixson ML, Stewart C. Microvascular anatomy of the radioscapholunate ligament of the wrist. *J Hand Surg Am.* 1990; 15(2): 279–282, doi: [10.1016/0363-5023\(90\)90108-4](https://doi.org/10.1016/0363-5023(90)90108-4), indexed in Pubmed: [2324457](https://pubmed.ncbi.nlm.nih.gov/2324457/).
11. Hua J, Kumar VP, Pereira BP, et al. Split flexor carpi radialis muscle. *Plast Reconstr Surg.* 1999; 103(3): 930–934, doi: [10.1097/00006534-199903000-00024](https://doi.org/10.1097/00006534-199903000-00024), indexed in Pubmed: [10077083](https://pubmed.ncbi.nlm.nih.gov/10077083/).
12. Kumar VP, Liu J, Lau HK, et al. Neurovascular supply of the gracilis muscle: a study in the monkey and human. *Plast Reconstr Surg.* 1998; 101(7): 1854–1860, doi: [10.1097/00006534-199806000-00012](https://doi.org/10.1097/00006534-199806000-00012), indexed in Pubmed: [9623827](https://pubmed.ncbi.nlm.nih.gov/9623827/).
13. Lim A, Kumar P, Hua J, et al. The Neuromuscular Compartments of the Flexor Carpi Ulnaris. *Plast Reconstr Surg.* 1999; 103(3): 1046–1051, doi: [10.1097/00006534-199903000-00048](https://doi.org/10.1097/00006534-199903000-00048).
14. Lim AYT, Pereira BP, Kumar VP, et al. Intramuscular innervation of upper-limb skeletal muscles. *Muscle Nerve.* 2004; 29(4): 523–530, doi: [10.1002/mus.10565](https://doi.org/10.1002/mus.10565), indexed in Pubmed: [15052617](https://pubmed.ncbi.nlm.nih.gov/15052617/).
15. Lin YT, Berger RA, Berger EJ, et al. Nerve endings of the wrist joint: a preliminary report of the dorsal radiocarpal ligament. *J Orthop Res.* 2006; 24(6): 1225–1230, doi: [10.1002/jor.20166](https://doi.org/10.1002/jor.20166), indexed in Pubmed: [16705705](https://pubmed.ncbi.nlm.nih.gov/16705705/).
16. Liu J, Kumar P, Shen Y, et al. Modified Sihler's technique for studying the distribution of intramuscular nerve branches in mammalian skeletal muscle. *Anat Record.* 1997; 247(1): 137–144, doi: [10.1002/\(sici\)1097-0185\(199701\)247:1<137::aid-ar16>3.0.co;2-q](https://doi.org/10.1002/(sici)1097-0185(199701)247:1<137::aid-ar16>3.0.co;2-q).
17. McCarthy C, Breen T. Arborization of the distal posterior interosseous nerve. *J Hand Surg.* 1995; 20(2): 218–220, doi: [10.1016/s0363-5023\(05\)80010-3](https://doi.org/10.1016/s0363-5023(05)80010-3).
18. Mu L, Sanders I. Sihler's whole mount nerve staining technique: a review. *Biotech Histochem.* 2010; 85(1): 19–42, doi: [10.3109/10520290903048384](https://doi.org/10.3109/10520290903048384), indexed in Pubmed: [19572223](https://pubmed.ncbi.nlm.nih.gov/19572223/).
19. Peker T, Gülekon N, Turgut BH, et al. Observation of the relationship between the shape of skeletal muscles and their nerve distribution patterns: a transparent and microanatomic study. *Plast Reconstr Surg.* 2006; 117(1): 165–176, doi: [10.1097/01.prs.0000186539.80555.27](https://doi.org/10.1097/01.prs.0000186539.80555.27), indexed in Pubmed: [16404263](https://pubmed.ncbi.nlm.nih.gov/16404263/).
20. Rhodes RH. Diagnostic Immunostaining of the Nervous System. In: Bennington JL (Ed.). *Major Problems in Pathology (vol 19): Immunomicroscopy: A Diagnostic Tool for the Surgical Pathologist.* Saunders, Philadelphia 1986: 334–343.
21. Van de Pol GJ, Koudstaal MJ, Schuurman AH, et al. Innervation of the wrist joint and surgical perspectives of denervation. *J Hand Surg Am.* 2006; 31(1): 28–34, doi: [10.1016/j.jhsa.2005.06.021](https://doi.org/10.1016/j.jhsa.2005.06.021), indexed in Pubmed: [16443100](https://pubmed.ncbi.nlm.nih.gov/16443100/).
22. Won SY, Kim DH, Yang HM, et al. Clinical and anatomical approach using Sihler's staining technique (whole mount nerve stain). *Anat Cell Biol.* 2011; 44(1): 1–7, doi: [10.5115/acb.2011.44.1.1](https://doi.org/10.5115/acb.2011.44.1.1), indexed in Pubmed: [21519543](https://pubmed.ncbi.nlm.nih.gov/21519543/).
23. Wong MT, Lim AY, Coninck CD, et al. Functional units within the latissimus dorsi muscle based on Sihler technique. *Ann Plast Surg.* 2007; 59(2): 152–155, doi: [10.1097/01.sap.0000252731.60748.cb](https://doi.org/10.1097/01.sap.0000252731.60748.cb), indexed in Pubmed: [17667408](https://pubmed.ncbi.nlm.nih.gov/17667408/).
24. Wu BL, Sanders I. A technique for demonstrating the nerve supply of whole larynges. *Arch Otolaryngol Head Neck Surg.* 1992; 118(8): 822–827, doi: [10.1001/archotol.1992.01880080044011](https://doi.org/10.1001/archotol.1992.01880080044011), indexed in Pubmed: [1379438](https://pubmed.ncbi.nlm.nih.gov/1379438/).
25. Wu BL, Sanders I, Mu L, et al. The human communicating nerve. An extension of the external superior laryngeal nerve that innervates the vocal cord. *Arch Otolaryngol Head Neck Surg.* 1994; 120(12): 1321–1328, doi: [10.1001/archotol.1994.01880360019004](https://doi.org/10.1001/archotol.1994.01880360019004), indexed in Pubmed: [7980895](https://pubmed.ncbi.nlm.nih.gov/7980895/).

# The variations and degenerative changes of sacroiliac joints in asymptomatic adults

Ö.F. Cihan<sup>1</sup> , M. Karabulut<sup>1</sup>, V. Kiliçoğlu<sup>2</sup>, N. Yavuz<sup>3</sup>

<sup>1</sup>Department of Anatomy, Faculty of Medicine, Gaziantep University, Gaziantep, Turkey

<sup>2</sup>Department of Orthopaedic Surgery, Faculty of Medicine, Gaziantep University, Gaziantep, Turkey

<sup>3</sup>Department of Radiology, Faculty of Medicine, Gaziantep University, Gaziantep, Turkey

[Received: 6 July 2019; Accepted: 25 February 2020]

**Background:** The sacroiliac joint has a structure in which the direction of the load relative to the articular surface is irrational, as the joint surface is not perpendicular to the trunk load axis; it is likely to incur more degenerative changes than other weight-bearing joints.

**Materials and methods:** This retrospective study consisted of a total of 145 cases — 104 (71.7%) men and 41 (28.3%) women — who were referred to Gaziantep University Medical Faculty Radiology Department Polyclinic for pelvic computed tomography (CT) from 2013 to 2018. The mean age was 33.5 years (range: 18–60 years). Pelvis CT images were performed according to the exclusion criteria specified by the experienced orthopaedic surgeon. Patients were excluded from the study if they were younger than the age of 18, had a condition involving the sacroiliac joint, had an endocrine disorder, or had a history of a trauma affecting the pelvis CT examination.

**Results:** In this current study, six types of anatomic variations were detected. Iliosacral complex variation has been determined as the most common type of variation. The incidence of variations of sacroiliac joint in all cases was 28.9%. Degenerative changes were seen in 5.5% of patients fewer than 30 years of age. When it comes to the patients whose age range is 30–60, the percentage of the degenerative changes is 12.4%. In patients who were 30 years and older, the prevalence of degenerative changes increased progressively with increasing age.

**Conclusions:** In this study, it is thought that the knowledge of variations in normal population and degenerative changes will contribute to the better understanding of normal morphological structure of sacroiliac joint and to the anatomical literature. It's seen that there is not a statistically significant relationship between degenerative changes and anatomical variations. (Folia Morphol 2021; 80, 1: 87–96)

**Key words:** sacroiliac joint, degenerative changes, anatomical variants, accessory joint

## INTRODUCTION

The sacroiliac joint (SJ) is the largest joint of the axial skeleton which is involved in a variety of pathological conditions that may affect individuals throughout their lives [23, 24, 36]. The joint has a synovial

portion and large ligamentous areas that are vertically orientated, which allow the entire body weight to be supported with an undulating surface [20, 24, 34]. It has a unique pattern of motion called nutation and counter-nutation. The sacrum essentially flexes and

extends. The normal motion is only  $2.5^\circ$  [16, 20, 29]. The emergence of a pronounced sexual dimorphism in joint structure occurs after puberty. These changes can progress into age-related degenerative processes, more in men than women, involving osteophyte formation and ankylosis [34].

Although some clinicians and researchers acknowledge that there is very limited movement in the SJ, and this movement decreases with aging due to degenerative changes, most physiotherapists, manual therapists and osteopaths have advocated the presence of a significant amount of movement in the SJ [12, 19, 35].

One possible cause of lower back pain is degeneration of the SJ [1, 2, 27, 37]. It has long been known that SJ degeneration is common [3, 6, 25, 26, 35]. The diagnosis of symptomatic SJ degeneration is difficult and based on a combination of patient history, clinical testing, diagnostic joint injections, and radiological examination. Among other radiological techniques, computed tomography (CT) is frequently used, but CT findings of SJ degeneration are also common in a normal population. A clear connection between CT findings and symptoms has not been established [5, 6, 10, 13, 18, 28, 33, 35]. Innovative progress has been made in the diagnosis of the SJ disorders following the use of imaging methods such as magnetic resonance imaging (MRI), and CT in particular [9, 15, 17].

Sacroiliac joints have a lot of structural variations and show some anatomical changes due to the age. Although the normal anatomy of the SJ has been meticulously discussed in the literature, there are only a few reports concerning the anatomical variants [4–6, 22] or the degenerative changes [1, 2, 6, 11, 26] on CT images.

Many studies have investigated accessory sacroiliac joints (ASJ) within the confines of the articulating area of the SJ [5, 8, 9, 14, 22, 30, 32]. Anatomical variants of SJs and the aetiology of the ASJ remain unclear. It is not certain if the ASJ is a congenital condition or if it is an acquired joint [8]. It is frequently found between the medial surface of the posterior superior iliac spine and the lateral crest of sacrum, opposite the second sacral foramen. Less commonly, it is found between the osseous projections at the iliac tuberosity and the lateral crest of sacrum, opposite the first sacral foramen [4, 5, 14, 22, 30, 32]. Comprehensive CT studies allow us to distinguish the normal and the pathologic appearance and they would be very useful

**Table 1.** Number of patients by age and gender

No. of patients	Age [years]				Total
	18–29	30–39	40–49	50–60	
Men	49	19	21	15	104
Women	25	5	4	7	41
Total	74	24	25	22	145

for the diagnosis of SJ diseases. Trotter [30] reported a similar increase associated with age. She concluded that the joints are acquired in most of the cases [30]. Prassopoulos et al. [22] reported that ASJs were more common in obese people over the age of 60 years, indicating that altered load-bearing stress at the SJs could lead secondarily to the formation of ASJs.

We reviewed the literature to determine underlying mechanism, symptomology, associated pathologies, and clinical importance of degenerative changes of the SJ. The purpose of the present study was to quantify degenerative changes and of the anatomical variations of the SJ in of asymptomatic patients evaluated with high-resolution CT scans. We hypothesized that SJ degeneration would be prevalent in asymptomatic individuals and that the prevalence would increase with age. The study was also to determine if there is a relationship between degenerative changes and anatomical variations.

## MATERIALS AND METHODS

This retrospective study consisted of a total of 145 cases — 104 (71.7%) men and 41 (28.3%) women — who were referred to Gaziantep University Medical Faculty Radiology Department Polyclinic for pelvic CT from 2013 to 2018. The mean age was  $33.5 \pm 12.68$  years (range: 18–60 years) (Table 1).

Pelvis CT images were performed according to the exclusion criteria specified by the experienced orthopaedic surgeon. Patients were excluded from the study if they were less than the age of 18, had a condition involving the SJ, had an endocrine disorder, or had a history of a trauma affecting the pelvis.

**CT examination.** The examinations were performed on CT scanner, one 32-slice scanner GE Healthcare Systems (USA) Lightspeed. CT images of all cases were obtained with the patients in the supine position. The images were reconstructed using a bone algorithm in axial and coronal directions with 7 mm thickness and 5 mm increment. After the SJ was scanned using these cross-sectional ranges,

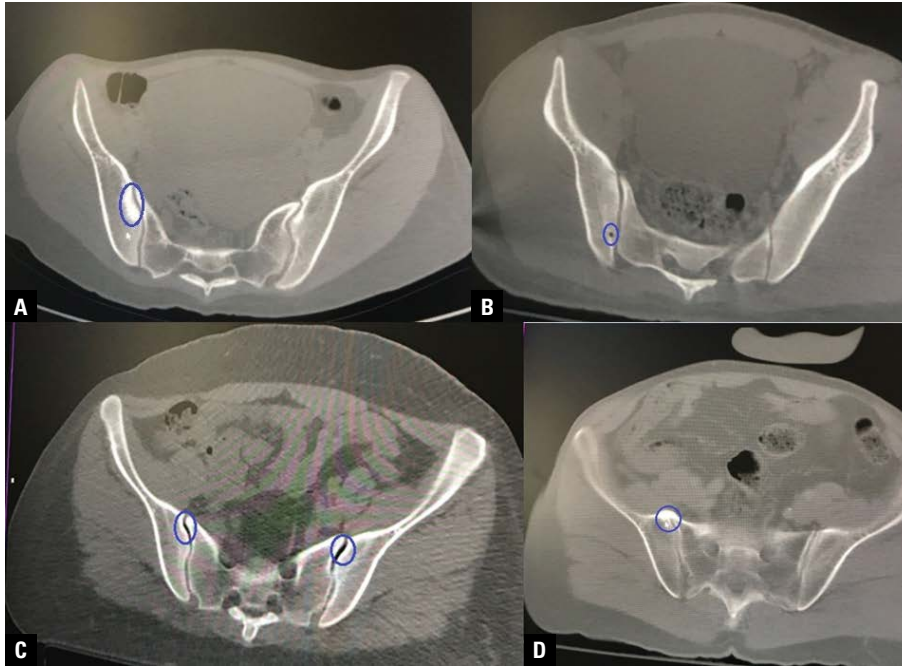


**Figure 1.** Degenerative changes in the periarticular tissues; **A.** Subchondral sclerosis; **B.** Subchondral cyst; **C.** Vacuum phenomenon; **D.** Ankylosis.

the images required for this current study were examined.

All patients were randomized prior to evaluation. Imaging review was performed in consensus by an orthopaedic surgeon, a radiologist and a PhD student (physiotherapist) in medical sciences (17 and 3 years of experience), blinded to clinical and other imaging findings. The patients were separated by gender and in age intervals of 18–29, 30–39, 40–49 and 50–60 years of age (Table 1).

There is the absence of a previously validated CT classification system for SJ degeneration [2, 6]. SJ degeneration was evaluated by adapting the scoring system described by Eno et al. [6]. Grading was performed according to a protocol designed for this purpose; subchondral sclerosis, vacuum phenomenon, subchondral cyst, joint space narrowing and ankylosis (Fig. 1) were assessed for each. Joints were classified as type 0 if there were no degenerative changes, as type 1 if there were degenerative changes, type 1 if anatomic variants are present and type 0 if anatomic variants are absent SJ. Degenerative changes were quantified in the overall patient population and by decade of life. Moreover, we analysed anatomical variants of the SJ, deviations from the usual appearance of the articular facets of the ilium and sacrum (Table 2).

**Table 2.** Grading protocol for sacroiliac joint degeneration and anatomical variants

Degenerative changes and anatomical variants	0	1
Subchondral cyst	None	Exist
Subchondral sclerosis	None	Minor or prominent
Vacuum phenomenon	None	Exist
Ankylosis	None	Exist
Joint space narrowing	Normal	Focal or general irregular
Anatomical variants	None	Exis

In addition, the SJ sections of 145 cases were reconstructed in three-dimensional format using the Horos v.3.0.1 software (<https://horosproject.org/>). The values obtained from the measurement of the SJ space on the narrowest and widest parts of the joint on the S1, S2 and S3 vertebra were averaged in the axial and coronal sections. Joint spacing of less than 2 mm indicated narrowing of the joint space [21].

#### Statistical analysis

The prevalence of degenerative changes was quantified in the overall patient population using Mann-Whitney U-test. Pearson and Spearman correlation analysis was used to determine the relationship between two quantitative variables. One-way

**Table 3.** Variations in appearance of normal sacroiliac joint on computed tomography examinations in relation to age, gender

No. of patients	Women (n = 41)	Men (n = 104)	18–29 (n = 74)		30–39 (n = 24)		40–49 (n = 25)		50–60 (n = 22)		Total (n = 145)
			Women	Men	Women	Men	Women	Men	Women	Men	
Accessory sacroiliac joint	3 (7.2%)	7 (7.8%)	2	1		2		3	1	1	10 (6.8%)
Iliosacral complex	6 (14.5%)	11 (10.7%)	3	4	2	1	1	3		3	17 (11.7%)
Bipartite iliac bony plate	6 (14.5%)	1 (1%)	4		1			1	1		7 (4.8%)
Crescent like iliac bony plate	—	1 (1%)		1							1 (0.6%)
Semicircular defects	1 (2.4%)	5 (4.9%)	1	1		1		2		1	6 (4.1%)
Ossification centres	—	1 (1%)						1			1 (0.6%)

ANOVA was used to compare variables with more than two groups. Student t-test was used to compare the variables which had only two groups. Analyses were made with statistical software SPSS (Windows version 22.0).  $P < 0.05$  was considered statistically significant.

#### Ethics statement

This retrospective study was initiated after approval from the Clinical Trials Ethical Committee of Gaziantep University ethics committee and carried out in accordance with The Code of Ethics of the World Medical Association (Declaration of Helsinki). (Decision no: 2018/197).

## RESULTS

In this study, six different variations were detected in the axial CT sections of the SJ and the distribution of the bilateral and unilateral views of these variations was examined by gender at Table 2. Accordingly, the most frequent variation was determined to be iliosacral complex variation (11 men, 10.7%) in men axial CT sections of the SJ. In addition, variations called accessory SJ (7 men, 7.8%), semicircular defects in iliac and sacral wings (5 men, 4.9%), bipartite iliac bony plate (1 man, 1%), crescent like iliac bony plate (1 man, 1%), and an ossification centres (1 man, 1%) were observed (Table 3).

In females, the most frequent variations were in the iliosacral complex (6 women, 14.5%), and the bipartite iliac bony plate (6 women, 14.5%). These variations were followed by accessory joints (3 women, 7.2%), and semicircular defects in the iliac and sacral wings (1 woman, 2.4%), respectively. Crescent like iliac bony plate or ossification centres variation was not detected in women (Table 3).

While the incidence of variation of SJ in all cases in this study was 28.9%, the incidence of ASJ was 6.8%. The incidence of accessory SJ was detected to be 7.8% in men and 7.2% in women. The ASJ



**Figure 2.** Image of right accessory sacroiliac joints at the S2 vertebra level on the axial computed tomography section in a 56-year-old man patient. A protrusion, extending from the iliac surface towards the sacral surface is observed.



**Figure 3.** Axial computed tomography section image of the bilateral iliosacral complex at the S2 vertebra level in a 60-year-old man patient. A protrusion and matching cavity is observed on the iliac surface.

was observed to be unilateral in 9 (12.6%) cases and bilateral in 1 (2.4%) case. This variation was determined to form a process from the iliac surface towards the sacral surface in the posterior aspect of the SJ (Fig. 2).

In addition, a total of 17 (11.7%) patients, 11 (10.7%) men and 6 (14.5%) women, were detected to have iliosacral complex variation. The iliosacral complex was unilateral in 12 (17.5%) patients and bilateral in 5 (7.7%) patients. In conclusion, it was detected to be in the form of a tubercle in the facies auricularis of the ilium and a cavity formation in the facies auricularis of the sacrum (Fig. 3).

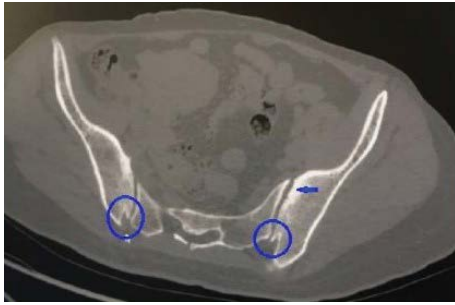


**Figure 4.** Axial computed tomography section image of the bilateral bipartite iliac bony plate variation (circled) at the S3 vertebral level in a 33-year-old woman patient. The blue arrow indicates subchondral sclerosis at the S1 vertebral level.

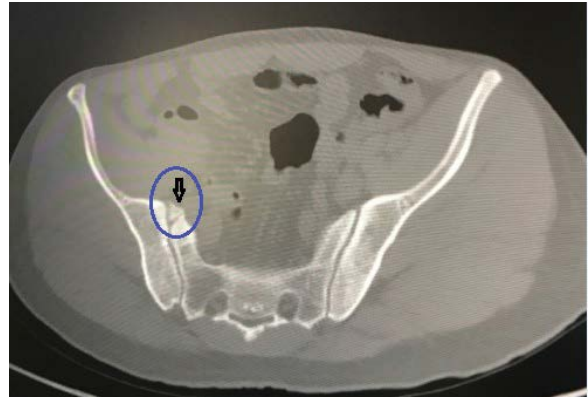


**Figure 7.** Axial computed tomography section image of the unilateral ossification centre at the S2 vertebral level in the anterior section of the joint space in a 44-year-old man patient.



**Figure 5.** Unilateral axial computed tomography section image of the crescent like iliac bony plate variation at the S2 vertebral level in a 26-year-old man patient.



**Figure 6.** Axial computed tomography section image of the semicircular defects variation at the S1 vertebral level in the sacral bony in a 40-year-old man patient.

In addition, the bipartite iliac bony plate variation was determined in a total of 7 (4.8%) patients, 1 (1%) man and 6 (14.5%) women. The bipartite iliac bony plate was observed to be unilateral in 4 (10.7%) patients and bilateral in 3 (4.8%) patients. As a result of this observation, the variation is characterized by a two-part shape, unlike the normal appearance of the ilium, as well as being mostly detected at the

S2 and S3 vertebral levels in the posterior aspect of the joint (Fig. 4).

In addition, while the crescent like iliac bony plate variation was observed in 1 (1%) man unilaterally, no such variation was observed in women. This formation is characterised by the lunette appearance of the ilium's facies auricularis and the convexity of the sacral surface corresponding to this part. The variation is localised at the S1 vertebral level in the posterior aspect of the joint (Fig. 5).

The variation called semicircular defects was seen in a total of 6 (4.1%) people, 5 (4.9%) men and 1 (2.4%) woman, in the iliac and sacral wings. This variation was observed at the S1 vertebral level in the posterior aspect of the joint, unilaterally in 2 (3%), and bilaterally in 3 (4.3%) patients (Fig. 6).

An ossification centre variation was observed unilaterally in 1 (1%) man. The variation was found to be localised in the anterior aspect of the joint at the S2 vertebral level (Fig. 7).

In our study, total degenerative changes in the SJ were found to be 26 (17.9%) case. The degenerative changes in the present study were also observed in the anterior aspect of the joint and mostly localised in ilium. When degenerative changes in periarticular tissues of SJ were examined; subchondral sclerosis (4.1%), ankylosis (0.7%), vacuum phenomenon (6.8%), subchondral cyst (4.1%) and joint space narrowing (2.1%) were observed (Fig. 1, Table 4).

Degenerative changes were also related to age. Degenerative changes were seen in 5.5% of patients under 30 years of age. When it comes to the patients whose age range is 30–60, the percentage of the degenerative changes is 12.4%. In patients who were

**Table 4.** Degenerative changes according to age and gender

No. of patients	18–29 (n = 74)		30–39 (n = 24)		40–49 (n = 25)		50–60 (n = 22)		Total (n = 145)
	Women	Men	Women	Men	Women	Men	Women	Men	
Subchondral cyst		4		1				1	6 (4.1%)
Subchondral sclerosis		2				2	1	1	6 (4.1%)
Vacuum phenomenon	1	1	1			2	3	2	10 (6.8%)
Ankylosis						1			1 (0.7%)
Joint space narrowing				1				2	3 (2.1%)
Total	8 (5.51%)		3 (2.07%)		5 (3.44%)		10 (6.89%)		26 (17.91%)

**Table 5.** Evaluation of joint space by genders in coronal and axial computed tomography sections (mm)

Sacral vertebra level of joint space	Coronal			Axial		
	Men (n = 104)	Women (n = 41)	P	Men (n = 104)	Women (n = 41)	P
Right S1 vertebra level	2.24 ± 0.81	2.18 ± 1.06	0.190	2.16 ± 0.58	2.02 ± 0.57	0.147
Right S2 vertebra level	2.08 ± 0.7	2.1 ± 1	0.887	2.2 ± 0.69	2.2 ± 1.05	0.317
Right S3 vertebra level	2.06 ± 0.64	1.92 ± 0.74	0.657	2.4 ± 0.89	2.46 ± 1.23	0.807
Left S1 vertebra level	2.33 ± 0.8	2.18 ± 0.74	0.292	2.14 ± 0.69	2.1 ± 0.71	0.724
Left S2 vertebra level	2.1 ± 0.77	2.01 ± 0.68	0.772	2.3 ± 0.77	2.28 ± 0.94	0.521
Left S3 vertebra level	2.14 ± 0.68	2.03 ± 0.76	0.261	2.54 ± 0.98	2.47 ± 1.11	0.634

30 years and older, the prevalence of degenerative changes increased progressively with increasing age. Significant differences were found when degenerative changes were evaluated according to age in Table 4. A logistic regression model calculating the increased probability of the presence of SJ degeneration revealed a progressive increase of 2.78 (95% confidence interval: 1.06–7.25) per year of life in the odds of having SJ degeneration. Separate logistic regression model SJ degeneration estimated a 2.78 increase per year of life, peaking at 6.6 in the fifth decade of life.

According to the correlations analysis results, it's seen that there is not a statistically significant relationship between degenerative changes and anatomical variations ( $p = 0.137$ ).

Besides, in this present study, the joint spaces of a total of 145 patients including men and women were measured in the axial and coronal CT sections at the S1, S2 and S3 vertebra levels. According to the measurement, the mean value of the joint space was found to be over 2 mm in both genders and no significant difference was found between the genders (Table 5).

In addition, the mean values of the joint spaces at the S1, S2 and S3 vertebra levels on both sides were found to be over 2 mm in 108 cases with no variation. However, as a result of the measurement

in the axial and coronal CT sections, it was observed that the mean values of the joint space in the joints with variation were less than 2 mm at the S1, S2 and S3 vertebra levels. For all measurements, the values in the joints with variation showed a significant decrease compared to the invisible variation (Table 6).

## DISCUSSION

Researchers stated that the synovial part of the SJ had a relatively vertical orientation in CT sections, and the ligamentous part of the joint showed a more oblique orientation [18, 28]. Prassopoulos et al. [22] observed that each SJ has its own subtle characteristics, and no patient in their series exhibited exactly the same SJ appearance as another. Slight differences in orientation and shape of the SJ existed between individuals. The SJ has a structure in which the direction of the load relative to the articular surface is irrational; as the joint surface is not perpendicular to the trunk load axis, it is likely to incur more degenerative changes than other weight-bearing joints [28]. In the present study, although the SJ has a general morphology, each joint was detected to have a unique appearance. Differences in appearance were accentuated by the various degrees and types of degenerative alterations that did not affect in a similar way asymptomatic



**Table 6.** Evaluation of joint space measurements of joints with and without variation in the axial and axial computed tomography sections (mm)

Sacral vertebra level of joint space	Without variation (n = 108)		With variation (n = 37)		P
	Axial	Coronal	Axial	Coronal	
Right S1 vertebra level	2.35 ± 0.39	2.52 ± 0.78	1.47 ± 0.56	1.29 ± 0.42	0.001
Right S2 vertebra level	2.5 ± 0.59	2.41 ± 0.55	1.35 ± 0.72	1.04 ± 0.47	0.001
Right S3 vertebra level	2.68 ± 0.62	2.32 ± 0.41	1.64 ± 1.41	1.08 ± 0.43	0.001
Left S1 vertebra level	2.38 ± 0.45	2.6 ± 0.57	1.4 ± 0.76	1.29 ± 0.48	0.001
Left S2 vertebra level	2.53 ± 0.49	2.39 ± 0.53	1.59 ± 1.14	1.11 ± 0.42	0.001
Left S3 vertebra level	2.78 ± 0.68	2.41 ± 0.46	1.74 ± 1.39	1.18 ± 0.48	0.001

adults of the same age and gender, and even the two SJs of the same individual. Although the normal anatomy of the SJ has been meticulously discussed in the literature, there are only a few studies concerning the anatomical variants [4, 5, 22] and degenerative changes [1, 2, 6, 7, 28, 38] of the SJ.

The ASJ is the most frequent anatomical variant of the SJ [8, 30]. A frequency of 3.6–50% of ASJ has been described through different studies, including CT scans evaluations [4, 5, 8, 22, 30–32]. Ehara et al. [5] identified the ASJ on 13 (13%) of 100 CT scans of the pelvis and in 9 (16%) of 56 dried skeletons. Prassopoulos et al. [22] in a study that examined the type and prevalence of anatomical variants of the SJ in patients without SJ disease on CT exam identified an ASJ in 19.1% of the 534 CT scans studied. Demir et al. [4], in their study including 400 patients, observed that ASJ was seen between the iliac and sacral articular surfaces in the posterior aspect of the SJ. They detected ASJ in 15.8% of women and in 19.1% of men. They reported the incidence of ASJ as 17.5% in all cases [4]. Valojerdy et al. [32] studied dried bone specimens and identified the ASJ in 18% of their 153 specimens. Although the numbers of Whites and Blacks in the age wise samples in Trotter's study [30] were markedly different, she reported occurrences of ASJs in the two races at 40% and 21%, respectively. In another study of Trotter [31] 50.5% of 485 white people's skeletons and 20.7% of 473 black people's skeletons showed one or more accessory sacroiliac articular facets. Several studies have contributed to our understanding of the prevalence of ASJs. Fortin et al. [8] reported a 3.6% incidence of ASJ from post SJ arthrography CT scans of 559 chronic SJ pain patients. The authors point out that there could be two important reasons why this study detected far fewer ASJs than previously reported studies involving samples of

SJ chronic pain patients. According to Fortin et al. [8], previous authors could have reported "interlocking articulations" present within the SJ as ASJs. Also point out that a focal area of degenerating ankylosis within the main SJ could have been misinterpreted as congenital ASJs in those populations. Although the ASJ is not a rare variant, it might not be very common since normal joint structure or degenerative changes in the SJ could masquerade as accessory joints [8]. In the present study, the incidence of ASJ was detected as 7.8% in men and 7.2% in women. While the incidence of SJ variants in all cases in the study was 28.9%, the incidence of ASJ was 6.8%. The contrasting findings between the current and previous reports may be attributed to a difference in patient population base because the subjects of our studies were asymptomatic adults and cases' mean age of the subjects in this study (33.5 years) is lower. Walker [36] had reported that there are evident discrepancies in the ASJ prevalence rates reported from different studies, possibly because of different imaging protocols or over- or underdetection of conditions due to overlapping normal joint structure or degenerative changes masquerading as accessory joints.

Prassopoulos et al. [22] detected iliosacral complex in a total of 31 (5.8%) cases in their study. Demir et al. [4] reported that they detected iliosacral complex in a total of 38 (9.5%) cases in their study. Prassopoulos et al. [22] reported in their study that iliosacral complex is more common in women. In this study, however, iliosacral complex was found in 17 (11.7%) cases and this variation was observed in men more frequently — 11 (10.7%) men.

Demir et al. [4] reported in their study that the bipartite iliac bony plate was not observed bilaterally and it was localized in the posterior aspect of the joint in 22 (5.5%) cases, and they observed that it was

more common in men. Prassopoulos et al. [22] found in their study that the bipartite iliac bony plate was localised in the posterior aspect of the joint in a total of 22 (4.1%) cases, unilaterally in 6 (1.1%) cases, and bilaterally in 16 (3.0%) cases. Prassopoulos et al. [22] reported that the bipartite iliac bony plate is more common in women. In the present study, the bipartite iliac bony plate was observed in the posterior aspect of the joint in a total of 7 (4.8%) cases, unilaterally in 4 (10.7%) cases and bilaterally in 3 (4.8%) cases. In addition, the bipartite iliac bony plate was seen more commonly in women, with 6 (14.5%) female patients compared to 1 (1%) male patient, which supports the study of Prassopoulos et al. [22].

Prossopoulos et al. [22] found crescent-like iliac bony plate variation in 20 (3.7%) cases. Demir et al. [4] found crescent-like iliac bony plate in 14 (3.5%) cases in their study. In this current study, unilateral crescent like iliac bony plate variation was observed in 1 (1%) men patient while it was not observed in women patients.

Prossopoulos et al. [22] reported in their study that they detected semicircular defect in the sacral and iliac bones in a total of 16 (3%) cases. Demir et al. [4] reported in their study that they detected semicircular defect in the sacral and iliac bones in a total of 19 (4.8%) cases. In this present study, the semicircular defect in sacral and iliac bones was observed in a total of 6 (4.1%) cases.

Prossopoulos et al. [22] reported that the ossification centres in the sacral wings in a total of 3 (0.6%) cases, 2 (0.9%) men and 1 (0.3%) woman. Demir et al. [4] reported in their study that they observed ossification centres in the sacral wings in a total of 4 (1.0%) cases, 1 (0.5%) man and 3 (1.5%) women. In this present study, while no ossification centres in the sacral wings was observed in women, it was detected a total of 1 (0.6%) case.

In concordance with other reports, SJ degeneration is common in non-symptomatic adults in the early decades of life and increases with age [2, 6, 28, 35]. Past studies have shown that degeneration of the SJ is more prevalent in the elderly population, but these changes tend to plateau in the higher age groups [1, 2, 6, 28, 38]. Given the high prevalence of pain-free SJ degeneration, physicians must be cautious in attributing low back pain to degenerative changes of the SJ seen on cross-sectional imaging [2, 6]. For this study a system was designed including established characteristics of subchondral sclerosis, vacuum phe-

nomenon, subchondral cyst, joint space narrowing and ankylosis. There are a number of limitations of this study. One of these limitations is related to age; in our study, the patient population was composed of asymptomatic adults aged 18–60 years. Eno et al. [6] examined SJs in patients aged 0 to 99 years, Bäcklund et al. [2] 20–70+ years of age, Asada et al. [1] 50–70+ years of age, Shibata et al. [28] 20–70+ years of age, Yagan et al. [38] 55 years and over, and Faglia et al. [7] aged 15 to 83 years. Further studies [2, 6, 7] were found that degenerative changes increased with age in asymptomatic patient groups similar to age group of this research. However, previous studies [1, 2, 6, 7, 28, 38] showed that the prevalence of degenerative changes in non-asymptomatic and 60+ age group was very high compared to our study.

Postacchini et al. [21] measured the SJ space in the axial and coronal CT sections on both sides, at the S1, S2 and S3 vertebral levels in their study. As a result of their measurements, they defined a joint space under 2 mm as narrowing of the joint space. In their study, Demir et al. [4] reported that the SJ space was less than 2 mm in the joints with variation. Ehara et al. [5] and Hadley [14] reported in their studies that narrowing of the joint space was observed in the joints with variation. However, the researchers did not provide a numeric value on the subjects. In this present study, the SJ space was measured in the axial and coronal CT sections on the right and left sides, at the S1, S2 and S3 vertebral levels. According to the measurements, while the joint space was over 2 mm in the people without variation in their joints, it was detected to be over 2 mm in the joints with variation. This study supports the studies related to the measurement of joint space of SJ.

## CONCLUSIONS

This study was carried out to contribute to the knowledge of anatomical variations in the normal population, to understand the normal morphological structure of SJ, and to the anatomical literature and radiologists to evaluate and interpret CT images. The prevalence of SJ degeneration in asymptomatic adults is high and increases significantly with age. It's seen that there is not a statistically significant relationship between degenerative changes and anatomical variants.

## REFERENCES

1. Asada M, Tokunaga D, Arai Y, et al. Degeneration of the sacroiliac joint in hip osteoarthritis patients: a three-dimensional image analysis. *J Belg Soc Radiol.* 2019;

- 103(1): 36, doi: [10.5334/jbsr.1648](https://doi.org/10.5334/jbsr.1648), indexed in Pubmed: [31149653](https://pubmed.ncbi.nlm.nih.gov/31149653/).
2. Bäcklund J, Clewett Dahl E, Skorpil M. Is CT indicated in diagnosing sacroiliac joint degeneration? *Clin Radiol*. 2017; 72(8): 693.e9–693.e13, doi: [10.1016/j.crad.2017.03.006](https://doi.org/10.1016/j.crad.2017.03.006), indexed in Pubmed: [28388969](https://pubmed.ncbi.nlm.nih.gov/28388969/).
  3. Cohen AS, McNeill JM, Calkins E, et al. The “normal” sacroiliac joint. Analysis of 88 sacroiliac roentgenograms. *Am J Roentgenol Radium Ther Nucl Med*. 1967; 100(3): 559–563, indexed in Pubmed: [6028970](https://pubmed.ncbi.nlm.nih.gov/6028970/).
  4. Demir M, Mavi A, Gümüşburun E, et al. Anatomical variations with joint space measurements on CT. *Kobe J Med Sci*. 2007; 53(5): 209–217, indexed in Pubmed: [18204297](https://pubmed.ncbi.nlm.nih.gov/18204297/).
  5. Ehara S, el-Khoury GY, Bergman RA. The accessory sacroiliac joint: a common anatomic variant. *Am J Roentgenol*. 1988; 150(4): 857–859, doi: [10.2214/ajr.150.4.857](https://doi.org/10.2214/ajr.150.4.857), indexed in Pubmed: [3258099](https://pubmed.ncbi.nlm.nih.gov/3258099/).
  6. Eno JJT, Boone CR, Bellino MJ, et al. The prevalence of sacroiliac joint degeneration in asymptomatic adults. *J Bone Joint Surg Am*. 2015; 97(11): 932–936, doi: [10.2106/JBJS.N.01101](https://doi.org/10.2106/JBJS.N.01101), indexed in Pubmed: [26041855](https://pubmed.ncbi.nlm.nih.gov/26041855/).
  7. Faflija CP, Prassopoulos PK, Daskalogiannaki ME, et al. Variation in the appearance of the normal sacroiliac joint on pelvic CT. *Clin Radiol*. 1998; 53(10): 742–746, doi: [10.1016/s0009-9260\(98\)80316-4](https://doi.org/10.1016/s0009-9260(98)80316-4), indexed in Pubmed: [9817091](https://pubmed.ncbi.nlm.nih.gov/9817091/).
  8. Fortin JD, Ballard KE. The frequency of accessory sacroiliac joints. *Clin Anat*. 2009; 22(8): 876–877, doi: [10.1002/ca.20772](https://doi.org/10.1002/ca.20772), indexed in Pubmed: [19173249](https://pubmed.ncbi.nlm.nih.gov/19173249/).
  9. Friedman L, Silberberg PJ, Rainbow A, et al. A limited, low-dose computed tomography protocol to examine the sacroiliac joints. *Can Assoc Radiol J*. 1993; 44(4): 267–272, indexed in Pubmed: [8348354](https://pubmed.ncbi.nlm.nih.gov/8348354/).
  10. Gilula LA, Murphy WA, Taylor CC, et al. Computed tomography of the osseous pelvis. *Radiology*. 1979; 132(1): 107–114, doi: [10.1148/132.1.107](https://doi.org/10.1148/132.1.107), indexed in Pubmed: [451181](https://pubmed.ncbi.nlm.nih.gov/451181/).
  11. Gohil I, Vilensky JA, Weber EC. Vacuum phenomenon: Clinical relevance. *Clin Anat*. 2014; 27(3): 455–462, doi: [10.1002/ca.22334](https://doi.org/10.1002/ca.22334), indexed in Pubmed: [24288359](https://pubmed.ncbi.nlm.nih.gov/24288359/).
  12. Grieve EF. Mechanical dysfunction of the sacro-iliac joint. *Int Rehabil Med*. 1983; 5(1): 46–52, doi: [10.3109/096388288309166940](https://doi.org/10.3109/096388288309166940), indexed in Pubmed: [6885271](https://pubmed.ncbi.nlm.nih.gov/6885271/).
  13. Ha KY, Lee JS, Kim KW, et al. Degeneration of sacroiliac joint after instrumented lumbar or lumbosacral fusion: a prospective cohort study over five-year follow-up. *Spine (Phila Pa 1976)*. 2008; 33(11): 1192–1198, doi: [10.1097/BRS.0b013e318170fd35](https://doi.org/10.1097/BRS.0b013e318170fd35), indexed in Pubmed: [18469692](https://pubmed.ncbi.nlm.nih.gov/18469692/).
  14. Hadley LA. Accessory sacroiliac articulations with arthritic changes. *Radiology*. 1950; 55(3): 403–409, doi: [10.1148/55.3.403](https://doi.org/10.1148/55.3.403), indexed in Pubmed: [14781347](https://pubmed.ncbi.nlm.nih.gov/14781347/).
  15. Kanberoglu K, Mihmanli I, Kurugoglu S, et al. Bone marrow changes adjacent to the sacroiliac joints after pelvic radiotherapy mimicking metastases on MRI. *Eur Radiol*. 2001; 11(9): 1748–1752, doi: [10.1007/s003300100819](https://doi.org/10.1007/s003300100819), indexed in Pubmed: [11511897](https://pubmed.ncbi.nlm.nih.gov/11511897/).
  16. Kibsgård TJ, Røise O, Stuesson B, et al. Radiostereometric analysis of movement in the sacroiliac joint during a single-leg stance in patients with long-lasting pelvic girdle pain. *Clin Biomech (Bristol, Avon)*. 2014; 29(4): 406–411, doi: [10.1016/j.clinbiomech.2014.02.002](https://doi.org/10.1016/j.clinbiomech.2014.02.002), indexed in Pubmed: [24602677](https://pubmed.ncbi.nlm.nih.gov/24602677/).
  17. Kozin F, Carrera GF, Ryan LM, et al. Computed tomography in the diagnosis of sacroiliitis. *Arthritis Rheum*. 1981; 24(12): 1479–1485, doi: [10.1002/art.1780241205](https://doi.org/10.1002/art.1780241205), indexed in Pubmed: [6976786](https://pubmed.ncbi.nlm.nih.gov/6976786/).
  18. Lawson TL, Foley WD, Carrera GF, et al. The sacroiliac joints: anatomic, plain roentgenographic, and computed tomographic analysis. *J Comput Assist Tomogr*. 1982; 6(2): 307–314, indexed in Pubmed: [6210717](https://pubmed.ncbi.nlm.nih.gov/6210717/).
  19. Lee D. *The Pelvic Girdle*. Churchill Livingstone. Longman Group, New York 1989.
  20. Polly DW. The Sacroiliac Joint. *Neurosurg Clin N Am*. 2017; 28(3): 301–312, doi: [10.1016/j.nec.2017.03.003](https://doi.org/10.1016/j.nec.2017.03.003), indexed in Pubmed: [28600004](https://pubmed.ncbi.nlm.nih.gov/28600004/).
  21. Postacchini R, Trasimeni G, Ripani F, et al. Morphometric anatomical and CT study of the human adult sacroiliac region. *Surg Radiol Anat*. 2017; 39(1): 85–94, doi: [10.1007/s00276-016-1703-0](https://doi.org/10.1007/s00276-016-1703-0), indexed in Pubmed: [27324173](https://pubmed.ncbi.nlm.nih.gov/27324173/).
  22. Prassopoulos PK, Faflija CP, Voloudaki AE, et al. Sacroiliac joints: anatomical variants on CT. *J Comput Assist Tomogr*. 1999; 23(2): 323–327, doi: [10.1097/00004728-199903000-00029](https://doi.org/10.1097/00004728-199903000-00029), indexed in Pubmed: [10096348](https://pubmed.ncbi.nlm.nih.gov/10096348/).
  23. Rana SH, Farjoodi P, Haloman S, et al. Anatomic evaluation of the sacroiliac joint: a radiographic study with implications for procedures. *Pain Physician*. 2015; 18(6): 583–592, indexed in Pubmed: [26606010](https://pubmed.ncbi.nlm.nih.gov/26606010/).
  24. Rebello da Veiga T, Custódio da Silva A, Gomes da Silva RT, et al. Intra-observer reliability in three-dimensional kinematic analysis of sacroiliac joint mobility. *J Phys Ther Sci*. 2015; 27(4): 1001–1004, doi: [10.1589/jpts.27.1001](https://doi.org/10.1589/jpts.27.1001), indexed in Pubmed: [25995542](https://pubmed.ncbi.nlm.nih.gov/25995542/).
  25. Resnick D, Niwayama G, Goergen TG. Comparison of radiographic abnormalities of the sacroiliac joint in degenerative disease and ankylosing spondylitis. *Am J Roentgenol*. 1977; 128(2): 189–196, doi: [10.2214/ajr.128.2.189](https://doi.org/10.2214/ajr.128.2.189), indexed in Pubmed: [401599](https://pubmed.ncbi.nlm.nih.gov/401599/).
  26. Resnick D, Niwayama G, Goergen TG, et al. Degenerative disease of the sacroiliac joint. *Invest Radiol*. 1975; 10(6): 608–621, doi: [10.1097/00004424-197511000-00008](https://doi.org/10.1097/00004424-197511000-00008), indexed in Pubmed: [1201940](https://pubmed.ncbi.nlm.nih.gov/1201940/).
  27. Shaffrey CI, Smith JS. Stabilization of the sacroiliac joint. *Neurosurg Focus*. 2013; 35(2 Suppl): Editorial, doi: [10.3171/2013.V2.FOCUS13273](https://doi.org/10.3171/2013.V2.FOCUS13273), indexed in Pubmed: [23829837](https://pubmed.ncbi.nlm.nih.gov/23829837/).
  28. Shibata Y, Shirai Y, Miyamoto M. The aging process in the sacroiliac joint: helical computed tomography analysis. *J Orthop Sci*. 2002; 7(1): 12–18, doi: [10.1007/s776-002-8407-1](https://doi.org/10.1007/s776-002-8407-1), indexed in Pubmed: [11819126](https://pubmed.ncbi.nlm.nih.gov/11819126/).
  29. Stuesson B, Uden A, Vleeming A. A radiostereometric analysis of movements of the sacroiliac joints during the standing hip flexion test. *Spine (Phila Pa 1976)*. 2000; 25(3): 364–368, doi: [10.1097/00007632-200002010-00018](https://doi.org/10.1097/00007632-200002010-00018), indexed in Pubmed: [10703111](https://pubmed.ncbi.nlm.nih.gov/10703111/).
  30. Trotter M. Accessory sacroiliac articulations in east african skeletons. *Am J Phys Anthropol*. 1964; 22(2): 137–141, doi: [10.1002/ajpa.1330220213](https://doi.org/10.1002/ajpa.1330220213), indexed in Pubmed: [14243699](https://pubmed.ncbi.nlm.nih.gov/14243699/).
  31. Trotter M. Accessory sacro-iliac articulations. *Am J Phys Anthropol*. 1937; 22(2): 247–261, doi: [10.1002/ajpa.1330220205](https://doi.org/10.1002/ajpa.1330220205).

32. Valojerdy MR, Hogg DA. Anatomical note: The occurrence of accessory sacroiliac joints in man. *Clin Anat.* 1990; 3(4): 257–260, doi: [10.1002/ca.980030403](https://doi.org/10.1002/ca.980030403).
33. van der Linden S, Valkenburg HA, Cats A. Evaluation of diagnostic criteria for ankylosing spondylitis. A proposal for modification of the New York criteria. *Arthritis Rheum.* 1984; 27(4): 361–368, doi: [10.1002/art.1780270401](https://doi.org/10.1002/art.1780270401), indexed in Pubmed: [6231933](https://pubmed.ncbi.nlm.nih.gov/6231933/).
34. Vleeming A, Van Wingerden JP, Dijkstra PF, et al. Mobility in the sacroiliac joints in the elderly: a kinematic and radiological study. *Clin Biomech (Bristol, Avon).* 1992; 7(3): 170–176, doi: [10.1016/0268-0033\(92\)90032-Y](https://doi.org/10.1016/0268-0033(92)90032-Y), indexed in Pubmed: [23915725](https://pubmed.ncbi.nlm.nih.gov/23915725/).
35. Vogler JB, Brown WH, Helms CA, et al. The normal sacroiliac joint: a CT study of asymptomatic patients. *Radiology.* 1984; 151(2): 433–437, doi: [10.1148/radiology.151.2.6709915](https://doi.org/10.1148/radiology.151.2.6709915), indexed in Pubmed: [6709915](https://pubmed.ncbi.nlm.nih.gov/6709915/).
36. Walker JM. The sacroiliac joint: a critical review. *Phys Ther.* 1992; 72(12): 903–916, doi: [10.1093/ptj/72.12.903](https://doi.org/10.1093/ptj/72.12.903), indexed in Pubmed: [1454866](https://pubmed.ncbi.nlm.nih.gov/1454866/).
37. Whang P, Cher D, Polly D, et al. Sacroiliac joint fusion using triangular titanium implants vs. Non-Surgical management: six-month outcomes from a prospective randomized controlled trial. *Int J Spine Surg.* 2015; 9: 6, doi: [10.14444/2006](https://doi.org/10.14444/2006), indexed in Pubmed: [25785242](https://pubmed.ncbi.nlm.nih.gov/25785242/).
38. Yagan R, Khan MA, Marmolya G. Role of abdominal CT, when available in patients' records, in the evaluation of degenerative changes of the sacroiliac joints. *Spine (Phila Pa 1976).* 1987; 12(10): 1046–1051, doi: [10.1097/00007632-198712000-00017](https://doi.org/10.1097/00007632-198712000-00017), indexed in Pubmed: [3502035](https://pubmed.ncbi.nlm.nih.gov/3502035/).

# Variations in the morphology of stylomastoid foramen: a possible solution to the conundrum of unexplained cases of Bell's palsy

S.K. Ghosh , R.K. Narayan

Department of Anatomy, All India Institute of Medical Sciences, Phulwarisharif, Patna, Bihar, India

[Received: 12 January 2020; Accepted: 2 February 2020]

**Background:** Stylomastoid foramen is the terminal part of facial canal and is the exit gateway for facial nerve from skull base. We hypothesized that anatomical variations of this foramen could be a risk factor for the injury of facial nerve resulting in unilateral facial nerve paralysis or Bell's palsy. Hence the present study was conducted to study the variations in size and shape of stylomastoid foramen in dry adult human skulls.

**Materials and methods:** The study was conducted on 37 dry adult human skulls of unknown age and sex. High resolution images of the skulls under study were processed by ImageJ software and observations were undertaken.

**Results:** Total eight variations of stylomastoid foramen were observed in terms of shape. The common variants were round, oval and square (present in 83.79% skulls on right side and 81.07% skulls on left side), whereas the rare variants were triangular, rectangular, serrated, bean-shaped and irregular. It was noted that stylomastoid foramen were associated with extensions (45.95% skulls) and also adjacent foramen (18.92% skulls). Exclusively unilateral observations included bifurcation of foramen (16.22% skulls), foramen situated deep inside skull groove (5.41% skulls) and foramen interrupted by bony spur (2.7% skulls). No significant differences were observed between the mean diameters (antero-posterior and transverse) of the stylomastoid foramen.

**Conclusions:** The unilateral variations along with rare variations in terms of shape such as serrated, bean-shaped and irregular foramen (which were also unilateral findings) could be potential risk factors towards injury of facial nerve at the point of exit from skull base leading to Bell's palsy. (Folia Morphol 2021; 80, 1: 97–105)

**Key words:** stylomastoid foramen, variations, risk factor, injury, facial nerve, Bell's palsy

## INTRODUCTION

The facial nerve or the VII<sup>th</sup> cranial nerve leaves the cranial cavity by travelling through a Z-shaped bony canal known as the facial or Fallopiian canal. The facial nerve lies in the tympanic cavity within the facial canal and leaves the skull via stylomastoid foramen [5]. The stylomastoid foramen is the termination of facial

canal and is a curved aperture located in the middle of the base of styloid and the mastoid process of the temporal bone, on the inferior aspect of the petrous temporal bone. The foramen along with the facial nerve also transmits the stylomastoid artery, a branch of posterior auricular artery [19]. The facial canal is approximately 3 cm long and is divided into three

parts, labyrinthine, tympanic and mastoid. Available literature suggests anatomical difference between the luminal size of facial canal along its entire length and diameter of facial nerve, which predisposes nerve to compression in varied conditions leading to neuritis and clinically presenting as ipsilateral facial palsy called as Bell's palsy [1, 12, 22].

Unilateral facial nerve paralysis is most commonly (70%) caused by Bell's palsy. It is an acute onset of temporary weakness in facial muscles, which mostly occurs due to swelling or inflammation of ipsilateral facial or VII<sup>th</sup> cranial nerve [4, 6]. For centuries, the acute onset, temporary, unilateral facial palsy was considered idiopathic and hence the diagnosis was that of exclusion of the known aetiologies. However, in recent literature it has been hypothesised that the inflammatory response to infection (commonly to herpes simplex virus type I) induces oedema of the facial nerve. Consequently the nerve being entrapped in the un-yielding, tortuous bony facial canal becomes ischaemic due to the increment of the endoneural pressure and compression of the neural vasculature. Hence, the swelling evidently leads to axonal degeneration and cessation of nerve conduction [7, 10, 25].

The compression of an inflamed facial nerve has previously been explained on the basis of irregularity between the lumen size of the un-yielding facial canal and the nerve width [3, 13]. However, the sporadic reports on the variation of size and shape of the stylomastoid foramen [17, 18], which can also have clinical implications in unexplained cases of facial nerve palsy, have never been discussed with regards to compression of the nerve. Hence the present study was conducted with an objective to study the variations in size and shape of the stylomastoid foramen in dry adult human skulls.

## MATERIALS AND METHODS

The study was conducted in the Department of Anatomy at All India Institute of Medical Sciences, Patna, India. Prior to the onset of the study, we obtained ethical approval from the Ethics Committee of the above mentioned institution. The study was conducted on 37 dry human skulls of unknown age and sex and all the bones were procured from the bone bank of the Department of Anatomy. It was ensured that all selected skulls were without any evident deformity or sign of injury.

At the onset high resolution digital images (horizontal and vertical resolutions: 300 dpi) of the of the

norma basalis of human skulls under study were taken along with a 15 cm ruler (Faber-Castell's grip ruler) with the help of Canon EOS 1300D 18MP digital single-lens reflex camera (utilising 18–55 mm lens). While taking the images of the skulls, uniformity was ensured with respect to sharpness, noise, dynamic exposure (exposure range), tone reproduction, contrast and colour accuracy of the images. Moreover it was ensured that for every image the distance between the skull and the lens of the camera remained uniform. Prior to undertaking the images the skulls were kept on a flat surface and stabilised appropriately. The images were then uploaded to an image processing software, ImageJ (1.52p version, 2019), for measurements. The images were converted with the help of the software to 8-bit colour and grayscale for proper analysis, the scale for measurement was set with the help of the grip ruler in the image and the values obtained were tabulated. All measurements were undertaken by two observers to reduce chances of error. Each measurement was taken twice by one observer and the final data were obtained as an average of the 4 measurements undertaken by the 2 observers. Finally mean and standard deviation was computed when data from all the skulls under study were available. Foramen's dimension was taken in two planes, maximum medio-lateral or transverse dimension and maximum antero-posterior dimension for both the right and left sides.

## Ethical clearance

The authors hereby declare that the study was conducted only after approval had been obtained from the Ethical Committee of All India Institute of Medical Sciences, Patna whose guidelines are in accordance with the Declaration of Helsinki (1964) and all subsequent revisions.

## Statistical analysis

Data was analysed using SPSS version 20.0 for Windows (SPSS Inc., Chicago, IL, USA). Paired t test was used to compare the left and right sides with the t value and  $p < 0.05$  considered significant. Quantitative data are represented as mean  $\pm$  standard deviation (SD) in the manuscript.

## RESULTS

We observed a total of eight types of variations with respect to the shape of the stylomastoid foramen in the human skulls included in the present study (Figs. 1–3). The most common variant observed was the round

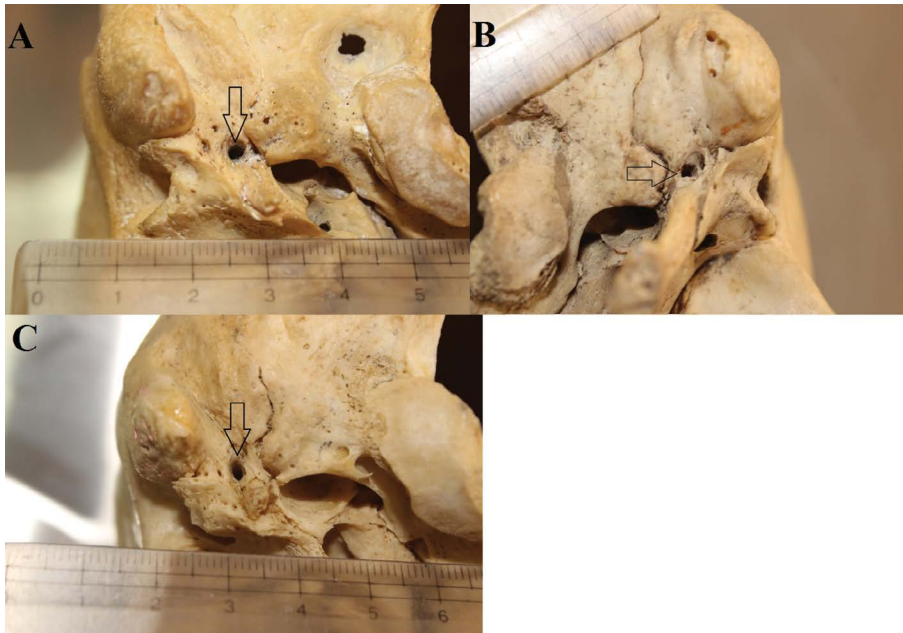


**Figure 1.** The common variants of stylomastoid foramen in terms of shape; **A.** Round stylomastoid foramen; **B.** Square stylomastoid foramen; **C.** Oval stylomastoid foramen. All the variants of foramen are shown as arrow marked area in the figures.

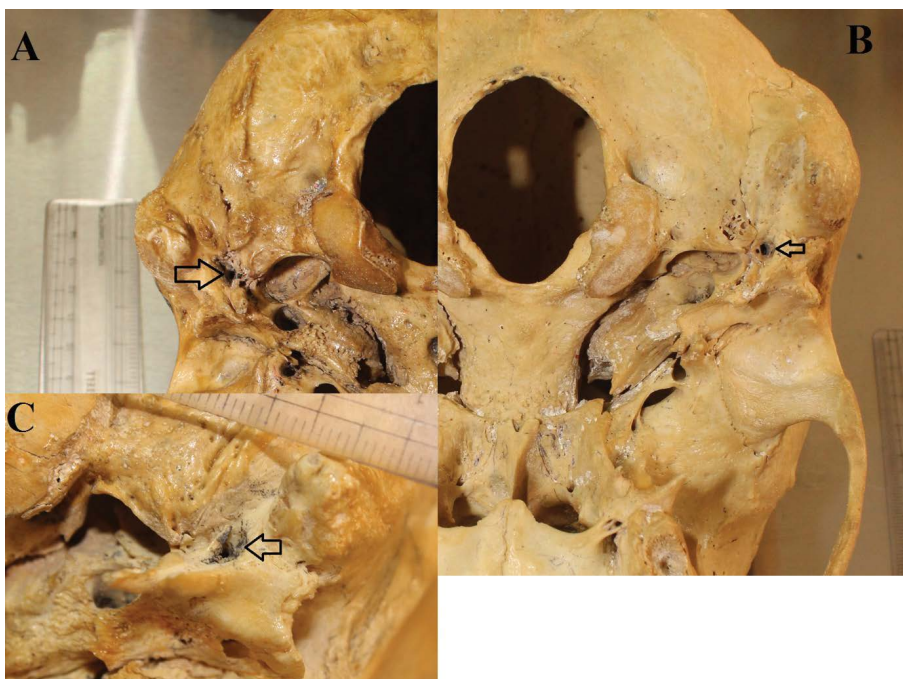


**Figure 2.** The uncommon variants of stylomastoid foramen in terms of shape; **A.** Triangular stylomastoid foramen; **B.** Rectangular stylomastoid foramen; **C.** Irregular stylomastoid foramen. All the variants of foramen are shown as arrow marked area in the figures.

shaped foramen which was noted in 20 (54.05%) skulls on left side and in 17 (45.95%) skulls on right side, respectively. Oval shaped foramen was the next common variant on the left side and was observed in 9 (24.32%) skulls. However, on the right side, square shaped foramen was the next common variant and was observed in 8 (21.62%) skulls, with oval shaped foramen noted in 6 (16.22%) skulls under study (Tables 1, 2).

In 17 (45.95%) skulls under study, the stylomastoid foramen along with its original shape had an

extension (Fig. 4). Extension of the foramen was observed bilaterally in 5 (13.51%) skulls. Overall extension of the foramen was observed in 22 cases (bilateral in 5 skulls and unilateral in 12 skulls). Among the eight variations of shape of the stylomastoid foramen reported in the present study, only oval foramen (15/22; 68.18%) and round foramen (7/22; 31.82%) were associated with extensions. It was noted that oval foramen was usually associated with antero-posterior extensions (13/15; 86.67%) and round foramen

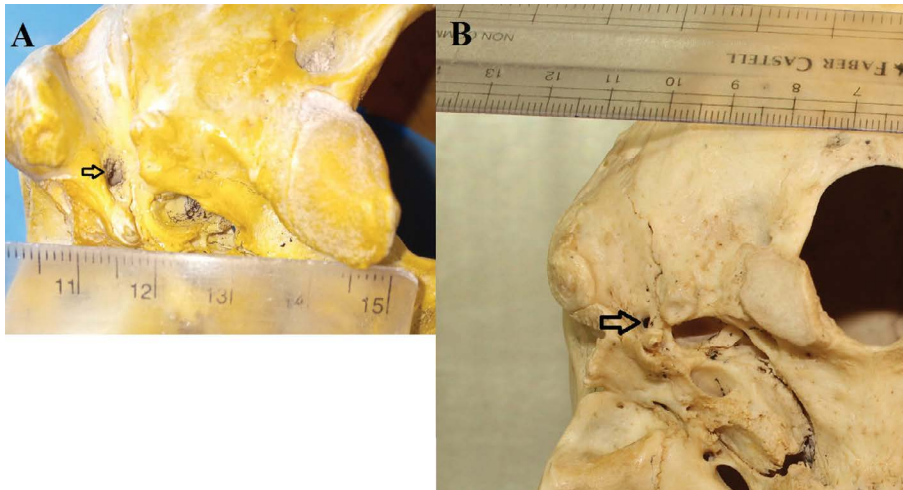


**Figure 3.** The uncommon variants of stylomastoid foramen in terms of shape; **A.** Serrated stylomastoid foramen; **B.** Bean-shaped stylomastoid foramen. Both the variants of foramen are shown as arrow marked area in the figures.

**Table 1.** Details of the shape of stylomastoid foramen and associated findings in the human skulls under study

Identification no. of skull	Location of foramen (side of skull)	Shape of foramen	Extensions when present (with direction)	Adjacent foramen when present (with direction)
1	Left	Oval	Antero-posterior	—
	Right	Oval	Antero-posterior	—
2	Left	Round	—	Anterior
	Right	Round	—	—
3	Left	Square	—	—
	Right	Round	Medial	—
4	Left	Round	Anterior	—
	Right	Round	Medial	—
5	Left	Round	—	—
	Right	Round	—	Anterior
6	Left	Round	—	—
	Right	Round	—	Anterior
7	Left	Round	—	—
	Right	Triangular	—	—
8	Left	Round	—	—
	Right	Square	—	—
9	Left	Round	Antero-medial	—
	Right	Serrated	—	—
10	Left	Round	—	—
	Right	Square	—	—
11	Left	Round	—	Anterior
	Right	Irregular (d/t bony spur projecting from posterior aspect of styloid process)	—	—
12	Left	Oval (bifurcated)	Antero-posterior	—
	Right	Round	—	—
13	Left	Round (situated deep inside the tympano-jugular groove)	—	—
	Right	Round (situated deep inside the tympano-jugular groove)	—	—
14	Left	Oval	Antero-posterior	—
	Right	Round	—	—



**Table 1. (cont.)** Details of the shape of stylomastoid foramen and associated findings in the human skulls under study

Identification no. of skull	Location of foramen (side of skull)	Shape of foramen	Extensions when present (with direction)	Adjacent foramen when present (with direction)
15	Left	Round	Lateral	—
	Right	Round	Medial	—
16	Left	Round	—	—
	Right	Square	—	—
17	Left	Oval	Antero-posterior	—
	Right	Square	—	—
18	Left	Round	—	—
	Right	Square	—	—
19	Left	Oval	Antero-posterior	—
	Right	Square	—	—
20	Left	Triangular	—	—
	Right	Rectangular	—	—
21	Left	Round	—	—
	Right	Oval	Medio-lateral	—
22	Left	Round	—	Medial
	Right	Round	—	—
23	Left	Serrated	—	—
	Right	Square (bifurcated)	—	—
24	Left	Bean-shaped	—	—
	Right	Round	Medial	—
25	Left	Round	—	—
	Right	Round	—	—
26	Left	Triangular (bifurcated)	—	—
	Right	Round	—	—
27	Left	Serrated	—	—
	Right	Oval	Antero-posterior	—
28	Left	Round	—	—
	Right	Round	—	—
29	Left	Round	—	—
	Right	Rectangular	—	Medial
30	Left	Rectangular	—	—
	Right	Triangular (bifurcated)	—	—
31	Left	Round	—	—
	Right	Round	—	Lateral
32	Left	Round	—	—
	Right	Round	—	—
33	Left	Oval	Antero-posterior	—
	Right	Oval	Medio-lateral	—
34	Left	Rectangular (bifurcated)	—	—
	Right	Oval (bifurcated)	Antero-posterior	—
35	Left	Oval	Antero-posterior	—
	Right	Square	—	—
36	Left	Oval	Antero-posterior	—
	Right	Round	—	—
37	Left	Oval	Antero-posterior	—
	Right	Oval	Antero-posterior	—

**Table 2.** Variations in the shape of stylomastoid foramen as observed in the present study

Serial number	Shape of foramen	Location on the skull (side)	
		Right	Left
1	Round	17 (45.95%)	20 (54.05%)
2	Oval	6 (16.22%)	9 (24.32%)
3	Square	8 (21.62%)	1 (2.7%)
4	Triangular	2 (5.41%)	2 (5.41%)
5	Rectangular	2 (5.41%)	2 (5.41%)
6	Serrated	1 (2.7%)	2 (5.41%)
7	Bean-shaped	0 (0%)	1 (2.7%)
8	Irregular	1 (2.7%)	0 (0%)

were usually associated with medial extensions (4/7; 57.14%). It was also observed that in case of oval foramen, extensions were more common on the left side (9/15; 60%); however, for round foramen extensions were more on the right side (4/7; 57.14%). Bilateral occurrence of extensions were more common in case of oval shaped foramen (3/5; 60%) (Tables 1, 3).

It was noted that the stylomastoid foramen was associated with an adjacent foramen in 7 skulls (7/37; 18.92%) under study (Fig. 4). The adjacent foramen,

when present was always found unilaterally and in most cases (4/7; 57.14%) it was located anterior to the actual foramen. Moreover it was observed on the right side in 4 skulls (4/7; 57.14%) and on the left side in 3 skulls (3/7; 42.86%), respectively (Table 1). Notably it was observed in 6 skulls (6/37; 16.22%) under study that the stylomastoid foramen was bifurcated (Fig. 5). Foramen with bifurcation was found in four variants of stylomastoid foramen in terms of shape (oval, triangular, rectangular and square) and was always a unilateral occurrence. It was also observed that in 2 skulls (2/37; 5.41%) the foramen (round in shape) was situated deep inside the tympano-jugular groove (Fig. 5). In one of the skulls under study, the stylomastoid foramen was partially obstructed by the presence of a bony spur projecting from posterior aspect of styloid process (Fig. 5, Table 1).

Measurements of dimensions of the stylomastoid foramen revealed that the mean antero-posterior diameter were more than the mean transverse diameter on both sides of the skull; however, the difference was not statistically significant. Moreover mean values of both the diameters (antero-posterior and transverse) were more on the left side of the skull; however, the difference was again not statistically significant (Table 4).



**Figure 4.** Additional morphological features of stylomastoid foramen; **A.** Round stylomastoid foramen showing medial extension; **B.** Round stylomastoid foramen with adjacent foramen on medial side. Both the features are shown as arrow marked area in the figures.

**Table 3.** Distribution of extensions of stylomastoid foramen as observed in the skulls under study

No. of skulls where extension observed	Distribution in the skulls		Distribution according to shape of foramen			
	Bilateral	Unilateral	Oval		Round	
			Right side	Left side	Right side	Left side
17	5	12	15		7	
			6	9	4	3
		Right side				
		5	7			

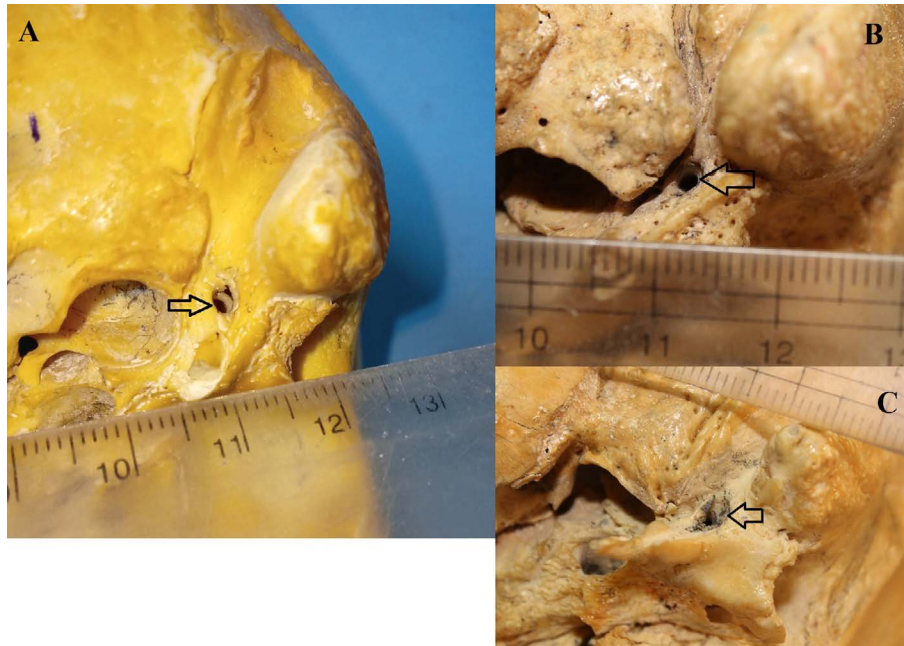


**Figure 5.** Exclusive unilateral features of stylomastoid foramen; **A.** Bifurcated oval foramen; **B.** Round foramen situated deep inside tympano-jugular groove; **C.** Irregular foramen with a bony spur projecting from posterior aspect of styloid process. All the features are shown as arrow marked area in the figures.

**Table 4.** Dimensions of the stylomastoid foramen as observed in the present study

Measurement values	Transverse diameter [mm]		Antero-posterior diameter [mm]	
	Right	Left	Right	Left
Mean $\pm$ standard deviation	2.02 $\pm$ 0.62	2.23 $\pm$ 0.57	2.21 $\pm$ 1.01	2.34 $\pm$ 0.64
p value	0.43		0.50	
Maximum	3.26	3.78	5.76	3.95
Minimum	0.85	1.08	0.98	1.13

## DISCUSSION

Idiopathic acute onset unilateral facial paralysis is commonly referred to as Bell's palsy [4]. Available literature suggests that herpes simplex virus (HSV-1) infection and subsequent oedema within the facial nerve attributed to inflammatory response as the possible aetiology of Bell's palsy in most cases [10, 15]. Nevertheless, researchers in recent times have tried to explore beyond the popular hypothesis and attempted to unravel other possible factors behind Bell's palsy [14, 16]. A trigger to this effect is the paradox that HSV-1 infection is relatively common whereas Bell's palsy is rather uncommon [22]. Researchers have tried to focus on the measurements related to the tortuous and uncompromising bony facial canal based on the hypothesis that anatomical variations within this canal could possibly lead to compression of the facial nerve eventually culminating as Bell's palsy [2, 8, 24]. Stylomastoid foramen is the termi-

nation of the facial canal and is the exit gateway for the facial nerve from skull base [19]. Variations in the dimensions (shape and size) of stylomastoid foramen could possibly have a significant influence in explained cases of Bell's palsy. There are considerable lacunae in the existing literature with regards to the anatomical details of stylomastoid. Hence the present study was undertaken to throw light on the variations in the size and shape of stylomastoid foramen.

There have been previous studies (conducted with the help of computed tomography and three dimensional models) on the anatomy of the facial canal and a recent study (on dry adult human skulls) was also conducted on the morphometry of the stylomastoid foramen [9, 11, 17, 20, 23]. However, to the best of our knowledge the present study is the first to explore the size and shape of stylomastoid foramen in dry adult human skulls. In this study as many as eight variations with regards to the shape of stylomastoid foramen were observed (Tables 1, 2). As noted in the present study, based on its shape, stylomastoid foramen can be broadly classified as common and rare variants. Whereas round, oval and square constitutes the common variants (present in 83.79% skulls on right side and 81.07% skulls on left side, respectively) shape wise triangular, rectangular, serrated, bean-shaped and irregular constitutes the rare variants of the stylomastoid foramen (Figs. 1–3, Table 2). It may be suggested that rare variants such as serrated (due to sharp edges), bean-shaped (due to narrow concave margin) and irregular stylomastoid foramen could interfere with the smooth exit of facial

nerve and thereby could have a bearing on unilateral injury of the nerve.

It was noted with interest that the stylomastoid foramen could be associated with extensions and adjacent foramen. In the present study, 17 skulls were associated with extensions of the stylomastoid foramen having both bilateral and unilateral incidence (Fig. 4). It was further observed that only round and oval shaped foramen (more common variants) were associated with extensions. Moreover the oval variants were more commonly (68.18% cases) associated with extensions as compared to round ones (31.82% cases). Notably extensions in oval variations of the foramen were commonly (86.67% cases) associated with antero-posterior orientation, whereas round foramen were usually associated with medial (57.14% cases) extensions (Table 3). In 7 skulls included in the present study, we observed that the stylomastoid foramen was associated with an adjacent foramen which was always unilateral in incidence (Fig. 4). Notably in most cases (57.14%) the adjacent foramen was situated anterior to the actual foramen (Table 1). On the basis of previously reported literature it may be suggested that extensions of the stylomastoid foramen and presence of adjacent foramen could be the allowance for the entry of stylomastoid artery (branch of posterior auricular artery) which is a normal anatomical companion of the facial nerve [19, 21]. In terms of size, it was observed that mean antero-posterior diameter was more than the mean transverse diameter; however, the difference was not statistically significant (Table 4). Hence it may be concluded that size of the stylomastoid foramen could be of little importance when considering the risk of facial nerve injury while passing through the stylomastoid foramen.

A notable observation was that 6 (16.22%) skulls under study had bifurcated stylomastoid foramen and this was always unilateral in occurrence (Fig. 5). Bifurcation when present was observed in oval shaped foramen (common variant) in 40% cases and in triangular, rectangular and square shaped foramen (rare variants) in the remaining 60% cases. In 2 skulls, the foramen (round shaped) were situated deep inside the tympano-jugular groove (Fig. 5). In 1 skull, the stylomastoid foramen was partially obstructed by a bony spur (Fig. 5, Table 1). Overall in 9 (24.32%) skulls as discussed above, the anatomical details of the stylomastoid foramen could possibly interfere with the smooth exit of the facial nerve from the skull base. In other words, in these skulls the

facial nerve was at the risk of injury while coming out of the stylomastoid foramen. Moreover in each of the 9 skulls, the observation was unilateral, which could lead to unilateral facial nerve palsy or Bell's palsy.

#### Limitations of the study

The present study has its inherent limitations as it is a single centre study conducted on a small number of dry human skulls. Nevertheless the findings reported could be considered as baseline information which may serve as a platform for future research. Knowledge about the variations in the shape of the stylomastoid foramen along with associated details such as presence of extensions of the foramen and existence of adjacent foramen could be useful during clinical interventions pertaining to facial nerve at the exit point from skull base. The most notable findings of the present study are the anatomical details of the stylomastoid foramen (bifurcated foramen, deeply situated foramen and presence of bony spur) which could be the cause of unilateral facial nerve lesion leading to Bell's palsy. Hence it may be opined that the findings of the present study do support the hypothesis that other than HSV-I infections, the aetiology of Bell's palsy could also partly be attributed to anatomical variations of stylomastoid foramen which is the terminal point of facial canal.

#### CONCLUSIONS

In the present study which was conducted on dry adult human skulls, eight variations of stylomastoid foramen were observed in terms of shape. The common variants were round, oval and square, whereas the rare variants were triangular, rectangular, serrated, bean-shaped and irregular. It was noted that stylomastoid foramen at times were associated with extension and even an adjacent foramen. It is quite possible that these entities are meant for the passage of stylomastoid artery which normally accompanies the facial nerve through the stylomastoid foramen. Variations of stylomastoid foramen, which were exclusively unilateral such as bifurcated foramen, presence of bony spur, deeply situated foramen within a groove were also observed. These unilateral variations along with rare variations in terms of shape such as serrated, bean-shaped and irregular foramen (which were also unilateral findings) could be potential risk factors towards injury of facial nerve at the point of exit from skull base leading to Bell's palsy. No significant differences were observed between the

mean diameters (antero-posterior and transverse) of the stylomastoid foramen thus limiting their role for any possible injury to the facial nerve.

### Acknowledgements

The authors express heartfelt gratitude to all the residents and faculty members of the Department of Anatomy, All India Institute of Medical Sciences, Phulwarisharif, Patna, India for their unconditional support throughout the study. We are grateful to the authorities of All India Institute of Medical Sciences, Phulwarisharif, Patna, India for their kind cooperation during the course of this study.

### REFERENCES

- Ahmed A. When is facial paralysis Bell palsy? Current diagnosis and treatment. *Cleve Clin J Med.* 2005; 72(5): 398–401, 405, doi: [10.3949/ccjm.72.5.398](https://doi.org/10.3949/ccjm.72.5.398), indexed in Pubmed: [15929453](https://pubmed.ncbi.nlm.nih.gov/15929453/).
- Celik O, Eskiizmir G, Pabuscu Y, et al. The role of facial canal diameter in the pathogenesis and grade of Bell's palsy: a study by high resolution computed tomography. *Braz J Otorhinolaryngol.* 2017; 83(3): 261–268, doi: [10.1016/j.bjorl.2016.03.016](https://doi.org/10.1016/j.bjorl.2016.03.016), indexed in Pubmed: [27217008](https://pubmed.ncbi.nlm.nih.gov/27217008/).
- Finsterer J. Management of peripheral facial nerve palsy. *Eur Arch Otorhinolaryngol.* 2008; 265(7): 743–752, doi: [10.1007/s00405-008-0646-4](https://doi.org/10.1007/s00405-008-0646-4), indexed in Pubmed: [18368417](https://pubmed.ncbi.nlm.nih.gov/18368417/).
- Fuller G, Morgan C. Bell's palsy syndrome: mimics and chameleons. *Pract Neurol.* 2016; 16(6): 439–444, doi: [10.1136/practneurol-2016-001383](https://doi.org/10.1136/practneurol-2016-001383), indexed in Pubmed: [27034243](https://pubmed.ncbi.nlm.nih.gov/27034243/).
- Ho ML, Juliano A, Eisenberg RL, et al. Anatomy and pathology of the facial nerve. *Am J Roentgenol.* 2015; 204(6): W612–W619, doi: [10.2214/AJR.14.13444](https://doi.org/10.2214/AJR.14.13444), indexed in Pubmed: [26001250](https://pubmed.ncbi.nlm.nih.gov/26001250/).
- Holland NJ, Weiner GM. Recent developments in Bell's palsy. *BMJ.* 2004; 329(7465): 553–557, doi: [10.1136/bmj.329.7465.553](https://doi.org/10.1136/bmj.329.7465.553), indexed in Pubmed: [15345630](https://pubmed.ncbi.nlm.nih.gov/15345630/).
- Kawiak W, Dudkowska A, Adach B. Diagnostic difficulties in etiology of the lesion of peripheral neuron of the facial nerve during the growth of sialoma. *Ann Univ Mariae Curie Skłodowska Med.* 1993; 48: 125–128, indexed in Pubmed: [8534144](https://pubmed.ncbi.nlm.nih.gov/8534144/).
- Kefalidis G, Riga M, Argyropoulou P, et al. Is the width of the labyrinthine portion of the fallopian tube implicated in the pathophysiology of Bell's palsy?: a prospective clinical study using computed tomography. *Laryngoscope.* 2010; 120(6): 1203–1207, doi: [10.1002/lary.20896](https://doi.org/10.1002/lary.20896), indexed in Pubmed: [20513040](https://pubmed.ncbi.nlm.nih.gov/20513040/).
- Mortazavi MM, Latif B, Verma K, et al. The fallopian canal: a comprehensive review and proposal of a new classification. *Childs Nerv Syst.* 2014; 30(3): 387–395, doi: [10.1007/s00381-013-2332-0](https://doi.org/10.1007/s00381-013-2332-0), indexed in Pubmed: [24322603](https://pubmed.ncbi.nlm.nih.gov/24322603/).
- Murakami S, Mizobuchi M, Nakashiro Y, et al. Bells palsy and herpes simplex virus: identification of viral DNA in endoneurial fluid and muscle. *Ann Intern Med.* 1996; 124: 27–30.
- Nakashima S, Sando I, Takahashi H, et al. Computer-aided 3-D reconstruction and measurement of the facial canal and facial nerve. I. Cross-sectional area and diameter: preliminary report. *Laryngoscope.* 1993; 103(10): 1150–1156, doi: [10.1288/00005537-199310000-00013](https://doi.org/10.1288/00005537-199310000-00013), indexed in Pubmed: [8412453](https://pubmed.ncbi.nlm.nih.gov/8412453/).
- Patel DK, Levin KH. Bell palsy: Clinical examination and management. *Cleve Clin J Med.* 2015; 82(7): 419–426, doi: [10.3949/ccjm.82a.14101](https://doi.org/10.3949/ccjm.82a.14101), indexed in Pubmed: [26185941](https://pubmed.ncbi.nlm.nih.gov/26185941/).
- Peitersen E. Bell's palsy: the spontaneous course of 2,500 peripheral facial nerve palsies of different etiologies. *Acta Otolaryngol Suppl.* 2002(549): 4–30, indexed in Pubmed: [12482166](https://pubmed.ncbi.nlm.nih.gov/12482166/).
- Phillips CD, Bubash LA. The facial nerve: anatomy and common pathology. *Semin Ultrasound CT MR.* 2002; 23(3): 202–217, doi: [10.1016/s0887-2171\(02\)90047-8](https://doi.org/10.1016/s0887-2171(02)90047-8), indexed in Pubmed: [12168997](https://pubmed.ncbi.nlm.nih.gov/12168997/).
- Powell HC, Myers RR, Costello ML, et al. Endoneurial fluid pressure in wallerian degeneration. *Ann Neurol.* 1979; 5(6): 550–557, doi: [10.1002/ana.410050610](https://doi.org/10.1002/ana.410050610), indexed in Pubmed: [475350](https://pubmed.ncbi.nlm.nih.gov/475350/).
- Salib RJ, Tziambazis E, McDermott AL, et al. The crucial role of imaging in detection of facial nerve haemangiomas. *J Laryngol Otol.* 2001; 115(6): 510–513, doi: [10.1258/0022215011908090](https://doi.org/10.1258/0022215011908090), indexed in Pubmed: [11429083](https://pubmed.ncbi.nlm.nih.gov/11429083/).
- Sharma N, Varshney R. Morphometry of stylomastoid foramen and its clinical application in facial nerve block. *Saudi J Anaesth.* 2015; 9(1): 60–63, doi: [10.4103/1658-354X.146314](https://doi.org/10.4103/1658-354X.146314), indexed in Pubmed: [25558201](https://pubmed.ncbi.nlm.nih.gov/25558201/).
- Shin KJ, Gil YC, Lee JY, et al. Three-dimensional study of the facial canal using microcomputed tomography for improved anatomical comprehension. *Anat Rec (Hoboken).* 2014; 297(10): 1808–1816, doi: [10.1002/ar.22977](https://doi.org/10.1002/ar.22977), indexed in Pubmed: [24990524](https://pubmed.ncbi.nlm.nih.gov/24990524/).
- Standing S. *Gray's Anatomy: The anatomical basis of clinical practice.* 41st Ed. Elsevier Health Sciences, Oxford, UK 2015: 1592.
- Tüccar E, Tekdemir I, Aslan A, et al. Radiological anatomy of the intratemporal course of facial nerve. *Clin Anat.* 2000; 13(2): 83–87, doi: [10.1002/\(SICI\)1098-2353\(2000\)13:2<83::AID-CA2>3.0.CO;2-Y](https://doi.org/10.1002/(SICI)1098-2353(2000)13:2<83::AID-CA2>3.0.CO;2-Y), indexed in Pubmed: [10679852](https://pubmed.ncbi.nlm.nih.gov/10679852/).
- Upile T, Jerjes W, Nouraei SA, et al. The stylomastoid artery as an anatomical landmark to the facial nerve during parotid surgery: a clinico-anatomic study. *World J Surg Oncol.* 2009; 7: 71, doi: [10.1186/1477-7819-7-71](https://doi.org/10.1186/1477-7819-7-71), indexed in Pubmed: [19785731](https://pubmed.ncbi.nlm.nih.gov/19785731/).
- Vianna M, Adams M, Schachern P, et al. Differences in the diameter of facial nerve and facial canal in bell's palsy: a 3-dimensional temporal bone study. *Otol Neurotol.* 2014; 35(3): 514–518, doi: [10.1097/MAO.0000000000000240](https://doi.org/10.1097/MAO.0000000000000240), indexed in Pubmed: [24518410](https://pubmed.ncbi.nlm.nih.gov/24518410/).
- Wang H, Northrop C, Burgess B, et al. Three-dimensional virtual model of the human temporal bone: a stand-alone, downloadable teaching tool. *Otol Neurotol.* 2006; 27(4): 452–457, doi: [10.1097/01.mao.0000188353.97795.c5](https://doi.org/10.1097/01.mao.0000188353.97795.c5), indexed in Pubmed: [16791035](https://pubmed.ncbi.nlm.nih.gov/16791035/).
- Yetiser S, Kazkayas M, Altinok D, et al. Magnetic resonance imaging of the intratemporal facial nerve in idiopathic peripheral facial palsy. *Clin Imag.* 2003; 27(2): 77–81, doi: [10.1016/s0899-7071\(02\)00485-0](https://doi.org/10.1016/s0899-7071(02)00485-0).
- Zhang W, Xu L, Luo T, et al. The etiology of Bell's palsy: a review. *J Neurol.* 2020; 267(7): 1896–1905, doi: [10.1007/s00415-019-09282-4](https://doi.org/10.1007/s00415-019-09282-4), indexed in Pubmed: [30923934](https://pubmed.ncbi.nlm.nih.gov/30923934/).

# The position of a duodenal diverticulum in the area of the major duodenal papilla and its potential clinical implications

E. Jakubczyk<sup>1</sup>, M. Pazurek<sup>2</sup>, A. Mokrowiecka<sup>2</sup>, B. Woźniak<sup>2</sup>, E. Małecka-Panas<sup>2</sup>, M. Podgórski<sup>3</sup>, M. Polgaj<sup>1</sup> , M. Topol<sup>4</sup> 

<sup>1</sup>Department of Normal and Clinical Anatomy, Chair of Anatomy and Histology, Medical University of Lodz, Poland

<sup>2</sup>Department of Digestive Tract Diseases, Chair of Gastroenterology, Medical University of Lodz, Poland

<sup>3</sup>Department of Diagnostic Imaging, Polish Mother's Memorial Hospital — Research Institute, Lodz, Poland

<sup>4</sup>Department of Angiology, Chair of Anatomy and Histology, Medical University of Lodz, Poland

[Received: 15 August 2019; Accepted: 7 January 2020]

**Background:** Although duodenal diverticula are associated with less frequent pathology than the colonic diverticula in the large intestine, their periampullary position may have significant clinical implications. The aim of the study was to identify any possible correlation between the type of localisation of the major duodenal papilla, duodenal diverticula, and some particular clinical issues.

**Materials and methods:** In total, 628 patients (408 females and 220 males; aged 21–91 years), who underwent endoscopic retrograde cholangiopancreatography were included in this study. The patients were divided into two groups: a study group comprising 66 (10.5%) patients with periampullary position of diverticula (group A), and a control group comprising 562 (89.5%) patients without diverticula (group B).

**Results:** A duodenal diverticulum was diagnosed in the periampullary position in 66/628 (10.5%) patients: 41 women (aged 52–91 years) and 25 men (aged 54–83 years).

**Conclusions:** Three types of localisation were observed for the major duodenal papilla with regard to the diverticula, with the most common type being next to each other (type III). In patients with diverticula, similar frequencies of gallstone occurrence are observed in men and women. Patients with papilla in the diverticulum who underwent cholecystectomy are more prone to develop lithiasis. (Folia Morphol 2021; 80, 1: 106–113)

**Key words:** endoscopic retrograde cholangiopancreatography (ERCP), duodenal diverticula, choledocholithiasis, major duodenal papilla

## INTRODUCTION

Diverticula of digestive tract are usually seen in the large intestine. They form “baggy intestine pouches” extending beyond the colonic wall. Diverticula have been shown to develop in response to increased pressure inside the intestinal lumen, weakness of the muscular membrane of intestine, a fibre-deficient

diet, low physical activity and chronic constipation. Furthermore, the incidence of diverticula increases with age [4, 21]. Two types of diverticulum have been recognised: true diverticula, caused by developmental disorders following the deformation of all layers of the intestine wall, and spurious diverticula, formed only by the mucous and submucous membrane; the

latter resemble hernias and develop in spots with decreased wall resistance [19, 21].

Duodenal diverticula (DD) are less frequently seen but are of significant importance, especially when they are located in close proximity to the major duodenal papilla (MDP). They are the second most common morphological pathology of the digestive tract after the colonic diverticula. This common entity was first described by Chomel in 1710 [see 32]. Their prevalence in particular populations ranges from 5% to 32.8% and has no sex predilection [3, 4, 19–21, 29, 32].

Duodenal diverticula are usually detected incidentally in patients during endoscopic retrograde cholangiopancreatography (ERCP) [4, 12, 15, 18, 24, 25, 34, 41, 43]. Congenital or true diverticula are rare, contain all layers of the duodenal wall, and may be subdivided into intraluminal and extraluminal forms [17, 32]. Intraluminal DD, first observed by Silcock in an autopsy specimen in 1885, are postulated to be secondary to congenital webs or membranes formed during the recanalization stage of the duodenal lumen after the seventh week of gestation — incomplete canalisation of the lumen. Extra-luminal duodenal diverticulum is a herniation acquired from a defect in the bowel wall due to entrance of vessels. The diagnosis in the literature has been almost exclusively based on the pathognomonic a barium-filled sac surrounded by a narrow radiolucent line entirely within the duodenum. The acquired or false type is more common, and is formed by protrusion of the mucosa, muscularis mucosa, or submucosa through a focal weakness in the duodenal wall. This is usually near blood vessels, the pancreatic duct, and the common bile duct [17, 32]. Spurious DD are mainly found next to the major duodenal ampulla, where they are associated with the healing of ulcerations in this area [20].

Duodenal diverticula are typically observed in patients older than 40 years old and their frequency increases with advancing age. Their formation is associated with the progression of duodenal motility disorders. The main underlying aetiologies for this defect are believed to be increased intraduodenal pressure and the progressive weakening of the intestinal smooth muscles. Diverticula are frequently asymptomatic, but they may be a cause of considerable morbidity [6, 14, 15, 32, 33].

Duodenal diverticula rarely cause any specific symptoms. A feeling of fullness or nausea may appear,

as well as postprandial pain related to the stretching of the large diverticula by the lingering chyme. These symptoms are often mistaken with signs of peptic ulcer disease [6]. However, DD may be of major clinical importance, especially when they are located close to the MDP [22, 24]. A few reports have proposed an association between the position of the MDP in the diverticulum and an increased frequency of bile duct disease, especially lithiasis and pancreatitis [3, 4, 9, 16, 18, 19, 21, 36, 38, 39].

Although DD are usually asymptomatic and discovered incidentally in patients during ERCP, DD can be associated with various pathological conditions such as common bile duct obstruction, pancreatitis, perforation, bleeding, and in rare cases, carcinoma [1–3, 8, 27, 30].

The aim of the study was to evaluate the frequency of MDP in the duodenal diverticulum with regard to diverticula characteristics, patient demographics, and the frequency of bile duct lithiasis, as well as of other pathologies or specific complaints. This data was approved by the ethics committee of the Medical University of Lodz (NR RNN/186/12/ KE).

## MATERIALS AND METHODS

This study was designed in a retrospective manner. Initially, 650 adult patients (421 women and 229 men), hospitalised in the Department of Digestive Tract Diseases Medical University of Lodz between 2010 and 2014 were evaluated for inclusion in the study. All individuals underwent an ERCP due to the following medical indications: clinical and biochemical features of jaundice, bile duct inflammation, severe gallstone, pancreatitis and suspected malignancy of the MDP, biliary ducts or pancreas, as in other hospitals [4, 10, 29]. Other indications in this group were based on previous ultrasonography and computed tomography examinations.

Twenty-two patients were excluded from the evaluated group because of cholangiocarcinoma and pancreatic cancer. Finally, 628 patients (408 women and 220 men), aged 21–91 years were included in the study (Table 1). Written informed consent was obtained from all patients who underwent ERCP.

During ERCP, the duodenal papilla was identified and catheterised. The bile duct was contrasted with a non-ionic contrast agent (Ultravist) and an X-rh ERCPay image was taken.

Among patients diagnosed with ERCP, the presence of stones in the biliary ducts or/and concre-

**Table 1.** Demography of examined patients

Gender	Demography					
	Patients with diverticulum			Patients without diverticulum		
	N	%	BMI	N	%	BMI
Female	41	62.1	31 ± 0.5	367	65.3	30 ± 0.5
Male	25	37.9	29 ± 0.5	195	34.7	27 ± 0.5
Total	66			562		

BMI — body mass index

tions in the gallbladder was recognised as primary choledocholithiasis; however, among those who had undergone cholecystectomy, choledocholithiasis in the biliary ducts was recognised as secondary [29].

The duodenal diverticulum was diagnosed as a depression of the intestine mucous membrane deeper than 5 mm.

The study population was divided into two groups: a study group comprising 66 patients (10.5% of the initial group) with periampullary position of diverticula (group A), and a control group comprising 562 (89.5%) patients without diverticula (group B).

The classification proposed by Boix et al. [4] was used to estimate the position of the duodenal major papilla in patients with the diverticula in the periampullary position. Three localisation types were identified for the major duodenal papilla: type I — MDP situated inside a diverticulum (centrally or at its internal edge), type II — MDP located between two diverticula, and type III — MDP situated 3 cm from a diverticulum, or at its external edge. All incidences were classified as type I, II or III, and the results for group A were compared with those for group B at ERCP.

### Statistical analysis

Statistical analysis was performed using Statistica 12.0 software (Statsoft, Cracow, Poland).  $P < 0.05$  was considered significant. The  $\chi^2$  test was employed to compare nominal data between two groups of patients divided according to the presence of a duodenal diverticulum.

## RESULTS

### Patient characteristics

Among 628 examined patients, the presence of at least one diverticulum in the area of the MDP was detected in 66 patients, and these were assigned to group A (10.5%). Within group A, 41 (62%) subjects were women, aged 52–91 years, and 25 (38%) were

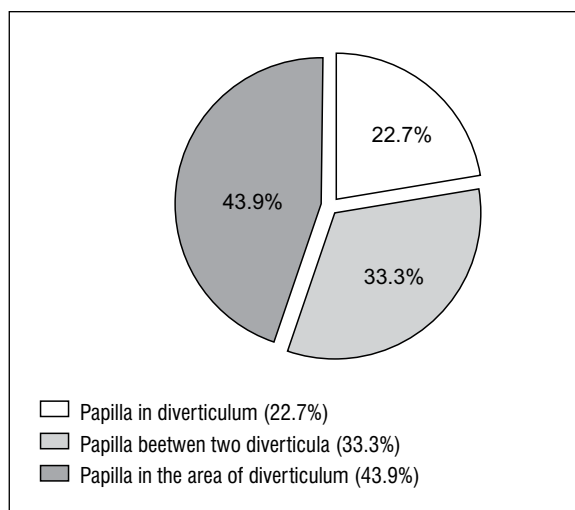


**Figure 1.** Location of major duodenal papilla in the area of the diverticulum.

men, aged 54–83. Similarly, in group B were 367/562 (65.3%) women and 195/562 (34.7%) men. The difference between the number of women in group A and B was not significant ( $p = 0.6083$ ). The majority of patients in group A (84.8%) and B (81.9%) were over the age of 60. The difference between these patients of the two groups was not significant ( $p = 0.5416$ ).

### DD and MDP

Of the MDP localisations, the most common was type III, i.e. where the MDP was situated next to the diverticula or at its external edge, which was observed in 29/66 cases (43.9%). This was followed by type II, i.e. where the MDP was located between two diverticula, observed in 22/66 cases (33.3%), and then type I, i.e. where the MDP was situated inside of the diverticula, in 15/66 cases (22.7%). Types II and III together were named as the juxtapaillary positions of the MDP (Fig. 1).

Juxtapaillary MDP was present significantly more often in woman (28/41; 68.3%) than in men (9/25; 36%;  $p = 0.002$ ). No significant difference in diverticulum location was observed with regard to age ( $p = 0.3486$ ).

### DD and clinical considerations

In 38/66 (57.5%) patients with diverticulum, biliary stones were detected with ERCP, and were removed during the same procedure. Only in 1 case was the size of the bile stone too large to be removed and the patient referred to surgery. Bile duct stones occurred less frequently in group B (262/562; 46.6%) than in



group A (38/66; 57.5%); however, the difference was not significant ( $p = 0.0918$ ; Fig. 2).

Biliary lithiasis was therefore detected in 262 cases in patients without diverticula: 192/367 (52.3%) women and 70/195 (35.9%) men. In this group, the frequency of choledocholithiasis was significantly higher in women than in men ( $p = 0.002$ ).

In contrast, no such significant difference in biliary lithiasis frequency was observed between male and female participants with the duodenal papilla located near the diverticulum: 25/41 (60.9%) women vs. 13/25 (52%) men ( $p = 0.646$ ).

Primary choledocholithiasis was detected in 28/66 (33.3%) patients of the whole of group A, and in 240/562 (42.7%) of the whole of group B ( $p = 0.1536$ ). However, among the patients with lithiasis, 28/38 (73.6%) from group A and 240/262 (91.6%) from group B suffered from primary choledocholithiasis. The difference between these groups was statistically significant ( $p = 0.0115$ ).

Of the patients with choledocholithiasis, additional gallbladder stones were detected in 4/28 (14.3%) in group A, and 36/240 (15%) in group B.

Secondary choledocholithiasis was found in 10 patients from group A and 10 (26.3%) with lithiasis. In group B, it was identified in 22 of all 562 (3.91%) patients or 22 of the 262 (8.4%) patients with lithiasis. The difference between these groups was significant ( $p = 0.0184$ ).

#### DD and clinical complications

A small number of complications such as bleeding were observed in the elderly patients (3/66; 4.5%). Pancreatitis was not observed.

Of the 66 patients with duodenal diverticulum, 12 (18.7%) individuals required prosthesis implantation into bile ducts due to incomplete stone evacuation. Among the 562 patients with the major duodenal papilla in the normal position, 141 (25%) required the prosthesis. The difference was not significant ( $p = 0.291$ ; Fig. 3).

Similar proportions of patients from group A (40/66 subjects; 60.6%) and group B (333/562 subjects; 59%) underwent endoscopic papillotomy ( $p = 0.8323$ ; Fig. 4).

In 21 of the 66 (42.2%) examined patients with diverticula, no other pathology was detected. It can be assumed that symptoms like pain and jaundice in this group were only caused by the presence of diverticula. However, the type of position of the diver-

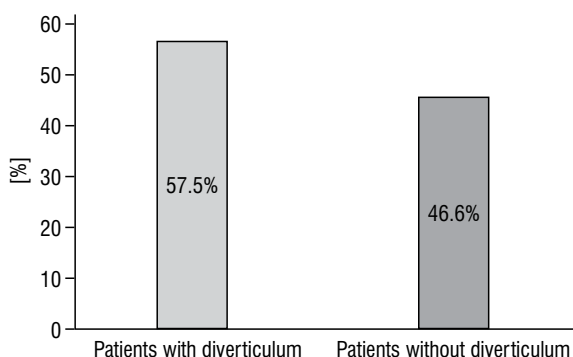


**Figure 2.** Frequency of lithiasis in patients with diverticulum, and in patients without diverticulum.

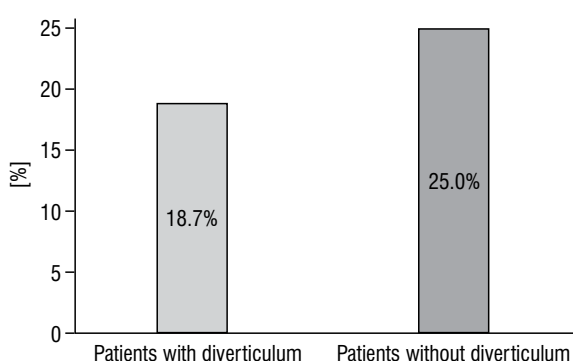


**Figure 3.** Frequency of prosthesis of the bile duct.

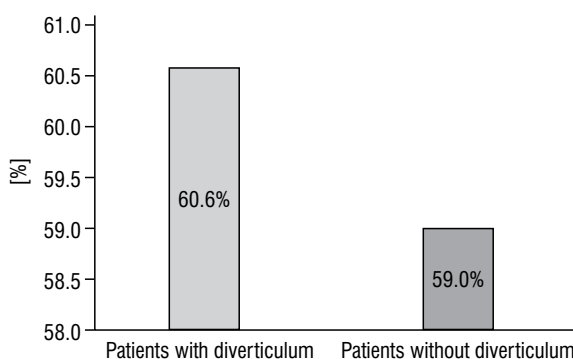


**Figure 4.** Frequency of endoscopic papillotomy.

ticulum was not connected with increasing frequency in any specific complaints.

## DISCUSSION

The incidence of DD ranges between 5% and 32.8% with the most common localisation being in the area of the MDP [4, 10, 20, 26]. Boix et al. [4] reports the frequency of periampullary diverticulum to be 32.8%, while Zoepf et al. [44] reports 12%, which is similar to our findings.

**Table 2.** The three types of papilla's location with respect to periampullary diverticula

Authors	Total (n)	Type I (%)	Type II (%)	Type III (%)
Boix et al. [4]	131	49%	30.5%	19.8%
Chandy et al. [7]	200	14%	17%	70%
Katsinelos et al. [15]	107	14%	72%	14%
Ozogul et al. [31]	249	41.3%	41.7%	17%
Yildirgan et al. [41]	51	52%	37.3%	9.8%
Zippi et al. [43]	77	28.6%	46.7%	24.7%
Present study	66	22.7%	33.3%	43%

The prevalence of DD increases with patient age. Our present findings indicate the majority of patients with duodenal diverticulum to be over 60 years old, which is confirmed by previous studies [21, 26, 29, 31]. Accordingly, roughly 40% of DD cases were found in patients aged 70 to 79 years [4, 7, 10, 37]. This relationship with advancing age suggests a degenerative process involving local supporting structures as an additional factor in the pathogenesis of DD [10]. This process may interfere with biliary drainage by establishing an unfavourable pressure gradient across the biliary tracts or by contraction of the duodenal wall and bile duct sphincter, thus obstructing the flow [10, 12]. In the case of secondary inflammation, the common bile duct can be obstructed by a juxtapapillary duodenal diverticulum filled with a food bezoar [24]. In turn, this may contribute to stasis in the biliary and pancreatic ductal systems, thereby promoting infection and increasing lithiasis [10, 23]. In most cases, DD are asymptomatic and are detected only by chance during ERCP examination [4, 19, 25, 28]. However, when symptoms occur, they often coexist with pathology in the hepato-pancreatic area.

Many authors consider DD to be a risk factor for choledocholithiasis and relapsing lithiasis [4, 8, 9, 11, 14, 18, 21, 25, 29, 40, 42]. Lithiasis tended to occur more frequently among patients with DD than in patients with the major duodenum in normal location. There are only a few reports on the role of diverticula in the pathogenesis of choledocholithiasis [3, 11, 19, 22, 33]. However, several hypotheses have been put forward to explain the observed higher incidence of biliary stone formation in the presence of DD. First, it was proposed that dysfunction in the sphincter of the common bile duct can lead to lithiasis by causing the reflux of pancreatic fluid and intestinal content. Second, it is possible that diverticula cause the sphincter to spasm, thereby increasing biliary duct pressure

that may in turn produce jaundice and cholangitis, as well as increase the chance of biliary stone formation. Finally, DD can compress the distal part of the common bile duct, causing functional biliary stasis [2, 5, 35].

Our present findings indicate a correlation between gender and choledocholithiasis only in the control group. In the study group, the frequency of lithiasis was similar in both sexes. The most common location of MDP in relation to the diverticulum was type III (43.9%), which is inconsistent with the reports of other authors (Table 2).

However, our findings are only confirmed by those of Zippi et al. [43]. So, the present study revealed that published data on the prevalence of papilla location with respect to DD is contradictory. This may be due to differences in the criteria used for classifying the position of the duodenal papilla and DD. For example, in contrast to all other articles, Katsinelos et al. [15] define type III as the intradiverticular position, i.e. papilla located between two adjacent diverticula [4, 7, 15, 31, 41, 43].

In our research, bile duct stones occurred less frequently in group B than in group A; however, the difference was not significant ( $p = 0.0918$ ).

Primary choledocholithiasis was detected less frequently in patients from group A than from group B ( $p = 0.1536$ ). However, a significantly greater proportion of the patients with lithiasis from group A (73.6%) suffered from primary choledocholithiasis than from group B ( $p = 0.0115$ ). Various other studies, including Tham and Kelly [37], report the greatest percentage to be among patients in whom choledocholithiasis was accompanied by cholecystolithiasis [3, 24, 43, 44]. Similarly, in our study secondary choledocholithiasis was found in 26.3% patients with lithiasis in group A, "and in 8.4% of patients with lithiasis in group B. The difference between these groups was significant ( $p = 0.0184$ ).

Our findings confirm a strong association between bile duct stones and DD. This is present both in subjects with common bile duct stones as primary choledocholithiasis and as secondary choledocholithiasis among patients with lithiasis in group A and group B. However, this difference was not significant between patients with lithiasis of both groups compared with all patients of both groups.

Consistent with our findings, Li et al. [23] also report a particularly close correlation between DD and choledocholithiasis after cholecystectomy.

A recent study by Bruno et al. [5] confirmed an association between diverticula and choledocholithiasis, cholangitis and common bile duct dilatation in an endoscopic ultrasound study of the prevalence of DD. In addition, no significant association was found between the presence of DD and acute, recurrent or chronic pancreatitis, as in the present study.

Khan et al. [17] present a case of Lemmel's syndrome, defined as obstructive jaundice, caused by DD in absence of choledocholithiasis or tumour [1, 13, 14]. Diagnosing Lemmel's syndrome is often challenging; to avoid delays in diagnosis and management, a side-viewing endoscope is used on patients with DD during ERCP. This approach is considered to be the gold-standard diagnostic test and diverticulectomy remains the standard of care.

The most frequent complications associated with ERCP are bleeding and severe acute pancreatitis [3, 4, 8, 25, 29]. The presence of a diverticulum did not affect the frequency of ERCP complication, which indicates that the location of the papilla close to the diverticulum does not hinder its catheterisation. In 31.8% patients with the papilla located near to the diverticulum, no other pathology was detected, which could explain the occurrence of the ailments reported by our patients. Chiang et al. [9] report a lower percentage of such patients (11%). However, unlike previous studies, our findings indicate that the type of diverticulum was not associated with the frequency of any specific complaints.

#### Limitations of the study

The present study has one key limitation: it was not possible to exclude the likelihood of the presence of microlithiasis among some of the patients.

### CONCLUSIONS

Gallstones were more common in the group of patients with periampullary diverticula than in the

control group; however, the difference was not significant. In patients with diverticula, this frequency is similar in men and women.

In patients with diverticula, the most common localization of the diverticulum is next to the major duodenal papilla (type III).

Duodenal diverticula can have a significant influence on the frequency of pathologies, especially in the area of the bile duct. Patients with papilla in the diverticulum who underwent cholecystectomy were found to be more prone to developing lithiasis.

It is possible that in the presence of DD, bile build-up and thickening may possibly lead to the development of gallstones and biliary duct stones.

The results also suggest that the presence of DD in the area of major duodenal papilla, accompanied by choledocholithiasis, is similar in both sexes; however, the type of diverticulum is not related to the incidence of any specific complaint.

### REFERENCES

1. Agúndez MC, Guerra DL, Pérez JF, et al. Síndrome de Lemmel: ictericia obstructiva secundaria a divertículo duodenal. *Cir Esp*. 2017; 95(9): 550–551, doi: [10.1016/j.ciresp.2017.02.003](https://doi.org/10.1016/j.ciresp.2017.02.003).
2. Altonbary AY, Bahgat MH. Endoscopic retrograde cholangiopancreatography in periampullary diverticulum: The challenge of cannulation. *World J Gastrointest Endosc*. 2016; 8(6): 282–287, doi: [10.4253/wjge.v8.i6.282](https://doi.org/10.4253/wjge.v8.i6.282), indexed in Pubmed: [27014423](https://pubmed.ncbi.nlm.nih.gov/27014423/).
3. Bergman S, Koumanis JD, Stein LA, et al. Duodenal diverticulum with retroperitoneal perforation. *Can J Surg*. 2005; 48(4): 332–336.
4. Boix J, Lorenzo-Zúñiga V, Añaños F, et al. Impact of periampullary duodenal diverticula at endoscopic retrograde cholangiopancreatography: a proposed classification of periampullary duodenal diverticula. *Surg Laparosc Endosc Percutan Tech*. 2006; 16(4): 208–211, doi: [10.1097/00129689-200608000-00002](https://doi.org/10.1097/00129689-200608000-00002), indexed in Pubmed: [16921297](https://pubmed.ncbi.nlm.nih.gov/16921297/).
5. Bruno M, Ribaldone D, Fasulo R, et al. Is there a link between periampullary diverticula and biliopancreatic disease? An EUS approach to answer the question. *Dig Liver Dis*. 2018; 50(9): 925–930, doi: [10.1016/j.dld.2018.07.034](https://doi.org/10.1016/j.dld.2018.07.034).
6. Branco C, Carneiro T, Luis D, et al. Perforated duodenal diverticulum: a rare complication in a common condition. *BMJ Case Rep*. 2017; 2017, doi: [10.1136/bcr-2017-219881](https://doi.org/10.1136/bcr-2017-219881), indexed in Pubmed: [28647710](https://pubmed.ncbi.nlm.nih.gov/28647710/).
7. Chandy G, Hart WJ, Roberts-Thomson IC. An analysis of the relationship between bile duct stones and periampullary duodenal diverticula. *J Gastroenterol Hepatol*. 1997; 12(1): 29–33, doi: [10.1111/j.1440-1746.1997.tb00341.x](https://doi.org/10.1111/j.1440-1746.1997.tb00341.x), indexed in Pubmed: [9076619](https://pubmed.ncbi.nlm.nih.gov/9076619/).
8. Chen L, Xia L, Lu Y, et al. Influence of periampullary diverticulum on the occurrence of pancreaticobiliary diseases and outcomes of endoscopic retrograde cholangiopancreatography. *Eur J Gastroenterol Hepatol*. 2017; 29(1): 105–111, doi: [10.1097/MEG.0000000000000744](https://doi.org/10.1097/MEG.0000000000000744), indexed in Pubmed: [27606949](https://pubmed.ncbi.nlm.nih.gov/27606949/).

9. Chiang TH, Lee YC, Chiu HM, et al. Endoscopic therapeutics for patients with cholangitis caused by the juxtapapillary duodenal diverticulum. *Hepatogastroenterology*. 2006; 53(70): 501–505.
10. Christoforidis E, Goulimaris I, Kanellos I, et al. The role of juxtapapillary duodenal diverticula in biliary stone disease. *Gastrointest Endosc*. 2002; 55(4): 543–547, doi: [10.1067/mge.2002.122615](https://doi.org/10.1067/mge.2002.122615), indexed in Pubmed: [11923769](https://pubmed.ncbi.nlm.nih.gov/11923769/).
11. Egawa N, Kamisawa T, Tu Y, et al. The role of juxtapapillary duodenal diverticulum in the formation of gallbladder stones. *Hepatogastroenterology*. 1998; 45(22): 917–920, indexed in Pubmed: [9755980](https://pubmed.ncbi.nlm.nih.gov/9755980/).
12. Farcas I, Patko A. The clinical significance of juxtapapillary diverticula: endoscopic and radiological study [abstract in English]. *Wien Klin Wochenschr*. 1981; 93(9): 296–303, indexed in Pubmed: [6789558](https://pubmed.ncbi.nlm.nih.gov/6789558/).
13. Frauenfelder G, Maraziti A, Ciccone V, et al. Computed Tomography Imaging in Lemmel Syndrome: A Report of Two Cases. *J Clin Imaging Sci*. 2019; 9: 23, doi: [10.25259/JCIS-17-2019](https://doi.org/10.25259/JCIS-17-2019), indexed in Pubmed: [31448174](https://pubmed.ncbi.nlm.nih.gov/31448174/).
14. Kang HS, Hyun JJ, Kim SY, et al. Lemmel's syndrome, an unusual cause of abdominal pain and jaundice by impacted intradiverticular enterolith: case report. *J Korean Med Sci*. 2014; 29(6): 874–878, doi: [10.3346/jkms.2014.29.6.874](https://doi.org/10.3346/jkms.2014.29.6.874), indexed in Pubmed: [24932093](https://pubmed.ncbi.nlm.nih.gov/24932093/).
15. Katsinelos P, Chatzimavroudis G, Tziomalos K, et al. Impact of periampullary diverticula on the outcome and fluoroscopy time in endoscopic retrograde cholangiopancreatography. *Hepatobiliary Pancreat Dis Int*. 2013; 12(4): 408–414, doi: [10.1016/s1499-3872\(13\)60063-6](https://doi.org/10.1016/s1499-3872(13)60063-6).
16. Kennedy RH, Thompson MH. Are duodenal diverticula associated with choledocholithiasis? *Gut*. 1988; 29(7): 1003–1006, doi: [10.1136/gut.29.7.1003](https://doi.org/10.1136/gut.29.7.1003), indexed in Pubmed: [3135249](https://pubmed.ncbi.nlm.nih.gov/3135249/).
17. Khan BA, Khan SH, Sharma A. Lemmel's syndrome: a rare cause of obstructive jaundice secondary to periampullary diverticulum. *Eur J Case Rep Intern Med*. 2017; 4(6): 000632, doi: [10.12890/2017\\_000632](https://doi.org/10.12890/2017_000632), indexed in Pubmed: [30755952](https://pubmed.ncbi.nlm.nih.gov/30755952/).
18. Kim DI, Kim MH, Lee SK, et al. Risk factors for recurrence of primary bile duct stones after endoscopic biliary sphincterotomy. *Gastrointest Endosc*. 2001; 54(1): 42–48, doi: [10.1067/mge.2001.115335](https://doi.org/10.1067/mge.2001.115335), indexed in Pubmed: [11427840](https://pubmed.ncbi.nlm.nih.gov/11427840/).
19. Kim CW, Chang JH, Kim JiH, et al. Size and type of periampullary duodenal diverticula are associated with bile duct diameter and recurrence of bile duct stones. *J Gastroenterol Hepatol*. 2013; 28(5): 893–898, doi: [10.1111/jgh.12184](https://doi.org/10.1111/jgh.12184), indexed in Pubmed: [23432035](https://pubmed.ncbi.nlm.nih.gov/23432035/).
20. Ko KS, Kim SH, Kim HC, et al. Juxtapapillary duodenal diverticula risk development and recurrence of biliary stone. *J Korean Med Sci*. 2012; 27(7): 772–776, doi: [10.3346/jkms.2012.27.7.772](https://doi.org/10.3346/jkms.2012.27.7.772), indexed in Pubmed: [22787373](https://pubmed.ncbi.nlm.nih.gov/22787373/).
21. Li X, Zhu K, Zhang L, et al. Periampullary diverticulum may be an important factor for the occurrence and recurrence of bile duct stones. *World J Surg*. 2012; 36(11): 2666–2669, doi: [10.1007/s00268-012-1716-8](https://doi.org/10.1007/s00268-012-1716-8), indexed in Pubmed: [22911215](https://pubmed.ncbi.nlm.nih.gov/22911215/).
22. Lee JJ, Brahm G, Bruni SG, et al. Biliary dilatation in the presence of a periampullary duodenal diverticulum. *Br J Radiol*. 2015; 88(1053): 20150149, doi: [10.1259/bjr.20150149](https://doi.org/10.1259/bjr.20150149), indexed in Pubmed: [26133074](https://pubmed.ncbi.nlm.nih.gov/26133074/).
23. Li X, Zhu K, Zhang L, et al. Periampullary diverticulum may be an important factor for the occurrence and recurrence of bile duct stones. *World J Surg*. 2012; 36(11): 2666–2669, doi: [10.1007/s00268-012-1716-8](https://doi.org/10.1007/s00268-012-1716-8), indexed in Pubmed: [22911215](https://pubmed.ncbi.nlm.nih.gov/22911215/).
24. Linde K, van der Linden GH, Beukers R, et al. Food impaction in a duodenal diverticulum as an unusual cause of biliary obstruction: case reports and review of the literature. *Eur J Gastroenterol Hepatol*. 1997; 9(6): 635–639, doi: [10.1097/00042737-199706000-00021](https://doi.org/10.1097/00042737-199706000-00021), indexed in Pubmed: [9222744](https://pubmed.ncbi.nlm.nih.gov/9222744/).
25. Linde K, van der Linden GH, Beukers R. Periampullary diverticula: consequences of failed ERCP. *Ann R Coll Surg Engl*. 1998; 80: 326–331, indexed in Pubmed: [9849331](https://pubmed.ncbi.nlm.nih.gov/9849331/).
26. Lobo DN, Balfour TW, Iftikhar SY, et al. Periampullary diverticula and pancreaticobiliary disease. *Br J Surg*. 1999; 86(5): 588–597, doi: [10.1046/j.1365-2168.1999.01121.x](https://doi.org/10.1046/j.1365-2168.1999.01121.x), indexed in Pubmed: [10361174](https://pubmed.ncbi.nlm.nih.gov/10361174/).
27. Loffeld RJ, Dekkers PEP. The impact of duodenal diverticuli and the execution of endoscopic retrograde cholangiopancreatography. *Int Sch Res Notices*. 2016; 2016: 5026289, doi: [10.1155/2016/5026289](https://doi.org/10.1155/2016/5026289), indexed in Pubmed: [27882342](https://pubmed.ncbi.nlm.nih.gov/27882342/).
28. Major P, Dembiński M, Winiarski M, et al. A periampullary duodenal diverticula in patient with choledocholithiasis: single endoscopic center experience. *Pol Przegl Chir*. 2016; 88(6): 328–333, doi: [10.1515/pjs-2016-0072](https://doi.org/10.1515/pjs-2016-0072), indexed in Pubmed: [28141552](https://pubmed.ncbi.nlm.nih.gov/28141552/).
29. Mohammad Alizadeh AH, Afzali ES, Shahnazi A, et al. ERCP features and outcome in patients with periampullary duodenal diverticulum. *ISRN Gastroenterol*. 2013; 2013: 217261, doi: [10.1155/2013/217261](https://doi.org/10.1155/2013/217261), indexed in Pubmed: [23984079](https://pubmed.ncbi.nlm.nih.gov/23984079/).
30. Örmeci N, Deda X, Kalkan Ç, et al. Impact of Periampullary Diverticula on Bile Duct Stones and Ampullary Carcinoma. *Euroasian J Hepatogastroenterol*. 2016; 6(1): 31–34, doi: [10.5005/jp-journals-10018-1162](https://doi.org/10.5005/jp-journals-10018-1162), indexed in Pubmed: [29201721](https://pubmed.ncbi.nlm.nih.gov/29201721/).
31. Ozogul B, Ozturk G, Kisaoglu A, et al. The clinical importance of different localizations of the papilla associated with juxtapapillary duodenal diverticula. *Can J Surg*. 2014; 57(5): 337–341, doi: [10.1503/cjs.021113](https://doi.org/10.1503/cjs.021113), indexed in Pubmed: [25265108](https://pubmed.ncbi.nlm.nih.gov/25265108/).
32. Pearl MS, Hill MC, Zeman RK. CT findings in duodenal diverticulitis. *Am J Roentgenol*. 2006; 187(4): W392–W395, doi: [10.2214/AJR.06.0215](https://doi.org/10.2214/AJR.06.0215), indexed in Pubmed: [16985110](https://pubmed.ncbi.nlm.nih.gov/16985110/).
33. Qi C, Zhaodong L, Shengwei L, et al. Diagnosis and treatment of juxta-ampullary duodenal diverticulum. *Clin Invest Med*. 2010; 33(5): E298–E303, doi: [10.25011/cim.v33i5.14355](https://doi.org/10.25011/cim.v33i5.14355), indexed in Pubmed: [20926036](https://pubmed.ncbi.nlm.nih.gov/20926036/).
34. Rajnakova A, Goh PM, Ngoi SS, et al. ERCP in patients with periampullary diverticulum. *Hepatogastroenterology*. 2003; 50(51): 625–628, indexed in Pubmed: [12828047](https://pubmed.ncbi.nlm.nih.gov/12828047/).

35. Song ME, Chung MJ, Lee DJ, et al. Cholecystectomy for prevention of recurrence after endoscopic clearance of bile duct stones in Korea. *Yonsei Med J.* 2016; 57(1): 132–137, doi: [10.3349/ymj.2016.57.1.132](https://doi.org/10.3349/ymj.2016.57.1.132), indexed in Pubmed: [26632393](https://pubmed.ncbi.nlm.nih.gov/26632393/).
36. Sun Z, Bo W, Jiang P, et al. Different types of periampullary duodenal diverticula are associated with occurrence and recurrence of bile duct stones: a case-control study from a Chinese Center. *Gastroenterol Res Pract.* 2016; 2016: 9381759, doi: [10.1155/2016/9381759](https://doi.org/10.1155/2016/9381759), indexed in Pubmed: [27143965](https://pubmed.ncbi.nlm.nih.gov/27143965/).
37. Tham TCK, Kelly M. Association of periampullary duodenal diverticula with bile duct stones and with technical success of endoscopic retrograde cholangiopancreatography. *Endoscopy.* 2004; 36(12): 1050–1053, doi: [10.1055/s-2004-826043](https://doi.org/10.1055/s-2004-826043), indexed in Pubmed: [15578293](https://pubmed.ncbi.nlm.nih.gov/15578293/).
38. Tomizawa M, Shinozaki F, Motoyoshi Y, et al. Association between juxtapaillary diverticulum and acute cholangitis determined using laboratory data. *Clin Exp Gastroenterol.* 2014; 7: 447–451, doi: [10.2147/CEG.S71539](https://doi.org/10.2147/CEG.S71539), indexed in Pubmed: [25429235](https://pubmed.ncbi.nlm.nih.gov/25429235/).
39. Tomizawa M, Shinozaki F, Hasegawa R, et al. Comparison of acute cholangitis with or without common bile duct dilatation. *Exp Ther Med.* 2017; 13(6): 3497–3502, doi: [10.3892/etm.2017.4401](https://doi.org/10.3892/etm.2017.4401).
40. Wijarnpreecha K, Panjawatanan P, Manatsathit W, et al. Association between juxtapaillary duodenal diverticula and risk of choledocholithiasis: a systematic review and meta-analysis. *J Gastrointest Surg.* 2018; 22(12): 2167–2176, doi: [10.1007/s11605-018-3865-z](https://doi.org/10.1007/s11605-018-3865-z), indexed in Pubmed: [30022443](https://pubmed.ncbi.nlm.nih.gov/30022443/).
41. Yildirgan MI, Başoğlu M, Yılmaz I, et al. Periampullary diverticula causing pancreaticobiliary disease. *Dig Dis Sci.* 2004; 49(11-12): 1943–1945, doi: [10.1007/s10620-004-9597-9](https://doi.org/10.1007/s10620-004-9597-9), indexed in Pubmed: [15628730](https://pubmed.ncbi.nlm.nih.gov/15628730/).
42. Zajac A, Solecki R, Kruszyna T, et al. Duodenal diverticula and choledocholithiasis in own material. [abstract in English]. *Przegl Lek.* 2005; 62(12): 1398–1400, indexed in Pubmed: [16786758](https://pubmed.ncbi.nlm.nih.gov/16786758/).
43. Zippi M, Traversa G, Pica R, et al. Efficacy and safety of endoscopic retrograde cholangiopancreatography (ERCP) performed in patients with Periampullary duodenal diverticula (PAD). *Clin Ter.* 2014; 165(4): e291–e294, doi: [10.7417/CT.2014.1745](https://doi.org/10.7417/CT.2014.1745), indexed in Pubmed: [25203345](https://pubmed.ncbi.nlm.nih.gov/25203345/).
44. Zoepf T, Zoepf DS, Arnold J. Juxtapaillary duodenal diverticula and biliopancreatic disease: analysis of 350 patients. *Gastrointest Endosc.* 2001; 54(1): 56–61, doi: [10.1067/mge.2001.115334](https://doi.org/10.1067/mge.2001.115334), indexed in Pubmed: [11427842](https://pubmed.ncbi.nlm.nih.gov/11427842/).

# Coeliac trunk and its anatomic variations: a cadaveric study

A. Juszczyk<sup>ORCID</sup>, A. Mazurek, J.A. Walocha, A. Pasternak

Department of Anatomy, Jagiellonian University Medical College, Krakow, Poland

[Received: 1 February 2020; Accepted: 30 March 2020]

**Background:** Coeliac trunk (CT) is the first major visceral branch of the abdominal aorta. The aim of this work was to present the CT division pattern and its anatomical variants in a sample of Polish population.

**Materials and methods:** Coeliac trunk dissection was performed in 50 adult cadavers in the Department of Anatomy, Jagiellonian University Medical College. Cadavers of Polish subjects were included. Cadavers with previous upper abdominal surgery, abdominal trauma, disease process that distorted arterial anatomy or signs of putrefaction were excluded. CT variations, accessory vessels, and vertebral level of origin were described. CT patterns were reported according to the Adachi classification. This study was reviewed and approved by the local Ethics Committee.

**Results:** Coeliac trunk consisting of the left gastric, common hepatic and splenic artery (type 1 according to the Adachi classification) was found in 82% of cadavers. The true tripod was found in 20% and the false one in 80%. Additional vessels were also found: greater pancreatic from the splenic artery and left inferior phrenic from the left gastric artery, which accounted for 2% sections. Type 2 according to the Adachi classification (i.e. the hepatosplenic trunk) was found in 16% of the sections. Other types of CT were not observed. The level of origin was found to be at the inter-vertebral disc between T12 and L1 in all of the cases.

**Conclusions:** Based on the analysis of the sectional material of the Department of Anatomy, it was found that the typical visceral segmental division is approximate to that observed by Adachi in its classification, whereas the second type of CT was twice as frequent and no other, less frequent types were found. (Folia Morphol 2021; 80, 1: 114–121)

**Key words:** tripod, anatomical variations, Adachi classification, coeliac trunk

## INTRODUCTION

The coeliac trunk (CT) is the first anterior visceral branch of the abdominal aorta (AA) and it arises from AA immediately below the aortic hiatus at the level of T12-L1 vertebra. It measures 1.5–2 cm. It runs down, right and slightly forward, lying back from the lesser omentum. Its ending lies just above the upper border of the pancreas. CT is surrounded by the coeliac plexus. It was first described by Albrecht von Haller

in 1756 [13], as “tripus Halleri”, which represents the classical type of branching, known as trifurcation in the left gastric artery (LGA), common hepatic artery (CHA) and splenic artery (SA). Anatomic variation of CT has been first classified by Adachi in 1928 [1], based on 252 dissections of Japanese cadavers, where six types of divisions were described (Fig. 1). However, two forms of trifurcation have been most commonly observed: a “true” tripod is considered when the

Address for correspondence: A. Pasternak, MD, PhD, Department of Anatomy, Jagiellonian University Medical College, ul. Kopernika 12, 31–034 Kraków, Poland, tel: +48 12 422 95 11, fax: +48 12 422 95 11, e-mail: artur.pasternak@uj.edu.pl

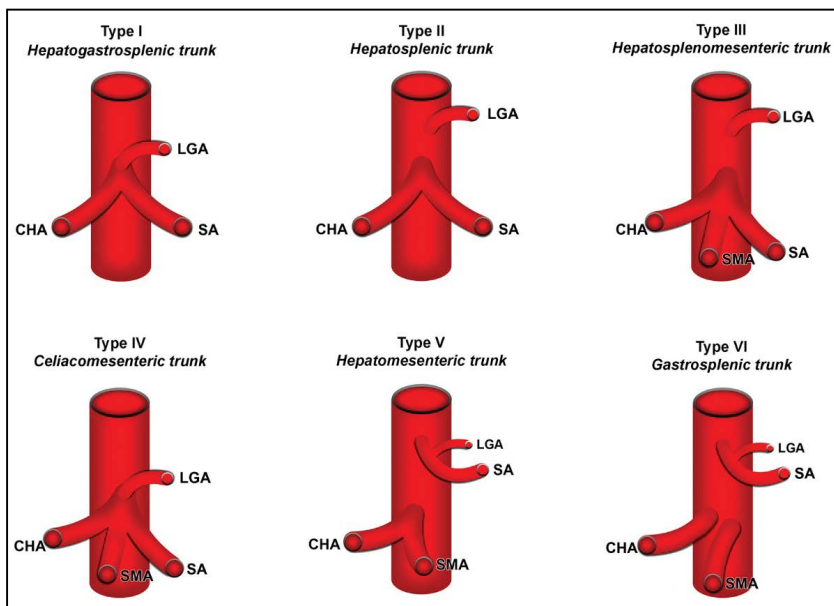


**Figure 1.** Coeliac trunk variations according to Adachi; CHA — common hepatic artery; LGA — left gastric artery; SA — splenic artery; SMA — superior mesenteric artery.

CHA, LGA and SA have a common origin, constituting a hepatogastrosplenic trunk. When one of these arteries arises before the remaining two in the course of the CT, it is called a false tripod [36]. CT supplies the structures derived from the foregut (liver, pancreas, abdominal part of the oesophagus, stomach and proximal duodenum). Surgery of the abdominal cavity requires an excellent knowledge of anatomical variations of the CT. Familiarity with the vascular supply of abdominal organs such as liver or pancreas is basic for numerous procedures (chemo-embolisation, liver resection, pancreatectomy) [15]. In the present modern era of imaging techniques, the cadaver still stands as an important and reliable mode of anatomical study [26, 51]. Hence, the aim of this cadaveric study was to analyse and report the vascular patterns of CT for the first time in a sample of Polish population according to the classification by Adachi [1].

## MATERIALS AND METHODS

Dissection of the CT was performed in 50 formalin-fixed abdomen specimens in the Department of Anatomy, Jagiellonian University Medical College. The inclusion criteria were cadavers of Polish nationality subjects. The sex and age was not taken into account. Cadavers with previous upper abdominal surgery, abdominal trauma, disease process that distorted the arterial anatomy or signs of putrefaction were excluded. This study was reviewed and approved by

the local Ethics Committee (no. 1072.6120.78.2019). Informed consent was not required. After dissection of the anterior abdominal wall, and entering the peritoneal cavity, the greater omentum of the stomach was dissected from the transverse colon, exposing the posterior wall of the stomach and opening the lesser sac. The pylorus was freed from adjacent connective tissue, and the omentum minus was opened along the minor curvature. Once the CHA, the LGA and the SA were identified, their course was followed to their site of origin. The presence of a “true tripod” or a “false tripod” was examined. CT variations, accessory vessels and site of origin were recorded and referred to Adachi’s classification. Care was taken not to overlook a left hepatic artery. The LGA was exposed as well as the coronary vein. The pancreas was also dissected to expose the origin of the superior mesenteric artery (SMA). The vertebral level of the CT origin was determined by palpation in cephalic direction beginning from the fifth lumbar vertebral body. The structures of the AA, its branches and variations were photographed using a digital camera.

## RESULTS

During routine dissection of abdomen we observed the following branching patterns of CT. Coeliac trunk divided into CHA, LGA and SA in 82% of the cadavers (41/50). This pattern corresponds to Adachi type I. Furthermore, two different trifurcation

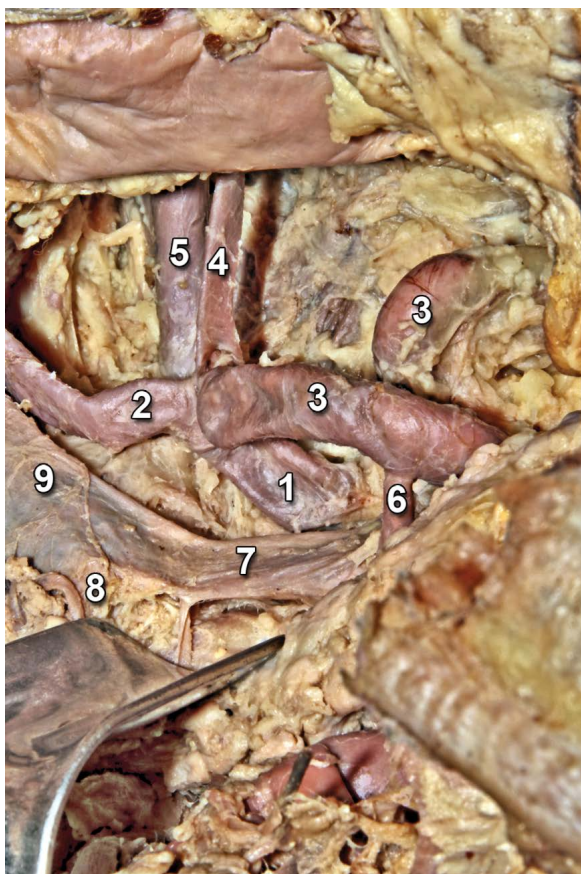


**Figure 2.** True tripod; 1 — coeliac trunk; 2 — common hepatic artery; 3 — splenic artery; 4 — left gastric artery; 5 — left gastric vein; 6 — greater pancreatic artery; 7 — splenic vein; 8 — superior mesenteric vein; 9 — portal vein.

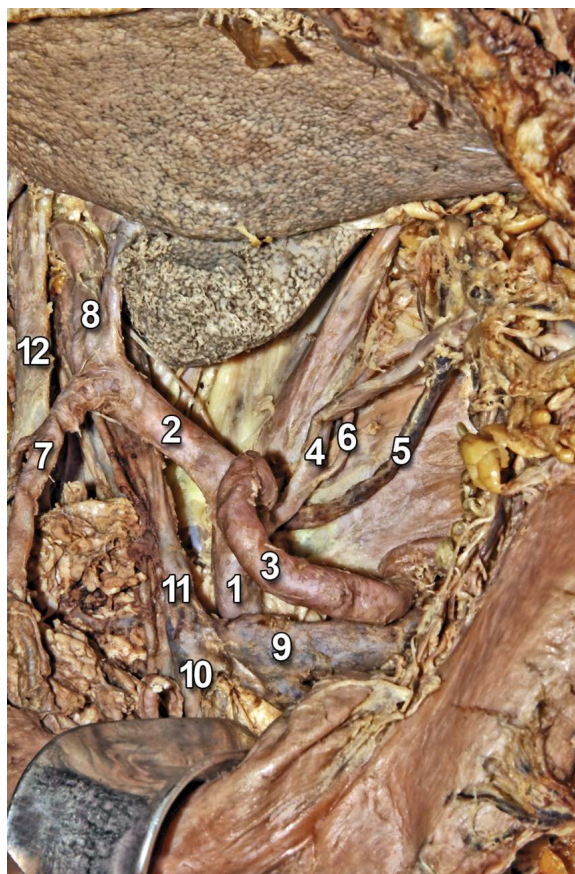


**Figure 3.** True tripod; 1 — coeliac trunk; 2 — common hepatic artery; 3 — splenic artery; 4 — left gastric artery; 5 — left gastric vein; 6 — right inferior phrenic artery; 7 — gastroduodenal artery; 8 — proper hepatic artery; 9 — splenic vein; 10 — superior mesenteric vein; 11 — portal vein; 12 — common bile duct.

patterns were observed; a classical or “true” tripod called “tripus Halleri” and a non-classical type. In the classical type, CHA, SA and LGA were found to arise from the CT. This was found in 20% of dissections (8/41) (Figs. 2, 3). In the non-classical type also known as “false” tripod the origin of LGA was located relatively proximal, between the AA and the bifurcation of CT, in 33 out of the 41 cadavers (80%) (Figs. 4, 5). Bifurcation of the CT (Adachi type II) was found in 16% of the cadaveric dissections (8/50). The CT divided into CHA and SA (hepatosplenic trunk) whereas LGA originated directly from the AA (Fig. 6). In 1 case, an accessory left inferior phrenic artery (LIPA) was found, rising from the LGA. The given variability was observed in 2%, which corresponds to 1/50 of cadavers. In addition, our attention was drawn by false tripod with two additional arteries: namely the LIPA from LGA and the greater pancreatic artery from SA. Such a variation occurred in 2% (1/50 of cadavers). The variations found in the present study in comparison to other cadaveric studies were

summarised in Table 1. Considering the prevalence of using the computed tomography angiography (CTA) in analysing anatomical variations, we also compared our results with the radiological studies in Polish population (Table 2). Correlation between gender and CT variation is given in Table 3. The level of CT origin was found to be at the inter-vertebral disc between T12 and L1 in all of the cases. Level of origin CT in different variations presented in Table 4.

## DISCUSSION

Anatomic variations of CT has been described by many authors in various classifications i.e. Rossi and Cova (1904) [38], Lariche and Villemin (1907) [23], Descomps (1910) [9], Picquand (1910) [35], de Rio Branco (1912) [37], Lipschutz (1917) [24], Eaton (1917) [10], Adachi (1928) [1], Tsukamoto (1929) [45], Imakoshi (1949) [16], Michels (1955) [27], Kozhevnikova (1977) [21], Katsume et al. (1978) [18], Vandamme and Bonte (1985) [46], Nelson et



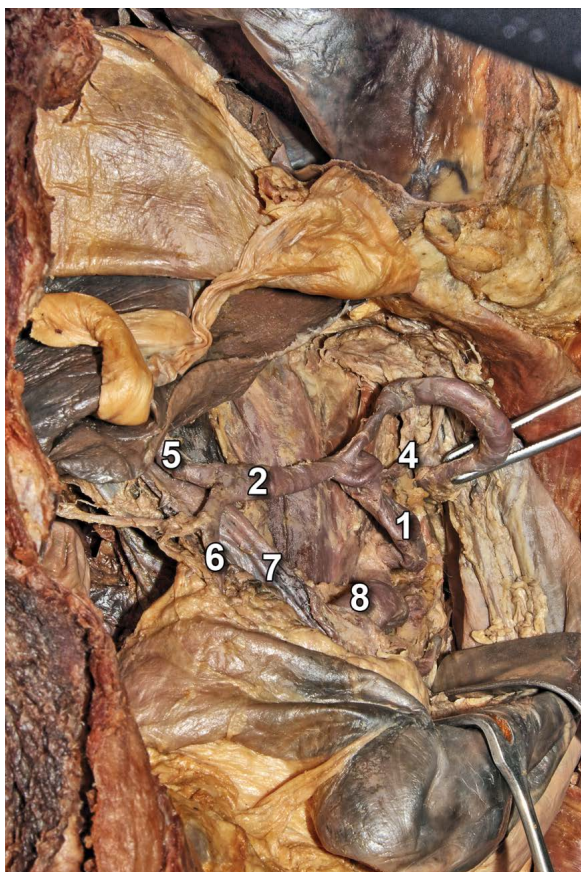


**Figure 4.** False tripod; 1 — coeliac trunk; 2 — common hepatic artery; 3 — splenic artery; 4 — left gastric artery; 5 — proper hepatic artery; 6 — gastroduodenal artery; 7 — portal vein; 8 — superior mesenteric artery.



**Figure 5.** False tripod; 1 — coeliac trunk; 2 — common hepatic artery; 3 — splenic artery; 4 — left gastric artery; 5 — proper hepatic artery; 6 — gastroduodenal artery.

al. (1988) [30], Kaneko (1990) [17], Chen (2009) [7], Shoumura et al. (1991) [40], Wadhwa Ambica (2011) [48], Panagouli (2013) [32], Olewnik et al. (2017) [31]. In our study we referred to Adachi [1] and Michels [27] who have classified the CT into six different types. However, these classifications do not include all observed variants of the CT as well as accessory or replaced hepatic arteries, both of them are still being mentioned and compared with newly described ones [8, 12, 26, 32, 34, 41, 44]. Furthermore, Adachi's and Michel's classifications described in textbooks were recently considered to create a scheme of the most frequent variants of the CT and anatomy of the hepatic circulation [7, 41]. Michel's classification was also used for depiction of CT and CHA variations in children [5]. Favelier et al. [11] mentioned that this classification provides the best anatomical approach. The types of CT according to Michels' classification are as follows: type 1 — normal branching; type 2 — hepatosplenic trunk and LGA

from aorta; type 3 — hepatosplenomesenteric trunk and left gastric from aorta; type 4 — hepatogastric trunk and SA from SMA; type 5 — splenogastric type; splenic and left gastric from the CT and CHA from SMA; and type 6 — coeliacomesenteric trunk; splenic, left gastric, common hepatic and superior mesenteric arteries arise from a common trunk [27, 40]. Indeed, the most prevalent is type 1, which occurs in 86% of the population [13]. We observed this type in 83.33% of cadavers. Type 2 occurring in 8% of population, was found in our study in 16.67% of cases. We did not observe other less common types i.e. type 3 (hepatosplenovisceral trunk), type 4 (visceromesenteric trunk), type 5 (hepatomesenteric trunk), type 6 (gastrosplenic trunk). Absence of the CT is the most infrequent variation, with a mean prevalence of 0.38%. In many studies, no CT absence has been found [2, 7, 15, 24]. In our study, no case of absence of CT was found (Table 1). It is important to notice that Olewnik et al. [31] revealed a shedload of CT variations non-classified by Adachi (27%)

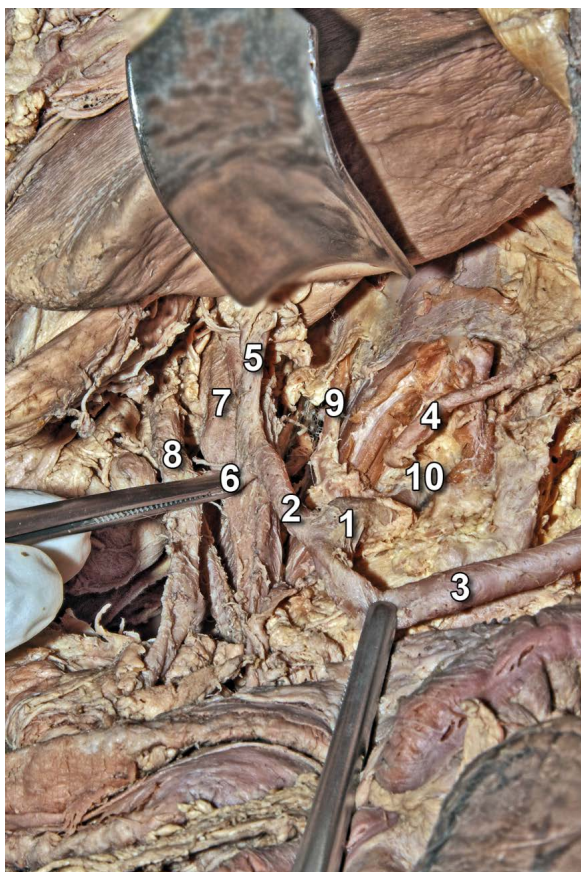


**Figure 6.** Hepatosplenic trunk + left gastric artery rising separately from abdominal aorta; 1 — coeliac trunk; 2 — common hepatic artery; 3 — splenic artery; 4 — left gastric artery; 5 — proper hepatic artery; 6 — gastroduodenal artery; 7 — portal vein; 8 — common bile duct; 9 — right inferior phrenic artery; 10 — abdominal aorta.

**Table 1.** Comparison between our study and the other cadaveric studies according to the Adachi's classification

Cadaveric study	I	II	III	IV	V	VI	Other
Our study	82.0%	16.0%	0.0%	0.0%	0.0%	0.0%	2.0%
Lipshutz [24]	73.5%	13.3%	0.0%	2.4%	0.0%	3.6%	7.2%
Adachi [1]	87.7%	6.4%	1.2%	2.4%	0.4%	2.0%	0.0%
Chen et al. [7]	89.8%	4.3%	0.7%	0.7%	1.5%	1.8%	1.0%
Marco-Clement et al. [26]	86.0%	14.0%	0.0%	0.0%	0.0%	0.0%	0.0%
Olewnik et al. [31]	62.5%	10.0%	0.0%	0.0%	0.0%	0.0%	27.5%

such as: 1) quadrifurcation — normal trifurcation + accessory hepatic artery: 7.5%; 2) coeliacophrenic trunk — normal trifurcation + LIPA: 12.5%; 3) trifurcation — hepatosplenic artery + accessory hepatic artery: 5.0%; 4) absence of the CT: 2.5% [31], so we

compared our results with other cadaveric studies of the non-Polish populations (Table 1).

Kornafel et al. [20] studied the variations of the main branches of the AA including CT and SMA using CTA and 64-detector computed tomography scanner in 201 patients. The authors did not base on the Adachi's or Michels' classification and observed 95.5% cases of the normal trifurcation. Other variations observed were hepatosplenic trunk (1.5%), coeliacomesenteric trunk (1.5%) and the gastrosplenic trunk (0.5%) [20]. Torres et al. [44] also analysed variations of the CT using multidetector computed tomography according to the Uflacker's classification. In this study the most common trifurcation was observed in 1455/1569 cases (92.7%), the other variants were: gastrosplenic trunk in 64/1569 cases (4.1%) and hepatosplenic trunk in 34 cases (2.2%). Coeliac-mesenteric trunk (8/1569; 0.5%), hepatogastric trunk (4/1569; 0.2%) were rarely observed. In 2 cases the absence of the CT was noted (0.1%). The hepatosplenomesenteric trunk and the coeliaco-colic trunk were not detected [44]. Kurcz et al. [22] presented results of the study on 240 patients. The most common patterns were: trifurcation (87.5%), hepatosplenic trunk (8.33%) and gastrosplenic trunk (3.33%). In 1 case CT was absent (0.42%) and hepatogastric trunk was observed in 0.42%. We compared our results on cadavers with radiologic studies (Table 2).

Due to high number of articles describing variations of the CT, there was a necessity to find appropriate results evaluated in one review. Santos et al. [39] and Whitley et al. [50] presented results of the previous studies about the CT and their findings were used to elaborate and compare our results with the other studies focused on the Polish population or the cadaveric studies.

Anson et al. [2] showed in cadaveric studies that almost 75% of cases had CT origin at the level of inter-vertebral disc between T12 and L1. In our study, the site of origin was also found to be at the above-mentioned level in most of the cases, which does not differ from the population norm.

The most common additional branches of the CT are single or double inferior phrenic arteries, which were described in 40% of cases in the study by Loukas et al. [25]. In our study, additional vessels were found in 2.77% of cadavers. In one autopsy specimen, the inferior phrenic artery arising from LGA and greater pancreatic artery arising from SA were found. In CTA scans Srivastava et al. [42] revealed visceral trifurca-

**Table 2.** Comparison between our cadaveric study and radiological studies in Polish population

Type of variation	Present study N = 50	Kornafel et al. [20] N = 201	Torres et al. [44] N = 1569	Kurcz et al. [22] N = 240
Normal branching	83.33%	95.50%	92.70%	87.50%
Hepatosplenic trunk	16.67%	1.50%	2.20%	8.33%
Hepatosplenomesenteric trunk	0.0%	0.0%	0.0%	0.0%
Hepatogastric trunk	0.0%	0.0%	0.20%	0.42%
Gastrosplenic trunk	0.0%	0.50%	4.10%	3.33%
Coeliacomesenteric trunk	0.0%	1.50%	0.50%	0.0%
Absence of coeliac trunk	0.0%	0.0%	0.10%	0.42%
Other (for example coeliac-colic trunk)	0.0%	1.0%	0.0%	0.0%

N — number of patients

**Table 3.** Correlation between gender and variation of the coeliac trunk (n = 50)

Type of variation	Male	Female
Hepatogastrosplenic trunk	28	13
Hepatosplenic trunk	7	2
Hepatosplenomesenteric trunk	0	0
Coeliacomesenteric trunk	0	0
Hepatomesenteric trunk	0	0
Gastrosplenic trunk	0	0

**Table 4.** Level of origin coeliac trunk in different variations (n = 50)

Type of variation	T12 (n)	L1 (n)
Hepatogastrosplenic trunk	27	14
Hepatosplenic trunk	3	6
Hepatosplenomesenteric trunk	0	0
Coeliacomesenteric trunk	0	0
Hepatomesenteric trunk	0	0
Gastrosplenic trunk	0	0

tion in 28%, bifurcation in 8%, quadrifurcation in 36%, pentafurcation in 20%, hexafurcation in 4%, while in 4% of cases visceral trunk was absent.

Anatomical variations of the CT are secondary to the embryonic developmental changes in the ventral segmental arteries [43]. Primitive segmental branches arise from the dorsal aorta and form the CT and the SMA. These branches are connected to the ventral longitudinal anastomotic channel. Retention or disappearance of parts of this primitive arterial plexus will give rise to variations of the CT and the SMA [14].

In studies carried out by Venieratos et al. [47] and Chen et al. [7] no differences were found between genders. However, the occurrence of different types of CT can be influenced by ethnicity [32]. Our study was carried out on the cadavers of Polish nationality presenting a trifurcated CT, either a common origin or with one of the three arteries arising first. This incidence is higher than those observed in Korean (10.9%), Caucasian (8.6%), Japanese (10.7%), Indian (30%) and Afro-American population (39%) [36].

Detailed knowledge of normal CT anatomy and its variations is very important during surgery such as pancreatoduodenectomy, liver transplant as well as

hepatic artery infusion chemotherapy. Preoperative imaging can help better preparation and planning by the surgical team. However, all arterial variations may not be detected in preoperative imaging (only up to 60–80% of cases). If detected, it can help the surgeons to identify the artery and prevent its injury during surgery and post-operative complications like bleeding and ischaemia [14]. Currently, arterial variations can also be predicted by the intrauterine ultrasonography examination and observations of the foetus' intestine position in the following stages of the foetal development [51]. Another modified ultrasonography examination — the three-dimensional contrast-enhanced ultrasonography — could be used in precisely non-invasive diagnosing the coeliac artery compression syndrome [49]. The pathologies of CT and SMA also could be detected by using new technique of the non-contrast magnetic resonance angiography [39].

Hepatic artery variations, such as anomalous right hepatic artery crossing posterior to the portal vein, are frequently seen (13%). These patients, when undergoing pancreatoduodenectomy, may require a change in the surgical approach to achieve an ad-

equate resection. Preoperative imaging can clearly identify such variations and help to achieve a safer pancreatic head dissection with proper surgical planning [3]. In transarterial chemoembolisation (TACE) or radioembolisation of hepatic cancers and metastases it is essential to analyse hepatic and extrahepatic perfusion in order to prevent iatrogenic postprocedural complications such as radiation induced ulcers in the stomach and duodenum or severe pancreatitis [4, 6, 33]. The variations of the CT are also significant during TACE in therapy of the pancreas cancer (especially the variations of the CHA) [29]. Anatomical variations of the CT are also significant to know in planning the bariatric procedures such as LGA embolisation or the sleeve gastrectomy [19, 28].

## CONCLUSIONS


Coeliac trunk variations are not uncommon findings, with different anatomic variants being reported. The classical visceral trifurcation was found in Polish population with a comparable frequency, as described by Adachi [1]. Only a low percentage of cases with additional vessels were found. Thus, the importance of knowing the possible variations of this structure is emphasized, which may have implications for surgical interventions and imaging studies related to the abdominal region.

## REFERENCES

- Adachi B. *Das arteriensystem der Japaner*, vol 2. Kenkyusha Press, Kyoto 1928: 18–71.
- Anson B, McVay C. The topographical positions and the mutual relations of the visceral branches of the abdominal aorta. A study of 100 consecutive cadavers. *Anat Rec.* 1936; 67(1): 7–15, doi: [10.1002/ar.1090670103](https://doi.org/10.1002/ar.1090670103).
- Balzan SM, Gava VG, Pedrotti S, et al. Prevalence of hepatic arterial variations with implications in pancreatoduodenectomy. *Arq Bras Cir Dig.* 2019; 32(3): e1455, doi: [10.1590/0102-672020190001e1455](https://doi.org/10.1590/0102-672020190001e1455), indexed in Pubmed: [31644675](https://pubmed.ncbi.nlm.nih.gov/31644675/).
- Boas FE, Bodei L, Sofocleous CT. Radioembolization of colorectal liver metastases: indications, technique, and outcomes. *J Nucl Med.* 2017; 58(Suppl 2): 1045–1115, doi: [10.2967/jnumed.116.187229](https://doi.org/10.2967/jnumed.116.187229), indexed in Pubmed: [28864605](https://pubmed.ncbi.nlm.nih.gov/28864605/).
- Caliskan E, Acar T, Ozturk M, et al. Coeliac trunk and common hepatic artery variations in children: an analysis with computed tomography angiography. *Folia Morphol.* 2018; 77(4): 670–676, doi: [10.5603/FM.a2018.0037](https://doi.org/10.5603/FM.a2018.0037), indexed in Pubmed: [29651794](https://pubmed.ncbi.nlm.nih.gov/29651794/).
- Catalano OA, Singh AH, Uppot RN, et al. Vascular and biliary variants in the liver: implications for liver surgery. *Radiographics.* 2008; 28(2): 359–378, doi: [10.1148/rj.282075099](https://doi.org/10.1148/rj.282075099), indexed in Pubmed: [18349445](https://pubmed.ncbi.nlm.nih.gov/18349445/).
- Chen H, Yano R, Emura S, et al. Anatomic variation of the celiac trunk with special reference to hepatic artery patterns. *Ann Anat.* 2009; 191(4): 399–407, doi: [10.1016/j.aanat.2009.05.002](https://doi.org/10.1016/j.aanat.2009.05.002), indexed in Pubmed: [19540742](https://pubmed.ncbi.nlm.nih.gov/19540742/).
- Cirocchi R, D'Andrea V, Lauro A, et al. The absence of the common hepatic artery and its implications for surgical practice: Results of a systematic review and meta-analysis. *Surgeon.* 2019; 17(3): 172–185, doi: [10.1016/j.surge.2019.03.001](https://doi.org/10.1016/j.surge.2019.03.001), indexed in Pubmed: [30948331](https://pubmed.ncbi.nlm.nih.gov/30948331/).
- Descomps P. *Le Tronc coeliaque*. G S Teinheil, Paris 1910.
- Eaton P. The coeliac axis. *Anat Rec.* 1917; 13(6): 369–374, doi: [10.1002/ar.1090130605](https://doi.org/10.1002/ar.1090130605).
- Favelier S, Germain T, Genson PY, et al. Anatomy of liver arteries for interventional radiology. *Diagn Interv Imaging.* 2015; 96(6): 537–546, doi: [10.1016/j.diii.2013.12.001](https://doi.org/10.1016/j.diii.2013.12.001), indexed in Pubmed: [24534562](https://pubmed.ncbi.nlm.nih.gov/24534562/).
- Fonseca-Neto OC, Lima HC, Rabelo P, et al. Anatomic variations of hepatic artery: a study in 479 liver transplantations. *Arq Bras Cir Dig.* 2017; 30(1): 35–37, doi: [10.1590/0102-6720201700010010](https://doi.org/10.1590/0102-6720201700010010), indexed in Pubmed: [28489166](https://pubmed.ncbi.nlm.nih.gov/28489166/).
- Haller VA. *Icones anatomicae in quibus peaeicipuae aliquae partes corporis humani delineatae proponuntur et arteriarum potissimum historia continetur*. Vandenhoeck, Gottingen 1756: 27–36.
- Hemamalini H. Variations in the branching pattern of the celiac trunk and its clinical significance. *Anat Cell Biol.* 2018; 51(3): 143–149, doi: [10.5115/acb.2018.51.3.143](https://doi.org/10.5115/acb.2018.51.3.143), indexed in Pubmed: [30310705](https://pubmed.ncbi.nlm.nih.gov/30310705/).
- Hiatt JR, Gabbay J, Busuttill RW. Surgical anatomy of the hepatic arteries in 1000 cases. *Ann Surg.* 1994; 220(1): 50–52, doi: [10.1097/0000658-199407000-00008](https://doi.org/10.1097/0000658-199407000-00008), indexed in Pubmed: [8024358](https://pubmed.ncbi.nlm.nih.gov/8024358/).
- Imakoshi K. Study of the abdominal arterial supply. Vol. 37. Achievements of Department Anat. Kanazawa Med. Univ, 1949, pp. 1-14: as cited by Chen et al. 2009.
- Kaneko O. The arterial distribution to the abdominal digestive organs in human fetuses. *Kaibogaku Zasshi.* 1990; 66: 452–461.
- Katsume K, Kanamura E, Sakai K, et al. Statistics report concerning variations in abdominal visceral arterial supply. *Kurume Igaku Zasshi.* 1978; 41: 266–273.
- Kordzadeh A, Lorenzi B, Hanif MA, et al. Left gastric artery embolisation for the treatment of obesity: a systematic review. *Obes Surg.* 2018; 28(6): 1797–1802, doi: [10.1007/s11695-018-3211-2](https://doi.org/10.1007/s11695-018-3211-2), indexed in Pubmed: [29616467](https://pubmed.ncbi.nlm.nih.gov/29616467/).
- Kornafel O, Baran B, Pawlikowska I, et al. Analysis of anatomical variations of the main arteries branching from the abdominal aorta, with 64-detector computed tomography. *Pol J Radiol.* 2010; 75(2): 38–45, indexed in Pubmed: [22802775](https://pubmed.ncbi.nlm.nih.gov/22802775/).
- Kozhevnikova TI. Age and individual characteristics in the structure of the celiac trunk in man. *Ark Anat Gistol Embriol.* 1977; 72: 19–25.
- Kurcz J, Nienartowicz E, Słonina J, et al. The usefulness of CT-angiography in detecting anatomical variants of arteries arising from the abdominal aorta and aortic arch. *Adv Clin Exp Med.* 2007; 16: 751–760.
- Leriche, Villemain. *Bibliogr. Anatom.* Paris, 1907, as cited by Bergman et al. 2006.
- Lipschutz B. A composite study of the celiac axie artery. *Ann Surg.* 1917; 65(2): 159–169, doi: [10.1097/0000658-191702000-00006](https://doi.org/10.1097/0000658-191702000-00006).

25. Loukas M, Hullett J, Wagner T. Clinical anatomy of the inferior phrenic artery. *Clin Anat.* 2005; 18(5): 357–365, doi: [10.1002/ca.20112](https://doi.org/10.1002/ca.20112), indexed in Pubmed: [15971218](https://pubmed.ncbi.nlm.nih.gov/15971218/).
26. Marco-Clement I, Martinez-Barco A, Ahumada N, et al. Anatomical variations of the celiac trunk: cadaveric and radiological study. *Surg Radiol Anat.* 2016; 38(4): 501–510, doi: [10.1007/s00276-015-1542-4](https://doi.org/10.1007/s00276-015-1542-4), indexed in Pubmed: [26267305](https://pubmed.ncbi.nlm.nih.gov/26267305/).
27. Michels NA. Blood supply and anatomy of the upper abdominal organs with a descriptive atlas. Observations on the blood supply of the liver and gallbladder (200 dissections). Lippincott, Philadelphia 1955: 139–140.
28. Mui WLM, Lee DWH, Lam KKY. Laparoscopic sleeve gastrectomy with loop bipartition: A novel metabolic operation in treating obese type II diabetes mellitus. *Int J Surg Case Rep.* 2014; 5(2): 56–58, doi: [10.1016/j.ijscr.2013.12.002](https://doi.org/10.1016/j.ijscr.2013.12.002), indexed in Pubmed: [24441436](https://pubmed.ncbi.nlm.nih.gov/24441436/).
29. Murata S, Onozawa S, Mine T, et al. Minimizing systemic leakage of cisplatin during percutaneous isolated pancreas perfusion chemotherapy: a pilot study. *Radiology.* 2015; 276(1): 102–109, doi: [10.1148/radiol.15141596](https://doi.org/10.1148/radiol.15141596), indexed in Pubmed: [25734552](https://pubmed.ncbi.nlm.nih.gov/25734552/).
30. Nelson T, Pollak R, Jonasson O, et al. Anatomic variants of the celiac, superior mesenteric, and inferior mesenteric arteries and their clinical relevance. *Clin Anat.* 1988; 1(2): 75–91, doi: [10.1002/ca.980010202](https://doi.org/10.1002/ca.980010202).
31. Olewnik Ł, Wysiadeci G, Polguj M, et al. Types of coeliac trunk branching including accessory hepatic arteries: a new point of view based on cadaveric study. *Folia Morphol.* 2017; 76(4): 660–667, doi: [10.5603/FM.a2017.0053](https://doi.org/10.5603/FM.a2017.0053), indexed in Pubmed: [28612916](https://pubmed.ncbi.nlm.nih.gov/28612916/).
32. Panagouli E, Venieratos D, Lolis E, et al. Variations in the anatomy of the celiac trunk: A systematic review and clinical implications. *Ann Anat.* 2013; 195(6): 501–511, doi: [10.1016/j.aanat.2013.06.003](https://doi.org/10.1016/j.aanat.2013.06.003), indexed in Pubmed: [23972701](https://pubmed.ncbi.nlm.nih.gov/23972701/).
33. Paprottka PM, Jakobs TF, Reiser MF, et al. Practical vascular anatomy in the preparation of radioembolization. *Cardiovasc Intervent Radiol.* 2012; 35(3): 454–462, doi: [10.1007/s00270-011-0169-z](https://doi.org/10.1007/s00270-011-0169-z), indexed in Pubmed: [21567273](https://pubmed.ncbi.nlm.nih.gov/21567273/).
34. Petrella S, Rodriguez C, Sgrott E, et al. Anatomy and variations of the celiac trunk. *Int J Morphol.* 2007; 25(2), doi: [10.4067/s0717-95022007000200002](https://doi.org/10.4067/s0717-95022007000200002).
35. Picquand G. Recherches sur l'anatomie du tronc coelia que et de ses branches. *Bibliogr Anat.* 1910; 19: 159–201.
36. Pinal-Garcia DF, Nuno-Guzman CM, Gonzalez-Gonzalez ME, et al. The celiac trunk and its anatomical variations: a cadaveric study. *J Clin Med Res.* 2018; 10(4): 321–329, doi: [10.14740/jocmr3356w](https://doi.org/10.14740/jocmr3356w), indexed in Pubmed: [29511421](https://pubmed.ncbi.nlm.nih.gov/29511421/).
37. Rio Branco P. Essais sur l'anatomie et la médecine opératoire du tronc coeliaque et de ses branches de l'artere hepatique en particulier. G Steinheil, Paris 1912: 828.
38. Rossi G, Cova E. Studio morfologico delle arterie dello stomaco. *Arch Ital di Anat e di Embryol.* 1904; 3: 485–526.
39. Santos PV, Barbosa AB, Targino VA, et al. Anatomical variations of the celiac trunk: a systematic review. *Arq Bras Cir Dig.* 2018; 31(4): e1403, doi: [10.1590/0102-672020180001e1403](https://doi.org/10.1590/0102-672020180001e1403), indexed in Pubmed: [30539978](https://pubmed.ncbi.nlm.nih.gov/30539978/).
40. Shoumura S, Emura S, Utsumi M. Anatomical study on the branches of the celiac trunk (IV). Comparison of the findings with Adachi's classification. *Kaibogaku Zasshi.* 1991; 66: 452–461.
41. Song SY, Chung JW, Yin YH, et al. Celiac axis and common hepatic artery variations in 5002 patients: systematic analysis with spiral CT and DSA. *Radiology.* 2010; 255(1): 278–288, doi: [10.1148/radiol.09090389](https://doi.org/10.1148/radiol.09090389), indexed in Pubmed: [20308464](https://pubmed.ncbi.nlm.nih.gov/20308464/).
42. Srivastava AK, Sehgal G, Sharma PK, et al. Various types of branching patterns of celiac trunk. *FASEB J.* 2012; 26(Suppl 1): 772.5.
43. Tandler J. Über die Varietäten der Arteria coeliaca und deren Entwicklung. Beiträge und Referate zur Anatomie und Entwicklungsgeschichte. 1904; 25(2): 473–500, doi: [10.1007/bf02300762](https://doi.org/10.1007/bf02300762).
44. Torres K, Staśkiewicz G, Denisow M, et al. Anatomical variations of the coeliac trunk in the homogeneous Polish population. *Folia Morphol.* 2015; 74(1): 93–99, doi: [10.5603/FM.2014.0059](https://doi.org/10.5603/FM.2014.0059), indexed in Pubmed: [25792402](https://pubmed.ncbi.nlm.nih.gov/25792402/).
45. Tsukamoto N. The branches of the abdominal visceral arteries in Japanese. *Kaibogaku Zasshi* 2. 1929: 780–829, as cited by Chen et al. 2009.
46. Vandamme JP, Bonte J. The branches of the celiac trunk. *Acta Anat (Basel).* 1985; 122(2): 110–114, doi: [10.1159/000145991](https://doi.org/10.1159/000145991), indexed in Pubmed: [4013640](https://pubmed.ncbi.nlm.nih.gov/4013640/).
47. Venieratos D, Panagouli E, Lolis E, et al. A morphometric study of the celiac trunk and review of the literature. *Clin Anat.* 2013; 26(6): 741–750, doi: [10.1002/ca.22136](https://doi.org/10.1002/ca.22136), indexed in Pubmed: [22886953](https://pubmed.ncbi.nlm.nih.gov/22886953/).
48. Wadhwa Ambica. A composite study of coeliac trunk in 30 adult human cadavers – its clinical implications. *Global J Med Res.* 2011; 11(1): 35–38.
49. Wang XM, Hua XP, Zheng GL. Celiac artery compression syndrome evaluated with 3-D contrast-enhanced ultrasonography: a new approach. *Ultrasound Med Biol.* 2018; 44(1): 243–250, doi: [10.1016/j.ultrasmedbio.2017.09.008](https://doi.org/10.1016/j.ultrasmedbio.2017.09.008), indexed in Pubmed: [29079396](https://pubmed.ncbi.nlm.nih.gov/29079396/).
50. Whitley A, Oliverius M, Kocián P, et al. Variations of the celiac trunk investigated by multidetector computed tomography: Systematic review and meta-analysis with clinical correlations. *Clin Anat.* 2020; 33(8): 1249–1262, doi: [10.1002/ca.23576](https://doi.org/10.1002/ca.23576), indexed in Pubmed: [32012339](https://pubmed.ncbi.nlm.nih.gov/32012339/).
51. Wozniak S, Florjanski J, Kordecki H, et al. Fetal sigmoid colon mesentery — In relevance in fetal ultrasound application. A pilot study. *Ann Anat.* 2018; 216: 152–158, doi: [10.1016/j.aanat.2017.12.003](https://doi.org/10.1016/j.aanat.2017.12.003), indexed in Pubmed: [29292173](https://pubmed.ncbi.nlm.nih.gov/29292173/).

# Age-related morphological peculiarities of human testes

K. Lasiene<sup>1</sup> , D. Gasiliunas<sup>2</sup>, N. Juodziukyniene<sup>1</sup>, A. Dabuzinskiene<sup>1</sup>, A. Vitkus<sup>1</sup>, B. Zilaitiene<sup>1</sup>

<sup>1</sup>Lithuanian University of Health Sciences, Kaunas, Lithuania

<sup>2</sup>Kaunas Division of State Forensic Medicine Service

[Received: 12 February 2020; Accepted: 25 February 2020]

**Background:** This study aimed to compare the isolated testes size, volume, weight and density changes with age and to establish the suitability of three formulas of testicular volume calculation for 18–50 and 51–70-year-old men groups.

**Materials and methods:** Two hundred and six testes of 103 men (59 of 18–50-year-old and 44 of 51–70-year-old men) were weighed and their size was measured by the sliding calliper. The accurate volume was determined by water displacement and compared with volume calculated using three formulas, and the density of testicular tissues was calculated.

**Results:** The mean length and height of both testes and length and height of right and left testes decreased significantly with age. The mean width of both testes and width of right and left testes decreased with age insignificantly. The mean of water displacement volume and weight and volume and weight of right and left testes decreased with age significantly. The mean density of testicular tissues and the density of the right and left testes increased significantly with age. In the same age group, the size, water displacement volume and weight of right testes was insignificantly higher than that of the left ones, and the density of testicular tissues was similar in the right and left testes.

**Conclusions:** The prolate spheroid formula was most suitable for calculation of testicular volume for 18–50-year-old men and prolate ellipsoid formula was most suitable for calculation of testicular volume in 51–70-year-old men. (Folia Morphol 2021; 80, 1: 122–126)

**Key words:** density, men, size, testis, weight, volume

## INTRODUCTION

Testicular function has a direct correlation with testicular volume. The seminiferous tubules and germinal elements comprise approximately 98% of testicular mass. Reduction in testicular size is mainly caused by reduction of these histological elements due to primary dysplasia or secondary damage and can therefore result in disturbed spermatogenesis [3, 14].

Mean size of testes had the significant correlation with total sperm count and sperm concentration,

sperm motility, percentage of live sperm, sperm morphology and serum follicle-stimulating hormone, luteinizing hormone and testosterone levels. Therefore, the measuring of size of the testis can be helpful to assess rapidly andrological status during the initial physical examination [14].

Evaluation of morphological parameters of living men and male animals is complicated. Various methods can be used for the measurement of the testicular size for the living male patients *in vivo*. The size of testes can be evaluated using vernier calliper, ruler,

orchidometer and ultrasound [2, 3, 7, 10, 12, 15]. Using the evaluated parameters of testes size, testicular volume can be calculated using various formulas such as prolate ellipsoid formula, the formula for a prolate spheroid or the empiric formula of Lambert. Results of these formulas can be very different and controversial [5]. However, the isolated testes' water displacement, weighing and measurement are most rigorous methods for the evaluation of testicular volume, weight and size [4, 11, 13].

The aim of this work was to compare changes of the morphological parameters (size, volume, weight and density) of isolated testes with age and establish the suitability of three formulas of testicular volume calculation for 18–50 and 51–70-year-old men groups.

## MATERIALS AND METHODS

This work was approved by the Kaunas Region Biomedical Research Ethics Committee (No. BE-2-1, 07.04.2015 and No. P1-BE-2-2/2015, 08.07.2016).

Pairs of testes from the men aged 18–70 year were obtained from Kaunas Division of State Forensic Medicine Service after autopsy at least 24 hours "post mortem". The left testes were marked using the cotton thread. The material was placed into 10% formaldehyde solution for 24 hours. Two hundred and six testes of 103 men were used for this investigation. Men were divided into two age groups: 18–50-year-old ( $n = 59$ ) and 51–70-year-old ( $n = 44$ ). Only testes without visible morphological pathologies were selected as suitable for this investigation. The testes were rinsed in streaming tap water, dried with blotting paper and the remnants of epididymis, adipose tissue and ligaments were removed. Then the testes were weighed using KERN 440-21N balance. The length, width and height of each testis were measured using the sliding calliper. The accurate volume was measured by water displacement of each testis. All obtained data were tabled in the Microsoft Excel 2003 programme. Using this program, the volume of each testis was calculated using three formulas: (1) for a prolate ellipsoid: volume = length  $\times$  width  $\times$  height  $\times$  0.52; (2) for a prolate spheroid: volume = length  $\times$  width<sup>2</sup>  $\times$  0.52; and (3) the empiric formula of Lambert: volume = length  $\times$  width  $\times$  height  $\times$  0.71 [4, 11, 13].

Also, the density of testicular tissues was calculated for each testis using the formula: density = weight/water displacement volume.

## Statistical analysis

The Statistica programme (Statistica Version 5, StatSoft Inc.) basic statistics was used for the calculation of the mean and standard deviation (SD). T-test for independent samples was used for statistical comparison of age groups ( $p$  values). Data were expressed as mean  $\pm$  standard deviation, and  $p < 0.05$  was taken as significant.

## RESULTS

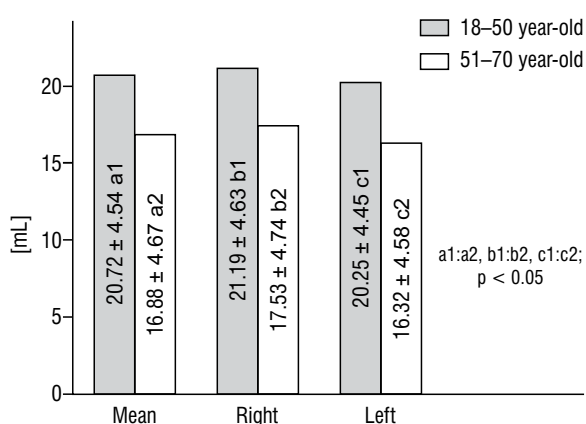
A mean size of the testes differed with age. The mean length of testes decreased significantly from  $4.54 \pm 0.42$  cm in 18–50-year-old men to  $4.17 \pm 0.49$  cm in 51–70-year-old men and their mean height decreased from  $2.6 \pm 0.3$  cm and  $2.34 \pm 0.38$  cm respectively ( $p < 0.05$ ). Only the mean width decreased non-significantly with age (from  $2.96 \pm 0.32$  cm and  $2.92 \pm 0.34$  cm). The size of the right and left testes of the 18–50-year-old group were higher than in 51–70-year-old men. The length and height of testes differed significantly ( $p < 0.05$ ). Also, the size of right testes was insignificantly higher than that of left testes in the same age group men, but, in 51–70-year-old men group, the height was the same in the right and left testes ( $p > 0.05$ ; Table 1).

The mean water displacement volume of both testes was significantly higher in 18–50-year-old men ( $0.72 \pm 4.54$  mL) than in the 51–70-year-old group ( $16.88 \pm 4.67$  mL;  $p < 0.05$ ). The volume of right and left testes was higher in 18–50-year-old men in comparison with the volume of testes in 51–70-year-old men ( $p < 0.05$ ). The volume of right testes was insignificantly higher than that of left testes in the same age group ( $p > 0.05$ ; Fig. 1).

Comparing the water displacement volume with the results of the three testicular volume calculation formulas, contradictory results were obtained (Table 2). In 18–50-year-old men group, mean of both testes volume and volumes of right and left testes, which were calculated using prolate ellipsoid formula and empiric formula of Lambert, differed significantly from the water displacement volume ( $p < 0.05$ ). Only results of prolate spheroid formula differed insignificantly from water displacement volume ( $p > 0.05$ ). In 51–70-year-old men group, the volumes calculated using prolate spheroid formula and empiric formula of Lambert, differed significantly from the water displacement volume ( $p < 0.05$ ). Only results of prolate ellipsoid formula differed insignificantly from water displacement volume in the testes of this age group men

**Table 1.** The length, width and height of the testes in 18–70-year-old men (mean  $\pm$  standard deviation)

	Length [cm]	Width [cm]	Height [cm]	P
<b>Mean</b>				
18–50-year-old	4.54 $\pm$ 0.42 a1	2.96 $\pm$ 0.32	2.6 $\pm$ 0.3 a3	a1:a2, a3:a4; p < 0.05
51–70-year-old	4.17 $\pm$ 0.49 a2	2.92 $\pm$ 0.34	2.34 $\pm$ 0.38 a4	
<b>Right</b>				
18–50-year-old	4.57 $\pm$ 0.44 b1	2.98 $\pm$ 0.31	2.63 $\pm$ 0.34 b3	b1:b2, b3:b4; p < 0.05
51–70-year-old	4.2 $\pm$ 0.51 b2	2.94 $\pm$ 0.37	2.34 $\pm$ 0.37 b4	
<b>Left</b>				
18–50-year-old	4.5 $\pm$ 0.4 c1	2.93 $\pm$ 0.33	2.58 $\pm$ 0.25 c3	c1:c2, c3:c4; p < 0.05
51–70-year-old	4.15 $\pm$ 0.48 c2	2.9 $\pm$ 0.32	2.34 $\pm$ 0.41 c4	

**Figure 1.** The water displacement volume of the testes in 18–70-year-old men (mean  $\pm$  standard deviation).

( $p > 0.05$ ). The obtained data showed that the Empiric formula of Lambert was completely unsuitable for the calculation of testicular volume in both age groups (the difference between results of water displacement and Empiric formula of Lambert was 20.69–25.98%).

The mean weight of testes in 18–50-year-old men (21.53  $\pm$  4.57 g) was significantly higher than in the 51–70-year-old men (17.91  $\pm$  5.01 mL;  $p < 0.05$ ). The weight of 18–50-year-old men right (22.03  $\pm$  4.63 g) and left (21.03  $\pm$  4.5 g) testes was higher than the weight of 51–70-year-old men testes (21.03  $\pm$  4.5 g and 17.26  $\pm$  4.88 g, respectively,  $p < 0.05$ ). The weight of right testes was higher than left testes in the same age men group ( $p > 0.05$ ; Fig. 2).

**Table 2.** The comparison of water displacement volume and volume calculated using three formulas in the 18–70-year-old men, mL (mean  $\pm$  standard deviation)

	Water displacement	Prolate ellipsoid	Prolate spheroid	Empiric formula of Lambert	P
<b>Mean</b>					
18–50-year-old	20.72 $\pm$ 4.54 a1	18.36 $\pm$ 4.4 a2	21.0 $\pm$ 5.45	25.07 $\pm$ 6.0 a3	a1:a2, a1:a3; p < 0.05
Difference with mean of water displacement volume	–	–2.36 (11.39%)	1.72 (8.3%)	4.35 (20.99%)	
51–70-year-old	16.88 $\pm$ 4.67 b1	15.28 $\pm$ 4.89	19.06 $\pm$ 5.69 b2	20.87 $\pm$ 6.67 d3	b1:b2, b1:b3; p < 0.05
Difference with mean of water displacement volume	–	–1.6 (9.48%)	2.18 (12.91%)	3.99 (23.64%)	
<b>Right</b>					
18–50-year-old	21.19 $\pm$ 4.63 c1	18.85 $\pm$ 4.69 c2	21.46 $\pm$ 5.5	25.74 $\pm$ 6.41 c3	c1:c2, c1:c3; p < 0.05
Difference with mean of water displacement volume	–	–2.34 (11.04%)	0.27 (1.27%)	4.55 (21.47%)	
51–70-year-old	17.43 $\pm$ 4.73 d1	15.51 $\pm$ 5.08	19.49 $\pm$ 6.18 d2	21.17 $\pm$ 6.93 d3	d1:d2, d1:d3; p < 0.05
Difference with mean of water displacement volume	–	–1.92 (11.02%)	2.06 (11.82%)	3.74 (21.46%)	
<b>Left</b>					
18–50-year-old	20.25 $\pm$ 4.45 e1	17.87 $\pm$ 4.06 e2	20.54 $\pm$ 5.44	24.44 $\pm$ 5.55 e3	e1:e2, e1:e3; p < 0.05
Difference with mean of water displacement volume	–	–2.38 (11.75%)	0.29 (1.43%)	4.19 (20.69%)	
51–70-year-old	16.32 $\pm$ 4.58 f1	15.06 $\pm$ 4.74	18.63 $\pm$ 5.18 f2	20.56 $\pm$ 6.47 f3	f1:f2, f1:f3; p < 0.05
Difference with mean of water displacement volume	–	–1.26 (7.72%)	2.31 (14.15%)	4.24 (25.98%)	



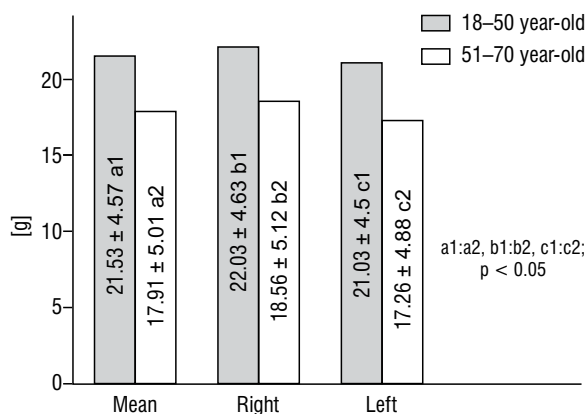


**Figure 2.** The testicular weight in 18–70-year-old men (mean ± standard deviation).

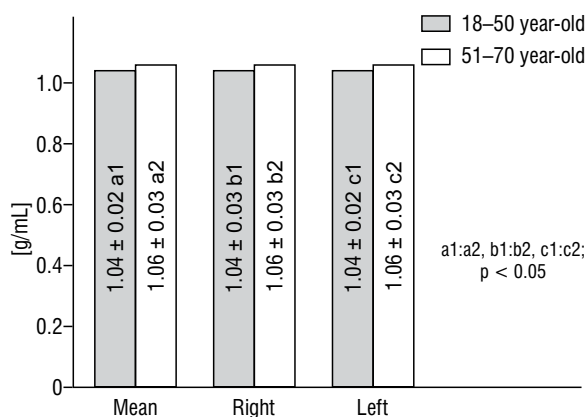


**Figure 3.** The density of testicular tissues in 18–70-year-old men (mean ± standard deviation).

The mean density of testicular tissues was lower in 18–50-year-old men than in 51–70-year-old men ( $1.04 \pm 0.02$  g/mL and  $1.06 \pm 0.03$  g/mL, respectively,  $p < 0.05$ ). The tissue density of right ( $1.04 \pm 0.03$  g/mL) and left ( $1.04 \pm 0.02$  g/mL) testes was lower in 18–50-year-old men in comparison with the density of testicular tissues in 51–70-year-old men ( $1.06 \pm 0.03$  g/L and  $1.06 \pm 0.03$  g, respectively,  $p < 0.05$ ). In the same age group, the tissue density of the right and left testes was identical ( $p > 0.05$ ; Fig. 3).

## DISCUSSION

The male fecundity begins to decline in the late thirties, or in the forties. This decline may be the consequence of an associated decline in semen quality. Age-related decrease evidences in semen volume, total sperm count, motility and proportion of sperm with normal [1].

Kelvin et al. [8] measured the size of left and right testes of 18–64-year-old men and calculated their vol-

ume. They estimated that the volume of right testes was lower than that of the left testes in patients aged 18–20 and 41–50 years. Also, the volume of right testes was higher in the patients of 51–64-year-old men group than in 18–50-year-old men. The volume of left testes was lower in the patients of 51–64-year-old group than in 41–50-year-old men [8]. Results of our investigation showed that the water displacement volume of the right testes was insignificantly higher than that of the left testes in the both investigated age groups. Also, the volume of right and left testes was significantly higher in 18–50-year-old men in comparison with 51–70-year-old men. Our results coincident with the results reported by Kothari and Gupta [9] and Tijani et al. [16] indicating that the volume of fertile men testes doesn't decline significantly with patient age.

Hsieh et al. [4], Mbaeri et al. [11] and Sakamoto et al. [13] compared volumes of patients' testes calculated using three formulas with water displacement volume. They estimated that the formula of Lambert is the optimal in clinical practice [4, 11, 13]. The results of our investigation contradict the proposition of these authors. Our obtained data show that the empiric formula of Lambert is completely unsuitable for the calculation of testicular volume. We ascertained that the prolate spheroid formula is most suitable for calculation of testes volume for 18–50-year-old men and prolate ellipsoid formula is most suitable for calculation of testes volume for 51–70-year-old men.

The density of testicular tissues varies with age. Johnson et al. [6] estimated that the testicular tunica weight increased, and the parenchyma weight decreased with age. Kothari and Gupta [9] predicated that ageing leads to a thickening of the tunica propria, inter-tubular fibrosis and progressive hyalinisation and atrophy of some tubules. The results of our investigation showed that mean density and density of testicular tissues of the left and right testes was significantly lower in 18–50-year-old men than in 51–70-year-old men. According to the data of the above-mentioned authors, the density of the tissues increases with age due to the proliferation of connective tissue and weight loss of parenchyma in the testes.

## CONCLUSIONS

1. The mean size and the size of right and left testes decreased with age. The length and height decreased significantly.

2. The water displacement volume's and weight's mean and the volume and weight of right and left testes decreased with age significantly.
3. The mean testicular tissues density and the density of the right and left testes increased significantly with age.
4. The prolate spheroid formula was most suitable for calculation of testicular volume for 18–50-year-old men and prolate ellipsoid formula was most suitable for calculation of testicular volume for 51–70-year-old men.

### Acknowledgements

We would like to thank the technical staff of the Kaunas Division of State Forensic Medicine Service for their help in collecting material for our study.

### REFERENCES

1. Auger J, Jouannet P. Age and male fertility: biological factors. *Rev Epidemiol Sante Publique*. 2005; 53 Spec No 2: 2S25–35, indexed in Pubmed: [16471142](#).
2. Cha M, Ahn B, Kim Y. Inaccuracy in Ultrasonographic Measurement of the Testicular Volume in Children. *Korean J Urol*. 2006; 47(8): 866, doi: [10.4111/kju.2006.47.8.866](#).
3. Goede J, Hack WWM, Sijstermans K, et al. Normative values for testicular volume measured by ultrasonography in a normal population from infancy to adolescence. *Horm Res Paediatr*. 2011; 76(1): 56–64, doi: [10.1159/000326057](#), indexed in Pubmed: [21464560](#).
4. Hsieh ML, Huang ST, Huang HC, et al. The reliability of ultrasonographic measurements for testicular volume assessment: comparison of three common formulas with true testicular volume. *Asian J Androl*. 2009; 11(2): 261–265, doi: [10.1038/aja.2008.48](#), indexed in Pubmed: [19151736](#).
5. Innocent M, Asomugha L, Ukamaka M, et al. Ultrasound measured testicular volume in Nigerian adults: Relationship of the three formulae with height, body weight, body-surface area, and body-mass index. *Int J Adv Med Health Res*. 2016; 3(2): 85, doi: [10.4103/2349-4220.195940](#).
6. Johnson L, Petty CS, Neaves WB. Influence of age on sperm production and testicular weights in men. *J Reprod Fertil*. 1984; 70(1): 211–218, doi: [10.1530/jrf.0.0700211](#), indexed in Pubmed: [6694139](#).
7. Karaman MI, Kaya C, Caskurlu T, et al. Measurement of pediatric testicular volume with Prader orchidometer: comparison of different hands. *Pediatr Surg Int*. 2005; 21(7): 517–520, doi: [10.1007/s00383-005-1470-1](#), indexed in Pubmed: [16010550](#).
8. Kelvin KE, Chukwuemeka NN, Adeyanju AR, et al. Ultrasound measurement of testicular volume in healthy nigerian adults. *J Asian Sci Res*. 2012; 2(2): 45–52.
9. Kothari LK, Gupta AS. Effect of ageing on the volume, structure and total Leydig cell content of the human testis. *Int J Fertil*. 1974; 19(3): 140–146, indexed in Pubmed: [4375123](#).
10. Mbaeri TU, Orakwe JC, Nwofor AM, et al. Accuracy of Prader orchidometer in measuring testicular volume. *Niger J Clin Pract*. 2013; 16(3): 348–351, doi: [10.4103/1119-3077.113460](#), indexed in Pubmed: [23771459](#).
11. Mbaeri TU, Orakwe JC, Nwofor A, et al. Ultrasound measurements of testicular volume: Comparing the three common formulas with the true testicular volume determined by water displacement. *Afr J Urol*. 2013; 19(2): 69–73, doi: [10.1016/j.afju.2012.11.004](#).
12. Sakamoto H, Ogawa Y, Yoshida H. Relationship between testicular volume and testicular function: comparison of the Prader orchidometric and ultrasonographic measurements in patients with infertility. *Asian J Androl*. 2008; 10(2): 319–324, doi: [10.1111/j.1745-7262.2008.00340.x](#), indexed in Pubmed: [18097521](#).
13. Sakamoto H, Saito K, Oohta M, et al. Testicular volume measurement: comparison of ultrasonography, orchidometry, and water displacement. *Urology*. 2007; 69(1): 152–157, doi: [10.1016/j.urology.2006.09.012](#), indexed in Pubmed: [17270639](#).
14. Takihara H, Cosentino MJ, Sakatoku J, et al. Significance of testicular size measurement in andrology: II. Correlation of testicular size with testicular function. *J Urol*. 1987; 137(3): 416–419, doi: [10.1016/s0022-5347\(17\)44053-5](#), indexed in Pubmed: [3102757](#).
15. Taskinen S, Taavitsainen M, Wikström S. Measurement of testicular volume: comparison of 3 different methods. *J Urol*. 1996; 155(3): 930–933, indexed in Pubmed: [8583610](#).
16. Tijani KH, Oyende BO, Awosanya GO, et al. Assessment of testicular volume: A comparison of fertile and sub-fertile West African men. *Afr J Urol*. 2014; 20(3): 136–140, doi: [10.1016/j.afju.2014.05.001](#).

# Histomorphometric evaluation of tibial subchondral bone after moderate running in male and female Wistar rats

M.N. Nazem<sup>1</sup>, M. Sahebozamani, R. Mosavian Naeini, S.M. Sajjadian

Shahid Bahonar University of Kerman, Iran

[Received: 7 May 20219; Accepted: 30 November 2019]

**Background:** Exercise has been shown to be beneficial to the skeleton, in both humans and animals. This study was done to test the sex-related difference in the risk of osteoarthritis (OA) of the knee joint and also on the subchondral bone after moderate running exercise.

**Materials and methods:** Forty male and female Wistar rats were randomly assigned to four equal groups (2 male and 2 female groups) in the same condition. Ten animals of each sex were selected as control groups, while running exercises were performed in remaining 20 male and female rats, using a motor treadmill to motivate rats to run daily distances of 1 km at 5 days/week within 6 weeks. On day 43, all animals were sacrificed and the knee articular cartilage and also histomorphometric parameters of subchondral bone and mid shaft of tibia were evaluated.

**Results:** Results showed mild OA in both male and female runner groups. Results in male runner rats were significantly lesser than that in female runners. On the other hand, the difference in female runner group showed significant changes in comparison with other groups in histomorphometric parameters in tibia.

**Conclusions:** Obtained results showed that the development of knee OA and subchondral bone changes may be related to the sex differences. Although there was no synovitis in male runners, female runner group showed mild hyperaemia dropsy with a moderate synovitis in this region. (Folia Morphol 2021; 80, 1: 127–132)

**Key words:** histomorphometry, running, subchondral bone, tibia, rat

## INTRODUCTION

According to human [7] and animal [12] studies, exercise and mechanical loading are beneficial to the skeleton. Despite the obvious effects of high mechanical loading on the skeleton, the capacity of skeleton to maintain the exercise-induced bone gain remains unknown [27].

Based on multiple studies with experimental models, increased mechanical loading or physical activity triggers bone formation and growth and has positive effects on the skeleton [9, 14, 29]. Studies show that

running exercise increases cortical and cancellous tibial bone mass in aged female rats [2].

The articular cartilage health is dependent on the mechanical features of its subchondral bone. It has been shown that bone changes are associated with osteoarthritis (OA) [25]. The architecture of subchondral metaphyseal bone is not uniform. The organisation of trabecular sheets is in a way that they can transfer stress from the overlying layers of articular cartilage, subchondral plate, and calcified cartilage to metaphyseal cortices [15, 18].

Address for correspondence: M.N. Nazem, Associate Professor of Anatomy, Histology and Embryology, Department of Basic Sciences, School of Veterinary Medicine, Shahid Bahonar University of Kerman, Pazhuhesh Square, Kerman, Iran. P.O. Box: 76169133, tel: +98 3431322954, fax: +98 3433257447, e-mail: nnazem@uk.ac.ir; nasernazem@yahoo.com

In this study, we aimed to evaluate the effects of moderate running exercise on the subchondral bone of tibia in the knee joint, histological assessment and grading of the synovial membrane changes and to conduct a histomorphometric assessment of the mid-shaft of tibia.

## MATERIALS AND METHODS

All procedures involving the experimental use of animals were approved by the Animal Ethics Committee, a branch of the Research Council of the Veterinary School in Shahid Bahonar University, Kerman Province, Iran.

Forty adult male and female Wistar rats (9–10 weeks of age) with no significant difference in their body weight ( $251.59 \pm 12.31$  g) were randomly divided into four equal groups. All rats were allowed a 5-day adaptation period in a room with controlled conditions (temperature 22–25°C and humidity 60–70%) before starting the experiment [28]. Ten animals of each sex were selected as male and female control groups while running exercises were performed in remaining 20 male and female rats for 6 weeks on a motor-driven rodent treadmill (Model T510, DRI Co., Taiyuan, Taiwan), speed of 20 m/min with inclination of 18° for 60 minutes each day on 5 days of every week.

During the exercise period, all animals were fed a standard diet (Javaneh Khorasan Co., Iran).

On day 43, all control and runner rats were sacrificed by overdose injection of pentobarbital sodium (100 mg/100 g body weight, intraperitoneal injection). The body weight was recorded. Then whole of both knee joints were taken and fixed in 10% buffered formaldehyde for 1 day and then was placed in a new solution of 10% buffered formaldehyde for 10 days. Decalcification in 10% formic acid solution was followed by embedding of the complete knee joints in this solution for 50 days. 5  $\mu$ m thickness serial sections of frontal whole left knee joint were prepared in order to obtain the thickest cartilage section from the lateral condyle of the tibia. Obtained thickest sections of each tibia were stained with haematoxylin-eosin method. Sections were evaluated using the Mankin's scheme [19]. We only differed safranin-O staining with haematoxylin-eosin method. The histological evaluation system for OA was classified into four categories: Mankin score of 0, no OA; Mankin scores of 1–5, mild OA; scores of 6–10, moderate OA; and scores of 11–14, severe OA [24]. In order to histological grading of synovial layer changes, Krenn et al.'s method was

used. Based on their results, 0 to 1 corresponds to no synovitis, 2 to 4 to a slight synovitis, 5 to 6 to a moderate synovitis, and 7 to 9 to a strong synovitis [16].

Histomorphometric analyses were taken on sections using method described by Renner et al. [26]. Thickness from subchondral bone to articular surface was measured at the middle of lateral condyle. In each section, chondrocyte cells were counted within a 120,000  $\mu$ m<sup>2</sup> area including both calcified layer and articular surface [26].

All right knee joints were opened and examined for gross knee articular surface evaluation.

On the other hand, the right tibia was dissected out. The tibia was cut into two equal parts. Thus, the proximal half of tibia was collected. The samples were proceeding similar to the left ones. Serial longitudinal sections were cut with a rotary microtome and mounted on saline-coated slides glass after preparation of histological specimens. Before staining, the sections were deparaffinised in 100% xylene and rehydrated in graded ethanol [1]. The longitudinal sections of the proximal tibia, between medial and lateral intercondyloid spines, and transverse sections of the mid shaft of tibia were cut at 5- $\mu$ m thickness with a microtome.

Histomorphometric measurements of the cancellous bone of the proximal tibia and the cortical bone of the tibial shaft were examined using an Olympus light microscope and photomicrographs were taken by an attached eyepiece camera (Dino-eye, AM-7023, 5Mp, Taiwan) on 40 $\times$  and 100 $\times$  magnification. Ten random fields were selected in each slide.

Histomorphometric parameters were described according to the American Society for Bone and Mineral Research nomenclature committee [30].

The histomorphometric parameters evaluated for cancellous bone were bone volume (BV; the percentage of occupied area by calcified bone in relation to the total area), ratio of BV to TV which included trabecular bone volume (BV/TV), trabecular number (TbN; number of trabeculae that a line through a trabecular compartment would hit per millimetre of its length), trabecular thickness (TbTh; the thickness of 40 complete trabecular bone packet on straight, rod-like trabecular structures in each section), osteoblast surface (ObS/BS; per cent of bone surface occupied by osteoblasts and osteoclast surface (OcS/BS; per cent of bone surface occupied by osteoclasts) [17, 30].

The histomorphometric parameters evaluated for tibial shaft were total tissue area (Tt Ar), marrow cavity area (Mc Ar) and cortical bone area (Cb Ar). These pa-

**Table 1.** The changes (mean  $\pm$  standard error) of weight (g) at the first day and end day of the exercise period

Groups		First day of exercise	End day of exercise
Control	Male	254.14 $\pm$ 18.54	256.2 $\pm$ 16.82
	Female	248.32 $\pm$ 12.32	254.14 $\pm$ 14.81
Runner	Male	253.32 $\pm$ 21.08	241.37 $\pm$ 17.03
	Female	249.23 $\pm$ 16.01 <sup>a</sup>	230.08 $\pm$ 17.01 <sup>b</sup>

<sup>a, b</sup>In the same row with no common superscript show significant difference ( $p < 0.05$ ).

**Table 2.** Mankin's histopathology and synovial gradings (mean  $\pm$  standard error) of distal extremity of lateral condyle of tibia

	Male		Female	
	Control	Runner	Control	Runner
Mankin*	0 <sup>a</sup>	1.02 $\pm$ 0.38 <sup>a</sup>	0 <sup>a</sup>	5.12 $\pm$ 0.89 <sup>b</sup>
Synovial layer**	0 <sup>a</sup>	0.8 $\pm$ 0.36 <sup>a</sup>	0 <sup>a</sup>	5.21 $\pm$ 0.32 <sup>b</sup>

<sup>a, b</sup>In the same row with no common superscript show significant difference ( $p < 0.05$ ), \*0: No osteoarthritis; 1–5: Mild osteoarthritis; 6–10: Moderate osteoarthritis; 11–14: Severe osteoarthritis, \*\*0 to 1 corresponds to no synovitis, 2 to 4 to a slight synovitis, 5 to 6 to a moderate synovitis, and 7 to 9 to a strong synovitis.

**Table 3.** Bone histomorphometry (mean  $\pm$  standard error) of cancellous and cortical parts of tibia

	Male		Female	
	Control	Runner	Control	Runner
<b>Cancellous part</b>				
TbN	6.75 $\pm$ 0.75 <sup>a</sup>	10.43 $\pm$ 0.75 <sup>b</sup>	7.25 $\pm$ 0.63 <sup>a</sup>	19.25 $\pm$ 0.75 <sup>c</sup>
TbTh [ $\mu$ m]	43.32 $\pm$ 5.47 <sup>a, b</sup>	46.54 $\pm$ 4.7 <sup>a, b</sup>	39.41 $\pm$ 4.01 <sup>a</sup>	54.93 $\pm$ 4.86 <sup>b</sup>
BV/TV [%]	58.32 $\pm$ 5.71 <sup>a</sup>	60.3 $\pm$ 5.32 <sup>a</sup>	55.43 $\pm$ 4.91 <sup>a</sup>	72.83 $\pm$ 6.32 <sup>b</sup>
OcS/BS [%]	8.42 $\pm$ 0.6 <sup>a</sup>	8.12 $\pm$ 0.52 <sup>a, b</sup>	8.51 $\pm$ 0.61 <sup>a</sup>	7.82 $\pm$ 0.42 <sup>b</sup>
ObS/BS [%]	53.41 $\pm$ 5.12 <sup>a</sup>	56.02 $\pm$ 4.01 <sup>a, b</sup>	51.07 $\pm$ 4.92 <sup>a</sup>	62.41 $\pm$ 3.12 <sup>b</sup>
<b>Cortical part</b>				
Tt Ar [mm <sup>2</sup> ]	541.48 $\pm$ 27.32 <sup>a, b</sup>	558.92 $\pm$ 31.27 <sup>a, b</sup>	524.61 $\pm$ 19.27 <sup>a</sup>	561.58 $\pm$ 23.97 <sup>b</sup>
Mc Ar [mm <sup>2</sup> ]	172.11 $\pm$ 10.27 <sup>a, c</sup>	161.92 $\pm$ 9.81 <sup>a</sup>	180.01 $\pm$ 14.31 <sup>bc</sup>	161.14 $\pm$ 9.97 <sup>a</sup>
Cb Ar [mm <sup>2</sup> ]	328.31 $\pm$ 24.03 <sup>a, b</sup>	333.12 $\pm$ 19.81 <sup>a, b</sup>	312.42 $\pm$ 16.81 <sup>a</sup>	348.91 $\pm$ 23.14 <sup>b</sup>

The abbreviations are mentioned in material and methods. <sup>a, b, c</sup> In the same row with no common superscript show significant difference ( $p < 0.05$ ).

rameters were chosen based on a previous study [1]. The results were obtained by using an Olympus light microscope and an attached eyepiece digital lens (Dino-eye, AM-7023, 5Mp, Taiwan).

### Statistical analysis

Results were expressed as means  $\pm$  standard error using the software SPSS 16 (version 16, Chicago, USA). Statistical analysis was carried out using an independent T-test and one-way ANOVA. Also the Tukey's test was used for post hoc analysis with significance set at  $p < 0.05$ .

## RESULTS

### Weight

In the female exercise group, body weight decreased markedly, compared to the control group at the end of the intervention (Table 1).

### Bone histomorphometry and histopathology

**Knee joint: Gross findings.** The surface of the femoral cartilage was found to be smooth in both

female and male control groups, whereas in four male runner rats, the articular surface was irregular after the sixth week. In the female exercise group, superficial cartilage irregularities were detected in the trochlea and femoral condyles.

### Histological finding

Our findings were indicative of mild OA in both female and male exercise groups. The results in male runner rats were less significant than those of female runners (Table 2).

Based on the findings, the synovial layer was normal in both female and male control groups. Most male runner rats in the control group had a normal condition.

There was no synovitis in male runners. However, the synovial joint seemed almost coarse and thick in the female runner group, with mild hyperaemia dropsy. There was also a moderate synovitis in this group (Table 2).

In the female exercise group, OcS/BS% was found to be significantly lower than that of the female control group (Table 3).

In the female runner group, ObS/BS% showed a significant increase compared to the female controls (Table 3).

The trabecular number (TbN) increased significantly in both female and male exercise groups, compared to the controls. On the other hand, the trabecular thickness (Tt Ar) difference between female runner and control rats was significant (Table 3).

The BV/TV ratio was higher in male and female exercise groups, compared to the corresponding control groups. The difference between female runner rats was significant (Table 3).

A greater total tissue area (Tt Ar) and a smaller marrow cavity area (Mc Ar) were found in both exercise groups, compared to the controls. The difference between the control and runner female groups was significant (Table 3). On the other hand, the cortical bone area (Cb Ar) was significantly greater in the female exercise group in comparison with the corresponding control group (Table 3).

## DISCUSSION

In the present study, moderate-intensity running was found to damage the articular cartilage; therefore, it is considered a strenuous exercise, especially for females. Based on our findings, in moderate-intensity exercise, women experience more cartilage changes, compared to men with a similar body weight. According to previous research, the cartilage volume of normal men is 33% to 42% larger than that of normal women, as indicated in radiographic analyses [3].

Moreover, Jones et al. [13] showed that the knee cartilage of men is significantly more than that of females. It was concluded that sex differences in cartilage development could explain the variations in OA of the knee in later stages of life. In addition, Faber et al. [6] reported that after adjustments for height and body weight, gender differences did not influence cartilage volume. Nevertheless, it was reported that body and bone size had significant effects on this difference, suggesting a direct relationship between cartilage volume and bone size [5, 13].

Evidence suggests the thicker cartilage of men, compared to women [22]. In contrast, no gender-related effects have been reported after adjustments for body weight and tibial head diameter [4]. Some significant changes were detected in rats with matching age and body weight; therefore, other parameters might explain gender differences

Previous studies show that running exercise decreases fat mass [7, 20]. Our obtained weight results were similar to this study.

The main bone function is to bear gravity-induced mechanical forces and muscle contraction and to facilitate efficient body locomotion [23]. In a study by Iwamoto et al. [11], to preserve the positive effects of exercise (for 8 weeks), continuous exercise was found to be necessary. To explain the mechanism through which exercise leads to increased bone mass on histomorphometry, Yeh et al. [31] showed that suppressed bone resorption and improved bone formation might be responsible for the positive effects of exercise on the cancellous bones of tibia in aged female rats. Moreover, Chen et al. [2] showed that exercise leads to cortical bone mass accumulation in the tibia of aged female rats. Our data demonstrated that moderate running exercise resulted in significant increases in both cancellous and cortical bone mass (BV/TV and Ct Ar, respectively) in a weight-bearing long bone, the tibia, in the female rats. The results of OcS/BS and ObS/BS percentage in female rats indicated that the response of cancellous bone to exercise differs according to the magnitude of mechanical loading to the bone. There is a threshold in mechanical loading to the bones when cancellous bone mass increases, with bone formation exceeding bone resorption (Table 3). These findings are consistent with the researchers' hypothesis [10, 11].

Joint tissues can sustain minimal damage without progressive change. It is known that cumulative micro-damage can lead to bone remodelling, stiffening, and cartilage lesion progression. Peak dynamic forces applied at a high rate cause subchondral bone remodelling and stiffening [8]. In this study, cortical and cancellous bone areas increased significantly in the tibia due to exercise. It should be noted that exercise duration and intensity were probably ideal for increasing cancellous bone mass in our study. Our results also demonstrated that the effect of exercise in females was more significant than males.

In a previous study, it was reported that moderate running exercise significantly increased cortical and cancellous bone mass in tibia [11]; our findings are in consistence with this study. This finding might be attributed to the position of tibia and mechanical loading on the tibia during treadmill running [11, 21]. Moreover, Chang et al. [1] showed that the cancellous bone response to exercise changes relative to the bone mechanical loading. This finding is consistent

with a previous study, which indicated the positive site-specific effect of treadmill exercise on bone mineral density, with predominant weight-bearing sites [11].

## CONCLUSIONS

Our results showed the moderate exercises are more harmful in females than males. Also subchondral bone changes in females may be more visible than in males.

## Acknowledgements

This research was financially supported by the research council of Shahid Bahonar University of Kerman (No: 1.7.1395). The authors would like to thank Mr. Mazhab Jaafari for providing histological laboratory methods and histology slides. The authors declared no conflict of interests.

## REFERENCES

- Chang TK, Huang CH, Huang CH, et al. The influence of long-term treadmill exercise on bone mass and articular cartilage in ovariectomized rats. *BMC Musculoskelet Disord.* 2010; 11: 185, doi: [10.1186/1471-2474-11-185](https://doi.org/10.1186/1471-2474-11-185), indexed in Pubmed: [20727126](https://pubmed.ncbi.nlm.nih.gov/20727126/).
- Chen MM, Yeh JK, Aloia JF, et al. Effect of treadmill exercise on tibial cortical bone in aged female rats: a histomorphometry and dual energy x-ray absorptiometry study. *Bone.* 1994; 15(3): 313–319, doi: [10.1016/8756-3282\(94\)90294-1](https://doi.org/10.1016/8756-3282(94)90294-1), indexed in Pubmed: [8068453](https://pubmed.ncbi.nlm.nih.gov/8068453/).
- Ding C, Cicuttini F, Scott F, et al. Sex differences in knee cartilage volume in adults: role of body and bone size, age and physical activity. *Rheumatology (Oxford).* 2003; 42(11): 1317–1323, doi: [10.1093/rheumatology/keg374](https://doi.org/10.1093/rheumatology/keg374), indexed in Pubmed: [12810930](https://pubmed.ncbi.nlm.nih.gov/12810930/).
- Eckstein F, Cicuttini F, Raynauld JP, et al. Magnetic resonance imaging (MRI) of articular cartilage in knee osteoarthritis (OA): morphological assessment. *Osteoarthritis Cartilage.* 2006; 14 Suppl A: A46–A75, doi: [10.1016/j.joca.2006.02.026](https://doi.org/10.1016/j.joca.2006.02.026), indexed in Pubmed: [16713720](https://pubmed.ncbi.nlm.nih.gov/16713720/).
- Eckstein F, Winzheimer M, Hohe J, et al. Interindividual variability and correlation among morphological parameters of knee joint cartilage plates: analysis with three-dimensional MR imaging. *Osteoarthr Cartil.* 2001; 9(2): 101–111, doi: [10.1053/joca.2000.0365](https://doi.org/10.1053/joca.2000.0365), indexed in Pubmed: [11237657](https://pubmed.ncbi.nlm.nih.gov/11237657/).
- Faber SC, Eckstein F, Lukas S, et al. Gender differences in knee joint cartilage thickness, volume and articular surface areas: assessment with quantitative three-dimensional MR imaging. *Skeletal Radiol.* 2001; 30(3): 144–150, doi: [10.1007/s002560000320](https://doi.org/10.1007/s002560000320), indexed in Pubmed: [11357452](https://pubmed.ncbi.nlm.nih.gov/11357452/).
- Howe T, Shea B, Dawson LJ, et al. Exercise for preventing and treating osteoporosis in postmenopausal women. *Cochrane Data Sys Rev.* 2015; 6(7): CD000333, doi: [10.1002/14651858.CD000333.pub2](https://doi.org/10.1002/14651858.CD000333.pub2), indexed in Pubmed: [21735380](https://pubmed.ncbi.nlm.nih.gov/21735380/).
- Hudelmaier M, Glaser C, Hausschild A, et al. Effects of joint unloading and reloading on human cartilage morphology and function, muscle cross-sectional areas, and bone density: a quantitative case report. *J Musculoskelet Neuronal Interact.* 2006; 6(3): 284–290, indexed in Pubmed: [17142951](https://pubmed.ncbi.nlm.nih.gov/17142951/).
- Iwamoto J, Sato Y, Takeda T, et al. Effectiveness of exercise for osteoarthritis of the knee: a review of the literature. *World J Orthop.* 2011; 2(5): 37–42, doi: [10.5312/wjo.v2.i5.37](https://doi.org/10.5312/wjo.v2.i5.37), indexed in Pubmed: [22474634](https://pubmed.ncbi.nlm.nih.gov/22474634/).
- Iwamoto J, Takeda T, Ichimura S. Effect of exercise on tibial and lumbar vertebral bone mass in mature osteopenic rats: bone histomorphometry study. *J Orthop Sci.* 1998; 3(5): 257–263, doi: [10.1007/s007760050051](https://doi.org/10.1007/s007760050051), indexed in Pubmed: [9732560](https://pubmed.ncbi.nlm.nih.gov/9732560/).
- Iwamoto J, Yeh JK, Aloia JF, et al. Effect of deconditioning on cortical and cancellous bone growth in the exercise trained young rats. *J Bone Miner Res.* 2000; 15(9): 1842–1849, doi: [10.1359/jbmr.2000.15.9.1842](https://doi.org/10.1359/jbmr.2000.15.9.1842), indexed in Pubmed: [10977004](https://pubmed.ncbi.nlm.nih.gov/10977004/).
- Järvinen TL, Kannus P, Sievänen H, et al. Effects of remobilization on rat femur are dose-dependent. *Scand J Med Sci Sports.* 2001; 11(5): 292–298, doi: [10.1034/j.1600-0838.2001.110507.x](https://doi.org/10.1034/j.1600-0838.2001.110507.x), indexed in Pubmed: [11696214](https://pubmed.ncbi.nlm.nih.gov/11696214/).
- Jones G, Glisson M, Hynes K, et al. Sex and site differences in cartilage development: a possible explanation for variations in knee osteoarthritis in later life. *Arthritis Rheum.* 2000; 43(11): 2543–2549, doi: [10.1002/1529-0131\(200011\)43:11<2543::AID-AN-R23>3.0.CO;2-K](https://doi.org/10.1002/1529-0131(200011)43:11<2543::AID-AN-R23>3.0.CO;2-K), indexed in Pubmed: [11083279](https://pubmed.ncbi.nlm.nih.gov/11083279/).
- Joo YI, Sone T, Fukunaga M, et al. Effects of endurance exercise on three-dimensional trabecular bone microarchitecture in young growing rats. *Bone.* 2003; 33(4): 485–493, doi: [10.1016/s8756-3282\(03\)00212-6](https://doi.org/10.1016/s8756-3282(03)00212-6), indexed in Pubmed: [14555251](https://pubmed.ncbi.nlm.nih.gov/14555251/).
- Kenneth D, Brandt M. Osteoarthritis. In: Kasper, Braunwald, Fauci, Hauser, Longo, Jameson, Editors: *Harrison's principles of internal medicine.* 15th ed. USA. Bmc Graw – Hill Incl, USA 2005: 2036–2045.
- Krenn V, Morawietz L, Häupl T, et al. Grading of chronic synovitis — a histopathological grading system for molecular and diagnostic pathology. *Path Res Pract.* 2002; 198(5): 317–325, doi: [10.1078/0344-0338-5710261](https://doi.org/10.1078/0344-0338-5710261).
- Kulak CA, Dempster DW. Bone histomorphometry: a concise review for endocrinologists and clinicians. *Arq Bras Endocrinol Metabol.* 2010; 54(2): 87–98, doi: [10.1590/s0004-27302010000200002](https://doi.org/10.1590/s0004-27302010000200002), indexed in Pubmed: [20485895](https://pubmed.ncbi.nlm.nih.gov/20485895/).
- Lee YJ, Park JiAh, Yang SH, et al. Evaluation of osteoarthritis induced by treadmill-running exercise using the modified Mankin and the new OARSI assessment system. *Rheumatol Int.* 2011; 31(12): 1571–1576, doi: [10.1007/s00296-010-1520-4](https://doi.org/10.1007/s00296-010-1520-4), indexed in Pubmed: [20490805](https://pubmed.ncbi.nlm.nih.gov/20490805/).
- Mankin H, Dorfman H, Lippiello L, et al. Biochemical and metabolic abnormalities in articular cartilage from osteo-arthritic human hips. *J Bone Joint Surg Am.* 1971; 53(3): 523–537, doi: [10.2106/00004623-197153030-00009](https://doi.org/10.2106/00004623-197153030-00009).
- Morseth B, Emaus N, Jørgensen L. Physical activity and bone: The importance of the various mechanical stimuli

- for bone mineral density. A review. *Norsk Epidemiologi*. 2011; 20(2), doi: [10.5324/nje.v20i2.1338](https://doi.org/10.5324/nje.v20i2.1338).
21. Mosavian NR, Sahebozamani M, Nazem MN. Effect of moderate treadmill exercise on hip osteoarthritis in male and female Wistar rats. *Novel Biomed*. 2017; 4: 177–184.
  22. Ni GX, Zhan LQ, Gao MQ, et al. Matrix metalloproteinase-3 inhibitor retards treadmill running-induced cartilage degradation in rats. *Arthritis Res Ther*. 2011; 13(6): R192, doi: [10.1186/ar3521](https://doi.org/10.1186/ar3521), indexed in Pubmed: [22114772](https://pubmed.ncbi.nlm.nih.gov/22114772/).
  23. Pajamäki I, Kannus P, Vuohelainen T, et al. The bone gain induced by exercise in puberty is not preserved through a virtually life-long deconditioning: a randomized controlled experimental study in male rats. *J Bone Miner Res*. 2003; 18(3): 544–552, doi: [10.1359/jbmr.2003.18.3.544](https://doi.org/10.1359/jbmr.2003.18.3.544), indexed in Pubmed: [12619940](https://pubmed.ncbi.nlm.nih.gov/12619940/).
  24. Pap G, Eberhardt R, Stürmer I, et al. Development of osteoarthritis in the knee joints of Wistar rats after strenuous running exercise in a running wheel by intracranial self-stimulation. *Path Res Pract*. 1998; 194(1): 41–47, doi: [10.1016/s0344-0338\(98\)80010-1](https://doi.org/10.1016/s0344-0338(98)80010-1).
  25. Radin EL, Rose RM. Role of subchondral bone in the initiation and progression of cartilage damage. *Clin Orthop Relat Res*. 1986(213): 34–40, indexed in Pubmed: [3780104](https://pubmed.ncbi.nlm.nih.gov/3780104/).
  26. Renner AF, Carvalho E, Soares E, et al. The effect of a passive muscle stretching protocol on the articular cartilage. *Osteoarthr Cartil*. 2006; 14(2): 196–202, doi: [10.1016/j.joca.2005.08.011](https://doi.org/10.1016/j.joca.2005.08.011), indexed in Pubmed: [16243547](https://pubmed.ncbi.nlm.nih.gov/16243547/).
  27. Seeman E. An exercise in geometry. *J Bone Miner Res*. 2002; 17(3): 373–380, doi: [10.1359/jbmr.2002.17.3.373](https://doi.org/10.1359/jbmr.2002.17.3.373), indexed in Pubmed: [11874229](https://pubmed.ncbi.nlm.nih.gov/11874229/).
  28. Seyyedini S, Nazem MN. Histomorphometric study of the effect of methionine on small intestine parameters in rat: an applied histologic study. *Folia Morphol*. 2017; 76(4): 620–629, doi: [10.5603/fm.a2017.0044](https://doi.org/10.5603/fm.a2017.0044), indexed in Pubmed: [28553855](https://pubmed.ncbi.nlm.nih.gov/28553855/).
  29. Tromp AM, Bravenboer N, Tanck E, et al. Additional weight bearing during exercise and estrogen in the rat: the effect on bone mass, turnover, and structure. *Calcif Tissue Int*. 2006; 79(6): 404–415, doi: [10.1007/s00223-006-0045-z](https://doi.org/10.1007/s00223-006-0045-z), indexed in Pubmed: [17160577](https://pubmed.ncbi.nlm.nih.gov/17160577/).
  30. Vidal B, Pinto A, Galvão MJ, et al. Bone histomorphometry revisited. *Acta Reumatol Port*. 2012; 37(4): 294–300, indexed in Pubmed: [24126421](https://pubmed.ncbi.nlm.nih.gov/24126421/).
  31. Yeh J, Aloia J, Chen M, et al. Influence of exercise on cancellous bone of the aged female rat. *J Bone Miner Res*. 1993; 8(9): 1117–1125, doi: [10.1002/jbmr.5650080913](https://doi.org/10.1002/jbmr.5650080913).



# Arthrogenic human synovial cysts: immunohistochemical profile of interleukin-1beta, interleukin-6, tumour necrosis factor-alpha

S. Taurone<sup>1\*</sup>, M.T. Santarelli<sup>1\*</sup>, C. De Ponte<sup>1</sup>, L. Bardella<sup>2</sup>, M. Ralli<sup>1</sup>, C. Morselli<sup>1</sup>, A. Nicolai<sup>1</sup>, A. Greco<sup>1</sup>, A. Ferretti<sup>3\*</sup>, M. Artico<sup>1\*</sup>

<sup>1</sup>Department of Sensory Organs, “Sapienza” University of Rome, Italy

<sup>2</sup>Department of Human Neurosciences, “Sapienza” University of Rome, Italy

<sup>3</sup>Orthopaedic Unit and Kirk Kilgour Sports Injury Centre, Sant’Andrea Hospital, “Sapienza” University of Rome, Italy

[Received: 28 October 2019; Accepted: 28 November 2019]

**Background:** Synovial cysts are currently classified as degenerative lesions affecting the joint capsule or adjacent structures.

**Materials and methods:** In our study we describe the results obtained in an immunohistochemical study comprising 18 patients with synovial cysts, performed to evaluate the pathophysiological role of some inflammatory cytokines such as: interleukin (IL)-1 $\beta$ , IL-6 and tumour necrosis factor-alpha (TNF- $\alpha$ ).

**Results:** Results showed an over-expression of TNF- $\alpha$ , IL-1 $\beta$  and IL-6 which appears to be involved in the onset and progression of the disease. At the present time it is not possible to affirm that these molecules play a direct role also due to the absence of further and more specific investigations. The authors therefore hypothesize that inhibition of inflammation may have a significant role in the pathogenesis and regression of synovial cysts.

**Conclusions:** Hence, these inflammatory cytokines may be considered potential therapeutic targets. The development of synthetic inhibitors of these inflammatory factors could lead to a reduction in the intensity of inflammation, thus inhibiting the onset and development of the disease. (Folia Morphol 2021; 80, 1: 133–139)

**Key words:** interleukins 1beta and 6, immunohistochemistry, synovial cysts, tumour necrosis factor-alpha

## INTRODUCTION

Synovial cysts (also known as “ganglion”, “synovial ganglion”, “arthrogenic cysts”) are benign neo-formations of the soft tissues which generally originate from the joint capsule or tendon sheath and contain fluid gelatinous material, usually appearing on the back of the wrist. Sometimes these cysts may involve neural structures, as in cases of peroneal nerve [1] or lumbar roots [11] involvement.

Arthrogenic cysts are cysts that occur at the level of the joint capsule. The most frequent location is at

the wrist. Since the joints are completely wrapped in a fibrous tissue (capsule) that favours the movements’ fluidity, a thinner capsular wall is responsible for a possible traumatic damage and so the cyst may develop in the joint. A herniation of the capsule occurs and it tends to move towards the superficial tissues and to form a revolving structure that we call cysts [4, 5].

The mechanism that gives rise to these cysts is still not clear. Synovial cysts are mostly found in young athletes or workers who use the wrist and hand joints a lot. In many cases synovial cysts are the result of joint

Address for correspondence: S. Taurone, PhD, Department of Sensory Organs, “Sapienza” University of Rome, V.le del Policlinico 155, 00161 Rome, Italy, tel/fax: 0649918054, e-mail: t.samanta@yahoo.it

\*Equally contributing

inflammation, arthrosis or previous trauma. However, the exact role of inflammation in this process has not yet been studied in detail. The synovial fluid contains inflammatory factors such as cytokines, prostaglandins and proteases. Previous studies have shown that angiogenic factors are released during the formation of the synovial cysts, suggesting a possible correlation between the proliferation of new vessels in synovial structures and the chronic inflammatory process that induces the progression of synovial cysts [10, 11, 13]. However, to date, no previous studies have analysed the modulation of the inflammatory process in the regression of synovial cysts. It has been shown that in the spinal joint tissue the induction of type 2 cyclooxygenases (COX-2) and phospholipase A2 stimulates the biosynthesis of different inflammatory mediators from synovial chondrocytes (chondrocytes from synovial joints), such as prostaglandin E2, interleukins (IL-1, IL-6, IL-8) and granulocyte-macrophage colony-stimulating factor (GM-CSF) [2]. COX-2 inhibitors have been shown to reduce synovitis, leukocyte infiltration and synovial hyperplasia in animal models, reducing the expression of IL-1 $\beta$ , IL-6 and tumour necrosis factor- $\alpha$  (TNF- $\alpha$ ) [7, 8]. Our study is based on previous experimental data that support the role played by inflammatory cytokines and growth factors in the development of arthrogenic synovial cysts. In the light of the data reported in the literature we hypothesize that inhibition of inflammation may play a significant role in the destiny and/or regression of arthrogenic synovial cysts. The aim of the present study was to evaluate the pathophysiological role of some inflammatory cytokines, such as IL-1 $\beta$ , IL-6 and TNF- $\alpha$ , in tissue samples of synovial cysts or tenosynovitis, obtained by surgical removal near a wrist joint. The main purpose of this was to evaluate the expression levels and localisation of inflammatory cytokines by immunohistochemical analysis to identify their involvement in the pathology and to evaluate the possible modulation of these factors as a potential therapeutic target.

## MATERIALS AND METHODS

### Clinical evaluation

Written informed consent concerning the donation of human tissues was provided by patients prior to tissue acquisition, following the protocol for the acquisition of human tissues of the Ethical Committee of our University Hospitals which approved the study protocol. All specimens were acquired according to the principles of the Helsinki Declaration.

Eighteen patients were included in the study, aged between 11 and 56 years (11 males and 7 females), undergoing surgical treatment for the removal of wrist synovial cysts, in the Orthopaedic Unit of the S. Andrea Hospital in Rome. Control samples (two specimens for each tissue fragment), characterised by normal palmar fascia tissues, were collected from patients undergoing hand surgery for carpal tunnel syndrome.

Patients with concomitant neoplastic, infectious, autoimmune diseases, peripheral vascular disorders or who had received anti-inflammatory therapy in the 6 months prior to the operation were excluded.

During excision, apart from anaesthesia, no other chemical products or pharmaceutical drugs were administered to the patients. Samples were fixed in formalin and embedded in paraffin to be processed for histological staining and immunohistochemistry. The sections were subjected to haematoxylin and eosin and Masson's trichromic staining.

### Immunohistochemistry

The immunohistochemical analysis was conducted using the ABC/HRP technique (avidin complexed with biotinylated peroxidase) on 4  $\mu$ m thick paraffin sections which were cut using a rotative microtome. These sections were deparaffinized and hydrated through decreasing ethanol series to distilled water, then subjected to microwave irradiation and immersed in citrate buffer (pH = 6) twice for 5 min each time. Subsequently, endogenous peroxidase activity was quenched using 0.3% hydrogenous peroxide in methanol for 30 min. To evaluate the immunolocalization of IL-1 $\beta$ , TNF- $\alpha$  and IL-6, the following antibodies were employed: i) rabbit anti-IL-1 $\beta$  polyclonal antibody (1:50, Santa Cruz Biotechnology, Santa Cruz, CA, USA); ii) mouse anti-TNF- $\alpha$  monoclonal antibody (1:100, Santa Cruz Biotechnology, Santa Cruz, CA, USA); iii) rabbit anti-IL-6 polyclonal antibody (1:200; Santa Cruz Biotechnology, Santa Cruz, CA, USA). Incubation with the primary antibodies was performed overnight at 4°C. Optimal antibody dilution and incubation times were assessed in preliminary experiments. As negative control, the primary antibodies were omitted. After exposure to the primary antibodies all slides were rinsed twice in phosphate buffer (pH = 7.4) and incubated for 1 hour with the appropriate secondary biotinylated antibody at the final dilution of 1:200. The secondary biotinylated antibodies against rabbit and mouse immunoglobulins were

purchased from Abcam (biotinylated goat anti-mouse antibody and biotinylated goat anti-rabbit antibody). The slides were then incubated with peroxidase-conjugated avidin (Vector Laboratories, Burlingame, CA, USA, Vectastain Elite ABC kit Standard\*PK 6-100) for 30 min. Slides were washed in phosphate buffer (pH = 7.4) and treated with 0.05% 3,3-diaminobenzidine (DAB) and 0.1% H<sub>2</sub>O<sub>2</sub>. Finally, sections were counterstained with Mayer's haematoxylin and dehydrated rapidly. The staining assessment was made by three experts. The intensity of the immune reaction was assessed microdensitometrically using an IAS 2000 image analyser (Delta Sistemi, Rome, Italy) connected via a TV camera to the microscope. Twelve 100  $\mu$ m<sup>2</sup> areas were delineated in each section by measuring the diaphragm. The system was calibrated taking the background obtained in sections exposed to non-immune serum as zero.

### Statistical analysis

Statistical analysis was performed with the Student's t-test, using the GraphPad Prism (La Jolla, CA). A p-value < 0.05 was considered for statistical significance.

## RESULTS

The histopathological alterations caused by human arthrogenic synovial cysts were evaluated using

**Table 1.** Expression levels of interleukin-1beta (IL-1 $\beta$ ), interleukin-6 (IL-6), tumour necrosis factor-alpha (TNF- $\alpha$ ) in synovial cysts and control specimens, and respective levels of statistical significance (t-test)

	Synovial cysts (%); n = 15	Control specimens (%); n = 15	P-value
IL-1 $\beta$	65.27 $\pm$ 12.91	12.61 $\pm$ 5.51	< 0.00001
IL-6	60.46 $\pm$ 10.70	11.66 $\pm$ 4.96	< 0.00001
TNF- $\alpha$	61.80 $\pm$ 10.22	13.13 $\pm$ 5.81	< 0.00001

The results were considered as statistically significant when p-value < 0.05.

the immunohistochemical technique. Immunohistochemical experiments have made it possible to visualise the distribution and localization of the cytokines analysed in the tissue samples obtained by surgical removal from patients with arthrogenic synovial cysts (Table 1). Through haematoxylin/eosin staining it was possible to detect, in the pathological tissues, the myo-fibroblastic proliferation site (Fig. A1–A3), not present in the control tissue (Fig. A4). In the pathological tissue (Fig. A1–A3) a thickening of fibroblasts and myo-fibroblasts was visible with areas of complete cellular overlapping. This tissue morphology is not present in normal tissue (Fig. A4), in which only connective tissue with dispersed fibroblasts and small blood vessels can be observed. Figures B1–B3 describe the immunohistochemical expression of

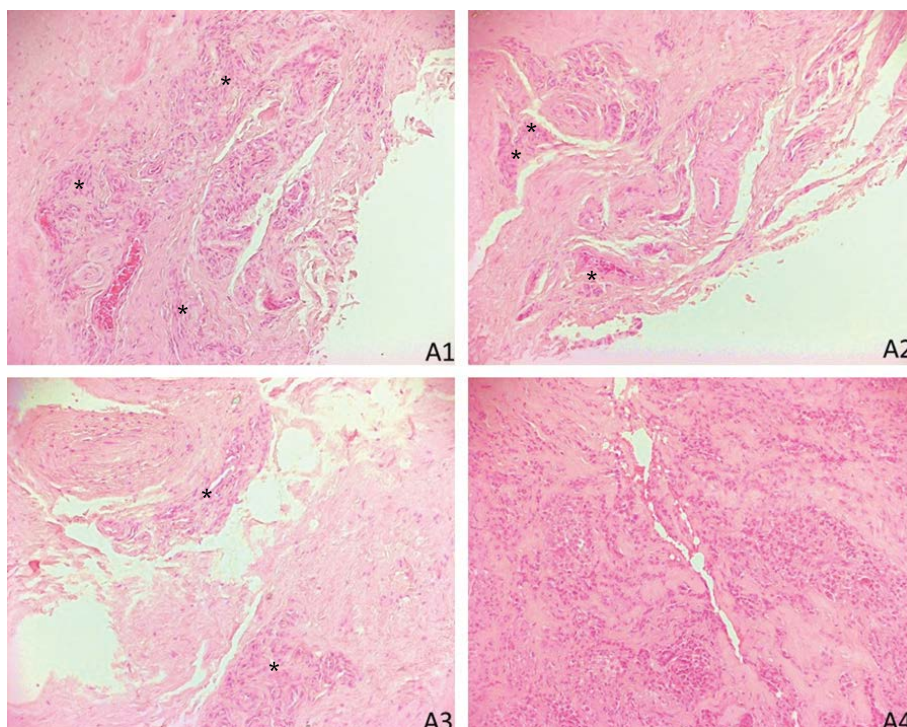


**Figure A.** Photomicrograph of histological preparations obtained by the haematoxylin/eosin staining method; **A1–A3.** Proliferation myofibroblast nodules (asterisks) obtained by surgical removal from a patient with synovial cyst (10 $\times$ ); **A4.** Normal palmar band consisting exclusively of connective tissue with fibroblasts and blood vessels (10 $\times$ ).

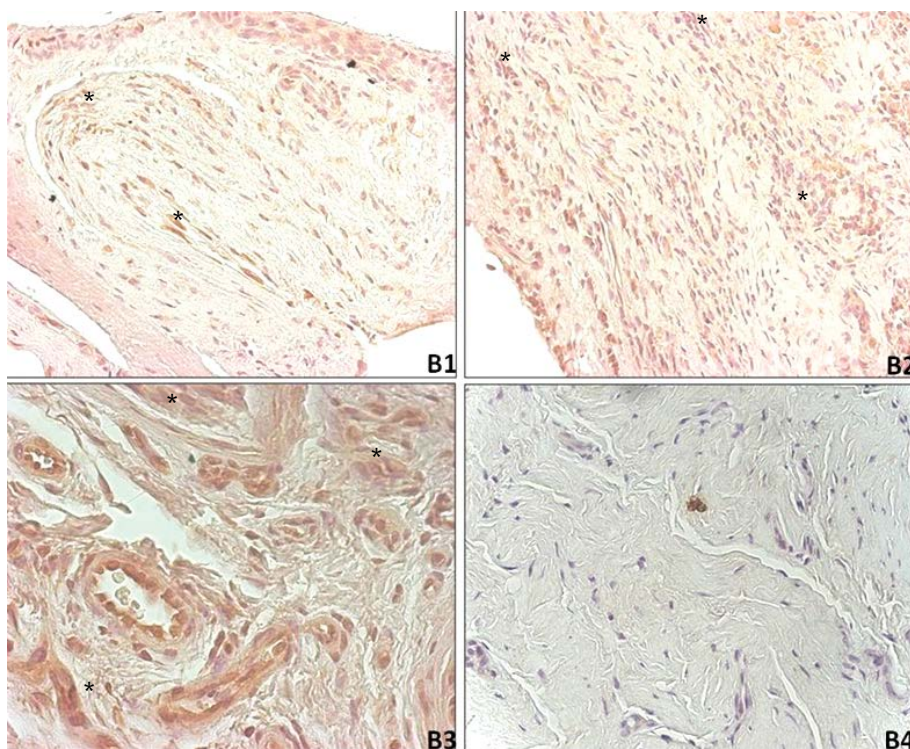


**Figure B.** Photomicrographs of the immunohistochemical reaction for the inflammatory cytokine interleukin-1beta (IL-1 $\beta$ ); **B1–B3.** Pathological tissue in which IL-1 $\beta$  is present in the extracellular matrix and in the cytoplasm of fibroblasts and myofibroblasts and in the endothelium of capillaries (B1, B2, 20 $\times$ ; B3, 40 $\times$ ). Myofibroblasts nodules (asterisks); **B4.** Control tissue (20 $\times$ ).

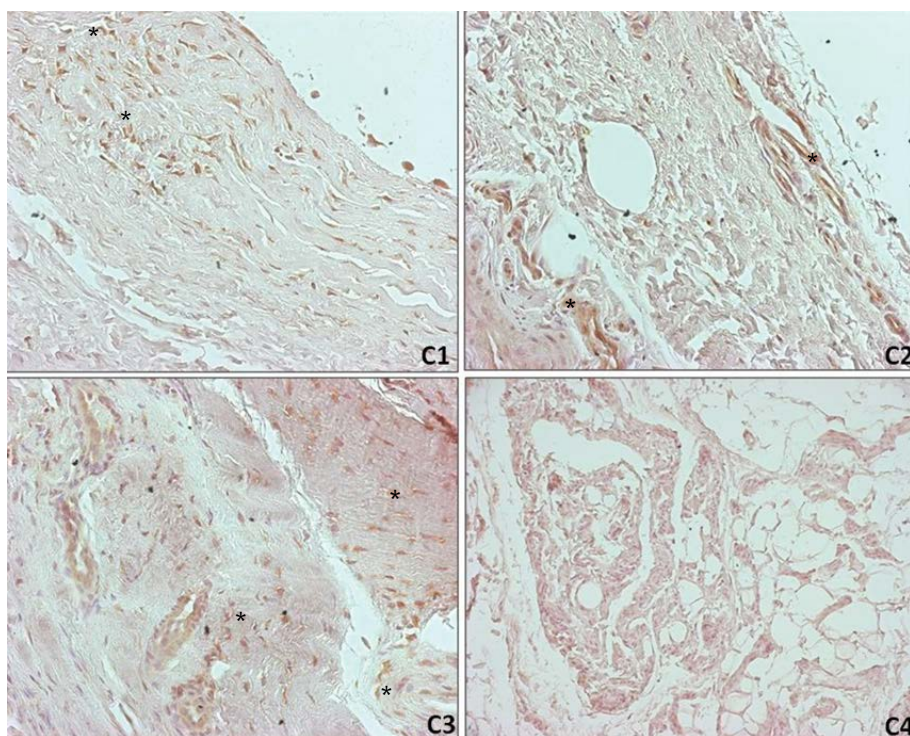


**Figure C.** Photomicrographs of the immunohistochemical reaction for the cytokine interleukin-6 (IL-6); **C1–C3.** Pathological tissue in which IL-6 is expressed at the level of proliferative nodules (asterisks: C1, C2, C3, 20 $\times$ ); **C4.** Control tissue (10 $\times$ ).

IL-1 $\beta$  in pathological samples, demonstrating positive reactions in the cytoplasm of myo-fibroblastic cells and in the extracellular matrix. IL-1 $\beta$  is completely absent in the extracellular matrix of the palmar control fascia specimens (Fig. B4). Moreover, this pro-inflammatory cytokine is highly expressed at the

level of the capillary endothelium, near the synovial cysts. IL-6 is appreciable in extracellular matrix, both in proliferating myo-fibroblasts and in fibroblasts at the level of proliferative nodules in patients affected by arthrogenic synovial cysts (Fig. C1). In the normal tissue of palmar fascia IL-6 appears to be completely

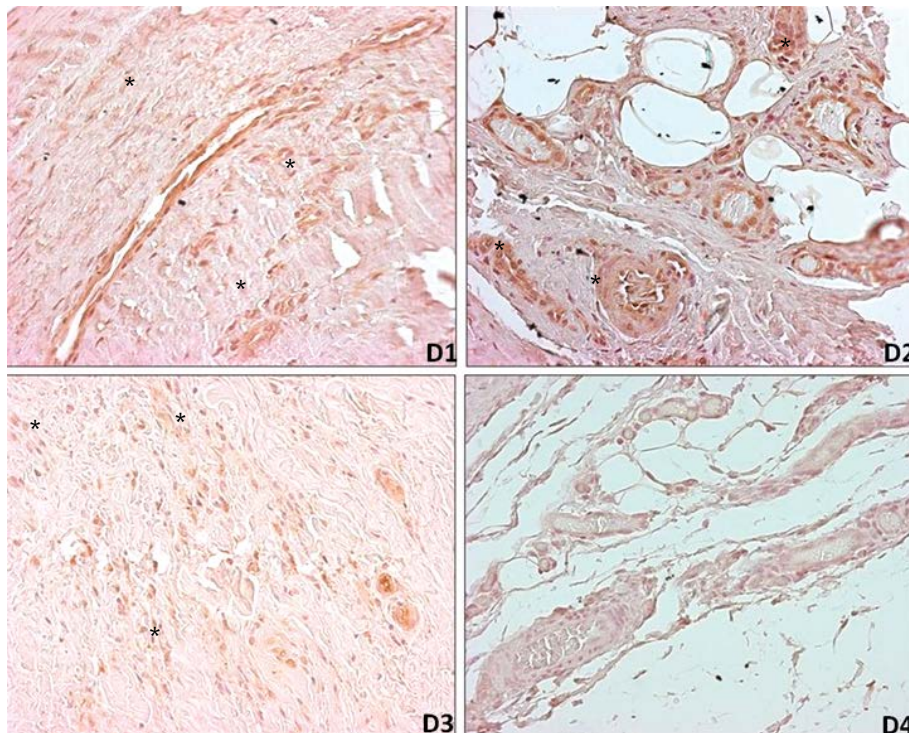


**Figure D.** Microphotographs of the immunohistochemical reaction for the proinflammatory cytokine tumour necrosis factor-alpha (TNF- $\alpha$ ) expressed in pathological myofibroblasts and in capillary endothelial cells (D1, D2, D3, 20 $\times$ ). Myofibroblasts nodules (asterisks); **D4.** Control tissue (20 $\times$ ).

absent at the level of the loose connective tissue, but moderately present in the endothelial cells of the blood vessels and in the fibroblasts scattered in the connective tissue (Fig. C2). Unlike the other cytokines, IL-6 shows an appreciable localisation in normal fibroblasts (Fig. C1) and a more evident cytoplasmic localisation in the pathological ones (Fig. C2). This cytokine appears to be involved in the inflammatory process that leads to the activation of the fibrotic process. Therefore, IL-6 appears to be synthesized in response to transforming growth factor-beta1 (TGF- $\beta$ 1) and acts by enhancing the proliferation and differentiation of fibroblasts into myo-fibroblasts with deposition of amorphous substance in association with TGF- $\beta$ 1. TNF- $\alpha$  is expressed in the extracellular matrix of the myo-fibroblastic tissue at the proliferation site observed in patients with synovial cysts (Fig. D1). TNF- $\alpha$  is present in pathological myo-fibroblasts and in capillary endothelial cells (Fig. D1). In the loose connective tissue of the normal palmar fascia this inflammatory factor is however moderately positive in the cytoplasm of fibroblastic cells and in the extracellular matrix (Fig. D2). This growth factor is also strongly expressed in the cytoplasm of secreting sweat glands (Fig. D2) in the dermis near the pathological proliferative nodules.

## DISCUSSION

Arthrogenic synovial cysts are benignly progressing fibro-proliferative disorders which often lead to severe functional damage. The lack of knowledge related to the aetiopathogenesis of the disease has meant that a specific therapy is not currently available until now. Therefore, it is difficult to prevent its onset or to avoid its recurrence after surgical excision. The absence of valid therapeutic targets has led to the development of empirical therapies, such as local injection of steroids [9]. Inflammation plays a fundamental role in the onset of fibrosis and this finding is confirmed by the presence of proinflammatory cytokines [17]. In physiological conditions of wound healing or tissue repair activation of the fibrotic process occurs. During this process fibroblastic cells may differentiate into myo-fibroblasts, because their contractile activity is essential for tissue remodelling. The formation of myo-fibroblasts, controlled by a variety of growth factors and numerous mechanical stimuli, leads to an excessive deposition of extracellular matrix. Their action ends when the tissue is completely repaired or reabsorbed. In some pathological conditions the contractile activity of myo-fibroblasts persists and leads to tissue deformation [16]. IL-1 $\beta$ , an important pro-inflammatory

cytokine, is involved in "in vitro" fibroblastic proliferation through the induction of the expression of transcriptional factors such as c-fos, c-jun and c-myc [6]. The excessive expression of IL-1 $\beta$  alone could be responsible for the local fibroblastic proliferation seen in the active phase of the disease. IL-1 $\beta$  seems to have an important function in the activation and feeding of the inflammatory process, inducing the synthesis of other cytokines such as IL-6 and IL-2, interferons or chemokines, which are able to attract macrophages and granulocytes towards the site of inflammation. It seems probable that the mitogenic effect of IL-1 $\beta$  is enhanced by the co-expression of other factors such as TGF- $\beta$  and platelet-derived growth factor alpha and beta. The combined expression of these growth factors are probably responsible for fibroblastic proliferation and excessive deposition of an amorphous substance and accumulation of synovial fluid, a condition typical of the disease. In our experiments we also evaluated the level of IL-6 expression. This cytokine is directly involved in the activation of the initial inflammatory process which subsequently leads to fibrosis. The pro-inflammatory cytokine IL-6 plays an important role in the regulation of inflammation and acts in association with TGF- $\beta$ 1, thus leading to an increased pro-fibrotic response [3, 14]. IL-6 acts by enhancing the TGF- $\beta$ 1 signal by increasing endocytosis mediated by non-lipid endosomes. This consequence is due to internalisation of the TGF- $\beta$ 1 receptors as a result of binding of their ligand through endocytosis mediated by caveolin lipid vesicles and by non-lipid vesicles, although the TGF- $\beta$ 1 signal increases when the receptor endocytosis is mediated by non-lipidic vesicles. Therefore, IL-6 and TGF- $\beta$ 1 act synergistically, causing an increase in the expression of proinflammatory cytokines that appear to be the primary cause of the onset of the disease. Verjee et al. [15] reported that TNF- $\alpha$  at low concentrations induce myo-fibroblastic contraction, while at high levels it induces reduction or complete inhibition of myo-fibroblastic contraction. It seems that the action of TNF- $\alpha$  depends strictly on the TNFR receptor type: TNFR2 causes fibroblastic proliferation, while TNFR1 activates programmed cell death. TNF- $\alpha$  could be considered a possible therapeutic target for the treatment of the disease in the primary stages or in preventing relapses following surgical removal. In our experimental study we found that TNF- $\alpha$  showed a greater localisation in pathological fibroblasts. Therefore, this factor appears to be directly involved in

the fibrotic reaction and its action depends exclusively on its TNFR2 receptor, which is strongly expressed in pathological conditions. Based upon our preliminary results, local injections of anti-TNF- $\alpha$  drugs could be useful in preventing the progression of the disease or avoiding its recurrence after surgical treatment. During the involutive phase a high ratio of collagen III on collagen I was detected, differently from the normal physiological condition [12].

## CONCLUSIONS

These experimental results suggest, therefore, a possible application of these pro-inflammatory factors in identifying the degree of disease progression and in the use of some of these markers as prognostic factors in the follow-up of patients undergoing surgical resection of synovial cysts. Innovative therapies could be characterised by the combined use of specific inhibitors of the factors TNF- $\alpha$ , IL-1 $\beta$  and IL-6 and their receptors in order to inhibit the progression of the disease through inactivation of the fibrotic process.

## Acknowledgments


This work was supported by a grant of the "Enrico ed Enrica Sovena" Foundation, Italy.

## REFERENCES

1. Artico M, Cervoni L, Carloia S, et al. Synovial cysts: clinical and neuroradiological aspects. *Acta Neurochir (Wien)*. 1997; 139(3): 176–181, doi: [10.1007/BF01844747](https://doi.org/10.1007/BF01844747), indexed in Pubmed: [9143581](https://pubmed.ncbi.nlm.nih.gov/9143581/).
2. Berenbaum F, Jacques C, Thomas G, et al. Synergistic effect of IL-1[beta] and TNF[alpha] on prostaglandin E2 production by articular chondrocytes. Involvement of cyclooxygenase without PLA2 stimulation. *Exp Cell Res*. 1996; 222(2): 379–384.
3. Bianchi E, Artico M, Di Cristofano C, et al. Growth factors, their receptor expression and markers for proliferation of endothelial and neoplastic cells in human osteosarcoma. *Int J Immunopathol Pharmacol*. 2013; 26(3): 621–632, doi: [10.1177/039463201302600306](https://doi.org/10.1177/039463201302600306), indexed in Pubmed: [24067459](https://pubmed.ncbi.nlm.nih.gov/24067459/).
4. Calderazzi A, Eligi C, Guidetti F, et al. [Synovial chondromatosis of the temporomandibular joint: an occasional finding in association with an arthroscopic cyst. A case report]. *Radiol Med*. 1995; 89(4): 522–525, indexed in Pubmed: [7597236](https://pubmed.ncbi.nlm.nih.gov/7597236/).
5. De Haas WH, Van Heerde P. Synovial nature of pathologic periarticular structures, including subcutaneous nodules descent from embryonic arthroscopic fibroblasts: a hypothesis. *Z Rheumatol*. 1979; 38(9-10): 318–329.
6. DiGiovine FS, Duff G. Interleukin 1: the first interleukin. *Immunology Today*. 1990; 11: 13–20, doi: [10.1016/0167-5699\(90\)90005-t](https://doi.org/10.1016/0167-5699(90)90005-t).
7. El-Ghazaly MA, Nada AS, El-Hazek RM, et al. Effect of selective COX-2 inhibitor, celecoxib on adjuvant-induced arthri-

- tis model in irradiated rats. *Int J Radiat Biol.* 2010; 86(12): 1079–1087, doi: [10.3109/09553002.2010.501839](https://doi.org/10.3109/09553002.2010.501839), indexed in Pubmed: [20698743](https://pubmed.ncbi.nlm.nih.gov/20698743/).
8. Gebhard HH, Zysk SP, Schmitt-Sody M, et al. The effects of Celecoxib on inflammation and synovial microcirculation in murine antigen-induced arthritis. *Clin Exp Rheumatol.* 2005; 23(1): 63–70, indexed in Pubmed: [15789889](https://pubmed.ncbi.nlm.nih.gov/15789889/).
  9. Huang AJ, Bos SA, Torriani M, et al. Long-term outcomes of percutaneous lumbar facet synovial cyst rupture. *Skeletal Radiol.* 2017; 46(1): 75–80, doi: [10.1007/s00256-016-2513-5](https://doi.org/10.1007/s00256-016-2513-5), indexed in Pubmed: [27771754](https://pubmed.ncbi.nlm.nih.gov/27771754/).
  10. Kusakabe T, Kasama F, Aizawa T, et al. Facet cyst in the lumbar spine: radiological and histopathological findings and possible pathogenesis. *J Neurosurg Spine.* 2006; 5(5): 398–403, doi: [10.3171/spi.2006.5.5.398](https://doi.org/10.3171/spi.2006.5.5.398), indexed in Pubmed: [17120888](https://pubmed.ncbi.nlm.nih.gov/17120888/).
  11. Nucci F, Artico M, Santoro A, et al. Intraneural synovial cyst of the peroneal nerve: report of two cases and review of the literature. *Neurosurgery.* 1990; 26(2): 339–344, doi: [10.1097/00006123-199002000-00028](https://doi.org/10.1097/00006123-199002000-00028), indexed in Pubmed: [2155391](https://pubmed.ncbi.nlm.nih.gov/2155391/).
  12. Shih B, Bayat A. Scientific understanding and clinical management of Dupuytren disease. *Nat Rev Rheumatol.* 2010; 6(12): 715–726, doi: [10.1038/nrrheum.2010.180](https://doi.org/10.1038/nrrheum.2010.180), indexed in Pubmed: [21060335](https://pubmed.ncbi.nlm.nih.gov/21060335/).
  13. Tatter SB, Cosgrove GR. Hemorrhage into a lumbar synovial cyst causing an acute cauda equina syndrome. Case report. *J Neurosurg.* 1994; 81(3): 449–452, doi: [10.3171/jns.1994.81.3.0449](https://doi.org/10.3171/jns.1994.81.3.0449), indexed in Pubmed: [8057153](https://pubmed.ncbi.nlm.nih.gov/8057153/).
  14. Taurone S, Bianchi E, Attanasio G, et al. Immunohistochemical profile of cytokines and growth factors expressed in vestibular schwannoma and in normal vestibular nerve tissue. *Mol Med Rep.* 2015; 12(1): 737–745, doi: [10.3892/mmr.2015.3415](https://doi.org/10.3892/mmr.2015.3415), indexed in Pubmed: [25738867](https://pubmed.ncbi.nlm.nih.gov/25738867/).
  15. Verjee LS, Midwood K, Davidson D, et al. Myofibroblast distribution in Dupuytren's cords: correlation with digital contracture. *J Hand Surg Am.* 2009; 34(10): 1785–1794, doi: [10.1016/j.jhsa.2009.08.005](https://doi.org/10.1016/j.jhsa.2009.08.005), indexed in Pubmed: [19910144](https://pubmed.ncbi.nlm.nih.gov/19910144/).
  16. Wu M, Ben Amar M. Growth and remodelling for profound circular wounds in skin. *Biomech Model Mechanobiol.* 2015; 14(2): 357–370, doi: [10.1007/s10237-014-0609-1](https://doi.org/10.1007/s10237-014-0609-1), indexed in Pubmed: [25183422](https://pubmed.ncbi.nlm.nih.gov/25183422/).
  17. Wynn TA, Ramalingam TR. Mechanisms of fibrosis: therapeutic translation for fibrotic disease. *Nat Med.* 2012; 18(7): 1028–1040, doi: [10.1038/nm.2807](https://doi.org/10.1038/nm.2807), indexed in Pubmed: [22772564](https://pubmed.ncbi.nlm.nih.gov/22772564/).

# The effect of N-acetylcysteine on the sensory retina of male albino rats exposed prenatally to cypermethrin

N. Mohey Issa, M.A. Al-Gholam 

*Human Anatomy and Embryology, Faculty of Medicine, Menoufia University, Menoufia, Shibin Al-koum, Egypt*

[Received: 12 February 2020; Accepted: 18 March 2020]

**Background:** *Cypermethrin (CYP), a pyrethroid that is globally used in the field and house to fight the pests. CYP can induce cellular toxicity and cross the placental barrier. N-acetylcysteine (NAC) can fight the prenatal exposure to the inflammation. This work aimed to study, for the first time, the effects of NAC on the sensory retina of male albino rats exposed prenatally to cypermethrin.*

**Materials and methods:** *Twenty-four sexually mature female albino rats and 12 male albino rats were allowed for mating and divided equally into the following groups: group I (control group): kept without treatment; group II (NAC group): received 1 g/kg/day NAC diluted in distilled water orally by gastric tube from the 7<sup>th</sup> day of gestation till delivery; group III (CYP group): received 12 mg/kg/day of cypermethrin orally by gastric tube from the 7<sup>th</sup> day of gestation till delivery; group IV (CYP and NAC group): received 12 mg/kg/day of cypermethrin and 1 g/kg/day of NAC. The ten male offspring of each group were divided into subgroups a and b that were sacrificed at the age of 7<sup>th</sup> and 14<sup>th</sup> days postnatal, respectively. At the end of the experiment, the eye samples were subjected to histological, immunohistochemical and morphometric studies.*

**Results:** *Concerning the different previous studies, the sensory retina of CYP subgroups showed vacuolation of the inner and outer plexiform layers, dilated congested blood vessels, hyalinisation and disorganisation of the photoreceptor layer. Also, the expression of collagen IV and caspase 3 (a marker of apoptosis) was up-regulated in the CYP subgroups.*

**Conclusions:** *N-acetylcysteine significantly protected the sensory retina from the damaging effects of CYP. NAC could be considered as a good protective agent against the damaging effect of CYP on the sensory retina. (Folia Morphol 2021; 80, 1: 140–148)*

**Key words:** cypermethrin N-acetylcysteine rat sensory retina

## INTRODUCTION

Pyrethrins are organic compounds, naturally derived from *Chrysanthemum cinerariifolium* flowers [18]. They have a potent insecticidal activity as their synthetic analogues which are called pyrethroids [19].

Cypermethrin (CYP), a pyrethroid that is globally used in the field and house to fight pests [13]. It is capable to disturb the cellular structure and function of pests [1]. CYP induced cellular toxicity may be due to reactive oxygen species (ROS) that cause destruction



of the cellular proteins, lipids and DNA [8]. CYP can cross the placental barrier causing toxic effects on the development of albino rats causing several congenital malformations and foetal death [10]. Cysteine is the basic amino acid for the synthesis of glutathione which combats the oxidative stress and the resultant free radicals by its antioxidant activity [11]. This activity is classified as enzymatic one through the promotion of glutathione peroxidase and reductase enzymes [14]. Besides this, N-acetylcysteine (NAC) has anti-inflammatory properties through inhibition of the cyclooxygenase enzyme together with its products as prostaglandins [6]. And so, NAC can fight the prenatal exposure to the inflammation preventing the occurrence of behavioural and memory alterations on the offspring [16]. This allows us to study the role of NAC on the retina of prenatally exposed rats to CYP.

## MATERIALS AND METHODS

### Materials

**Cypermethrin.** A trade name to an oily solution containing 250 g/L of the active ingredient CYP, it was diluted with distilled water to concentration levels convenient to be used throughout the whole experiment, in which 1 mL of diluted working solution contained 12 mg of CYP.

**N-acetylcysteine.** A pharmacological preparation (Acetylcystein 600 mg, Effervescent Instant Granules, SEDICO Pharmaceutical Co., 6 October City-Egypt) was diluted with tap water and given to the rats orally.

### Animals

Twenty-four sexually mature female albino rats and 12 male albino rats, weighing between 200 and 250 g were allowed for laboratory rat chow diet and water ad-libitum.

Every 2 female rats were housed overnight with a sexually mature male albino rat for mating; every morning, vaginal smears were taken and microscopically examined for the presence of sperms. The detection of sperms in the smears was considered as the 1<sup>st</sup> day of gestation. All experimental procedures were performed with the approval of the Research Ethics Committee, Faculty of Medicine, Menoufia University, Egypt.

### Experimental design

The pregnant mothers were divided equally into the following groups:

- Group I (control group): the pregnant rats were fed ad libitum and allowed free water supply from the 7<sup>th</sup> day of gestation. Ten male offspring were divided into subgroup Ia and Ib that were sacrificed at the age of 7<sup>th</sup> and 14<sup>th</sup> days postnatal, respectively;
- Group II (NAC group): the pregnant rats received 1 g/kg/day of NAC [3] diluted in distilled water orally by gastric tube from the 7<sup>th</sup> day of gestation till delivery. Ten male offspring were divided into subgroup IIa and IIb that were sacrificed at the age of 7<sup>th</sup> and 14<sup>th</sup> days postnatal, respectively;
- Group III (CYP group): the pregnant rats received 12 mg/kg/day of CYP [7] orally by gastric tube from the 7<sup>th</sup> day of gestation till delivery. Ten male offspring were divided into subgroup IIIa, and IIIb that were sacrificed at the age of 7<sup>th</sup> and 14<sup>th</sup> days postnatal, respectively;
- Group IV (CYP and NAC group): the pregnant rats received 12 mg/kg/day of CYP and 1 g/kg/day of NAC diluted in distilled water orally by gastric tube from the 7<sup>th</sup> day of gestation till delivery. Ten male offspring were divided into subgroup IVa and IVb that were sacrificed at the age of 7<sup>th</sup> and 14<sup>th</sup> days postnatal, respectively.

At the end of each detected period, the eye samples were removed from each animal. The eye samples were fixed in 10% formol saline and processed to prepare 5  $\mu$ m-thick paraffin sections for use in the following histological techniques:

### Histological study

Haematoxylin and eosin stain and toluidine blue stain.

### Immunohistochemical study

For detection of the immunoreactivity of collagen IV and caspase 3, the sections were deparaffinised, rehydrated, and after antigen retrieval with 10 mmol/L citrate acid solution (pH 6), the specimens were pre-incubated with goat serum for 5 min and were then incubated overnight at 4°C with anti-collagen IV (Abcam, 6586) and anti caspase 3 (Abcam, 2302) (Working dilution 1:500). The binding was detected using biotinylated secondary antibody (goat anti-mouse IgG; Sigma Aldrich) for 10 min. The specimens were then incubated with streptavidin-peroxidase complex for 5 min, followed by incubation with 3,3-diaminobenzidinetetrahydrochloride (DAB; Sigma Aldrich) for 3 min. Slides were counterstained with haematoxylin and mounted.

### Morphometric study

Data were obtained from five different sections from each rat of all subgroups and examined using image J analyser software, version 1.47 v to determine:

- the colour intensity in toluidine blue-stained sections;
- area per cent in collagen IV immune-stained sections;
- the number of positive cells in caspase 3 immune-stained sections.

### Statistical analysis

Data obtained from the morphometric study was subjected to statistical analysis using SPSS software version 20 (SPSS, Inc., Chicago, IL, USA). Data were presented as mean  $\pm$  standard deviation. Differences among the study groups were detected by using Mann-Whitney U test. The results were considered statistically significant with  $p$  value  $< 0.05$  [15].

## RESULTS

### Histological study

#### *Haematoxylin and eosin (H and E) stain*

Haematoxylin and eosin-stained retinal sections of the control and NAC groups revealed the same histological features of the sensory retina.

The sensory retina of postnatal rats aged 7 days from control mothers (control group) consisted of the photoreceptor layer, 2 nuclear (outer and inner) layers that were separated from each other by the outer plexiform layer. Moreover, the inner nuclear layer was followed internally by the inner plexiform layer then the ganglion cell layer. The nerve fibre layer was followed by the inner limiting membrane with the developing blood vessels.

However, the sensory retina of 7 days old postnatal rats from mothers treated with cypermethrin (CYP group) showed vacuolations of inner and outer plexiform layers. The nuclear layers showed pyknosis of their nuclei, also the blood vessels showed vasodilatations and congestion. On the treatment of the mothers with cypermethrin and N-acetylcysteine (CYP and NAC group), the sensory retina of their 7 days old postnatal offspring showed preservation of normal development and differentiation, so the retina appeared more or less normal. The sensory retinal layers of postnatal rats aged 14 days from control mothers (control group) appeared more differentiated than that of the age of 7 days (Fig. 1).

On the treatment of the mothers with cypermethrin (CYP group), the sensory retina of their 14 days postnatal offspring showed hyalinisation and disorganisation of the photoreceptor layer. Also, the vacuolations of the plexiform layers and nuclear pyknosis of the nuclear layers appeared. On the treatment of the mothers with cypermethrin and N-acetylcysteine (CYP and NAC group), the sensory retina of their 14 days old postnatal offspring showed preservation of normal development and differentiation, so the sensory retina appeared more or less normal (Fig. 2).

### *Toluidine blue stain*

The sensory retina of postnatal rats aged (7 and 14) days from control mothers (control group) showed dark blue staining of its neural cells indicating the presence of dense Nissl's bodies in their cytoplasm. The CYP sensory retinae showed a significant decrease in the colour intensity as compared to that of the control group, while the NAC treated sensory retinae showed a significant increase in the colour intensity of the toluidine blue stain as compared to that of CYP group (Figs. 3, 4).

### Immunohistochemical study

The sensory retina of postnatal rats aged (7 and 14) days from CYP mothers (CYP group) showed significant increase in the percentage of positively reacting area for collagen IV as compared to that of control group, while the NAC treated sensory retinae showed significant decrease in the percentage of positively reacting area for collagen IV as compared to that of CYP group (Figs. 5, 6).

The sensory retina of postnatal rats aged (7 and 14) days from control mothers (control group) showed minimal expression of caspase 3. The CYP sensory retinae (CYP group) showed significant increase in the number of positively immunostaining cells for caspase 3 as compared to that of control group, while the NAC treated sensory retinae (CYP and NAC group) showed significant decrease in the number of positively immunostaining cells for caspase 3 as compared to that of CYP group (Figs. 7, 8).

## DISCUSSION

The postnatal exposure to CYP leads to neurodegenerative effects on human and rat [22], so the aim of this work was to study for the first time, the effect of prenatal exposure to CYP on the development of the sensory retina and the possible role of

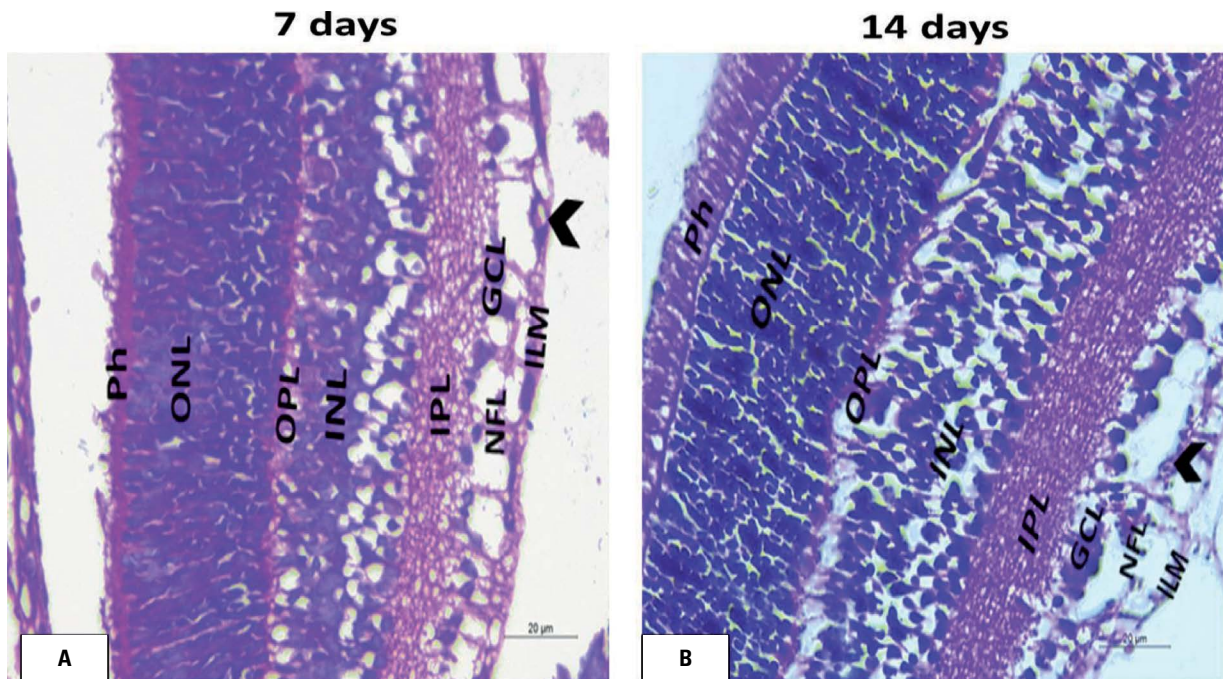


**Figure 1.** Haematoxylin and eosin stained sensory retinal sections ( $\times 400$ ) of 7 and 14 days postnatal offspring of control group: the sensory retina of 7 (A) and 14 (B) days postnatal offspring of (control) group showing photoreceptor layer (ph), outer nuclear layer (ONL), outer plexiform layer (OPL), inner nuclear (INL), inner plexiform layer (IPL), ganglionic cell layer (GCL), nerve fibre layer (NFL) and inner limiting membrane (ILM). Also, the normal blood vessels (arrowhead) are present on the inner limiting membrane.

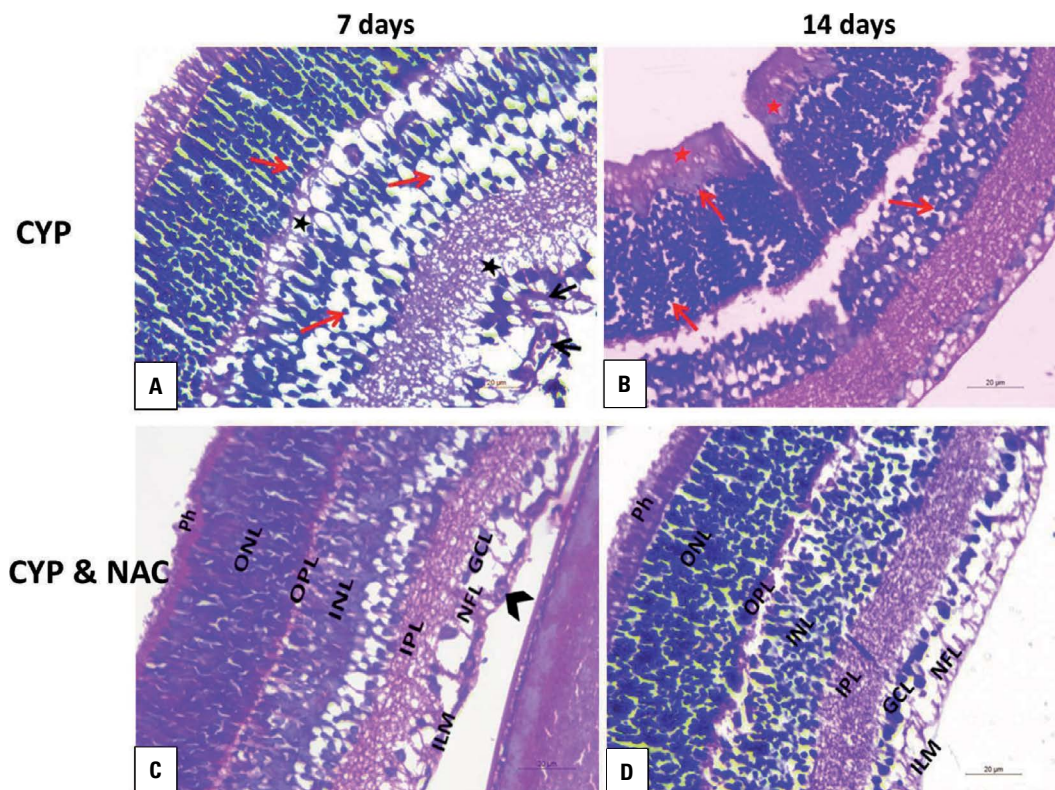


**Figure 2.** Haematoxylin and eosin stained sensory retinal sections ( $\times 400$ ) of 7 and 14 days postnatal offspring of cypermethrin (CYP) and cypermethrin and N-acetylcysteine (CYP and NAC) groups. A, B. Sensory retina of 7 and 14 days postnatal offspring of CYP group showing vacuolations (black star) of plexiform layers, pyknosis (red arrow) of nuclear layers, vasodilatation and congestion of the blood vessels (black arrow). Moreover, hyalinization and disorganisation (red star) are present in the photoreceptor layer; C, D. Sensory retina of 7 and 14 days postnatal offspring of CYP and NAC group showing preservation of normal development and differentiation.

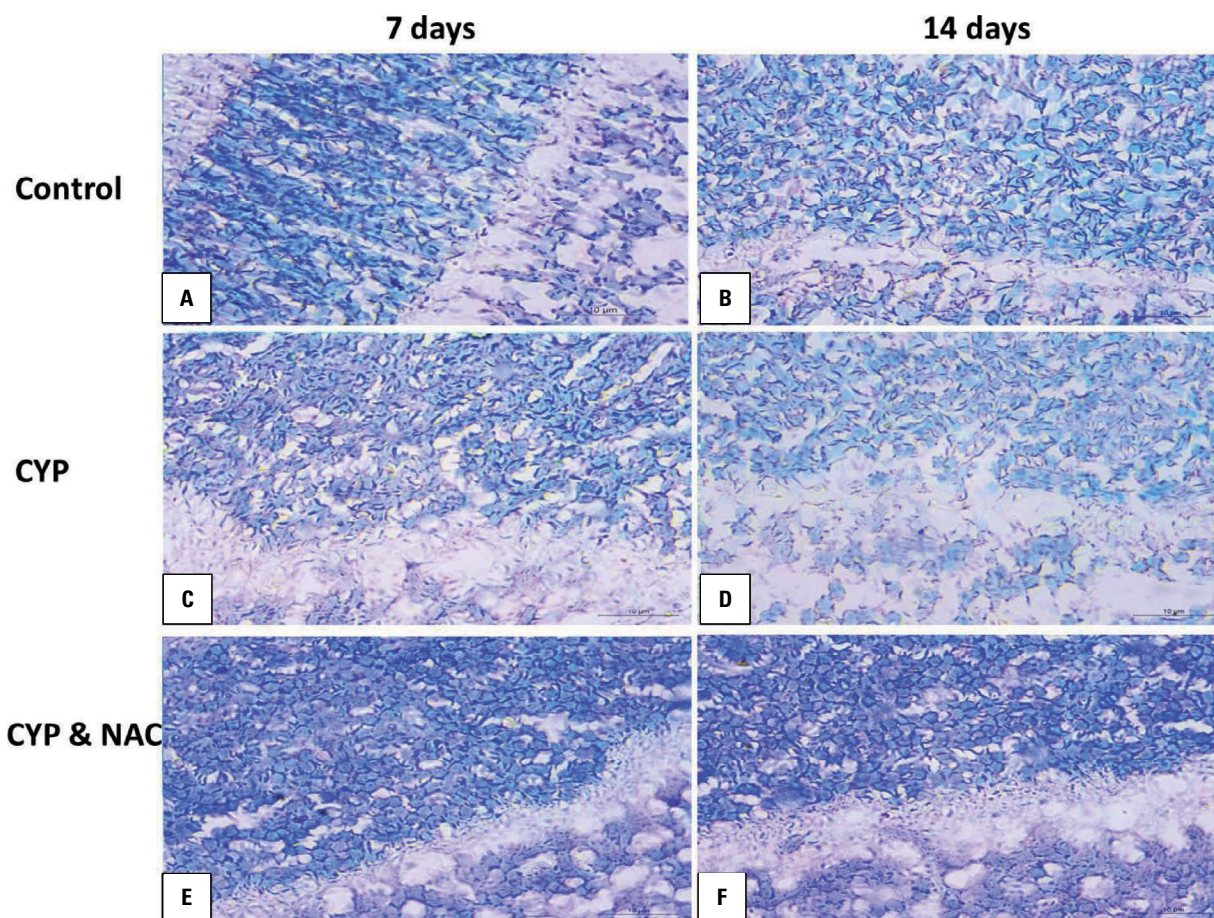


**Figure 3.** Representative toluidine blue-stained sensory retina ( $\times 1000$ ) of all experimental groups; **A, B.** Dark blue staining of Nissl's bodies in retinal neural cells of control group; **C, D.** Significant decrease ( $p$  value  $< 0.05$ ) in colour intensity of the sections of cypermethrin (CYP) group as compared to control group; **E, F.** Significant increase ( $p$  value  $< 0.05$ ) in colour intensity of the sections of CYP and N-acetylcysteine (NAC) group as compared to CYP group.

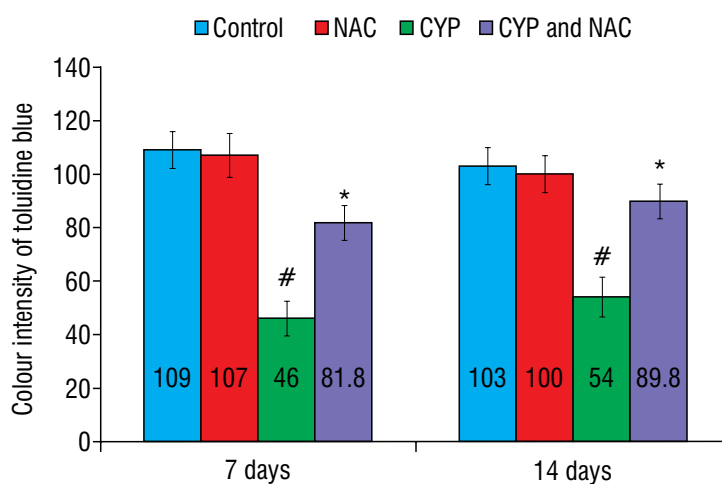


**Figure 4.** Regarding the colour intensity of toluidine blue staining, the cypermethrin (CYP) group showing a significant decrease ( $\#p$  value  $< 0.05$ ) as compared to the control group while the CYP and N-acetylcysteine (NAC) group showing a significant increase ( $*p$  value  $< 0.05$ ) as compared to CYP group.

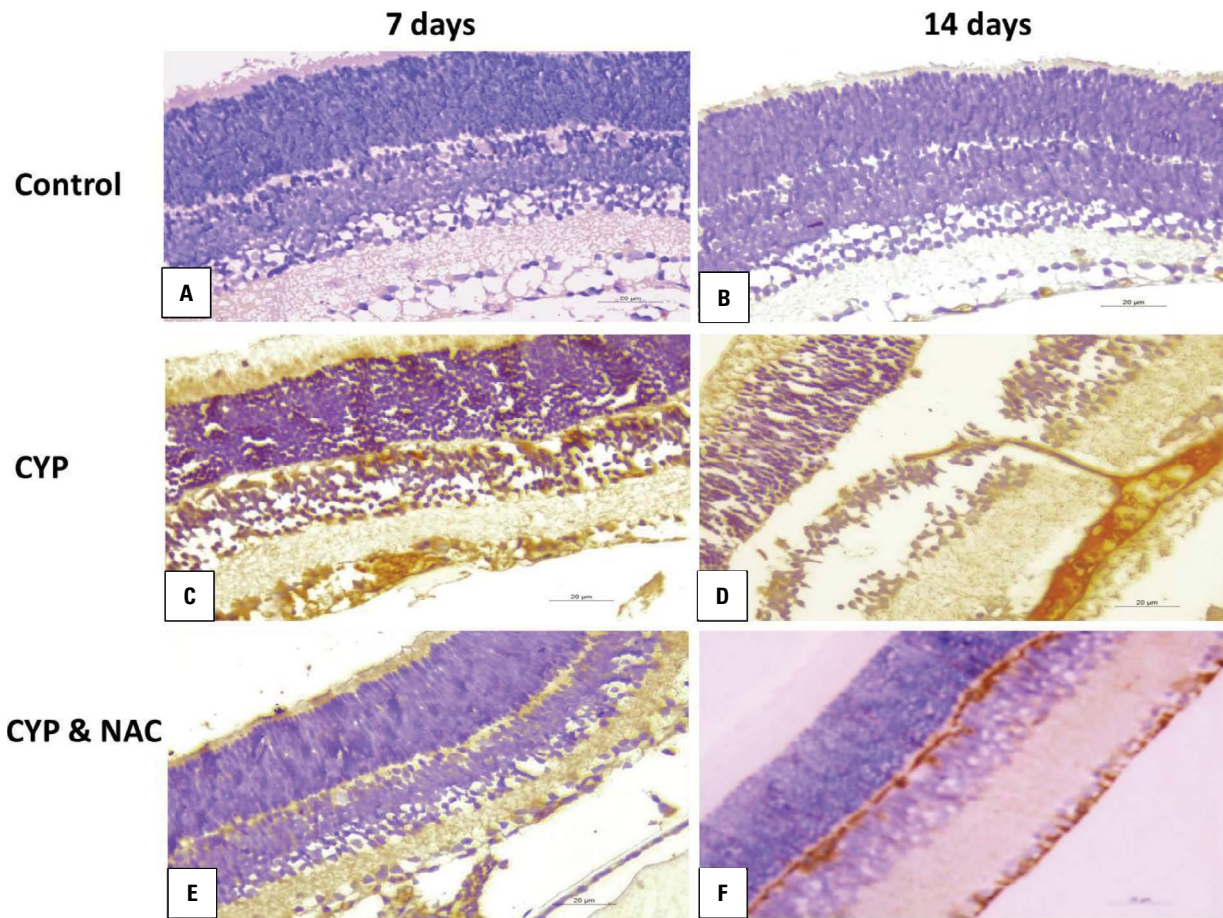


**Figure 5.** Representative collagen IV immunostained sensory retina ( $\times 400$ ) of all experimental groups; **A, B.** Normal expression of collagen IV in retinal blood vessels of (control) group; **C, D.** Significant up-regulation ( $p$  value  $< 0.05$ ) in percentage of collagen IV immunoreacting area in retinae of cypermethrin (CYP) group as compared to those of control group; **E, F.** Significant down-regulation ( $p$  value  $< 0.05$ ) in percentage of collagen IV immunoreacting area in retinae of CYP and N-acetylcysteine (NAC) group as compared to CYP group.

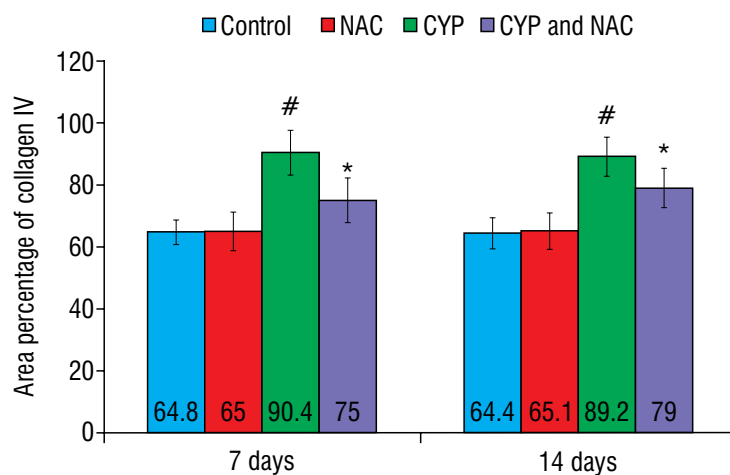


**Figure 6.** Regarding the expression of collagen IV immunostaining, the cypermethrin (CYP) group showing a significant increase ( $\#p$  value  $< 0.05$ ) as compared to the control group while the CYP and N-acetylcysteine (NAC) group showing a significant decrease ( $*p$  value  $< 0.05$ ) as compared to CYP group.

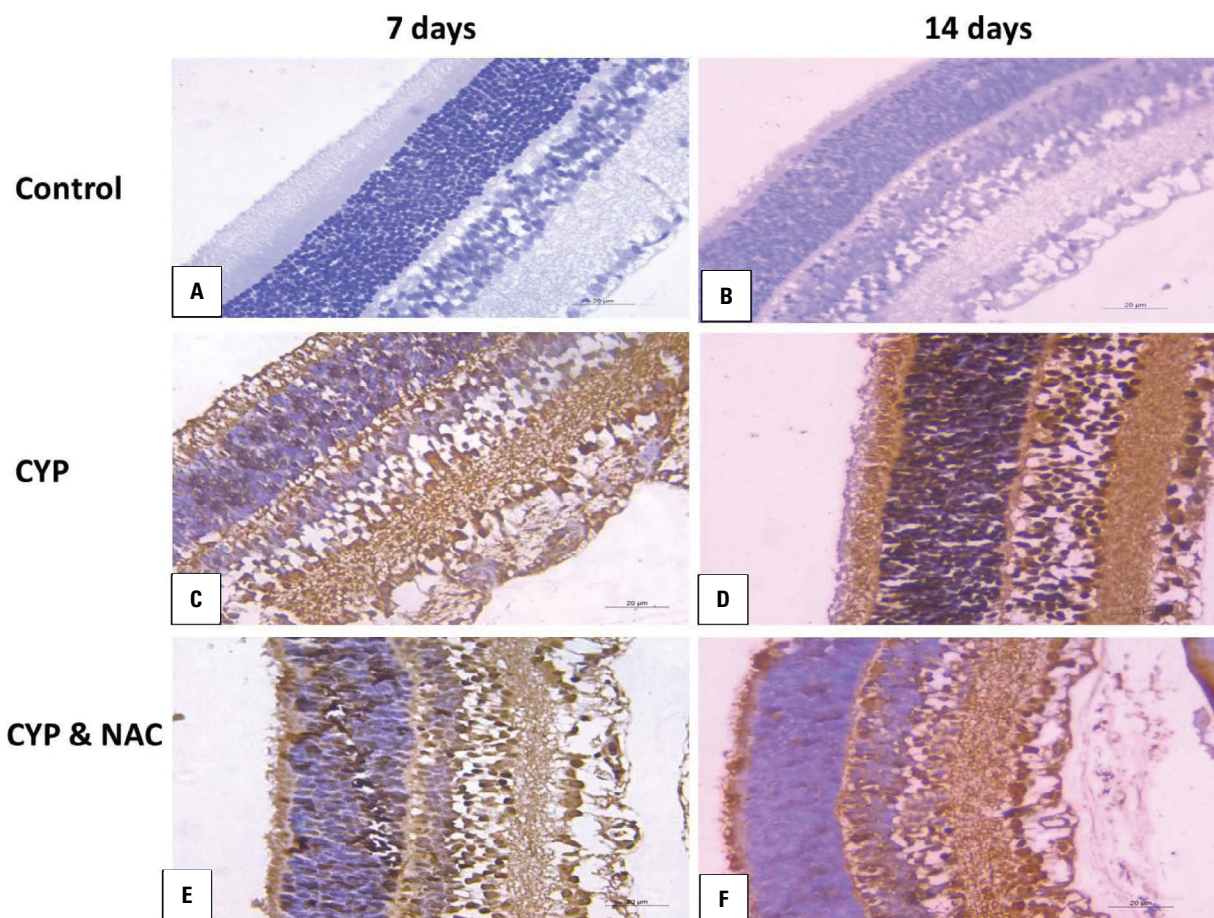


**Figure 7.** Representative caspase 3 immunostained sensory retina ( $\times 400$ ) of all experimental groups. The retinae of control group showing negative (A) and minimal (B) expression of caspase 3; C, D. Significant increase ( $p$  value  $< 0.05$ ) in number of caspase 3 immunopositive cells in retinae of cypermethrin (CYP) group as compared to those of control group; E, F. Significant decrease ( $p$  value  $< 0.05$ ) in number of caspase 3 immunopositive cells in retinae of CYP and N-acetylcysteine (NAC) group as compared to those of CYP group.

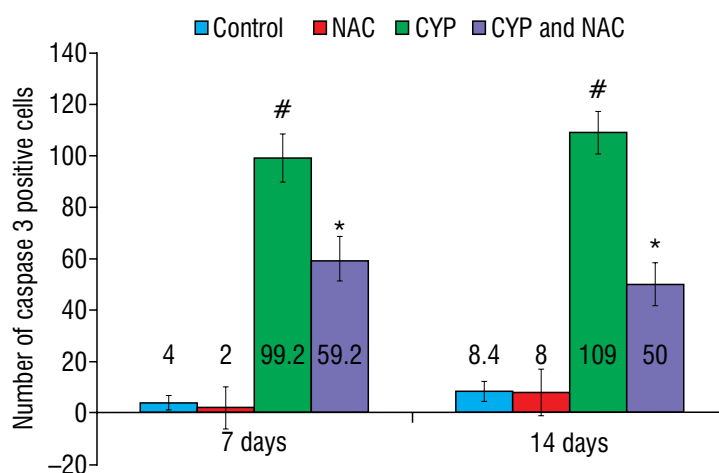


**Figure 8.** Regarding the expression of caspase 3 immunostaining, the cypermethrin (CYP) group showing a significant increase ( $\#p$  value  $< 0.05$ ) as compared to the control group, however, the CYP and N-acetylcysteine (NAC) group showing downregulation of caspase 3 expression ( $\#p$  value  $< 0.05$ ) compared to CYP group.

NAC. The sensory retina of 7 days old postnatal rats from mothers treated with cypermethrin (CYP group) showed vacuolations of inner and outer plexiform layers. The nuclear layers showed pyknosis of their nuclei, also the blood vessels showed vasodilatations and congestion. Moreover, the sensory retina of 14 days postnatal rats from mothers treated with CYP showed hyalinisation and disorganisation of the photoreceptor layer. These degenerative changes were explained by the toxic effect on the retinal blood vessels causing retinal hypoxia. Hypoxia-induced reactive changes in glial cells (responsible for retinal vasculature development), which, in turn, result in an imbalance of pro-angiogenic and anti-angiogenic factors leading to retinal degeneration during vascular development and migration of blood vessels in the neural retina [17]. Massengill et al. [12] explained the retinal degeneration by the occurrence of the inflammation. The inflammation was mediated by the accumulation of cyclic guanosine monophosphate causing the opening of calcium channels in the rod cells and subsequent rod cell death which was followed by the degeneration of other retinal layers [9]. Our results also showed a concomitant significant decrease in the intensity of the toluidine blue-stained retinae (CYP group) as compared to the control group. The reduced intensity was explained by the loss of Nissl's bodies (basophilic ribosomal ribonucleic acid substances) as reported by Ajibade et al. [2] which added that neuronal degeneration followed by defective protein synthesis and loss of neuronal function. Our immunohistochemical results showed a significant increase in the expression of collagen IV in the sensory retina of the CYP group as compared to the control group denoting the neovascularisation (proliferation and abnormal organization) of retinal blood vessels, as reported by Dorrell et al. [5]. The retinal neovascularisation was owed to two factors (hypoperfusion and inflammation), but the inflammatory process might precede the ischaemia [21]. The inflammatory cytokines (IL-1 $\beta$ , IL-6, IL-8 and TNF- $\alpha$ ) were claimed to cause endothelial proliferation and pathologic angiogenesis [4]. Also, the sensory retina of the CYP group showed a significant increase in the number of caspase 3 immune-positive cells as compared to that of the control group, this explained that the retinal neuro-degeneration occurred through caspase-dependent apoptotic mechanism stimulated by the oxidative stress [23]. NAC allowed significant protection of the sensory

retina of the CYP and NAC group by preventing the neural degeneration and pathological apoptosis with the preservation of its Nissl's bodies. Moreover, NAC allowed normal development of retinal blood vessels preventing neovascularisation. The protective role of NAC could be explained by acting as a glutathione precursor (cysteine is required for endogenous antioxidant glutathione production), down regulator of the expression of several inflammatory cytokines genes and microglia proliferation inhibitor [20].

## CONCLUSIONS

The prenatal exposure of the rats to CYP led to damage to their sensory retina and the use of NAC as a protective agent resulted in the preservation of the normal structure of the sensory retina.

The experiment was conducted at Human Anatomy and Embryology Department, Faculty of Medicine, Menoufia University.

## REFERENCES

1. Abdul-Hamid M, Moustafa N, Asran AA, et al. Cypermethrin-induced histopathological, ultrastructural and biochemical changes in liver of albino rats: The protective role of propolis and curcumin. *Beni-Suef Univ J Basic Appl Sci.* 2017; 6(2): 160–173, doi: [10.1016/j.bjbas.2017.03.002](https://doi.org/10.1016/j.bjbas.2017.03.002).
2. Ajibade AJ, Adenowo TK, Fegemilehin ME, et al. Some histological observations on the cerebellar cortex of adult Wistar rats following quinine administration. *Sci Focus.* 2006; 11(2): 97–100.
3. Berry A, Bellisario V, Panetta P, et al. Administration of the antioxidant N-acetyl-cysteine in pregnant mice has long-term positive effects on metabolic and behavioral endpoints of male and female offspring prenatally exposed to a high-fat diet. *Front Behav Neurosci.* 2018; 12: 48, doi: [10.3389/fnbeh.2018.00048](https://doi.org/10.3389/fnbeh.2018.00048), indexed in Pubmed: [29599711](https://pubmed.ncbi.nlm.nih.gov/29599711/).
4. Curnow SJ, Murray PI. Inflammatory mediators of uveitis: cytokines and chemokines. *Curr Opin Ophthalmol.* 2006; 17(6): 532–537, doi: [10.1097/ICU.0b013e32801094b5](https://doi.org/10.1097/ICU.0b013e32801094b5), indexed in Pubmed: [17065921](https://pubmed.ncbi.nlm.nih.gov/17065921/).
5. Dorrell MI, Aguilar E, Friedlander M. Retinal vascular development is mediated by endothelial filopodia, a preexisting astrocytic template and specific R-cadherin adhesion. *Invest Ophthalmol Vis Sci.* 2002; 43: 3500–3510.
6. Farshid AA, Tamaddonfard E, Yahyae F. Effects of histidine and N-acetylcysteine on diclofenac-induced anti-inflammatory response in acute inflammation in rats. *Indian J Exp Biol.* 2010; 48(11): 1136–1142, indexed in Pubmed: [21117455](https://pubmed.ncbi.nlm.nih.gov/21117455/).
7. Huang C, Li X. Maternal cypermethrin exposure during the perinatal period impairs testicular development in C57BL male offspring. *PLoS One.* 2014; 9(5): e96781, doi: [10.1371/journal.pone.0096781](https://doi.org/10.1371/journal.pone.0096781), indexed in Pubmed: [24810582](https://pubmed.ncbi.nlm.nih.gov/24810582/).
8. Huang F, Liu Q, Xie S, et al. Cypermethrin induces macrophages death through cell cycle arrest and oxidative

- stress-mediated JNK/ERK signaling regulated apoptosis. *Int J Mol Sci.* 2016; 17(6), doi: [10.3390/ijms17060885](https://doi.org/10.3390/ijms17060885), indexed in Pubmed: [27322250](https://pubmed.ncbi.nlm.nih.gov/27322250/).
9. Luodan A, Zou T, He J, et al. Rescue of retinal degeneration in rd1 mice by intravitreally injected metformin. *Front Mol Neurosci.* 2019; 12: 102, doi: [10.3389/fnmol.2019.00102](https://doi.org/10.3389/fnmol.2019.00102), indexed in Pubmed: [31080404](https://pubmed.ncbi.nlm.nih.gov/31080404/).
  10. Madu EP. Teratogenic and embryotoxic effects of orally administered cypermethrin in pregnant albino rats. *J Toxicol Environ Health Sci.* 2015; 7(7): 60–67, doi: [10.5897/jtehs2015.0336](https://doi.org/10.5897/jtehs2015.0336).
  11. Massaad CA, Klann E. Reactive oxygen species in the regulation of synaptic plasticity and memory. *Antioxid Redox Signal.* 2011; 14(10): 2013–2054, doi: [10.1089/ars.2010.3208](https://doi.org/10.1089/ars.2010.3208), indexed in Pubmed: [20649473](https://pubmed.ncbi.nlm.nih.gov/20649473/).
  12. Massengill MT, Ahmed CM, Lewin AS, et al. Neuroinflammation in retinitis pigmentosa, diabetic retinopathy, and age-related macular degeneration: a minireview. *Adv Exp Med Biol.* 2018; 1074: 185–191, doi: [10.1007/978-3-319-75402-4\\_23](https://doi.org/10.1007/978-3-319-75402-4_23), indexed in Pubmed: [29721943](https://pubmed.ncbi.nlm.nih.gov/29721943/).
  13. Molavi M, Razi M, Cheraghi H, et al. Protective effect of vitamin E on cypermethrin-induced follicular atresia in rat ovary: Evidence for energy dependent mechanism. *Vet Res Forum.* 2016; 7(2): 125–132.
  14. Monks TJ, Ghersi-Egea JF, Philbert M, et al. Symposium overview: the role of glutathione in neuroprotection and neurotoxicity. *Toxicol Sci.* 1999; 51(2): 161–177, doi: [10.1093/toxsci/51.2.161](https://doi.org/10.1093/toxsci/51.2.161), indexed in Pubmed: [10543018](https://pubmed.ncbi.nlm.nih.gov/10543018/).
  15. Mould RF. *Introductory Medical Statistics.* Adam Hilger, Bristol, Philadelphia, USA 1999: 22–126.
  16. Phensy A, Duzdabaniyan HE, Brewer S, et al. Antioxidant Treatment with N-acetyl Cysteine Prevents the Development of Cognitive and Social Behavioral Deficits that Result from Perinatal Ketamine Treatment. *Front Behav Neurosci.* 2017; 11: 106, doi: [10.3389/fnbeh.2017.00106](https://doi.org/10.3389/fnbeh.2017.00106), indexed in Pubmed: [28634445](https://pubmed.ncbi.nlm.nih.gov/28634445/).
  17. Pinilla I, Fernández-Sánchez L, Segura F, et al. Long time remodeling during retinal degeneration evaluated by optical coherence tomography, immunocytochemistry and fundus autofluorescence. *Exp Eye Res.* 2016; 150: 122–134, doi: [10.1016/j.exer.2015.10.012](https://doi.org/10.1016/j.exer.2015.10.012).
  18. Saka WA, Akhigbe RE, Azeez OM, et al. Effects of Pyrethroid Insecticide Exposure on Haematological and Haemostatic Profiles in Rats. *Pak J Biol Sci.* 2011; 14(22): 1024–1027, doi: [10.3923/pjbs.2011.1024.1027](https://doi.org/10.3923/pjbs.2011.1024.1027).
  19. Sankar P, Telang AG, Manimaran A. Protective effect of curcumin on cypermethrin-induced oxidative stress in Wistar rats. *Exp Toxicol Pathol.* 2012; 64(5): 487–493, doi: [10.1016/j.etp.2010.11.003](https://doi.org/10.1016/j.etp.2010.11.003), indexed in Pubmed: [21130633](https://pubmed.ncbi.nlm.nih.gov/21130633/).
  20. Santos P, Herrmann AP, Elisabethsky E, et al. Anxiolytic properties of compounds that counteract oxidative stress, neuroinflammation, and glutamatergic dysfunction: a review. *Braz J Psychiatry.* 2019; 41(2): 168–178, doi: [10.1590/1516-4446-2018-0005](https://doi.org/10.1590/1516-4446-2018-0005), indexed in Pubmed: [30328963](https://pubmed.ncbi.nlm.nih.gov/30328963/).
  21. Sapiaha P, Hamel D, Shao Z, et al. Proliferative retinopathies: angiogenesis that blinds. *Int J Biochem Cell Biol.* 2010; 42(1): 5–12, doi: [10.1016/j.biocel.2009.10.006](https://doi.org/10.1016/j.biocel.2009.10.006), indexed in Pubmed: [19836461](https://pubmed.ncbi.nlm.nih.gov/19836461/).
  22. Wang Y, Zhang Y, Ji L, et al. Prenatal and postnatal exposure to organophosphate pesticides and childhood neurodevelopment in Shandong, China. *Environ Int.* 2017; 108: 119–126, doi: [10.1016/j.envint.2017.08.010](https://doi.org/10.1016/j.envint.2017.08.010), indexed in Pubmed: [28843140](https://pubmed.ncbi.nlm.nih.gov/28843140/).
  23. Wu J, Gorman A, Zhou X, et al. Involvement of caspase-3 in photoreceptor cell apoptosis induced by in vivo blue light exposure. *Invest Ophthalmol Vis Sci.* 2002; 43: 3349–3354.



# Ameliorating effect of pomegranate peel extract supplement against type 1 diabetes-induced hepatic changes in the rat: biochemical, morphological and ultrastructural microscopic studies

K.A.J. Faddladdeen 

Biology Department, Faculty of Science, King Abdulaziz University, Jeddah, Saudi Arabia

[Received: 16 December 2019; Accepted: 2 March 2020]

**Background:** Diabetes mellitus could result from disorders in insulin secretion or receptors mainly characterised by hyperglycaemia. Natural antioxidants including pomegranate are traditionally used as hypoglycaemic agents. The present research was designed to evaluate the possible therapeutic role of pomegranate peel extract (PPE) against type 1 diabetic-induced hepatic biochemical and histological alteration.

**Materials and methods:** Adult male Wistar rats ( $n = 48$ ) were sorted into four groups: G1: control group, G2: normal rats received PPE, G3: streptozotocin (STZ)-diabetic rats, received IP STZ (55 mg/kg body weight), and G4: diabetic rats post-treated with PPE (200 mg/kg body weight/day). Effectiveness of PPE was assessed by measuring serum glucose, liver enzymes, and morphological features of liver tissue using light and electron microscopy.

**Results:** Histological examination showed degenerative necrotic changes in diabetic rat liver which were improved by post-treatment with PPE. Biochemical results confirmed microscopic morphological and ultrastructural findings.

**Conclusions:** Pomegranate peel extract was found to have a moderate therapeutic effect against hepatic alterations in male rats. It could be advised for diabetic patients suffering from early alterations of liver functions. (Folia Morphol 2021; 80, 1: 149–157)

**Key words:** pomegranate peel extract, therapeutic, streptozotocin, liver, diabetes, liver enzymes, ultrastructure

## INTRODUCTION

Diabetes is a challenging clinical condition with many drastic complications on body organs [15, 49] including the liver [46]. Hyperglycaemia is the main feature of diabetes mellitus [20]. It has many impacts on the structure and function of many organs [32, 51] including the liver [2, 44]. Hepatocytes are well-

known to be involved in the metabolism of different nutrients including carbohydrate [34].

Transmission electron microscopy (TEM) is used to give subcellular details of cells and define cell organelles involved in protein synthesis, energy production and lysosomal functions that can undergo alteration upon exposure to oxidative stress [31]. Researches

regarding hepatocyte alteration in diseases and therapeutic modulation were found in the literature [26].

Alteration of mitochondrial electron transport chain which may be reflected in mitochondrial ultrastructure and their energy production was reported [6]. Pomegranate is a famous fruit highly rich in antioxidants [9, 24] and its products were used as natural remedies for many diabetic oxidative-stress-induced lesions including liver [33]. This study showed that pomegranate juice significantly reduced hepatocyte lipid peroxidation and oxidative stress in type 2 diabetic rats through improving antioxidant status in liver tissue. Therapeutic uses of pomegranate were reviewed, and it was proved to be effective against many diseases such as dental infection, cardiovascular disease, and diabetes [23].

A study was done [28] that proved its effective role in the amelioration of diabetic induced nephropathy in the rat.

The previous study by the author showed that pomegranate peel extract (PPE) provided a prophylactic effect against diabetes-induced changes in rat liver [17]. Diabetes was reported to induce oxidative stress leading to tissue damage and this mostly occurs via alteration in mitochondria [14]. Thus, in the present study electron microscopy was used to confirm light microscopic morphological finding and describe mitochondrial and other organelles changes in the liver of diabetic rats besides demonstrating the therapeutic anti-diabetic effect of PPE together with confirming biochemical assay of liver enzymes alteration.

#### Ethical approval

This study was conducted according to guidelines and protocols approved by the ethical committee for animal care and use in King Fahd Medical Research Centre (KFMRC), King Abdulaziz University (KAU), Jeddah, Saudi Arabia, which are in accordance with the guidelines of the Canadian Council on Animal Care.

## MATERIALS AND METHODS

### Drugs and chemicals

Pomegranate fresh fruits were obtained from Taif region (Al Bustan farm), Saudi Arabia. Methanol was purchased from Sigma-Aldrich, Chemie GmbH, Germany. Streptozotocin (STZ) was obtained from Sigma-Aldrich Corp, St. Louis, MO, USA. Mouse alanine transaminase (ALT) ELISA Kit was obtained from Geno Technology, Inc. (USA). Rat total alkaline phosphatase (ALP) ELISA Kit as well as rat aspartate aminotrans-

ferase (AST) ELISA Kit were purchased from My Bio-Source, Inc., California, San Diego (USA).

### Animals

Adult (3 months old) male Wistar rats (n = 48) with an average body weight of 200–250 g were obtained from animal house (animal care unit in KFMRC, KAU, Jeddah, Saudi Arabia) according to the guidelines for animal research approved by the Unit of Biomedical Ethics Research Committee, Faculty of Medicine, King Abdulaziz University. Rats were divided into four groups (12 rats per cage) and allowed to adapt to lab conditions for 1 week, temperature 23°C and 22 Co humidity with 12 h/12 h light/dark cycle. They were fed with normal standard diet and water ad libitum.

### Methods

**PPE preparation.** Air-dried peel was prepared from fresh pomegranate (*Punica granatum*). Dried peels (50 g) was pulverized and extracted for 24 h using 500 mL absolute methanol using ULTRA-TUR-RAX disperser (T50 basic IKA-Werke, Germany). The resulted extract was filtered and evaporated using rotary evaporation (Rotavap, BUCHI, Switzerland). The extract was kept at 20°C.

**Diabetes induction.** STZ (55 mg/kg body weight) was dissolved in 0.05 M citrate buffer (1 mL) at pH 4.5 and injected immediately after preparation through intraperitoneal route to fasting rats. Glucose (5%) was given in drinking water to overcome STZ induced hypoglycaemia.

Three days later, blood glucose from fasted rats was taken from tail vein then measured using glucometer. Animals having blood glucose ranged from 300 to 500 mg/dL were chosen as a model for type 1 diabetes and included in the experimental procedure [8].

**Animal grouping and study design.** The experimental procedure last for 12 consecutive weeks where rats were divided into four groups: G1 — served as the control; G2 — rats received an oral dose of PPE (200 mg/kg body weight/day); G3 — STZ-diabetic rats, G4 — diabetic rats administrated PPE in a similar dose to G2. The following parameters were recorded.

**Body weight.** The body weight of all animal groups was recorded at the end of the experiment before sacrificing and was statically analysed.

**Blood glucose.** For evaluation of treatment response fasting glucose level was measured weekly all through the experiment using a blood glucometer

**Table 1.** Effects of streptozotocin (STZ) and pomegranate peel extract (PPE) on body weight, blood glucose, and liver enzymes in rats

	G1 (control)	G2 (PPE)	G3 (STZ)	G4 (STZ + PPE)
Body weight [g]	276.379 ± 21.92	259.4444 ± 28.58	202.1667 ± 3.85 <sup>a</sup>	227.8283 ± 13.72
Blood glucose [mg/dL]	91.89394 ± 3.54	97.12963 ± 4.72	464.9583 ± 26.45 <sup>a</sup>	392.8485 ± 9.67 <sup>b</sup>
Alanine aminotransferase [U/L]	23.16667 ± 7.34	26.83333 ± 7.67	56.5 ± 7.65 <sup>a</sup>	41.83333 ± 6.62 <sup>b</sup>
Aspartate aminotransferase [U/L]	54.33333 ± 12.23	54.66667 ± 9.30	154.8333 ± 26.62 <sup>a</sup>	78 ± 15.52 <sup>b</sup>
Alkaline phosphatase [U/L]	100.5 ± 14.68	80.66667 ± 9.45	209.5 ± 54.70 <sup>a</sup>	146.6667 ± 9.83 <sup>b</sup>

The number of animals was 12 for each group; all values are expressed as means ± standard deviation. <sup>a</sup>Significance versus G1 (control); <sup>b</sup>Significance versus G3 (STZ); p < 0.05

(ACCU-CHEK; Roche Mannheim, Germany). Blood glucose levels measured for all groups at the end of the experiment and were subjected to statistical analysis.

**Biochemical study for liver enzymes.** Blood samples were collected from the retro-orbital venous plexus lightly anesthetized animals before animal sacrifice. Serum was obtained by centrifugation at 4°C, 3000 rpm for 10 min then stored at -20°C for liver enzyme (ALT, AST, ALP) analysis [40]. The analysis was done in Mansour Scientific Foundation for Research and Development, Jeddah, Saudi Arabia.

**Tissue processing for morphological and ultrastructural microscopic features.** The rats were anesthetised lightly by diethyl ether inhalation (1 mL in soaked cotton pellets) and the abdominal cavity was incised at the midline. The liver was removed and samples from the large lobe (2 × 2 mm) were fixed either in 10% neutral buffered formalin or in 3% glutaraldehyde in phosphate buffer pH 7.4 at 4°C. Routine processing for light paraffin sections and electron microscopy was carried out in highly specialised lab in KAU hospital and electron microscopy unit. Paraffin sections are stained by haematoxylin and eosin (H&E) while semi-thin sections (0.5–1 mm) were stained with 1% toluidine blue for general orientation using light microscope. Ultrathin sections (60 nm thick) were done by ultra-tome then processed for staining using 2% uranyl acetate and lead citrate [37]. Photographing of ultrathin stained sections was done using a TEM (80 kV, JEM-100 Cx11, JEOL) in an Electron Microscopic Unit, Assuit University, Egypt.

### Statistical analysis

Statistical analysis using IBM SPSS Statistics ver. 20.0 was applied to evaluate and test the hypothesis. The results were presented as means ± standard deviations (SD). One-way analysis of variance (ANOVA) was used to find the significant differences between

the four groups' means followed by a post hoc test, Tukey HSD for multiple comparisons. Results were considered statistically significant when p < 0.05.

## RESULTS

### Body weight changes

Table 1 showed the body weight of G3 (STZ) was decreased significantly (p < 0.01) as compared with G1 (control) and G2 (PPE). The rats in G4 (STZ + PPE) showed an increased in body weight as compared with G3. PPE did not alter body weight of control rats. However, it was observed that the decrease in body weight in the diabetic rat was restored by PPE administration.

### Fasting blood glucose alteration

Table 1 showed that fasting blood glucose (FBG) of G3 was increased significantly (p < 0.01) as compared with control G1 and G2. The rats in G4 showed a decrease in FBG as compared with G3. PPE was found to lower blood glucose of diabetic rats but insignificantly compared with control. PPE, on the other hand, did not alter the blood glucose of control animals.

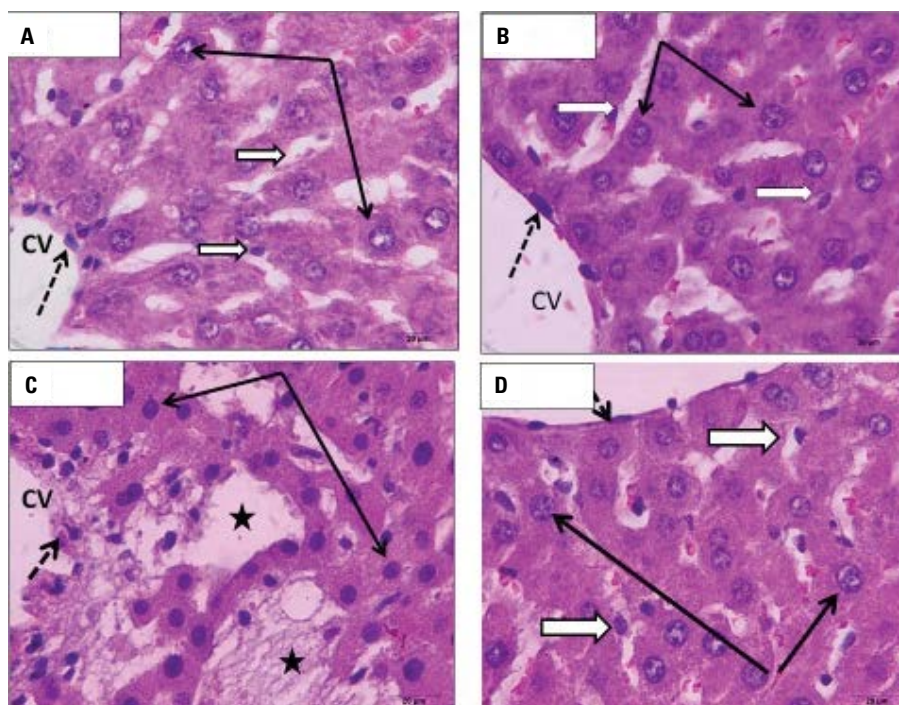
### Liver enzymes (ALT, AST, ALP) serum levels alteration

Table 1 showed the liver enzymes level in G3 was increased significantly (p < 0.01) as compared with control G1 and G2. The rats in G4 showed decreased in liver enzymes as compared with G3. Liver enzymes were assayed in this study to demonstrate any hepatocyte cell injury or necrosis that may lead to the release of enzymes into blood circulation.

### Histopathological study

#### *Effects of type 1 diabetes and PEE treatment on the morphology of liver tissue using light microscopy*

Figure 1 shows photographs from the light microscopic examination of paraffin (H&E stain) rat



**Figure 1.** Photomicrographs of transverse sections of rat liver. Magnified power (1000 $\times$ ) stained by H&E to show: **A.** G1: control. Part of central vein (CV) with intact endothelial lining (dotted arrows). Hepatocytes cell cords with rounded vesicular nuclei (black arrows) and slightly basophilic cytoplasm. Blood sinusoids are of normal appearance (white arrows); **B.** G2: pomegranate peel extract (PPE). No alteration in liver histology, CV is lined by intact endothelium (dotted arrow). Normal hepatocytes with normal nuclei (black arrows) and blood sinusoids (white arrows); **C.** G3: streptozotocin (STZ) diabetes. Showing damage to CV endothelial cell lining (dotted arrows). Hepatocytes are shrunken with their nuclei looked smaller darker and degenerated (black arrows) all are features of apoptosis. Many hepatocytes are lost leaving necrotic regions (stars); **D.** G4: STZ + PPE. Liver parenchyma with both hepatocytes (black arrows) and blood sinusoids (white arrows) looked normal and similar to control.

liver sections from control group 1 rats (Fig. 1A), PPE extract group (Fig. 1B), diabetic STZ group (Fig. 1C) and diabetic STZ + PPE group (Fig. 1D).

In Figure 1A hepatocytes were found to be arranged radially around the central vein. Cells had rounded central vesicular nuclei and showed an acidophilic cytoplasm. Thin-walled blood sinusoids were observed between hepatocyte cell cords. They were lined by flat endothelial cells. Occasionally, Kupffer cells nuclei could be seen in some sinusoids. Figure 1B showed no alteration of normal structure. In Figure 1C the liver showed scattered apoptotic hepatocytes (smaller in size than normal cells and having deeply stained acidophilic cytoplasm and small dark nuclei). Some samples showed necrotic cells with ill-defined outlines. In Figure 1D marked improvement was observed where the liver showed nearly normal radially arranged hepatocytes around the central vein. Blood sinusoidal spaces and their Kupffer cells also looked like that of control animals.

#### ***Effects of type 1 diabetes and PEE treatment on the morphology of liver tissue using electron microscopy***

**Semithin sections (toluidine blue stain).** The technique of semithin sectioning provided more detailed features of liver parenchyma. In control animals, hepatocytes with polyhedral shapes are normally arranged around the central vein were observed. The cells have vesicular nuclei with prominent one or two nucleoli. Blood sinusoids between hepatocytes are lined by endothelial and Kupffer cells (Fig. 2A).

In Figure 2B no alteration was observed. Alterations by STZ-induced diabetes were shown in Figure 2C; marked damage to central vein endothelial cell lining was observed. Hepatocytes appeared shrunken. Their nuclei looked smaller, darker and degenerated.

Blood sinusoids were dilated. Nearby hepatocytes showed necrosis leaving empty spaces.

In Figure 2D hepatocytes showed normal rounded central nuclei and prominent nucleoli; the cytoplasm

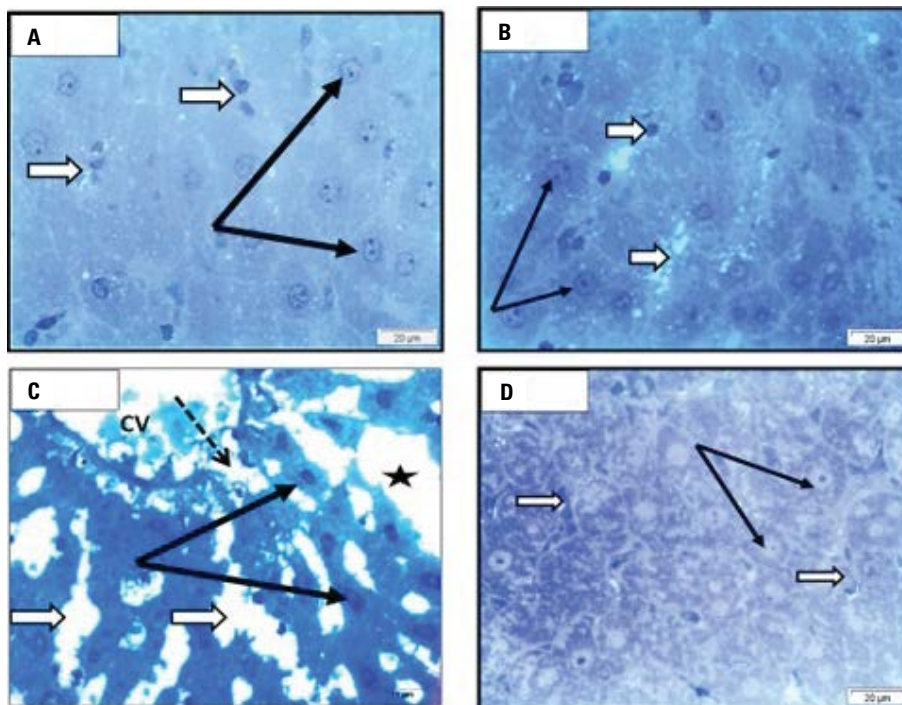


**Figure 2.** Photomicrographs of semithin sections from rat liver. Magnified power (1000×) stained by toluidine blue to show: **A.** G1: control. Notice the normal hepatocyte with their central rounded vesicular nuclei with prominent nucleoli (black arrows). Thin wall blood sinusoids with blood cells could be seen among hepatic cell cords (white arrows); **B.** G2: pomegranate peel extract (PPE). Showing also normal hepatocytes with rounded vesicular nuclei (black arrows). Blood sinusoids showed prominent Kupffer cell nuclei (white arrow); **C.** G3: streptozotocin (STZ). Marked damage to central vein (CV) endothelial cell lining (dotted arrows). Apoptotic hepatocytes are shrunken with their nuclei looked smaller, darker and degenerated (black arrows). Blood sinusoidal lumina are dilated (white arrow). Many hepatocytes are lost leaving necrotic regions (stars); **D.** G4: STZ + PPE. Showing hepatocytes with normal rounded central nuclei and prominent nucleoli (black arrows). The cytoplasm of some cells showed dark stained granules. Blood sinusoids between the cells are thin (white arrows).

of some cells dark stained granules. Blood sinusoids between the cells were thin.

**Ultra-structural changes in rat hepatocytes.**

The ultra-structural study was used to confirm what was seen by light microscopy as it showed cell organelles' changes in all experimental groups compared to control.

Electron microscopy micrographs from control liver (Fig. 3A, B) showed that hepatocytes have a normal population of mitochondria, rough endoplasmic reticulum and glycogen granules with few fat globules. The nuclei showed a euchromatic appearance.

Blood sinusoids are lined by normal Kupffer cells.

In Figure 3C there was no alteration in ultrastructure features of hepatocytes.

In Figure 3D, E electron microscopic photographs of diabetic rat hepatocytes showed enlarged nuclei, which is called karyomegaly. Binucleated hepatocytes with double nuclei were observed. Hepatocyte cytoplasm showed focal regions of organelle degeneration, few swollen mitochondria, lipid droplets, and

dark lysosomal bodies. In Figure 3F where diabetic rats were treated with PPE, ultrastructure features of hepatocytes showed absence of changes seen in treated diabetic group. The nucleus was normal. The cytoplasm contained rough endoplasmic reticulum beside numerous normal mitochondria. Smooth endoplasmic reticulum beside few cytoplasm vacuoles was observed.

**DISCUSSION**

The liver is considered the largest important organ that deals with metabolic processing of many nutrient materials including carbohydrate beside toxin and drug detoxification in both normal and diseased conditions [19]. Diabetes is associated with the increased process of oxidative stress induced by hyperglycaemia [11]. The increased free radicles in oxidative stress damaged many organs including the liver [30, 50].

Light microscopic examination in the present study showed alteration in diabetic rat liver in the form of disordered hepatic cords, appearance of

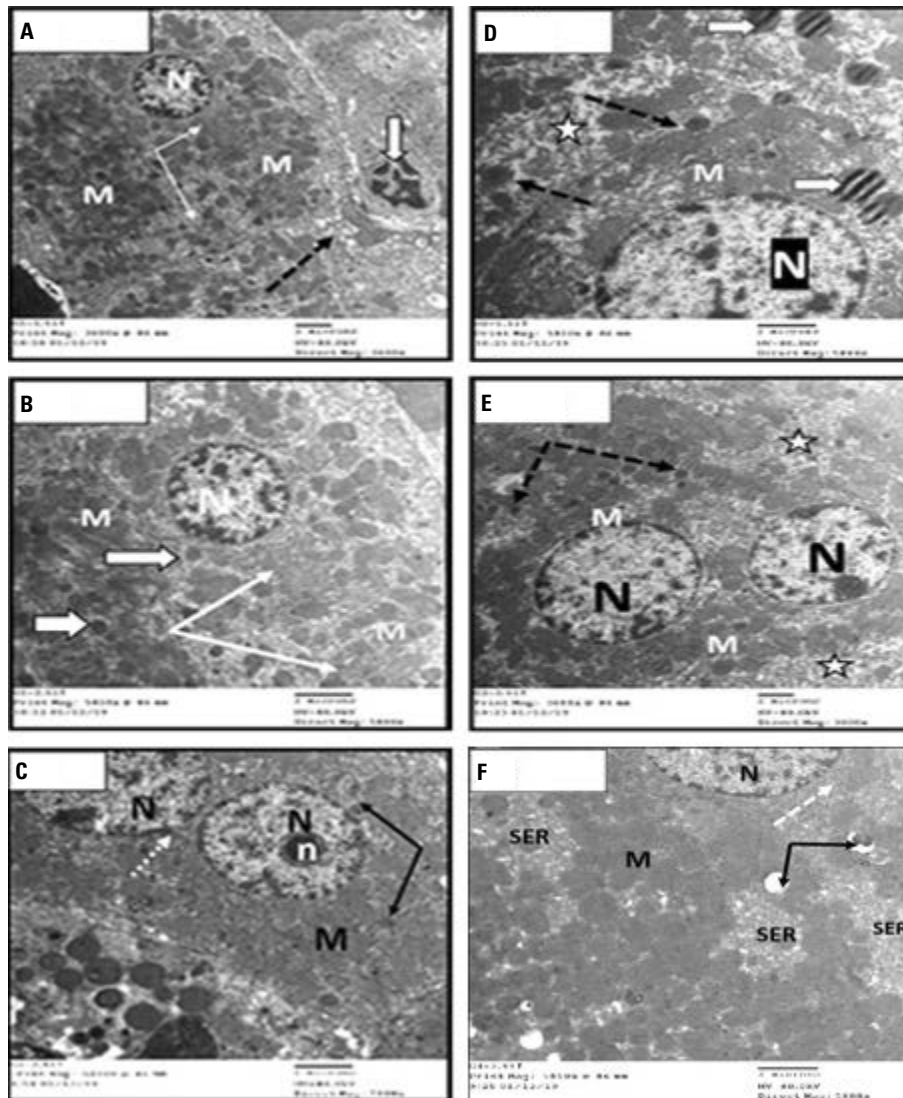


**Figure 3.** Electron micrographs of ultrathin sections from hepatocytes showing: G1: control; **A.** Low magnification (3600 $\times$ ) to show hepatocyte and part of nearby sinusoids lined by Kupffer cells (white arrow). Hepatocytes nucleus (N), mitochondria (M), rough endoplasmic reticulum (white arrows). Smooth endoplasmic as small vesicles (dotted arrows); **B.** Higher magnification (5800 $\times$ ) to show details of hepatocyte organelles and nucleus; **C.** G2: pomegranate peel extract (PPE). Showing binucleated hepatocyte (N) with prominent nucleoli (n). The cytoplasm showed numerous mitochondria (M), rough endoplasmic reticulum (white dotted arrows) and few small dense lysosomal bodies (black arrows) (5800 $\times$ ); **D, E.** G3: streptozotocin (STZ). Showing hepatocytes from diabetic rat liver; **D.** Hepatocytes with enlarged nuclei — karyomegaly (N). Focal area of cell organelle degeneration. Cytoplasm contains few swollen mitochondria (M), lipid droplets (white arrows), dark lysosomal dense bodies (dotted arrows) (5800 $\times$ ); **E.** Binucleated hepatocytes with double nuclei (N). One showed peripherally located nucleolus (n). Cytoplasm showed regions of organelle degeneration (white stars). Lysosomal bodies (dotted arrows) and mitochondria (M) (3600 $\times$ ); **F.** G4: STZ + PPE. Showing absence of changes seen in pomegranate treated diabetic group (STZ + PPE), the nucleus is normal (N). The cytoplasm contains rough endoplasmic reticulum (white arrows) numerous normal mitochondria (M). Few vacuoles (black arrows). Notice, regions of smooth endoplasmic reticulum (SER) (5800 $\times$ ).

scattered apoptotic cells, dilation in central vein and sinusoids, damaged lining of central veins. Similar results were reported by Aboonabi et al. [1], Al-Attar et al. [5], and Rodríguez et al. [38]. STZ-cytotoxicity on pancreatic islet  $\beta$ -cells resulting in hyperglycaemic status that interferes with cellular metabolic oxidative mechanisms [35]. Animal diabetic models exhibit high oxidative stress due to chronic hyperglycaemia

that results in depletion of the antioxidant defence system and promotes de novo generation of free radicals [29].

In the present study, semithin sections beside ultrastructural features of normal rat hepatocytes reflected what was seen in H&E stained paraffin. In electron microscopy micrographs the central vesicular nuclei appeared euchromatic where chromatin was seen

dispersed in the nucleoplasm with prominent nuclei. Such appearance indicated normal cellular activity [3]. On the other hand, hepatocytes from diabetic rats showed altered ultrastructure in the form of nuclear chromatin condensation (heterochromatic appearance), loss chromatin condensation (heterochromatic appearance), loss and damage to rough endoplasmic reticulum which appeared as electron-lucent regions with reticulated appearance. There was also a decreased mitochondria population. A similar observation was seen in many cases of hepatocyte cell injury in toxic conditions [11]. In diabetic status, similar ultrastructure alterations of hepatocytes in case of alloxan-induced diabetes in rat liver were described [26].

Loss of endoplasmic reticulum and decreased mitochondria population in hepatocytes of STZ-induced type 2 diabetes were also reported [7]. Also, Farid et al. [18] described disorganisation and degenerative changes in hepatocyte cytoplasmic organelles of diabetic rats.

Mitochondria integrity is critical for cellular health. In the present study, hepatocyte mitochondria showed a marked decrease in G3 diabetic rats. The decrease in mitochondria may affect energy production with subsequent derangement of functional activity. Hyperglycaemia was reported to cause damage to mitochondrial structure and function in tubular and mesangial cells of the diabetic rat kidney [14].

In a study done by Chang et al. [13], hyperglycaemia was found to affect mitochondrial replication and fusion needed to face nutrient depletion [13]. Hyperglycaemia was reported to increase Ca<sup>2+</sup> within mitochondria and this may cellular function [10]. Mitochondrial integrity and function were affected in the case of hepatic insulin resistance [39].

Accumulation of lipid droplets and lysosomal bodies in hepatocytes of the diabetic rats was demonstrated in this study at the level of electron microscopy. Similar observations were reported using HepG2 cells and were attributed to alteration of enzymes (inducible kinase) involved in the process of lipogenesis [36, 45]. Hyperlipidaemia associated with type 2 diabetes mellitus results in lipid deposition in different tissue including the liver [25, 42]. Steatosis or hepatic liver accumulation of lipids was also described in detail in the rat model [12].

Dense bodies observed in rat hepatocytes of G3: diabetic rats were most probably lysosomal structures that were previously described and associated with hepatocellular autophagy in alloxan-induced diabetes

in male mice [27]. The increase in the lysosomal structure was attributed to oxidative stress and increased free radical formation in diabetic status [21, 43].

In animals receiving PEE, hepatocytes showed the absence of changes induced by diabetes and looked similar to those of control.

Ultrastructure features of rat hepatocytes showed less features of necrosis, apoptosis, Bioactivities of pomegranate peel extract as an antioxidant was reported by Akhtar et al. [4]. It was used for the protection of many organs as in case diabetic nephropathic changes [28] and was used to antagonise oxidative stress induced by diabetes [16]. Diabetic rats were given extracts of pomegranate peel (*Punica granatum*) showed improved diabetic status [41]. The effect was reported by the authors to be via increasing antioxidants enzymes that antagonise oxidative stress of diabetic status.

Hepatic steatosis in diabetic patients was reported to be prevented by ellagic acid, the active ingredient of pomegranate [48]. Most previous researches regard pomegranate products deal with preventive activities against diabetic induced hepatic changes [22]. This study, however, proved its potential therapeutic effect against diabetic changes in liver parenchyma

However, an updated review about the health benefit of pomegranate products including PPE was done by Vučić et al. [47] who reported that more investigations have to be done to clarify the mechanism of its antidiabetic action before use as a therapy.

## CONCLUSIONS

It could be concluded that morphological features of liver tissue using both light and ultrastructural microscopic studies provided an idea concerning cellular and subcellular changes in case of diabetes compared to control. Mitochondrial alteration observed here confirmed that diabetic changes are due to oxidative stress, which explained the improvement occurred via administration of PPE; the natural supplement that proved to possess high antioxidant activity. Further studies on the same samples are running to confirm this mechanism. More work must be done via clinical trials to evaluate its beneficial effect in controlling diabetic hyperglycaemia and its complication especially hepatic in humans.

## Acknowledgements

This project was funded by the Deanship of Scientific Research (DRS), King Abdulaziz University, Jed-

dah, under grant no. D267-130-1441. The author, therefore, acknowledges with thanks to DSR technical and financial support.

## REFERENCES

- Aboonabi A, Rahmat A, Othman F. Effect of pomegranate on histopathology of liver and kidney on generated oxidative stress diabetic induced rats. *J Cytol Histol.* 2015; 6(1).
- Ahmadieh H, Azar ST. Liver disease and diabetes: association, pathophysiology, and management. *Diabetes Res Clin Pract.* 2014; 104(1): 53–62, doi: [10.1016/j.diabres.2014.01.003](https://doi.org/10.1016/j.diabres.2014.01.003), indexed in Pubmed: [24485856](https://pubmed.ncbi.nlm.nih.gov/24485856/).
- Ahmed RR, Abdul-Hamid M, Galaly SR, et al. Monosodium glutamate-induced liver microscopic and biochemical changes in male rats, and the possible amendment of quercetin. *Egypt J Zoo.* 2019; 71(71): 44–55.
- Akhtar S, Ismail T, Layla A. Pomegranate bioactive molecules and health benefits. *Bioactive Molecules Food.* 2019; 1253–1279, doi: [10.1007/978-3-319-78030-6\\_78](https://doi.org/10.1007/978-3-319-78030-6_78).
- Al-Attar AM, Alsalmi FA. Influence of olive leaves extract on hepatorenal injury in streptozotocin diabetic rats. *Saudi J Biol Sci.* 2019; 26(7): 1865–1874, doi: [10.1016/j.sjbs.2017.02.005](https://doi.org/10.1016/j.sjbs.2017.02.005), indexed in Pubmed: [31762669](https://pubmed.ncbi.nlm.nih.gov/31762669/).
- Alejandra Sánchez-Muñoz M, Valdez-Solana MA, Campos-Almazán MI, et al. Streptozotocin-Induced adaptive modification of mitochondrial supercomplexes in liver of wistar rats and the protective effect of lam. *Biochem Res Int.* 2018; 2018: 5681081, doi: [10.1155/2018/5681081](https://doi.org/10.1155/2018/5681081), indexed in Pubmed: [29686903](https://pubmed.ncbi.nlm.nih.gov/29686903/).
- Alshathly MR. Efficacy of ginger (*Zingiber officinale*) in ameliorating streptozotocin-induced diabetic liver injury in rats: histological and biochemical studies. *J Microsc Ultrastruct.* 2019; 7(2): 91–101, doi: [10.4103/JMAU.JMAU\\_16\\_19](https://doi.org/10.4103/JMAU.JMAU_16_19), indexed in Pubmed: [31293891](https://pubmed.ncbi.nlm.nih.gov/31293891/).
- Althunibat O, Al-Mustafa A, Tarawneh K, et al. Protective role of *Punica granatum* L. peel extract against oxidative damage in experimental diabetic rats. *Proc Biochem.* 2010; 45(4): 581–585, doi: [10.1016/j.procbio.2009.12.004](https://doi.org/10.1016/j.procbio.2009.12.004).
- Ardekani MRS, Hajimahmoodi M, Oveisi MR, et al. Comparative antioxidant activity and total flavonoid content of Persian pomegranate (*Punica granatum* L.) cultivars. *Iran J Pharmaceut Research: IJPR.* 2011; 10(3): 519.
- Arruda AP, Hotamisligil GS. Calcium homeostasis and organelle function in the pathogenesis of obesity and diabetes. *Cell Metab.* 2015; 22(3): 381–397, doi: [10.1016/j.cmet.2015.06.010](https://doi.org/10.1016/j.cmet.2015.06.010), indexed in Pubmed: [26190652](https://pubmed.ncbi.nlm.nih.gov/26190652/).
- Asmat U, Abad K, Ismail K. Diabetes mellitus and oxidative stress-A concise review. *Saudi Pharm J.* 2016; 24(5): 547–553, doi: [10.1016/j.jsps.2015.03.013](https://doi.org/10.1016/j.jsps.2015.03.013), indexed in Pubmed: [27752226](https://pubmed.ncbi.nlm.nih.gov/27752226/).
- Bae JS, Lee JY, Lee DH, et al. Quantitative evaluation of hepatic steatosis using normalized local variance in a rat model: comparison with histopathology as the reference standard. *Korean J Radiol.* 2019; 20(9): 1399–1407, doi: [10.3348/kjr.2019.0068](https://doi.org/10.3348/kjr.2019.0068), indexed in Pubmed: [31464118](https://pubmed.ncbi.nlm.nih.gov/31464118/).
- Chang JYA, Yu F, Shi L, et al. Melatonin affects mitochondrial fission/fusion dynamics in the diabetic retina. *J Diabetes Res.* 2019; 2019: 8463125, doi: [10.1155/2019/8463125](https://doi.org/10.1155/2019/8463125), indexed in Pubmed: [31098384](https://pubmed.ncbi.nlm.nih.gov/31098384/).
- Czajka A, Malik AN. Hyperglycemia induced damage to mitochondrial respiration in renal mesangial and tubular cells: Implications for diabetic nephropathy. *Redox Biol.* 2016; 10: 100–107, doi: [10.1016/j.redox.2016.09.007](https://doi.org/10.1016/j.redox.2016.09.007), indexed in Pubmed: [27710853](https://pubmed.ncbi.nlm.nih.gov/27710853/).
- Duru OK, Middleton T, Tewari MK, et al. The landscape of diabetic kidney disease in the united states. *Curr Diab Rep.* 2018; 18(3): 14, doi: [10.1007/s11892-018-0980-x](https://doi.org/10.1007/s11892-018-0980-x), indexed in Pubmed: [29457196](https://pubmed.ncbi.nlm.nih.gov/29457196/).
- El-Hadary AE, Ramadan MF. Phenolic profiles, antihyperglycemic, antihyperlipidemic, and antioxidant properties of pomegranate (*Punica granatum*) peel extract. *J Food Biochem.* 2019; 43(4): e12803, doi: [10.1111/jfbc.12803](https://doi.org/10.1111/jfbc.12803), indexed in Pubmed: [31353600](https://pubmed.ncbi.nlm.nih.gov/31353600/).
- Faddladdeen KA, Ojaimi AA. Protective effect of pomegranate (*Punica granatum*) extract against diabetic changes in adult male rat liver: histological study. *J Microsc Ultrastruct.* 2019; 7(4): 165–170, doi: [10.4103/JMAU.JMAU\\_6\\_19](https://doi.org/10.4103/JMAU.JMAU_6_19), indexed in Pubmed: [31803570](https://pubmed.ncbi.nlm.nih.gov/31803570/).
- Farid O, Zeggwagh NA, Ouadi FEI, et al. aqueous extract exhibits antidiabetic and hepatoprotective effects in streptozotocin-induced diabetic rats. *Endocr Metab Immune Disord Drug Targets.* 2019; 19(3): 292–301, doi: [10.2174/1871530318666181005102247](https://doi.org/10.2174/1871530318666181005102247), indexed in Pubmed: [30289084](https://pubmed.ncbi.nlm.nih.gov/30289084/).
- Ferrell JM, Chiang JYL. Circadian rhythms in liver metabolism and disease. *Acta Pharm Sin B.* 2015; 5(2): 113–122, doi: [10.1016/j.apsb.2015.01.003](https://doi.org/10.1016/j.apsb.2015.01.003), indexed in Pubmed: [26579436](https://pubmed.ncbi.nlm.nih.gov/26579436/).
- George B, Cebioglu M, Yeghiazaryan K. Inadequate diabetic care: global figures cry for preventive measures and personalized treatment. *EPMA J.* 2010; 1(1): 13–18, doi: [10.1007/s13167-010-0006-5](https://doi.org/10.1007/s13167-010-0006-5), indexed in Pubmed: [23199037](https://pubmed.ncbi.nlm.nih.gov/23199037/).
- Gheorghe G, Stoian A, Gaman MA, et al. The benefits and risks of antioxidant treatment in liver diseases. *Revista de Chimie.* 2019; 70(2): 651–655, doi: [10.37358/rc.19.2.6977](https://doi.org/10.37358/rc.19.2.6977).
- Hou C, Zhang W, Li J, et al. Beneficial effects of pomegranate on lipid metabolism in metabolic disorders. *Mol Nutr Food Res.* 2019; 63(16): e1800773, doi: [10.1002/mnfr.201800773](https://doi.org/10.1002/mnfr.201800773), indexed in Pubmed: [30677224](https://pubmed.ncbi.nlm.nih.gov/30677224/).
- Jurenka JS. Therapeutic applications of pomegranate (*Punica granatum* L.): a review. *Altern Med Rev.* 2008; 13(2): 128–144, indexed in Pubmed: [18590349](https://pubmed.ncbi.nlm.nih.gov/18590349/).
- Khaled SA. Herbal medicine in diabetes mellitus: effectiveness of punica granatum peel powder in prediabetics, diabetics and complicated diabetics. *J Biol Agriculture Healthcare.* 2015; 5(16): 34–42.
- Lisha V, John P, Sujith S, et al. Effect of Averrhoa bilimbi fruit powder on Histopathology and the functional Indices of the Liver and Kidney of Rats fed with high fat diet. *Pharma Innov J.* 2019; 8(1): 48–51.
- Lucchese AN, Cassetari LL, Spadella CT. Alloxan-induced diabetes causes morphological and ultrastructural changes in rat liver that resemble the natural history of chronic fatty liver disease in humans. *J Diabetes Res.* 2015; 2015: 494578, doi: [10.1155/2015/494578](https://doi.org/10.1155/2015/494578), indexed in Pubmed: [25789328](https://pubmed.ncbi.nlm.nih.gov/25789328/).
- Mahmoud A, Elgheri A, Shakor AA. Hyperglycemia and hyperinsulinemia induced hepatocellular autophagy in male mice. *Egypt Acad J Biol Sci, D. Histology Histochemistry.* 2015; 7(1): 1–10, doi: [10.21608/eajbsd.2015.14113](https://doi.org/10.21608/eajbsd.2015.14113).



28. Manna K, Mishra S, Saha M, et al. Amelioration of diabetic nephropathy using pomegranate peel extract-stabilized gold nanoparticles: assessment of NF- $\kappa$ B and Nrf2 signaling system. *Int J Nanomedicine*. 2019; 14: 1753–1777, doi: [10.2147/IJN.S176013](https://doi.org/10.2147/IJN.S176013), indexed in Pubmed: [30880978](https://pubmed.ncbi.nlm.nih.gov/30880978/).
29. Maritim AC, Sanders RA, Watkins JB. Diabetes, oxidative stress, and antioxidants: a review. *J Biochem Mol Toxicol*. 2003; 17(1): 24–38, doi: [10.1002/jbt.10058](https://doi.org/10.1002/jbt.10058), indexed in Pubmed: [12616644](https://pubmed.ncbi.nlm.nih.gov/12616644/).
30. Masarone M, Rosato V, Dallio M, et al. Role of oxidative stress in pathophysiology of nonalcoholic fatty liver disease. *Oxid Med Cell Longev*. 2018; 2018: 9547613, doi: [10.1155/2018/9547613](https://doi.org/10.1155/2018/9547613), indexed in Pubmed: [29991976](https://pubmed.ncbi.nlm.nih.gov/29991976/).
31. Mielańczyk Ł, Matysiak N, Klymenko O, et al. Transmission electron microscopy of biological samples. *Transmission Electron Microscope Theory Applications*. 2015, doi: [10.5772/60680](https://doi.org/10.5772/60680).
32. Mohammad G, Duraisamy AJ, Kowluru A, et al. Functional regulation of an oxidative stress mediator, rac1, in diabetic retinopathy. *Mol Neurobiol*. 2019; 56(12): 8643–8655, doi: [10.1007/s12035-019-01696-5](https://doi.org/10.1007/s12035-019-01696-5), indexed in Pubmed: [31300985](https://pubmed.ncbi.nlm.nih.gov/31300985/).
33. Nadia M, Ramadan G, El-Husseiny E, et al. Effects of pomegranate aril juice and its punicalagin on some key regulators of insulin resistance and oxidative liver injury in streptozotocin-nicotinamide type 2 diabetic rats. *Mol Biol Rep*. 2019; 46(4): 3701–3711, doi: [10.1007/s11033-019-04813-8](https://doi.org/10.1007/s11033-019-04813-8), indexed in Pubmed: [31006095](https://pubmed.ncbi.nlm.nih.gov/31006095/).
34. Nagarajan SR, Paul-Heng M, Krycer JR, et al. Lipid and glucose metabolism in hepatocyte cell lines and primary mouse hepatocytes: a comprehensive resource for in vitro studies of hepatic metabolism. *Am J Physiol Endocrinol Metab*. 2019; 316(4): E578–E589, doi: [10.1152/ajpendo.00365.2018](https://doi.org/10.1152/ajpendo.00365.2018), indexed in Pubmed: [30694691](https://pubmed.ncbi.nlm.nih.gov/30694691/).
35. Papaccio G, Pisanti F, Latronico M, et al. Multiple low-dose and single high-dose treatments with streptozotocin do not generate nitric oxide. *J Cell Biochem*. 2000; 77(1): 82–91, doi: [10.1002/\(sici\)1097-4644\(20000401\)77:1<82::aid-jcb9>3.0.co;2-v](https://doi.org/10.1002/(sici)1097-4644(20000401)77:1<82::aid-jcb9>3.0.co;2-v).
36. Qin H, Chen H, Zou Y, et al. Systematic investigation of the mechanism of Cichorium glandulosum on type 2 diabetes mellitus accompanied with non-alcoholic fatty liver rats. *Food Funct*. 2019; 10(5): 2450–2460, doi: [10.1039/c8fo02284d](https://doi.org/10.1039/c8fo02284d), indexed in Pubmed: [30969285](https://pubmed.ncbi.nlm.nih.gov/30969285/).
37. Reynolds ES. The use of lead citrate at high pH as an electron-opaque stain in electron microscopy. *J Cell Biol*. 1963; 17: 208–212, doi: [10.1083/jcb.17.1.208](https://doi.org/10.1083/jcb.17.1.208), indexed in Pubmed: [13986422](https://pubmed.ncbi.nlm.nih.gov/13986422/).
38. Rodríguez V, Plavnik L, Tolosa de Talamoni N. Naringin attenuates liver damage in streptozotocin-induced diabetic rats. *Biomed Pharmacother*. 2018; 105: 95–102, doi: [10.1016/j.biopha.2018.05.120](https://doi.org/10.1016/j.biopha.2018.05.120), indexed in Pubmed: [29852394](https://pubmed.ncbi.nlm.nih.gov/29852394/).
39. Rogers RS, Wheatley JL, Archer AE, et al. Heat shock protein 72 regulates mitochondrial integrity and function in the prevention of hepatic insulin resistance. *FASEB J*. 2016; 30(suppl 1): 1015–1011.
40. Saad EA, Hassanien MM, El-Hagrasy MA, et al. Antidiabetic, hypolipidemic and antioxidant activities and protective effects of Punica granatum peels powder against pancreatic and hepatic tissues injuries in streptozotocin induced IDDM in rats. *Int J Pharm Pharm Sci*. 2015; 7(7): 397–402.
41. Salwe KJ, Sachdev DO, Bahurupi Y, et al. Evaluation of antidiabetic, hypolipidemic and antioxidant activity of hydroalcoholic extract of leaves and fruit peel of Punica granatum in male Wistar albino rats. *J Nat Sci Biol Med*. 2015; 6(1): 56–62, doi: [10.4103/0976-9668.149085](https://doi.org/10.4103/0976-9668.149085), indexed in Pubmed: [25810635](https://pubmed.ncbi.nlm.nih.gov/25810635/).
42. Seng YH, Chang CW, Chiang W, et al. Adlay bran oil suppresses hepatic gluconeogenesis and attenuates hyperlipidemia in type 2 diabetes rats. *J Med Food*. 2019; 22(1): 22–28, doi: [10.1089/jmf.2018.4237](https://doi.org/10.1089/jmf.2018.4237), indexed in Pubmed: [30673500](https://pubmed.ncbi.nlm.nih.gov/30673500/).
43. Shaw JP, Moore MN, Readman JW, et al. Oxidative stress, lysosomal damage and dysfunctional autophagy in molluscan hepatopancreas (digestive gland) induced by chemical contaminants. *Mar Environ Res*. 2019; 152: 104825, doi: [10.1016/j.marenvres.2019.104825](https://doi.org/10.1016/j.marenvres.2019.104825), indexed in Pubmed: [31668363](https://pubmed.ncbi.nlm.nih.gov/31668363/).
44. Smith BW, Adams LA. Nonalcoholic fatty liver disease and diabetes mellitus: pathogenesis and treatment. *Nat Rev Endocrinol*. 2011; 7(8): 456–465, doi: [10.1038/nrendo.2011.72](https://doi.org/10.1038/nrendo.2011.72), indexed in Pubmed: [21556019](https://pubmed.ncbi.nlm.nih.gov/21556019/).
45. Song D, Yin L, Wang C, et al. Adenovirus-mediated expression of SIK1 improves hepatic glucose and lipid metabolism in type 2 diabetes mellitus rats. *PLoS One*. 2019; 14(6): e0210930, doi: [10.1101/514299](https://doi.org/10.1101/514299).
46. Targher G, Lonardo A, Byrne CD. Nonalcoholic fatty liver disease and chronic vascular complications of diabetes mellitus. *Nat Rev Endocrinol*. 2018; 14(2): 99–114, doi: [10.1038/nrendo.2017.173](https://doi.org/10.1038/nrendo.2017.173), indexed in Pubmed: [29286050](https://pubmed.ncbi.nlm.nih.gov/29286050/).
47. Vučić V, Grabež M, Trchounian A, et al. Composition and potential health benefits of pomegranate: a review. *Curr Pharm Des*. 2019; 25(16): 1817–1827, doi: [10.2174/1381612825666190708183941](https://doi.org/10.2174/1381612825666190708183941), indexed in Pubmed: [31298147](https://pubmed.ncbi.nlm.nih.gov/31298147/).
48. Zhang C, Hu J, Sheng L, et al. Ellagic acid ameliorates AKT-driven hepatic steatosis in mice by suppressing de novo lipogenesis via the AKT/SREBP-1/FASN pathway. *Food Funct*. 2019; 10(6): 3410–3420, doi: [10.1039/c9fo00284g](https://doi.org/10.1039/c9fo00284g), indexed in Pubmed: [31123744](https://pubmed.ncbi.nlm.nih.gov/31123744/).
49. Zheng Y, Ley SH, Hu FB. Global aetiology and epidemiology of type 2 diabetes mellitus and its complications. *Nat Rev Endocrinol*. 2018; 14(2): 88–98, doi: [10.1038/nrendo.2017.151](https://doi.org/10.1038/nrendo.2017.151), indexed in Pubmed: [29219149](https://pubmed.ncbi.nlm.nih.gov/29219149/).
50. Zhou B, Zhao J, Liu J, et al. Fluoride-induced oxidative stress is involved in the morphological damage and dysfunction of liver in female mice. *Chemosphere*. 2015; 139: 504–511, doi: [10.1016/j.chemosphere.2015.08.030](https://doi.org/10.1016/j.chemosphere.2015.08.030), indexed in Pubmed: [26295688](https://pubmed.ncbi.nlm.nih.gov/26295688/).
51. Zhou B, Li Q, Wang J, et al. Ellagic acid attenuates streptozotocin induced diabetic nephropathy via the regulation of oxidative stress and inflammatory signaling. *Food Chem Toxicol*. 2019; 123: 16–27, doi: [10.1016/j.fct.2018.10.036](https://doi.org/10.1016/j.fct.2018.10.036), indexed in Pubmed: [30342113](https://pubmed.ncbi.nlm.nih.gov/30342113/).

# Effect of vitamin B17 on experimentally induced colon cancer in adult male albino rat

W. Badr El-Kholy, S.A. Abdel-Rahman, F.E.-N. Abd El-Hady El-Safti, N. Mohey Issa

Human Anatomy and Embryology, Faculty of Medicine, Menoufia University, Menoufia, Shibin Al-koum, Egypt

[Received: 13 December 2019; Accepted: 23 January 2020]

**Background:** Colon cancer is considered to be the third most common cancer worldwide. At diagnosis of colon cancer, 3.7–11% developed bone metastasis. Diet based strategies are important for prevention and treatment of colon cancer. This study investigated the effect of vitamin B17 on a DMH induced rat model of colon cancer.

**Materials and methods:** Eighty young adult male albino rats were divided into five groups: group I (control group), group II (vitamin B17), group III (colon cancer), group IV (protected) and group V (treated). Distal colon sections were prepared for light and scanning electron microscopic examination. Lumbar vertebrae specimens were prepared for light microscopic study. Morphometric and statistical analysis were done.

**Results:** In comparison with the control, both colon cancer and treated groups showed invasion of the colonic tissue by pleomorphic branching colonic glands of variable shapes and sizes lined with dysplastic elongated hyperchromatic nuclei with frequent mitotic figures or stratified multi-layered crowded nuclei with an extremely significant ( $p < 0.0001$ ) reduction of goblet cell number when compared to the control together with major pathological bone changes were observed in colon cancer and the treated groups.

**Conclusions:** While the protected group showed impressive improvement of all previously mentioned diameters. (Folia Morphol 2021; 80, 1: 158–169)

**Key words:** colon cancer rat, vitamin B17

## INTRODUCTION

Colon cancer is often found in patients aged 50 years or older. However, recent interest in Egyptian colon cancer has been raised when epidemiological studies revealed a high incidence of this disease among young Egyptian population aged between 30 and 35 years [14]. The aetiology of colon cancer is multifactorial, including genetic, environmental and dietary factors [2]. At diagnosis of colon cancer, 3.7–11% developed bone metastasis [12]. Animal models are good ways to study the disease development. In addition, these models allow for studying the pre-

vention of colon cancer [7]. Currently, experimental models use 1,2-dimethylhydrazine (DMH) which is a potent colon carcinogen and the most widely used colon cancer inducer. DMH causes oxidative stress by methylating the molecules of colonic epithelial cells [5]. Colon cancer is considered to be a preventable disease [17, 25].

Vitamin B17, commonly known as Laetrile or Amygdalin, is claimed to be a potential natural chemotherapeutic agent found particularly in the seeds of common fruits such as apricots, peaches and apples [9]. The anti-neoplastic effect of vitamin B17 is attribut-

ed to its ability to induce apoptosis in tumour cells. It is also claimed to reduce the mitotic activity of these cells [18]. It would be therefore worthwhile to experimentally induce a rat model of colon cancer and study the possible role of vitamin B17 whether protective or curative.

## MATERIALS AND METHODS

**DMH.** A product of Sigma-Aldrich (Munich, Germany), was available in the form of white powder. It was dissolved in 1 mM EDTA-Normal saline. It was given to the rat by intra-peritoneal injection (IP) at a dose of 20 mg/kg/body weight once weekly for 5 consecutive weeks [23].

**Vitamin B17.** It was obtained online from (IHerb, California) in the form of capsules. The container served 100 capsules, each capsule served 100 mg Apricot seed extract (vitamin B17; Amygdalin). It was given at a dose of 300 mg/kg bodyweight daily by oral tube [24].

Eighty young adult male albino rats, weighing between 160 and 180 g were obtained from Theodor Bilharz Institute's animal house, El-Warraq, Giza, Egypt. They were fed standard diet. Ethical approval was obtained from the animal house of Theodor Bilharz Institute. Animals were divided into five main groups:

- Group I (control group): this group consisted of 10 male albino rats; they were subdivided into subgroup Ia: consisted of 5 rats; they were kept without any treatment until the end of the study; subgroup Ib: consisted of 5 rats, they received 1 mM EDTA intra-peritoneal once weekly until the end of the study;
  - Group II (vitamin B17 group): consisted of 10 rats, they received the calculated dose of vitamin B17 orally daily for 5 weeks;
  - Group III (colon cancer [CC] induced group): consisted of 20 rats, received the calculated dose of DMH IP once weekly for 5 weeks;
  - Group IV (protected group): consisted of 20 rats; received first the calculated dose of vitamin B17 orally daily for 5 weeks then colon cancer was induced for the following 5 weeks;
  - Group V (treated group): consisted of 20 rats; colon cancer was induced first with DMH injection by the dose mentioned above for 5 weeks, and then received the calculated dose of vitamin B17 for 5 consecutive weeks.
- All rats were then sacrificed after 10 weeks.

## Clinical assessment

Initial and final weights were recorded [11]; blood samples were taken for assessment of carcino-embryonic antigen (CEA) levels [12, 26].

## Light microscopic study

A small piece of the distal colon and lumbar vertebrae (cleaned of all soft tissue) were fixed for 24 hours in 10% neutral buffered formalin then dehydrated in ascending grades of alcohol, cleared and embedded in paraffin. After deparaffinizing, the 3–5 microns thick tissue sections were cut by microtome and were subjected to: haematoxylin and eosin (H&E) staining for routine histological examination, Masson trichome staining (for colon sections) for detection of collagen fibre deposition, toluidine blue (for bone sections) for assessment of bone mineralisation and immunohistochemical stains for colon sections (Ki-67 [marker of proliferation and detecting the mitotic activity], cytokeratin 20 [CK20 for detecting adenocarcinoma arising from epithelia that normally contain this protein], vascular endothelial growth factor [VEGF for detecting angiogenesis], and Caudal Type Homeobox 2 [CDx2 protein involved in the proliferation and differentiation of intestinal epithelial cells via regulation of intestine-specific gene transcription with a tumour suppressor role]).

## Scanning electron microscopic (SEM) study

Samples from distal colon were subjected to post-fixation in 2% osmium tetroxide for 2 hours. They were then washed in distilled water for 5 minutes and passed through a series of graded acetones to achieve dehydration. Critical point drying was carried out with liquid carbon dioxide. The specimens were mounted on aluminium slabs using silver conductive paint and gold palladium sputter coating was achieved using a Polaron E5100 sputter coating instrument. The biopsies were examined by a SEM (JEOL JSM35) at an acceleration voltage of 20 kV at electron microscopy unit at Faculty of Medicine, Tanta University [14].

## Morphometric study

Haematoxylin and eosin stain (colon sections): goblet cells number and Mitotic index, H&E stain (bone sections): number of bone resorption pits, Masson trichome stain: percentage of surface area of collagen fibre deposition, toluidine blue stain: colour intensity and immune-stains: percentage of Ki-67 immuno-positive nuclei, percentage of CK20

immuno-positive nuclei, area percentage of VEGF and percentage of surface area of CDx2 positive immune-staining in all groups by using image analyser software (Image J analyser version 1.43o8, National Institutes of Health, USA and Digimizer version 4.3.5, MedCalc software). This was done in the Anatomy and Embryology Department, Menoufia University.

### Statistical analysis

Statistical analysis was performed for the initial and final weights, CEA and for the morphometric results. Results were collected, tabulated and statistically analysed by statistical package for social science (SPSS) version 20 on IBM compatible computer. Results were expressed as mean ( $\bar{X}$ )  $\pm$  standard deviation (SD). Student t-test (a test for significance comparing two groups) was performed [6]. A value of  $p < 0.05$  was considered significant. Ten rats were used for each [15].

## RESULTS

### General results

Both CC induced group and the treated group showed decreased physical activity when compared to the control group. 20% and 30% mortality was recorded for the CC induced group and the treated group, respectively.

### Body weight

Figure 1 shows the body weight changes among the studied groups. Both CC induced group and the treated group showed significant ( $p < 0.001$ ) decrease in their final body weight when compared to their initial ones. The protected group showed a non-significant decrease ( $p > 0.05$ ) in their final weight when compared to their initial one.

### Biochemical results

Figure 2 shows the CEA level among the studied groups. Compared to the control group, animals of the CC induced group showed a statistically significant increase ( $p < 0.001$ ) in their CEA level. The protected group showed a non-significant increase ( $p > 0.05$ ) in its level. The treated one showed a significant increase ( $p < 0.001$ ) in the serum CEA concentration.

### Histological results

All sections of both control and vitamin B17 groups showed nearly similar histological features with no statistically significant differences between them.

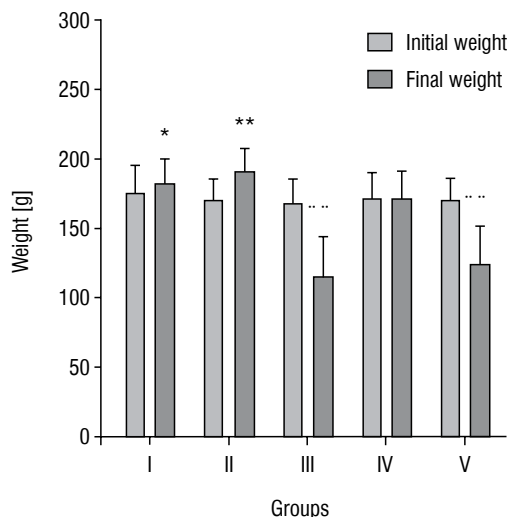


**Figure 1.** Mean initial and final body weight of all rats (in grams); \*, \*\*Significant increase ( $p < 0.05$  and  $p < 0.001$ , respectively) from the initial body weight; \*\*\*Significant decrease ( $p < 0.001$ ) from the initial body weight.

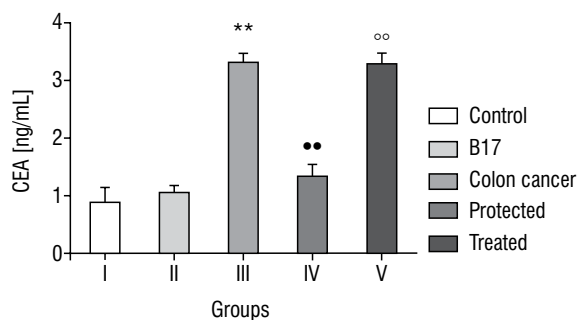


**Figure 2.** Mean serum carcino-embryonic antigen (CEA) concentration in all groups (ng/mL); \*\*Significant increase compared with the control group ( $p < 0.0001$ ); ••Significant decrease compared with the colon cancer induced group ( $p < 0.0001$ ); ••Significant increase compared with the protected group ( $p < 0.0001$ ).

### Light microscopic study

#### H&E stain

**Colon sections.** The colonic tissue of control group consisted of: the innermost layer is the mucosa, underneath there is the submucosa, followed by the muscularis propria and finally, the outermost layer — the adventitia. The structure of these layers varies, in different regions of the digestive system, depending on their function. The mucosa showed parallel straight crypts (colonic glands or acini) extending to the muscularis mucosa and separated by the lamina propria. The lining epithelium was composed of principle simple columnar epithelial cells with oval vesicular nuclei and mucous secreting goblet flask-shaped cells with basal dense nuclei. CC induced group (group III) showed disrupted mucosal

continuity with abnormal sloughing and extrusion of the necrotic debris into the colonic lumen, invasion of the colonic tissue by pleomorphic branching colonic glands of variable shapes and sizes. The abnormal glands were lined with dysplastic elongated hyperchromatic nuclei with an extremely significant ( $p < 0.0001$ ) increase in the number of mitotic figures or stratified multi-layered crowded nuclei with an extremely significant ( $p < 0.0001$ ) reduction of goblet cell number when compared to the control. Group IV showed preservation of the normal colonic architecture of the mucosa which appeared with preserved continuity. Most of the lining epithelial cells appeared with oval vesicular euchromatic nuclei; however, few lining epithelial cells showed mild to moderate dysplasia with elongated hyperchromatic nuclei. Some disruption of the muscularis mucosa with congested blood vessels in the sub-mucosa was evident. This group showed an extremely significant ( $p < 0.0001$ ) decrease in the mitotic index and an extremely significant increase ( $p < 0.0001$ ) in the goblet cell percentage when compared to the CC group. Group V showed more or less distorted colonic architecture with extensive sloughing of the abnormal mucosa into the lumen. The lining epithelial cells showed elongated hyperchromatic nuclei and a non-significant decrease in number of mitotic figures when compared to CC group. An extremely significant ( $p < 0.0001$ ) reduction of goblet cell number was clearly evident. The muscularis mucosa layer was disrupted and the submucosa showed congested dilated blood vessel (Figs. 3–6).

**Lumbar vertebra sections.** The bone tissue control group showed regular well-organised parallel arrangement of the bone lamellae. The osteocytes within the bone matrix were resident inside their lacunae. The bone marrow space was filled with haematopoietic cells and scattered adipocytes. CC induced group showed an extremely significant increase ( $p < 0.0001$ ) in bone resorption pits in the vicinity of multi-nucleated osteoclasts. The osteocytes appeared with wide lacunae. The bone lamellae lost their parallel well-organised arrangement with areas of sub-periosteal bone necrosis. The bone marrow spaces were widened and invaded by tumour cell nests with signet ring cells. The protected group revealed more or less preserved parallel arrangement of bone lamellae with an extremely significant decrease ( $p < 0.0001$ ) in number of bone resorption pits compared to the CC group, together with presence of several multi-nucleated osteoclasts. The treated group

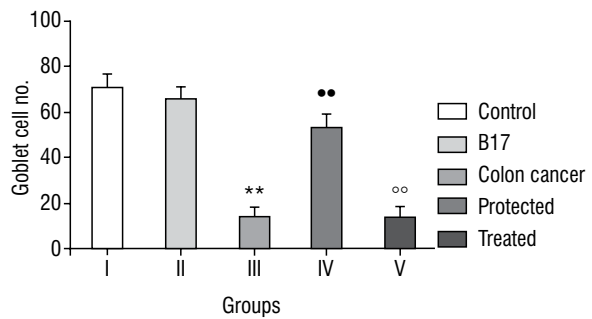


**Figure 3.** Mean Goblet cells percentage in all groups; \*\*Significant decrease compared with the control group ( $p < 0.0001$ ); ••Significant increase compared with the colon cancer induced group ( $p < 0.0001$ ); ooSignificant decrease compared with the protected group ( $p < 0.0001$ ).

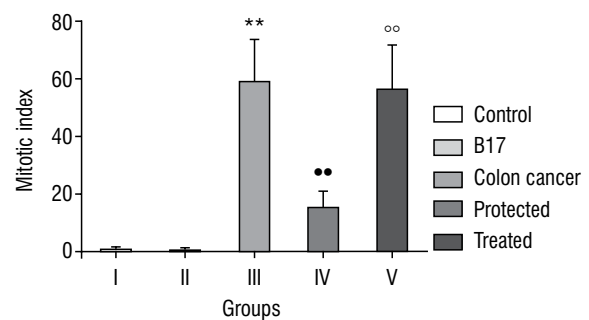


**Figure 4.** Mean mitotic index in all groups; \*\*Significant increase compared with the control group ( $p < 0.0001$ ); ••Significant decrease compared with the colon cancer induced group ( $p < 0.0001$ ); ooSignificant increase compared with the protected group ( $p < 0.0001$ ). Mitotic index = Number of mitotic figures  $\times$  100 / Number of all evaluated cells.

showed tumour cell nests invading the bone marrow space and surrounding the destructed trabecular bone that showed a non-significant decrease ( $p > 0.05$ ) of bone resorption pits number compared to CC group, with multi-nucleated osteoclasts (Figs. 7, 8).

### Special stains

**Masson trichome stain.** When compared with the control group, CC induced group showed an extremely significant increase ( $p < 0.0001$ ) in the surface area percentage of collagen fibre deposition. The protected group showed an extremely significant decrease ( $p < 0.0001$ ) in the same percentage when compared to the CC group. When compared to the CC group, the treated group showed no statistically significant difference ( $p > 0.05$ ) of the same percentage. When compared to the protected group, the treated group showed an extremely significant increase ( $p < 0.0001$ ) in this percentage (Fig. 9).

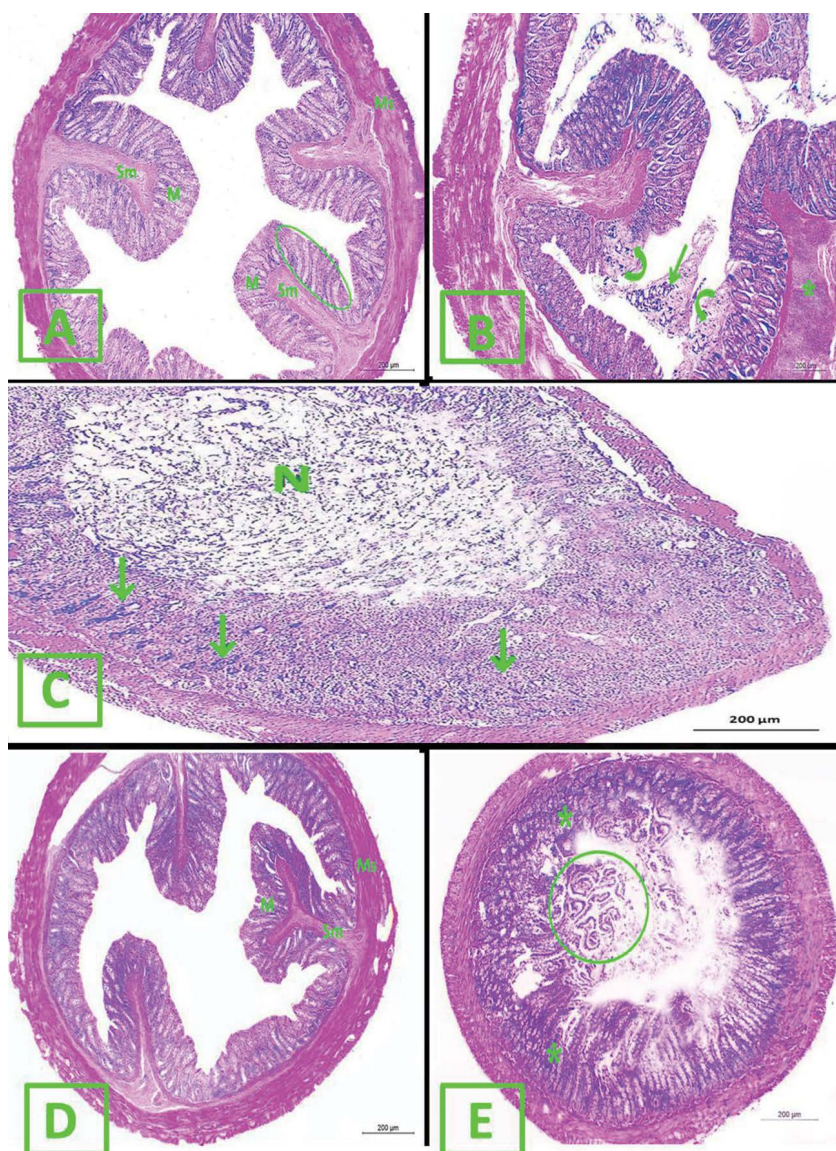


**Figure 5.** A photomicrograph of colon section in all experimental groups (H&E,  $\times 40$ ); **A.** Control group: mucosa (M) with parallel colonic crypts (encircled), submucosa (Sm) and muscularis (Ms); **B, C.** Colon cancer induced group: disrupted mucosal continuity (curved arrows) with abnormal sloughed tissue extruded into the lumen (thin arrow); **C.** Severely distorted colonic architecture with complete morphological loss of the mucosa and submucosa (arrows). Necrotic debris filling the colonic lumen (N); **D.** Protected group: preservation of normal mucosal continuity (M). The submucosa (Sm) and muscularis (Ms) layers appear more or less normal; **E.** Treated group: more or less distorted architecture. The mucosa and submucosa are infiltrated by irregular crowded colonic glands (asterisks). Sloughing of the crypts into the colonic lumen (encircled).

**Toluidine blue stain.** When compared with the control group, CC group showed an extremely significant decrease ( $p < 0.0001$ ) in the toluidine blue colour intensity. The protected group showed a very significant increase ( $p < 0.001$ ) in the same percentage when compared to the CC induced group. The treated group showed a non-significant decrease ( $p > 0.05$ ) in toluidine blue colour intensity when compared to the CC group, while showed an extremely significant decrease ( $p < 0.0001$ ) in toluidine blue colour intensity when compared to the protected group (Fig. 10).

**Immuno-stains.** Control group showed negative immune-staining for Ki-67, VEGF, mild positive immune-staining for CK20 and marked positive immune-staining for CDx2. CC group showed strong positive immune-staining for Ki-67, VEGF and CK20,

while showed negative immune-staining for CDx2. The protected group showed mild to moderate positive reactions for all immune-stains. The treated group showed marked positive immune-reaction for Ki-67, VEGF and CK20, while showed negative reaction to CDx2 (Figs. 11, 12).

#### SEM study

The control group revealed that the colonic surface mucosa was composed of rounded to oval well-arranged cryptal units. Each unit was covered with concentrically arranged epithelial cells with a central rounded lumen. The crypts were well-delineated by furrows. The cryptal units were loaded with mucous secretion. The CC group showed total loss of the epithelial cells covering the crypts. Moreover, necrotic areas

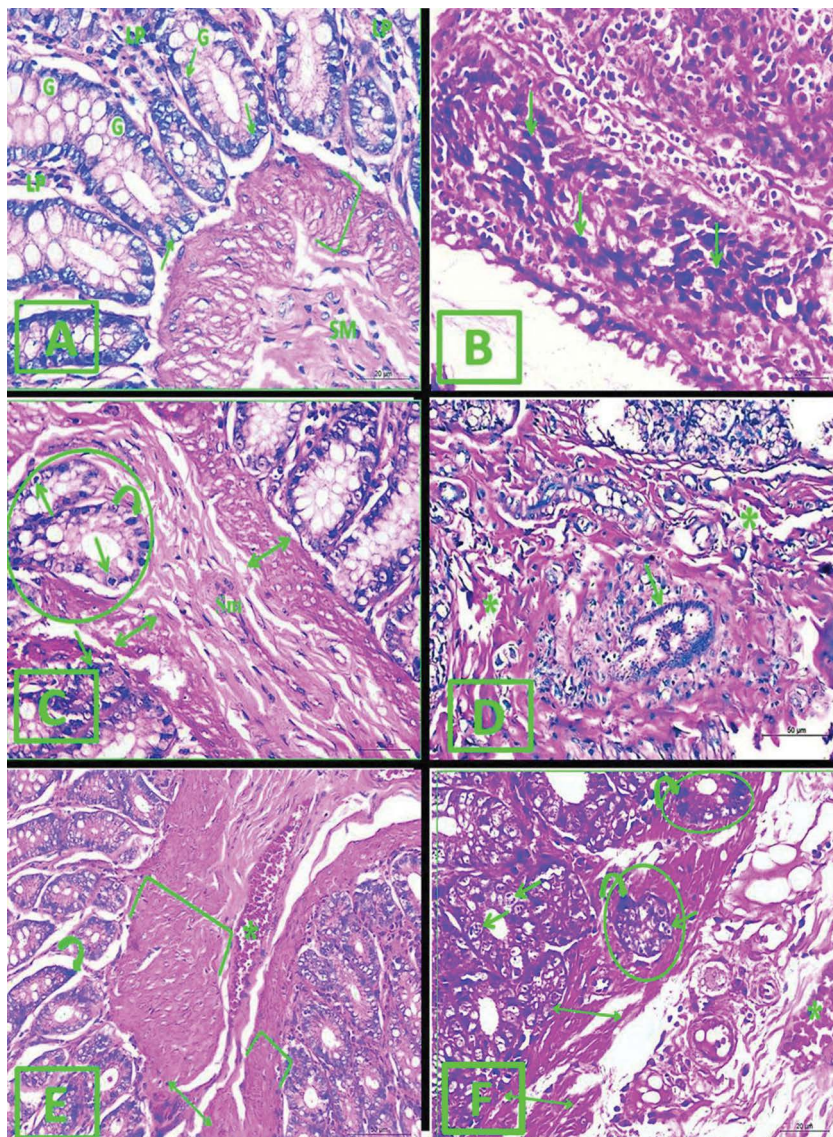


**Figure 6.** A photomicrograph of colon section in all groups (H&E,  $\times 400$ ); **A.** Control group: normal parallel colonic glands lined by simple columnar epithelial cells with oval vesicular nucleus (arrows) and mucous secreting goblet cells (G) with basal flat nuclei. Lamina propria (LP). Muscularis mucosa (bracketed). Submucosa (Sm); **B, C, D.** Colon cancer group: the atypical crypts lined with epithelial cells with elongated crowded hyperchromatic nuclei (arrows); **C.** Atypical colonic glands (encircled) invading the muscularis mucosa layer (double headed arrows) reaching the submucosa (Sm). Some nuclei show frequent mitotic figures (thin arrow); **D.** Abnormal pleomorphic colonic gland (thin arrow) lined with stratified multi-layered hyperchromatic crowded nuclei invading the muscularis layer (asterisks); **E.** Protected group: the majority of the crypts appear more or less normal. One abnormal shape crypt (curved arrow). Disrupted muscularis mucosa layer (double headed arrow). Asymmetrical appearance of muscularis mucosa (brackets). Congested dilated blood vessel in the submucosa (asterisk); **F.** Treated group: abnormal glands (encircled) invading a disorganised muscularis mucosa layer (double headed arrow). The lining epithelial cells possess either elongated hyperchromatic nuclei (curved arrows) or frequent mitotic figures (thin arrows). Congested dilated blood vessel in the submucosa (asterisk).

of the surface mucosa were clearly evident. The surface mucosa was depleted of mucous secretion. The protected group showed more or less normal crypt units bathed with mucous secretion with preserved both covering epithelium and central lumen. However, some sections showed few abnormal crypts which lost their covering epithelium. The cryptal units of the treated group showed loss of their covering epithelium, others showed obliteration of the central lumen. Necrotic areas of the surface mucosa were clearly evident (Fig. 13).

## DISCUSSION

With the increasing incidence of colon cancer worldwide with its very high morbidity and mortality rates and poor prognosis, several attempts were done to convert it to a preventable disease [5, 11]. Vitamin B17 (Amygdalin), as a natural substance, may have

anti-inflammatory and anti-cancerous effects. The role of vitamin B17 in treating colon cancer is still a matter of controversy. In this study, the elevated serum CEA levels of the colon cancer induced group judged the occurrence of colon cancer which was further supported by the highly significant reduction in the final body weight of this group when compared to the initial one. Furthermore, colon cancer was evidenced by the major pathological lesions affecting the colon; this was in accordance with Moharib et al. [15]. In the current work, the earliest hallmark for colon cancer was the presence of hyperplastic aberrant crypt foci which are abnormal crypts diverging from the normal shape. This was in agreement with Youssef et al. [28]. Hyperplasia of the crypts was further evidenced in this study by the SEM results that showed hyperplastic elevated crypts' epithelial covering. This

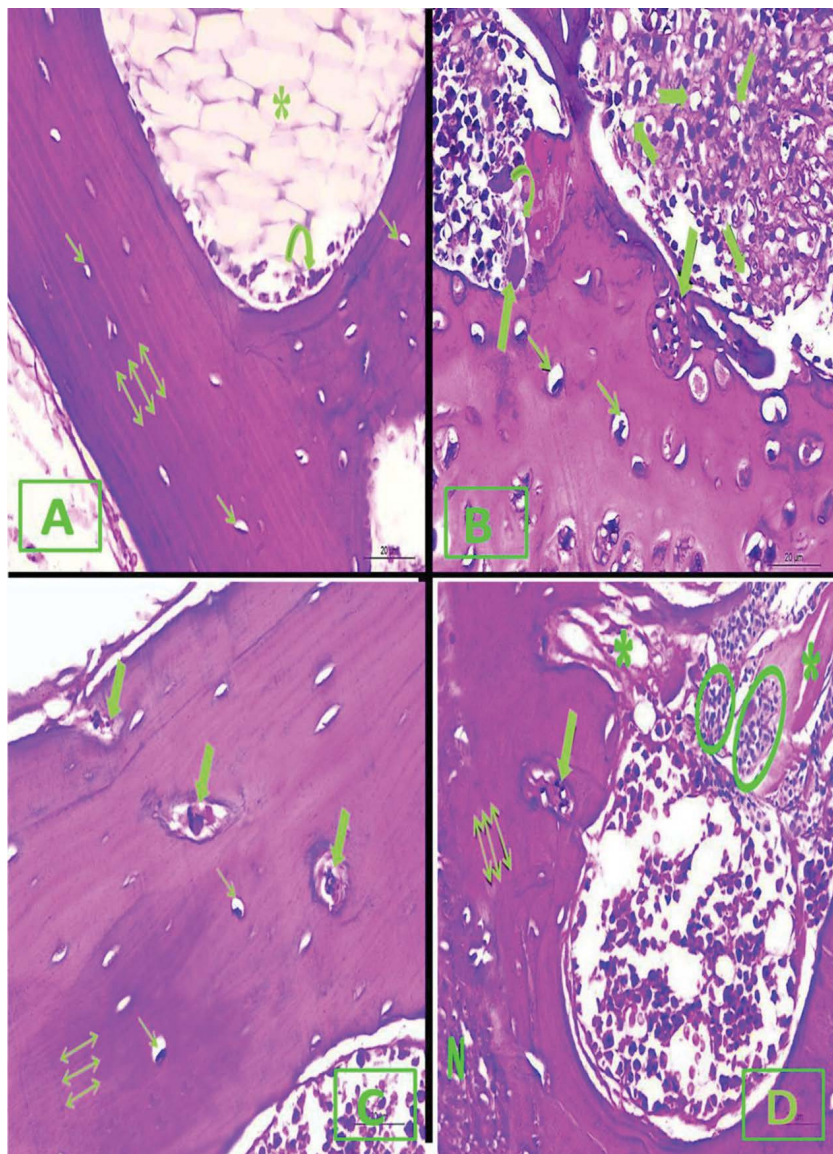


**Figure 7.** A photomicrograph of lumbar vertebrae section in all groups (H&E,  $\times 400$ ); **A.** Control group: regular well-organised parallel arrangement of the bone lamellae (double headed arrows). Osteocytes inside their lacunae (thin arrows). The bone marrow spaces can be seen with large vacuolated adipocytes (asterisk) and haematopoietic cells (curved arrow); **B.** Colon cancer group: multinucleated osteoclasts (thick arrows) at the site of bone scalloping (curved arrow). Osteocytes with wide lacunae (thin arrows). Invasion of the bone marrow spaces by tumour cell nest with signet ring cells (notched arrows); **C.** Protected group: more or less preserved arrangement of the bone lamellae (double headed arrows). Multi-nucleated osteoclasts (thick arrows). Widening of the osteocytes' lacunae (thin arrows); **D.** Treated group: distorted arrangement of the bone lamellae (double headed arrows). Tumour cell nests (encircled) invading destructed bone trabeculae (asterisks). Multi-nucleated osteoclast (thick arrows). Area of bone necrosis (N).

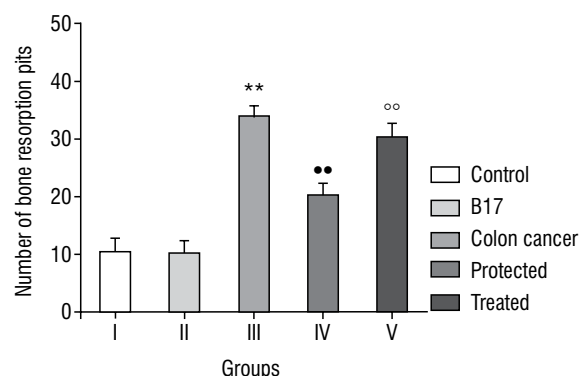


**Figure 8.** Mean number of bone resorption pits; \*\*Significant increase compared with the control group ( $p < 0.0001$ ); ••Significant decrease compared with the colon cancer induced group ( $p < 0.0001$ ); ooSignificant increase compared with the protected group ( $p < 0.0001$ ).

was supported by Paulsen et al. [20]. Sanganna and Kulkarni [21] stated that hyperplasia might be due to the oxidative stress involved in the process of tumour development. This mechanism might explain the highly significant increase in the mitotic index of this group when compared to control as shown in our results. Furthermore, in the present work, the CC induced group showed intense positive immunoreaction for Ki-67 which might prove the enhanced proliferative activity. All degrees of dysplasia have been reached; mild, moderate and severe dysplasia with finally the anaplasia or the carcinoma stage. This was in agreement with Jucaa et al. [11] who used the same methodology for completion of experimental carcinogenesis by DMH. Colon cancer group in this



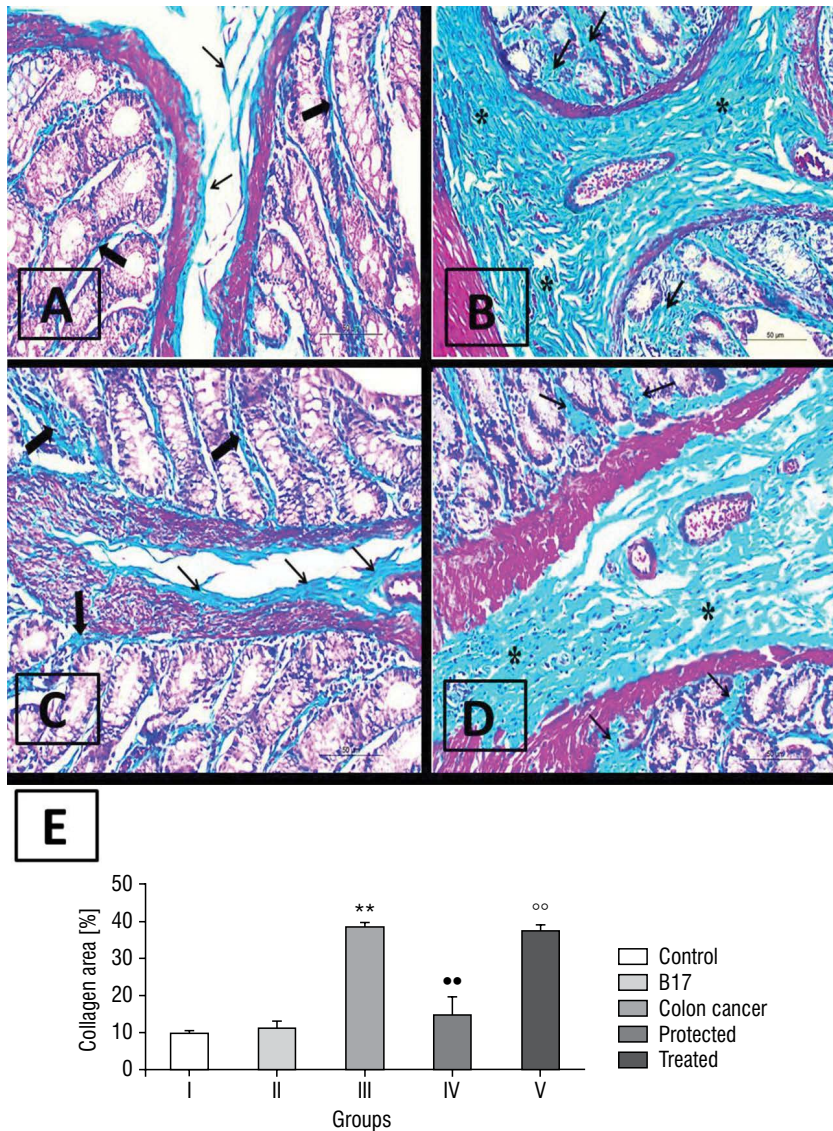


**Figure 9.** Photomicrographs of Masson trichrome stained colon sections of all groups ( $\times 400$ ); **A.** Control group: minimal amount of collagen fibre deposition (arrows); **B.** Colon cancer induced group: large amount of collagen fibre deposition (arrows and asterisks); **C.** Protected group: small amount of collagen deposition (thick and thin arrows); **D.** Treated group: large amount of collagen fibre deposition (arrows and asterisks); **E.** Foote notes: \*\*Significant increase compared with the control group ( $p < 0.0001$ ); ••Significant decrease compared with the CC group ( $p < 0.0001$ ); ∞∞Significant increase compared with the protected group ( $p < 0.0001$ ).

study showed strong positive immune-reaction for CK20; which emphasized reaching the adenocarcinoma stage; this was in accordance with Nabil et al. [16]. In the present study, CC induced group showed a highly significant decrease in the number of Goblet cells or their complete absence. This was further evidenced by our SEM study which revealed absence of the mucous secretion in this group. In this study, CC group showed a highly significant increase in the percentage of collagen fibre deposition. Fibrosis might suggest the presence of chronic inflammation, thus chronic exposure of fibroblasts to inflammatory mediators may drive their transition to activated myofibroblasts with consequent abnormal collagen production. Colon cancer induced group showed highly significant decrease in the percentage of CDx2 positively stained surface area; this was in agree-

ment with Sangeetha and Nalini [22]. In the current study, angiogenesis (formation of new capillaries from pre-existing blood vessels) as one of the most leading factors to develop bone metastasis has been proved as CC group showed strong positive expression of VEGF. Lumbar spine was the site of choice to assess the possibility of bone metastasis. This was in accordance with Jimi et al. [10], who postulated that the lumbar spine, followed by the pelvis were the most common sites of bone metastasis in colon cancer (62.16–55.40%, respectively). Cassar et al. [3] attributed vertebral metastasis from colon cancer to a vertebral venous plexus named Baston’s plexus which was considered to be the main source of spreading. In the present study, bone metastasis was evident due to presence of multiple osteolytic lesions and resorption pits. Increased activity of the

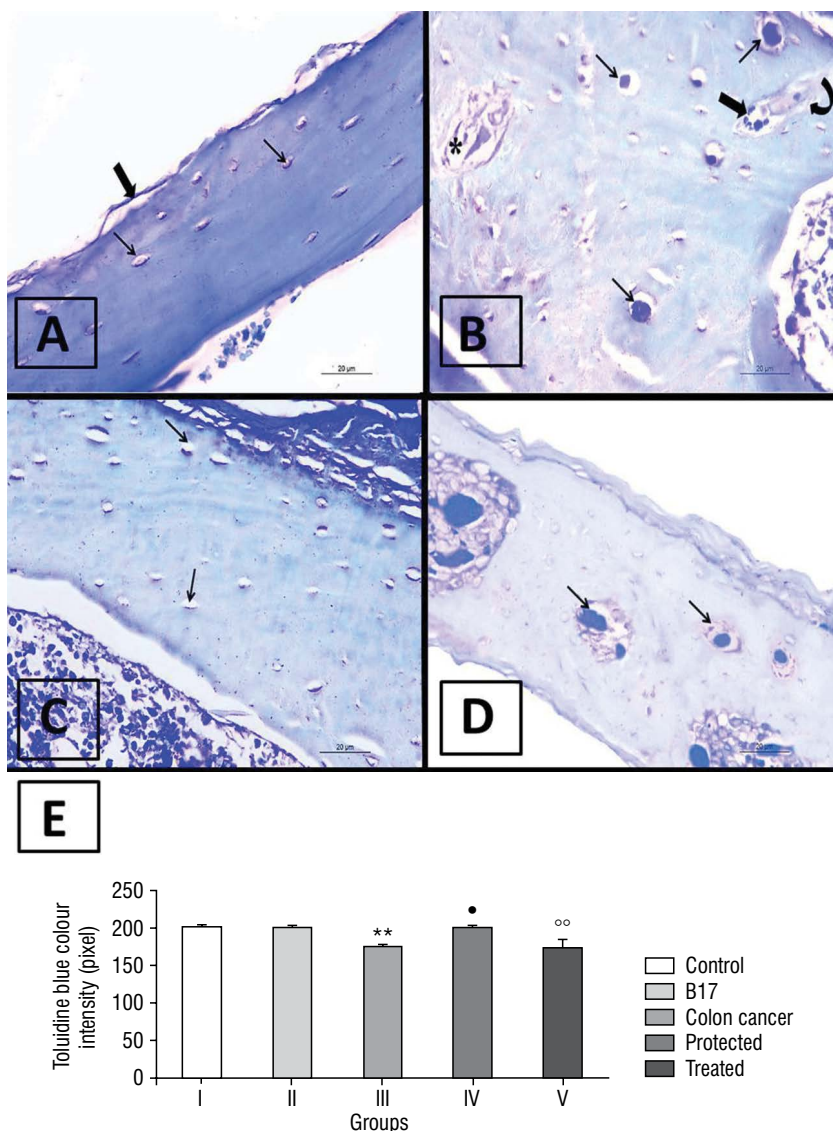


**Figure 10.** Photomicrographs of toluidine blue stained lumbar vertebral sections of all groups ( $\times 400$ ); **A.** Control group: dark blue staining of the bone sections; **B.** Colon cancer group: faint blue staining of the bone sections; **C.** Protected group: average blue staining of the bone sections; **D.** Treated group: pale blue staining of the bone sections; **E.** Foote notes: \*\*Significant decrease compared with the control group ( $p < 0.0001$ ); •Significant increase compared with the colon cancer induced group ( $p < 0.05$ ); °°Significant decrease compared with the protected group ( $p < 0.0001$ ).

osteoclasts revealed the presence of osteolytic type of bone metastasis. This was in accordance with Macedo et al. [13]. The presence of tumour cell nests inside the bone marrow cavity emphasized the metastasis. These results were in line with Vatandoust et al. [27] who reported that signet ring cell stage of colon cancer had a high rate of bone osteolytic metastasis. In the current work, when compared to the CC group, the protected group showed nearly normal physical activity, average food intake, a non-significant difference between their final body weight and their initial one. No deaths occurred among this group, marvelous regenerative changes proved by the significant improvement in serum CEA level and the impressive improvement of the disrupted histology that appeared very close to reach the normal appearance.

On the contrary, the treated group did not show any impressive improvement compared with CC induced and protected groups. The present study showed significant decrease in collagen fibre deposition of the protected group when compared to the treated one. This might suggest the anti-fibrotic action of vitamin B17. This could be explained as vitamin B17 caused regression of inflammation with subsequent regressed fibrosis. This was in accordance with Bottinger and Bitzer [1] who reported that vitamin B17 might enhance serum butyrate concentration which caused suppression of pro-fibrotic cytokine transforming growth factor beta 1 (TGF- $\beta 1$ ). Moreover, Guo et al. [8] studied the effect of amygdalin in suppressing kidney fibroblast proliferation and TGF- $\beta 1$  secretion in the lymphocytes and thus was able to

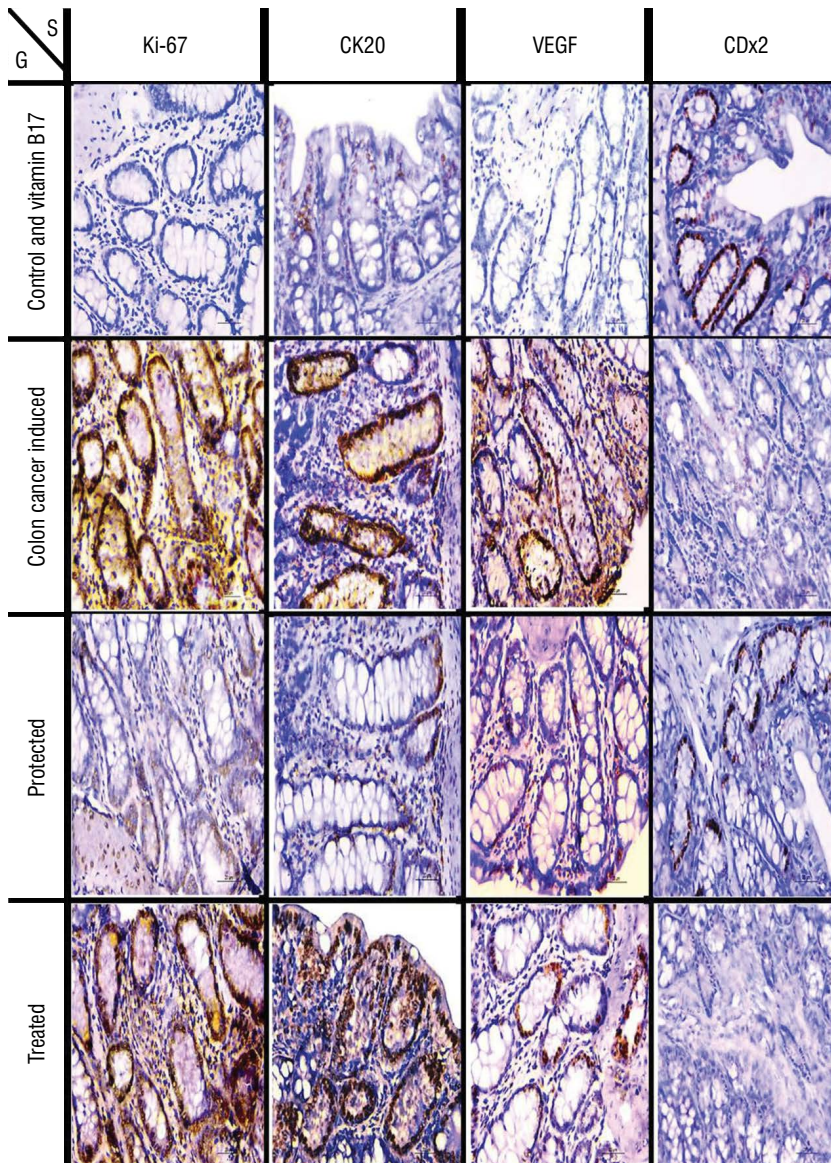


**Figure 11.** Photomicrographs of immuno-stained colon sections of all groups ( $\times 400$ ); Control and vitamin B17 groups: negative immune-staining for Ki-67, CK20, VEGF and positive for CDx2. CC induced group: strong positive immune-staining for Ki-67, CK20, VEGF and negative for CDx2; Protected group: mild to moderate immune-reaction for all immune-stains; Treated group: strong positive immune-staining for Ki-67, CK20 and VEGF, but negative reaction to CDx2 immuno-stain; S — stain; G — group; rest abbreviations — see text.

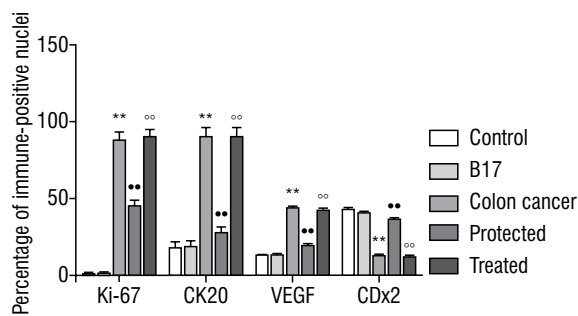


**Figure 12.** Mean area percentage of immune-positive nuclei (%) in all groups: \*\*Significant increase ( $p < 0.0001$ ) compared with the control group (for Ki-67, CK20 and VEGF) and significant decrease ( $p < 0.0001$ ) compared with the control group for CDx2; ••Significant decrease compared with the colon cancer group for Ki-67, CK20 and VEGF and significant increase compared with colon cancer group for CDx2 ( $p < 0.0001$ ); °°Significant increase from compared with the protected group for Ki-67, CK20 and VEGF and significant decrease from protected group for CDx2 ( $p < 0.0001$ ); abbreviations — see text.

significantly postpone the process of renal interstitial fibrosis, which further proved the anti-fibrotic effect of Amygdalin. Furthermore, they hypothesized that the mechanisms which might be involved include increasing the secretion of type I collagenase, inhibiting kidney fibroblast proliferation, accelerating apoptosis and suppressing type I collagen synthesis. In the present study, the protected group showed mild positive immunoreaction for Ki-67 which might prove the inhibition of proliferative activity. This finding was in agreement with Park et al. [19]. The mechanisms of vitamin B17 in defeating cancer cells were uncertain; however, Cassiem and De-Kock [4] performed a very recent study on vitamin B17's anti-cancer role. Being selective for destructing cancer cells which lack rhodanese enzyme, vitamin B17 exerts its anti-oxidant

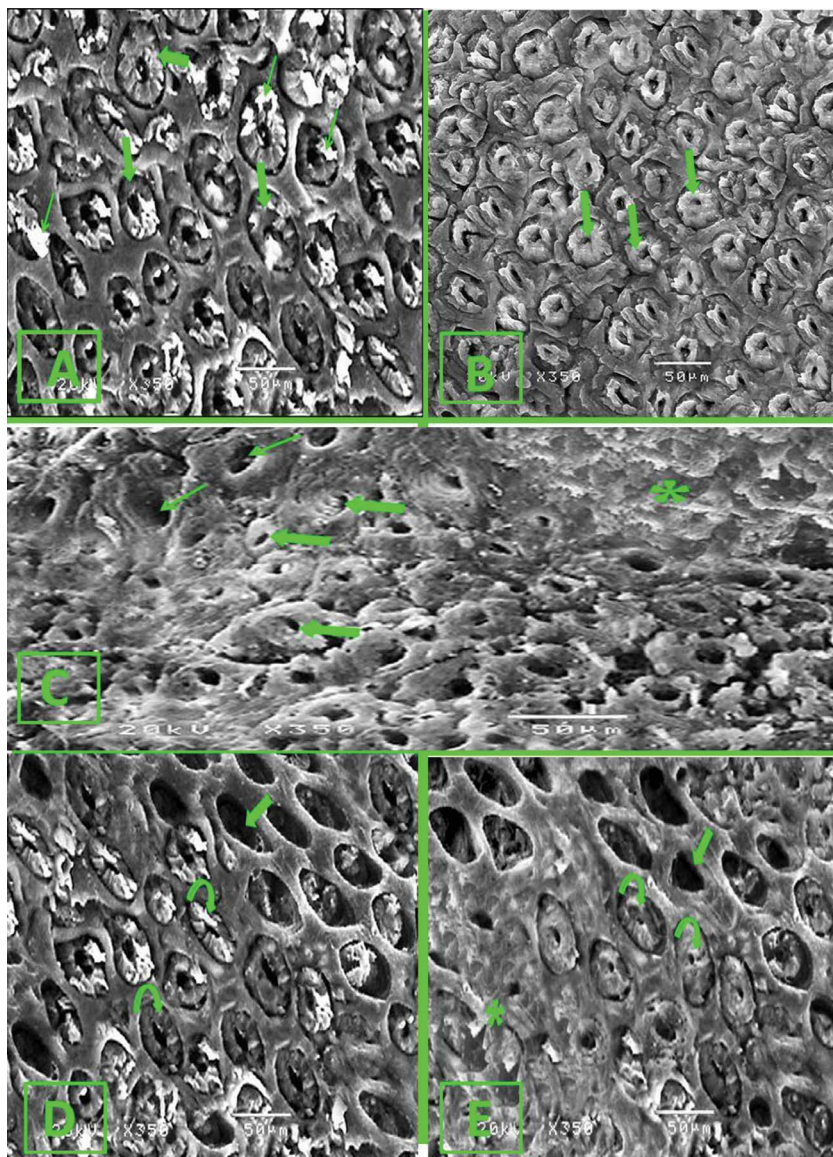


**Figure 13.** Scanning electron micrographs of colon sections of all groups (SEM,  $\times 350$ ); **A.** Control group: rounded to oval crypt units (encircled) covered with concentrically arranged epithelial cells, each unit is demarcated by a furrow (thick arrow) with a lumen at the centre (asterisk). Mucous secretion can be noticed (thin arrows); **B.** Colon cancer induced group: elevated crypt units with hyperplasia (arrows); **C.** Colon cancer group: crypts with narrowed slit like lumen (thick arrows); others show wide crypt lumen with total loss of the cells covering the crypts (thin arrows). A necrotic area can be observed (asterisk); **D.** Protected group: some crypts appear more or less normal (curved arrows); others show complete loss of their covering cells (thick arrow); **E.** Treated group: crypts with obliterated lumen (curved arrows); others show total loss of their covering epithelium (thick arrow). A large necrotic area can be noticed (asterisk).

action. Normal cells do have the rhodanese enzyme which neutralizes vitamin B17 converting it to a harmless compound; thiocyanate. Meanwhile, cancer cells lack rhodanese enzyme, so cyanide radical is liberated. Moreover, Song and Xu [24] added that Amygdalin could significantly increase polyhydroxyalkanoates that induced human peripheral blood T lymphocyte proliferation with secretion of interleukin 2 and interferon gamma, and then inhibiting the secretion of TGF- $\beta 1$ , therefore enhancing the immune function. In the current work, treatment of colon cancer with vitamin B17 did not either induce improvement or reversal of the pathological changes that occurred. This might be due to the progressive and irreversible uncontrolled progressive cancer cell division and

bone metastasis. Ki-67, CK20 and VEGF all showed intense positive immunostaining when compared to the control group.

## CONCLUSIONS

Our findings revealed that daily intake of vitamin B17 may play an important role as a chemo-preventive, anti-cancer, anti-inflammatory, anti-fibrotic and anti-oxidant agent. Furthermore, this study proved the uselessness of vitamin B17 in curing colon cancer.



## Acknowledgements

Acknowledgment to all members of Human Anatomy and Embryology Department Faculty of Medicine, Menoufia University, Egypt.

## REFERENCES

1. Bottinger EP, Bitzer M. TGF-beta signaling in renal disease. *J Am Soc Nephrol*. 2002; 13(10): 2600–2610, doi: [10.1097/01.asn.0000033611.79556.ae](https://doi.org/10.1097/01.asn.0000033611.79556.ae).
2. Carethers JM. Clinical and genetic factors to inform reducing colorectal cancer disparities in African Americans. *Front Oncol*. 2018; 8: 531, doi: [10.3389/fonc.2018.00531](https://doi.org/10.3389/fonc.2018.00531), indexed in Pubmed: 30524961.
3. Cassar N, Cresswell AB, Moran B. Oligometastatic colorectal cancer: is single-site bony colorectal metastasis a treatable condition? *Int J Colorectal Dis*. 2017; 32(8): 1229–1231, doi: [10.1007/s00384-017-2780-1](https://doi.org/10.1007/s00384-017-2780-1), indexed in Pubmed: 28213624.
4. Cassiem W, de Kock M. The anti-proliferative effect of apricot and peach kernel extracts on human colon cancer cells in vitro. *BMC Complement Altern Med*. 2019; 19(1): 32, doi: [10.1186/s12906-019-2437-4](https://doi.org/10.1186/s12906-019-2437-4), indexed in Pubmed: 30696432.
5. Chari KY, Polu PR, Shenoy RR. An appraisal of pumpkin seed extract in 1, 2-dimethylhydrazine induced colon cancer in Wistar rats. *J Toxicol*. 2018; 2018: 6086490, doi: [10.1155/2018/6086490](https://doi.org/10.1155/2018/6086490), indexed in Pubmed: 30245714.
6. De Muth JE. Presentation Models in Basic Statistics and Pharmaceutical Statistical Applications, 3rd edition. CRC Press. 2014; 4: 95, doi: [10.1201/b16842](https://doi.org/10.1201/b16842).
7. De-Souza AS, Costa-Casagrande TA. Animal models for colorectal cancer. *Arq Bras Cir Dig*. 2018; 31(2): e1369, doi: [10.1590/0102-672020180001e1369](https://doi.org/10.1590/0102-672020180001e1369), indexed in Pubmed: 29972397.
8. Guo J, Wu W, Sheng M, et al. Amygdalin inhibits renal fibrosis in chronic kidney disease. *Mol Med Rep*. 2013; 7(5): 1453–1457, doi: [10.3892/mmr.2013.1391](https://doi.org/10.3892/mmr.2013.1391), indexed in Pubmed: 23525378.
9. Jaswal V, Palanivelu J, C R. Effects of the Gut microbiota on Amygdalin and its use as an anti-cancer therapy: Substantial review on the key components involved in altering dose efficacy and toxicity. *Biochem Biophys Rep*. 2018; 14: 125–132, doi: [10.1016/j.bbrep.2018.04.008](https://doi.org/10.1016/j.bbrep.2018.04.008), indexed in Pubmed: 29872744.
10. Jimi Si, Yasui T, Hotokezaka M, et al. Clinical features and prognostic factors of bone metastases from colorectal cancer. *Surg Today*. 2013; 43(7): 751–756, doi: [10.1007/s00595-012-0450-z](https://doi.org/10.1007/s00595-012-0450-z), indexed in Pubmed: 23224335.
11. Jucaa M, Bandeira B, Carvalho D, et al. Comparative study of 1,2-dimethylhydrazine and azoxymethane on the induction of colorectal cancer in rats. *J Coloproctol*. 2014; 34(3): 167–173, doi: [10.1016/j.jcol.2014.06.003](https://doi.org/10.1016/j.jcol.2014.06.003).
12. Li AA, Yuan ZC, Jia-Ming L, et al. The risk factors for bone metastases in patients with colorectal cancer. *Medicine*. 2018; 97(40): e12694.
13. Macedo F, Ladeira K, Pinho F, et al. Bone metastases: an overview. *Oncol Rev*. 2017; 11(1): 321, doi: [10.4081/oncol.2017.321](https://doi.org/10.4081/oncol.2017.321), indexed in Pubmed: 28584570.
14. Metwally IH, Shetiwy M, Elalfy AF, et al. Epidemiology and survival of colon cancer among Egyptians: a retrospective study. *J Coloproctol (Rio J)*. 2018; 38(1): 24–29.
15. Moharib SA, Abd El Maksoud N, Ragab HM, et al. Anticancer activities of mushroom polysaccharides on chemically-induced colorectal cancer in rats. *J Applied Pharmaceutical Sci*. 2014; 4(7): 54–63, doi: [10.7324/japs.2014.40710](https://doi.org/10.7324/japs.2014.40710).
16. Nabil HM, Hassan BN, Tohamy AA, et al. Radioprotection of 1,2-dimethylhydrazine-initiated colon cancer in rats using low-dose  $\gamma$  rays by modulating multidrug resistance-1, cytokeratin 20, and  $\beta$ -catenin expression. *Hum Exp Toxicol*. 2016; 35(3): 282–292, doi: [10.1177/0960327115584687](https://doi.org/10.1177/0960327115584687), indexed in Pubmed: 25926526.
17. Nasir NL, Kamsani NE, Mohtarrudin N, et al. Anticarcinogenic activity of Muntingia calabura leaves methanol extract against the azoxymethane-induced colon cancer in rats involved modulation of the colonic antioxidant system partly by flavonoids. *Pharm Biol*. 2017; 55(1): 2102–2109, doi: [10.1080/13880209.2017.1371769](https://doi.org/10.1080/13880209.2017.1371769), indexed in Pubmed: 28872373.
18. Nour A, Azar B, Rabata A. The effect of amygdalin in the treatment of squamous cell carcinoma induced in the buccal pouch of golden syrian hamster. *J Dental Med Sci*. 2016; 15(2): 75–79.
19. Park HJ, Yoon SH, Han LS, et al. Amygdalin inhibits genes related to cell cycle in SNU-C4 human colon cancer cells. *World J Gastroenterol*. 2005; 11(33): 5156–5161.
20. Paulsen JE, Namork E, Alexander J. Scanning electron microscopy of colonic lesions in 1,2-dimethylhydrazine-treated rats. *Anticancer Res*. 2005; 25(6B): 3883–3888, indexed in Pubmed: 16309175.
21. Sanganna B, Kulkarni AR. Effect of citrus reticulata essential oil on aberrant crypt foci (acf) development in 1,2-dimethylhydrazine induced colon carcinogenesis rats. *Int J Pharmac App*. 2013; 4(1): 29–37.
22. Sangeetha N, Nalini N. Silibinin modulates caudal-type homeobox transcription factor (CDX2), an intestine specific tumor suppressor to abrogate colon cancer in experimental rats. *Hum Exp Toxicol*. 2015; 34(1): 56–64, doi: [10.1177/0960327114530741](https://doi.org/10.1177/0960327114530741), indexed in Pubmed: 24740923.
23. Shewatatek G, Wajana LL, Getinet Y. Coffee arabica complies chemo-preventive activity against DMH induced colorectal cancer in experimental rat model. *J Med Diagn Meth*. 2017; 6: 1–3.
24. Song Z, Xu X. Advanced research on anti-tumor effects of amygdalin. *J Cancer Res Ther*. 2014; 10 Suppl 1: 3–7, doi: [10.4103/0973-1482.139743](https://doi.org/10.4103/0973-1482.139743), indexed in Pubmed: 25207888.
25. Usher-Smith J, Walter F, Emery J, et al. Risk prediction models for colorectal cancer: a systematic review. *Cancer Prev Res*. 2015; 9(1): 13–26, doi: [10.1158/1940-6207.capr-15-0274](https://doi.org/10.1158/1940-6207.capr-15-0274).
26. Van Herck H, Baumans V, Brandt CJ, et al. Blood sampling from the retro-orbital plexus, the saphenous vein and the tail vein in rats: comparative effects on selected behavioural and blood variables. *Lab Anim*. 2015; 35(2): 131–139, doi: [10.1258/0023677011911499](https://doi.org/10.1258/0023677011911499), indexed in Pubmed: 11315161.
27. Vatandoust S, Price TJ, Karapetis CS. Colorectal cancer: Metastases to a single organ. *World J Gastroenterol*. 2015; 21(41): 11767–11776, doi: [10.3748/wjg.v21.i41.11767](https://doi.org/10.3748/wjg.v21.i41.11767), indexed in Pubmed: 26557001.
28. Youssef KM, Ezzo AM, El-Sayed MI, et al. Chemopreventive effects of curcumin analogs in DMH-Induced colon cancer in albino rats model. *Future J Pharmac Sci*. 2015; 1: 57–72.

# Applied anatomy and clinical significance of the maxillofacial and mandibular regions of the barking deer (*Muntiacus muntjak*) and sambar deer (*Rusa unicolor*)

K. Keneisenuo<sup>1</sup>, O.P. Choudhary<sup>1</sup> , P. Priyanka<sup>2</sup> , P.C. Kalita<sup>1</sup>, A. Kalita<sup>1</sup>, P.J. Doley<sup>1</sup>, J.K. Chaudhary<sup>3</sup>

<sup>1</sup>Department of Veterinary Anatomy and Histology, College of Veterinary Sciences and Animal Husbandry, Central Agricultural University (I), Selesih, Aizawl, Mizoram, India

<sup>2</sup>Department of Veterinary Microbiology, College of Veterinary Sciences and Animal Husbandry, Central Agricultural University (I), Jalukie, Peren, Nagaland, India

<sup>3</sup>Department of Animal Genetics and Breeding, College of Veterinary Sciences and Animal Husbandry, Central Agricultural University (I), Selesih, Aizawl, Mizoram, India

[Received: 15 January 2020; Accepted: 20 February 2020]

**Background:** There is no previously reported information on the applied anatomy and clinical significance of the maxillofacial and mandibular regions of the barking deer and sambar deer.

**Materials and methods:** Therefore, the present study was designed to provide some important clinical landmarks related to tracking of the infraorbital, mental and mandibular nerves with its clinical implications in regional anaesthesia in both the species.

**Results:** In the present study, the distance between the most lateral bulging of the facial tuberosity to the infraorbital foramen and from the latter to the root of the alveolar tooth directly ventral to it was found to be  $2.65 \pm 0.01$  cm and  $0.90 \pm 0.02$  cm in males;  $2.75 \pm 0.01$  cm,  $1.11 \pm 0.01$  cm in females of barking deer and  $4.57 \pm 0.01$  cm and  $1.83 \pm 0.02$  cm in males;  $4.52 \pm 0.02$  cm and  $1.76 \pm 0.02$  cm in females of sambar deer. The infraorbital foramen was small, elliptical and was located at the level of first superior premolar teeth in barking deer and sambar deer. The facial tuberosity was located above the third superior premolar teeth in the barking deer but was located at the level of the first superior molar teeth in sambar deer. The distance between the lateral alveolar root of the third inferior incisor tooth to the mental foramen was  $2.84 \pm 0.01$  cm in males,  $2.78 \pm 0.01$  cm in females of barking deer and  $3.04 \pm 0.02$  cm in males,  $2.96 \pm 0.01$  cm in females of sambar deer which is an important landmark for achieving the location of the mental foramen nerve for the regional nerve block in both the species. The mandible of both the species showed oval-shaped mental foramen with unossified mandibular symphysis.

**Conclusions:** The present study revealed that most of the parameters showed a statistically significant difference between the sexes in barking deer and sambar deer; however, from the practical point of view, these differences were meager. The results were discussed with regard to their clinical applications in various regional anaesthesia performed in maxillofacial and mandibular regions of both the species. (Folia Morphol 2021; 80, 1: 170–176)

**Key words:** barking deer, sambar deer, infraorbital, mental, mandibular, nerve, regional anaesthesia

## INTRODUCTION

The barking deer (*Muntiacus muntjak*) is a cervid species deer native to South and Southeast Asia that has been listed as 'least concern' on the International Union for the Conservation of Nature (IUCN) red list [32]. They are relatively small tropical deer that have a solitary lifestyle [21] and wide natural distribution, ranging throughout the large parts of South-east Asia [24]. The males have short antlers protruding from long body hair-covered pedicles above the eyes, while females have small bony knobs. Males have preorbital glands which are larger than in females [2] and they use these glands to mark the ground [1, 3].

The sambar deer (*Rusa unicolor*) is a large deer of cervid species native to the Indian subcontinent, Southern China and Southeast Asia, that has been listed as 'vulnerable' by the IUCN red list since 2008 due to decrease in their population year by year [20, 33]. The males have rugged antlers having simple brow tines along with forked beams at its tip and are dropped annually. The barking and sambar deer are protected under Schedule III of the Indian Wildlife Protection Act, 1972.

The regional anatomy is the important branch of anatomy that deals with the form and relationships of various anatomic structures present in a specific area. It is one of the major foundations of clinical and surgical practice as it enables the clinician/surgeon to visualise the details of the structures relevant to the case at hand [12]. The knowledge of the regional anatomy of the head is crucial due to the presence of the vital organs and structures such as the brain, tongue, eye, ears, nose, lips, horn and skull. Due to the presence of these structures, the function of the head is to coordinate the body, deglutition, olfaction and defence [12]. Numerous investigations have been done on the regional anatomy of the head region of the domestic and wild animals including ox, horse, sheep, goat, dog, pig and camel [4–6, 12, 15, 26, 28].

The relationship and forms of all organs that are located in a particular area are directly concerned with regional anatomy helping the clinician as well as surgeon to visualise details of the structures relevant to the case at hand and form one of the important foundations for clinical and surgical practice [12]. It has been reported previously that the infraorbital nerve and mental nerve pass from the infraorbital foramen and mental foramen, respectively [13, 14]. In an emergency situation that requires surgical intervention, it is very easy to locate this region as a topographical landmark for quick and easy anaesthesia

to block the infraorbital and mental nerve. Knowing the topographic and morphometric anatomy of the infraorbital and mental foramen provides simplicity in veterinary surgery during an emergency [12, 27].

There is no previously reported information on the applied anatomy and clinical significance of the maxillofacial and mandibular region of barking deer and sambar deer. Therefore, the present study has been carried out to provide information on some clinically important parameters and landmarks on the maxillofacial and mandibular region in both the species. Thus, the results shown in this study will aid the clinicians in the implication of regional anaesthesia in the maxillofacial and mandibular regions in both the species.

## MATERIALS AND METHODS

The study was conducted on the maxillofacial and mandibular regions of eight adult barking deer and sambar deer of either sex. The skull samples were collected from the Aizawl Zoological park, Aizawl, Mizoram after taking official permission from the Principal Chief Conservator of Forest and Chief Wildlife Warden, Government of Mizoram, Aizawl vide letter no. A. 33011/5/2017-CWLW/91 dated 15.03.2019. After collection, the samples were processed by the hot water maceration technique. The present study was carried out in the Department of Veterinary Anatomy and Histology, College of Veterinary Sciences and Animal Husbandry, Selesih, Aizawl, Mizoram and Interpretation Centre, Aizawl Zoological Park, Aizawl, Mizoram. The radiograph of the mandible was carried out by the Siemens X-Ray machine (500 mA) at Diagnostic Division Radiology and Imaging, Mizoram Health Care, Aizawl, Mizoram.

Altogether a total of eleven measurements were taken in the upper jaw and mandibles of both the species by using digital vernier calliper (Resolution 0.01 mm or 0.0005 inches: Accuracy  $\pm$  0.03 mm) and the results were expressed as mean  $\pm$  standard deviation (SD). The parameters taken in maxillofacial and mandibular regions are delineated below and revealed in Figures 1–3.

- A. Facial tuberosity to the infraorbital foramen: It was measured from the level of most lateral bulging of facial tuberosity to mid-level of the infraorbital foramen.
- B. Infraorbital foramen to root of alveolar tooth: It was measured from the mid-level of the infraorbital foramen to the alveolar root of the superior first premolar tooth.

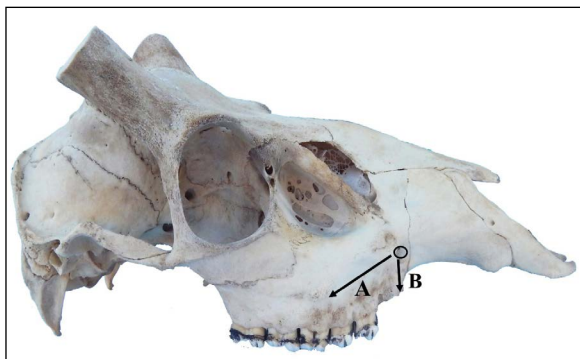


**Figure 1.** Lateral view of the skull of sambar deer showing facial tuberosity to infraorbital foramen (A) and infraorbital foramen to root of the superior first premolar tooth (B).

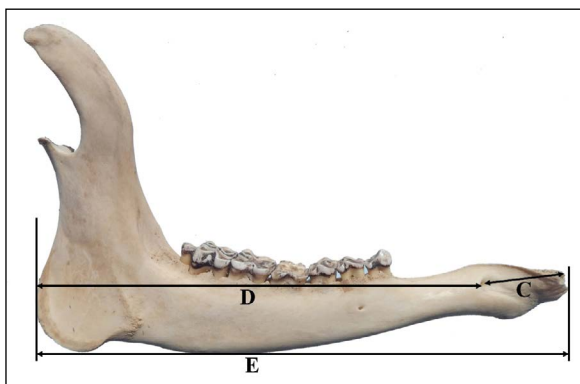


**Figure 2.** Lateral view of the mandible of sambar deer showing measurements; lateral alveolar root of inferior third incisor tooth to mental foramen (C), mental foramen to the caudal mandibular border (D) and mandibular length (E).



**Figure 3.** Medial view of mandible of sambar deer showing measurements; mandibular foramen to the horizontal plane at the level of the ventral margin of the mandible (F), below mandibular foramen to caudal mandibular border (G), maximum height of mandible to the condylar process (H), maximum mandibular height (I), condylar process to the ventral margin of the mandible (J) and mandibular foramen to the border of mandibular angle (K).

- C. Lateral alveolar root to mental foramen: It was measured from the lateral extent of the alveolar root of the third inferior incisor tooth to the mental foramen.
- D. Mental foramen to the caudal mandibular border: It was measured from the level of the mental foramen to caudal border of the ramus of the mandible.
- E. Mandibular length: It was measured from the level of the rostral extremity of the alveolar root of the central inferior incisor tooth to the transversal plane at the level of the caudal border of the mandible.
- F. Mandibular foramen to the horizontal plane at the level of the ventral margin of the mandible: It was measured from the ventral limit of the mandibular foramen to the horizontal plane at the level of the ventral margin of the mandible.
- G. Caudal border of the mandible to below mandibular foramen: It was measured from the caudal most border of the mandible to the vertical line produced by a description of measurement of mandibular foramen to the ventral margin of the mandible.
- H. Condylar process to the height of mandible: It was measured from the condylar process to the maximum height of the mandible.
- I. Maximum mandibular height: It was measured from the highest level of the coronoid process perpendicularly to the ventral mandibular margin of the mandible.
- J. Condylar process to the ventral margin of the mandible.
- K. Mandibular angle to mandibular foramen: It was measured from the extreme caudal border of angle of the mandible to mandibular foramen.

**Statistical analysis**

All the above parameters of the maxillofacial and mandibular regions of barking deer and sambar deer were obtained. All the measurements obtained were analysed by routine statistical analysis [30] and Student "t" test by the Statistical Package for the Social Sciences (IBM, SPSS, 20.0 version) programme.

**RESULTS**

The infraorbital foramen, mandibular foramen and mental foramen on the medial and lateral surface of the maxillofacial and mandibular regions are shown



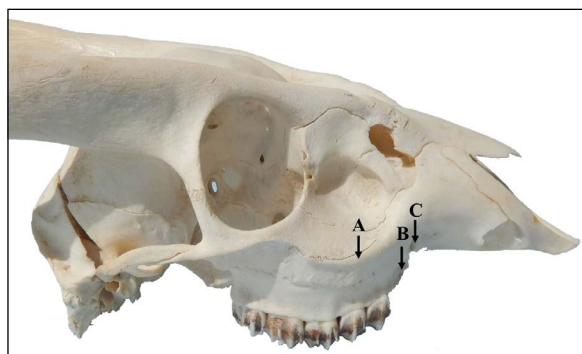


**Figure 4.** Lateral view of the skull of barking deer showing facial tuberosity (A); root of the superior first premolar tooth (B) and infraorbital foramen (C).

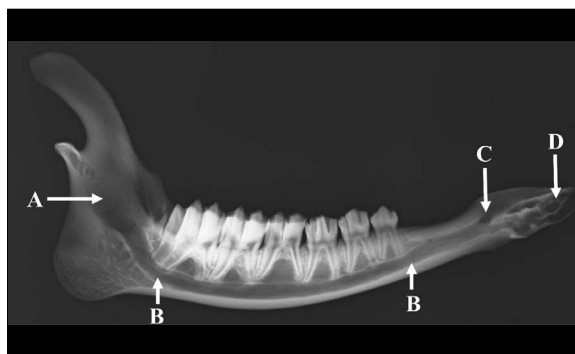


**Figure 5.** Mediolateral radiographical view of the mandible of barking deer showing mandibular foramen (A), mandibular foramen (B), mental foramen (C) and root of the lateral alveolar tooth (D).

**Table 1.** The measurements of the maxillofacial and mandibular region in barking deer and sambar deer in centimetres (mean  $\pm$  standard deviation)

Parameters#	Barking deer		P	Sambar deer		P
	Male	Female		Male	Female	
A	2.65 $\pm$ 0.01	2.75 $\pm$ 0.01	< 0.01**	4.57 $\pm$ 0.01	4.52 $\pm$ 0.02	< 0.05*
B	0.90 $\pm$ 0.02	1.11 $\pm$ 0.01	< 0.01**	1.83 $\pm$ 0.02	1.76 $\pm$ 0.02	< 0.01**
C	2.84 $\pm$ 0.01	2.78 $\pm$ 0.01	< 0.01**	3.04 $\pm$ 0.02	2.96 $\pm$ 0.01	< 0.01**
D	12.87 $\pm$ 0.01	14.46 $\pm$ 0.02	< 0.01**	23.66 $\pm$ 0.01	23.59 $\pm$ 0.01	< 0.01**
E	15.77 $\pm$ 0.01	17.27 $\pm$ 0.02	< 0.01**	28.10 $\pm$ 0.01	27.96 $\pm$ 0.01	< 0.01**
F	2.49 $\pm$ 0.01	2.39 $\pm$ 0.02	< 0.01**	5.17 $\pm$ 0.01	5.10 $\pm$ 0.02	< 0.01**
G	2.15 $\pm$ 0.01	2.09 $\pm$ 0.01	< 0.01**	3.80 $\pm$ 0.01	3.71 $\pm$ 0.01	< 0.01**
H	2.89 $\pm$ 0.01	2.79 $\pm$ 0.01	< 0.01**	5.29 $\pm$ 0.01	5.21 $\pm$ 0.01	< 0.01**
I	7.88 $\pm$ 0.01	7.78 $\pm$ 0.02	< 0.01**	15.96 $\pm$ 0.01	15.78 $\pm$ 0.02	< 0.01**
J	4.89 $\pm$ 0.01	4.39 $\pm$ 0.01	< 0.01**	10.60 $\pm$ 0.01	10.50 $\pm$ 0.01	< 0.01**
K	2.49 $\pm$ 0.03	2.39 $\pm$ 0.02	< 0.01**	5.16 $\pm$ 0.02	5.11 $\pm$ 0.01	< 0.01**

#As mentioned in alphabetical order in materials and method. Level of significance at 5%; \*Significant ( $p < 0.05$ ); \*\*Highly significant ( $p < 0.01$ ).

in Figures 4, 5. The measurement points taken to determine the topographic and morphometric location of the mental foramen are shown in Figures 2, 3. In the present study, the infraorbital foramen was small, elliptical and was located at the level of first superior premolar tooth in barking deer and sambar deer (Figs. 1, 4). The alveolar border of mandible presented 6 alveoli for the 3 superior premolar and 3 superior molar teeth. The facial tuberosity was located dorsally to the third superior premolar tooth in barking deer but was at the first superior molar tooth in sambar deer. The preorbital fossa was wide and deep in both the species with upper canine teeth on the maxilla. The mandible of both the species showed oval mental foramen with unossified mandibular symphysis. The results of the measurements are listed in Table 1.

The present study revealed that all the obtained parameters differed statistically significantly ( $p < 0.01$  and  $p < 0.05$ ) between the males and females of barking deer and sambar deer respectively; however, from the practical point of view, these differences were meager.

## DISCUSSION

In the present study, facial tuberosity of barking deer was located above the third superior premolar tooth which has also been reported in ox [13], chital [18] and blackbuck [9], while it was located at the level of first superior molar tooth in sambar deer. However, the facial tuberosity of the Madras Red sheep was prominent and placed at the level of 5<sup>th</sup> cheek tooth (second superior molar tooth) [31]. The distance between the most lateral bulging of the

facial tuberosity to the infraorbital foramen and from the latter to the root of the alveolar tooth directly ventral to it was  $2.65 \pm 0.01$  cm and  $0.90 \pm 0.02$  cm in males;  $2.75 \pm 0.01$  cm,  $1.11 \pm 0.01$  cm in females of barking deer and  $4.57 \pm 0.01$  cm and  $1.83 \pm 0.02$  cm in males;  $4.52 \pm 0.02$  cm and  $1.76 \pm 0.02$  cm in females of sambar deer (Table 1). However, the same parameter was reported as 1.6–1.8 cm and 1.3–1.6 cm in West African Dwarf goats [26];  $2.06 \pm 0.14$  cm and  $1.13 \pm 0.11$  cm in Gwembe Valley dwarf goat [17]; 2.8 cm and 2.5 cm in Iranian native cattle [23];  $1.85 \pm 0.14$  cm and  $1.75 \pm 0.19$  cm in black Bengal goat [34] and  $2.37 \pm 0.00$  cm and  $0.72 \pm 0.00$  cm in blackbuck [10]. The infraorbital nerve block can be achieved extraorally by injecting anaesthetic drugs approximately 1 cm in barking deer and 1.8 cm in sambar deer above the root of the first superior premolar tooth in the infraorbital foramen. The infraorbital nerve block is used in the surgical interventions related to the upper lip, nose and skin supplied by the infraorbital nerve.

The above-recorded parameters were of clinical importance because the facial tuberosity is remarkable even in live animals providing a clear guide for tracking the infraorbital nerve and its desensitisation during the manipulations in the skin of the upper lip, nostril and face at the level of the foramen. The infraorbital foramen was small, elliptical and located at the level of the first superior premolar tooth in barking deer and sambar deer which was also reported in chital [18] and blackbuck [9]. However, the same foramen was located dorsal to the second premolar in red Sokoto (Maradi) goats [25].

The distance between the lateral alveolar root of the third inferior incisor tooth to the mental foramen was  $2.84 \pm 0.01$  cm in males,  $2.78 \pm 0.01$  cm in females of barking deer and  $3.04 \pm 0.02$  cm in males,  $2.96 \pm 0.01$  cm in females of sambar deer (Fig. 2, Table 1) which is an important landmark for achieving the location of the mental foramen nerve for the regional nerve block in both the species, whereas it was  $1.6 \pm 0.22$  cm in West African Dwarf goat [26];  $2.0 \pm 0.3$  cm in red Sokoto (Maradi) goats [25];  $2.45 \pm 0.00$  cm in blackbuck [8];  $9.22 \pm 0.05$  cm in dromedary camel [5] and  $3.57 \pm 0.04$  cm in local pig of Mizoram [6]. The mental nerve block can be achieved extraorally by injecting anaesthetic drugs approximately 2.8 cm in barking deer and 3 cm in of sambar deer from the lateral extent of the alveolar root of inferior third incisor tooth into the mental

foramen. The mental nerve block is useful for desensitizing the lower lip during its surgical interventions.

The distance from the mental foramen to caudal border of the ramus of the mandible was  $12.87 \pm 0.01$  cm in males,  $14.46 \pm 0.02$  cm in females of barking deer and  $23.66 \pm 0.01$  cm in males,  $23.59 \pm 0.01$  cm in females of sambar deer, while the same parameters were  $13.43 \pm 0.08$  cm in blackbuck [8];  $11.69 \pm 0.40$  cm in black Bengal goat [34];  $13.74 \pm 0.18$  cm in Mehraban sheep [16];  $9.26 \pm 0.49$  cm in Gwembe Valley Dwarf goat [17];  $32.12 \pm 0.16$  cm in dromedary camel [5];  $15.23 \pm 1.46$  cm in Barbados black belly sheep [22];  $11.8 \pm 0.89$  cm in black Bengal goat [29],  $12.38 \pm 1.52$  cm in Abaza goats [11] and  $18.47 \pm 0.01$  cm in local pig of Mizoram [6].

The length and height of the mandible was  $15.77 \pm 0.01$  cm,  $7.88 \pm 0.01$  cm in males and  $17.27 \pm 0.02$  cm,  $7.78 \pm 0.02$  cm in females of barking deer; and  $28.10 \pm 0.01$ ,  $15.96 \pm 0.01$  cm in males and  $27.96 \pm 0.01$  cm,  $15.78 \pm 0.02$  cm in females of sambar deer, respectively. The same mandibular parameters were  $12.00 \pm 0.89$  cm,  $6.90 \pm 1.09$  cm for West African Dwarf goats [26];  $11.24 \pm 0.52$  cm,  $6.64 \pm 0.44$  cm in Gwembe Valley Dwarf goat [17];  $16.53 \pm 0.12$  cm,  $10.69 \pm 0.02$  cm in blackbuck [7];  $42.98 \pm 0.62$  cm,  $22.58 \pm 0.28$  cm in dromedary camel [5] and  $25.02 \pm 0.09$ ,  $10.54 \pm 0.07$  cm in local pig of Mizoram [6].

The distance between the condylar process to the height of the mandible, condylar process to the ventral margin of the mandible was  $2.89 \pm 0.01$  cm,  $4.89 \pm 0.01$  cm in males and  $2.79 \pm 0.01$  cm,  $4.39 \pm 0.01$  cm in females of barking deer; and  $5.29 \pm 0.01$  cm,  $10.60 \pm 0.01$  cm in males and  $5.21 \pm 0.01$  cm,  $10.50 \pm 0.01$  cm in females of sambar deer. However, the same parameter has been reported to be  $3.09 \pm 0.00$  cm,  $7.57 \pm 0.02$  cm in blackbuck [7].

The distance between the vertical line drawn downward from the caudal border of the mandible (I) and the vertical line drawn from the mandibular foramen downwards (F) was (G)  $2.15 \pm 0.01$  cm in males,  $2.09 \pm 0.01$  cm in females of barking deer and  $3.80 \pm 0.01$  cm in males,  $3.71 \pm 0.01$  cm in females of sambar deer (Fig. 3). However, the same parameter was observed as  $1.85 \pm 0.01$  cm in blackbuck [7].

The mandibular nerve block is used to anaesthetise the mandibular nerve during the clinical examinations and surgical procedures involving the alveoli and teeth of the lower jaw in animals [19]. The distances from the mandibular foramen to the ventral margin of the mandible, caudal border of mandible to the

level of mandibular foramen, mandibular foramen to the border of mandibular angle were  $2.49 \pm 0.01$  cm,  $2.15 \pm 0.01$  cm,  $2.49 \pm 0.03$  cm in males;  $2.39 \pm 0.02$  cm,  $2.09 \pm 0.01$  cm,  $2.39 \pm 0.02$  cm in females of barking deer and  $5.17 \pm 0.01$  cm,  $3.80 \pm 0.01$  cm,  $5.16 \pm 0.02$  cm in males;  $5.10 \pm 0.02$  cm,  $3.71 \pm 0.0$  cm,  $5.11 \pm 0.01$  cm in females of sambar deer (Fig. 3). Whereas, the same parameters were recorded as  $4.18 \pm 0.01$  cm,  $1.36 \pm 0.01$  cm,  $3.07 \pm 0.00$  cm in blackbuck [8];  $8.84 \pm 0.08$  cm,  $5.88 \pm 0.05$  cm,  $8.29 \pm 0.07$  cm in dromedary camel [5] and  $4.56 \pm 0.01$  cm,  $3.81 \pm 0.00$  cm,  $4.84 \pm 0.00$  cm in local pig of Mizoram [6]. Equivalent figures for West African dwarf goats of Nigeria were  $1.57 \pm 0.44$  cm,  $2.58 \pm 0.34$  cm for the caudal border of the mandible to below mandibular foramen and the mandibular foramen to the ventral margin of the mandible [26]. In horse and dogs, the distance between the mandibular foramen and the ventral margin of the mandible was 3 cm and 1.5 to 2 cm, respectively [15]. The mandibular nerve is useful during the treatment of the injuries related to the lower incisors and premolar tooth, i.e. dental extraction, tumours etc. An extraoral mandibular nerve block can be achieved by injecting anaesthetic drugs approximately 2.5 cm in barking deer and 5.0 cm in sambar deer from the horizontal plane at the level of the ventral margin of the mandible to the ventral limit of the mandibular foramen.

## CONCLUSIONS

It is concluded that the measurements obtained from the present study will be useful for the surgeons to locate the site for infiltration of the anaesthetic drugs for the nerves of maxillofacial and mandibular regions and can aid the veterinary practitioners in treating the head injuries related to both the species. Further, it will be very useful in the future endeavours involving applied research works leading towards the massive improvement in the livestock sector of the international economy as well as conservation of wildlife.

## Acknowledgements



The authors are thankful to the Dean, College of Veterinary Sciences and Animal Husbandry, Central Agricultural University (I), Aizawl, Mizoram; Principal Chief Conservator of Forest and Chief Wildlife Warden (PCCF and CWW), Government of Mizoram, Aizawl and Director, Aizawl Zoological Park, Aizawl, Mizoram for providing all the necessary facilities to carry out the research work.

## REFERENCES

1. Adnyane IKM, Zuki ABZ, Noordin MM, et al. Morphological study of the infraorbital gland of the male barking deer, *muntiacus muntjak*. *Afr J Biotech*. 2011; 10(77), doi: [10.5897/ajb10.2634](https://doi.org/10.5897/ajb10.2634).
2. Barrette C. Musculature of facial scent glands in the muntjac. *J Anat*. 1976; 122(Pt 1): 61–66, indexed in Pubmed: [977477](https://pubmed.ncbi.nlm.nih.gov/977477/).
3. Barrette C. Social behavior of muntjac. Ph.D. Thesis submitted to the University of Calgary, Calgary, Alberta, Canada. 1975.
4. Choudhary O, Kalita P, Doley P, et al. Applied anatomy of the head region of the indian wild pig (*sus scrofa*) and its clinical value during regional anesthesia. *J Anim Res*. 2017; 7(2): 339, doi: [10.5958/2277-940x.2017.00049.3](https://doi.org/10.5958/2277-940x.2017.00049.3).
5. Choudhary OP, Kalita PC, Kalita A, et al. Applied anatomy of the maxillofacial and mandibular regions of the dromedary camel (*Camelus dromedarius*). *J Camel Prac Res*. 2016; 23(1): 127, doi: [10.5958/2277-8934.2016.00021.7](https://doi.org/10.5958/2277-8934.2016.00021.7).
6. Choudhary O, Kalita P, Konwar B, et al. Morphological and Applied Anatomical Studies on the Head Region of Local Mizo Pig (Zovawk) of Mizoram. *Int J Morphol*. 2019; 37(1): 196–204, doi: [10.4067/s0717-95022019000100196](https://doi.org/10.4067/s0717-95022019000100196).
7. Choudhary O, Singh I, Bharti S, et al. Gross and Morphometrical Studies on Mandible of Blackbuck (*Antelope cervicapra*). *Int J Morphol*. 2015; 33(2): 428–432, doi: [10.4067/s0717-95022015000200003](https://doi.org/10.4067/s0717-95022015000200003).
8. Choudhary O, Singh I. Applied Anatomy of the Maxillofacial and Mandibular Regions of the Indian Blackbuck (*Antelope cervicapra*). *J Anim Res*. 2015; 5(3): 497, doi: [10.5958/2277-940x.2015.00085.6](https://doi.org/10.5958/2277-940x.2015.00085.6).
9. Choudhary O, Singh I. Morphological and Radiographic Studies on the Skull of Indian Blackbuck (*Antelope cervicapra*). *Int J Morphol*. 2016; 34(2): 775–783, doi: [10.4067/s0717-95022016000200055](https://doi.org/10.4067/s0717-95022016000200055).
10. Choudhary O, Singh I. Morphometrical Studies on the Skull of Indian Blackbuck (*Antelope cervicapra*). *Int J Morphol*. 2015; 33(3): 868–876, doi: [10.4067/s0717-95022015000300011](https://doi.org/10.4067/s0717-95022015000300011).
11. Dalga S. Topographic and morphometric study of the mental foramina of Abaza goats with its clinical implication for regional anesthesia. *Folia Morphol*. 2019 [Epub ahead of print], doi: [10.5603/FM.a2019.0122](https://doi.org/10.5603/FM.a2019.0122), indexed in Pubmed: [31750539](https://pubmed.ncbi.nlm.nih.gov/31750539/).
12. Dyce KM, Sack WO, Wensing CJG. *Textbook of Veterinary Anatomy*. 2nd edn. Elsevier, Philadelphia 1996.
13. Getty R. *Sisson and Grossman's The Anatomy of the Domestic Animals*, 2nd edn. Vol. I. W.B. Saunders Co., Philadelphia 1975.
14. Ghosh RK. *Primary Veterinary Anatomy*, 5th edn. Current books international, Kolkata, West Bengal, India 2012.
15. Hall LW, Clarke KW, Trim CM. *Wright's Veterinary Anesthesia*. 10th edn. ELBS and Bailliere Tindall, London 2000.
16. Karimi I, Onar V, Pazvant G, et al. The cranial morphometric and morphologic characteristics of Mehraban sheep in western Iran. *Global Vet*. 2011; 6(2): 111–117.
17. Kataba A, Mwaanga ES, Simukoko H, et al. Clinical anatomy of the head Region of Gwembe Valley dwarf goat in Zambia. *Int J Vet Sci*. 2014; 3(3): 142–146.
18. Kumawat R, Joshi S, Mathur R, et al. Gross morphological studies on mandible of Indian spotted deer (*Axis axis*). *Indian Vet J*. 2014; 91(9): 105–107.

19. Lahunta ADE, Habel RE. Applied veterinary anatomy. W.B. Saunders Co., Philadelphia 1986.
20. Leslie D. *Rusa unicolor* (Artiodactyla: Cervidae). Mammalian Species. 2011; 43: 1–30, doi: [10.1644/871.1](https://doi.org/10.1644/871.1).
21. Long JL. Introduced mammals of the world: their history, distribution and influence. CSIRO Publishing, Collingwood Victoria, Australia 2003.
22. Mohamed R, Drisco M, Mootoo N. Clinical anatomy of the skull of the Barbados black belly sheep in Trinidad. Int J Curr Res Med Sci. 2016; 2(8): 8–19.
23. Monfared AL. Gross anatomical measurements of the head region of the Iranian native cattle (*Bos taurus*) and their clinical value for regional anesthesia. Global Vet. 2013; 10(2): 219–222, doi: [10.5829/idosi.gv.2013.10.2.724](https://doi.org/10.5829/idosi.gv.2013.10.2.724).
24. Ohtaishi N, Gao Y. A review of the distribution of all species of deer (Tragulidae, Moschidae and Cervidae) in China. Mammal Review. 1990; 20(2-3): 125–144, doi: [10.1111/j.1365-2907.1990.tb00108.x](https://doi.org/10.1111/j.1365-2907.1990.tb00108.x).
25. Olopade JO, Onwuka SK. Osteometric studies of the red Sokoto (Maradi) goats (*Capra hircus*): Implication for regional anaesthesia of the head. Int J Morphol. 2007; 25(2): 407–410, doi: [10.4067/S0717-95022007000200027](https://doi.org/10.4067/S0717-95022007000200027).
26. Olopade J, Onwuka S. Some Aspects of the Clinical Anatomy of the Mandibular and Maxillofacial Regions of the West African Dwarf Goat in Nigeria. Int J Morphol. 2005; 23(1), doi: [10.4067/s0717-95022005000100006](https://doi.org/10.4067/s0717-95022005000100006).
27. Ommer PA, Harshan KR. Applied Anatomy of Domestic Animals, 1st edn. Jaypee brother's medical publisher, New Delhi, India 1995.
28. Onar V, Ozcan S, Pazvant G. Skull typology of adult male Kangal dogs. Anat Histol Embryol. 2001; 30(1): 41–48, doi: [10.1046/j.1439-0264.2001.00292.x](https://doi.org/10.1046/j.1439-0264.2001.00292.x), indexed in Pubmed: [11284162](https://pubmed.ncbi.nlm.nih.gov/11284162/).
29. Poddar S, Faruq AA, Dey T, et al. Topographic and morphometric anatomy of mental foramen of black Bengal goat (*Capra hircus*) in Bangladesh with its clinical implication for regional anesthesia. Int J Zoo Anim Biol. 2018; 1(1), doi: [10.23880/izab-16000102](https://doi.org/10.23880/izab-16000102).
30. Snedecor GW, Cochran WG. Statistical Methods. 8th edn. Iowa State University Press, Ames, Iowa, USA 1994.
31. Sundaram V, Dharani P, Gnanadevi R, et al. Studies on clinical anatomy of the maxillofacial and mandibular regions of the Madras Red sheep (*Ovis aries*) in India. Folia Morphol. 2019; 78(2): 389–393, doi: [10.5603/FM.a2018.0098](https://doi.org/10.5603/FM.a2018.0098), indexed in Pubmed: [30371934](https://pubmed.ncbi.nlm.nih.gov/30371934/).
32. Timmins RJ, Duckworth JW, Hedges S. *Muntiacus muntjak*. The IUCN Red List of Threatened Species. International Union for Conservation of Nature and Natural Resources, IUCN 2016.
33. Timmins RJ, Kawanishi K, Gimán B, et al. *Rusa unicolor*. The red list of threatened species. IUCN 2015.
34. Uddin M, Ahmed S, Islam K, et al. Clinical anatomy of the head region of the black bengal goat in bangladesh. Int J Morphol. 2009; 27(4), doi: [10.4067/s0717-95022009000400048](https://doi.org/10.4067/s0717-95022009000400048).

# Evaluation of the middle ear in water buffaloes (*Bubalus bubalis*) by gross anatomy and cone-beam computed tomography

J. Nourinezhad<sup>1</sup>, M. Abedini<sup>2</sup>, M.M. Shamsi<sup>3</sup>, A. Dabbaghi<sup>4</sup>, M. Janeczek<sup>5</sup>

<sup>1</sup>Division of Anatomy and Embryology, Department of Basic Sciences, Faculty of Veterinary Medicine, Shahid Chamran University of Ahvaz, Ahvaz, Iran

<sup>2</sup>D.V.M. Student of the Faculty of Veterinary Medicine, Shahid Chamran University of Ahvaz, Ahvaz, Iran

<sup>3</sup>Graduated Ph.D. Student of Comparative Anatomy and Embryology, Faculty of Veterinary Medicine, Shahid Chamran University of Ahvaz, Ahvaz, Iran

<sup>4</sup>Department of Oral and Maxillofacial Radiology, Dental School, Ahvaz Jundishapur University of Medical Sciences, Ahvaz, Iran

<sup>5</sup>Division of Animal Anatomy, Department of Biostructure and Animal Physiology, Faculty of Veterinary Medicine, Wrocław University of Environmental and Life Sciences, Wrocław, Poland

[Received: 10 February 2020; Accepted: 26 February 2020]

**Background:** The purpose of this study was to provide a description of gross middle ear morphology in water buffaloes, augmented with additional data on the osseous structures of middle ear derived from cone-beam computed tomography (CBCT).

**Materials and methods:** Skulls of 10 young adult male water buffaloes were used to examine their middle ears.

**Results:** Anatomical features noted included the presence of tympanic cells in the tympanic bulla, the location of malleus head and neck, and all of incus in the dorsal epitympanic recess, the oval tympanic membrane, absence of a prominent notch on the articular surface of malleus, positional variations of the lateral process of malleus relative to the muscular process and muscular process relative to the rostral process of malleus, absence of complete coverage of the articular facet of malleus head by incus body, and presence of the lenticular process of incus. In CBCT images, the osseous part of external acoustic meatus, the petrous part of temporal bone and the details of the ossicles were seen, except for stapes.

**Conclusions:** Although tympanic membrane, malleus and stapes of water buffaloes are similar to those of ox, the incus of water buffaloes is more similar to that of goats. The heaviest ossicles among the ruminants studied belonged to water buffaloes; the mean length of malleus head and neck, total length and width of incus body as well as length of stapes head were greatest in water buffaloes too. The auditory ossicles of water buffaloes show 'transitional type' morphological characteristics. These features suggest a relatively wide frequency range of hearing, but not one biased towards especially low or especially high frequencies. (Folia Morphol 2021; 80, 1: 177–185)

**Key words:** anatomy, auditory ossicles, cone-beam computed tomography, middle ear, morphometry, water buffalo

## INTRODUCTION

The middle ear cavity is an irregular space within the temporal bone that is filled with air. It contains the malleus, incus, and stapes, which form a chain and serve to convey vibrations from the tympanic membrane (TM) across the cavity to the internal ear [11]. Many studies on the middle ear have been conducted from morphological, functional, and surgical viewpoints, with physiological experiments typically having been performed on relatively small laboratory animals such as gerbils, guinea pigs and cats. There is considerable variation in middle ear architecture among the many species studied [7, 15, 20, 21]. Body size, phylogeny, style of life, ecology, and acoustic environment can all be reflected in aspects of ear morphology [29].

Recently, there has been more interest in the middle ear of larger animals such as sheep and pig, which potentially represent better models of the human middle ear [18, 28]. However, the gross morphology of middle ear of ox, sheep, and goat is not described or illustrated in any detail in most veterinary anatomical textbooks, atlases and dissection guides [5, 8, 14, 24, 25, 32]. Only Getty [11], in his veterinary anatomical textbook, included detailed comparative descriptions of this area, but did not present any schematic pictures and photographs. There are a few descriptive anatomical accounts of sheep and ox ears [4, 34, 35], but there remains much to be clarified regarding the comparative anatomy of ruminant auditory systems.

Cone-beam computed tomography (CBCT) acquires data volumetrically, providing accurate, three-dimensional (3D) radiographic imaging which is ideal for the assessment of osseous structures of the maxillofacial region at sub-millimeter resolution [17]. This has proved to be an excellent technology for the identification and description of the normal anatomy of middle ear structures in veterinary research [31]. CT studies on the normal anatomy of middle ear structures have been conducted in sheep [33], and horses [3].

Water buffaloes (*Bubalus bubalis*) are placed in the family Bovidae, within the order Artiodactyla. Some archeological evidence suggests that water buffaloes were first domesticated in Iran and migrated to southern Europe from this region [23]. The Khuzestan ecotype of Iranian water buffaloes are likely to be the biggest buffalo breed in the world [22], the morphological appearance of which differs from that of Mediterranean water buffaloes [23]. No description of the middle ear of water buffaloes seems to have been published. The goals of this study

were, therefore, (1) to provide a detailed description of the middle ear of water buffaloes, (2) to determine the similarities and differences between water buffaloes ears and those of other ruminants, and (3) to describe the osseous structures of the middle ear of water buffaloes using CBCT.

## MATERIALS AND METHODS

Skulls of 10 young adult male water buffaloes, without any external abnormality or pathology, were collected from a local slaughterhouse in Ahvaz, southwest Iran. The age of animals, as estimated from the eruption of teeth [9], ranged between 2 to 3 years. The animals' live weight (316–383 kg) was estimated based on carcass weight (190–230 kg). There was no need of approval from the Local Ethical Committee as the animal skulls were collected from the slaughterhouse. The maceration of skull and the dissection of tympanic cavity were performed according to the procedures of Nummela [27], and Martonos et al. [19], respectively. Afterwards, the following measurements for separated auditory ossicles were taken according to Martonos et al. [19]. Malleus: total length (TL), length of the manubrium (LM), head diameter (HD), and head and neck length (HNL). Incus: total length (TL), body width (BW), length of short crus (LSC), and length of long crus (LLC). Stapes: total length (TL), head length (HL), and thickness of crura at the middle (TCM). All variables were measured three times by a single researcher using a digital calliper (150 mm, Mitutoyo, Japan) and presented as means and standard deviations. The masses of ossicles were measured to an accuracy of 0.001 g on laboratory scales (A&D Company, MA 3000, Japan). Photographs of the ossicles were taken under a stereomicroscope (Nikon, SMZ800, Japan) using a Canon digital camera (G9, Tokyo, Japan).

Cone-beam CT images were acquired using New Tom VGi scanner (New Tom GRsrl; Verona, Italy) with a field of view 12 cm × 8 cm at a 0.15 mm voxel resolution with the scanning parameter of 110 kVp, 9.18 mA (for left side) and 7.33 mA (for right side), and 5.4 seconds exposure time. CBCT data were evaluated in the dorsal and sagittal planes by an expert maxillofacial radiologist.

## RESULTS

### Tympanic membrane

The mean and standard deviation of rostrocaudal and dorsoventral dimensions of TM were  $11.66 \pm 0.63$  mm and  $9.12 \pm 0.12$  mm, respectively. The TM

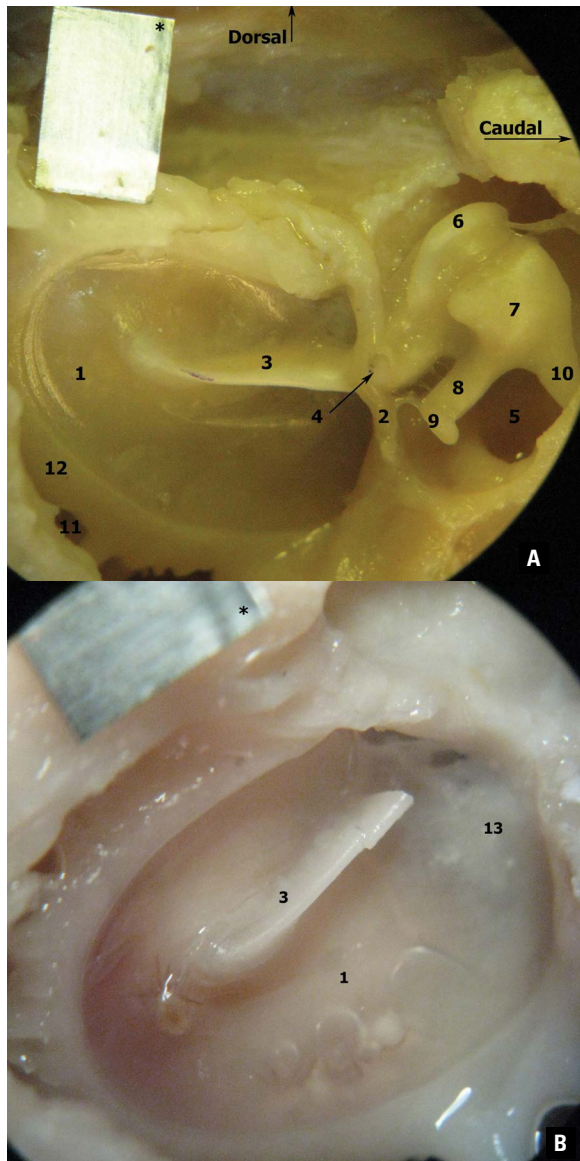


**Figure 1.** Medial aspect of right ossicles and tympanic membrane in water buffaloes (in situ); **A. B.** 1 — pars tensa; 2 — chorda tympani nerve; 3 — manubrium; 4 — muscular process; 5 — epitympanic recess; 6 — malleus head; 7 — incus body; 8 — long process; 9 — lenticular process; 10 — short process; 11 — tympanic cell; 12 — tympanic ring; 13 — pars flaccida; \*Scale = 5 mm.

was made up of two major parts, the pars flaccida (PF) and pars tensa (PT). The PF, an irregular triangle, was small and extended from the surrounding parts of the tympanic incisures of squamous temporal bone to the lateral process of malleus (Fig. 1B). The shape of PT was a regular oval. The medial surface of TM appeared to be irregularly concavo-convex. The entire length of manubrium was embedded in PT. The manubrium almost in its middle was very strongly attached to the medial surface of PT (Fig. 1A, B).

**Table 1.** Means (mm) ± standard deviations of the ossicles (water buffaloes)

Malleus	TL	ML	HNL	HD
	11.07 ± 0.46	6.54 ± 0.6	5.73 ± 0.29	3.17 ± 0.4
Stapes	TL	BL	HL	TMB
	3.6 ± 0.57	2.7 ± 1.27	1.44 ± 0.33	0.7 ± 0.16
Incus	TL	LCL	SCL	BW
	5.74 ± 0.88	2.78 ± 0.16	2.74 ± 0.18	3.3 ± 0.22

TL — total length; ML — malleus length; HNL — head and neck length; HD — head diameter; BW — body width; HL — head length; BL — body length; TMB — thickness in the middle of bone; LCL — long crus length; SCL — short crus length

The epitympanic recess housed the head and neck of malleus, and all of the incus (Fig. 1A). The ventral part of middle ear cavity was divided into tympanic cells (see Fig. 5A).

#### Auditory ossicles

The morphometric data obtained from the ossicles are presented in Tables 1 and 2.

**Malleus head.** Caudally, the head was slightly convex and its edges rounded and somewhat pressed (Fig. 2A, C) and there was a small, shallow fossa just rostral to the root of the lamina on the lateral surface of head (Fig. 2A, C). The head had a concave facet on its caudomedial aspect for articulation with incus. The facet was divided by a shallow notch into dorsal and ventral parts (Fig. 2B).

**Malleus neck.** The curved neck was not very distinct below the head (Fig. 2A, B). The well-developed lamina was thin and irregularly triangular in shape: it originated from the dorsolateral surface of neck and extended rostrally, dorsally and laterally. The rostral process was a delicate projection in continuity with lamina, and was lateral to the large muscular process (Fig. 2A). The rostral process was attached by a ligament to the wall of tympanic cavity (not shown). There was a very distinct shallow fossa caudal to the muscular process on the mediodorsal side (Fig. 2B). The medial surface of neck, just rostral to the muscular process, was crossed by chorda tympani branch of facial nerve (Fig. 1A). The muscular process was a very well-developed and prominent spur which arose medially from the distal part of the neck (Fig. 1A, 2B).

**Malleus manubrium.** The manubrium had four sides. The lateral edge of manubrium was convex. It was attached to TM, whereas the medial edge of the manubrium was free. The rostradorsal surface of the manubrium was slightly concave longitudinally

**Table 2.** Comparison of mean masses (mg) ± standard deviations of the ossicles (water buffaloes) with those obtained in various ruminates

	Malleus	Incus	Stapes
Present study	0.050 ± 0.030	0.048 ± 0.008	0.006 ± 0.001
Ox [11] [27]	0.032 ± 0.006 0.022	0.030 ± 0.005 0.026	0.005 ± 0.0005 0.002
Sheep [11] [27]	0.008 ± 0.001 0.007	0.008 ± 0.001 0.055	0.001 ± 0.0003
Goat [11]	0.010 ± 0.001	0.008 ± 0.001	0.001 ± 0.0004
Dromedary camel [21]	0.039 ± 0.080	0.030 ± 0.003	0.004 ± 0.0004
Bactrian camel [2] [27]	0.037 ± 0.02 0.037	0.032 ± 0.008 0.038	0.005 ± 0.0005 0.004
Human [12] [27]	0.023 ± 0.002 0.028	0.025 ± 0.002 0.033	0.003 ± 0.0006 0.002

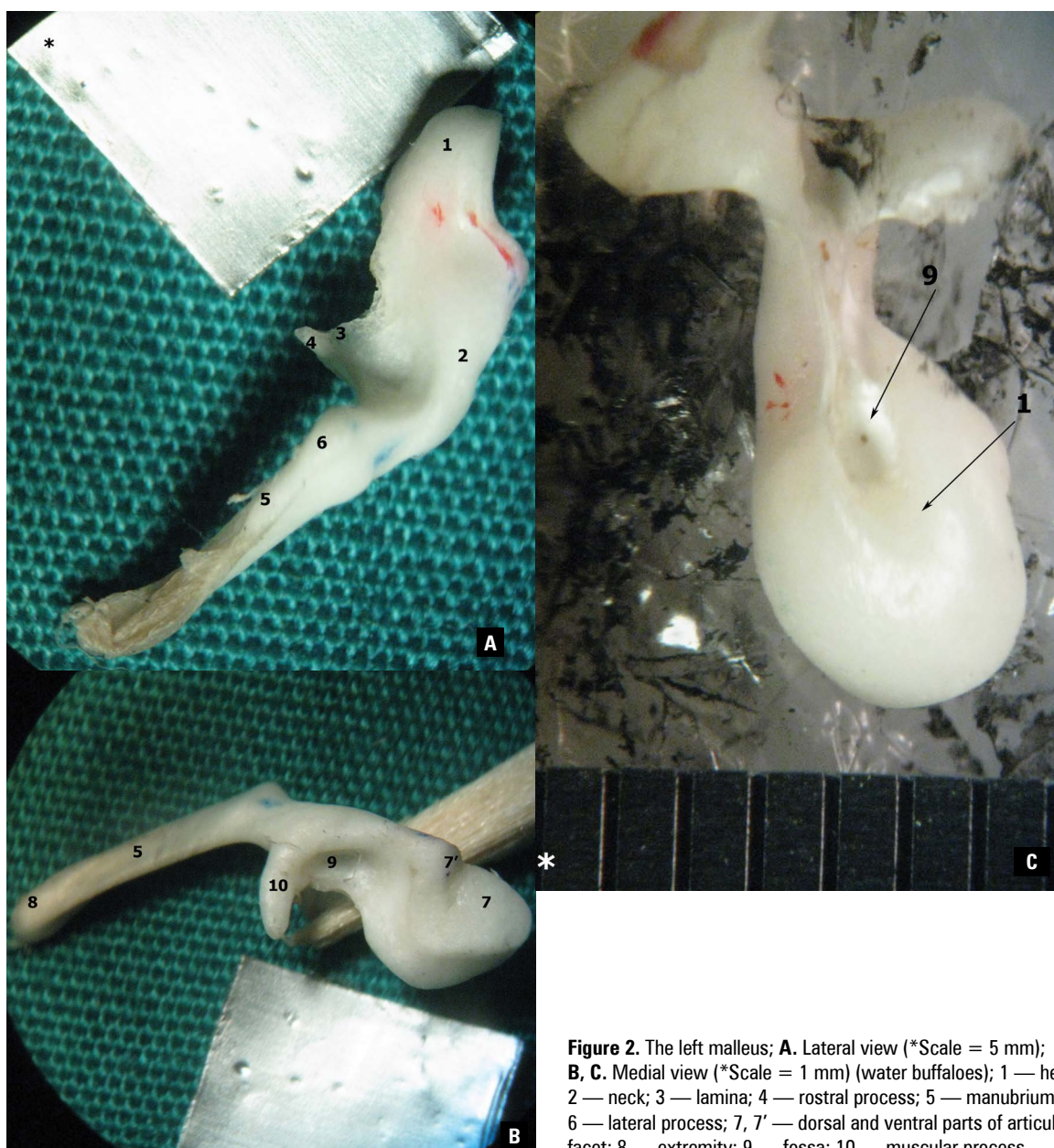


**Figure 2.** The left malleus; **A.** Lateral view (\*Scale = 5 mm); **B, C.** Medial view (\*Scale = 1 mm) (water buffaloes); 1 — head; 2 — neck; 3 — lamina; 4 — rostral process; 5 — manubrium; 6 — lateral process; 7, 7' — dorsal and ventral parts of articular facet; 8 — extremity; 9 — fossa; 10 — muscular process.



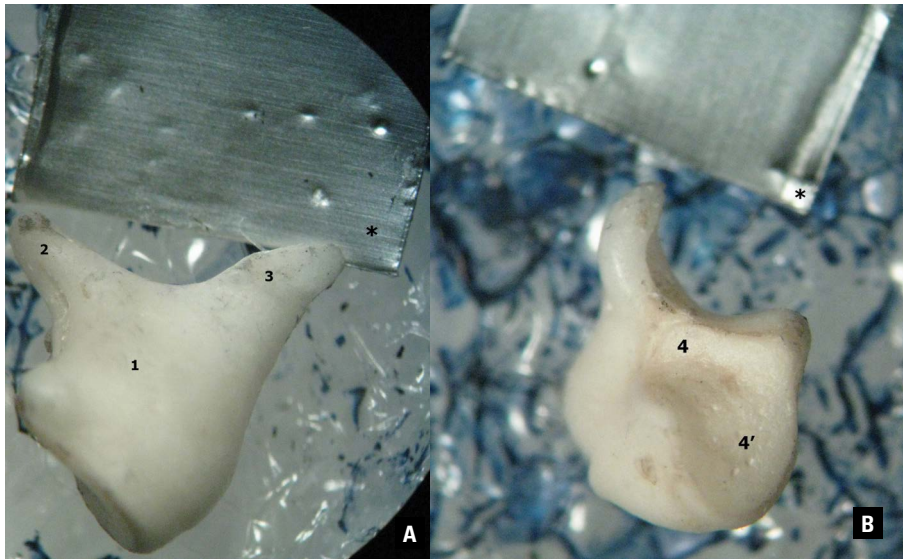


**Figure 3.** The left incus (water buffaloes); **A.** Lateral view; **B.** Articular surface; 1 — body; 2 — long process; 3 — short process; 4, 4' — dorsal and ventral parts of articular facet; \*Scale = 5 mm.

from body to tip, whereas the caudoventral surface was convex. The lateral process was a right-angled triangular protuberance which arose from the base of the manubrium at the same level as the muscular process on the opposite side (Fig. 2A, B).

The imaginary line extending between the anterior process of malleus and the short process of the incus, two points where the ossicles are tethered to skull, has been called the 'anatomical axis' [16]. The manubrium took an intermediate orientation relative to the anatomical axis, i.e. between perpendicular and parallel (Fig. 1A).

**Incus.** The medial surface of body was convex with a distinct oval facet (Fig. 3A), while the lateral surface was almost smooth (not shown). The shape of the articular facet was slightly saddle-shaped and occupied virtually the whole width of incus, and was divided by a ridge into two facets (Fig. 3B). The long process extended in a rostroventral direction. The lenticular process seemed to ossify with the extremity of long process. It was directed mainly caudally and formed a small, nodular projection. The pyramidal short process was oriented in a caudoventral direction. The incudo-malleolar joint was easily separable (Fig. 1A).

**Stapes.** The head of stapes was convex. The stapes was quadrilateral in shape. The rostral crus of spates was slightly inclined rostrally, while the caudal crus was almost straight below the level of junction of caudal crus and neck at its caudomedial aspect, there was a small but prominent muscular process. The intercrural foramen was a regular oval in shape (Fig. 4A). Cross-section of the rostral crus was as a narrow semicircle near footplate, but caudal crus was somewhat

appeared as an irregular c-shaped (Fig. 4C). Footplate was an irregular oval in shape (Fig. 4B), its extremities extending considerably beyond the limits of insertion of crura. However, it extended farther beyond the insertion of caudal crus than beyond the rostral crus. The well-developed labrum was thick at the extremities, especially at the caudal extremity. The caudal extremity was relatively pointed, whereas the rostral one was rounded when viewed from its vestibular aspect. The center of footplate was relatively thin and was slightly concave towards the vestibule (Fig. 4A). The footplate was placed in fossa ovalis leading to the oval window at its bottom (Fig. 4C).

**CBCT anatomy.** Osseous structures of water buffaloes middle ear were very well visualized with CBCT. The sagittal plane images provided excellent depictions of anatomical structures. No significant anatomic variations were noted between right and left sides of temporal bone. In the sagittal plane tomogram shown in Figure 5A, the body, short and long processes of incus, the head, neck, rostral process, and manubrium of malleus, incudo-malleolar joint, tympanic bulla, tympanic cells and epitympanic recess were readily identified. In the dorsal plane tomogram shown in Figure 5B, the osseous part of external acoustic meatus, the bony rim supporting the tympanic membrane, part of the malleus, and the petrous part of temporal bone were seen clearly.

## DISCUSSION

**Tympanic membrane.** Although the typical mammalian TM has a PT and smaller PF, the outline of PT differs among the species, from nearly circular to an

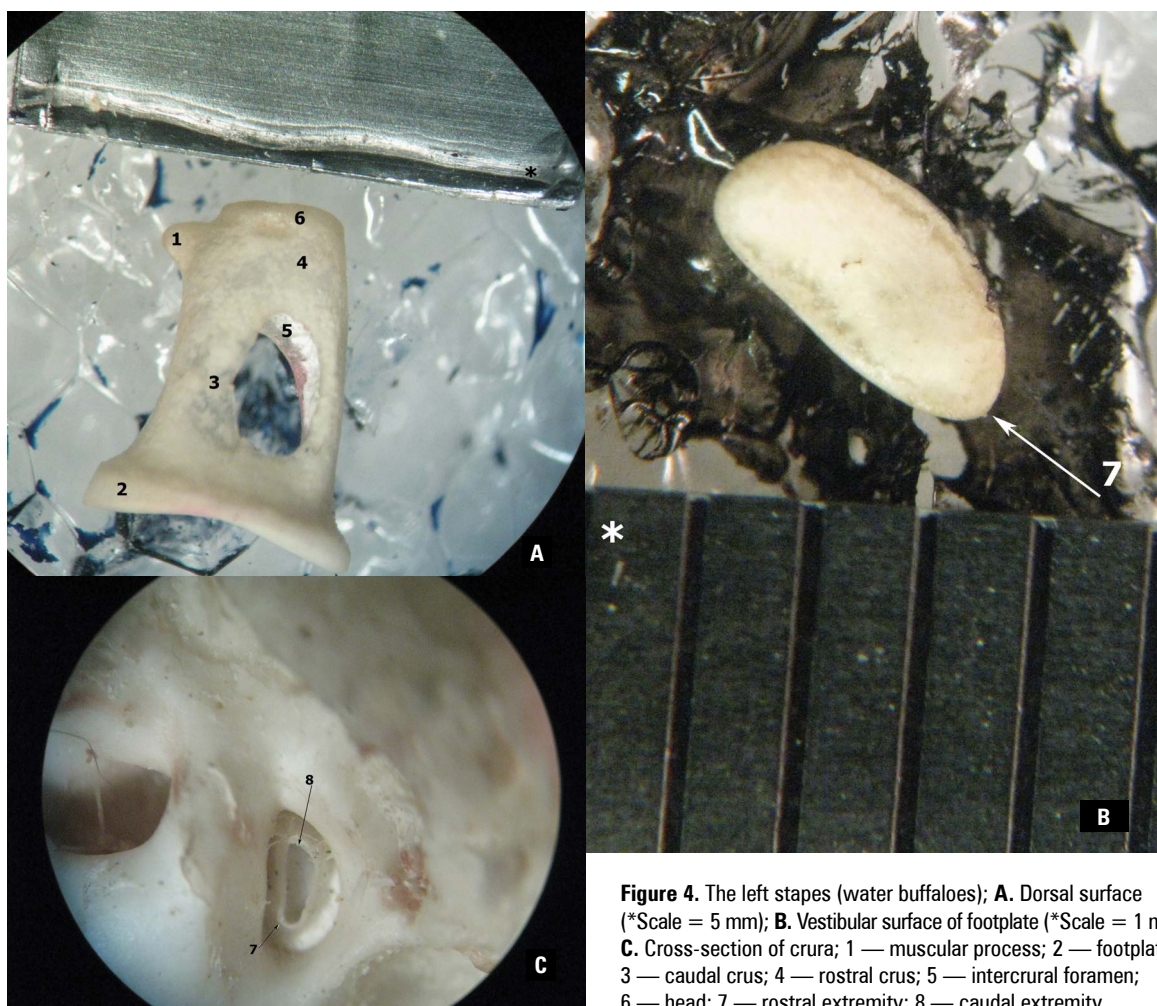


**Figure 4.** The left stapes (water buffaloes); **A.** Dorsal surface (\*Scale = 5 mm); **B.** Vestibular surface of footplate (\*Scale = 1 mm), **C.** Cross-section of crura; 1 — muscular process; 2 — footplate; 3 — caudal crus; 4 — rostral crus; 5 — intercrural foramen; 6 — head; 7 — rostral extremity; 8 — caudal extremity.

approximately elongated oval [6]. Like that of the ox, the PT of TM in water buffaloes was a regular oval, whereas the shape of PT in sheep and goats takes the form of a regular circle [11]. The shape of PF is more or less rectangular [11] or roughly triangular [35] in the ox and irregularly triangular in sheep and goats [11], as it was in water buffaloes. The TM is circular in one-humped camels [21].

Like the ox, sheep, dog, cat, and pig [6] the manubrium divides PT into asymmetrical dorsal and ventral sections in water buffaloes. Puria and Steele [30] hypothesize that a similar asymmetry in cats and humans ears could lead to a force differential on the manubrium, resulting in a rotation of malleus about its long axis. Because such a change in rotatory axis would reduce the moment of inertia, they suggest that this change in ossicular vibratory mode could improve the efficiency of sound transmission at higher frequencies.

As in the goat and ox [11], the entire length of manubrium in water buffaloes was embedded in PT,

whereas in the sheep part of manubrium was superficially placed over PT [11]. The medial surface of PT on its central part was strongly convex in the ox or regularly convex in goats and sheep [11]. In water buffaloes, it was not convex; it appears to be irregularly concavo-convex.

The size of PF is very variable among mammals; out of humans, cats, dogs, the ox, sheep and rodents, the biggest PF belongs to the sheep [6]. Although we did not measure PF separately in water buffaloes, it is likely very similar in size to that of the ox as illustrated by Decraemer and Funnell [6]. In short, the TM of water buffaloes resembled that of the ox rather than those of goats and sheep.

**Tympanic cavity.** The epitympanic recess in water buffaloes was occupied by head and neck of the malleus, as well as all of the incus, whereas in small ruminants the head, neck and rostral process of malleus, along with its articulation with incus, are all situated in the recess [11]. In the ox only the head

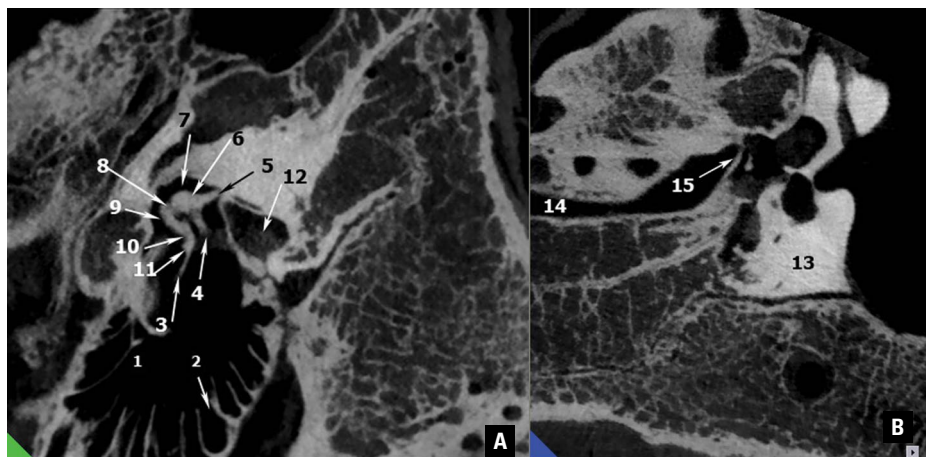


**Figure 5.** Sagittal (A) and dorsal (B) planes tomogram created by cone-beam computed tomography of right temporal bone (water buffaloes); 1 — tympanic cavity; 2 — tympanic cell; 3 — manubrium; 4 — long process of incus; 5 — short process of incus; 6 — incus body; 7 — epi-tympanic recess; 8 — incus-malleus joint; 9 — malleus head; 10 — malleus neck; 11 — rostral process of malleus; 12 — facial and vestibulocochlear nerves; 13 — petrosal part of temporal bone; 14 — external acoustic meatus; 15 — tympanic rim.

**Table 3.** Comparison of means (mm) ± standard deviations of the ossicles (water buffaloes) with those obtained in various ruminates

		Present study	Ox	Sheep	Goat	Dromedary camel	Bactrian camel [2]	Human [26]
Malleus	TL	11.07 ± 0.46	11.26 ± 0.61	8.28 ± 0.39	8.40 ± 0.41	10.25 ± 0.54	—	7.15 ± 0.31
	ML	6.54 ± 0.60	7.32 ± 0.13	5.56 ± 0.31	5.10 ± 0.55	7.60 ± 0.46	—	4.22 ± 0.35
	HNL	5.73 ± 0.20	3.17 ± 0.40	2.60 ± 0.21	2.60 ± 0.21	2.72 ± 0.17	—	4.85 ± 0.29
	HD	3.17 ± 0.40	1.76 ± 0.08	1.26 ± 0.16	2.18 ± 0.32	3.25 ± 0.17	1.60 ± 0.20	2.36 ± 0.21
Incus	TL	5.74 ± 0.88	6.20 ± 0.38	3.22 ± 0.13	3.10 ± 0.10	4.84 ± 0.20	—	3.14 ± 0.19
	BW	3.30 ± 0.22	2.92 ± 0.28	2.08 ± 0.08	2.14 ± 0.15	3.04 ± 0.15	—	—
Stapes	TL	3.60 ± 0.57	3.60 ± 0.57	2.72 ± 0.20	2.27 ± 0.20	4.12 ± 0.35	4.30 ± 0.60	3.12 ± 0.21
	HL	1.44 ± 0.33	1.42 ± 0.05	1.26 ± 0.11	1.07 ± 0.09	1.35 ± 0.17	—	—
	BL	2.70 ± 1.27	2.57 ± 0.09	2.08 ± 0.08	2.02 ± 0.05	3.25 ± 0.37	—	2.68 ± 0.27

Note: The author did not record the related parameters which are empty in Bactrian camel and human. TL — total length; ML — malleus length; HNL — head and neck length; HD — head diameter; BW — body width; HL — head length; BL — body length. The parameters are based on millimeters (mm).

of malleus and part of the incus [11] or the head of malleus and incus [4] are housed in the recess. In Bactrian camels, the malleus head and main part of incus are located in the recess [2].

The cellular divisions of the bullar cavity in water buffaloes resemble what has been described in the ox [1, 35]. This is not the case in other domestic ruminant species in veterinary anatomical textbooks [11, 25] nor in Bactrian camels [2]. According to Fleischer [10] and Plestilova et al. [29], similar bony septa which divide the middle ear cavities of several types of mammals are expected to change the resonance properties of such cavities, but experimental data are lacking.

**Morphometry of ossicles.** Differences in ossicle size in animals correlate with variations in their auditory range [13, 27]. Nummela [27] found that although there is a correlation between skull mass and ossicular mass among mammals in general; the ossicular mass cannot be reliably predicted from skull mass in mammals with large skulls. There are very few morphometric studies documented for ossicles of ruminants. Mohammadpour [21] reported masses

and other measurements of the different parts and process of the ossicles in the ox, sheep, goat, and dromedary camel. Bai et al. [2] weighed all ossicles and measured malleus head and length of stapes in Bactrian camels. Nummela [27] reported average masses of ossicles in various mammals including Bactrian camels, cattle and sheep.

According to Table 2, the heaviest ossicles belonged to water buffaloes although it is not the largest animal among the reported animals. The mean values for HNL of malleus, TL and BW of incus, as well as HL stapes, were all greatest in water buffaloes among the other ruminants. However, the mean values of BL and TL of stapes were greatest in dromedary and Bactrian camels, respectively (Table 3). In the ox, the long crus was almost twice the length of short crus, whereas in the sheep the long crus was nearly three times longer than the short crus. The two crura of goats were almost equal in length [11], like water buffaloes, while high frequency hearing is limited by middle ear size and in particular ossicular mass [13].

**Malleus head.** Unlike small ruminants [11], caudally the malleus head is smoothly convex in the ox [11],

as it was in water buffaloes. Wilkie [35] also reported that malleus head has very pronounced features in the flatness of head caudally.

Unlike the ox and water buffalo, the notch on the articular surface of head is very prominent in goat and sheep [11], which is the most striking difference among the mallei of these animals.

The articular surface of malleus head was covered by the incus body completely in the ox [11], while it was covered partly in goat and sheep [11], as it was in water buffaloes.

**Malleus neck.** As in the ox [11, 35], the curved neck was not very distinct in water buffaloes, whereas in the sheep the neck was the thickest part [11].

**Malleus processes.** The best-developed muscular process belonged to one-humped camels [11], followed by the ox and small ruminants [11, 21]. The process of water buffaloes resembled the ox in this respect.

The rostral process arises from the medial and just rostral to the muscular process in small ruminants, whereas the rostral process arises medially from the neck at the same level as at which the muscular process arises in the ox [11], as it was in water buffaloes.

In water buffaloes, the rostral process was attached by a ligament to the wall of tympanic cavity. According to Getty [11], the ossicles in domestic animals are connected with walls of tympanic cavity by ligaments. While in the rodents there is an osseous connection between the process and tympanic cavity [20].

**Manubrium.** In goats [11], the manubrium is three-sided, whereas the manubrium of water buffaloes was four-sided, like those of ox and sheep [11].

As in the goat and ox [11], in water buffaloes the entire length of manubrium were embedded in PT, whereas in the sheep part of manubrium lies superficially over PT, almost in its middle [11].

The best-developed lateral process belonged to one-humped camels [21], followed by the goat, sheep, and ox [11]. In water buffaloes, the process resembled that of the ox.

In the goat, the lateral process arises almost at the same level as the muscular process [11], whereas in the sheep and ox this process arises caudal to the muscular process, on the opposite side [11], similar to that of water buffaloes.

One of distinguishing features of ossicle morphology among mammals is the orientation of the manubrium relative to the anatomical axis, but this has not been the focus of attention in the larger domestic animals. The manubrium is roughly parallel to the axis

in many very small mammals, but it is perpendicular in humans, rabbits, guinea pigs, and chinchillas [20]. In water buffaloes, the manubrium took an intermediate position (not perpendicular or parallel).

**Incus.** Unlike the ox [35] and water buffalo, the articular surface of body had a concave depression in sheep and goat because of the presence of a high ridge on the surface [11]. The incus body of the ox [35] and water buffalo were a large, well-developed, unlike those of small ruminants [11].

In water buffaloes, the lenticular process was located at the extremity of long crus of incus, as in goats [11], dromedary [21], and Bactrian camels [2]. However, in the sheep and ox the process was absent [11] or present [34, 35].

**Stapes.** Like the ox [35], this ossicle was nearly rectangular in shape in water buffaloes, whereas it is more trapezoidal in sheep [34].

As in the ox [11], the head of stapes in water buffaloes was convex, whereas the head was flattened in goats [11].

The footplate of mammalian stapes was oval or bean-shaped, as in man. It is elongated, thus having a long and a short axis [10]. As in the ox [35], the shape of footplate was an irregular oval in water buffaloes, whereas it has a squarer shape in sheep [34] and is elliptical in Bactrian camels [2].

## CONCLUSIONS

Although general anatomical characteristics of the middle ear structures and the relationship of the ossicles in the water buffalo was almost similar to those in the ox and small ruminates, several distinctive morphologic and morphometric variations of the middle ear structures are recognized in the water buffalo.

In general, among the mammals, there seems to be correlations between ossicle morphology and the frequency that an animal can hear [13, 29]. Therefore, although some of morphological characteristics of middle ear described here remain of unknown functional significance, the middle ear of water buffaloes shows characteristics of the transitional type ear, following the terminology of Fleischer [10]. These characteristics consist of an enlarged malleus head, heavy ossicles, a ligamentous connection of a reduced rostral process to the skull, reduction of malleus anterior lamina, the possession of a relatively large incus, and oblique manubrial orientation to the anatomical axis [20]. Such a transitional type ear leads to the prediction of quite a wide frequency range: not es-

pecially low nor especially high. Water buffaloes, like the cattle, belong to the Bovidae family and cattle are able to hear a much wider range of sound frequencies (16 to 40,000 Hz) than humans (20 to 20,000 Hz). This should permit them to hear, in principle, both low-frequency rumbles of elephants and the ultrasonic screams of flying bats [13]. However, intraspecific variations in ossicle morphology among water buffaloes and other ruminants remain to be examined.



### Acknowledgements

We thank Prof. Dr. Matthew Mason from Department of Physiology, Development and Neuroscience of University of Cambridge for his very thoroughly editing of our manuscript and giving valuable advice and comments that improved significantly this research. The study was supported by grant (Grant Number: SCU.VB98.770) from Research Council of Shahid Chamran University of Ahvaz.

### REFERENCES

- Ardouin P. Anatomie comparée de la chaîne des osselets de l'ouïe dans la série des mammifères. *Rev Laryngol Otol Rhinol.* 1935; 56: 427–489.
- Bai Z, Wang H, Yuan G, et al. functional anatomy of the external and middle ear of the Bactrian camel. *J Camel Pract Res.* 2009; 16(1): 115–120.
- Blanke A, Ohlerth S, Hollerrieder J, et al. Computed tomographic features of the osseous external ear canal, tympanic membrane, and tympanic bulla in clinically normal horses. *J Equine Vet Sci.* 2016; 45: 17–21, doi: [10.1016/j.jevs.2016.03.001](https://doi.org/10.1016/j.jevs.2016.03.001).
- Botti M, Secci F, Ragionieri L, et al. Auditory ossicles in the ruminants: comparative morphological analysis with the analogous formations of horse. *Ann Fac Medic Vet di Parma.* 2006; 26: 91–96.
- Budras KD, Habel E, Wunsche A, Buda S. Anatomy of the bovine: An illustrated text. Schluetersche GmbH, Hanover 2003.
- Decraemer WF, Funnel WR. Anatomical and mechanical properties of the tympanic membrane. In: ARS B. (ed.) Chronic otitis media: pathogenesis-oriented therapeutic management. Kugler, The Netherlands 2005: 51–84.
- Doran AHG. Morphology of the mammalian ossicula auditūs. *Trans Linn Soc Lond 2nd Ser.* 1878; 13(68): 185–189.
- Dyce KM, Sack WO, Wensing CJG. Textbook of veterinary anatomy. WB Saunders Company, Philadelphia 2018.
- FAO. The water buffaloes, Food and agriculture organization of the United Nations, Italy 1977.
- Fleischer G. Evolutionary principles of the mammalian middle ear. *Adv Anat Embryol Cell Biol.* 1978; 55(5): 3–70, doi: [10.1007/978-3-642-67143-2](https://doi.org/10.1007/978-3-642-67143-2), indexed in Pubmed: [735912](https://pubmed.ncbi.nlm.nih.gov/735912/).
- Getty R. Sisson and Grossman's the anatomy of the domestic animals. WB Saunders Company, Philadelphia 1975.
- Harneja NK, Chaturvedi RP. A study of the human ear ossicles. *Ind J Otol.* 1973; 25: 154, doi: [10.1007/BF02991177](https://doi.org/10.1007/BF02991177).
- Hemilä S, Nummela S, Reuter T. What middle ear parameters tell about impedance matching and high frequency hearing. *Hearing Res.* 1995; 85(1-2): 31–44, doi: [10.1016/0378-5955\(95\)00031-x](https://doi.org/10.1016/0378-5955(95)00031-x).
- König HE, Liebich HG. Veterinary anatomy of domestic mammals, text book and colour atlas. Schattauer, New York 2004.
- Kurtul I, Cevik A, Bozkurt EU, et al. A detailed subgross morphometric study on the auditory ossicles of the New Zealand rabbit. *Anat Histol Embryol.* 2003; 32(4): 249–252, doi: [10.1046/j.1439-0264.2003.00483.x](https://doi.org/10.1046/j.1439-0264.2003.00483.x), indexed in Pubmed: [12919078](https://pubmed.ncbi.nlm.nih.gov/12919078/).
- Lavender D, Taraskin SN, Mason MJ. Mass distribution and rotational inertia of “microtype” and “freely mobile” middle ear ossicles in rodents. *Hear Res.* 2011; 282(1-2): 97–107, doi: [10.1016/j.heares.2011.09.003](https://doi.org/10.1016/j.heares.2011.09.003), indexed in Pubmed: [21951489](https://pubmed.ncbi.nlm.nih.gov/21951489/).
- Mallya S, Lam E. White and Pharoah's oral radiology: principles and interpretation. Mosby, USA 2018.
- Mantokoudis G, Huth ME, Weisstanner C, et al. Lamb temporal bone as a surgical training model of round window cochlear implant electrode insertion. *Otol Neurotol.* 2016; 37(1): 52–56, doi: [10.1097/MAO.0000000000000921](https://doi.org/10.1097/MAO.0000000000000921), indexed in Pubmed: [26649606](https://pubmed.ncbi.nlm.nih.gov/26649606/).
- Martonos C, Damian A, Gudea A, et al. Morphological and morphometrical study of the auditory ossicles in chinchilla. *Anat Histol Embryol.* 2019; 48(4): 340–345, doi: [10.1111/ahc.12446](https://doi.org/10.1111/ahc.12446), indexed in Pubmed: [31041818](https://pubmed.ncbi.nlm.nih.gov/31041818/).
- Mason MJ. Of mice, moles and guinea pigs: functional morphology of the middle ear in living mammals. *Hear Res.* 2013; 301: 4–18, doi: [10.1016/j.heares.2012.10.004](https://doi.org/10.1016/j.heares.2012.10.004), indexed in Pubmed: [23099208](https://pubmed.ncbi.nlm.nih.gov/23099208/).
- Mohammadpour AA. Comparative anatomical and morphological study of the middle ear bones between camel and other ruminants. *Pajouhesh and Sazandegi.* 2005; 64: 70–75.
- Moioli B, Borghese A. Buffalo breeds and management systems. In: Borghese A (ed.). Buffalo Production and research. Food and Agriculture Organization of the United Nations, Rome 2005: 51–108.
- Naserian AA, Saremi B. Water buffalo industry in Iran. *Itali J Anim Sci.* 2016; 6(sup2): 1404–1405, doi: [10.4081/ijas.2007.s2.1404](https://doi.org/10.4081/ijas.2007.s2.1404).
- Nickel R, Schummer A, Seiferle E. Lehrbuch der Anatomie der Haustiere: Nervensystem, Sinnesorgan, Endokrine Drüsen. Verlag Paul Parey, Berlin 1975.
- Nickel R, Schummer A, Seiferle E. The Anatomy of the domestic animals, the locomotor system of the domestic mammals. Verlag Paul Parey, Berlin 1986.
- Noussios G, Chouridis P, Kostretzis L, et al. Morphological and Morphometrical Study of the Human Ossicular Chain: A Review of the Literature and a Meta-Analysis of Experience Over 50 Years. *J Clin Med Res.* 2016; 8(2): 76–83, doi: [10.14740/jocmr2369w](https://doi.org/10.14740/jocmr2369w).
- Nummela S. Scaling of the mammalian middle ear. *Hearing Res.* 1995; 85(1-2): 18–30, doi: [10.1016/0378-5955\(95\)00030-8](https://doi.org/10.1016/0378-5955(95)00030-8).
- Péus D, Dobrev I, Prochazka L, et al. Sheep as a large animal ear model: Middle-ear ossicular velocities and intracochlear sound pressure. *Hearing Res.* 2017; 351: 88–97, doi: [10.1016/j.heares.2017.06.002](https://doi.org/10.1016/j.heares.2017.06.002), indexed in Pubmed: [28601531](https://pubmed.ncbi.nlm.nih.gov/28601531/).
- Pleštilová L, Hrouzková E, Burda H, et al. Does the morphology of the ear of the Chinese bamboo rat (*Rhizomys sinensis*) show “Subterranean” characteristics? *J Morphol.* 2016; 277(5): 575–584, doi: [10.1002/jmor.20519](https://doi.org/10.1002/jmor.20519), indexed in Pubmed: [26880690](https://pubmed.ncbi.nlm.nih.gov/26880690/).
- Puria S, Steele C. Tympanic-membrane and malleus-incus-complex co-adaptations for high-frequency hearing in mammals. *Hearing Res.* 2010; 263(1-2): 183–190, doi: [10.1016/j.heares.2009.10.013](https://doi.org/10.1016/j.heares.2009.10.013), indexed in Pubmed: [19878714](https://pubmed.ncbi.nlm.nih.gov/19878714/).
- Russo M, Covelli EM, Meomartino L, et al. Computed tomographic anatomy of the canine inner and middle ear. *Vet Radiol Ultrasound.* 2002; 43(1): 22–26, doi: [10.1111/j.1740-8261.2002.tb00437.x](https://doi.org/10.1111/j.1740-8261.2002.tb00437.x), indexed in Pubmed: [11866039](https://pubmed.ncbi.nlm.nih.gov/11866039/).
- Schaller O, Ghsrge M, Constaninescu G. Illustrated veterinary anatomical nomenclature. Enke Verlag, Germany 2007.
- Seibel VA, Lavinsky L, De Oliveira JA. Morphometric study of the external and middle ear anatomy in sheep: a possible model for ear experiments. *Clin Anat.* 2006; 19(6): 503–509, doi: [10.1002/ca.20218](https://doi.org/10.1002/ca.20218), indexed in Pubmed: [16287111](https://pubmed.ncbi.nlm.nih.gov/16287111/).
- Wilkie HC. The ossicula auditūs of the sheep (*Ovis aries*). *J Comp Pathol. Ther.* 1925; 38: 298–301, doi: [10.1016/s0368-1742\(25\)80051-1](https://doi.org/10.1016/s0368-1742(25)80051-1).
- Wilkie HC. The auditory organ of the ox (*Bos taurus*). *Proc Zool Soc Lond.* 2009; 106(4): 985–1009, doi: [10.1111/j.1469-7998.1936.tb06299.x](https://doi.org/10.1111/j.1469-7998.1936.tb06299.x).

# Morphometric analysis and three-dimensional computed tomography reconstruction of the long bones of femoral and crural regions in Van cats

O. Yılmaz<sup>1</sup> , İ. Demircioğlu<sup>2</sup> 

<sup>1</sup>Department of Anatomy, Faculty of Veterinary Medicine, Van Yüzüncü Yıl University, Van, Turkey

<sup>2</sup>Department of Anatomy, Faculty of Veterinary Medicine, Harran University, Şanlıurfa, Turkey

[Received: 21 June 2020; Accepted: 6 September 2020]

**Background:** This study was conducted to determine the morphometric features and to make the three-dimensional (3D) reconstruction of the images obtained by computed tomography (CT) of the main long bones (femur, tibia, fibula) in Van cats, and to reveal the biometric differences between these measurement values of both sexual dimorphism and homotypic variations.

**Materials and methods:** A total of 16 adult Van cats, 8 male and 8 female, were used in the study. The pelvic limb long bones of the cats, which were anesthetized with the ketamine-xylazine combination, were scanned with a CT device and their images were obtained. These images were converted to a 3D structure by means of MIMICS 20.1 (The Materialise Group, Leuven, Belgium) software programme. Then, morphometric, volumetric, surface area measurements of these bones were calculated and statistical analyses were performed.

**Results:** In the analysis, it was observed that right greatest length (GL), left GL, right greatest length from caput ossis femoris (GLc), left greatest breadth of the distal end (Bd), right volume (V), and left V measurement values of the femur; left GL1, right greatest breadth of the proximal end (Bp), right Bd, left Bd, right smallest breadth of the diaphysis (SD), right V, left V, and right surface area (SA) measurement values of the tibia; right V, left V, right SA, and left SA measurement values of the fibula were statistically significantly higher in male cats than in female cats ( $p < 0.05$ ). The volume and surface area measurement values of the femur, tibia and fibula of male and female cats were determined as  $8.57 \pm 1.33 \text{ cm}^3$  and  $7.00 \pm 0.49 \text{ cm}^3$ ,  $64.28 \pm 6.72 \text{ cm}^2$  and  $59.42 \pm 4.72 \text{ cm}^2$ ;  $7.56 \pm 1.28 \text{ cm}^3$  and  $6.15 \pm 0.52 \text{ cm}^3$ ,  $56.89 \pm 6.47 \text{ cm}^2$  and  $52.72 \pm 3.15 \text{ cm}^2$ ;  $1.10 \pm 0.17 \text{ cm}^3$  and  $0.83 \pm 0.05 \text{ cm}^3$ ,  $14.18 \pm 1.61 \text{ cm}^2$  and  $11.95 \pm 0.48 \text{ cm}^2$ , respectively.

**Conclusions:** The statistical differences between the sexes in terms of the measurement parameters of the femur, tibia and fibula in adult Van cats were determined. We believe that these differences can be used in determining morphological variations of Van cats. In addition, it is thought that the data obtained from the present study would be beneficial to veterinary physicians in the clinical application areas in order to evaluate the pathological conditions related to these bones and to the studies in the field of zooarchaeology. (Folia Morphol 2021; 80, 1: 186–195)

**Key words:** computed tomography, femur, fibula, three-dimensional reconstruction, tibia, Van cat

## INTRODUCTION

Living around and named after the Van Lake region of Turkey, Van cats are an attractive breed of domestic cats with their distinctive eye coloration (one eye can be yellow and the other can be blue, both can be yellow, or both can be blue), soft fur, affection for swimming, hunting capabilities, cleanliness, and intelligence. In 22 April 2006, Van cats were licensed and registered with the communiqué no. 2006/16 as a breed of domestic cat with all their distinctive properties, and are now officially under protection of the Republic of Turkey [6]. There are only a handful of studies in literature, however, regarding the osteological properties of these cats [46–48].

Known also as “the thigh bone”, femur (os femoris) is the strongest of all the long bones. It usually has a cranioventral bearing along the skeletal structure, and it plays a significant role during the forward motion of the body [14]. Meanwhile, “the ossa cruris” structure is another formation of the long bones of the pelvic limbs, and consists of the combination of the tibia and fibula bones. Tibia is a long, tubular bone and is the stronger of the two as it shoulders the weight of the body. It is located towards the medial surface of the leg, and has joints with the femur at the proximal end and with ossa tarsi at the distal end. Located towards the lateral surface, the fibula is weaker and does not have a joint with femur at the proximal end. On the distal end, however, it has a limited amount of contact with ossa tarsi [4]. In ruminants, the proximal end of the fibula is found in contact with the outer rim of the condyles lateralis tibiae, and it has a regressed corpus. Its distal end, it joins the formation of os malleolare. In equidae, the proximal end of the fibula makes a joint with tibia, but the distal end only reaches halfway down the range of tibia where it ends with a pointy edge. Sus and carnivore species have a fully developed fibula, but it's separated from tibia with a formation known as “spatium interosseum cruris”. This gap, which is enclosed with soft tissue, goes almost all the way down to the distal edge in Sus species, while it's only limited to the proximal region in carnivores [15].

In recent years, medical imaging systems, computed tomography (CT), and three-dimensional (3D) reconstruction software become commonly utilized tools when trying to determine the morphological properties of the anatomical structures in the skeletal systems of animals, particularly those of small, pet animals like cats and dogs. These systems are also being used to obtain osteometric and volumetric

measurement results, to evaluate any potential developmental, metabolic, inflammatory, or degenerative anomalies, and to investigate numerous other pathological situations like traumas, dislocations, fractures, or neoplasia [26, 45]. Anthropological studies also commonly use these methods and 3D modelling in tandem to determine the morphological properties of long bones and to perform various measurements on them [8, 17, 21].

Various studies have been performed to determine the anatomical and osteometrical properties of the main long bones of the pelvic limbs (femur, tibia, fibula) of different animal species, like mole-rats (*Spalax leucodon Nordmann*) [34], African giant rats (*Cricetomys gambianus Waterhouse*) [27], grasscutter rodents (*Thryonomys swinderianus*, Temminck-1827) [29], guinea pigs (*Cavia porcellus*) [37], feral pigs (*Sus scrofa*) [19], martens (*Martes foina*) [3], badgers (*Meles meles*) [32], squirrels (*Sciurus vulgaris*) [31], hedgehogs hedgehog (*Erinaceus europaeus L.*) [35], porcupines (*Hystrix Cristata*) [49], chinchillas (*Chinchilla lanigera*) [10], lumholtz tree-kangaroo (*Dendrolagus lumholtzii*) [40], Anatolian bobcats (*Lynx lynx*) [30], New Zealand rabbits (*Oryctolagus cuniculus*) [1, 16, 36], marmosets (*Callithrix jacchus*) [9], brown bears (*Ursus arctos*) [13], deers (*Hippocamelus bisulcus*) [41], sheeps (*Ovis aries*) [2], gazelles (*Gazella subgutturosa*) [12], foxes (*Vulpes vulpes* and *Alopex lagopus*) [24], dogs (*Canis lupus familiaris*) [28, 43], and domestic cats (*Felis catus* and *Felis domestica*) [5, 16]. No study was found when the existing literature was searched for long bones of the pelvic limbs of Van cats, however. This study was, therefore, performed with the aim of creating 3D models of the pelvic limb long bones of Van cats using CT scans and imaging of different anatomical structures of these bones, and to obtain osteometric and volumetric measurements and to determine any potential biometrical difference in these measured values with regards to sexual dimorphism and homotypic variations.

## MATERIALS AND METHODS

A total of 16 adult Van cats (8 males and 8 females) obtained from Van Yuzuncu Yil University Van Cat Research and Application Centre was used in this study. The ages of the cats varied between 3 and 8 years, and their live body masses (W) varied between 5810 and 8050 grams. *Ad libitum* cat feed and tap water was provided to these cats until the day before the study. The study received the approval of the Van Yuzuncu Yil

**Table 1.** Studied parameters and abbreviations (according to Von den Driesch, 1976 [44])

Parameter	Abbreviation	Definition
<b>Measurement points and abbreviations of the femur in Van cats</b>		
1	GL	Greatest length: distance between the proximal and the distal end [mm]
2	GLc	Greatest length from caput ossis femoris: distance between the caput ossis femoris and the distal end [mm]
3	Bp	Greatest breadth of the proximal end [mm]
4	Bd	Greatest breadth of the distal end [mm]
5	Dc	Greatest depth of the caput ossis femoris [mm]
6	SD	Smallest breadth of the diaphysis (Corpus ossis femoris) [mm]
7	V	Volume of the femur [cm <sup>3</sup> ]
8	SA	Surface area of the femur [cm <sup>2</sup> ]
<b>Measurement points and abbreviations of the tibia in Van cats</b>		
1	GL1	Greatest length: distance between the proximal and the distal end [mm]
2	Bp	Greatest breadth of the proximal end [mm]
3	Bd	Greatest breadth of the distal end [mm]
4	SD	Smallest breadth of the diaphysis (Corpus tibiae) [mm]
5	V	Volume of the tibia [cm <sup>3</sup> ]
6	SA	Surface area of the tibia [cm <sup>2</sup> ]
<b>Measurement points and abbreviations of the fibula in Van cats</b>		
1	GL2	Greatest length: distance between the proximal and the distal end [mm]
2	V	Volume of the fibula [cm <sup>3</sup> ]
3	SA	Surface area of the fibula [cm <sup>2</sup> ]

University Local Ethical Board for Animal Experimentation (Decision no: 2020/02-27.02.2020). The cats included in the study were numbered, and were not provided any feed starting the day before the study. Anaesthesia of the cats for the scanning process was performed using a combination of ketamine (15 mg/kg, IM, Ketazol® 10% injectable, Interhas Veterinary Medicines, Ankara) and xylazine (1–2 mg/kg, IM, Alfazyn® 2% injectable, Ege – Vet Veterinary Medicines, İzmir).

A 16-section multi-sequential CT device (Somatom Sensation 16; Siemens Medical Solutions, Erlangen, Germany) located in Van Yuzuncu Yil University Medical Faculty Radiology Department was used to obtain the CT scans of the cats. A disposable sheet was placed onto the gantry of the device, and the cats were laid onto this sheet head-first in prone position (ventral decubitus) to achieve symmetry. The device parameters for the CT scan were as follows: KV/Effective mAs/Rotation time (sec) 120/120/0.75; gantry rotation period 420 ms; physical detector collimation, 16 × 0.6 mm; section thickness 0.4 mm; final section collimation 32 × 0.63 mm; feed/rotation 6 mm; Kernel, U90u; increment 0.5 mm; and resolution 512 × 512 pixels. Setting of the dosage parameters and the scanning process itself were performed on the basis of standard

protocols established by the literature [18, 39]. The images obtained were saved in DICOM format.

These images were then transported to the MIM-ICS 20.1 (The Materialise Group, Leuven, Belgium) software and were reconstructed. Osteometric measurements were then performed on the 3D models of the femur, tibia, and fibula bones. The measurement points specified in the literature were used during the morphometric measurements [44]. Once the morphometric measurements were complete, the surface area and volume of each of the bones were calculated. The definitions and abbreviations for the measured osteometric parameters are presented in Table 1. Nomina Anatomica Veterinaria [25] was used as the terminology basis throughout the study. Weighing of the cats included in the study was performed using a digital scale (TESS®, RP-LCD, Çomak Terazı, İstanbul).

#### Statistical analysis

Van cat pelvic limb long bones (femur, tibia, and fibula) were modelled in 3D environment based on the CT images of the cats obtained as part of study, and Shapiro-Wilk test ( $n < 50$ ) was used to determine if the value distribution of the data obtained from these models was normal. Since the distribution of the values



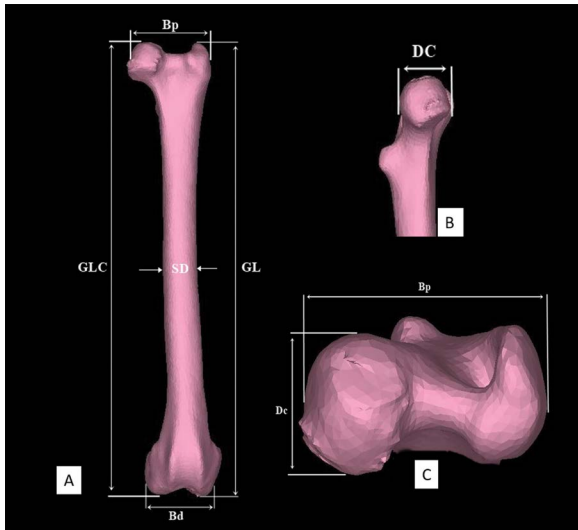


**Figure 1.** Measurement points from cranial (A), upper medial (B), and dorsal (C) of the femur in Van cats; GL — greatest length; GLC — greatest length from caput ossis femoris; Bp — greatest breadth of the proximal end; Bd — greatest breadth of the distal end; Dc — greatest depth of the caput ossis femoris; SD — smallest breadth of the diaphysis (*Corpus ossis femoris*).

weren't normal in general, a number of non-parametric tests were performed throughout the rest of the study. The defining statistics for the measured properties in this study are presented as mean, standard deviation, and minimum and maximum values. Wilcoxon test was used to compare the measurements for left and right side bones. Comparisons between the sexes were performed using Mann-Whitney-U test. The correlations between the measurements were investigated through Spearman Correlation coefficient calculations, and were separately performed for each sex. Statistical significance threshold was taken as ( $\alpha$ ) 5%, and SPSS (IBM SPSS for Windows, Ver.23) package software was used for calculations.

## RESULTS

The volume and surface area measurements of the Van cat pelvic limb femur, tibia, and fibula were performed as part of this study. The morphometric measurement parameters and 3D reconstructions are presented in Figures 1–3 with regards to the measurement point locations on bones. These results were then compared in terms of sexual dimorphism and homotypic variations, and are presented in Tables 2–7. Any statistically significant differences between the results ( $p < 0.05$ ) were recorded.

Table 2 presents the defining statistics for femurs' morphometric measurement results and the comparison of the sexes in terms of homotypic variations.

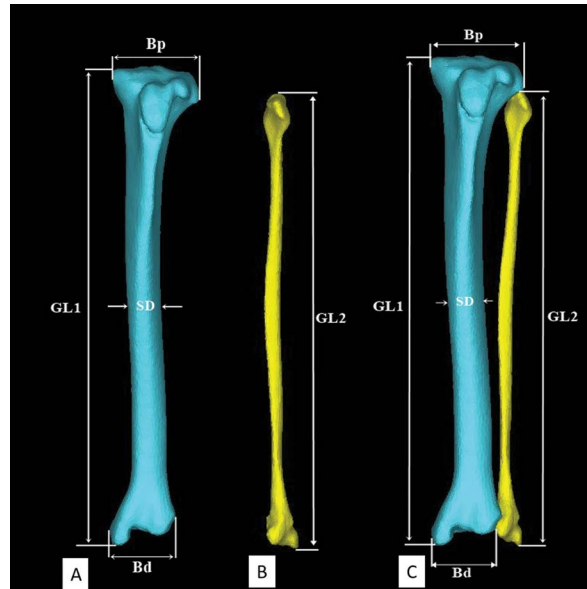


**Figure 2.** Measurement points from cranial of the tibia (A), fibula (B), and ossa cruris (C) in Van cats; GL1 — greatest length of the femur; Bp — greatest breadth of the proximal end; Bd — greatest breadth of the distal end; SD — smallest breadth of the diaphysis (*Corpus tibiae*); GL2 — greatest length of the fibula.

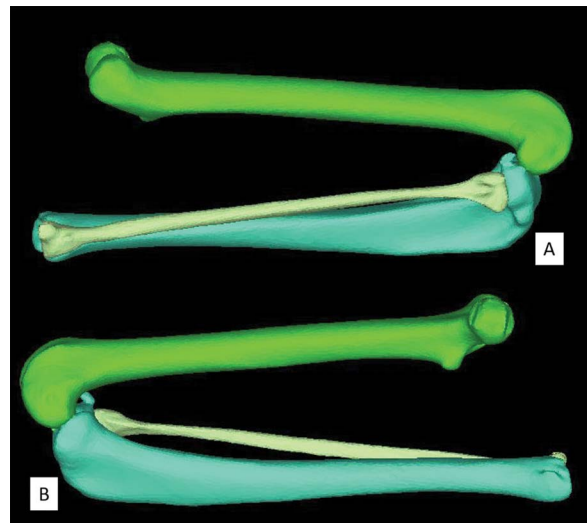


**Figure 3.** Three-dimensional reconstruction of the pelvic limb long bones (femur, tibia, fibula) from lateral (A) and medial (B) in Van cats (flexion position).

Accordingly, right greatest length (GL), left GL, right greatest length from caput ossis femoris (GLC), left greatest breadth of the distal end (Bd), right volume (V), and left V values were found to be higher in males in a statistically significant manner, compared to females ( $p < 0.05$ ). When the left and right femur defining statistics were compared within each sex, right smallest breadth of the diaphysis (SD)

**Table 2.** Descriptive statistics and homotypic variations of the biometric parameters of the femur obtained from three-dimensional reconstruction of computed tomography images in Van cats

Parameter	Male			Female			P*
	Mean ± SD	Minimum	Maximum	Mean ± SD	Minimum	Maximum	
Right GL	108.79 ± 4.81	102.47	117.60	103.44 ± 2.84	100.01	107.30	0.016
Left GL	108.88 ± 5.04	103.07	118.01	103.18 ± 3.02	99.31	107.46	0.016
Right GLc	110.23 ± 5.34	101.55	117.31	103.99 ± 3.24	99.44	110.27	0.021
Left GLc	109.12 ± 5.11	102.36	118.23	104.84 ± 2.79	102.24	110.22	0.059
Right Bp	20.48 ± 0.82	19.14	21.37	19.63 ± 0.95	18.24	20.91	0.059
Left Bp	20.27 ± 1.05	19.13	22.03	19.20 ± 0.98	17.56	20.77	0.066
Right Bd	18.40 ± 0.82	17.08	19.40	18.12 ± 0.94	16.85	19.60	0.462
Left Bd	18.91 ± 0.53	18.11	19.44	18.14 ± 0.59	17.26	18.86	0.021
Right Dc	9.98 ± 0.68	8.93	11.16	9.75 ± 0.57	8.84	10.51	0.529
Left Dc	10.05 ± 0.69	9.31	11.29	9.89 ± 0.54	9.02	10.94	0.793
Right SD	9.35 ± 0.94	8.08	10.62	9.51 ± 0.57	8.88	10.57	0.674
Left SD	9.33 ± 0.85	8.45	10.59	9.22 ± 0.35	8.88	9.91	0.958
Right V	8.57 ± 1.31	6.96	10.57	7.06 ± 0.43	6.55	8.57	0.012
Left V	8.57 ± 1.35	6.94	10.71	6.93 ± 0.55	6.03	8.57	0.012
Right SA	64.15 ± 6.52	50.96	71.02	59.24 ± 4.81	54.42	64.15	0.074
Left SA	64.41 ± 6.92	51.36	71.48	59.59 ± 4.62	55.67	64.41	0.093

\*p < 0.05; Mann-Whitney U test; SD — standard deviation; rest abbreviations — see Table 1

**Table 3.** “r” values of Spearman’s rho nonparametric correlations coefficients between the morphometric measurements of the femur in Van cats by gender

	Female		Male											
	Age (A)	Body mass (W)	Right GL	Left GL	Right GLc	Left GLc	Right Bp	Left Bp	Right Bd	Left Bd	Right Dc	Left Dc	Right SD	Left SD
Age (A)		0.957**	0.878**	0.878**	0.293	0.830*	0.683	0.683	0.244	-0.244	0.586	0.781*	0.732*	0.586
Body mass (W)	0.390		0.946**	0.946**	0.431	0.898**	0.659	0.659	0.228	-0.156	0.479	0.731*	0.874**	0.683
Right GL	-0.098	0.286		0.999**	0.619	0.976**	0.524	0.595	0.429	0.119	0.524	0.738*	0.881**	0.714*
Left GL	-0.098	0.357	0.952**		0.619	0.976**	0.524	0.595	0.429	0.119	0.524	0.738*	0.881**	0.714*
Right GLc	-0.098	0.286	0.999**	0.952**		0.571	-0.095	0.262	0.310	0.476	0.381	0.405	0.571	0.333
Left GLc	0.244	0.524	0.881**	0.857**	0.881**		0.500	0.643	0.524	0.190	0.571	0.690	0.810*	0.643
Right Bp	0.488	0.643	0.476	0.405	0.476	0.524		0.643	0.143	-0.167	0.429	0.738*	0.595	0.667
Left Bp	-0.098	0.429	0.619	0.690	0.619	0.548	0.548		0.167	-0.143	0.833*	0.619	0.405	0.167
Right Bd	0.634	0.333	-0.214	-0.143	-0.214	-0.048	0.595	0.357		0.786*	0.500	0.548	0.286	0.381
Left Bd	0.785*	0.515	0.096	0.108	0.096	0.323	0.802*	0.347	0.886**		0.190	0.238	0.143	0.262
Right Dc	0.488	0.405	-0.190	-0.095	-0.190	0.071	0.452	0.405	0.881**	0.802*		0.738*	0.238	0.095
Left Dc	0.195	0.429	0.048	0.238	0.048	0.000	0.500	0.571	0.714*	0.563	0.571		0.690	0.690
Right SD	-0.293	0.500	0.143	0.048	0.143	0.024	0.381	0.214	-0.143	-0.108	-0.190	0.071		0.881**
Left SD	0.049	0.667	0.167	0.071	0.167	0.190	0.714*	0.452	0.333	0.395	0.333	0.286	0.833*	

\*p < 0.05; \*\*p < 0.01; abbreviations — see Table 1

values were found to be higher than left SD values in females and the difference was statistically significant (p = 0.036). Furthermore, male left Bd

values were statistically higher than right Bd values (p = 0.017). No meaningful difference was determined for any other right and left side average femur values

**Table 4.** Descriptive statistics and homotypic variations of the biometric parameters of the tibia obtained from three-dimensional reconstruction of computed tomography images in Van cats

Parameter	Male			Female			P*
	Mean ± SD	Minimum	Maximum	Mean ± SD	Minimum	Maximum	
Right GL1	113.27 ± 4.84	105.43	120.74	108.14 ± 3.06	103.27	112.80	0.059
Left GL1	113.57 ± 5.48	105.09	123.31	107.86 ± 2.97	102.42	110.81	0.036
Right Bp	19.12 ± 0.70	18.17	19.95	18.31 ± 0.54	17.37	19.10	0.021
Left Bp	19.07 ± 0.90	17.41	20.21	18.37 ± 0.33	17.81	18.77	0.052
Right Bd	15.02 ± 0.72	14.34	16.11	13.80 ± 0.61	12.79	14.58	0.006
Left Bd	15.31 ± 0.67	14.33	16.40	13.65 ± 0.61	12.71	14.47	0.001
Right SD	8.16 ± 0.68	7.17	9.16	7.40 ± 0.43	6.89	8.05	0.036
Left SD	7.91 ± 0.79	7.12	9.40	7.58 ± 0.46	6.99	8.08	0.674
Right V	7.55 ± 1.27	6.05	9.50	6.18 ± 0.51	5.36	6.91	0.036
Left V	7.57 ± 1.28	6.02	9.62	6.11 ± 0.53	5.30	7.01	0.021
Right SA	56.84 ± 6.48	42.70	63.21	52.53 ± 2.95	47.49	57.00	0.027
Left SA	56.94 ± 6.46	43.05	62.66	52.91 ± 3.35	47.81	56.94	0.093

\*p < 0.05: Mann-Whitney U test; SD — standard deviation; other abbreviations — see Table 1

**Table 5.** “r” values of Spearman’s rho nonparametric correlations coefficients between the morphometric measurements of the tibia in Van cats by gender

Female	Male									
	Age (A)	Body mass (W)	Right GL1	Left GL1	Right Bp	Left Bp	Right Bd	Left Bd	Right SD	Left SD
Age (A)		0.957**	0.878**	0.878**	0.781*	0.830*	0.634	0.390	0.830*	0.781*
Body mass (W)	0.390		0.898**	0.922**	0.814*	0.814*	0.707	0.599	0.719*	0.731*
Right GL1	-0.488	0.119		0.952**	0.762*	0.786*	0.595	0.476	0.643	0.571
Left GL1	-0.342	0.262	0.929**		0.690	0.714*	0.619	0.476	0.667	0.571
Right Bp	0.098	0.595	0.476	0.405		0.905**	0.762*	0.429	0.500	0.714*
Left Bp	0.390	0.571	0.167	0.333	0.690		0.476	0.357	0.571	0.810*
Right Bd	0.488	-0.310	-0.786*	-0.714*	-0.333	0.167		0.357	0.357	0.333
Left Bd	0.098	-0.476	-0.429	-0.405	-0.095	0.286	0.810*		0.238	0.381
Right SD	-0.025	0.060	0.431	0.467	0.407	0.192	-0.443	-0.084		0.833*
Left SD	0.537	0.524	-0.024	0.214	0.048	0.167	-0.262	-0.452	0.515	

\*p < 0.05; \*\*p < 0.01; abbreviations — see Table 1

**Table 6.** Descriptive statistics and homotypic variations of the biometric parameters of the fibula obtained from three-dimensional reconstruction of computed tomography images in Van cats

Parameter	Male			Female			P*
	Mean ± SD	Minimum	Maximum	Mean ± SD	Minimum	Maximum	
Right GL2	105.09 ± 5.08	97.92	113.15	100.78 ± 2.32	97.28	103.99	0.074
Left GL2	105.67 ± 6.22	97.33	115.56	100.66 ± 2.64	96.84	104.18	0.074
Right V	1.09 ± 0.16	0.90	1.29	0.83 ± 0.05	0.76	0.90	0.001
Left V	1.10 ± 0.18	0.83	1.30	0.82 ± 0.05	0.73	0.90	0.003
Right SA	14.07 ± 1.60	11.72	15.97	11.95 ± 0.43	11.15	12.60	0.012
Left SA	14.28 ± 1.62	11.77	16.07	11.95 ± 0.53	11.21	12.56	0.012

\*p < 0.05: Mann-Whitney U test; SD — standard deviation; other abbreviations — see Table 1

**Table 7.** “r” values of Spearman’s rho nonparametric correlations coefficients between the morphometric measurements of the fibula in Van cats by gender

Female	Male			
	Age (A)	Body mass (W)	Right GL2	Left GL2
Age (A)		0.957**	0.781*	0.878**
Body mass (W)	0.390		0.838**	0.922**
Right GL2	-0.195	0.333		0.976**
Left GL2	-0.293	0.310	0.952**	

\*\*p < 0.01; \*p < 0.05; abbreviations — see Table 1

(p > 0.05). Femur volume was found as  $8.57 \pm 1.33 \text{ cm}^3$  in males and as  $7.00 \pm 0.49 \text{ cm}^3$  in females on average, while the surface area was calculated as  $64.28 \pm 6.72 \text{ cm}^2$  for males and as  $59.42 \pm 4.72 \text{ cm}^2$  for females, on average.

Table 3 shows the relationship between the morphometric values for femur based on sex. Accordingly, female cats have positive correlations between the following values (p < 0.05): age and left Bd; right GL with left GL, right GLc, and left GLc; left GL with right GLc and left GLc; right GLc, and left GLc; right greatest breadth of the proximal end (Bp) with left Bd and left SD; right Bd with left Bd, right greatest depth of the caput ossis femoris (Dc), and left Dc; left Bd and right Dc; and finally, right SD and left SD. The male cats, on the other hand, were found to have positive correlations between the following values (p < 0.05): between ‘age and W’ with right GL, left GL, left GLc, left Dc, and right SD values; right GL with left GL, left GLc, left Dc, right SD, and left SD; left GL with left GLc, left Dc, right SD, and left SD; left GLc and right SD; right Bp and left Dc; left Bp and right Dc; right Bd and left Bd; right Dc and left Dc; and finally, right SD and left SD.

The defining statistics for the morphometric values of tibia, and the comparisons in terms of homotypic variations, are provided in Table 4. Accordingly, male cats were found to have higher left GL1, right Bp, right Bd, left Bd, right SD, right V, left V, and light surface area (SA) values compared to females, and this difference was determined to be statistically significant (p < 0.05). No statistical difference in terms of measured left and right average tibia values was found, however (p > 0.05). Tibia volume was found as  $7.56 \pm 1.28 \text{ cm}^3$  on average for males and as for  $6.15 \pm 0.52 \text{ cm}^3$  females, while its SA was determined as  $56.89 \pm 6.47 \text{ cm}^2$  for males and as  $52.72 \pm 3.15 \text{ cm}^2$  for females, on average.

Table 5 presents the relationships between the morphometric values of tibia per sex. Accordingly, a positive correlation with 92.9% ratio was determined between the right GL1 and left GL1 values of the female cats, while a positive correlation with 81% ratio was determined between their right Bd and left Bd values (p < 0.05). Meanwhile, negative correlations for females between right Bd with right GL1 and left GL1 values were determined with 78.6% and 71.4% ratio, respectively (p < 0.05). For male cats, a positive correlation was shown between age and W values with right GL1, left GL1, right Bp, left Bp, right SD, and left SD values; between right GL1 with left GL1, right Bp and left Bp values; between left GL1 and left Bp values; between right Bp with left Bp, right Bd, and left SD values; and between left SD with left Bp and right SD values (p < 0.05).

The defining statistics for the morphological values of fibula per sex and homotypic variations are provided in Table 6. Accordingly, male cats were found to have a higher left side SA value compared to the right side, and the difference was statistically significant (p = 0.012). No other statistical difference was determined between the right and left side tibia average values per sex (p > 0.05). That being said, right V, left V, right SA, and left SA values were found to be higher in males compared to females in a statistically significant manner (p < 0.05). Fibula average volume was determined as  $1.10 \pm 0.17 \text{ cm}^3$  for males and as  $0.83 \pm 0.05 \text{ cm}^3$  for females, while its surface area was determined as  $14.18 \pm 1.61 \text{ cm}^2$  for males and as  $11.95 \pm 0.48 \text{ cm}^2$  for females.

Table 7 presents the relationship between the measured morphometric values for fibula bones. Accordingly, a positive correlation in male cats between age with W, right GL2 and left GL2 values with 95.7%, 78.1%, and 87.8% ratio, respectively, while a positive correlation was found between W with right GL2 and left GL2 values with 83.8% and 92.2% ratios, and between right GL2 and left GL2 values with 97.6% ratio (p < 0.05). Similarly, a positive correlation between right GL2 and left GL2 values was determined for females with 95.2% as well (p < 0.01).

## DISCUSSION

Studies on the morphology of animal bones yield important data for a variety of developmental, evolutionary and forensic sciences. Studies on the morphometric and volumetric analyses and morphology of the long bones, in particular, are of great help in

determining crucial behavioural activities that differ among animal species, such as foraging, hunting, evading hunters, and migration; as well as their phylogeny, allometry and postures. In addition, these measurements hold an important place in determining morphological variations and taxonomic classifications among different species of the same genus; as well as identifying the differences between sexes [5, 23, 38]. For this purpose, many studies have been conducted on humans [21, 22, 42] and animals [2, 5, 9, 10, 14, 16, 29, 33, 36] that involved obtaining osteometric measurements on the long bones of their pelvic limbs. In our study, the morphometric, volumetric and surface area measurements of the femur, tibia, and fibula of adult Van cats were obtained via CT scans and 3D modelling, in order to identify the differences between the two sexes. According to these statistics, the right GL, left GL, right GLc, left Bd, right V, and left V values of the femur, the left GL1, right Bp, right Bd, left Bd, right SD, right V, left V, and right SA values of the tibia, and the right V, left V, right SA, and left SA values of the fibula are higher in male cats than that of female cats in a statistically significant fashion ( $p < 0.05$ ). Most of the other measurements were likewise found to be higher in male cats. We can, therefore, surmise that the femur, tibia and fibula of the male cats are larger than that of the female cats. We think that the larger bones of the pelvic limbs in male Van cats are correlates to the body mass as well as the bones in thoracic limbs according to data obtained from the previous studies by Yılmaz [48].

In the study conducted by Pazar and Kahvecioğlu [36] on 15 male and 15 female New Zealand rabbits, the researchers found no significant difference between the morphometric properties on the long bones of the right and left pelvic limbs ( $p > 0.05$ ). In the present study, although no statistically significant difference was found between the morphometric values of the right and left tibia and fibula of different sexes ( $p > 0.05$ ), it has been observed that in female cats, the femur right SD value is higher than the left SD value, and in male cats, the femur left Bd value is higher than the right Bd value in a statistically significant manner ( $p < 0.05$ ). These results are thought to be important for the evaluation of unilateral studies of the pelvic limb long bones in Van cats.

In their study, Boonsri et al. [5] report that the GL values of the femur, tibia and fibula of cats with the dolichocephalic and mesaticephalic

skulls are  $108.95 \pm 5.14$  and  $95.37 \pm 12.39$  mm,  $110.12 \pm 5.39$  mm and  $96.88 \pm 12.69$  mm, and  $101.75 \pm 6.01$  and  $84.53 \pm 17.50$  mm, respectively. In the same study, the measurements of these bones belonging to male and female domestic cats were reported to be  $103.64 \pm 12.80$  mm and  $101.22 \pm 10.74$  mm,  $105.65 \pm 12.48$  mm and  $102.07 \pm 10.57$  mm, and  $94.79 \pm 17.13$  mm and  $93.21 \pm 12.07$  mm, respectively. In Turkish Van cats, these values in male and female cats were, respectively,  $108.84 \pm 4.93$  mm and  $103.31 \pm 2.93$  mm,  $113.42 \pm 5.16$  mm and  $108.00 \pm 3.02$  mm, and  $105.38 \pm 5.65$  mm and  $100.72 \pm 2.48$  mm. It is thought that in general, the marginal differences among these values that are otherwise in compliance with literature, and the difference can be attributed to factors such as age, length, body weight, breed and measuring techniques. In addition, according to these values, the Van cats are similar to cats with a dolichocephalic skull shape in terms of pelvic limb long bone dimensions.

Studies show that there is a close relation between age and body weight with the evaluation of long bones of the hind legs; or the development of these bones, especially from a young age [2, 7, 20]. It has also been found that there is a generally positive correlation between the morphometric measuring parameters of these bones [5]. Our study shows, regarding the properties of the femur based on sex, that there is a significant positive relationship between the age and body mass (W) with right GL, left GL, left GLc, left Dc, and right SD values of male cats, as well as the age and left Bd values of female cats ( $p < 0.05$ ). On the other hand, while there is a positive correlation between body mass and morphometric parameters, no significant relationship could be found ( $p > 0.05$ ). Regarding the measurements of tibia based on sex, while a positive relationship between the age and body mass with right GL1, left GL1, right Bp, left Bp, right SD, and left SD values in male cats was observed, no statistically significant relationship between age and body mass and these values were noted in female cats ( $p > 0.05$ ). Regarding fibula measurements and sex, although there was a positive relationship between age and body mass (W) with right GL2 and left GL2 in male cats; there was only a positive relationship of 95.2% in right GL2 and left GL2 values in female cats ( $p < 0.01$ ). The correlation between the measurements of femur, tibia, and fibula of male and

female cats are provided in the Tables 3, 5, and 7. In general, we can interpret that there is a positive correlation between age and body mass with the measurement values of the long bones in the pelvic limbs in Van cats.

Thanks to the recent developments in CT and 3D reconstruction software, it has become possible to obtain images of any desired width from an anatomical section without any physical harm to the animal, and the morphometric, volumetric and surface area measurements can now be obtained in a fast and efficient way. In this manner, the efficacy of the diagnosis and treatment of various pathological conditions afflicting the anatomical area of interest can also be evaluated [21, 26, 46]. A literature survey has shown that, while the volumetric and surface area measurements of the long bones of pelvic limbs belonging to humans [21], brown bears [13], chinchillas [33], guinea pigs [11], and gazelles [12] have been obtained using CT and 3D imaging software, no information regarding the long bones of pelvic limbs of cats could be found in literature in that regard. The mean volumetric values of the femur were  $8.57 \pm 1.33 \text{ cm}^3$  in males and  $7.00 \pm 0.49 \text{ cm}^3$  in females; while their mean surface areas were  $64.28 \pm 6.72 \text{ cm}^2$  in males and  $59.42 \pm 4.72 \text{ cm}^2$  in females. The mean volumetric values of the tibia were  $7.56 \pm 1.28 \text{ cm}^3$  in males and  $6.15 \pm 0.52 \text{ cm}^3$  in females; while their mean surface areas were  $56.89 \pm 6.47 \text{ cm}^2$  in males and  $52.72 \pm 3.15 \text{ cm}^2$  in females. The mean volumetric values of the fibula were  $1.10 \pm 0.17 \text{ cm}^3$  in males and  $0.83 \pm 0.05 \text{ cm}^3$  in females; while their mean surface areas were  $14.18 \pm 1.61 \text{ cm}^2$  in males and  $11.95 \pm 0.48 \text{ cm}^2$  in females. The average volume and surface area measurement values in pelvic limb long bones are higher in male Van cats. It is thought that this difference detected between the measurement values of these bones may be related to body mass.

## CONCLUSIONS



In conclusion, the sex-based differences of the measured parameters of the femur, tibia and fibula belonging to adult Van cats were detected. We believe that the information gathered in this study can be utilised in determining morphological variations and the taxonomy of different lineages of Van cats. Moreover, this study has hopefully uncovered information that will be beneficial to the clinical studies of veterinarians that seek to treat Van cats' pathological conditions of the osteological structure, and for zooarchaeologists.

## REFERENCES

1. Ajayi IE, Shawulu JC, Zachariya TS, et al. Osteomorphometry of the bones of the thigh, crus and foot in the New Zealand white rabbit (*Oryctolagus cuniculus*). *Ital J Anat Embryol.* 2012; 117(3): 125–134, indexed in Pubmed: [23420943](#).
2. Alpak H, Onar V, Mutuş R. The relationship between morphometric and long bone measurements of the Morkaraman sheep. *Turk J Vet Anim Sci.* 2009; 33(3): 199–207, doi: [10.3906/vet-0709-23](#).
3. Atalar Ö, Özdemir D. Macro-anatomical investigations on the skeletons of marten (*Martes foina*). II. Ossa Membri Pelvini. *Firat Univ J Health Sci.* 2002; 16: 233–236.
4. Bahadır A, Yıldız H. *Veteriner Anatomi: Hareket Sistemi & İç Organlar*. Ezgi Kitabevi Bursa, Turkey 2014.
5. Boonsri B, Pitakarnnop T, Buddhachat K, et al. Can feline (*Felis catus*) flat and long bone morphometry predict sex or skull shape? *Anat Sci Int.* 2019; 94(3): 245–256, doi: [10.1007/s12565-019-00480-8](#), indexed in Pubmed: [30771106](#).
6. Cak B. Turkish Van Cat and Turkish Angora Cat: A Review. *J Agric Sci Technol A.* 2017; 7(3): 151–159, doi: [10.17265/2161-6256/2017.03.002](#).
7. Campbell KE, Marcus L. The relationships of hindlimb bone dimensions to body weight in birds. *Nat Hist Mus Los Angeles Co Sci Ser.* 1992; 36: 395–412.
8. Carew RM, Morgan RM, Rando C. A preliminary investigation into the accuracy of 3D modeling and 3D printing in forensic anthropology evidence reconstruction. *J Forensic Sci.* 2019; 64(2): 342–352, doi: [10.1111/1556-4029.13917](#), indexed in Pubmed: [30296344](#).
9. Casteleyn C, Bakker J, Breugelmanns S, et al. Anatomical description and morphometry of the skeleton of the common marmoset (*Callithrix jacchus*). *Lab Anim.* 2012; 46(2): 152–163, doi: [10.1258/la.2012.011167](#), indexed in Pubmed: [22517992](#).
10. Çevik-Demirkan A, Özdemir V, Türkmenoğlu İ, et al. Anatomy of the hind limb skeleton of the chinchilla (*Chinchilla lanigera*). *Acta Veterinaria Brno.* 2007; 76(4): 501–507, doi: [10.2754/avb200776040501](#).
11. Dayan MO, Beşoluk K, Eken E, et al. Three-dimensional modelling of the femur and humerus in adult male guinea pigs (guinea pig) with computed tomography and some biometric measurement values. *Folia Morphol.* 2019; 78(3): 588–594, doi: [10.5603/FM.a2019.0002](#), indexed in Pubmed: [30644082](#).
12. Demircioğlu I, Gezer Ince N. Three-dimensional modelling of computed tomography images of limb bones in gazelles (*Gazella subgutturosa*). *Anat Histol Embryol.* 2020; 49(6): 695–707, doi: [10.1111/ahe.12564](#), indexed in Pubmed: [32319123](#).
13. Demircioğlu İ, Kirbaş Doğan G, Aksünger Karaavci F, et al. Three-dimensional modelling and morphometric investigation of computed tomography images of brown bear's (*Ursus arctos*) ossa cruris (*Zeugopodium*). *Folia Morphol.* 2020; 79(4): 811–816, doi: [10.5603/FM.a2019.0125](#), indexed in Pubmed: [31777947](#).
14. Dursun N. *Veterinary anatomy I*. Medisan Publisher, Ankara, Turkey 2008.
15. Dyce KM, Sack WO, Wensing CJG. *Textbook of veterinary anatomy*, 4th ed. Saunders Elsevier Inc., Missouri, United States 2010: 490–500.
16. El-Ghazali HM, El-Behery EI. Comparative morphological interpretations on the bones of the pelvic limb of New Zea-

- land rabbit (*Oryctolagus cuniculus*) and domestic cat (*Felis domestica*). *J Adv Vet Anim Res.* 2018; 5(4): 410–419, doi: [10.5455/javar.2018.e292](https://doi.org/10.5455/javar.2018.e292), indexed in Pubmed: [31453151](https://pubmed.ncbi.nlm.nih.gov/31453151/).
17. Imai N, Funayama K, Suzuki H, et al. Stature estimation formulae based on bony pelvic dimensions and femoral length. *Homo.* 2020; 71(2): 111–119, doi: [10.1127/homo/2020/1116](https://doi.org/10.1127/homo/2020/1116), indexed in Pubmed: [31944200](https://pubmed.ncbi.nlm.nih.gov/31944200/).
  18. Kalra MK, Maher MM, Toth TL, et al. Strategies for CT radiation dose optimization. *Radiology.* 2004; 230(3): 619–628, doi: [10.1148/radiol.2303021726](https://doi.org/10.1148/radiol.2303021726), indexed in Pubmed: [14739312](https://pubmed.ncbi.nlm.nih.gov/14739312/).
  19. Karan M. Macro-anatomical study of ossa membri pelvini in the feral pigs (*Sus scrofa*). *Firat Univ Vet J Hlth Sci.* 2012; 26: 31–34.
  20. Kumaş M, Ayaz D. Age determination and long bone histology in *Stellagama stellio* (Linnaeus, 1758) (Squamata: Sauria: Agamidae) populations in Turkey. *Vertebr Zool.* 2014; 64(1): 113–126.
  21. Lee UY, Kim IB, Kwak DS. Sex determination using discriminant analysis of upper and lower extremity bones: New approach using the volume and surface area of digital model. *Forensic Sci Int.* 2015; 253: 135.e1–135.e4, doi: [10.1016/j.forsciint.2015.05.017](https://doi.org/10.1016/j.forsciint.2015.05.017), indexed in Pubmed: [26117502](https://pubmed.ncbi.nlm.nih.gov/26117502/).
  22. Mahakkanukrauh P, Khanpetch P, Prasitwattanseree S, et al. Stature estimation from long bone lengths in a Thai population. *Forensic Sci Int.* 2011; 210(1-3): 279.e1–279.e7, doi: [10.1016/j.forsciint.2011.04.025](https://doi.org/10.1016/j.forsciint.2011.04.025), indexed in Pubmed: [21616616](https://pubmed.ncbi.nlm.nih.gov/21616616/).
  23. Martín-Serra A, Figueirido B, Palmqvist P. A three-dimensional analysis of the morphological evolution and locomotor behaviour of the carnivoran hind limb. *BMC Evol Biol.* 2014; 14: 129, doi: [10.1186/1471-2148-14-129](https://doi.org/10.1186/1471-2148-14-129), indexed in Pubmed: [24927753](https://pubmed.ncbi.nlm.nih.gov/24927753/).
  24. Monchot H, Gendron D. Disentangling long bones of foxes (*Vulpes vulpes* and *Alopex lagopus*) from arctic archaeological sites. *J Archaeol Sci.* 2010; 37(4): 799–806, doi: [10.1016/j.jas.2009.11.009](https://doi.org/10.1016/j.jas.2009.11.009).
  25. Nomina Anatomica Veterinaria. International committee on veterinary gross anatomical nomenclature (ICVGAN), Published by the Editorial Committee, Hannover, 2017.
  26. Ohlerth S, Scharf G. Computed tomography in small animals--basic principles and state of the art applications. *Vet J.* 2007; 173(2): 254–271, doi: [10.1016/j.tvjl.2005.12.014](https://doi.org/10.1016/j.tvjl.2005.12.014), indexed in Pubmed: [16516508](https://pubmed.ncbi.nlm.nih.gov/16516508/).
  27. Olude MA, Olopade JO, Mustapha OA. Macro-anatomical investigations of the skeletons of the African giant rat (*Cricetomys gambianus* Waterhouse): Pelvic limb. *Eur J Anat.* 2009; 13(3): 127–131.
  28. Onar V, Belli O. Estimation of shoulder height from long bone measurements on dogs unearthed from the Van-Yoncatepe early Iron Age necropolis in Eastern Anatolia. *Rev Med Vet (Toulouse).* 2005; 156(1): 53–60, doi: [10.1007/s12565-019-00480-8](https://doi.org/10.1007/s12565-019-00480-8).
  29. Onwuama KT, Ojo SA, Hambolu JO, et al. Macro-anatomical and morphometric studies of the hindlimb of grasscutter (*Thryonomys swinderianus*, Temminck-1827). *Anat Histol Embryol.* 2018; 47(1): 21–27, doi: [10.1111/ahe.12319](https://doi.org/10.1111/ahe.12319), indexed in Pubmed: [29139158](https://pubmed.ncbi.nlm.nih.gov/29139158/).
  30. Ozgel O, Aykut M. Macroanatomical investigation on the ossa membri pelvini of Anatolian bobcat, *Lynx lynx*. *Pakistan J Zool.* 2015; 47(5): 1492–1494.
  31. Özdemir D, Atalar Ö. Macro-anatomical investigations on the skeletons of squirrel (*Sciurus vulgaris*). II. Ossa Membri Pelvini. *Firat Univ J Health Sci.* 2003; 17: 151–154.
  32. Özdemir D, Karan M. Macroanatomical investigations on the skeletons of badger (*Meles meles*). II. Ossa membri pelvini. *Firat Univ J Health Sci.* 2001; 15: 397–400.
  33. Özkadif S, Varlik A, Kalaycı İ, et al. Morphometric evaluation of chinchillas (*Chinchilla lanigera*) femur with different modelling techniques. *Kafkas Univ Vet Fak Derg.* 2016; 22(6): 945–951, doi: [10.9775/kvfd.2016.15683](https://doi.org/10.9775/kvfd.2016.15683).
  34. Özkan ZE. Macro-anatomical investigations on the hind limb skeleton of mole-rat (*Spalax leucodon* Nordmann). *Vet Arhiv.* 2002a; 72: 159–166.
  35. Özkan ZE. Macro-anatomical investigations on the skeletons of hedgehog (*Erinaceus europaeus* L.) II Ossa membri pelvini. *Vet Arhiv.* 2002b; 72: 213–220.
  36. Pazvant G, Kahvecioğlu KO. Studies on homotypic variation of forelimb and hindlimb long bones of rabbits. *J Fac Vet Med Istanbul Univ.* 2009; 35: 23–39.
  37. Pazvant G, Kahvecioğlu KO. Studies on homotypic variations of forelimb and hindlimb long bones of guinea pigs. *J Fac Vet Med Istanbul Univ.* 2013; 39: 20–32.
  38. Polly PD. Limbs in Mammalian Evolution. In: *Fins into Limbs. Evolution, development and transformation*, Chapter 15, Hall BK (ed.). University of Chicago Press, Chicago 2007: 245–268.
  39. Prokop M. General principles of MDCT. *Eur J Radiol.* 2003; 45(Suppl 1): S4–10, doi: [10.1016/s0720-048x\(02\)00358-3](https://doi.org/10.1016/s0720-048x(02)00358-3), indexed in Pubmed: [12598021](https://pubmed.ncbi.nlm.nih.gov/12598021/).
  40. Saber A, K. B. Some morphological and radiological studies on the pelvic limb skeleton of Lumholtz Tree-Kangaroo (*Dendrolagus lumholtzii*). *Journal of Veterinary Anatomy.* 2019; 12(1): 19–34, doi: [10.21608/jva.2019.67223](https://doi.org/10.21608/jva.2019.67223).
  41. Salinas P, Arenas-Caro A, Núñez-Cook S, et al. Morphometric, anatomic and radiographic study of bone of the pelvic limb of endangered patagonian huemul deer (*Hippocamelus bisulcus*). *Int J Morphol.* 2020; 38(3): 747–754, doi: [10.4067/s0717-95022020000300747](https://doi.org/10.4067/s0717-95022020000300747).
  42. Saulsman B, Oxnard CE, Franklin D. Long bone morphometrics for human from non-human discrimination. *Forensic Sci Int.* 2010; 202(1-3): 110.e1–110.e5, doi: [10.1016/j.forsciint.2010.05.009](https://doi.org/10.1016/j.forsciint.2010.05.009), indexed in Pubmed: [20837249](https://pubmed.ncbi.nlm.nih.gov/20837249/).
  43. Shahar R, Milgram J. Morphometric and anatomic study of the hind limb of a dog. *Am J Vet Res.* 2001; 62(6): 928–933, doi: [10.2460/ajvr.2001.62.928](https://doi.org/10.2460/ajvr.2001.62.928), indexed in Pubmed: [11400852](https://pubmed.ncbi.nlm.nih.gov/11400852/).
  44. Von Den Driesch A. A guide to the measurement of animal bones from archaeological sites. Peabody Museum Bulletin 1. Harvard University, Cambridge, MA 1976.
  45. Wisner ER, Zwingenberger AL. Atlas of small animal CT and MRI. Willey-Blackwell Publishing, USA 2015: 40–68.
  46. Yilmaz O, Soyguder Z, Yavuz A, et al. Three-dimensional computed tomographic examination of pelvic cavity in Van Cats and its morphometric investigation. *Anat Histol Embryol.* 2020; 49(1): 60–66, doi: [10.1111/ahe.12484](https://doi.org/10.1111/ahe.12484), indexed in Pubmed: [31486129](https://pubmed.ncbi.nlm.nih.gov/31486129/).
  47. Yilmaz O, Soyguder Z, Yavuz A. Three-dimensional investigation by computed tomography of the clavicle and scapula in van cats. *Van Vet J.* 2020; 31(1): 34–41, doi: [10.36483/vanvetj.644080](https://doi.org/10.36483/vanvetj.644080).
  48. Yilmaz O. Three-dimensional investigation by computed tomography of the forelimb skeleton in van cats. Van Yuzuncu Yil University, Institute of Health Sciences, Faculty of Veterinary, Department of Anatomy, Van, Turkey 2018.
  49. Yilmaz S, Dinç G, Aydın A. Macro-Anatomical Investigations on the Skeletons of Porcupine (*Hystrix Cristata*) II. Ossa Membri Pelvini. *Turk J Vet Anim Sci.* 1999; 23(3): 297–300.

# Morphometric profile of tendocalcaneus of South Africans of European ancestry using a cadaveric approach

S. Latiff<sup>1</sup> , M.A. Bidmos<sup>2</sup> , O.I. Olateju<sup>1</sup> 

<sup>1</sup>School of Anatomical Sciences, Faculty of Health Sciences, University of the Witwatersrand, Johannesburg, South Africa  
<sup>2</sup>College of Medicine, QU Health, Qatar University, Doha, Qatar

[Received: 29 January 2020; Accepted: 13 February 2020]

**Background:** Tendocalcaneus is a strong tendon that is vital for bipedalism in humans. Despite its tremendous strength, the tendocalcaneus is prone to damage and degeneration causing mobility problems and pain. Morphometric dimension of the tendocalcaneus is of benefit to the surgical repair and reconstruction of the damaged tendon. Cadaveric approach provides a realistic method for determining tendocalcaneus morphometry and as at present only two cadaveric studies on Indian population is available. Thus this study presents data on tendocalcaneus morphometry in South Africans of European ancestry using a cadaveric approach. **Materials and methods:** A total of 66 lower limbs (32 left and 34 right legs) sourced from 49 male and female cadavers were used. After careful dissection of the posterior aspect of leg, the medial and lateral length, distal width, distal circumference and proximal width of the tendocalcaneus were measured. **Results:** The data showed a high degree of reproducibility indicating that the measurements obtained using cadaveric approach were precise and accurate. There was no difference in measurements between the sides. Measurements in the males were generally higher than in the females. Strong associations were observed between the paired measurements of the medial and lateral tendon length and between the distal width and distal circumference. **Conclusions:** The data obtained will be useful in predicting tendocalcaneus size during the surgical reconstruction of the tendocalcaneus. (Folia Morphol 2021; 80, 1: 196–203)

**Key words:** cadavers, European ancestry, Achilles morphometry, tendon, South African

## INTRODUCTION

Tendocalcaneus (TC) is a strong, whitish and poorly vascularized tendon in the posterior compartment of the leg where it serves as the insertion, via a conjoint tendon, for the gastrocnemius and soleus and sometimes the plantaris [9, 10, 33]. The conjoint tendon inserts to the supero-posterior aspect of the calcaneal tuberosity [31]. With this arrangement, the calf muscles are able to plantarflex the foot at the ankle joint thus make the

TC vital for bipedalism in humans [31]. In addition, the TC transmits force from the muscle to the foot bones during walking and as such it endures a significant strain and stress which may explain the reason for its high mechanical strength and flexibility [40, 43, 44]. Mechanical strength is also reinforced by the tightly packed bundles of collagen fibres in the tendon [13, 25].

The TC is one of the most commonly injured tendons in humans [14, 22, 29, 32, 45]. The most com-



mon site of rupture is 2–6 cm from its insertion point due to the small cross sectional area (CSA) at this region, its large eccentric loads and reduced vascularity [9, 38]. TC rupture is due to a sudden or aggressive dorsiflexion of a plantar-flexed foot which then causes the sudden displacement of the weight-bearing foot with the knee in extension [14]. Most TC injuries are related to sport [14, 15, 21] or could be as a result of overuse or age-related stiffness that reduces the ability of an individual to withstand stress [39, 48]. Similarly, spontaneous TC rupture has been reported in dialysis and renal transplant patients [42]. Although the exact cause remains controversial however calcium phosphate build-up and the use of steroid treatment in renal failure often cause weakening of tendons [5, 28, 42]. Interestingly, there is reduced injury incidence in older individuals unless the tendon is subjected to sudden rapid contractions which can then cause the tendon to tear [14, 27, 43]. Age-related reduction in collagen content also makes the tendon more prone to repetitive tears due to a decrease in the mechanical strength of the tendon [35]. Whereas in athletes or physically active individuals, the constant use of the tendon predisposes them to higher risk of injury than in less active individuals [37, 39] because the mechanical properties are dependent on the extent of mechanical strain put on each of the limbs i.e. a case of loading versus strength of the tendon [2].

The propensity of TC to damage and the subsequent surgical repair or management makes it crucial to understand its morphometry in different population groups. Only two studies are available on the morphometry of TC using a cadaveric approach and both studies utilized cadavers of Indian population [19, 41]. Data that closely match the TC dimensions in the living in different population groups will be of benefit to surgical repair and management of tendinopathy. The present study assessed the TC morphometry of South Africans of European ancestry using a cadaveric approach. Cadavers were utilised as they provide a realistic measurement and a better morphological description in a three-dimensional [19, 34] compared to a highly-subjective two-dimensional ultrasound scans [47]. According to Thoirs and Childs [47], image acquisition using ultrasound is identified as the major contributor to measurement errors of the TC. These errors are due to variations in equipment, positioning of the subject and stabilisation of the lower limb, non-standardized transducer pressure, transducer orientation and equipment settings [46, 47].

**Table 1.** Demographics of cadavers and distribution of lower limbs

Sex	Age		Side		
	Mean	SD	Left	Right	Total
Female	76.9	11.2	17	18	35
Male	74.6	11.3	15	16	31
			32	34	66

SD — standard deviation

## MATERIALS AND METHODS

### Sample population

A total of 34 right (18 female and 16 male) and 32 left (17 female and 15 male) lower limbs from cadavers of South Africans of European ancestry (Table 1) were used which were housed in the School of Anatomical Sciences at the University of the Witwatersrand, Johannesburg, South Africa for teaching purposes. Approval was granted (Ethics Number: W-CJ-140604-1) by the Human Research Ethics Committee (Medical) of the same university. Therefore the study was conducted in accordance with the ethical standards. From the cadavers available for this study, 17 left and 17 right limbs (i.e. both limbs) were sourced from the same cadavers and the rest were from 32 cadavers. The mean age of the female cadavers was 76.9 years (range: 53–94 years) and that of the male cadavers was 74.6 years (range: 52–93 years) (Table 1). Cadavers with any physical scars or deformity on the lower limb were excluded from the study.

### Anatomical dissection

With the body in the prone position and the lower limb in full extension, a longitudinal incision was made on the posterior surface of each lower limb extending from the popliteal fossa to the inferior aspect of the calcaneus bone. The skin was carefully reflected to reveal the underlying structures. The subcutaneous fascia and fat were also removed. The crural fascia was then cut open to expose the muscles in the posterior compartment of the leg. At the popliteal fossa, a 2.5 cm transverse incision was made in the medial and the lateral direction (perpendicular to the longitudinal incision) to allow for adequate space to examine the deep structures without compromising the use of the cadavers for teaching purposes. Similarly, at the heel, about 5 cm long incisions were made on the medial and lateral sides of the foot (also perpendicular to the longitudinal incision).

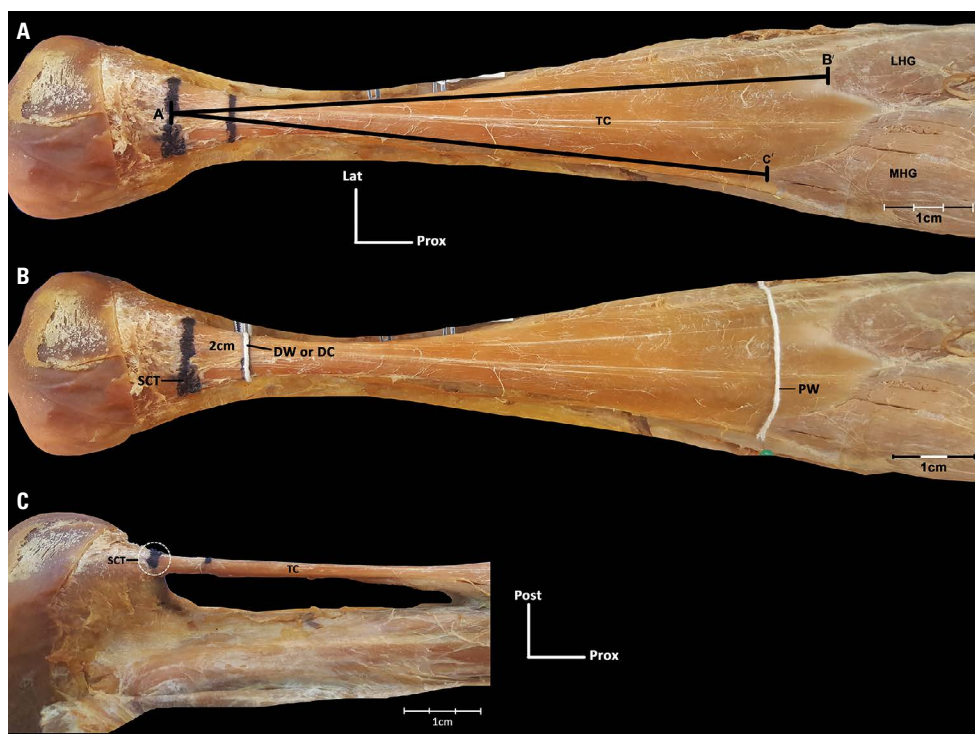


**Figure 1.** Photographs showing the tendocalcaneus (TC) on the posterior compartment of the left leg and the description of the measured parameters; **A.** The dissection revealing the level of the superior aspect of calcaneal tuberosity (SCT) and measurement of the medial length of tendon ( $LOT_M$ ; point A' to B') and lateral length of tendon ( $LOT_L$ ; point A' to C'); **B.** The levels at which measurement for the distal width (DW) and distal circumference (DC; 2 cm from the level of SCT) and then the proximal width (PW; lowest level of musculotendinous junction of the gastrocnemius) were performed; **C.** The lateral view of the SCT and a portion of the length of TC; LHG — lateral head of gastrocnemius; MHG — medial head of gastrocnemius; Lat — lateral; Prox — proximal; Post — posterior.

### Measurements

With the knee in full extension and the foot in a dorsiflexed position (approximately  $90^\circ$ ), modified measurements (Fig. 1) previously described by Kumar et al. [19] were taken on each limb. Soft tissue within the area of the calcaneus and deep to the TC was cleared until the superior aspect of the calcaneus was visible (Fig. 1C). Similar to Liem et al. [23], Ebeling et al. [11] and Kumar et al. [19], the superior aspect of the calcaneal tuberosity was used as the reference point from which all measurements were taken in order to reduce variability in the measurements. Also for repeatability, the distal width and circumference (Fig. 1B) were measured 2 cm from the reference point [11, 23] while the proximal width was determined at the lowest level of the musculotendinous junction of the gastrocnemius [3, 35, 36]. Due to ease of access, visibility and without cutting the TC that may compromise measuring its actual length, the medial and lateral lengths of the tendon (Fig. 1A) were considered to be the actual length of the TC which is a slight modification to the measurements by Kumar et al. [19]. This modification was used because there

is a significant variation to the extent or level at which the gastrocnemius and the soleus muscles contribute to the formation of the TC due to the non-constant orientation of the tendon fibrils [7, 9, 10].

The measurements used in the present study are summarized below:

- medial length of the tendon ( $LOT_M$ ) — distance from the superior aspect of the calcaneal tuberosity to the lowest point of the musculotendinous junction of the medial head of the gastrocnemius muscle (Metre rule);
- lateral length of the tendon ( $LOT_L$ ) — distance from the superior aspect of the calcaneal tuberosity to the lowest point of the musculotendinous junction of the lateral head of the gastrocnemius muscle (Metre rule);
- distal width (DW) — measurement taken at a level 2 cm above the superior aspect of the calcaneal tuberosity (Vernier calliper);
- proximal (PW) width — measurement taken at the lowest point on the musculotendinous junction of the gastrocnemius muscle (Thread and metre rule);

— distal circumference (DC) — measurement taken at a level 2 cm above the superior aspect of the calcaneal tuberosity (around the distal width) (Thread and metre rule). The superior aspect of the calcaneal tuberosity was used as a reference point for the DW and DC (Fig. 1B).

### Statistical analyses

An inter-observer reliability test (Lin's concordance test) was used to determine the level of precision and accuracy between the measurements [20, 24]. This test was performed to determine the degree of agreement between test and retest measurements. After establishing that the measuring technique is adequate, data were collected separately for male and female groups. Descriptive statistics including means and standard deviation was obtained for each measurement. A Student's t-test was used to determine side and sex differences for each measurement. In addition, a Pearson's correlation coefficient was used to assess the strength of the association between the different dimensions of the TC. All statistical analyses were performed using SPSS software (version 22.0; IBM, US). Statistical difference of 5% was regarded significant for all the statistical analyses.

## RESULTS

### Test of reliability of measurements

The Lin's concordance correlation coefficient ( $P_c$ ) for all measurements is shown in Table 2. The  $P_c$  ranged between 0.971 for DW and 0.995 for  $LOT_L$ , which indicates a high degree of reproducibility. The measurement technique is therefore precise and accurate based on the result of the  $P_c$ . The measurement error from subsequent data collected and analysed for the current study is considered minimal and acceptable.

### Assessment of side difference

A comparison of mean measurements from both sides were made separately for male and female samples from cadavers whose both lower limbs were dissected. Table 3 shows that there is no statistically significant differences between the two sides indicating a lack of side dominance.

### Descriptive statistics

The mean and standard deviation for each measurement of the left and right TC are presented in Table 4. The  $LOT_M$ ,  $LOT_L$ , DC and DW (right leg) of the

**Table 2.** Lin's concordance correlation of reproducibility

Measurements	$P_c$
$LOT_M$	0.993
$LOT_L$	0.995
DW	0.971
DC	0.990
PW	0.990

$LOT_M$  — medial length of tendon;  $LOT_L$  — lateral length of tendon; DW — distal width; DC — distal circumference; PW — proximal width

TC displayed sexual dimorphism but not the PW and the DW (left leg).

### Correlation analyses

The associations for the different TC dimensions were separated to give clear details about the relationship between any paired measurements with respect to sex and side. Using the Pearson's correlation coefficients [1], strong associations were observed between the paired measurements of  $LOT_L$  and  $LOT_M$  ( $R \geq 0.8$ ) for both sexes and sides. Association between DC and DW ( $R \geq 0.7$ ) was similarly strong except for the male left leg. In addition, association between DW and PW showed a negative strong association ( $R = -0.7$ ) in the male left leg. Other paired measurements displayed moderate associations ( $R = 0.4-0.6$ ). The association between measurements of the right and left TC for both sexes showing only the strong and moderate associations is presented in Table 5.

## DISCUSSION

Ultrasound is the most preferred method for diagnosing TC rupture and which is also commonly utilised in determining the TC morphometry [3, 8, 11, 17, 35, 36]. There is usually a high variability in the TC dimension when measurement is obtained from images acquired using ultrasound. This variability is due to the non-uniformities of equipment, different resolutions of equipment and image acquisition parameters [46, 47]. For example, Pang and Ying [35] observed that the measurement outcome for CSA did not correspond with the TC thickness in their study on TC morphometry using an ultrasound. They concluded that this was so because the measured CSA was more accurate than the TC thickness. Thus the approach used (i.e. ultrasound) was implicated as the source of errors or variability [35]. This therefore means that there is a need to present data on TC morphometry that is more precise and accurate. The results of the present study showed a high degree

**Table 3.** Comparison between mean measurements of left and right tendocalcaneus

	Female							Male						
	Left			Right				Left			Right			
	N	Mean	SD	Mean	SD	t	p	N	Mean	SD	Mean	SD	t	p
LOT <sub>M</sub>	10	173.0	22.4	162.4	15.9	1.22	0.24	7	193.4	22.9	191.4	26.0	0.15	0.88
LOT <sub>L</sub>	10	194.4	23.1	186.3	10.3	1.01	0.33	7	228.5	28.8	220.1	21.2	0.62	0.55
DW	10	12.9	3.8	13.2	3.6	0.18	0.86	7	14.9	2.2	15.6	1.7	0.67	0.52
DC	10	40.3	8.0	40.4	8.1	0.03	0.98	7	45.3	4.2	43.7	4.3	0.71	0.49
PW	10	73.2	9.5	71.3	6.3	0.53	0.61	7	66.1	5.9	73.6	11.6	1.52	0.15

LOT<sub>M</sub> — medial length of tendon; LOT<sub>L</sub> — lateral length of tendon; DW — distal width; DC — distal circumference; PW — proximal width; SD — standard deviation

**Table 4.** Descriptive statistics of measurements of the tendocalcaneus

	Female			Male			t	p
	N	Mean	SD	N	Mean	SD		
<b>Left</b>								
LOT <sub>M</sub>	17	178.4	25.3	15	202.5	20.7	3.04	0.005
LOT <sub>L</sub>	17	197.0	19.4	15	227.5	24.3	4.04	0.000
DW	17	13.9	3.3	15	15.8	2.1	1.98	0.057*
DC	17	41.2	6.7	15	46.1	4.5	2.42	0.022
PW	17	72.8	9.4	15	71.6	13.7	0.61	0.766*
<b>Right</b>								
LOT <sub>M</sub>	18	173.4	21.4	16	195.1	22.5	2.88	0.007
LOT <sub>L</sub>	18	194.7	16.4	16	219.4	18.3	4.17	0.000
DW	18	13.1	2.8	16	15.3	1.9	2.63	0.013
DC	18	38.4	6.5	16	43.2	3.7	2.62	0.013
PW	18	71.2	7.5	16	75.4	13.6	1.12	0.273*

\*No significant difference at  $p \leq 0.05$ ; LOT<sub>M</sub> — medial length of tendon; LOT<sub>L</sub> — lateral length of tendon; DW — distal width; DC — distal circumference; PW — proximal width; SD — standard deviation

**Table 5.** Correlation coefficient between measurements of the left and right tendocalcaneus

	Female					Male				
	LOT <sub>M</sub>	LOT <sub>L</sub>	DW	DC	PW	LOT <sub>M</sub>	LOT <sub>L</sub>	DW	DC	PW
<b>Left</b>										
LOT <sub>M</sub>										
LOT <sub>L</sub>	0.9					0.8				
DW	0.4									
DC			0.9					0.6		
PW			0.5	0.4			0.4	-0.7		
<b>Right</b>										
LOT <sub>M</sub>										
LOT <sub>L</sub>	0.8					0.8				
DW	0.5	0.5				0.4				
DC	0.6	0.6	0.9					0.7		
PW								0.6	0.4	

LOT<sub>M</sub> — medial length of tendon; LOT<sub>L</sub> — lateral length of tendon; DW — distal width; DC — distal circumference; PW — proximal width

of reproducibility indicating that the measurements obtained were precise and accurate. Cadaveric approach seems to be a more idealistic approach as it provides a three-dimensional view of the structure from which measurements of different parameters and direct observations can be conducted. Only few data on the TC morphometry using cadaveric approach is available (e.g. Kumar et al. [19]); however, its benefits have been utilised in similar studies such as patella-patellar ligament morphometry [34].

The result of the present study is consistent with that obtained for other studies in that the TC dimensions were not significantly different between the sides [8]. The base-line morphometric profile of the TC is very useful as it has been shown that the tendon properties of both TC are asymmetrical [2]. Thus a morphometric distinction between a pathological and a non-pathological tendon is of paramount importance in the surgical repair of the TC and post-surgery mobility recovery. In addition, the differences in the TC morphometry between sides may not be entirely pathological but may be as a result of sidedness [2]. Leg dominance with respect to TC is particularly interesting in that some studies [2, 12, 35] reported the left leg as the dominant leg despite the fact that a significant number of people are right-sided [26, 35]. In the study by Pang and Ying [35], the participants were asked to elect a limb to kick a ball. A significant number elected the right limb but their elected limb was considered non-dominant. This makes sense in that the left ankle in right-sided individuals endures significant tension while acting as push off during certain activities e.g. ball kicking. This also accounts for the high prevalence of left TC injuries owing to the fact that many individuals are right-sided [26, 35].

Several factors, e.g. subjects' physical activities, sex and age, have been suggested to be contributing factors to the differences in the TC morphometry [2, 34, 35]. Differences in foot types also have a direct relationship with the TC morphometry [30] as a thin TC is often associated with a flat-arched foot type due to the reduced effectiveness of the transfer of force from the heel to the forefoot during the propulsion phase of walking [18, 49]. Likewise, a thin TC is also more prone to rupture and it is more vulnerable to developing tendinopathy than a thicker TC [16]. It is thus logical to observe morphometric variations in measurements taken within any population group (e.g. athlete vs. non-athlete) and the variation could be more significant between different population

groups. Despite the differences in approaches used (e.g. ultrasound or cadaveric) for TC morphometry, the mean values for the distal width in the present study is within close range with other ultrasound studies [4, 8, 17, 36]. However it differs from Kumar et al. [19] and Singhal et al. [41] that measured the tendon near their insertions unlike the present the study that took measurements at the region where the TC is most prone to injury. The mean values also fall within the range that were reported for white, non-white or black population groups [8, 36]. This consistency could be attributed to the superficial position of this section of the TC (i.e. distal part) that makes it easy to measure when using any of the two approaches.

Tendon degeneration is common in old age due to a reduction in the collagen fibrils but results in an increase in tendon fibrils [35]. These two factors contribute to the differences in TC morphometric. The reduction in collagen in-turn lowers the mechanical strength of tendon making aged individuals to be more prone to repetitive tears [6, 16]. As tendon constantly remodels in order to repair the repetitive tears, the healing tendon hypertrophies which could thus introduce more variability in the TC dimension across any population group. Most cadavers in our facility are aged and it is thus a limitation for the present cadaveric study.

In the present study, strong associations were found between the medial and lateral lengths of the TC and between the distal width and distal circumference of the TC of both legs while moderate to weak associations were reported for other paired measurements in the legs for both sexes. Kumar et al. [19] similarly reported weak to moderate associations in the TC dimensions in the male cadavers. In the latter study, weak associations were reported for paired measurements between the tendon length and the tendon circumferences (proximal and distal) similar to the findings of the present study for the male cadavers. There was also a weak association between the tendon length and the rest of the measurements [19]. Moderate associations were reported between proximal and distal widths as well as between distal width and distal circumference [19] which are similar to the results of the present study. The significant similarities between the present findings and the report by Kumar et al. [19] further indicates the adequacy of a cadaveric method for determining the TC morphometry. Based on the strong associations, it seems that the TC length, distal width and distal circumference could be dependable factors for predicting the normal

size of the TC. This will be of help to surgeons during the surgical repairs of the TC.

## CONCLUSIONS

The presented morphometric profiles of the TC using a cadaveric approach are considered highly accurate suggesting that the measurements obtained may closely match that in the living of similar age. Although cadaveric approach is faced with numerous limitations (e.g. age range owing to cadaveric collection, sample size, population group etc.), it still offers a realistic approach for morphometric measurements. A more comprehensive morphometric data of the TC that takes into account the body weight, stature, physical activities and pathologies etc. still need to be conducted as this will be helpful during the surgical repair of the tendon. Future studies should also incorporate the measurement of CSA of the TC across different population groups using histological approach. This may shed more light into the associations between the tendon length, the TC distal width and distal circumference where most TC injuries often occur.

## Acknowledgements

This study would not be possible without the aid of those who donated their bodies toward the advancement of medical science. We are grateful to the School of Anatomical Sciences of the University of the Witwatersrand for giving us access to the Human Collections. The National Research Foundation of South Africa provided Student Financial aid to S. Latiff (first author).

## REFERENCES

- Akoglu H. User's guide to correlation coefficients. *Turk J Emerg Med.* 2018; 18(3): 91–93, doi: [10.1016/j.tjem.2018.08.001](https://doi.org/10.1016/j.tjem.2018.08.001), indexed in Pubmed: [30191186](https://pubmed.ncbi.nlm.nih.gov/30191186/).
- Bohm S, Mersmann F, Marzilger R, et al. Asymmetry of Achilles tendon mechanical and morphological properties between both legs. *Scand J Med Sci Sports.* 2015; 25(1): e124–e132, doi: [10.1111/sms.12242](https://doi.org/10.1111/sms.12242), indexed in Pubmed: [24798645](https://pubmed.ncbi.nlm.nih.gov/24798645/).
- Brouwer EF, Myhrvold SB, Benth JS, et al. Ultrasound measurements of Achilles tendon length using skin markings are more reliable than extended-field-of-view imaging. *Knee Surg Sports Traumatol Arthrosc.* 2018; 26(7): 2088–2094, doi: [10.1007/s00167-017-4815-0](https://doi.org/10.1007/s00167-017-4815-0), indexed in Pubmed: [29185003](https://pubmed.ncbi.nlm.nih.gov/29185003/).
- Canbolat M, Özbağ D, Özdemir Z, et al. Effects of physical characteristics, exercise and smoking on morphometry of human Achilles tendon: an ultrasound study. *Anatomy.* 2016; 9(3): 128–134, doi: [10.2399/ana.15.022](https://doi.org/10.2399/ana.15.022).
- Cohen IK, Diegelmann RF, Johnson ML. Effect of corticosteroids on collagen synthesis. *Surgery.* 1977; 82(1): 15–20, indexed in Pubmed: [877852](https://pubmed.ncbi.nlm.nih.gov/877852/).
- Cook JL, Khan KM, Kiss ZS, et al. Asymptomatic hypoechoic regions on patellar tendon ultrasound: A 4-year clinical and ultrasound followup of 46 tendons. *Scand J Med Sci Sports.* 2001; 11(6): 321–327, doi: [10.1034/j.1600-0838.2001.110602.x](https://doi.org/10.1034/j.1600-0838.2001.110602.x), indexed in Pubmed: [11782263](https://pubmed.ncbi.nlm.nih.gov/11782263/).
- Cummins EJ, Anson BJ. The structure of the calcaneal tendon (of Achilles) in relation to orthopedic surgery, with additional observations on the plantaris muscle. *Surg Gynecol Obstet.* 1946; 83: 107–116, indexed in Pubmed: [20988044](https://pubmed.ncbi.nlm.nih.gov/20988044/).
- Mello R, Marchiori E, Santos A, et al. Avaliação morfológica do tendão de Aquiles por ultra-sonografia. *Radiol Bras.* 2006; 39(3): 161–165, doi: [10.1590/s0100-39842006000300003](https://doi.org/10.1590/s0100-39842006000300003).
- Del Buono A, Chan O, Maffulli N. Achilles tendon: functional anatomy and novel emerging models of imaging classification. *Int Orthop.* 2013; 37(4): 715–721, doi: [10.1007/s00264-012-1743-y](https://doi.org/10.1007/s00264-012-1743-y), indexed in Pubmed: [23254856](https://pubmed.ncbi.nlm.nih.gov/23254856/).
- Doral MN, Alam M, Bozkurt M, et al. Functional anatomy of the Achilles tendon. *Knee Surg Sports Traumatol Arthrosc.* 2010; 18(5): 638–643, doi: [10.1007/s00167-010-1083-7](https://doi.org/10.1007/s00167-010-1083-7), indexed in Pubmed: [20182867](https://pubmed.ncbi.nlm.nih.gov/20182867/).
- Ebeling T, Farin P, Pyörälä K. Ultrasonography in the detection of Achilles tendon xanthomata in heterozygous familial hypercholesterolemia. *Atherosclerosis.* 1992; 97(2-3): 217–228, doi: [10.1016/0021-9150\(92\)90134-3](https://doi.org/10.1016/0021-9150(92)90134-3), indexed in Pubmed: [1466665](https://pubmed.ncbi.nlm.nih.gov/1466665/).
- Egwu A. Normal thickness of the tendo calcaneus (TCT) in an adult nigerian population: an imaging based normographic study. *Br J Med Med Res.* 2014; 4(10): 2100–2111, doi: [10.9734/bjmmr/2014/5678](https://doi.org/10.9734/bjmmr/2014/5678).
- Eriksen HA, Pajala A, Leppilähti J, et al. Increased content of type III collagen at the rupture site of human Achilles tendon. *J Orthop Res.* 2002; 20(6): 1352–1357, doi: [10.1016/S0736-0266\(02\)00064-5](https://doi.org/10.1016/S0736-0266(02)00064-5), indexed in Pubmed: [12472252](https://pubmed.ncbi.nlm.nih.gov/12472252/).
- Hess GW. Achilles tendon rupture: a review of etiology, population, anatomy, risk factors, and injury prevention. *Foot Ankle Spec.* 2010; 3(1): 29–32, doi: [10.1177/1938640009355191](https://doi.org/10.1177/1938640009355191), indexed in Pubmed: [20400437](https://pubmed.ncbi.nlm.nih.gov/20400437/).
- Järvinen TAH, Kannus P, Maffulli N, et al. Achilles tendon disorders: etiology and epidemiology. *Foot Ankle Clin.* 2005; 10(2): 255–266, doi: [10.1016/j.fcl.2005.01.013](https://doi.org/10.1016/j.fcl.2005.01.013), indexed in Pubmed: [15922917](https://pubmed.ncbi.nlm.nih.gov/15922917/).
- Jhingan S, Perry M, O'Driscoll G, et al. Thicker Achilles tendons are a risk factor to develop Achilles tendinopathy in elite professional soccer players. *Muscles Ligaments Tendons J.* 2011; 1(2): 51–56, indexed in Pubmed: [23738247](https://pubmed.ncbi.nlm.nih.gov/23738247/).
- Kallinen M, Suominen H. Ultrasonographic measurements of the Achilles tendon in elderly athletes and sedentary men. *Acta Radiol.* 1994; 35(6): 560–563, indexed in Pubmed: [7946678](https://pubmed.ncbi.nlm.nih.gov/7946678/).
- Koivunen-Niemelä T, Parkkola K. Anatomy of the Achilles tendon (tendo calcaneus) with respect to tendon thickness measurements. *Surg Radiol Anat.* 1995; 17(3): 263–268, doi: [10.1007/BF01795061](https://doi.org/10.1007/BF01795061), indexed in Pubmed: [7502192](https://pubmed.ncbi.nlm.nih.gov/7502192/).
- Kumar N, Aithal AP, Nayak SB, et al. Morphometric evaluation of human tendocalcaneus: a cadaveric study of south indian male population. *Muscles Ligaments Tendons J.* 2017; 7(1): 62–68, doi: [10.11138/mltj/2017.7.1.062](https://doi.org/10.11138/mltj/2017.7.1.062), indexed in Pubmed: [28717613](https://pubmed.ncbi.nlm.nih.gov/28717613/).
- Landis JR, Koch GG. The measurement of observer agreement for categorical data. *Biometrics.* 1977; 33(1): 159–174, indexed in Pubmed: [843571](https://pubmed.ncbi.nlm.nih.gov/843571/).

21. Lantto I, Heikkinen J, Flinkkilä T, et al. Epidemiology of Achilles tendon ruptures: increasing incidence over a 33-year period. *Scand J Med Sci Sports*. 2015; 25(1): e133–e138, doi: [10.1111/sms.12253](https://doi.org/10.1111/sms.12253), indexed in Pubmed: [24862178](https://pubmed.ncbi.nlm.nih.gov/24862178/).
22. Leppilahti J, Puranen J, Orava S. Incidence of Achilles tendon rupture. *Acta Orthop Scand*. 1996; 67(3): 277–279, doi: [10.3109/17453679608994688](https://doi.org/10.3109/17453679608994688), indexed in Pubmed: [8686468](https://pubmed.ncbi.nlm.nih.gov/8686468/).
23. Liem MS, Leuven JA, Bloem JL, et al. Magnetic resonance imaging of Achilles tendon xanthomas in familial hypercholesterolemia. *Skeletal Radiol*. 1992; 21(7): 453–457, doi: [10.1007/BF00190990](https://doi.org/10.1007/BF00190990), indexed in Pubmed: [1439898](https://pubmed.ncbi.nlm.nih.gov/1439898/).
24. Lin LK. A concordance correlation coefficient to evaluate reproducibility. *Biometrics*. 1989; 45(1): 255, doi: [10.2307/2532051](https://doi.org/10.2307/2532051).
25. Maffulli N, Ewen SW, Waterston SW, et al. Tenocytes from ruptured and tendinopathic achilles tendons produce greater quantities of type III collagen than tenocytes from normal achilles tendons. An in vitro model of human tendon healing. *Am J Sports Med*. 2000; 28(4): 499–505, doi: [10.1177/03635465000280040901](https://doi.org/10.1177/03635465000280040901), indexed in Pubmed: [10921640](https://pubmed.ncbi.nlm.nih.gov/10921640/).
26. Maffulli N, Waterston SW, Squair J, et al. Changing incidence of Achilles tendon rupture in Scotland: a 15-year study. *Clin J Sport Med*. 1999; 9(3): 157–160, doi: [10.1097/00042752-199907000-00007](https://doi.org/10.1097/00042752-199907000-00007), indexed in Pubmed: [10512344](https://pubmed.ncbi.nlm.nih.gov/10512344/).
27. Magnusson SP, Beyer N, Abrahamsen H, et al. Increased cross-sectional area and reduced tensile stress of the Achilles tendon in elderly compared with young women. *J Gerontol A Biol Sci Med Sci*. 2003; 58(2): 123–127, doi: [10.1093/gerona/58.2.b123](https://doi.org/10.1093/gerona/58.2.b123), indexed in Pubmed: [12586849](https://pubmed.ncbi.nlm.nih.gov/12586849/).
28. Mirahmadi KS, Coburn JW, Bluestone R. Calcific peri-arthritis and hemodialysis. *JAMA*. 1973; 223(5): 548–549, indexed in Pubmed: [4739139](https://pubmed.ncbi.nlm.nih.gov/4739139/).
29. Möller A, Astron M, Westlin N. Increasing incidence of Achilles tendon rupture. *Acta Orthop Scand*. 1996; 67(5): 479–481, doi: [10.3109/17453679608996672](https://doi.org/10.3109/17453679608996672), indexed in Pubmed: [8948254](https://pubmed.ncbi.nlm.nih.gov/8948254/).
30. Murley GS, Tan JM, Edwards RM, et al. Foot posture is associated with morphometry of the peroneus longus muscle, tibialis anterior tendon, and Achilles tendon. *Scand J Med Sci Sports*. 2014; 24(3): 535–541, doi: [10.1111/sms.12025](https://doi.org/10.1111/sms.12025), indexed in Pubmed: [23301865](https://pubmed.ncbi.nlm.nih.gov/23301865/).
31. Nickisch F. Anatomy of the Achilles Tendon. *Achilles Tendon*. 2008; 2–16, doi: [10.1007/978-0-387-79205-7\\_1](https://doi.org/10.1007/978-0-387-79205-7_1).
32. Nillius SA, Nilsson BE, Westlin NE. The incidence of Achilles tendon rupture. *Acta Orthop Scand*. 1976; 47(1): 118–121, doi: [10.3109/17453677608998983](https://doi.org/10.3109/17453677608998983), indexed in Pubmed: [1266586](https://pubmed.ncbi.nlm.nih.gov/1266586/).
33. O'Brien M. The anatomy of the Achilles tendon. *Foot Ankle Clin*. 2005; 10(2): 225–238, doi: [10.1016/j.fcl.2005.01.011](https://doi.org/10.1016/j.fcl.2005.01.011), indexed in Pubmed: [15922915](https://pubmed.ncbi.nlm.nih.gov/15922915/).
34. Olateju O, Philander I, Bidmos M. Morphometric analysis of the patella and patellar ligament of South Africans of European ancestry. *South African J Sci*. 2013; 109(9/10): 1–6, doi: [10.1590/sajs.2013/20130069](https://doi.org/10.1590/sajs.2013/20130069).
35. Pang B, Ying M. Sonographic measurement of Achilles tendons in asymptomatic subjects. *J Ultrasound Med*. 2006; 25(10): 1291–1296, doi: [10.7863/jum.2006.25.10.1291](https://doi.org/10.7863/jum.2006.25.10.1291).
36. Patel NN, Labib SA. The Achilles tendon in healthy subjects: an anthropometric and ultrasound mapping study. *J Foot Ankle Surg*. 2018; 57(2): 285–288, doi: [10.1053/j.jfas.2017.10.005](https://doi.org/10.1053/j.jfas.2017.10.005), indexed in Pubmed: [29275904](https://pubmed.ncbi.nlm.nih.gov/29275904/).
37. Rosager S, Aagaard P, Dyhre-Poulsen P, et al. Load-displacement properties of the human triceps surae aponeurosis and tendon in runners and non-runners. *Scand J Med Sci Sports*. 2002; 12(2): 90–98, doi: [10.1034/j.1600-0838.2002.120205.x](https://doi.org/10.1034/j.1600-0838.2002.120205.x), indexed in Pubmed: [12121426](https://pubmed.ncbi.nlm.nih.gov/12121426/).
38. Saltzman CL, Tearse DS. Achilles tendon injuries. *J Am Acad Orthop Surg*. 1998; 6(5): 316–325, doi: [10.5435/00124635-199809000-00007](https://doi.org/10.5435/00124635-199809000-00007), indexed in Pubmed: [9753759](https://pubmed.ncbi.nlm.nih.gov/9753759/).
39. Schepsis AA, Jones H, Haas AL. Achilles tendon disorders in athletes. *Am J Sports Med*. 2002; 30(2): 287–305, doi: [10.1177/03635465020300022501](https://doi.org/10.1177/03635465020300022501), indexed in Pubmed: [11912103](https://pubmed.ncbi.nlm.nih.gov/11912103/).
40. Sharma P, Maffulli N. Biology of tendon injury: healing, modeling and remodeling. *J Musculoskelet Neuronal Interact*. 2006; 6(2): 181–190, indexed in Pubmed: [16849830](https://pubmed.ncbi.nlm.nih.gov/16849830/).
41. Singhal M, Parmar N, Singhal D, et al. Morphometric analysis of tendoachilles tendon with its clinical implications. *Int J Anat Res*. 2019; 7(2.2): 6550–6555, doi: [10.16965/ijar.2019.165](https://doi.org/10.16965/ijar.2019.165).
42. Spencer JD. Spontaneous rupture of tendons in dialysis and renal transplant patients. *Injury*. 1988; 19(2): 86–88, doi: [10.1016/0020-1383\(88\)90079-4](https://doi.org/10.1016/0020-1383(88)90079-4), indexed in Pubmed: [3058609](https://pubmed.ncbi.nlm.nih.gov/3058609/).
43. Stenroth L, Peltonen J, Cronin NJ, et al. Age-related differences in Achilles tendon properties and triceps surae muscle architecture in vivo. *J Appl Physiol* (1985). 2012; 113(10): 1537–1544, doi: [10.1152/jappphysiol.00782.2012](https://doi.org/10.1152/jappphysiol.00782.2012), indexed in Pubmed: [23042907](https://pubmed.ncbi.nlm.nih.gov/23042907/).
44. Strocchi R, De Pasquale V, Guizzardi S, et al. Human Achilles tendon: morphological and morphometric variations as a function of age. *Foot Ankle*. 1991; 12(2): 100–104, doi: [10.1177/107110079101200207](https://doi.org/10.1177/107110079101200207), indexed in Pubmed: [1773989](https://pubmed.ncbi.nlm.nih.gov/1773989/).
45. Suchak AA, Bostick G, Reid D, et al. The incidence of Achilles tendon ruptures in Edmonton, Canada. *Foot Ankle Int*. 2005; 26(11): 932–936, doi: [10.1177/107110070502601106](https://doi.org/10.1177/107110070502601106), indexed in Pubmed: [16309606](https://pubmed.ncbi.nlm.nih.gov/16309606/).
46. Syha R, Grau S, Nieß AM, et al. Computer-based quantification of the Achilles tendon thickness in sequential B-mode ultrasound images: a study of feasibility and reliability. *Arch Orthop Trauma Surg*. 2014; 134(10): 1443–1449, doi: [10.1007/s00402-014-2043-3](https://doi.org/10.1007/s00402-014-2043-3), indexed in Pubmed: [25052771](https://pubmed.ncbi.nlm.nih.gov/25052771/).
47. Thoires KA, Childs J. Are ultrasound measurements of achilles tendon size reliable? A systematic review of rater reliability. *Ultrasound Med Biol*. 2018; 44(12): 2476–2491, doi: [10.1016/j.ultrasmedbio.2018.07.011](https://doi.org/10.1016/j.ultrasmedbio.2018.07.011), indexed in Pubmed: [30154035](https://pubmed.ncbi.nlm.nih.gov/30154035/).
48. van Dijk CN, van Sterkenburg MN, Wiegerinck JI, et al. Terminology for Achilles tendon related disorders. *Knee Surg Sports Traumatol Arthrosc*. 2011; 19(5): 835–841, doi: [10.1007/s00167-010-1374-z](https://doi.org/10.1007/s00167-010-1374-z), indexed in Pubmed: [21222102](https://pubmed.ncbi.nlm.nih.gov/21222102/).
49. Van Ginckel A, Thijs Y, Hesar NG, et al. Intrinsic gait-related risk factors for Achilles tendinopathy in novice runners: a prospective study. *Gait Posture*. 2009; 29(3): 387–391, doi: [10.1016/j.gaitpost.2008.10.058](https://doi.org/10.1016/j.gaitpost.2008.10.058), indexed in Pubmed: [19042130](https://pubmed.ncbi.nlm.nih.gov/19042130/).

# Macroanatomical and histological study of the structure of intercornual gland in Abaza (*Capra Aegagrus*) and Gurcu (*Capra Falconeri*) goats breeds

S. Dalga<sup>1</sup>, S. İlhan Aksu<sup>2</sup>, K. Aslan<sup>1</sup>, T. Deprem<sup>2</sup>

<sup>1</sup>Department of Anatomy, Faculty of Veterinary Medicine, Kafkas University, Kars, Turkey

<sup>2</sup>Department of Histology and Embriology, Faculty of Veterinary Medicine, Kafkas University, Kars, Turkey

[Received: 10 January 2020; Accepted: 18 February 2020]

**Background:** The anatomical localisation of the odour glands, which increase activity during the reproduction period and help goat species to find each other, varies.

**Materials and methods:** In our study, the anatomical and histological structures of the glands around the horn were examined in the Gurcu and Abaza goats, which are native breeds. In this study a total of 12 Abaza and Gurcu goat heads were used.

**Results:** The area between the two horns and area at the back of the horns were shaved to remove all hair. The distance between the horns of both goat breeds was measured using an electronic calliper. The mean distance between the horns of the Abaza goats was determined as  $36.80 \pm 8.62$  mm while this distance was  $39.63 \pm 4.10$  mm for the Gurcu goats. Gland tissue that could not be seen anatomically under the skin was examined histologically. For the histological examination, skin samples were taken from the anterior, middle, right posterior and left posterior of the area between the two horns of both breeds. Crossman triple staining and haematoxylin and eosin staining were applied to the samples.

**Conclusions:** Glandula intercornualis was found to be slightly caudal between the horns in both breeds and normal sebaceous glands were almost absent in the areas where these glands were found. Lobes and branched alveolar glands were located around the hair follicles. (Folia Morphol 2021; 80, 1: 204–209)

**Key words:** horn gland, Abaza goat, Gurcu goat

## INTRODUCTION

Abaza goats are farmed in the province of Artvin in Turkey and are generally bronze, white, black or brown [1]. Their mouths, horns, legs and the area around their eyes are generally black. They have a thin body structure and therefore likened to gazelles. The bucks have sword-like flat broad horns, while the females may or may not have horns. It is also known that Abaza goats are of *Capra aegagrus* origin [3].

Gurcu goats, also known as Tbilisi goats or Caucasian goats, are originally from the Caucasus and are bred in the North-Eastern region of Turkey, especially in the province of Kars and Ardahan. Gurcu goats, which are mostly black, grey or white, originate from the auger horned goat *Capra falconeri*, and are particularly similar to Abaza goats reared in Şavşat or Borçka [3, 14]. Gurcu goats have long and straight horns that meet at the end which distinguishes



them from hair goats. Gurcu goats can also be hornless [3, 16].

The horn glands in the horn roots of goats are sebaceous glands and the goats emit an odour through these glands to find their mates during breeding periods [8]. The secretion of the modified sebaceous glands was also believed to be involved in the production of this fragrance [2, 4, 10, 13]. French [9] stated that the presence of horns in male goats was a characteristic of Italian goats. Sar and Calhoun [13] reported large, branched, alveolar and sebaceous glands at the base of the horns and ears of American goats. Jenkinson et al. [10] reported that the odour of British Saanen goats mainly comes from enlarged sebaceous glands located in the head and neck. Bal and Ghoshal [2] reported that the cross-section diameters of female and castrated male fat cells are larger than male fat cells American goats, and the glands are more active during breeding season. Sar and Calhoun [13] and Bal and Ghoshal [2] described the sebaceous glands between the horn glands as being simple, branched or alveolar. According to Bal and Ghoshal [2], although females had sebaceous glands, they had no characteristic odour. In other studies in the literature, it has been reported that testosterone increases the size and activity of the sebaceous glands [7, 15].

Various anatomical and histological studies have been conducted on the horn glands and sebaceous glands of goats found in different parts of their bodies [5, 12].

Various studies have been conducted on goat breeds native to Turkey [6, 11]. However, no anatomical and histological studies have been conducted on Abaza and Gurcu goats. Thus, in the present study, the glandula intercornualis, special skin glands located between the two horns of Abaza and Gurcu goats, was studied.

## MATERIALS AND METHODS

This study was approved by the local Ethics Commission of Experimental Animals of Kafkas University. A total of 12 Abaza and Gurcu goat heads were used in the present study (regardless of gender). The materials were supplied during the sale of the Abaza and Gurcu goat herd sacrificial and forbearance from Kafkas University Education, Research and Application Farm. The head samples were obtained between June and December. Firstly, the anterior and posterior of the heads and the area between the two

horns were shaved to remove all hair. The distance between the two horns of both goat breeds was then measured using an electronic calliper. The left and right horn lengths and the transverse surface of the horns of both goat breeds were measured using a tape measure. Subsequently, for the histological examination, skin samples of approximately 1 × 1 size were taken from the anterior, middle, right posterior and left posterior of the area between the two horns of both breeds. The skin samples were kept in 10% formaldehyde for 24 hours and then underwent routine histological follow-up (alcohol-xylol) series and paraffin-blocked. Crossman triple staining and haematoxylin and eosin staining were applied to the samples by taking 5–6 sections with microtome from these blocks. After the staining, the samples were examined under a light microscope (Olympus B×51, Japan). The locations of the horn glands detected in both goat breeds were photographed.

## RESULTS

### Macroanatomic findings

The distance between the horns of the Abaza and Gurcu goat was measured using an electronic calliper. The mean distance between the horns of the Abaza goats was  $36.80 \pm 8.62$  mm while this distance was  $39.63 \pm 4.10$  mm for the Gurcu goats. The mean horn lengths for the Abaza and Gurcu goats were 276.66 mm and 288.66 mm, and the transverse surface lengths of the horns were 193.33 mm and 218.33 mm, respectively. Similarly, the mean horn lengths of the right and left horns of the Gurcu goats were 382.5 mm and 395 mm and their transverse surface lengths were 170 mm and 175 mm, respectively. As a result of the macro-anatomical analyses performed, the presence of glandula intercornualis, which can be seen in various goat breeds macroscopically, was not found in the samples used in this study (Figs. 1, 2).

### Histological findings

As a result of the light microscopic examinations conducted on the skin samples, it was observed that both goat breeds contained layers of epidermis, dermis and muscle (Fig. 3). The epidermis layer was found to be multi-layered and have a flat epithelium and microscopic papillae. Under the epidermis, there were the stratum papillare (str. superficiale) and stratum reticular (str. profundum) substrates of the dermis, as well as the connective tissue of the dermis, vessels, veins, hair roots and hair muscles (Figs. 4, 5). It was



Figure 1. The horns of an Abaza goat.



Figure 2. The horns of a Gurcu goat.

seen that the sebaceous glands that have a plurivacuolar structure and contain oil droplets were open at the hair roots (Fig. 6). In addition, the presence of sweat gland drainage duct structure was determined in both goat breeds (Fig. 5).

After the gland structures of the two goat breeds were determined, normal sebaceous gland structure

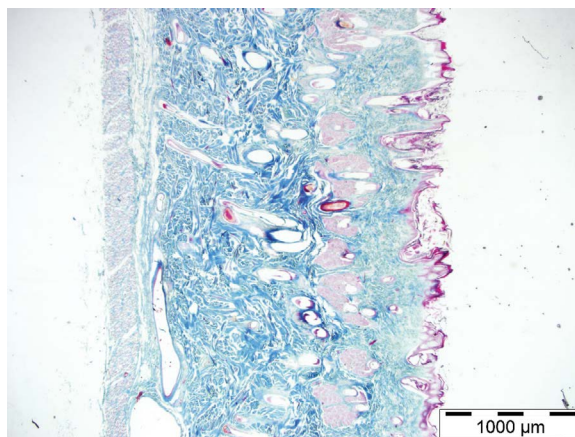


Figure 3. Microscopic view of the skin of goats; triple  $\times 2$ .

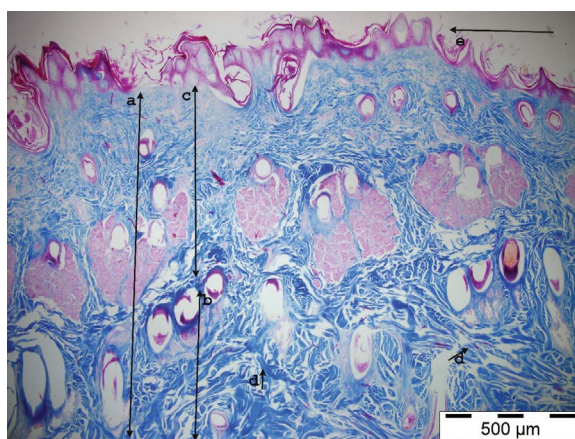


Figure 4. Dermis layers of in the goats; a — dermis; b — stratum polymorphic; c — stratum superficial; d — collagen yarns; e — epidermis.

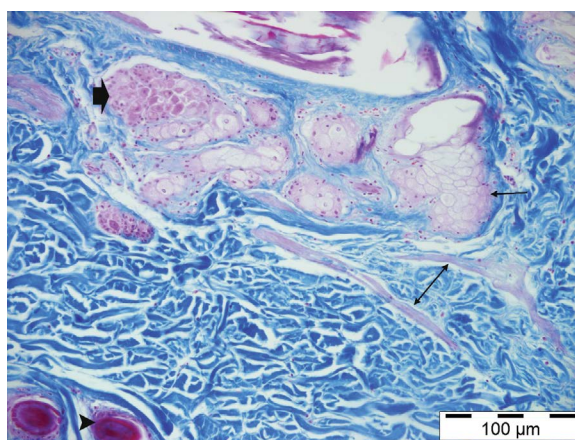
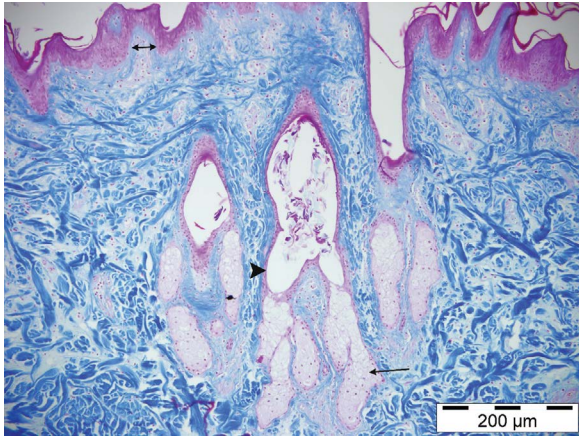
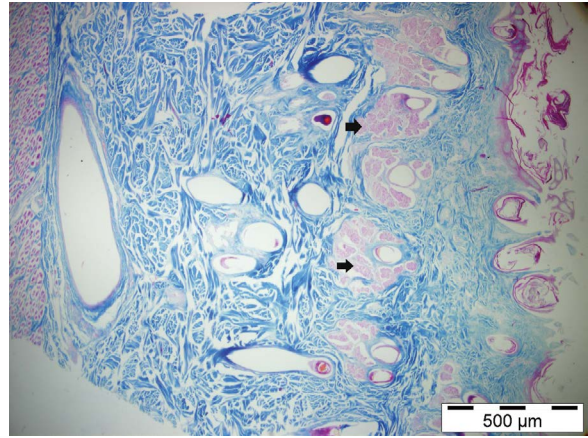


Figure 5. Dermis structures of the goats. Arrowhead: hair root; thin arrow: sebaceous glands; thick arrow: sebaceous gland-like structures; double headed arrow: muscle erector battery; triple  $\times 20$ .

(Fig. 7) was observed to be intense behind the horn and less localised in the anterior parts. In the present



**Figure 6.** The opening of the sebaceous glands to the hair root in the dermis. Thin arrow: sebaceous glands, arrowhead: hair root, double-headed arrow: multi-layer epithelial structure.



**Figure 9.** Localisation of the glands in the stratum superficiale of the Abaza goats. Thick arrow: triple  $\times 4$ , similar to the sebaceous gland structures.

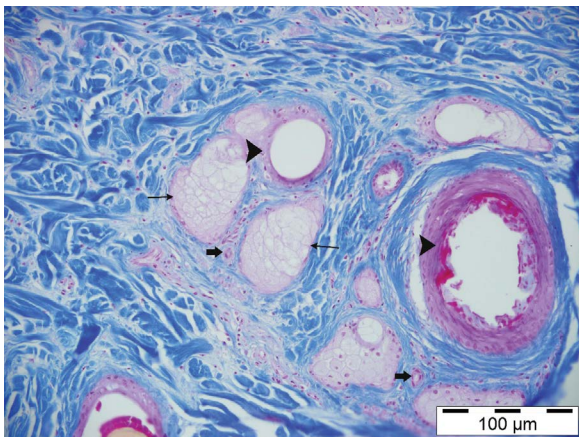


**Figure 7.** Microscopic view of a hair follicle, sebaceous gland and sweat gland drainage duct. Arrowhead: hair root, thin arrow: oil glands, thick arrow: sweat gland duct.

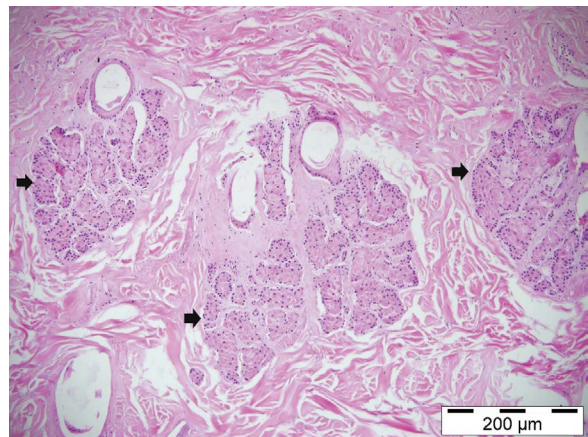


**Figure 10.** Lobe (alveolar) structure of the glands of the Abaza goats. Thick arrow: oil cloth-like structures, haematoxylin and eosin.

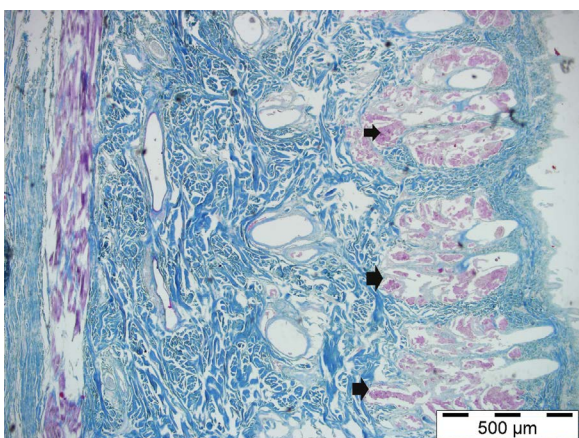


**Figure 8.** Localisation of the glands in stratum superficiale of the Gurcu goats. Thick arrow: triple  $\times 4$ , similar to the sebaceous gland structures.

study, it was observed that these gland structures were in the back part of the middle part of the horn as we thought that there might be horn glands. It was determined that these gland structures were located parallel to the epidermis in the stratum superficiale layer of the dermis in both goat breeds (Figs. 8, 9). In the Abaza goats, these gland structures were found in the middle part of the superficial region of the dermis layer, in a more regular and broadly located lobed form (Fig. 10). In the Gurcu goats, the localisation of these glands was more superficial, in other words, close to the epidermis and had a narrower structure with more lobes (Fig. 11). In both breeds, it was observed that the normal sebaceous glands were negligible in the regions containing this gland

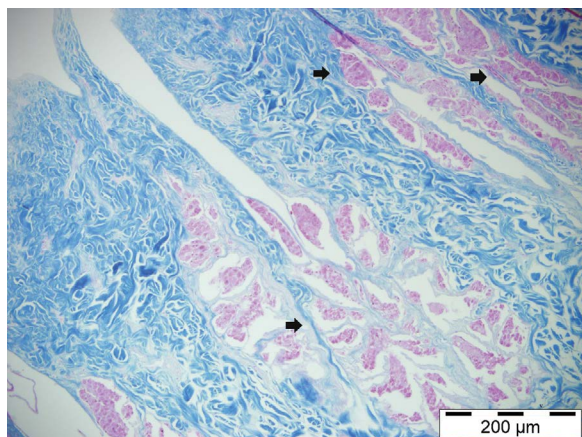


**Figure 11.** Multi-lobed structure of the glands of the Gurcu goats. Thick arrow: triple, similar to the sebaceous gland structures,  $\times 10$ .

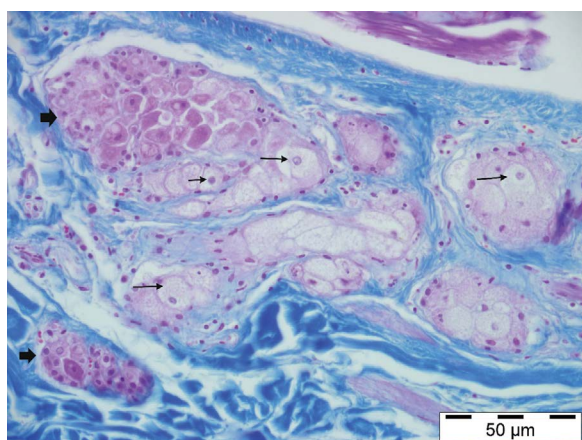


**Figure 12.** Different cell groups located between the fat cells in the dermis. Thick arrow: oil gland-like structures; triple  $\times 40$ .

structure. It was thought that these glands, which had more lobes and branched alveolar structures, may be the horn glands as they were different from the typical sebaceous glands found around the hair root. In some cases, these glands which were thought to be the horn glands and the sebaceous glands were found together; however, they contained cells with different structures and staining properties (Fig. 12). In addition, when the sebaceous gland structures of the two breeds were examined, it was observed that the fat cells in the Gurcu goats were structurally smaller than those of the Abaza goats.

## DISCUSSION

In the present study, the front, back and side of the horn glands were determined by cross-section in two different, but morphologically similar, breeds of the Abaza goat and Gurcu goat.

Lancker et al. [12] reported that the horned glands of the polled goat breeds were located on the caudal surface of the head under the skin folds [12]. This, however, was not observed in the present study for the Abaza goats or the Gurcu goats.

In a study on the horn glands of West African dwarf goats and red Sokoto goats conducted in Nigeria, the horn glands were reported to be simple or branched alveolar sebaceous glands. It was stated that the horn glands were structurally similar to the sebaceous glands located in other parts of the body in both the males and the females. As with other sebaceous glands, the horn glands are often said to be associated with hair follicles. However, in a few cases, it has been reported that one or more sebaceous glands are associated with a hair follicle, and each of these glands has a separate secretion portion, as well as a separate secretory channel opening to the hair follicle. In the Abaza and Gurcu goats, it was observed that the glands were simply branched and alveolar, and their secretions were drained through the hair follicles [5]. The structures specified as horn glands in the present study were found to be similar to the glands of the Nigerian goat breeds. However, unlike the breeds in Nigeria, a secretion channel was not found in the Abaza and Gurcu goats.

Some authors reported that two sebaceous glands associated with a single hair follicle had two lobes [2, 10]. This was found to be similar for the Abaza goats examined in the present study; however, more lobed glands were found around a hair follicle in the Gurcu goats.

In a study conducted on American goats, horn glands and other sebaceous glands were compared and it was reported that the sebaceous glands had larger alveoli [13]. In the present study, it was seen that the sebaceous glands had more alveoli than the horn glands in the goat breeds, and that the structures that were thought to be horn glands in both of the goat breeds were more than the sebaceous glands.

West African dwarf goats are found in the tropical forest areas of Southern Nigeria, while red Sokoto goats are found in the savannah regions of Northern Nigeria. It was reported that climate can have an impact on the glands of these goats, and that seasonal changes alter the size of the British and American goat horn glands [2, 10].

It has been reported that the differences in the cross-sectional area of the horn glands and other sebaceous glands were more prominent in male Nigerian

goats than the female ones and that these glands were involved in odour production [5]. In the present study, the reason for the glands being larger and more active was thought to be because the samples used were collected during the breeding season of the goats.

## CONCLUSIONS

In the present study, horn glands could not be detected macroanatomically in the Abaza and Gurcu goat breeds; however, they were found histologically and their structure were seen to be similar to those mentioned in the literature. This study can help guide future studies.

## REFERENCES

1. Anonim. Abaza keçisi koruma altında, Artvin İl Gıda Tarım ve Hayvancılık Müdürlüğü (28.11.2016).
2. Bal HS, Ghoshal NG. The scent glands of the goat (*Capra hircus*). Zentralbl. Veterinärmed C. 1976; 5(104).
3. Batu S. Türkiye Keçi Irkları. Ankara Üniversitesi Veteriner Fakültesi Yayınları, Ankara. 1951.
4. Brouwer E, Nijkamp HJ. Volatile acids in the secretion products, hair grease, of the skin. *Biochem J.* 1952; 52(1): 54–58, doi: [10.1042/bj0520054](https://doi.org/10.1042/bj0520054), indexed in Pubmed: [13018162](https://pubmed.ncbi.nlm.nih.gov/13018162/).
5. Chukwu DO, Ihemelandu EC. Morphometric studies on horn glands of Nigerian breeds of goat. *Small Ruminant Res.* 1989; 2(4): 367–374, doi: [10.1016/0921-4488\(89\)90031-x](https://doi.org/10.1016/0921-4488(89)90031-x).
6. Dalga S. Topographic and morphometric study of the mental foramina of Abaza goats with its clinical implication for regional anesthesia. *Folia Morphol.* 2019 [Epub ahead of print], doi: [10.5603/FM.a2019.0122](https://doi.org/10.5603/FM.a2019.0122), indexed in Pubmed: [31750539](https://pubmed.ncbi.nlm.nih.gov/31750539/).
7. Ebling F. The effects of testosterone and oestradiol on the sebaceous glands and epidermis of therat. *J Embryol Exp Morphol.* 1957; 5: 74–82.
8. Erençin Z. Genel Histoloji, Ankara Üniversitesi Veteriner Fakültesi Yayınlar. 1958; 98.
9. French MH. Observations on the goat. FAO, Rome. 1970; 2.
10. Jenkinson DM, Blackburn PS, Proudfoot R. Seasonal changes in the skin glands of the goat. *Br Vet J.* 1967; 123(12): 541–549, doi: [10.1016/s0007-1935\(17\)39654-9](https://doi.org/10.1016/s0007-1935(17)39654-9).
11. Kuru M, Kuru B, Kulaksız R, et al. Abaza Keçilerinde Progesteron Destekli Östrus Senkronizasyonunun Bazı Reprodüktif Parametrelere Etkileri. *Kocatepe Vet J.* 2017; 10(3): 164–171.
12. Lancker S, Van den Broeck W, Simoens P. Morphology of caprine skin glands involved in buck odour production. *Vet J.* 2005; 170: 351–358, doi: [10.1016/j.tvjl.2004.08.017](https://doi.org/10.1016/j.tvjl.2004.08.017).
13. Sar M, Calhoun ML. Microscopic anatomy of the integument of the common erican goat. *Am J Vet Res.* 1966; 27: 444–456.
14. Sezgin E, Kopuzlu S, Yüksel S. Abaza keçisi. Ulusal Keçicilik Kongresi, Çanakkale. 2010: 241–244.
15. Strauss JS, Kligman AM, Pochi PE. The effect of androgens and estrogens on human sebaceous glands. *J Invest Dermatol.* 1962; 39: 139–155, doi: [10.1038/jid.1962.94](https://doi.org/10.1038/jid.1962.94), indexed in Pubmed: [13917704](https://pubmed.ncbi.nlm.nih.gov/13917704/).
16. Yalçın BC, Türkiye’de yetiştirilen keçi ırkları. “Koyun-Keçi Hastalıkları ve Yetiştiriciliği”, Ed; Aytuğ CN, Alaçam E, Özkoç Ü, Yalçın BC, Gökçen H, Türker H, Tüm Vet. Hayvancılık Hizmetleri Yayını, Teknografik Matbaası, İstanbul, Türkiye, 1990.

# A stereological study of the renal and adrenal glandular structure of red-legged partridge (*Alectoris chukar*)

N. Colcimen<sup>1</sup>, G. Cakmak<sup>2</sup>

<sup>1</sup>Department of Histology and Embryology, Faculty of Medicine, Van Yuzuncu Yil University, Van, Turkey

<sup>2</sup>Department of Anatomy, Faculty of Veterinary Medicine, Van Yuzuncu Yil University, Van, Turkey

[Received: 4 December 2019; Accepted: 19 January 2020]

**Background:** Partridge is a major bird species that has recently gained an increasing importance as an alternative food source and a game animal in hunting tourism. Herein, we aimed to examine the histological structure and stereological properties of the renal and adrenal glands of red-legged partridge.

**Materials and methods:** Seven healthy adult red-legged partridges (*Alectoris chukar*) of both genders were used in this study. The *Alectoris chukars* were perfused with the intracardiac method and were kept in 10% formaldehyde for 72 h for optimal fixation. The tissues were embedded in paraffin after routine light microscopic processes. Then, 5- $\mu$ m thick sections were taken, which were stained with haematoxylin and eosin, photographed, and examined in light microscope. Modified Cavalieri principle was used for volume calculation as stereological analysis. Total tissue volume ratios were calculated with the help of a point grid provided by the Shtereom 1.5 packaged programme. Mann Whitney-U test was used for inter-group comparisons. The significance level was set at 5% SPSS (ver: 13) statistical software was used for all statistical analyses.

**Results:** Renal histological structure was found to resemble those of other bird species and contained a mixed type (mammalian, reptilian) glomerular structure. It was also found that the adrenal histology was not in the form of separate layers but composed of cell groups with different properties. Stereological renal volume assessment revealed statistically similar right and left renal size ( $p > 0.05$ ). In adrenal gland volume assessment, the right and left adrenal volumes were also statistically similar ( $p > 0.05$ ).

**Conclusions:** The obtained data in the present study is thought to contribute to the understanding of the stereological, morphological and histological structure of the red-legged partridge (*Alectoris chukar*) kidney and adrenal gland. (Folia Morphol 2021; 80: 1: 210–214)

**Key words:** adrenal gland, kidney, partridge, stereology

## INTRODUCTION

The partridge is the common name for belonging to the *Alectoris* and *Perdix* species of the Phasianidae family [4]. The partridge is a major bird species that has recently gained an increasing importance as an

alternative food source and a game animal in hunting tourism.

The kidneys are located on both sides of the abdominal aorta and inferior vena cava in the dorsal part of the abdominal cavity, and the adrenal glands are



**Figure 1.** Transverse section of kidney photographed ( $\times 4$  objective) and a point counting grid superposed onto it for the volume calculation.

located on the cranial pole of both kidneys [16]. The kidneys of bird species have an intermediate structure between mammals and reptilians. The bird species do not possess a renal pelvis, urinary bladder, or urethra [14]. Histologically, their kidneys have a multilobulated pattern and isolated cortex and medulla which are separated by a fine connective tissue. They have two types of nephron structures. The first one is designated as the mammalian or medullary type and is composed of a renal corpuscle, a proximal convoluted tubule, a distal convoluted tubule, a collecting tubule, and thin and thick segments of Henle's loop. The second type is the reptilian type also called as the cortical type, which has a smaller renal corpuscle but no Henle's loop; additionally, there is a short section between proximal convoluted tubule and distal convoluted tubule, which is named the intermediate tubule [13]. Adrenal glands are anatomic structures that play an important role for accommodation to all types of stress and, by hormones they produce, they contribute to many metabolic processes. In bird species the shape of the adrenal glands is highly variable, with inter-species and even inter-individual variations being possible. Experimental removal of adrenal glands results in death of birds [16]. It was showed in a review of the literature that there have been anatomic studies on red-legged partridge, but not specifically on its renal and adrenal gland structure. It was aimed to perform a detailed histological and stereological study of red-legged partridge's renal and adrenal glandular structures in this study.

## MATERIALS AND METHODS

Seven healthy adult red-legged partridges (*Alectoris chukar*) of the both genders were used in this study. The animals were obtained from Van Yuzuncu Yil University Wildlife Protection Centre. It was approved by Van Yuzuncu Yil University Local Ethics Committee (27/06/2019/ 06) complied with the study procedures. The partridges were anesthetised with 10 mg/kg Xylazine HCL (Rompun 2%, 50 mL, Bayer) and with 40 mg/kg i.m. Ketamine HCL (Ketalar 50 mg/mL, 10 mL vial, Pfizer). The animals were perfused with intracardiac method and dissected tissues were kept in 10% formaldehyde for 72 h for optimal fixation [18]. The tissues were embedded in paraffin after completion of routine histological light microscopy procedures. Then, 5- $\mu$ m thick sections were obtained. The first section was randomly selected and then the 40<sup>th</sup> section was taken. The sections were stained with haematoxylin and eosin, photographed, and examined in light microscope.

### Stereological analysis

Stereology, random and systematic sampling is utilised to gain unbiased and quantitative information. Among stereological analyses, modified Cavalieri principle was used for volume calculation. Then, total tissue volume ratios were calculated using a point grid provided by the Shtereom 1.5 packaged programme (Fig. 1). Volume calculation was carried out using the following formula:  $V(\text{obj}) = t \times a/p \times \Sigma p$ .  $V(\text{obj})$  is the volume of the objective,  $t$  is the section

**Table 1.** Descriptive statistics and comparison of the results

	Right					Left					P
	Median	Mean	SD	Min.	Max.	Median	Mean	SD	Min.	Max.	
Kidney tot. vol. [mm <sup>3</sup> ]	2.28	3.34	2.18	1.61	6.88	3.02	2.61	0.85	1.52	3.80	0.499
Cortex vol. [mm <sup>3</sup> ]	1.55	2.02	1.14	1.03	3.94	2.43	2.09	0.88	0.70	3.08	0.735
Kidney tot. vol./Cortex vol. [mm <sup>3</sup> ]	1.67	1.60	0.27	1.22	1.91	1.24	1.36	0.38	1.06	2.17	0.310
Medulla vol. [mm <sup>3</sup> ]	0.91	1.32	1.08	0.30	2.94	0.59	0.53	0.24	0.18	0.82	0.091
Kidney tot. vol./Medulla vol. [mm <sup>3</sup> ]	2.50	3.24	1.53	2.10	5.52	5.14	6.60	4.93	1.85	16.74	0.176
Cortex vol./Medulla vol. [mm <sup>3</sup> ]	1.50	2.24	1.53	1.10	4.52	4.14	5.60	4.93	0.85	15.74	0.259
Adrenal gland tot. vol. [mm <sup>3</sup> ]	0.02	0.02	0.01	0.01	0.03	0.02	0.02	0.01	0.02	0.03	0.499

Max. — maximum; Min. — minimum; SD — standard deviation

thickness,  $a/p$  represents the area of each point on the point counting grid and  $\Sigma p$  is the total number of points hitting the renal and adrenal areas [9, 10]. Coefficient of error (CE) and coefficient of variation (CV) were used to determine the optimum sample size in each group in the standard stereological approach [8]. The values of the CE and CV in our study were in accordance with the literature data.

### Statistical analysis

Descriptive statistics included median, mean, standard deviation, minimum and maximum. Inter-group differences were analysed with Mann-Whitney U test. The significance level was set at 5%. All statistical analyses were performed with SPSS (ver.13) statistical software package programme.

## RESULTS

The stereological analysis revealed that the left and right kidneys had similar sizes. A stereological volume calculation showed a right renal volume of 2.28 mm<sup>3</sup> and a left kidney volume of 3.02 mm<sup>3</sup>. Comparison of both renal volumes revealed a slight but statistically non-significant difference between both kidneys ( $p > 0.05$ ) (Table 1). The microscopic examination of the histological sections demonstrated that the kidney was composed of lobules, each being composed of the cortical and medullary parts and encapsulated by connective tissue containing blood vessels. The renal structure was composed of 60% cortex and 40% medulla on the right side and 80% cortex and 20% medulla on the left kidney. The nephrons had structure two type of nephrons that the reptile and mammalian nephrons (Fig. 2). The number of reptilian nephrons was larger than the mammalian nephrons. The two nephron types also had different distributions so that they were more numerous in

the cortex but there were only tubal structures in the medulla. The mammalian type nephrons were located in deep cortex, close to the medullary cone, whereas the reptilian nephrons were located in the peripheral and middle parts of the cortex, aligned in horseshoe shape around the central vein (Fig. 3).

Examination of the adrenal glandular structure showed that the left and right adrenal glands had some differences in shape but not in size, and a stereological volume assessment revealed that the volume of both adrenal glands was 0.02 mm<sup>3</sup> ( $p > 0.05$ ) (Table 1). A general histological examination showed that the adrenal gland did not have three distinct different layers but only cellular differentiation (dark, light coloured; having different nuclear structures); the glands were encapsulated by a connective tissue containing blood vessels capsule separating them from the kidneys. The adrenal gland had a separate vascular supply (Fig. 4).

## DISCUSSION

It was showed that the renal structure of red-legged partridge was similar to those of other bird species in this study. Red-legged partridge had two kidneys encapsulated by connective tissue containing blood vessels sheaths and composed of multiple lobules containing the cortical and medullary parts. The stereological volume assessment has shown that the right and left renal size were similar statistically. Previous studies on the right and left renal size of bird species have revealed variable results. One study reported that there were no difference between the right and left renal size [6] whereas another study reported difference between the left and right renal size [17]. Similarly, studies assessing the cortical and medullary volumes of bird species have reported variable results. A study has reported that 90% of the total



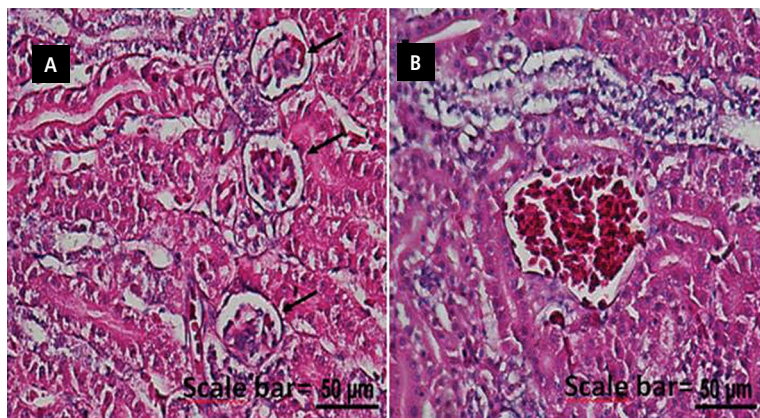


**Figure 2. A.** Haematoxylin and eosin (H&E) staining. Kidney nephron structure. The reptilian-type nephrons (black arrows). Scale bar = 50 µm; **B.** H&E staining. The mammalian-type nephron. Scale bar = 50 µm.

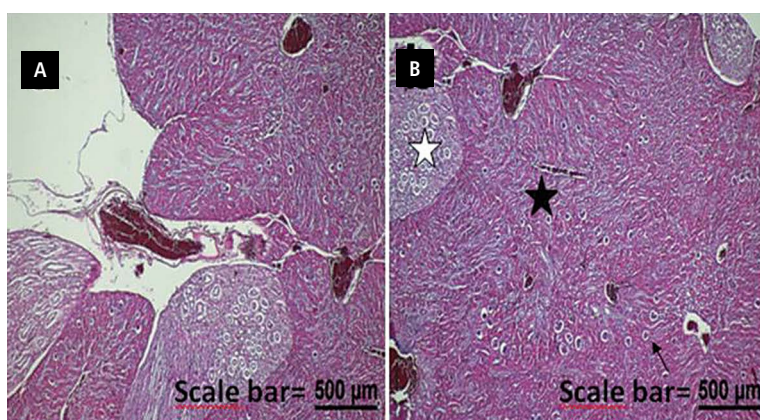


**Figure 3. A.** Haematoxylin and eosin (H&E) staining. The general appearances, lobular structure and vascularisation of kidney. Scale bar = 500 µm; **B.** H&E staining. The histological structure of kidney. Medulla (white asterisk), cortex (black asterisk), horseshoe-shaped reptile glomerular structure (black arrow). Scale bar = 500 µm

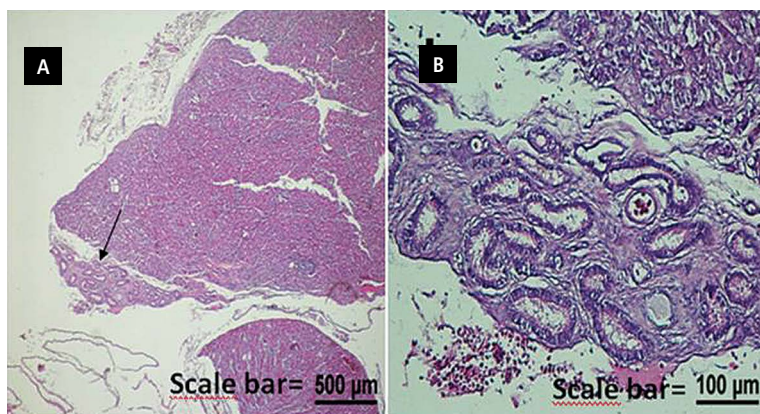


**Figure 4. A.** Haematoxylin and eosin (H&E) staining. The general appearance of the adrenal gland (arrow). Scale bar = 500 µm; **B.** H&E staining. The adrenal gland structure and vascularization. Scale bar = 100 µm.

volume of bird kidney was composed of the cortex and 2% of the medulla [3]; another one has reported corresponding figures of 77% and 10%, respectively [19]. It was founded that the cortical ratio similar to the literature data, but the medullary ratio was slightly higher in this study. Casotti and Braun [5] reported that renal volume varied by the living environment of the bird species. Literature data suggest that a bird's renal shape, size, and structure change by its diet, phylogeny, and environmental factors [17].

All animals were in the same region and climatic conditions (maximum temperature 30–33°C). The basic renal structure is composed of nephrons. The bird kidney is different from the mammalian one because it is composed of a two types of nephrons resembling mammalian and reptilian nephrons [2, 12]. Similarly, in our study, two types of nephrons were observed. Prior studies have shown that more numerous reptile nephrons are located in the periphery of the lobule, a small renal corpuscle, and no loop

of Henle. It has been reported that the mammalian nephrons are larger and had a more complex renal corpuscle and are located deep in the cortex neighbouring the medulla; additionally, they contain a loop of Henle, and are less in number [1]. Herein, it was shown a similar number and distribution of nephrons. The nephrons are responsible for filtration, reabsorption, and secretion, thereby forming urine. The bird's nephrons are composed of a glomerulus, a proximal tubule, a distal tubule, and collecting ducts [14]. This study also revealed similar results.

The present study demonstrated that the adrenal glands were located at the cranial pole of the kidneys and medial to them, as Nickel et al. [15] has reported. It was found the adrenal histology was not in the form of separate layers but composed of cell groups with different properties (having a dark or light colour and varying nuclear structure). It was also shown that the right and left adrenal glands had different shapes and there were also inter-individual differences. The adrenal gland was separated from the kidney tissue with a connective tissue sheath and had a separate vascular supply. The results of this study are in accordance with the previous studies on bird species [16]. Among the studies on adrenal gland size, Humayun et al. [11] and Wells and Wight [20] reported that the left adrenal gland was larger than the right one in chickens of both genders whereas Ozudogru et al. [16] as well as Elbajory [7] reported that the right adrenal gland was larger than the left one. The weight, length, width, and thickness of the adrenal glands vary by a number of factors, such as species, breed, age, health status, and environment [11]. In this study it was detected that there is no difference between stereologically calculated volumes between the right and left adrenal glands.

## CONCLUSIONS

The obtained data in the present study is thought to contribute to the understanding of the stereological, morphological and histological structure of the red-legged partridge (*Alectoris chukar*) kidney and adrenal gland. We think that it will be a guide for the studies about red-legged partridge (*Alectoris chukar*).

## REFERENCES

- Akaydin Y, Ozcan Z. Hindi (*Meleagris gallopavo*) böbreğinin yapısı üzerinde ışık ve elektron mikroskopik çalışmalar. Ankara Üniv Vet Fak Derg. 2005; 52(1): 149–155, doi: [10.1501/vetfak\\_0000000047](https://doi.org/10.1501/vetfak_0000000047).
- Aslan S. Üriner sistem. In: Aslan S (Ed): Kanatlı Histolojisi. Dora Basım Yayın Dağıtım, Bursa, Turkey. 2018: 85–98.
- Batah AL. Morphological and histological study for the kidneys of coot bird (*Fulica atra*). Bas J Vet Res. 2012; 11(1): 128–136, doi: [10.33762/bvetr.2012.54767](https://doi.org/10.33762/bvetr.2012.54767).
- Can M, Ozdemir D. Kaya kekliği (*Alectoris graeca*) plexus sacralis'i üzerinde makro-anatomik araştırmalar. Kafkas Univ Vet Fak Derg. 2012; 18(1): 141–146, doi: [10.9775/kvfd.2011.5226](https://doi.org/10.9775/kvfd.2011.5226).
- Casotti G, Braun E. Renal anatomy in sparrows from different environments. J Morphol. 2000; 243(3): 283–291, doi: [10.1002/\(sici\)1097-4687\(200003\)243:3<283::aid-jmor5>3.0.co;2-b](https://doi.org/10.1002/(sici)1097-4687(200003)243:3<283::aid-jmor5>3.0.co;2-b).
- Dhyaa AA, Ali FR, Azhar SK, et al. Comparative anatomical and histological features of the kidney in harrier (*Circus aeruginosus*), chicken (*Gallus domesticus*) and mallard duck (*Anas platyrhynchos*). Iraqi J Vet Sci. 2014; 38(1): 107–113.
- Elbajory SIA. Morphometric study of the adrenal gland of the adult Sudanese Chicken (*Gallus domesticus*) and Duck (*Anas platyrhynchos*). Cur Res J Biol Sci. 2012; 4: 239–241.
- Gundersen HJ, Jensen EB. The efficiency of systematic sampling in stereology and its prediction. J Microsc. 1987; 147(Pt 3): 229–263, doi: [10.1111/j.1365-2818.1987.tb02837.x](https://doi.org/10.1111/j.1365-2818.1987.tb02837.x), indexed in Pubmed: [3430576](https://pubmed.ncbi.nlm.nih.gov/3430576/).
- Gundersen HJ, Bendtsen TF, Korbo L, et al. Some new, simple and efficient stereological methods and their use in pathological research and diagnosis. APMIS. 1988; 96(5): 379–394, doi: [10.1111/j.1699-0463.1988.tb05320.x](https://doi.org/10.1111/j.1699-0463.1988.tb05320.x), indexed in Pubmed: [3288247](https://pubmed.ncbi.nlm.nih.gov/3288247/).
- Howard CV, Reed MG. Unbiased stereology, three-dimensional measurements in microscopy. BIOS Scientific Publishers, Oxford, UK 1998: 39–68.
- Humayun K, Aoyama M, Sugita S. Morphological and histological studies on the adrenal gland of the chicken (*Gallus domesticus*). J Poult Sci. 2012; 49(1): 39–45, doi: [10.2141/jpsa.011038](https://doi.org/10.2141/jpsa.011038).
- Kocamis H, Aslan S, Deprem T. Kazların böbrek yapısı üzerine histolojik ve histometrik inceleme. Kafkas Univ Vet Fak Derg. 2003; 9(2): 157–160.
- Koral Tasci S, Gulmez N, Aslan S, et al. Immunohistochemical localization of Catalase in Geese (*Anser anser*) kidney. Kafkas Univ Vet Fak Derg. 2020; 26(1): 41–46, doi: [10.9775/kvfd.2019.22152](https://doi.org/10.9775/kvfd.2019.22152).
- Mutus R. Tavuk ve bildircında böbrek arterleri. İstanbul Üniv Vet Fak Derg. 1995; 21(1): 59–67.
- Nickel R, Schummer A, Seiferle E. The anatomy of the domestic birds. 1st ed. Verlag Paul Parley, Berlin, Germany 1977: 40–61.
- Ozudogru Z, Özdemir D, Balkaya H, et al. Civcivlerde Adrenal Bezin Gelişimi Üzerine Farklı Fotoperiyotların Etkisi. Atatürk Üniv Vet Bil Derg. 2017; 12(3): 250–258, doi: [10.17094/ataunivbd.295548](https://doi.org/10.17094/ataunivbd.295548).
- Richardson KC, Wooller RD, Casotti G. The relative sizes and asymmetry of kidneys in passerine birds from Australia and North America. J Anat. 1991; 175: 181–185, indexed in Pubmed: [2050563](https://pubmed.ncbi.nlm.nih.gov/2050563/).
- Romeis B. Microscopic technique. R. Oldenburg, München, Germany 1948: 51–52.
- Warui CN. Light microscopic morphometry of the kidneys of fourteen avian species. J Anat. 1989; 162: 19–31, indexed in Pubmed: [2808116](https://pubmed.ncbi.nlm.nih.gov/2808116/).
- Wells JW, Wight PAL. The adrenal glands, In: Physiology and biochemistry of the domestic fowl. Bell DJ and Freeman GM eds. Academic Press, London 1971: 489–520.

# Bilateral inferior renal polar arteries with a high origin from the abdominal aorta

Y. Cho<sup>1</sup> , S.-P. Yoon<sup>2, 3</sup> 

<sup>1</sup>Medical Course, Jeju National University School of Medicine, Jeju, Republic of Korea

<sup>2</sup>Department of Anatomy, Jeju National University School of Medicine, Jeju, Republic of Korea

<sup>3</sup>Institute for Medical Science, Jeju National University, Jeju, Republic of Korea

[Received: 14 February 2020; Accepted: 30 March 2020]

*Bilateral multiple renal arteries are not-so-rare variations. However, inferior renal polar arteries with a high origin from the abdominal aorta have rarely been reported. We found bilateral inferior renal polar arteries with a high origin from the abdominal aorta in an 84-year-old Korean female cadaver. Two right and three left renal arteries were seen with the lowest as the main renal artery bilaterally. The highest artery crossed the main renal artery and penetrated into the inferior pole of the kidney, respectively. After dissection, each inferior polar artery could be classified as the inferior segmental branch. A further understanding on its embryogenesis might be important since variations in renal arteries are of particular interest to clinicians as well as anatomists. (Folia Morphol 2020; 80, 1: 215–218)*

**Key words:** multiple renal arteries, inferior renal polar artery, inferior segmental branches, anatomical variation, cadaver

## INTRODUCTION

The renal vascular system is extensive and has significant variability, and detailed anatomical knowledge of renovascular varieties is important for clinical and radiologic procedures. The reported incidence of multiple renal arteries is approximately 20% and varies with ethnicity ranging from 4% in a Malaysian population to 61.5% in a Brazilian population [8]. The frequency is lowest in eastern and southern Asia (from 4% to 18.4%), reported to be 13.0% in Korean. Double and triple renal arteries have been reported, with respective incidences of 18.7% and 3.0% [18], 17.4% and 0.9% [10], and 19.7% and 3.6% [19]. The incidence of bilaterality was much lower, reported in approximately one-fifth of multiple renal arteries [14].

Among these variations, the inferior renal polar arteries usually arise from the aorta or the renal artery, and much less frequently from a suprarenal, common iliac, or superior mesenteric artery [1].

The incidence of inferior renal polar arteries at an extrahilar level originating in the abdominal aorta varies between 0.6% (71/1237) [1] and 9.7% (24/250) [19]. Because the metanephros receives more new cranial branches from vessels close to it during ascent while the former lower branches are degenerated [7], incomplete degeneration of the former lower branches leads to the presence of the inferior renal polar artery below the renal artery. Therefore, the inferior renal polar arteries showing upward course have been implicated as an etiological factor in a form of hydronephrosis surgically correctable [1].

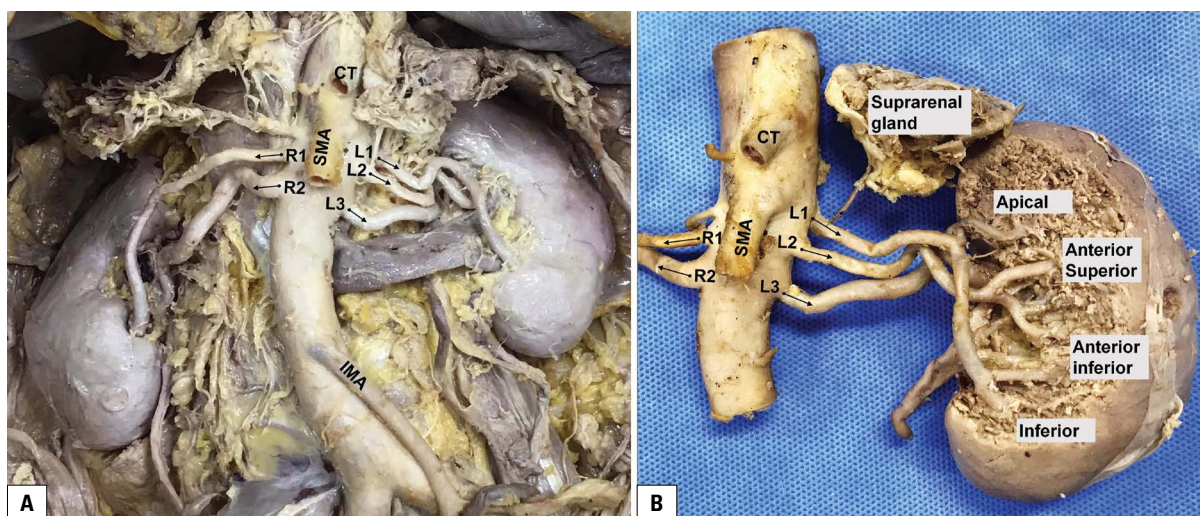
The inferior renal polar arteries with a high origin from the abdominal aorta may cross the lower renal arteries to supply the inferior pole of the kidney, which has rarely been reported to date [2, 13, 16]. Herein, we presented a case of bilateral inferior renal polar arteries originating from a high aortic position and discussed its embryological significance.

Address for correspondence: Dr. S.-P. Yoon, Department of Anatomy, Jeju National University School of Medicine, 102 Jejudaehak-ro, Jeju-Si, Jeju-Do 63243, Republic of Korea, tel: +82-64-7543823, fax: +82-64-7252593, e-mail: spyoon@jejunu.ac.kr

**Table 1.** Morphologic parameters of the bilateral multiple renal arteries. Renal segments classified into superior, anterior superior, anterior inferior, inferior, and posterior according to a previous report [19]

Variables	Distance from the bifurcation of the abdominal aorta [mm]	Vertebrae level at origin	External diameter [mm]	Segmental distribution
<b>Right</b>				
R1	95	Intervertebral space between LV 1–2	3	Inferior
R2 (main)	91	Upper half of LV 2 body	7	Apical; anterior superior; anterior inferior; posterior
<b>Left</b>				
L1	101	Intervertebral space between LV 1–2	4	Apical; anterior inferior; inferior
L2	97	Intervertebral space between LV 1–2	3	Anterior superior; anterior inferior
L3 (main)	89	Upper half of LV 2 body	5	Apical; posterior

LV — lumbar vertebrae

**Figure 1.** Photographs of bilateral inferior renal polar arteries before (A) and after (B) dissection to clarify the segmental distribution. The multiple renal arteries were designated R1 to R2 from the highest to the lowest on the right side and, similarly, L1 to L3 on the left side. The highest artery (R1 and L1) arose from above the main renal artery (R2 and L3), crossed it, and entered the inferior pole of the kidneys, respectively. Dashed arrow — left suprarenal artery; CT — coeliac trunk; IMA — inferior mesenteric artery; SMA — superior mesenteric artery.

## CASE REPORT

During routine educational dissection, we found a rare variation of bilateral inferior renal polar arteries (Fig. 1) in an 84-year-old Korean female cadaver, whose cause of death was 'cerebral infarction'.

The renal arteries were designated R1 to R2 from the highest to the lowest on the right side and, similarly, L1 to L3 on the left side, in which the lowest was the main renal artery bilaterally. We analysed the distance from the bifurcation of the abdominal aorta, the vertebral level at the origin, the external diameter, the segmental distribution, and other characteristics of each renal artery (Table 1).

On the right side (Fig. 1A), two renal arteries arose from the anterolateral aspect of the abdominal aorta. The superior additional artery (R1) arose from above the main renal artery (R2) and crossed the main renal artery anteriorly into the inferior pole of the right kidney.

On the left side (Fig. 1A), three renal arteries arose from the abdominal aorta. The superior additional artery (L1) arose from the posterolateral aspect of the abdominal aorta just below the superior mesenteric artery, and ran forward the main renal artery (L3), then divided and entered the superior and inferior pole of the left kidney, respectively. The left suprarenal

artery arose from L1 (Fig. 1B). The middle additional artery (L2) arose from the anterolateral aspect of the abdominal aorta just below the L1, ran forward the main renal artery, and entered the kidney through the hilum below the main renal artery.

## DISCUSSION

The inferior segmental artery variations of the kidney are subdivided into four types based on their origin: I — from the anterior division of the renal artery; II — from the posterior division of the renal artery, III — from the renal artery directly, and IV — from the aorta. The incidence of the inferior segmental branch arising from the aorta was approximately 2.2% (10/459) [3], in which most of the inferior segmental branches arose below the renal artery from the aorta. Meanwhile, the incidence of the inferior segmental branches detached from the superior renal artery was 1.6% (4/250) [19]. However, the authors did not mention whether the superior renal artery directly originated from the aorta or not. Only a few reports have been published on the inferior renal polar arteries with a high origin from the abdominal aorta [2, 13, 16]. The reported inferior renal polar arteries with a high origin from the abdominal aorta were right-sided, arose above the main renal artery from the aorta, and entered just below the renal hilum, but clear explanations were lacking. The present case, the bilateral inferior segmental branch from the inferior renal polar arteries with a high origin from the abdominal aorta, might be the first report. A very similar case was reported in bilateral ectopic kidney in the pelvic cavity [7].

Nine pairs of arteries, the cranial (the 1<sup>st</sup> and the 2<sup>nd</sup> pair), middle (the 3<sup>rd</sup> to the 5<sup>th</sup> pair), and the caudal (the 6<sup>th</sup> to the 9<sup>th</sup> pair), form a vascular network from the lateral aorta, the so-called rete arteriosum urogenitale between 6<sup>th</sup> cervical and 3<sup>rd</sup> lumbar vertebrae, and supply the mesonephros, metanephros, gonads, and the suprarenal glands [5]. The differing origins and/or additional numbers of renal arteries around the renal hilum are usually explained by this 'ladder theory'. Insufficient degeneration of mesonephric arteries leads to the presence of more than one renal artery, with or without different origins. We agree with the previous report on the bilateral multiple renal arteries, and attempted to suggest a feasible explanation for the present case since the reason why the inferior renal polar arteries develop with a high origin from the abdominal aorta is not known.

The existence of the inferior renal polar arteries with a high origin from the abdominal aorta could be explained by the persistence of a mesonephric artery from the cranial part with a longer oblique course to reach the lower pole of the kidneys as suggested in the case of high-positioned gonadal artery [4]. As in the high-positioned gonadal artery, an extremely high-positioned inferior renal polar artery was also reported with a thoracic origin at the lower thoracic vertebrae [6, 15]. Compared to normal renal arteries, the ectopic renal arteries arose more posteriorly or posterolaterally in origin from the aorta [7]. In the present case, L1 arose from the posterolateral aspect of the aorta and supplied the left kidney as the apical, anterior inferior and inferior segments, which might reinforce the previous hypotheses [4, 7].

Due to the very complex embryogenesis of the kidneys [8, 9], renal vascularisation variants are not uncommon, which is primarily important in surgery, nephrology, and radiology. In any surgical and interventional procedures, including renal transplants, aneurysmorrhaphy, and other vascular reconstructions, unawareness of the presence of multiple renal arteries may result in a fatal outcome. The inferior renal polar artery with a high origin from the abdominal aorta showed a narrow calibre which has suggested as an etiological factor of renovascular hypertension [2]. Although the mean renal artery diameter found in cadavers casted with synthetic resin (4.87 mm) was slightly less than that reported in angiographic studies (5.9 mm) [17], the diameter of multiple renal arteries was significantly smaller than when a single renal artery was present [11] and the presence of a supernumerary renal artery should be predicted when the main renal artery has a luminal diameter less than 4.15 mm in a cadaveric study [17]. Recently, the sum of the luminal areas of smaller, additional renal vessels needs to be equal to or a little higher than that of a single renal artery to compensate for based on the renal-aortic ratio [12]. In the present case, the right main renal artery was thicker than the left one, and more additional arteries on left side were expected, as suggested.

## CONCLUSIONS

Taken together, we clearly showed bilateral inferior renal polar arteries with a high origin from the abdominal aorta for the first time based on embryological explanation. The renal artery presents a variety of spectra in morphological representations of num-

bers, length, diameter, and branching level, which is extremely important as it enables efficient clinical interventions and reduces the risk of complications. Because the renal artery is an end artery, a deeper understanding on the renovascular development is important to clinicians as well as anatomists.

### Acknowledgements

This research was supported by the 2020 scientific promotion program funded by Jeju National University.

### REFERENCES

- Bergman RA, Afifi AK, Miyachi R. Illustrated encyclopedia of Human Anatomic Variation: Opus II: Cardiovascular System: Arteries: Abdomen: Variations in Branches of Celiac Trunk. <https://www.anatomyatlases.org/AnatomicVariants/Cardiovascular/Text/Arteries/RenalInferiorPolar.shtml> (Cited Jan 28, 2020).
- Chan PL, Tan FH. Renin dependent hypertension caused by accessory renal arteries. *Clin Hypertens*. 2018; 24: 15, doi: [10.1186/s40885-018-0100-x](https://doi.org/10.1186/s40885-018-0100-x), indexed in Pubmed: [30410790](https://pubmed.ncbi.nlm.nih.gov/30410790/).
- Chandragirish S, Nanjiah CM, Shirur SY, et al. Study on variations of inferior segmental branch of renal artery. *Int J Anat Res*. 2014; 2(4): 716–719, doi: [10.16965/ijar.2014.534](https://doi.org/10.16965/ijar.2014.534).
- Çiçekcibaşı AE, Salbacak A, Seker M, et al. The origin of gonadal arteries in human fetuses: anatomical variations. *Ann Anat*. 2002; 184(3): 275–279, doi: [10.1016/S0940-9602\(02\)80126-1](https://doi.org/10.1016/S0940-9602(02)80126-1), indexed in Pubmed: [12056759](https://pubmed.ncbi.nlm.nih.gov/12056759/).
- Felix W. The development of the urogenital organs. In: Keibel F, Mall FP eds. *Manual of human embryology*. J.B. Lippincott Company, Philadelphia 1912: 752–880.
- Gadabanahalli K, Bhat V. Thoracic origin of single right renal artery: some interesting facets. *Int J Angiol*. 2017; 26(4): 264–266, doi: [10.1055/s-0037-1604328](https://doi.org/10.1055/s-0037-1604328), indexed in Pubmed: [29142495](https://pubmed.ncbi.nlm.nih.gov/29142495/).
- Gokalp G, Hakyemez B, Erdogan C. Vascular anomaly in bilateral ectopic kidney: a case report. *Cases J*. 2010; 3: 5, doi: [10.1186/1757-1626-3-5](https://doi.org/10.1186/1757-1626-3-5), indexed in Pubmed: [20076808](https://pubmed.ncbi.nlm.nih.gov/20076808/).
- Gulas E, Wysiadecki G, Cecot T, et al. Accessory (multiple) renal arteries - Differences in frequency according to population, visualizing techniques and stage of morphological development. *Vascular*. 2016; 24(5): 531–537, doi: [10.1177/1708538116631223](https://doi.org/10.1177/1708538116631223), indexed in Pubmed: [26945775](https://pubmed.ncbi.nlm.nih.gov/26945775/).
- Gulas E, Wysiadecki G, Szymański J, et al. Morphological and clinical aspects of the occurrence of accessory (multiple) renal arteries. *Arch Med Sci*. 2018; 14(2): 442–453, doi: [10.5114/aoms.2015.55203](https://doi.org/10.5114/aoms.2015.55203), indexed in Pubmed: [29593819](https://pubmed.ncbi.nlm.nih.gov/29593819/).
- Khamanarong K, Prachaney P, Utravichien A, et al. Anatomy of renal arterial supply. *Clin Anat*. 2004; 17(4): 334–336, doi: [10.1002/ca.10236](https://doi.org/10.1002/ca.10236), indexed in Pubmed: [15108340](https://pubmed.ncbi.nlm.nih.gov/15108340/).
- Majos M, Stefańczyk L, Szemraj-Rogucka Z, et al. Does the type of renal artery anatomic variant determine the diameter of the main vessel supplying a kidney? A study based on CT data with a particular focus on the presence of multiple renal arteries. *Surg Radiol Anat*. 2018; 40(4): 381–388, doi: [10.1007/s00276-017-1930-z](https://doi.org/10.1007/s00276-017-1930-z), indexed in Pubmed: [28980056](https://pubmed.ncbi.nlm.nih.gov/28980056/).
- Majos M, Polguy M, Stefańczyk L, et al. Renal-aortic ratio as an objective measure of renal artery diameter a computed tomography angiography study. *BMC Cardiovasc Disord*. 2019; 19(1): 181, doi: [10.1186/s12872-019-1163-7](https://doi.org/10.1186/s12872-019-1163-7), indexed in Pubmed: [31362712](https://pubmed.ncbi.nlm.nih.gov/31362712/).
- Mantraratnam PP, Bhattam NR. A study on accessory renal arteries in cadavers and its clinical correlation. *Int J Health Sci Res*. 2016; 6: 148–150.
- Ozkan U, Oğuzkurt L, Tercan F, et al. Renal artery origins and variations: angiographic evaluation of 855 consecutive patients. *Diagn Interv Radiol*. 2006; 12(4): 183–186, indexed in Pubmed: [17160802](https://pubmed.ncbi.nlm.nih.gov/17160802/).
- Patel K, Gandhi S, Modi P. Unusual origin of right renal artery: a report of two cases. *J Clin Diagn Res*. 2016; 10(5): TJ03–TJ04, doi: [10.7860/JCDR/2016/18428.7823](https://doi.org/10.7860/JCDR/2016/18428.7823), indexed in Pubmed: [27437328](https://pubmed.ncbi.nlm.nih.gov/27437328/).
- Ramesh Rao T, Shetty P, Rao S. Unusual course of accessory renal artery and its clinical significance: a case report. *Int J Anat Var*. 2011; 4: 197–199.
- Saldarriaga B, Pinto S, Ballesteros L. Morphological expression of the renal artery: a direct anatomical study in a colombian half-caste population. *Int J Morphol*. 2008; 26(1), doi: [10.4067/s0717-95022008000100005](https://doi.org/10.4067/s0717-95022008000100005).
- Vilhova I, Kryvko YY, Maciejewski R. The radioanatomical research of plural renal arteries. *Folia Morphol*. 2001; 60(4): 337–341, indexed in Pubmed: [11770346](https://pubmed.ncbi.nlm.nih.gov/11770346/).
- Zăhoi DE, Sztika D, Dăescu E. Morphological variability of arterial sources of the renal polar parenchyma and its clinical importance. *Rom J Morphol Embryol*. 2015; 56(4): 1403–1409, indexed in Pubmed: [26743287](https://pubmed.ncbi.nlm.nih.gov/26743287/).

# The sphenozygomatic fissure

M.C. Rusu<sup>1</sup> , F. Pop<sup>2</sup>, M. Săndulescu<sup>3</sup>

<sup>1</sup>Division of Anatomy, Faculty of Dental Medicine, “Carol Davila” University of Medicine and Pharmacy, Bucharest, Romania

<sup>2</sup>Division of Pathologic Anatomy, Faculty of Medicine, “Carol Davila” University of Medicine and Pharmacy, Bucharest, Romania

<sup>3</sup>Division of Implant Prosthetic Rehabilitation, Faculty of Dental Medicine, “Carol Davila” University of Medicine and Pharmacy, Bucharest, Romania

[Received: 3 January 2020; Accepted: 3 February 2020]

*The lateral (temporal) wall of the orbit separates it from the temporal fossa and the anterior part of the temporal muscle. Within this wall, the sphenozygomatic suture joins the greater wing of the sphenoid bone and the zygomatic bone. We retrospectively documented in cone-beam computed tomography the anatomy of the orbit in a 56-year-old female and we found a previously unreported anatomic variant. The greater wing of the sphenoid bone and the zygomatic bone were separated, bilaterally, by a large unossified space which we termed the sphenozygomatic fissure. This was merged inferiorly with the inferior orbital fissure. A possible imbalanced mechanism of membranous ossification of both the zygomatic bone and the orbital surface of the greater wing could be speculated as a possible cause for such sphenozygomatic fissure. This previously undocumented anatomic variant is of high clinical relevance, since it may allow orbital fat to herniate (or bulge) toward the temporal fossa, it may be easily damaged during minor trauma and it should be carefully approached during the surgery of the orbit through the lateral wall. (Folia Morphol. 2021; 80, 1: 219–221)*

**Key words:** orbit, cone-beam computed tomography, temporal fossa, orbital hernia, hiatus

## INTRODUCTION

The orbit is a 4-sided pyramid with walls that are built-up by either viscerocranial, or neurocranial bones [7]. The sphenozygomatic suture connects the greater wing of the sphenoid bone and the zygomatic bone on the lateral wall of the orbit [7].

The development of the orbit at the junction between the cranial membranous bones and the basal endochondral bones is complex [3]. Orbital bones initially form as a network of tiny bony ossification zones centrally, separated by large non-ossified areas [10]. As ossification proceeds, separate ossification zones gradually approach each other leaving unossified spaces in between [10].

Various cranial abnormalities are caused by a cessation of the development of specific structures at specific times. For example, defects in the apposition of the junctions of embryological fissures lead to clefting syndromes [3].

The inferior orbital fissure (IOF) was described by Lang (2011) [6]: it is wider laterally and narrower medially, being bordered superiorly by the greater sphenoidal wing and inferiorly by the maxillary bone. According to Lang’s description, further quoted in Bergman’s Comprehensive Encyclopedia of Human Anatomic Variation [2], the anterolateral segment of the IOF may be formed by either the zygomatic bone (50%) or the sphenoid and maxillary bones (50%). In rare

---

Address for correspondence: M.C. Rusu, MD, PhD (Med.), PhD (Biol.), Dr. hab., Prof., “Carol Davila” University of Medicine and Pharmacy, 8 Eroilor Sanitari Blvd., RO-050474, Bucharest, Romania, tel: +40722363705, e-mail: anatomon@gmail.com

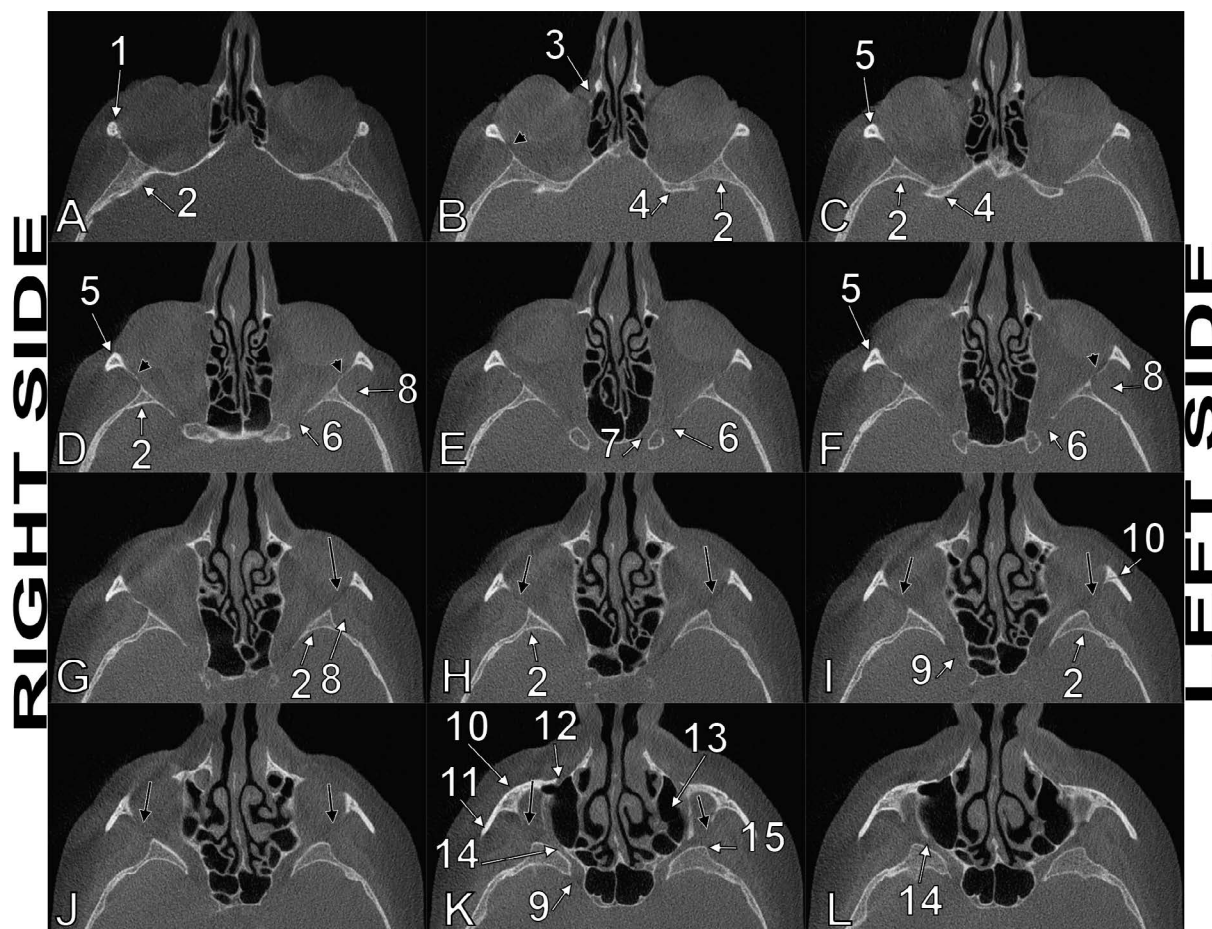


**Figure 1.** Axial slices through the orbits, superior-to-inferior series (A–L); 1 — zygomatic process of the frontal bone; 2 — greater wing of the sphenoid bone; 3 — lacrimal fossa; 4 — lesser wing of the sphenoid bone; 5 — frontal process of the zygomatic bone; 6 — superior orbital fissure; 7 — optic canal; 8 — deep anterior portion of the temporal muscle; 9 — foramen rotundum; 10 — zygomatic bone; 11 — temporal process of the zygomatic bone; 12 — infraorbital foramen; 13 — maxillary sinus; 14 — inferior orbital fissure; 15 — infratemporal spine (sphenoidal tubercle). The lateral walls of each orbit are superiorly thinned (black arrowheads) and inferiorly dehiscent (black arrows) at the sphenozygomatic junction (sphenozygomatic fissure).

cases, especially in older persons, the antero-lateral segment of the IOF may be thinned, which allows the orbital fat to herniate toward the temporal fossa [6]. Anatomical restrictions for such “fat hernia” relate to the deepest portion of the temporal muscle that originates, occasionally, from the periorbital region and the pericranium covering the orbital muscles thus forming the closing plate of the IOF [6]. This single previous report on the possibilities of variation of the IOF does not cover, however, the possibility of a superior extension of the IOF, as a sphenozygomatic fissure, or hiatus, within the lateral orbit wall.

### CASE REPORT

A retrospective cone-beam computed tomography (CBCT) study of the archived files of a 56-year-old female patient was performed.

The subject had been scanned using a CBCT machine — iCat (Imaging Sciences International), the DICOM file being further documented with the Planmeca Romexis Viewer 3.5.0.R software, according to a previously detailed study protocol [9]. We evaluated the orbit walls in all the three anatomical planes, as well as the three-dimensional volume renderisations. The orbit floor was fitted in the horizontal plane. Relevant anatomical features were exported as image files. The patient has given written informed consent for all medical data to be used for research, provided they are anonymised.

The patient had the temporal walls of both orbits largely incomplete on the entire height, this being accurately documented on serial axial slices (Fig. 1). The lack of bone was identified at the junction of the greater sphenoidal wing with the zygomatic bone,



thus in the anatomical situs of the sphenozygomatic suture. We termed sphenozygomatic fissure the dehiscence of the lateral orbital wall. We also observed it was continuous with the IOF, thus extending the IOF upwards, between the orbit and the temporal fossa. The anterior part of the temporal muscle was located immediately posterior to that sphenozygomatic fissure and was inserted onto the pericranium obturating the fissure. We did not find any evidence of tissue hernias from the orbit into the temporal fossa.

## DISCUSSION AND CONCLUSIONS

Different imaging techniques are currently used to study the skull bones; however, CBCT images are superior over others for the bony anatomy and muscle attachments [5, 8]. Therefore, the CBCT method is reliable enough to assess this possible, but previously unreported, anatomic variant of the temporal wall of the orbit — the sphenozygomatic fissure.

This bilateral anatomical “defect”, or cleft, of the orbit can predispose the patient to fractures of the orbital wall, even after a moderate trauma, or change the fracture pattern, as it changes the resistance structure of the cranium. Moreover, it is likely that orbital fat hernias could enter the temporal fossa not only through the IOF, but also via such a sphenozygomatic fissure, which is a wider passage. Therefore, if the anterior section of the temporal fossa is approached, extreme traction of orbital fat hernias should be avoided [6]. These large sphenozygomatic defects of the temporal wall of the orbit recommend delicate manoeuvres during lateral orbital approaches when the surgeon uses a pure zygomatic osteotomy [11]. Also, as the zygomatic bone is commonly involved in facial trauma, zygomatic fractures with displacement could lead to blow-in orbital fractures, especially when the temporal fossa anterior wall is thinned or incomplete, as in this case.



The bones of the chondrocranium usually have endochondral ossification centres, while the facial bones are formed by membranous ossification [12]; this however does not apply to the greater wing of the sphenoid bone (alisphenoid), which has both intramembranous and endochondral components [4]. The intramembranous part of the alisphenoid replaces the orbital cartilage [4], thus participating in the lateral wall of the orbit. While the ossification of the zygomatic bone starts in weeks 23–31, that of the greater wing of the sphenoid bone begins later, in weeks 55–68 [10]. Therefore, an incomplete

membranous ossification of the temporal wall of the may explain the formation of these bilateral sphenozygomatic fissures. This mechanism could mirror the congenital anomalies of the sphenoid bone that are likely to occur at the fusion planes of the ossified cartilaginous precursors during development [1].

## REFERENCES

1. Bendersky DC, Landriel FA, Ajler PM, et al. Sternberg's canal as a cause of encephalocele within the lateral recess of the sphenoid sinus: a report of two cases. *Surg Neurol Int.* 2011; 2: 171, doi: [10.4103/2152-7806.90034](https://doi.org/10.4103/2152-7806.90034), indexed in Pubmed: [22145089](https://pubmed.ncbi.nlm.nih.gov/22145089/).
2. Bergman RA, Tubbs RS, Shoja MM, Loukas M. Bergman's comprehensive encyclopedia of human anatomic variation. John Wiley & Sons, Hoboken, New Jersey 2016.
3. Dollfus H, Verloes A. Dysmorphology and the orbital region: a practical clinical approach. *Survey Ophthalmology.* 2004; 49(6): 547–561, doi: [10.1016/s0039-6257\(04\)00133-x](https://doi.org/10.1016/s0039-6257(04)00133-x).
4. Gray H, Standring S, Anand N, Birch R, Collins P, Crossman A, Gleeson M, Jawaheer G, Smith AL, Spratt JD, Stringer MD, Tubbs SR, Tunstall R, Wein AJ, Wigley CB. *Gray's anatomy: The anatomical basis of clinical practice.* 41 ed. Elsevier, London, UK 2016.
5. Hegde S, Praveen B, Shetty S. Morphological and radiological variations of mandibular condyles in health and diseases: a systematic review. *Dentistry.* 2013; 3(1), doi: [10.4172/2161-1122.1000154](https://doi.org/10.4172/2161-1122.1000154).
6. Lang J. Skull base and related structures: Atlas of clinical anatomy. Schattauer, Verlag 2001.
7. Maliborski A, Różycki R. Diagnostic imaging of the nasolacrimal drainage system. Part I. Radiological anatomy of lacrimal pathways. *Physiology of tear secretion and tear outflow. Med Sci Monit.* 2014; 20: 628–638, doi: [10.12659/MSM.890098](https://doi.org/10.12659/MSM.890098), indexed in Pubmed: [24743297](https://pubmed.ncbi.nlm.nih.gov/24743297/).
8. Rusu MC, Dincă D. Accessory pterygoid fovea of the human mandibular condyle. *Cranio.* 2019 [Epub ahead of print]: 1–5, doi: [10.1080/08869634.2019.1635674](https://doi.org/10.1080/08869634.2019.1635674), indexed in Pubmed: [31241001](https://pubmed.ncbi.nlm.nih.gov/31241001/).
9. Rusu MC, Sava CJ, Ilie AC, et al. Agger nasi cells versus lacrimal cells and uncinata bullae in cone-beam computed tomography. *Ear Nose Throat J.* 2019; 98(6): 334–339, doi: [10.1177/0145561319840836](https://doi.org/10.1177/0145561319840836), indexed in Pubmed: [31012345](https://pubmed.ncbi.nlm.nih.gov/31012345/).
10. Tawfik HA, Dutton JJ. Embryologic and fetal development of the human orbit. *Ophthalmic Plast Reconstr Surg.* 2018; 34(5): 405–421, doi: [10.1097/IOP.0000000000001172](https://doi.org/10.1097/IOP.0000000000001172), indexed in Pubmed: [30134385](https://pubmed.ncbi.nlm.nih.gov/30134385/).
11. Villalonga JF, Sáenz A, Revuelta Barbero JM, et al. Surgical anatomy of the orbit. A systematic and clear study of a complex structure. *Neurocirugia (Astur).* 2019; 30(6): 259–267, doi: [10.1016/j.neucir.2019.04.003](https://doi.org/10.1016/j.neucir.2019.04.003), indexed in Pubmed: [31221573](https://pubmed.ncbi.nlm.nih.gov/31221573/).
12. Zhang Q, Wang H, Udagawa J, et al. Morphological and morphometric study on sphenoid and basioccipital ossification in normal human fetuses. *Congenit Anom (Kyoto).* 2011; 51(3): 138–148, doi: [10.1111/j.1741-4520.2011.00322.x](https://doi.org/10.1111/j.1741-4520.2011.00322.x), indexed in Pubmed: [21848997](https://pubmed.ncbi.nlm.nih.gov/21848997/).

# A case of individual variation of the rhomboid muscles

M. Ulkir<sup>1</sup> , M.F. Sargon<sup>2</sup> 

<sup>1</sup>Department of Anatomy, Faculty of Medicine, Hacettepe University, Ankara, Turkey

<sup>2</sup>Department of Anatomy, Faculty of Medicine, Lokman Hekim University, Ankara, Turkey

[Received: 9 January 2020; Accepted: 1 February 2020]

*During the routine gross anatomic dissection of a Turkish male cadaver; a variation of rhomboid muscles was observed on the left side. There were two rhomboid minors and three rhomboid majors coursing under the trapezius muscle. The origins of the upper and lower rhomboid minor muscles were C5, C6 and C7 vertebrae, respectively. Their insertions were to medial border of scapula, to upper part and to lower part of the spine of scapula, respectively. The origins of the upper, middle and lower rhomboid majors were C7, T1–T3 and T4–T5 vertebrae, respectively. Their insertions were to the 2/3 most inferior part of the medial border of scapula, from superior to inferior in sequence. In the examination of the literature, we could not observe such a variation of these muscles. In surgical procedures these types of variations have a clinical importance for intrathoracic muscle flap transfers and in cases with the paralysis of trapezius muscle. (Folia Morphol 2021; 80, 1: 222–224)*

**Key words:** dissection, anatomy, cadaver

## INTRODUCTION

The rhomboid minor and rhomboid major muscles are inferior to levator scapulae muscle. Rhomboid minor is a small, cylindrical muscle and rhomboid major is a quadrilateral sheet of muscle [8]. These two muscles work together to retract or pull the scapula towards the vertebral column. With other muscles; they may also rotate lateral aspect of the scapula inferiorly [1]. In the literature; there are only a few reports related with the variation of these two muscles [4, 5, 9]. In the present case; to our knowledge, we report a unique variation of these two muscles on the left side of a cadaver.

## CASE REPORT

During the routine gross anatomic dissection of the superficial back muscles of a 67-year-old Turkish male cadaver, a variation of rhomboid muscles was

observed on the left side. There were two rhomboid minors and three rhomboid majors coursing under the trapezius muscle. The origins of the upper and lower rhomboid minor muscles were C5, C6 and C7 vertebrae, respectively. Their insertions were to medial border of scapula, to upper part and to lower part of the spine of scapula, respectively. The origins of the upper, middle and lower rhomboid majors were C7, T1–T3 and T4–T5 vertebrae, respectively. Their insertions were to the 2/3 most inferior part of the medial border of scapula, from superior to inferior in sequence. In the examination of the literature, we could not observe such a variation of these muscles. In the cadaver, the left superficial back muscles, the right half of the hemithorax and right superficial back muscles were normal in every aspect (Fig. 1). There was any abnormality on the cadaver and it was a healthy specimen.



**Figure 1.** Variation of rhomboid muscles; 1, 2 — rhomboid minor muscles; a, b, c — rhomboid major muscles.

## DISCUSSION

The variations of the rhomboid muscles are very rare. During the superficial back dissection of a 72-year-old male cadaver, Jeleu and Landzhov [4] observed an aberrant muscle bilaterally below the lower border of the rhomboideus major. The unusual muscle arose by a thin aponeurosis from the spinous process of the mid-thoracic vertebrae and was attached laterally to the lowest part of the medial border of the scapula [4]. In the study of Mori [5], a muscular slip called “musculus rhomboideus minus” was described in 11–14% of the Japanese population. This muscle was originated from the spinous process above the latissimus dorsi origin, was coursing laterally and gradually disappearing or passing into the fascia of the teres major muscle [5]. Von Haffner [9] observed a small muscle on the right side of a cadaver, stretched between the sixth thoracic vertebra and the inferior angle of the scapula. The author named this muscle as “musculus rhomboideus minimus”. Additionally, in his case, bilateral incomplete agenesis of the trapezius muscles was present [9]. In another study, Saberi et al. [7] investigated the embryonic origins of the rhomboid muscles by following the derivatives of medial and lateral somite halves using

quail-chick chimeras. Their results showed that the rhomboid muscles were made up of cells derived mainly from the lateral portion of the somite [7].

In animals: the rhomboid muscles always present cervical and thoracic parts and in carnivores there is an additional, capital part. Rhomboid muscles are innervated from the brachial plexus in the dog, but in some species they are also innervated by dorsal branches of local spinal nerves [2].

In the examination of the literature, our variation is unique and is clinically important. When found during surgical procedures, it can be used together with the usual rhomboid muscles for intrathoracic muscle flap transfers [3]. Additionally, the transfer of the rhomboid muscles to the infraspinous fossa (the Eden-Lange procedure) is important in cases with the paralysis of the trapezius muscle [6].

## CONCLUSIONS

In the literature, variations of rhomboid muscles are scarce. The present case report describes a variation of the rhomboid muscles. In surgical procedures these types of variations have a clinical importance for intrathoracic muscle flap transfers and in cases with the paralysis of trapezius muscle.

## Acknowledgements

The authors of this case report declare no relationships with any companies, whose products or services may be related to the subject matter of the article. No complex statistical methods were necessary for this paper. The cadaver belongs to the Hacettepe University, Faculty of Medicine, Department of Anatomy, Turkey.

## REFERENCES

1. Chang KV, Wu WT, Mezian K, et al. Sonoanatomy of muscles attaching to the medial scapular border (levator scapulae, rhomboid minor, and serratus anterior) revisited. *Am J Phys Med Rehabil.* 2019; 98(7): e79–e80, doi: [10.1097/PHM.0000000000001136](https://doi.org/10.1097/PHM.0000000000001136), indexed in Pubmed: [30640725](https://pubmed.ncbi.nlm.nih.gov/30640725/).
2. Dyce KM, Sack WO, Wensing CJG. *Textbook of Veterinary Anatomy.* 4. ed. Saunders 2009: p. 84.
3. Grima R, Krassas A, Bagan P, et al. Treatment of complicated pulmonary aspergillomas with cavernostomy and muscle flap: interest of concomitant limited thoracoplasty. *Eur J Cardiothorac Surg.* 2009; 36(5): 910–913, doi: [10.1016/j.ejcts.2009.05.007](https://doi.org/10.1016/j.ejcts.2009.05.007), indexed in Pubmed: [19595606](https://pubmed.ncbi.nlm.nih.gov/19595606/).
4. Jeleu L, Landzhov B. A rare muscular variation: the third of the rhomboids. *Anatomy.* 2013; 6-7: 63–64, doi: [10.2399/ana.11.218](https://doi.org/10.2399/ana.11.218).
5. Mori M. Statistics on the musculature of the Japanese. *Okajimas Folia Anat Jpn.* 1964; 40: 195–300, doi: [10.2535/ofaj1936.40.3\\_195](https://doi.org/10.2535/ofaj1936.40.3_195), indexed in Pubmed: [14213705](https://pubmed.ncbi.nlm.nih.gov/14213705/).

6. Romero J, Gerber C. Levator scapulae and rhomboid transfer for paralysis of trapezius. The Eden-Lange procedure. *J Bone Joint Surg Br.* 2003; 85(8): 1141–1145, doi: [10.1302/0301-620x.85b8.14179](https://doi.org/10.1302/0301-620x.85b8.14179), indexed in Pubmed: [14653596](https://pubmed.ncbi.nlm.nih.gov/14653596/).
7. Saberi M, Pu Q, Valasek P, et al. The hypaxial origin of the epaxially located rhomboid muscles. *Ann Anat.* 2017; 214: 15–20, doi: [10.1016/j.aanat.2017.05.009](https://doi.org/10.1016/j.aanat.2017.05.009), indexed in Pubmed: [28655569](https://pubmed.ncbi.nlm.nih.gov/28655569/).
8. Standring S. *Gray's Anatomy*. 41. ed. Elsevier 2016: p. 818.
9. Von Haffner H. Eine seltene doppelseitige Anomalie des Trapezius. *Internationale Monatsschrift für Anatomie und Physiologie.* 1903; 20: 213–218 (as cited by Jelev L, Landzhov B. A rare muscular variation: the third of the rhomboids. *Anatomy* 2013; 6-7: 63–64, doi: [10.2399/ana.11.218](https://doi.org/10.2399/ana.11.218)).

<b>Age-related morphological peculiarities of human testes .....</b>	<b>122</b>
K. Lasiene, D. Gasiliunas, N. Juodziukyniene, A. Dabuzinskiene, A. Vitkus, B. Zilaitiene	
<b>Histomorphometric evaluation of tibial subchondral bone after moderate running in male and female Wistar rats.....</b>	<b>127</b>
M.N. Nazem, M. Sahebozamani, R. Mosavian Naeini, S.M. Sajjadian	
<b>Arthrogenic human synovial cysts: immunohistochemical profile of interleukin-1beta, interleukin-6, tumour necrosis factor-alpha .....</b>	<b>133</b>
S. Taurone, M.T. Santarelli, C. De Ponte, L. Bardella, M. Ralli, C. Morselli, A. Nicolai, A. Greco, A. Ferretti, M. Artico	
<b>The effect of N-acetylcysteine on the sensory retina of male albino rats exposed prenatally to cypermethrin .....</b>	<b>140</b>
N. Mohey Issa, M.A. Al-Gholam	
<b>Ameliorating effect of pomegranate peel extract supplement against type 1 diabetes-induced hepatic changes in the rat: biochemical, morphological and ultrastructural microscopic studies .....</b>	<b>149</b>
K.A.J. Faddladdeen	
<b>Effect of vitamin B17 on experimentally induced colon cancer in adult male albino rat.....</b>	<b>158</b>
W. Badr El-Kholy, S.A. Abdel-Rahman, F.E.-N. Abd El-Hady El-Safti, N. Mohey Issa	
<b>Applied anatomy and clinical significance of the maxillofacial and mandibular regions of the barking deer (<i>Muntiacus muntjak</i>) and sambar deer (<i>Rusa unicolor</i>) .....</b>	<b>170</b>
K. Keneisenuo, O.P. Choudhary, P. Priyanka, P.C. Kalita, A. Kalita, P.J. Doley, J.K. Chaudhary	
<b>Evaluation of the middle ear in water buffaloes (<i>Bubalus bubalis</i>) by gross anatomy and cone-beam computed tomography .....</b>	<b>177</b>
J. Nourinezhad, M. Abedini, M.M. Shamsi, A. Dabbaghi, M. Janeczek	
<b>Morphometric analysis and three-dimensional computed tomography reconstruction of the long bones of femoral and crural regions in Van cats.....</b>	<b>186</b>
O. Yilmaz, İ. Demircioğlu	
<b>Morphometric profile of tendocalcaneus of South Africans of European ancestry using a cadaveric approach .....</b>	<b>196</b>
S. Latiff, M.A. Bidmos, O.I. Olateju	
<b>Macroanatomical and histological study of the structure of intercornual gland in Abaza (<i>Capra Aegagrus</i>) and Gurcu (<i>Capra Falconeri</i>) goats breeds .....</b>	<b>204</b>
S. Dalga, S. İlhan Aksu, K. Aslan, T. Deprem	
<b>A stereological study of the renal and adrenal glandular structure of red-legged partridge (<i>Alectoris chukar</i>) .....</b>	<b>210</b>
N. Colcimen, G. Cakmak	
<b>CASE REPORTS</b>	
<b>Bilateral inferior renal polar arteries with a high origin from the abdominal aorta .....</b>	<b>215</b>
Y. Cho, S.-P. Yoon	
<b>The sphenozygomatic fissure.....</b>	<b>219</b>
M.C. Rusu, F. Pop, M. Săndulescu	
<b>A case of individual variation of the rhomboid muscles .....</b>	<b>222</b>
M. Ulkir, M.F. Sargon	

## CONTENTS

### REVIEW ARTICLES

- Vertebral artery variations revised: origin, course, branches and embryonic development** ..... 1  
 E.-P. Magklara, E.-T. Pantelia, E. Solia, E. Panagouli, M. Piagkou, A. Mazarakis, P. Skandalakis,  
 T. Troupis, D. Filippou
- The morphology and application of stem cells in digestive system surgery** ..... 13  
 M. Pucufek, J. Baj, P. Portincasa, M. Sitarz, C. Grochowski, E. Radzikowska

### ORIGINAL ARTICLES

- Course variability of the atlantic (V3) segment of vertebral artery: anatomical study with clinical implications** ..... 20  
 M.K. Ciołkowski, B. Ciszek
- Stereological analysis of hippocampus in rat treated with chemotherapeutic agent oxaliplatin** ..... 26  
 J. Sadeghinezhad, I. Amrein
- Quantitative analysis of healthy olfactory sulcus depth, olfactory tract length and olfactory bulb volume in the paediatric population: a magnetic resonance study** ..... 33  
 S. Sahin, A.H. Baykan, E. Altunisik, C.A. Vural, F.D. Sahin, I. Inan
- Tractography-guided surgery of brain tumours: what is the best method to outline the corticospinal tract?** ..... 40  
 T. Szmuda, S. Kierońska, S. Ali, P. Słoniewski, M. Pacholski, J. Dzierżanowski, A. Sabisz, E. Szurowska
- Comparison of colour difference formulas to best distinguish resected areas of malignant brain tumours from their background using 5-aminolevulinic acid fluorescence** ..... 47  
 T. Szmuda, S. Ali, P. Słoniewski
- The craniofacial indicators of aggression: a cross-sectional multiparametric anthropometry study** ..... 55  
 B. Gülçen, İ.C. Pelin, E.B. Özener
- Anatomical study on branching pattern and variations of orbital segment of the oculomotor nerve** ..... 63  
 R. Haładaj, Ł. Olewnik, M. Polgaj
- Anatomy of the superior hypogastric plexus and its application in nerve-sparing paraortic lymphadenectomy** ..... 70  
 H. Kim, Y.S. Nam, U.-Y. Lee, I.-B. Kim, Y.-S. Kim
- The terminal branch of the posterior interosseous nerve: an anatomic and histologic study** ..... 76  
 T. Bonczar, J.A. Walocha, M. Bonczar, E. Mizia, M. Koziej, P. Piekos, M. Kujdowicz
- Assessing the innervation of the dorsal wrist capsule using modified Sihler's staining** ..... 81  
 T. Bonczar, J.A. Walocha, M. Bonczar, E. Mizia, J. Filipowska
- The variations and degenerative changes of sacroiliac joints in asymptomatic adults** ..... 87  
 Ö.F. Cihan, M. Karabulut, V. Kiliçoğlu, N. Yavuz
- Variations in the morphology of stylomastoid foramen: a possible solution to the conundrum of unexplained cases of Bell's palsy** ..... 97  
 S.K. Ghosh, R.K. Narayan
- The position of a duodenal diverticulum in the area of the major duodenal papilla and its potential clinical implications** ..... 106  
 E. Jakubczyk, M. Pazurek, A. Mokrowiecka, B. Woźniak, E. Małecka-Panas, M. Podgórski, M. Polgaj, M. Topol
- Coeliac trunk and its anatomic variations: a cadaveric study** ..... 114  
 A. Juszcak, A. Mazurek, J.A. Walocha, A. Pasternak



**INDEXED in:** BIOSIS Previews, CAS, CINAHL, CrossRef, Dental Abstracts, EBSCO, Elsevier BIOBASE, EMBIOLOGY, FMJ, Google Scholar, Index Copernicus (154.80), Index Medicus/MEDLINE, Index Scholar, Ministry of Science and Higher Education (70), NCBI/National Center for Biotechnology Information, Polish Medical Bibliography, Scopus, SJR, Thomson Reuters, Thomson Scientific Products — Biological Abstracts, Ulrich's Periodicals Directory, Veterinary Bulletin, WorldCat and Zoological Record.

*Cover picture: Typical variant in which muscular branch to the levator palpebrae superioris (marked by white arrow) wraps around the medial border of the superior rectus muscle (sr) to reach its target muscle. Superior view to the left orbit; lps — levator palpebrae superioris muscle (cut from its origin and reflected); so — superior oblique muscle. For details see: Haładaj et al., Folia Morphol 2021; 80, 1: 63–69.*